INTER

International Network on Timber Engineering Research

INTER - International Network on Timber Engineering Research

2014 the International Network on Timber Engineering Research (INTER) was founded.

Scope
Presentation, discussion and documentation of research results in timber engineering and development of application rules for timber design codes or standards related to timber engineering.
Approach
Annual meetings in different countries/places hosted by meeting participants
Presentation and discussion of papers
Peer review of the abstracts before the meeting and of the papers during the meeting
Decision of the acceptance of the abstracts before the meeting by a well-defined review process
Decision of the acceptance of the papers for the proceedings during the meeting
Publication of the papers and the discussion in proceedings
Rules
All decisions including the appointment of the chairperson or the location of annual meetings are made by the participants attending a meeting.
Membership
Persons contributing to or being interested in research related to timber engineering.

INTER PROCEEDINGS MEETING FIFTY 2017

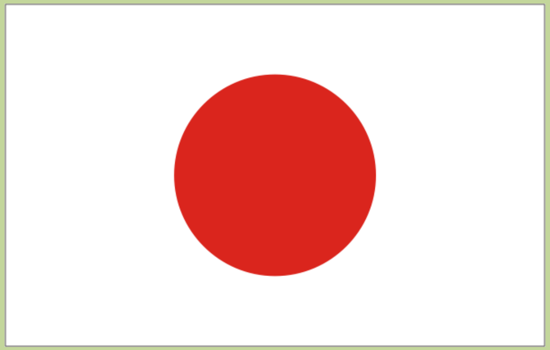

MEETING FIFTY

KYOTO, JAPAN

AUGUST 2017

INTER

International Network on Timber Engineering Research

Proceedings

Meeting 50

28 - 31 August 2017

Kyoto, Japan

Edited by Rainer Görlacher

Timber Scientific Publishing
KIT Holzbau und Baukonstruktionen
Karlsruhe, Germany
2017

Publisher:
Timber Scientific Publishing
KIT Holzbau und Baukonstruktionen
Reinhard-Baumeister-Platz 1
76131 Karlsruhe
Germany
2017

ISSN 2199-9740

Table of Contents

1 List of participants

AUSTRALIA	
K Crews	University of Technology Sydney
CANADA	
F Lam	University of British Columbia, Vancouver
A Salenikovich	Université Laval, Québec
CHINA	
Minjuan He	Tongji University
Zheng Li	Tongji University
CROATIA	
V Rajcic	University of Zagreb
SPAIN	
J M Cabrero	Universidad de Navarra
ESTONIA	
A Just	Tallinn University of Technology
J Liblik	Tallinn University of Technology
K N Mäger	Tallinn University of Technology
M Tiso	Tallinn University of Technology
FRANCE	
C Faye	FCBA - Bordeaux
GERMANY	
S Aicher	MPA University Stuttgart
H J Blaß	Karlsruhe Institute of Technology (KIT)
P Dietsch	Technical University of Munich
M Danzer	Technical University of Munich

M Frese	Karlsruhe Institute of Technology (KIT)
R Görlacher	Karlsruhe Institute of Technology (KIT)
S Loebus	Technical University of Munich
C Sandhaas	Karlsruhe Institute of Technology (KIT)
T Schmidt	Karlsruhe Institute of Technology (KIT)
P Stapel	Technical University of Munich
C Tapia Camu	MPA University Stuttgart
S Winter	Technical University of Munich
J-W van der Kuilen	Technical University of Munich/TU Delft

ITALY

A Ceccotti	University of Venice
R Scotta	University of Padova

JAPAN

K Aoki	The University of Tokyo
H Isoda	Kyoto University
Y Karube	University of Tokyo
K Kobayashi	Shizuoka University
H Kato	Kogakuin University
T Miyake	Nihon System Skkei Architects & Engineers
T Nagashima	Sumitomo Forestry CO.,LTD., Tsukuba
M Okabe	Tsukuba Building Research and Testing Laboratory
T Tsuchimoto	Building Research Institute, Tsukuba
Wonwoo Lee	KEYTEC CO., LTD., Tokyo
M Yasumura	Shizuoka University

KOREA

Chul-Ki Kim	Seoul National University

NEW ZEALAND

A Buchanan	PTL Structural Timber Consultants, Christchurch
Minghao Li	University of Canterbury
P Quenneville	University of Auckland
A Palermo	University of Canterbury

NORWAY

K Nore	Norwegian Institute of Wood Technology, Oslo

SWEDEN

D Brandon	RISE, Stockholm
H Danielsson	Lund University
E Serrano	Lund University

SWITZERLAND

T Ehrhart	ETH Zürich
R Jockwer	ETH Zürich

USA

M Gershfeld	California State Polytechnic University, Pomona
B Yeh	APA - The Engineered Wood Association, Tacoma

2 Minutes of the Meeting

by F Lam, Canada

CHAIRMAN'S INTRODUCTION

Prof. Hans Blass welcomed the delegates to the International Network on Timber Engineering Research (INTER) which constitutes the 50th meeting of the group including the series of former CIB-W18 meetings. INTER continues the tradition of yearly meetings to discuss research results related to timber structures with the aim of transferring them into practical applications. Chairman gave a review of the history of the group which was started by a group of scientists in March 1973 from eight European countries, Canada, Brazil and the USA establishing a working group during a meeting at Princes Risborough UK. Australia was also kept in special correspondence. Two other groups, IUFRO S5.02 and RILEM TT3 dealing with timber structures also existed. IUFRO S5.02 focused more on wood science and RILEM TT3 focused on test methods. There was a need for a group to facilitate idea exchange on timber engineering before these topics were introduced in commissions of standardization organizations such as ISO or CEN dealing with codes. The elaboration of a “CIB Code” was also started as a harmonized international design code for timber structures as a basis for the drafting of ISO standard for ISO/TC 165 – Timber Structures as well as Eurocode 5. The attendance of the yearly meetings is a clear indication of the high interest in the work of the group.

The chair thanked M. Yasumura and his team from Shizuoka University for hosting the meeting. The chair announced the sad news that our friend and colleague Hans Jørgen Larsen passed away on January 14, 2017 and asked for a minute of silence to remember our friend and colleague Hans Larsen.

There were 27 papers accepted for this meeting. The papers were selected based on a review process for the abstracts with 4 acceptance criteria (state of the art, originality, assumed content, and relation to standards or codes).

Papers brought directly to the meeting would not be accepted for presentation, discussions, or publication. Same rule applied to papers where none of the authors was present or papers which were not defended by one of the authors. The presentations were limited to 20 minutes each, allowing time for meaningful discussions after each presentation. The Chair asked the presenters to conclude the presentation with a general proposal or statements concerning impact of the research results on existing or future potential applications and development in codes and standards.

The topics covered in this meeting were: Stress grading (1), Stresses for solid timber (1), Timber joints and fasteners (4), Duration of load (1), Timber beams (1), Laminated members (7), Structural stability (6), Fire (5), Statistics and data analysis

(1). Numbers in parentheses are the number of papers presented in each topic based on initial allocation.

The participants could present notes towards the end of the technical session. R Görlacher brought a list of intended note presentations. Participants intending to present notes that were not on the list would need to notify R Görlacher accordingly.

An address list of the participants was circulated for verification of accuracy.

M. Yasumura welcomed the participants and made housekeeping announcements.

GENERAL TOPICS

None

STRESS GRADING

50 - 5 - 1 Assignment of Timber to Bending and Tension Strength Classes - Effects of Calculation Procedures - P Stapel, A Kovryga, J W G van de Kuilen

Presented by P Stapel

H Blass commented that the study showed application of k_v would lead to non-conservative results yet it was also applied k_v to the tension data. P Stapel responded that the problem was kept but when applying k_v to the tension data one would be consistent to allow for comparisons.

T Ehrhart asked about the propensity matching technique. P Stapel responded that there was a need to get two data sets to be very similar so that inferring from one set to the other was possible.

S Winter stated as a structural engineer he would be interested in real values. Would it be an option to assume EN384 tension values? P Stapel agreed that it was also possible.

STRESSES FOR SOLID TIMBER

50 - 6 - 1 Shear Strength Values for Soft- and Hardwoods - J W G van de Kuilen, W Gard, G Ravenshorst, V Antonelli, A Kovryga

Presented by J W G van de Kuilen

H Blass commented that the long overhang in the 5 point bending tests would influence the results. JWG van de Kuilen responded that he did not take this into consideration but this was more similar to the case of an application in a Dutch bridge. H Blass also commented that the FEM calculation showing beam curvature over the end support was not reasonable. JWG van de Kuilen agreed and would look into it.

F Lam commented UBC and USFPL also worked with the 5 point bending tests in the 1990's. Even though shear failures were observed, the influence of combined shear and compression perpendicular grain stresses would lead to the higher shear capacity. This was difficult to quantify for general application. As a result 5 point bending was not accepted as standard test method in timber. Instead centre point bending with I cross sec-tion at a short span to depth ratio 7:1 to 10:1 worked well. JWG van de Kuilen agreed.

P Quenneville asked how to explain the formula limiting shear strength at 5 MPa. JWG van de Kuilen stated that this was conservative with limited knowledge. Also D class shear strength values of tropical hardwood and European hardwood were very different.

K Crews commented in Australia the 5 point bending test method is no longer used. Centre point loading at span to depth ratio of 6:1 would give very good results compared to the 5 point test.

A Salenikovich stated that N. American hardwood shear strengths are also low because of lack of data.

BJ Yeh asked for comments on volume effects in shear. JWG van de Kuilen stated that the volume difference between two groups was so small that it would not be possible to make a comment.

H Blass stated that the notched beam equation used in the first slide was not appropriate. JWG van de Kuilen agreed.

T Ehrhart and JWG van de Kuilen discussed failure mechanism as influenced by growth ring orientation and plane.

TIMBER JOINTS AND FASTENERS

50 - 7 - 1 Steel-to-Timber Connections: Failure of Laterally Loaded Dowel-Type Fasteners - H J Blass, C Sandhaas, N Meyer

Presented by H Blass

S Winter asked about the appropriateness of calculations of screw using fu. H Blass replied there will be another paper discussing this point but the moment capacity from tests would have included strain hardening, so this would be appropriate.

P Quenneville asked about the assumption of no rope effect even though slide 4 seemed to show rope effect existed. H Blass agreed that slide 4 case did show rope effect; however, this was not yet considered because it would be difficult to tell practical engineers when to consider it and when not.

JWG van de Kuilen commented that although steel dowel shear failure was observed in single dowel connection one would not see this in a group of dowel in a row. H Blass agreed but this would depend on the connection layout.

P Quenneville asked about the observed failure of fasteners in the table. H Blass explained failures were a combined action of bending moment, shear and normal force.

F Lam received clarification of the concept of interaction of MNV.

A Salenikovich commented on their own work on screws and nails.

A Buchanan commented about seismic design on the issue of cyclic loading and capacity design principles. He asked if this could be used to look into the upper limit for capacity design as well as lower limits. H Blass stated yes.

R Jockwer received clarification on the effect of interaction between embedding stress and shear stress in wood on the connection. H Blass also commented that they did work in the past to investigate embedment influence on withdrawal capacity which was not significant.

50 - 7 - 2 The Embedment Strength as a System Property - M Yurrita, J M Cabrero

Presented by J M Cabrero

R Jockwer asked about the embedment strength as a system parameter. How could one use this information as the parameter for the capacity of joints as there could be other non-linear effects in the joint. JM Cabrero stated that they were trying to verify the embedment strength and check the results against design provisions.

H Blass stated that it was unreasonable to use yield strength. He also commented on how would one test hardness influence on embedment strength. It would be difficult to accept this as it was not a parameter that could physically explain the differences.

S Aicher agreed with H Blass's comment. He stated however that the results seemed to indicate hardness as a parameter provided the best fit; hence, there could be some indication that hardness might be important.

JWG van de Kuilen discussed some of the past test results of hardwood where achieving the target moisture content was difficult. The decision to ignore dowel diameter in estimating embedment strength was an engineering decision. JM Cabrero agreed and stated they might consider such issues in the future.

A Salenikovich received clarification about the smallest diameter of dowel considered was 8 mm. He questioned also what was measured, for example in the perpendicular to grain case was it the maximum load?

JWG van de Kuilen commented that the quality of hole surface could have strong influence on the results.

P Quenneville asked why some of the data was ignored. JM Cabrero stated they did not fit. JWG van de Kuilen said that some of the data might be based on ½ hole tests and some on full hole tests; therefore, some of the data would not fit.

50 - 7 - 3 Nailed joints: Investigation on Parameters for Johansen Model - C Sandhaas, R Görlacher

Presented by C Sandhaas

M Li asked about the diameter of nails as larger nails could split the wood. C Sandhaas responded that wood splitting was not recorded in the database.

P Quenneville asked about the issue related to quality of nail production. He said this would be seldom checked and asked how one would propose to check this. C Sandhaas said that this could be considered via careful choice of the maximum value and strict external quality control measurements.

A Salenikovich and C Sandhaas discussed about density control. C Sandhaas said that each nail test had an associated density measurement.

A Buchanan commented on engineered wood products such as LVL when density of the product might not reflect on the quality as the product would be densified during production. C Sandhaas responded in such cases one should conduct tests.

R Jockwer and C Sandhaas discussed in the last slide the COV of each test series that was used. There were test results with high COV. It would be interesting to see the real COV for the proper evaluation of the capacity. C Sandhaas said only if this reflects material property which was however not the case.

50 - 7 - 4 Cyclic Bending Fatigue Properties of Dowel Type Fasteners - K Kobayashi, M Yasumura

Presented by K Kobayashi

H Blass received clarification of the term “severe combination”.

A Ceccotti asked about the speed of the cyclic test. K Kobayashi responded 1 to 2 mm/s.

C Sandhaas received clarification that the clamping distance was 2d.

A Buchanan commented that the quality of the material was important. For example higher quality screws from Europe would be very different from lower quality products from other parts of the world. Kobayashi explained the influence of screw quality.

P Quenneville received confirmation that some of the screws were Japanese and some were European.

V Rajcic received clarification that both screw and joint tests were performed.

Z Li commented that boundary conditions might be different from the real case. H Blass pointed out again that joint tests were done.

M Gershfeld asked whether CLT was edge glued. K Kobayashi said that the CLT was not edge glued.

DURATION OF LOAD

50 - 9 - 1 Design Equations to Predict Losses in Post-Tensioned Timber Frames - G Granello, C Leyder, A Palermo, A Frangi, S Pampanin

Presented by A Palermo

P Dietsch commented about humidity demand over one year period as they had monitored many service class 1 buildings over the years. He stated the assumption for service class II is incorrect and should be checked against real data.

JW Van de Kuilen asked about pure creep and why there would be such a large variability in parameter “a” for the creep function. A Palermo said that they were based on test results. JW Van de Kuilen stated that the findings might be influenced by the time frame of the experiments. A Palermo agreed.

A Ceccotti asked about the situation of 90% loss. A Palermo said that it was an extreme case where almost all post tension was lost and it would be unlikely to happen.

JW Van de Kuilen discussed the consideration of starting date would be important as large moisture variation in the start dates would have a strong influence on the result. A Palermo explained that the plates were not stiff enough in the building. The influence might be reduced if the right size of plates were used. Also one could include a factor for the construction phase. A Palermo also stated that a 10% loss in 3 years would be expected.

K Crews stated that on-going monitoring and building maintenance would be important.

P Quenneville discussed whether the building was truly closed.

TIMBER BEAMS

50 - 10 - 1 Glued Thin-webbed Beams - Amendments to EC 5 for Safe ULS Design - S Aicher, C Stritzke

Presented by S Aicher

E Serrano commented about the slender web and the splitting of flange failure mode.

S Aicher agreed that this type of beam could result in many types of failure modes including splitting of flange. E Serrano asked how common this type of beam design would be needed. S Aicher said that the work was done in the framework of another testing project where they did the testing. He was not sure who would produce such product regularly. He commented that even though they would not be used commonly the design method should be correct. He also stated that this type of beams could have high bearing loads.

LAMINATED MEMBERS

50 - 12 - 1 In-Grade Evaluation of U.S. Glulam Beams, End Joints, and Tension Laminations - B J Yeh, J Chen, T Skaggs

Presented by BJ Yeh

A Buchanan asked do you have limitation on end-joint spacing in US. BJ Yeh responded that end-joints within a lamination must be at least 6 feet apart. End-joints distance between adjacent lamination must be greater than 6 inches. Proof loading of end-joints would allow the longitudinal requirements to be waived.

F Lam commented that there was a large difference between the DF and SYP species with the SYP having higher values. If DF were taken alone they would be slightly below the target level. Statistical analysis could probably show that there was no difference. BJ Yeh agreed and he said that the DF values were only slightly lower than target which could be attributed to the inclusion of off grade beams in the database. F Lam stated that although inclusion of the off grade data was conservative but this would be against in-grade testing philosophy.

JWG van de Kuilen questioned whether there would be any difference between vertical and horizontal finger joints. BJ Yeh said that in N. America there is no distinction between the types of finger joints unless wider width lamina was considered.

JWG van de Kuilen and BJ Yeh agreed that machine rated lamina would make a difference.

S Winter asked about proof loading experience in N. American glulam production. BJ Yeh said end joint proof loading is available in 1/3 of the plants and there is a standard for proof loading.

50 - 12 - 2 In-plane Loaded CLT Beams – Tests and Analysis of Element Lay-up - H Danielsson, E Serrano, M Jelec, V Rajcic

Presented by H Danielsson

BJ Yeh commented that in the C and E test series bending fracture occurred which would not be not a surprise. H. Danielsson said that this was what the results show. BJ Yeh asked about the difference in the strength between the vertical and horizontal layers assumed in the finite element analysis. H. Danielsson said that they did not consider the strengths in the finite element analysis and they only obtained the stress estimates.

P Dietsch asked whether there was an influence from the random location of the laminae within the beam. H Danielsson said that the coefficient of variation was very small. H Blass commented that the layup and the consequent homogenisation must have an influence.

S Aicher and H Danielsson discussed the strength values assumed for the beams. He asked whether these were board values or CLT values. H Danielsson said that they were values of the CLT beam and not a single board. S Aicher said that these values would still be high.

50 - 12 - 3 Experimental Investigation on the Mechanical Behaviour of Glued Laminated Beams Made of Oak - C Faye, G Legrand, D Reuling, J-D Lanvin

Presented by C Faye

H Blass commented that the compression strength values with moisture content of 10 to 12 % were high. If this product would also be used in service class 2, you would need to decrease the value by 1/3 to account for the lower compression strength in service class 2.

H Blass asked about the difference in MOE of laminae and finish glulam being different from 1:1. It was clarified that the MOE of the laminae was based on localized tension MOE.

P Stapel and C Faye further discussed the relationship between local and glulam MOE in that all data was used.

JWG van de Kuilen questioned about the scatter in the data as it would be too low to cover the usual grade. C Faye said that it might be low but all the data was used.

P Stapel said that the 5th percentile value for tension strength of laminae was too low. How was it possible to get such high bending strength? C Faye said that they used more data in the statistical analysis. P Stapel suggested one should use an adjusted value in the model to account for the low sample size.

T Ehrhart said that the height of the beams was not too large. If one wanted the information to apply to large beams then size effect would be an issue. C Faye agreed as they planned to work on large beams and as such there would be lots of finger joints in such beams.

50 - 12 - 4 Effective Flange Width of a CLT Slab in Timber Composite Beams - R Masoudnia, A Hashemi, P Quenneville

Presented by P Quenneville

A Buchanan questioned if you try to develop a long span floor system for say a 9 m x 9m grid you would be strengthening the case in one direction and weakening it for the other direction. P Quenneville disagreed and provided an explanation.

K Crews stated this type of system would be limited by what one could transport. Furthermore secondary effects such as vibration would be more important.

S Aicher asked what was assumed when calculating the shear resistance of the lowest cross layer. If they were edge bonded this would be a different issue. P Quenneville stated that the model assumed elastic behaviour only and did not consider failures.

P Dietsch stated that rolling shear modulus would be important and asked what value was used and what would be the influence of the number of screws in terms of composite action. P Quenneville said that the rolling strength properties of the material were assumed and the influence of number of screws would be dealt with in a future paper.

S Winter asked what would be the practical implication of this model. P Quenneville responded that the effective width can be up to 2.5 m.

S. Winter and P Quenneville discussed the support conditions and shear lag effect at the end of the beam. H Blass commented that the laminae were not edge glued so one would have a low shear modulus within the plane and the cantilever action would also have shear deformation. They also discussed putting high transverse stiffness at the beginning of the span.

A Buchanan queried the possibility of putting the panel in the opposite direction. H Blass and P Quenneville agreed that this would not work because one would not have composite action.

50 - 12 - 5 Improved Design Equations for the Resultant Tensile Forces in Glulam Beams with Holes - C Tapia Camú, S Aicher

Presented by C Tapia Camú

S Winter received clarification of the meaning of conservative results in this paper.

P Dietsch commented about the eccentricity creating shear and moments. He questioned about be the influence of moving the hole along the length of the beam towards the middle. Also the recommendation of corner radius seemed to require a large diameter drill which would be impractical.

F Lam asked about the case of interaction between tensile perpendicular to grain stress and shear stress. C Tapia said that this was not considered as the aim was to get a more accurate equation for estimating tensile perpendicular to grain stress.

H Danielsson asked if the inclusion of normal forces were considered as well. C Tapia denied.

R Jockwer asked about the influence of stressed volume on reduction of strength. C Tapia said that the equation allowed calculation of internal forces needed for reinforcement. Size effect on strength exists but was not under consideration. S Aicher added the work aimed to quantify the forces needed for reinforcement calculations. Material properties were separate issues.

50 - 12 - 6 Round Holes in Glulam Beams Arranged Eccentrically or in Groups - M Danzer, P Dietsch, S Winter

Presented by M Danzer

S Aicher received clarification that in Figure 17 effect of multiple holes in horizontal direction the minimum clear distance used was 1d.

50 - 12 - 7 Two-way Spanning CLT-Concrete-Composite-Slab - S Loebus, P Dietsch, S Winter

Presented by S Loebus

H Blass asked what would be the typical application. S Loebus responded 6 m x 6 m or 7 m x 7 m rooms such as classroom in schools as well as cases with posts and concentrated supports.

H Blass asked what would be the advantage over a pure CLT plate. S Loebus responded that this system would be much stiffer and the concrete would be available for acoustic control already. A Ceccotti added that in this system control of floor vibration would be advantageous also. H Blass further asked would the same advantage be available for a pure CLT system of equal height. S Loebus agreed that CLT is a two way system. S Winter said that in this study they used weak concrete on purpose. Better results would be achieved if higher quality concrete was used.

A Palermo asked about the effect of shrinkage of the concrete. S Loebus discussed about shrinkage effects and stated that the study had not yet been extended to long term studies.

A Buchanan commented that the shrinkage in the concrete on top would lead to higher deformation. S Loebus said that minimum reinforcement for shrinkage crack control was used. Also fire performance for two way spanning system should be better because of more levels of redundancy. A Buchanan agreed as tensile membrane action would be available.

M Gershfeld and S Loebus discussed the efficiency of Ly/Lx ratio. S Loebus said that the reinforcing bar needed to be introduced in the second layer and Ly/Lx ratio of one would be more efficient. M Gershfeld said that no need for drop beam would be a great advantage.

R Jockwer asked whether changes in load sharing were observed when screws began to fail versus the notched case. S Loebus said that the distribution of load did not seem to change. When screws failed in one area, concrete uplifting was observed in the region with screw pull out of the CLT. Support loads were only obtained from linear elastic FEM and not from tests.

M Li asked about installation of screws as double incline installation in some locations could lead to confusion in practice. H Blass commented that putting two full grids of screws in the two main axes would be a practical solution. S Loebus said that the slip modulus of the screws not applied in the direction of the principle axis would be an issue. H Blass disagreed. S Winter said that too many screws would be too expensive and notches would be more cost effective.

STRUCTURAL STABILITY

50 - 15 - 1 Shake Table Tests on Large-Scale Hybrid Steel Frame and Timber Shear Wall System with Slotted-Bolted Friction Dampers - Hanlin Dong, Zheng Li, Qi Luo, Minjuan He

Presented by Zheng Li

S Aicher asked how such system would re-center. Z Li said that they would need to untighten the bolts and rely on gravity to re-center the building. He said post tension tendon could be considered in a later study.

A Ceccotti received confirmation that Kobe JAM record with PGA of 0.8 g was considered and the amplification factor of 2 was found resulting in upper floor acceleration of 1.6 g.

A Palermo asked about the ductility for friction system and how would one design this. Z Li said that force based design was considered initially. A Palermo asked why it would be important to lock this device. Z Li said that it was needed to provide some robustness.

M Gershfeld asked if the test structure was the core of a building as there were few openings. Z Li said yes it was the core with a corridor between the two cores.

F Lam commented that the fundamental period of the structure was between 0.5 s to 1 sec and the various earthquake spectra were conditioned between these periods. He asked what the period of the higher mode for the building were as there were some high peaks in the conditioned spectra just below 0.5 sec. Z Li would check into this.

50 - 15 - 2 Dissipative Joints for CLT Shear Walls - T Schmidt, H Blass

Presented by T Schmidt

P Quenneville commented whether the geometry of the plate would stay “as-is” if rope effect was mobilized.

P Dietsch commented that the test set up was intended to avoid friction between two components.

M Li commented about gaps from the test set up. Gaps might be produced by the system after a few cycles resulting different hold down forces. H Blass agreed but said that this would lead to much higher forces on the hold-downs.

A Buchanan commented that the CLT system activating the damping was important. He asked how to do this if two walls came together at 90 degrees. H Blass responded that the same connection could be used in a corner.

A Palermo commented that location of plastic hinge would move during loading which could lead to better performance for fatigue. H Blass agreed that this was observed.

M Gershfeld asked whether changes in steel cross section could improve the situation. For example changes the width towards the middle may enhance the performance. H Blass responded that this was considered already and might not be needed.

F Lam commented that UBC work with a different damper system indicated that damping might not be mobilized when higher capacity dampers were used and suggested that dynamic analysis could be used to optimize the approach. H Blass agreed.

50 - 15 - 3 Required Seismic Performance of CLT Panel Buildings from Japanese Standard - T Miyake, M Yasumura, N Kawai, H Isoda, M Koshihara, T Tsuchimoto, Y Araki, T Nakagawa

Presented by T Miyake

A Buchanan asked why platform framing and not balloon framing was considered. T Miyake commented that construction with through walls would be allowed based on a different design method. 5 story buildings would also be possible under another method.

H Blass asked about LP1 and LP2. LP1 was expected to have cracks and LP2 was not expected to have cracks. How would one know this ahead of time? T Miyake said the CLT panels were first considered using structural models.

A Ceccotti asked if the CLT walls were compared with reinforced concrete walls what would be the thicknesses of the walls for this type of building. T Miyake said that the CLT walls would be 90 to 150 mm in thickness and reinforced concrete walls would be 150 to 200 mm in thickness.

R Jockwer commented that high performance connections with dowels and bolts were considered. Would the use of self tapping screw connections be possible? T Miyake responded that this was not within the scope of the study.

50 - 15 - 4 Shaking Table Tests for Verification of Seismic Design of CLT Panel Buildings - H Isoda, N Kawai, T Miyake, M Yasumura, M Koshihara, T Tsuchimoto, Y Araki, T Nakagawa

Presented by H Isoda

M Gershfeld asked about the acceleration at the upper storey level. H Isoda said ~ 1.2 g. M Gershfeld received clarification that the deformations were based on inter-story drift and the weak story was designed to be the first story as the walls were the same in all levels.

A Ceccotti commented about the CLT failure and suggested that the weak SUGI material with low MOE might be an issue. He also received clarification that 3 ply CLT was used. He commented that 3 ply CLT only has one transverse layer and in Italy at least 5 ply CLT for walls for this type of building would be used.

A Buchanan commented that even if the material was not strong it could be possible to design the building with no damage. He asked if the Japanese standards would be interested in no damage philosophy. H Isoda said that the residents are interested. Performance based design principles are available for high performance buildings at say 1.5 times minimum requirements stipulated in Building standard law. H Isoda also stated that the high performance system would carry financial incentives with mortgages.

A Palermo stated that large acceleration could lead to failure of non-structural components. He queried with partial damages how would one do the repair and retrofit. H Isoda said that damage control systems could be used via using a stiffer system or base isolation system.

JW van de Kuilen commented about the extreme seismic event was based on large event occurred in the past. It might be better to define such event via Gamma function.

M Li and H Isoda discussed the return period and the level of the Kobe earthquake.

50 - 15 - 5 Capacity Design of CLT Structures with Traditional or Innovative Seismic-Resistant Brackets - R Scotta; D Trutalli; L Marchi, L Pozza, A Ceccotti

Presented by R Scotta

H Blass commented about nail connection tests with one nail in that the scatter would be reduced had connections with more nails were considered. R Scotta agreed.

M Li asked about the sample size for the connection tests. R Scotta said that 3 replicates in some cases and the statistical method used had an adjustment procedure to account for sample size.

R Jockwer and A Palermo both commented about rope effects influence on values in ETA. A Palermo suggested to check more credible equations and see how this could influence the procedure. R Scotti responded that similar procedures would be used and would consider the capacity based on the required loading.

50 - 15 - 6 Post-Tensioned CLT Wall Systems with Multiple Rocking Segments - D Sanscartier Pilon, A Salenikovich, A Palermo, F Sarti

Presented by A Salenikovich

A Buchanan commented that looking at deflection seemed to indicate not much gap opening. Shear stress and crushing under the steel plate must be high. He received confirmation about the size of the window being 1.2 m in width. He commented that the details were important. A Palermo responded that cutting out the high mode would be the intent of post tension system. With large opening would imply large bending moments and more expensive connection designs.

M Li commented about the shear connection design. Local bearing would imply needing large plates. He asked what their thickness was. A Salenikovich responded 35 mm thick washer + C Channel.

R Scotta asked would buckling and compression effects at the end of the wall require additional bracing elements. A Salenikovich said that this could be done.

P Quenneville and A Salenikovich discussed the dampers and the connections between the CLT and dampers.

H Blass commented that rocking could lead to crushing at the compression end. This could lead to permanent deformation. A Salenikovich said that there was experimental work in US looking into improvement with reinforcement. A Buchanan stated that experience in NZ indicated that it was not a problem. F Lam commented that the NZ work would be based on LVL which would have higher compression strength compared to CLT. H Blass commented that after strong motion localized damage could occur which might need repair and therefore not damage-free. A Palermo agreed that compression of CLT could be a problem but would try to avoid this issue via design calculations. H Blass further commented that the compression strength would decrease by 10 to 15 % considering end grain to end grain compression.

FIRE

50 - 16 - 1 Design Parameters for Timber Members Protected by Clay Plaster at Elevated Temperatures - J Liblik, A Just

Presented by J Liblik

A Buchanan asked about the non standard product considered. For example can one buy the reed mat? J Liblik said this could be bought in Estonia and Germany. There is strong interest to use natural material in buildings.

H Blass asked how to guarantee that plaster would conform to the product. J Liblik said that the clay plaster was tested as standardized product.

J W Van de Kuilen discussed fitting of the data shown in Slide 18. J Liblik said that the fitting results were considered safe and conservative.

A Buchanan commented about the ISO fire in small scale versus full scale tests as there was no standardization.

H Blass commented that test standard to determine charring rate was missing. D Brandon responded that it was difficult to standardize this test procedure as the procedure aimed to simulate the charring rate and there would be difficulties with respect to control and measurement of heat flux etc.

50 - 16 - 2 Parametric Fire Design – Zero-Strength-Layers and Charring Rates - D Brandon, A Just, D Lange, M Tiso

Presented by D Brandon

A Buchanan commented that as the fire went out the temperature would decrease; however, the temperature within the panel would keep increasing. He wondered if the simulation work extended beyond the fire going out. He stated that this was a huge problem and there was a lot of work going on worldwide. He suggested to the authors to coordinate with others.

J W Van de Kuilen asked whether the modified charring rate included delamination of layers. D Brandon responded that falling off did not seem to occur when char reached the bond line in this study. Depending on the type of adhesive delaminating could occur at around 220°C. This would be a complicated problem

50 - 16 - 3 Zero Strength Layers for Timber Frame Assemblies in a Standard Fire - M Tiso, A Just, M Klippel, J Schmid, D Brandon

Presented by M Tiso

H Blass commented that comparison of test results with calculated results would need assumption or prediction of bending strength. It would not make sense to present the results with this level of accuracy. H Blass further asked about the in- or out- of plane buckling load. Which model was used to determine the compression capacity? M Tiso said a model developed by T Konig on constitutive properties was used.

A Buchanan discussed the approach used and one equation should be good enough considering the accuracy. M Tiso said that in the buckling situation there would be panel on side of wall. He further discussed about the type of product used and they planned to investigate other products.

50 - 16 - 4 Improved Fire Resistance of Connected Nail-Plate Trusses - G Glasø, K Nore, A Sagen

Presented by K Nore

H Blass asked if protection of the timber was needed. K Nore said it was not needed as the timber were screwed together and did not char in between.

A Buchanan received confirmation that fully threaded screws were used.

D Brandon commented about embedment failure versus steel failures at high temperature. He commented that it would be interesting to do some tests.

50 - 16 - 5 Protection by Fire Rated Claddings in the Component Additive Method - K N Mäger, A Just, A Frangi, D Brandon

Presented by K N Mäger

A Buchanan commented that this study tried to make something complicated simpler for designers. He asked if it would be possible to use this type of method for structural components. In NZ different manufacturers would have their own data and would not rely on same method. K N Mäger responded that different factors and parameters would be needed. He also responded that in Europe manufacturers might not be happy with the current conservative method; hence, this study was needed. M Gershfeld also commented on approaches in US.

STATISTICS AND DATA ANALYSIS

50 - 17 - 1 Reliability of Large Glulam Members - Part 2: Data for the Assessment of Partial Safety Factors for the Tensile Strength - M Frese, S Egner, H J Blaß

Presented by M Frese

F Lam commented that the scope of the paper is wider than the title suggested. The author should consider changing the title to reflect the paper content. M Frese responded that this paper was the second part of a paper from last year with similar title and would be appropriate to keep the title for consistency.

F Lam asked about the use of Normal distribution rather than extreme value distribution to represent the load in reliability study. M Frese responded that Normal distribution can be used to represent some loads in Eurocode approach.

P Dietsch asked about the assumption of 30 mm laminate thickness. There are many producers in Europe producing glulam with 40 mm thick laminates. Why 40 mm thick laminates were not considered. M Frese said that the database is based on 30 mm thick material and changing the laminate thickness might yield different results. H Blass responded that if 40 mm thick material was used fewer laminates would be used for a given beam depth. Results would have already considered laminate number and hence thickness effects.

There were discussions about the normal forces in truss lower chord might not be constant and what would be a length to be used for consideration. F Lam said that UBC had done work in this area and results were presented in CIB W18 paper which could be considered here.

S Aicher commented that the results indicated no significant depth effect whereas volume effect existed in bending of timber.

R Jockwer commented that consideration of minimum value rather than 5th percentile value would be confusing.

S Aicher received clarification of the mean and standard deviation of the laminate length.

NOTES

Four Notes were presented.

ANY OTHER BUSINESS

K Crews discussed topics related to publication in general. He suggested that key findings from this group could be published in Special issues of a Journal such as Journal of Construction and Materials. JW Van de Kuilen commented about not very positive past experience because invited authors might assume their work would be automatically published. H Blass also commented about the commercial nature of some publishing house. There were further discussions that in Wood Science and Technology ~ 700 submission per year in which ~1/3 would be published. There are issues regarding the practice of self-citation and referencing.

P Dietsch has been elected to succeed H Blass as the Chair of this group. H Blass would still chair the next meeting in 2018.

VENUE AND PROGRAMME FOR NEXT MEETING

Venue for 2018 INTER meeting will be Tallinn Estonia (August 13-16). Tentative venue for future years are: 2019 Seattle USA; 2020 Chile; 2021 Munich Germany; 2022 Biel Switzerland; 2023 Shanghai China; 2024 Padova Italy

CLOSE

H Blass thanked M Yasumura and K Kobayashi for organizing a perfect meeting especially the technical excursion and dinner. Good quality of papers is the foundation of this group. H Blass encouraged audience to speak out to continue the tradition of this group.

3 INTER Papers, Kyoto, Japan 2017

50 - 5 - 1	Assignment of Timber to Bending and Tension Strength Classes - Effects of Calculation Procedures - P Stapel, A Kovryga, J W G van de Kuilen
50 - 6 - 1	Shear Strength Values for Soft- and Hardwoods - J W G van de Kuilen, W Gard, G Ravenshorst, V Antonelli, A Kovryga
50 - 7 - 1	Steel-to-Timber Connections: Failure of Laterally Loaded Dowel-Type Fasteners - H J Blass, C Sandhaas, N Meyer
50 - 7 - 2	The Embedment Strength as a System Property - M Yurrita, J M Cabrero
50 - 7 - 3	Nailed joints: Investigation on Parameters for Johansen Model - C Sandhaas, R Görlacher
50 - 7 - 4	Cyclic Bending Fatigue Properties of Dowel Type Fasteners - K Kobayashi, M Yasumura
50 - 9 - 1	Design Equations to Predict Losses in Post-Tensioned Timber Frames - G Granello, C Leyder, A Palermo, A Frangi, S Pampanin
50 - 10 - 1	Glued Thin-webbed Beams - Amendments to EC 5 for Safe ULS Design - S Aicher, C Stritzke
50 - 12 - 1	In-Grade Evaluation of U.S. Glulam Beams, End Joints, and Tension Laminations - B Yeh, J Chen, T Skaggs
50 - 12 - 2	In-plane Loaded CLT Beams – Tests and Analysis of Element Lay-up - H Danielsson, E Serrano, M Jelec, V Rajcic
50 - 12 - 3	Experimental Investigation on the Mechanical Behaviour of Glued Laminated Beams Made of Oak - C Faye, G Legrand, D Reuling, J-D Lanvin
50 - 12 - 4	Effective Flange Width of a CLT Slab in Timber Composite Beams - R Masoudnia, A Hashemi, P Quenneville
50 - 12 - 5	Improved Design Equations for the Resultant Tensile Forces in Glulam Beams with Holes - C Tapia Camú, S Aicher
50 - 12 - 6	Round Holes in Glulam Beams Arranged Eccentrically or in Groups - M Danzer, P Dietsch, S Winter
50 - 12 - 7	Two-way Spanning CLT-Concrete-Composite-Slab - S Loebus, P Dietsch, S Winter

50 - 15 - 1 Shake Table Tests on Large-Scale Hybrid Steel Frame and Timber Shear Wall System with Slotted-Bolted Friction Dampers - Hanlin Dong, Zheng Li, Qi Luo, Minjuan He

50 - 15 - 2 Dissipative Joints for CLT Shear Walls - T Schmidt, H Blass

50 - 15 - 3 Required Seismic Performance of CLT Panel Buildings from Japanese Standard - T Miyake, M Yasumura, N Kawai, H Isoda, M Koshihara, T Tsuchimoto, Y Araki, T Nakagawa

50 - 15 - 4 Shaking Table Tests for Verification of Seismic Design of CLT Panel Buildings - H Isoda, N Kawai, T Miyake, M Yasumura, M Koshihara, T Tsuchimoto, Y Araki, T Nakagawa

50 - 15 - 5 Capacity Design of CLT Structures with Traditional or Innovative Seismic-Resistant Brackets - R Scotta; D Trutalli; L Marchi, L Pozza, A Ceccotti

50 - 15 - 6 Post-Tensioned CLT Wall Systems with Multiple Rocking Segments - D Sanscartier Pilon, A Salenikovich, A Palermo, F Sarti

50 - 16 - 1 Design Parameters for Timber Members Protected by Clay Plaster at Elevated Temperatures - J Liblik, A Just

50 - 16 - 2 Parametric Fire Design – Zero-Strength-Layers and Charring Rates - D Brandon, A Just, D Lange, M Tiso

50 - 16 - 3 Zero Strength Layers for Timber Frame Assemblies in a Standard Fire - M Tiso, A Just, M Klippel, J Schmid, D Brandon

50 - 16 - 4 Improved Fire Resistance of Connected Nail-Plate Trusses - G Glasø, K Nore, A Sagen

50 - 16 - 5 Protection by Fire Rated Claddings in the Component Additive Method - K N Mäger, A Just, A Frangi, D Brandon

50 - 17 - 1 Reliability of Large Glulam Members - Part 2: Data for the Assessment of Partial Safety Factors for the Tensile Strength - M Frese, S Egner, H J Blaß

Assignment of timber to bending and tension strength classes - Effects of calculation procedures

Peter Stapel, Andriy Kovryga
Technische Universität München, Holzforschung München

Jan Willem G. van de Kuilen
Technische Universität München, Holzforschung München
& TU Delft Faculty of Civil Engineering

Keywords: safety factors, material properties, machine grading, m_k-factor, k_v-factor

1 Introduction

EN 338 provides strength classes for structural timber. Timber can be assigned to C-classes if edgewise bending tests have been performed or since 2016 (EN 338:2016) T-classes if tension tests have been performed. Research with focus on the underlying relationships and on the basic concept of the strength class system was the primary interest of research before (Burger&Glos 1995, Burger&Glos 1997, Denzler& Glos 2007, Hanhijärvi et al. 2007, Rouger 2004, Steiger&Arnold 2009).

For an initial assignment to a strength class characteristic strength, modulus of elasticity parallel to the grain and density are required. Both strength classes give full strength profiles. Properties that are not actually tested are derived on the basis of known relationships. For bending strength as the major characteristic property, tension strength is derived on the safe side and vice versa, leading to different strength ratios and class profiles.

In order to assign timber to a strength class at all, the timber needs to be graded. In general, grading machines are used for the classification of timber to be used in engineered products. The derivation of machine settings is being influenced by a number of factors.

Factors that may differ depending on the intended strength class (a C- or T-class) and have an influence on the final classification of the tested samples are:

- timber quality of the representative sample

- prediction quality of the grading parameter
- the grading method
- different "safety" factors used (e.g. k_h, k_v)
- different coefficients of variation of the material properties
- statistical distribution of the material properties
- the cross-section

These factors are given or are the basis for calculations as part of different standards dealing with classifications and testing (EN 338, EN 384, EN 408, EN 14081-2, EN14358). Some factors have an influence when assigning timber to a strength class as well as during grading operations.

Whether T- or C-classes are graded, usually depends on the intended application. If timber is used for glulam the tensile properties are of interest. Therefore, obviously, T-Classes would be the preferred option.

The analysis presented here focuses on the comparison of strength properties for machine grading to T- and C-classes and includes guidelines on how to choose the favourable class system in order to optimize resource and product efficiency. The benefit of having two classes is questioned and an alternative is being proposed. Suggestions for the adjustment of related standards are included to avoid situations in which shortcomings of the current procedures are misused to maximise the grading results.

2 Data basis and calculation procedures

2.1 Available date and data pre-processing

2.1.1 Description of the data set

For the current analysis, 800 specimens of Norway spruce (P*icea abies*) tested in tension and 800 specimens tested in bending are selected and analysed. In order to compare the grading results for tension strength classes to bending strength classes, specimens resulting in a similar distribution of certain properties were selected from a large data set. The approach is explained in section 2.1.2.

The dimensions for tensile specimens range between 30-45 in the depth and 70-250mm in the width and for bending specimens between 35-65mm in the depth and 65 to 250mm in the width.

The tension test was applied in accordance with EN 408:2010 with the testing span of 9**h*, where h is the width of the specimens. The four point bending test was carried out according to EN 408:2010 with the distance between the supports of 18**h*, where h is the depth of the timber. For all the specimens the grade determining properties density, modulus of elasticity and strength were measured. Additionally, the visual grading parameter total knot area ratio (*tKAR*) was measured considering all knots with a diameter above 5mm. The machine grading parameter E_{dyn} using the eigenfrequency method was determined.

2.1.2 Matching the data

To analyse the mechanical property values of specimens graded to bending and tension strength classes, a data set with similar characteristics is required. Therefore, bias resulting from non-random selection should be, if possible, removed or at least reduced. Particularly, the values of covariates, or confounder variables, should be regarded. In our case both bending and tension test data should reveal the same values of the quality characteristics - dynamic MOE and visible grading parameter tKAR - as the key confounding variable. Furthermore, the values of strength and static MOE are not to be considered for matching.

To create tension and bending groups with matched characteristics (equally distributed covariates) and particularly eliminate the bias, the propensity score matching was used. The propensity score matching is dated back to Rosenbaum and Rubin (1983) and is frequently used in various fields like epidemiology, sociology, economics and political (Stuart 2010). It is used e.g. in observational or quasi-experimental studies in which the assignment of treatments to a research subjects is not random and, therefore, results in bias (Adelson 2013).

The propensity score matching is a statistical method to select units from a pool of data to produce a control group with respect to background covariates (Rosenbaum & Rubin 1985). The method aims to balance the distribution of covariates in the treated and control group (Stuart 2010). Therefore, the propensity score as distinct match variable, that summarizes all of the covariates into one scalar, is used. The propensity score is a conditional probability of being treated based on observed covariates (Rosenbaum & Rubin 1983). As the real propensity score is seldom known the estimate is used. The most common estimation for propensity score is the logistic regression (Stuart 2010). Therefore, logit models using the covariates are being created. Afterwards, based on the distance measure the specimens are assigned to the control group using matching algorithms, such as nearest-neighbour matching. Particularly, in easiest case, for each "treated" individual, individuals with the smallest calculated distance are selected (Stuart 2010). For more information on propensity score, see Stuart (2010), Adelson (2013), Rosenbaum and Rubin (1983), Rosenbaum and Rubin (1985), Stuart (2010).

For the present study, the initial dataset prior to matching included 1385 tension test specimens and 2159 bending test specimens. For the matching, one sample should define the desired covariate distribution (treatment) and the other should be matched to the desired distribution (control sample). As, after Rosenbaum & Rubin (1983) the control group should be large compared to the treatment group, the tension test sample was assumed as a "treated" group and the bending strength sample as "control group". For a more precise match, the group size for tension and bending strength was limited to 800 specimens. Particularly, 800 specimens were randomly sampled from the tension data set and afterwards the matching was applied to sample 800 bending specimens.

The covariates used to create the propensity score are the E_{dyn} and the *tKAR*. The strength or the static MOE are not involved in matching. Even though, the initial data accounted 3544 specimens, the timber cross section could not be handled as a separate confounding variable. The use of dimensions would require a considerably larger data pool for matching. To exclude possible size effect as good as possible, the data is limited to board dimensions.

The matching is performed in R using the MatchIt package. To match the specimens using the propensity score the nearest-neighbour algorithm is used.

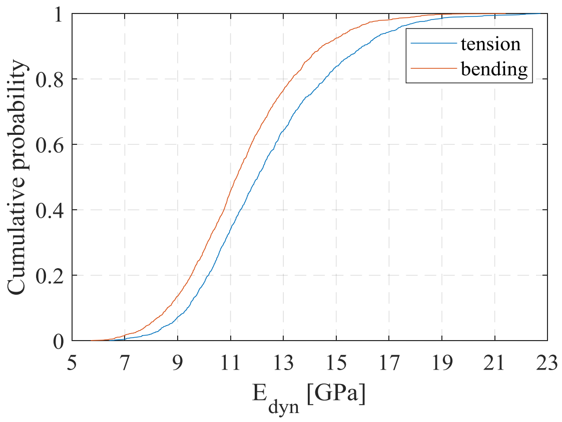

E_{dyn} before match

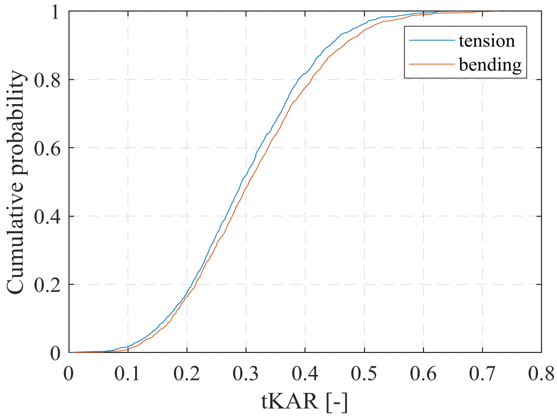

tKAR before match

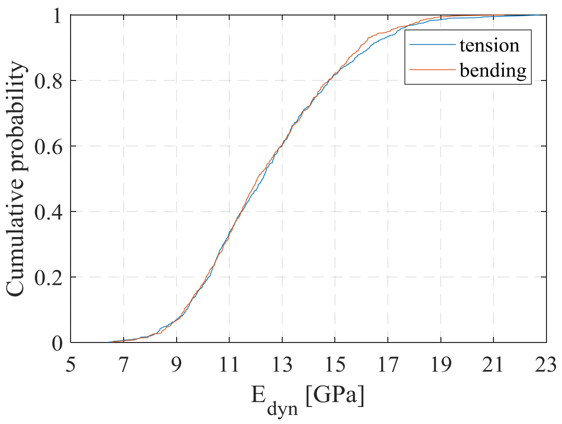

E_{dyn} after match

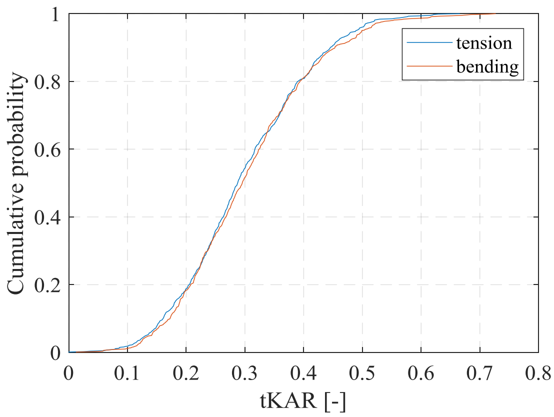

tKAR after match

Figure 2-1: CDF of dynamic modulus Elasticity and tKAR for specimens before matching and after matching for tension test and bending test specimens

Figure 2-1 shows the matching results. The empirical cdf after matching shows similar distribution of E_{dyn} and tKAR compared to the distribution before match. Some deviation between the distribution of covariates for bending and tension is observed for high values. This is possibly caused by an average higher quality of timber for tensile test specimens compared to the bending test specimens.

2.1.3 Properties of matched data

Table 1 gives an overview of the matched bending and tension specimens taken for the current analysis. The overall quality of spruce tested in tension corresponds to the average quality reported previously for Central Europe (Ranta-Maunus 2009, Ranta- Maunus et al. 2011). The values for the grading properties *tKAR* and E_{dyn} of matched bending and tension samples are almost identical. Prior to matching the bending test specimens revealed by 1GPa lower mean values for the E_{dyn} compared to the tension test specimens. After the matching, no difference is visible Table 1.

Table 1: Descriptive statistics of the materials used in the current study

Testing mode	N	Statistic	tKAR [-]	$E_{dyn,12}$ [GPa]	MC [%]	ρ_{12} [kg/m³]	$E_{0,12}$ [GPa]	f_{150} [MPa]
bending	800	*μ*	0.305	1.24	11.5	452	1.22	39.9
		s	0.112	0.258	1.2	56	0.313	12.9
		CoV	0.369	0.208	0.100	0.125	0.257	0.322
		$Q_{0.05}$	0.142	0.875	9.59	371	0.762	20.98
tension	800	*μ*	0.299	1.25	10.4	455	1.19	28.7
		s	0.109	0.273	1.3	60	0.286	12.5
		CoV	0.366	0.217	0.125	0.131	0.242	0.436
		$Q_{0.05}$	0.135	0.864	8.32	372	0.768	12.7

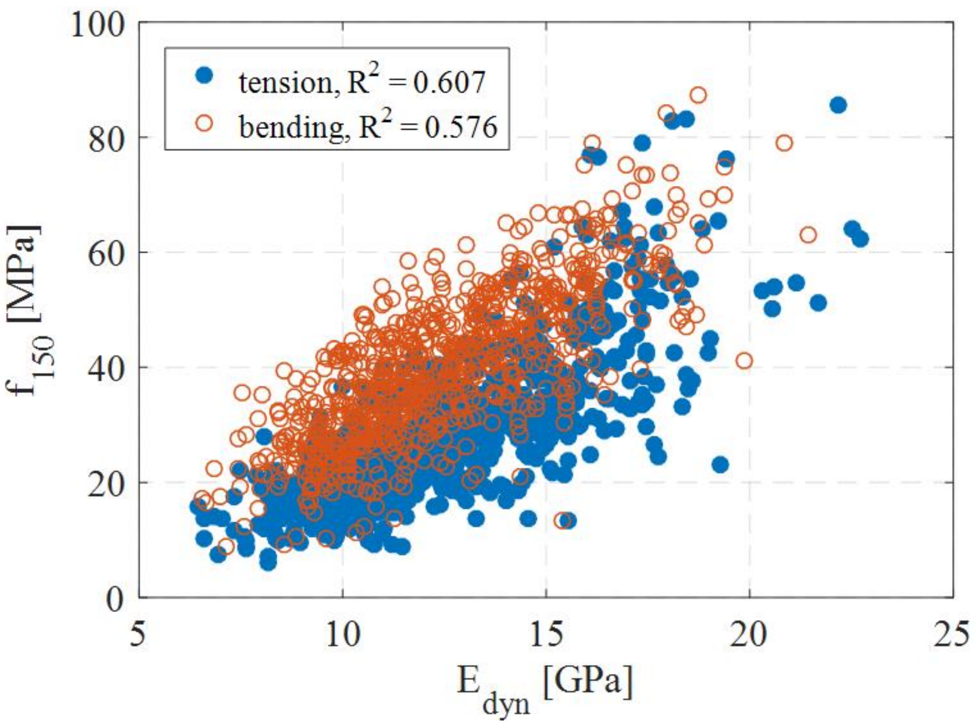

Figure 2-2: Scatter plot between dynamic Modulus of elasticity and strength from bending and tension test.

Figure 2-2 shows the relationship between E_{dyn} and bending or tension strength. For both tension and bending strength, the E_{dyn} shows high prediction strength. The R^2

values for tension strength prediction are usually higher than the ones for the bending strength prediction.

For spruce tested in tension, R^2 values for describing the relation between E_{dyn} and strength range from 0.58 to 0.61 (Bacher 2008, Ranta-Maunus 2009). For bending strength the R^2 values range between 0.43 and 0.60 (Hanhijärvi et al. 2005, Ranta-Maunus 2009). The R^2 value of 0.576 for bending strength is on the upper boundary of the reported values. This could be a result of the matching procedure, as the lower quality specimens are left out during the matching procedure allowing for a more pronounced relationship between E_{dyn} and stiffness.

2.2 Factors applied

2.2.1 Depth factor

The revision of EN 384:2010 brought the calculation of the depth factor in line with Eurocode 5. Hence, during the determination of characteristic values the test values are only being decreased. Having large cross-sections (above a 150mm depth) in a sample no longer increases the characteristic strength of a sample.

2.2.2 Factors EN 14358

EN 384 requires the calculation of characteristic strength values for machine graded timber according to EN 14081-2 which in turn references EN 14358. EN 14358 offers parametric and non-parametric approaches for the calculation of characteristic strength values. Based on comparative calculations (Stapel et al., 2015) and the fact that during the revision process of the standard industry insisted on keeping the non-parametric method in the standard, it is expected that the non-parametric methods result in the highest strength values. As this method is the one being most likely to be used by industry, this method was checked. Only relevant factors for this method are being discussed. In order to check a possible influence of the coefficient of variation, the option of taking the factor $k_{0.5,0.75}$ as 1 (allowed for type testing of machine controlled systems for non-parametric calculations) was not considered.

Based on a characteristic strength value for a tested sample the value m_k is calculated. m_k is the 5-percent lower tolerance limit with 75 % confidence. The number of specimens used for the determination and the effect the final result. The combination of factors used to reduce the strength values to m_k is focused on in connection with the grading results.

2.2.3 Variability factor

The variability factor k_v is a factor to allow for the lower variability of characteristic strength values between sub-samples for machine grades in comparison with visual grades. For machine grades based on bending tests (C-classes) with $f_{m,k}$ equal or less than 30 N/mm^2, k_v = 1.12. Although, the assumption of a lower variability was shown to be suitable only for higher strength classes (Stapel & van de Kuilen, 2012), it is still in use. Whether the factor itself is justified will not be discussed here. When strength classes are assigned k_v is only used for classes that are derived based on bending tests. Hence, it is crucial to consider this factor during the comparison.

2.3 V-Class – Comparing tension and bending strength

V-classes in this paper are derived on order to check, whether it is possible to derive settings for machine grades on a mixed dataset of bending and tension data. This would open up the opportunity to grade T- and C-classes in one pass. Additionally, the testing efforts, required to get approvals for grading machines, could be reduced if no separation for bending and tension data was needed. In order to use that approach, data in the same order of magnitude are required. The following three options are obvious:

- Calculate the settings on a bending strength level (calculate the expected bending strength from the tension strength values)
- Calculate the settings on a tension strength level (calculate the expected tension strength from the bending strength values)
- Calculate the settings on a virtual strength level (calculate an artificial value from both tension strength and bending strength values)

Here, we decided to use the last approach to make clear that the strength values we need to compare are only actual test values for the corresponding loading mode in 50% of the cases. Additionally, the average value of the test sample is expected to have an influence during the calculation procedure.

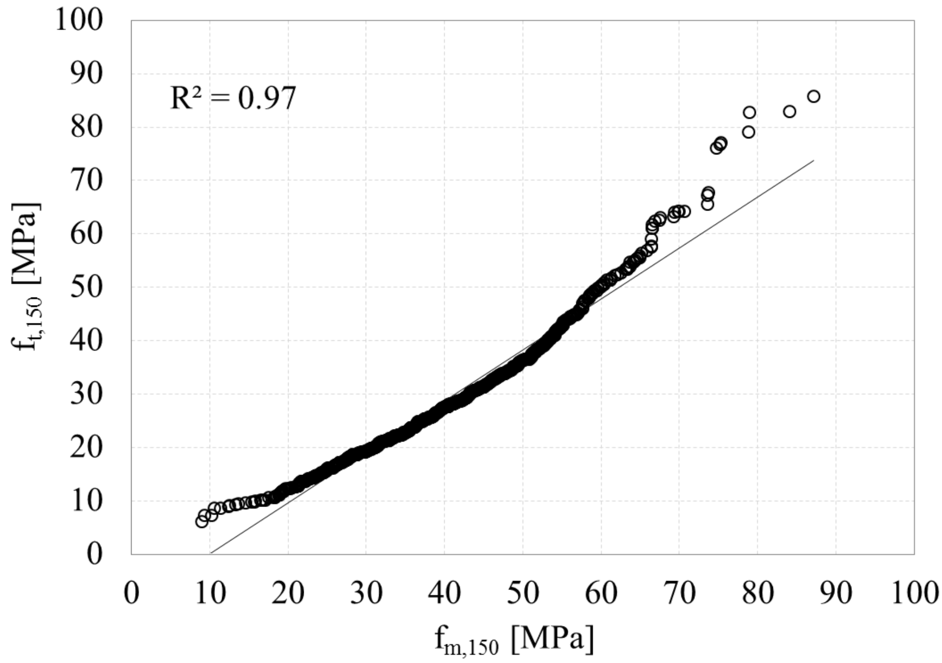

Figure 2-3: Bending and tension specimens ranked by strength and plotted against each other, n=2x800.

For the conversion on a single piece level, the following approach was used. The 800 bending and the 800 tension specimens were ranked by strength (after applying k_h)

compared (Figure 2-3). Based on this comparison each virtual strength value $f_{virt,150}$ can be calculated from the bending strength $f_{m,150}$ or the tension strength $f_{t,150}$ value. A linear approach was chosen in order to keep the ratio between indicating property used for machine grading and the strength values unchanged.

$$f_{virt,150} = -4.73 + 0.98 \cdot f_{m,150} \tag{1}$$

$$f_{virt,150} = 5.50 + 1.00 \cdot f_{t,150} \tag{2}$$

Figure 2-4 shows the resulting $f_{virt,150}$ for the different loading modes.

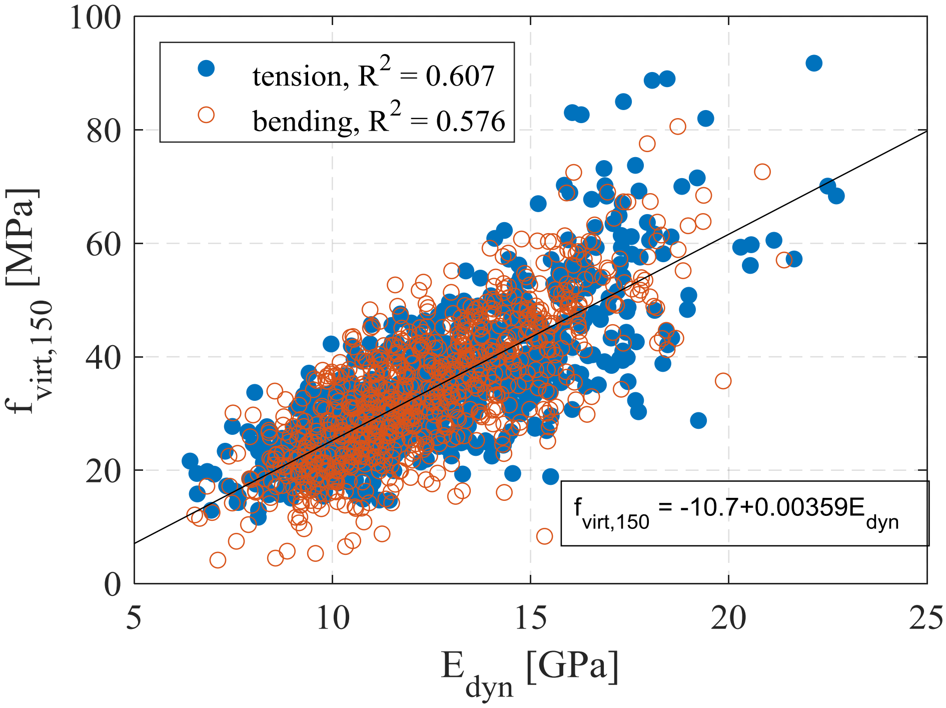

Figure 2-4: Values for $f_{virt,150}$ after the conversion according to equations 1 and 2.

In case that characteristic 5th percentile strength values are calculated directly from characteristic bending strength $f_{m,k}$ and characteristic tension strength $f_{t,k}$ values, the calculation is not based on the data available for this study. Here, the equations given in EN 384:2016 (EN 384:2016 Table 2 - Equations for calculating of other properties) are the basis for the conversion:

$$f_{virt,k,EN384} = -1.4 + 0.89 \cdot f_{m,k} \tag{3}$$

$$f_{virt,k,EN384} = 1.81 + 1.15 \cdot f_{t,k} \tag{4}$$

Figure 2-5 summarizes the used factors and visualizes the calculation of the virtual strength values intended to be used for the proposed V-classes.

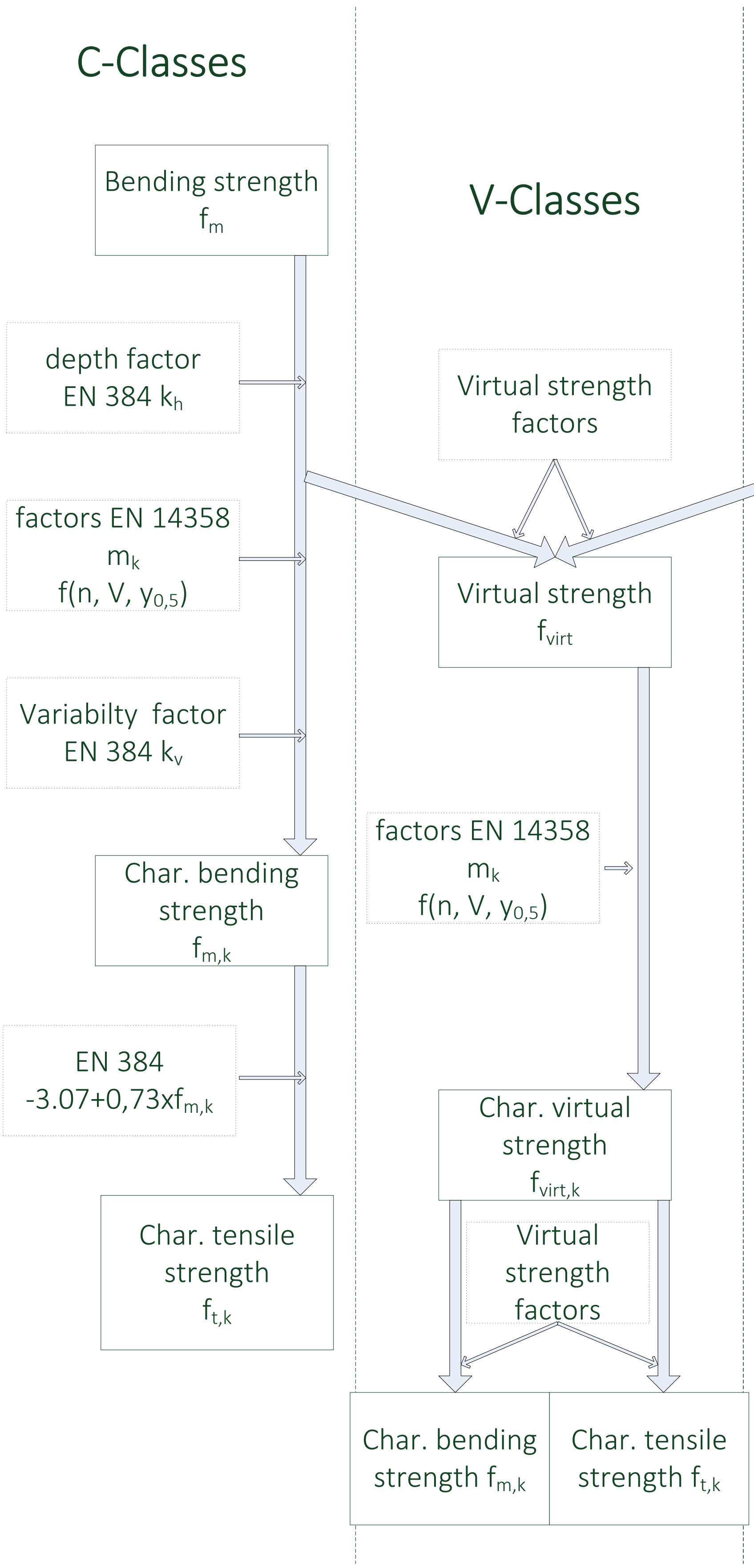

Figure 2-5: Calculation of the characteristic strength values for C-Classes, T-classes and the proposed V-classes.

2.4 Strength grading

In order to achieve required strength values, the material needs to be graded. In this study only the most frequently used machine grading principle (E_{dyn}) is applied. This matches the method featured for the fixed settings in prEN 14081-2:2016. The analysis is limited to a basic machine controlled systems. Aspects such as the currently required sub-samples analysis or the cost-matrix are not considered (EN 14081-2:2010). A detailed analysis is carried out for a single strength class, using settings ranging between 6400 MPa and 16100 MPa and intervals of 100 MPa. Grading results are used to judge the effect of the mentioned factors as well as for checking the applicability of V-classes.

3 Results and Discussion

3.1 Factors

3.1.1 Depth factor

While the number of pieces with cross-sections below 150mm is almost equal for bending and tension specimens, the distribution in this range leads to a mean k_h-factor of 1.049 for bending and 1.031 for tension. As the factor was applied before determining the factors used for calculating the virtual strength, an influence from k_h on the virtual values is not expected. Obviously, it has a direct influence on the strength values. Resulting bending strength values are lower compared to tension strength values. This means, that if the same cross-sections for bending and tension would have been available, the absolute difference between bending and tension strength values would increase by 2%.

3.1.2 Factors EN 14358

The EN 14358 safety factor is influenced by the number of pieces in the analysed sample and its coefficient of variation. The number of specimens is obviously decreasing with increasing settings. The difference in the number of bending and tension is neglect able. The number of specimens of the virtual strength results from the sum of both (Figure 3-1).

The fact that the tension strength is lower than the bending strength results in higher cov-values for the tension samples (Figure 3-2). The cov for the virtual strength values can be found between the ones for bending and tension. Accordingly, the calculated safety factor for tension samples reaches the highest values (Figure 3-3), while the factor for the virtual strength shows the lowest values due to doubled sample size in comparison to bending or tension samples. The absolute values for the safety factor increases with decreasing sample size, as the decreasing cov values cannot compensate for the decreasing number of pieces.

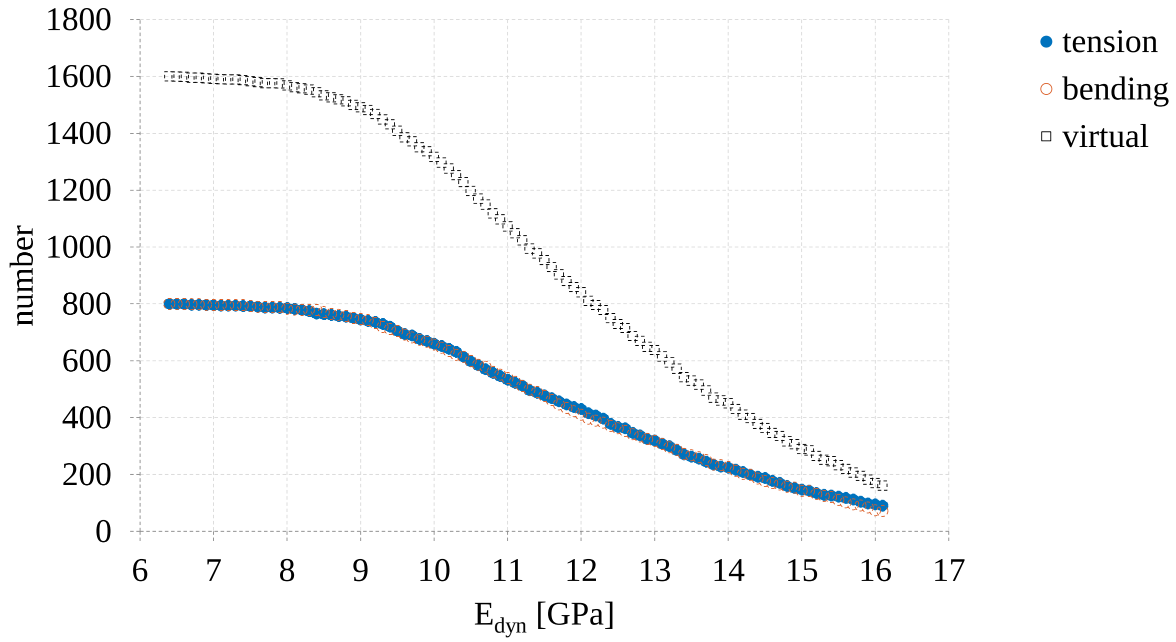

Figure 3-1: Number of pieces depending on the used setting for the bending,the tension and the combined virtual datasets.

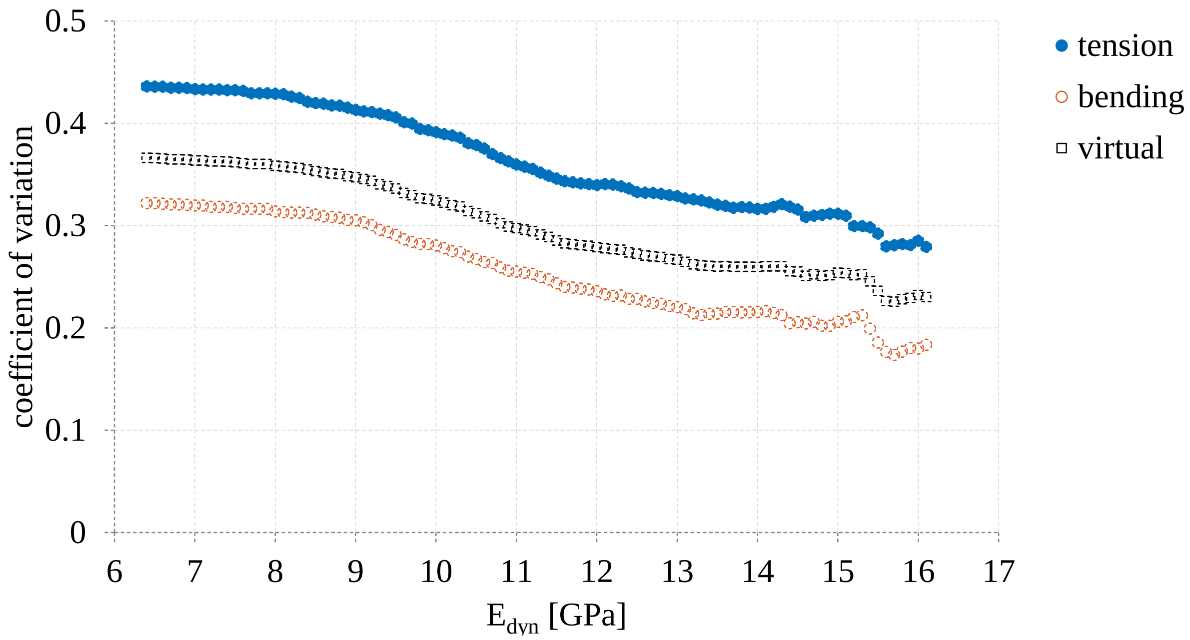

Figure 3-2: Coefficient of variation depending on the used setting for the bending,the tension and the combined virtual datasets.

Here, a separation into sub-samples, as required during a derivation of settings strictly according to the standard was not analysed. Factors in reality would exceed the values illustrated in Figure 3-3 as sample sizes would be significantly lower.

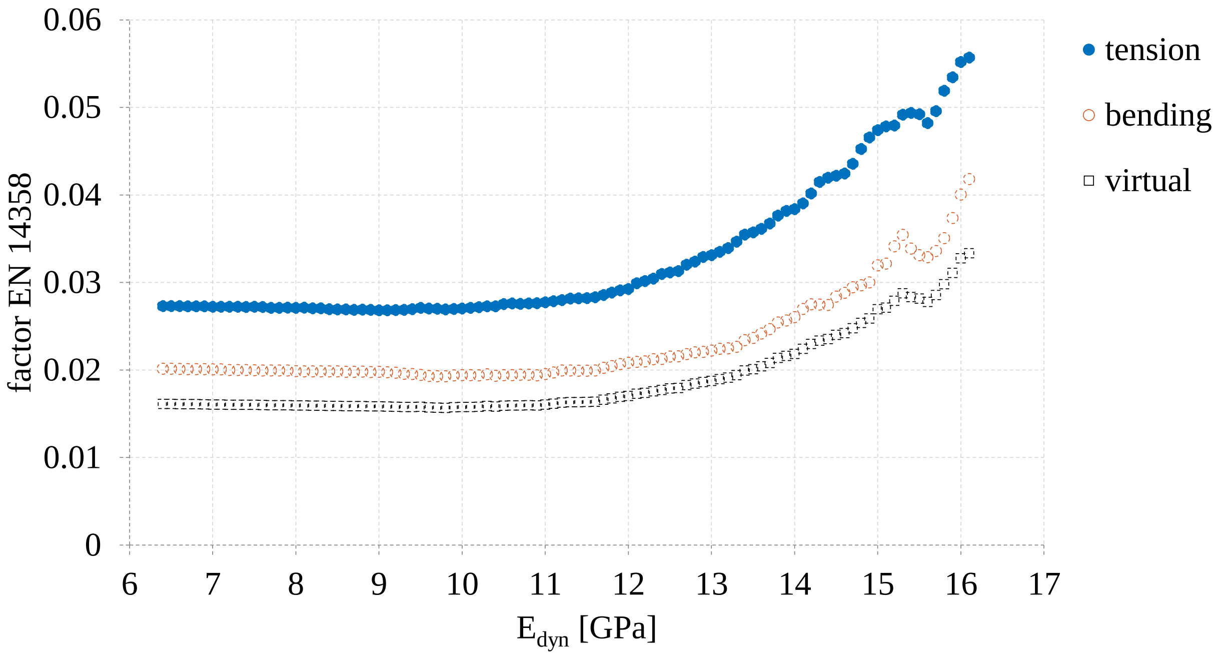

Figure 3-3: Factor used in EN 14358 depending on the used setting for the bending,the tension and the combined virtual datasets.

3.1.3 Variability factor

The variability factor k_v is only used on characteristic bending strength values. Hence, the tension strength values can only be affected in cases in which they are derived from the bending strength. The fact that the bending strength is increased by 12% up to characteristic bending strength values of 30 MPa is not further surprising. Figure 3-4 gives the strength values for increasing settings. Tension strength values derived from the bending strength using the equation from EN 384 are above the tension strength values that result from tension tests directly. Even for higher characteristic strength values (for which the k_v factor is not allowed), the strength values derived from the bending strength are close to the values resulting from tension tests.

When bending strength values are derived from tension strength values, using the formula given in EN 384, no such effect can be observed.

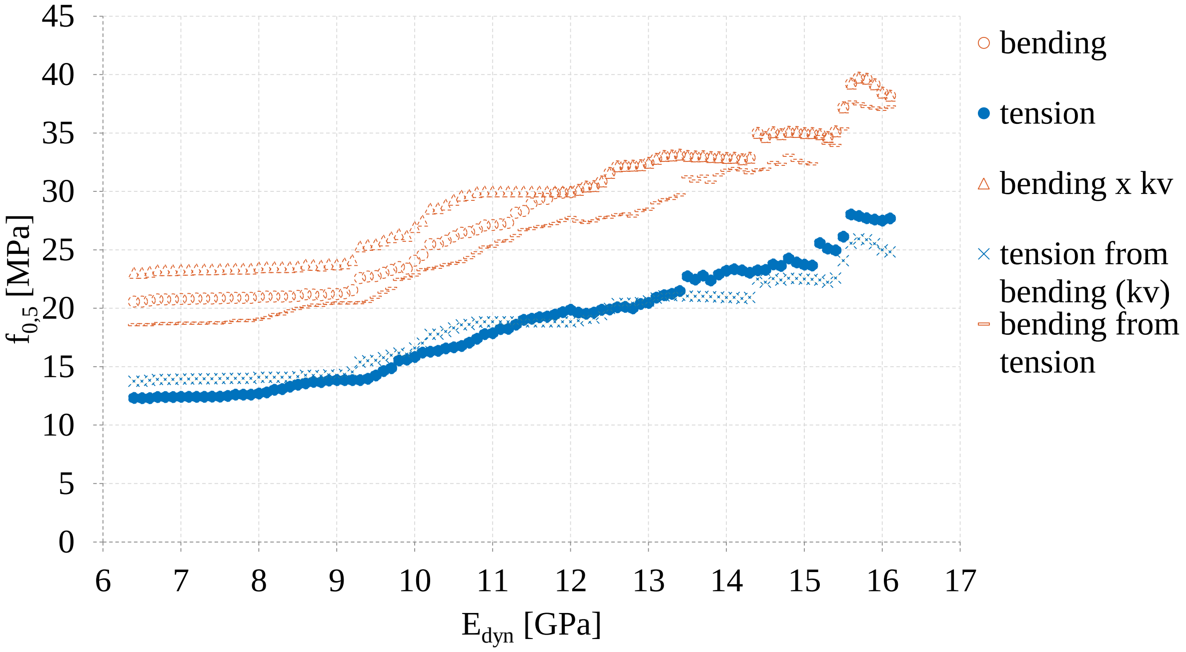

Figure 3-4: Characterisitic strength values for both loading modes and strength values calculated using conversion factors and partly the variability factor k_v.

While the differences between the tension strength values seem small, the effect on the yield is strong. Differences in yield of more than 10% can be found. The economic relevance is even bigger, as in the range of the shown strength values boards not getting assigned to the respective strength class are usually rejected.

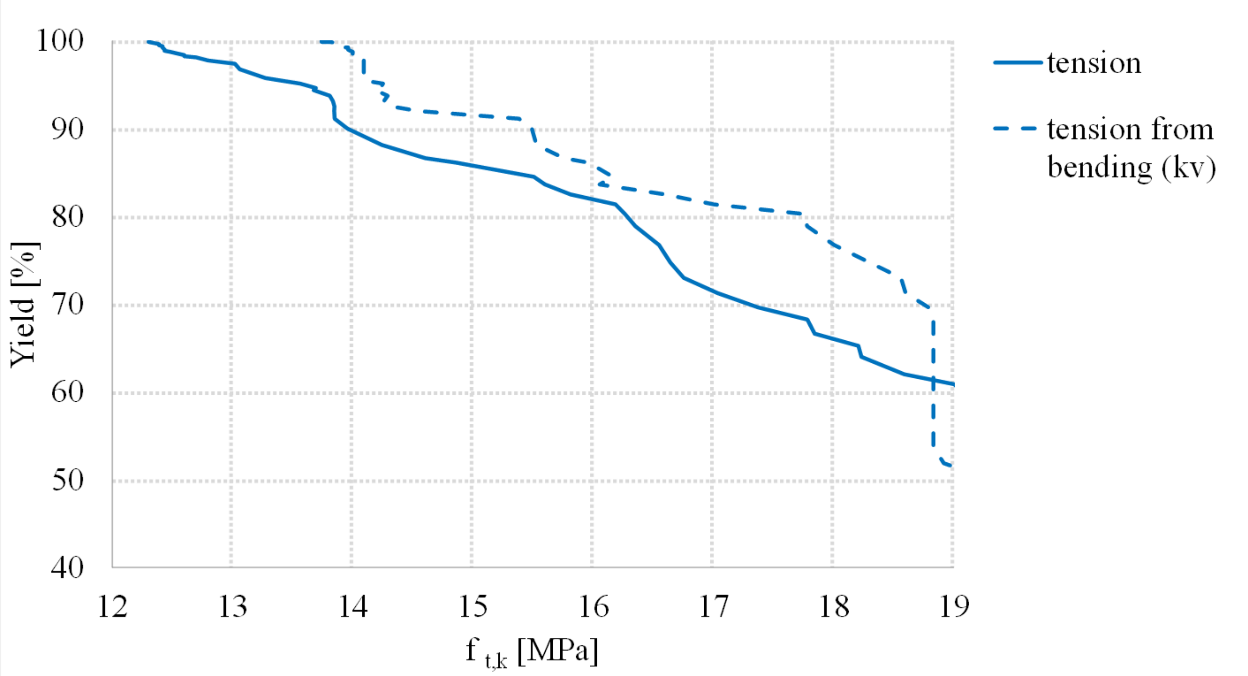

Figure 3-5: Yield by required characterisitic tension strength values for different derivation methods.

3.2 V-Class – Comparing tension and bending strength

The characteristic strength values for bending and tension strength derived from the combined virtual strength data is compared to the real strength values reached for tension and bending datasets separately (Figure 3-6). Of course, for certain E_{dyn} settings slight deviations are found. The respective value of the other loading mode usually deviates in the opposite direction (e.g. E_{dyn} ~ 13000). The derivation of characteristic tension and bending strength values based on the virtual strength data works well independent of the used setting.

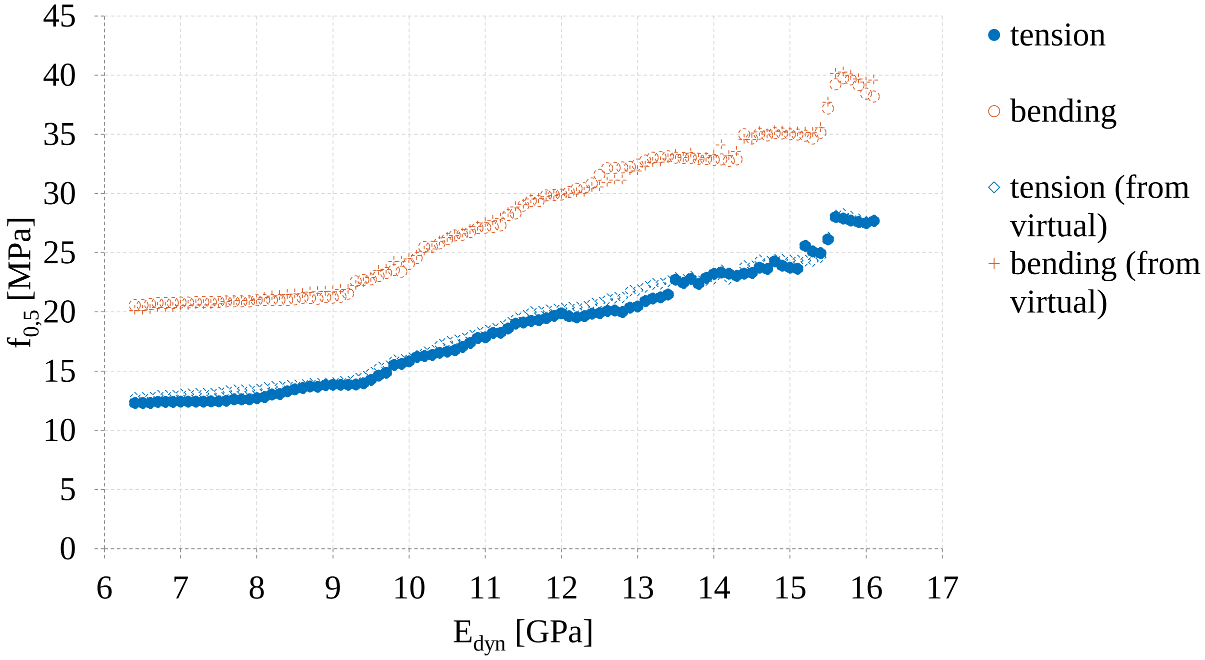

Figure 3-6: Comparison of the characteristic bending and tension strength values compared to the corresponding strength values derived from the virtual strength.

By using the virtual strength values in the proposed way, the disadvantage of lower characteristic strength values coming from the conversion factor to calculate tension from bending strength values or vice versa disappears (Figure 3-7). Strength values are above the derived characteristic strength values across the whole range of considered E_{dyn} settings. As the k_v factor was not accounted for during the calculation of the virtual strength, the corresponding part of the distribution shows higher characteristic strength values for the bending strength compared to the new calculated strength values.

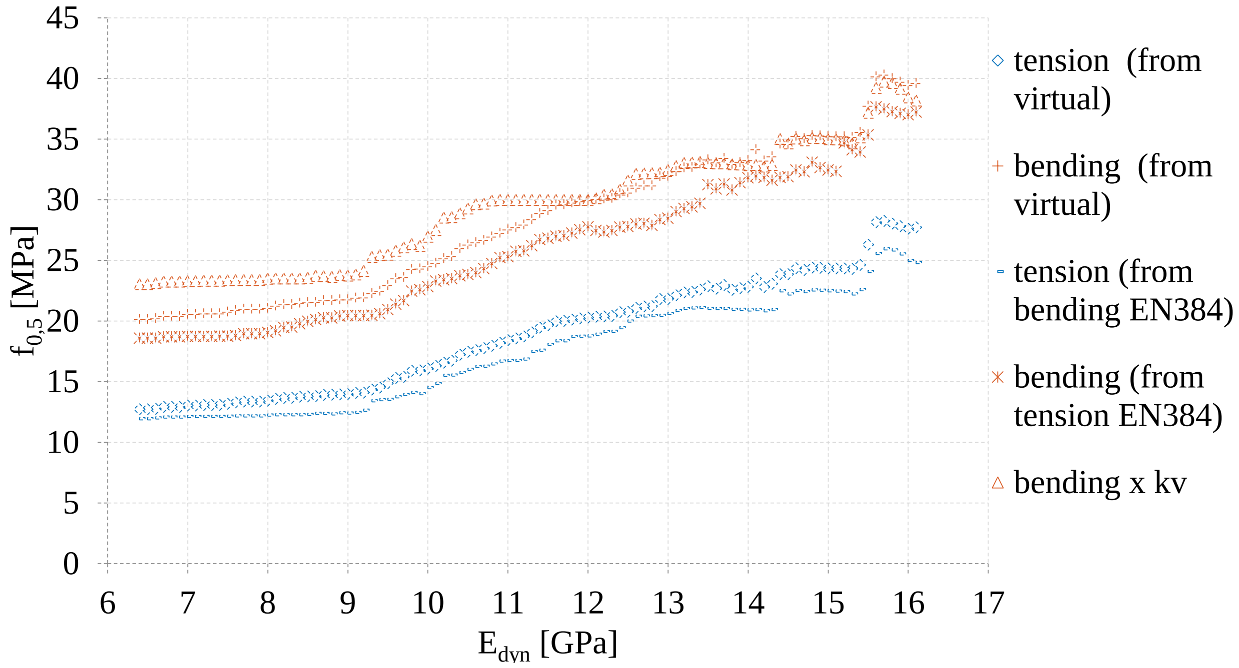

Figure 3-7: Derived characteristic bending and tension strength values using different approaches.

4 Conclusions

For grading machines using E_{dyn} it is easier to predict tensile strength than bending strength. However, the currently used procedure for the derivation of settings makes sure that this natural advantage gets lost. A combination of factors used during the derivation process of settings leads to the odd fact that grading to C-classes results in higher tension strength values (derived from the tested bending strength) compared to a direct assignment to T-classes. Instead of performing tension tests, calculating tension strength values from bending tests can lead to an increase in yield of more than 10%.
This artificial effect should be avoided by either adjusting the conversion factor from the characteristic bending to the characteristic tension strength or introducing k_v for tension strength classes (for classes with a characteristic tension strength of below 20 MPa).

Both options could easily be considered when data from bending and tension strength tests are analysed together for the derivation of settings. The analysis presented in this paper shows that deriving settings on a mix of bending and tension data leads to grading results that are similar compared to the ones derived on separate datasets. The main advantage is that no safety margin for the conversion from bending to tension and vice versa is needed. In addition, sampling efforts could be reduced and existing test data can be used more efficiently.

5 References

Adelson, J. L. (2013) Educational research with real-world data: Reducing selection bias with propensity scores. Practical Assessment, Research & Evaluation, 18(15), 2.

Bacher, M. (2008) Comparison of different machine strength grading principles, COST E53Conference Proceedings, Delft, Netherlands, pp. 183–193.

Burger, N.; Glos, P. (1995) Relationship of moduli of elasticity in tension and in bending of solid timber. Paper 28-5-2. In: Proceedings of CIB-W18 Meeting 28, April 1995, Copenhagen, Denmark.

Burger, N.; Glos, P. (1997) Strength relationships in structural timber subjected to bending and tension. Paper 30-6-1. In: Proceedings of CIB-W18 Meeting 30, August 1997, Vancouver, Canada.

Denzler, J.; Glos, P. (2007) Determination of shear strength values according to EN 408. Material and Structures, 40: 79-86.

EN 338:2016 Structural timber – Strength classes.

EN 384: 2010 Structural timber - Determination of characteristic values of mechanical properties and density.

EN 384: 2016 Structural timber - Determination of characteristic values of mechanical properties and density.

EN 408:2010+A1:2012 Timber structures – Structural timber and glued laminated timber – Determination of some physical and mechanical properties

EN 14080:2013 Timber structures. Glued laminated timber and glued solid timber. Requirements.

EN 14081-2:2010+A1:2012 Timber structures – Strength graded structural timber with rectangular cross section – Part 2: Machine grading; additional requirements for initial type testing

EN 14358:2016 Timber structures – Calculation and verification of characteristic values

EN 1995-1-1:2004 Eurocode 5: Design of timber structures – Part 1-1: General – Common rules and rules for buildings

Hanhijärvi, A.; Ranta-Maunus, A.; Sarkama, H.; Kohsaku, M.; Poussa, M.; Puttonen, .J (1997) Analysis of Tension and Bending strength of Graded Spruce Timber. Paper 40-6-3. In: Proceedings of CIB-W18 Meeting 40, August 2007, Bled, Slovenia.

Hanhijärvi, A.; Ranta-maunus, A.; Turk, G. (2005) Potential of strength grading of timber with combined measurement techniques. Combigrade-project-phase 1. VTT Publications 568. Espoo, Finland, 2005.
http://www.vtt.fi/inf/pdf/publications/2005/P568.pdf

prEN 14081-2:2016 Timber structures – Strength graded structural timber with rectangular cross section – Part 2: Machine grading; additional requirements for initial type testing

Ranta-Maunus, A. (2009) Strength of European timber: Part 1. Analysis of growth area based on existing test results, VTT, Espoo.

Ranta-Maunus, A.; Denzler, J. K.; Stapel, P. (2011) Strength of European timber: Part 2.Properties of spruce and pine tested in Gradewood project, Vol. 179 of VTT Working Papers:, VTT, Finnland.

Rosenbaum, P. R.; Rubin, D. B. (1983) The Central Role of the Propensity Score in Observational Studies for Causal Effects. In Biometrika 70 (1), pp. 41–55.

Rosenbaum, P. R.; Rubin, D. B. (1985) Constructing a Control Group Using Multivariate Matched Sampling Methods That Incorporate the Propensity Score. In The American Statistician 39 (1), pp. 33–38.

Rouger, F. (2004) A Review of Existing Standards Related to Calculation of Characteristic Values of Timber. Paper 37-6-4. In: Proceedings of CIB-W18 Meeting 37, August 2004, Edinburgh, Scotland.

Stapel, P.; Denzler, J.; van de Kuilen, J.-W. (2015) Analysis of determination methods for characteristic timber properties as related to growth area and grade yield. Wood Material Science &Engineering. DOI: 10.1080/17480272.2014.987317

Stapel, P.; van de Kuilen, J.-W. (2012) Effects of grading procedures on the scatter of characteristic values of European grown sawn timber. Material and Structures. DOI 10.1617/s11527-012-9999-7

Steiger, R.; Arnold, M. (2009) Strength grading of Norway spruce structural timber: Revisiting property relationships used in EN 338 classification system. Wood Science and Technology, 43(3-4):259-278.

Stuart, E. A. (2010) Matching methods for causal inference. A review and a look forward. In Statistical science : a review journal of the Institute of Mathematical Statistics 25 (1), pp. 1–21. DOI: 10.1214/09-STS313.

Discussion

The paper was presented by P Stapel

H Blass commented that the study showed application of k_v would lead to non-conservative results yet it was also applied k_v to the tension data. P Stapel responded that the problem was kept but when applying k_v to the tension data one would be consistent to allow for comparisons.

T Ehrhart asked about the propensity matching technique. P Stapel responded that there was a need to get two data sets to be very similar so that inferring from one set to the other was possible.

S Winter stated as a structural engineer he would be interested in real values. Would it be an option to assume EN384 tension values? P Stapel agreed that it was also possible.

Shear strength values for soft- and hardwoods

Jan Willem van de Kuilen, TU Munich Wood Technology, TU Delft Faculty of Civil Engineering and Geosciences

Wolfgang Gard, TU Delft, Faculty of Civil Engineering and Geosciences

Geert Ravenshorst, TU Delft, Faculty of Civil Engineering and Geosciences

Valeria Antonelli, TU Munich, Wood Technology

Andriy Kovryga, TU Munich, Wood Technology

Keywords:

Shear strength values, softwood, medium dense and tropical hardwoods, shear strength testing, strength classes.

1 Introduction

Shear strength values as given in the European strength classes are primarily based on tests on pure shear samples in accordance with test standard EN 408. The values obtained from such tests are included in the strength class table of EN 338. However, shear testing has traditionally been focused on softwoods, without taking into account that many hardwoods with a large range of densities are used in structural applications as well.

The shear strength values for softwoods in EN 338 are primarily based on shear tests according to EN 408, based on research by Denzler and Glos [2007]. With regard to tropical hardwoods, it seems that hardly any test data is available derived from shear tests in accordance with EN 408. Due to lack of data, the characteristic value of the shear strength was topped-off by the CEN standardization committee, not only for softwood, but over the full range of strength classes for hardwoods as well. In the current version of EN 338 the characteristic values of the shear strength are based on the following relationships with the bending strength, as given in EN 384.

For softwoods: f_(v,k)= min(1.6+0.1*$f_{m,k}$; 4.0) (1)

For hardwoods: f_(v,k)= min (3.0+0.03*$f_{m,k}$; 5.0) (2)

In the 2010 version of EN 338 fixed values were given with a maximum of 4.0 N/mm2 for softwoods and 5.0 N/mm2 for hardwoods. In the 2003 version of EN 338 the following relationship was given:

$$f_{v,k} = 0.2\, f_{m,k}^{0.8} \tag{3}$$

leading to an increase in shear strength for higher strength classes. On the basis of this equation, the shear strength ratio between D70 and C24 is about 2.35. This ratio is about equal to the ratio of the characteristic densities for these strength classes, namely 2.4, characteristic densities of 850 kg/m^3 and 350 kg/m^3 respectively (EN 338:2016). However, the characteristic shear strength value for C24 is given as 4.0 N/mm^2, whereas the characteristic shear strength value of dense hardwoods topped off at 5.0 N/mm^2. This is only a slight difference and clearly underestimates the shear capacity of dense hardwoods that have their typical applications in bridges and a variety of hydraulic structures (Van de Kuilen et al, 2014). On the basis of the study performed by Van de Kuilen and Leijten (2002), specific bridge decks made with dense hardwoods may be designed with shear strength values of 10 to 13 MPa, depending on the configuration and species.

In this paper, the increase in shear strength of wood in relation to the density will be shown, starting with softwood (spruce), passing through medium dense hardwoods like beech and oak, to dense tropical hardwoods such as azobé and massaranduba. Furthermore, this increase in shear strength will be shown applying two different test methods for determining the shear strength. The first determination method is the standardized method as given in EN 408. As this test set-up is particularly applicable to low strength species a study has been performed as to which kind of modifications are needed for more dense hardwoods. The study included:

- the influence of the taper of the steel plates that are glued onto the specimens,
- the type of glue/epoxy suitable for testing,
- the specimen shape in relation to the interface between the glue/epoxy and the wood.

In addition, five-point bending tests have been performed on specimens having an I-profile [van de Kuilen and Leijten, 2002]. These tests were performed to have a more practice-oriented result, for instance for beams spanning over more supports. Species spruce, oak, bilinga, azobé and massaranduba were tested in accordance with EN 408, whereas for the five-point bending tests, spruce, karri (South-Africa), azobè, massaranduba, angelim vermelho, piquia and uchi torrado were selected.

2 Materials and methods

2.1 Materials

For the determination of the shear strength according to EN 408 (method A) the following wood species were tested:

Table 1: Wood species and number of samples tested according to method A.

Wood species	origin	N	Test institute
spruce A	Germany	11	TU Delft
spruce B	Germany	26	TU Munich
Azobé	Cameroon	45	TU Delft
massaranduba	Brazil	44	TU Delft
Bilinga	Cameroon	26	TU Delft
oak	Germany	24	TU Delft
ash	Germany	73	TU Munich
beech	Germany	85	TU Munich

For the determination of the shear strength according to a 5-point set-up (method B) the wood species given in Table 2 were tested.

Table 2: Wood species and number of samples tested according to method A.

Wood species	origin	N	Test instituite
Karri	South-Africa	7	TU Delft
massaranduba	Brazil	25	TU Delft
Uchi torrado	Brazil	22	TU Delft
Angelim vermelho	Brazil	23	TU Delft
piquia	Brazil	22	TU Delft
azobé	Cameroon	18	TU Delft

Spruce	Sweden	20	TU Delft

2.2 Methods

Determination of the shear strength according to EN 408 (method A)

The test set-up according to EN 408 is used for the experiments of method A. The intention is to determine the “pure” shear strength with as little interaction with other stresses as possible. Tapered glued steel plates of 10 mm thickness are glued on both sides. See figure 1. The test piece is positioned at an angle of 14 degrees with the loading direction in the test set-up. See figure 2.

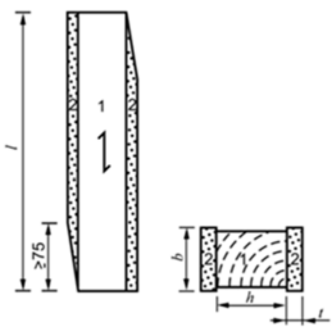

Figure 1: Timber test piece with glued on steel plates according to EN 408.

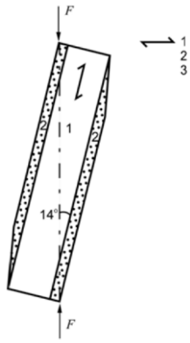

Figure 2: Loading arrangement of the test piece according to EN 408.

The shear strength f_v of a test piece is calculated according to equation (4).

$$f_v = \frac{F_{max} \cos 14°}{l\,b} \tag{4}$$

Where F_{max} is the maximum-recorded force in N, l is length of the specimen parallel to the grain and b is the thickness of the specimen.

This set-up has been used to determine the shear strength of spruce as reported in [Denzler and Glos, 2007].EN 408 gives as a provision that the test result is only valid when the failure area in the timber test piece/steel plate interface is less than 20% of the total bonding area. The intention is that the failure will occur in the middle of the specimen. To prevent failure at the interface peak stresses have to be avoided. In Denzler and Glos [2007] 260 specimens were tested, and for 7.5% of these specimens a failure area larger than 20% of the total bonding area was found. When the failure is in the interface the shear strength of the timber is higher and cannot be determined. The 20%-requirement therefore is a requirement to determine the correct timber shear strength, and to prevent low values. However, when species with a higher density are tested there is a risk of a higher amount of specimen with a failure area larger than 20% at the bonding area. This will be investigated in the next section.

Determination of the shear strength accord to a 5 point bending set-up (method B)

To determine the shear strength closer to the actual loading situation in practice the species according to table 2 were tested according to the set-up in figure 3. The specimen were shape to I beams according to figure 4 from full cross section of 60 mm x 110 mm. The shear force at both sides of the middle supports is $V = \frac{11}{32}F$.

The shear strength then becomes:

$$f_v = \frac{11}{32}\frac{FS}{bI} \tag{5}$$

where *F* is the total force, *S* the static moment of the sheared of part, *b* is the thickness of the web of the I-beam and *I* is the 2nd moment of inertia of the entire *I*-section.

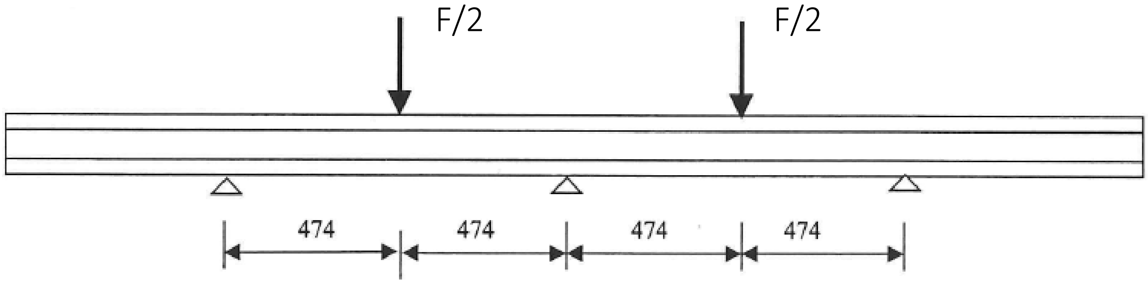

Figure 3: Loading arrangement according to the 5 point bending test

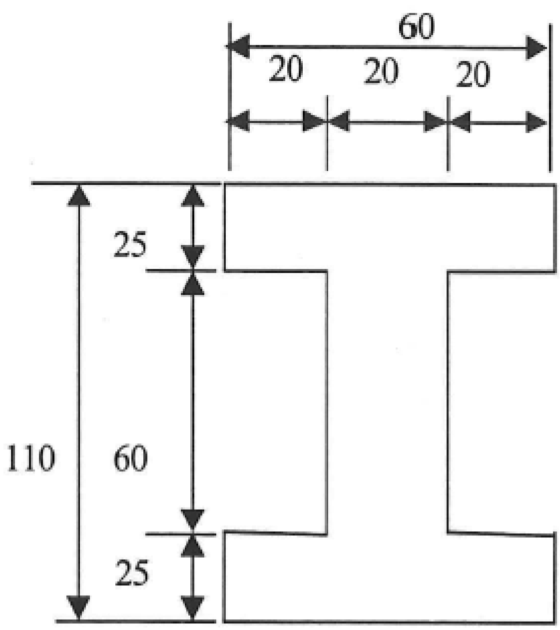

Figure 4: Cross section of the test pieces in the 5 point bending test

3 Test experiences

The method for shear testing as given in EN 408 has been validated mainly for softwoods. EN 408 advices a 2-part epoxy as suitable for gluing the wood to the steel plates. For the steel plates tapered plates of 10 mm thickness are advised but it is recognized that for hardwoods thicker plates might be necessary. This however leads to changes in the specimen dimensions when the loading angle at 14 degrees of the grain direction is to be maintained. Consequently, tested volumes are no longer the same and volume effects may influence the comparisons made between wood species.

A pre-test with a normal epoxy adhesive, (Griffon combi) and wood species massaranduba (with a mean density of 1050 kg/m3 was performed according to the test set-up of EN 408 (figures 1 and 2). This glue requires a thin glue line. However, the results were not satisfactory. The failure occurred 100% at the interface timber-steelplate at one side. The steel plates popped of spontaneously at a low load. The retrieved values were even lower than the values for softwood, indicating that the stiffer hardwood and the absence of the taper introduced peak stresses causing the failure.

To investigate the influence of the difference in stiffness and the influence on the taper a numerical study was performed [Ravenshorst et al, 2016], with the following conclusions for softwood:

- The application of the taper gives an almost evenly distributed shear stress in the glue line with the steel plate over the length of the steel plate, although at the taper the shear stress increases.
- Tension stresses perpendicular to the grain do almost not occur, both for the tapered and the non-tapered configuration
- The taper gives a more evenly distributed shear stress in the middle of the timber.

For hardwoods, the following conclusions could be drawn:

- Peak shear stresses do occur for both tapered and non-tapered steel plates at the interface.
- peak tension stresses perpendicular to the grain may occur for non-tapered steel plates.
- For the shear stress in the middle of the timber there is not much difference between the two configurations.

It can be concluded that the main function of the taper is to limit the shear stresses at the interface steel-timber, but that even then some peak stresses do occur. This is in line with the experiments from Denzler and Glos [2007] where most of the specimen failed in the timber, but a small portion still failed in the interface.

The magnitude of the peak stresses may also be dependent on the stiffness of the adhesive, which was not included in the analysis. However, the results indicate that special attention has to be taken for the glue line, to achieve the desired shear failure mechanism.

In tests with beech and ash, the steel plates deformed plastically to an extent that they influenced the test. It was decided to increase the thickness of the steel plates to 20 mm and use non-tapered steel plates. To maintain the angle of 14 degrees with the loading, the width of the specimens was reduced to 35 mm. The adhesive used was an epoxy Scotch-Weld 9323 B/A from 3M, applied in accordance with the manufacturers specifications. For the 26 spruce specimen tested in TU Munich the standard test set-up with 10 mm tapered steel plates were used (Hunger and Van de Kuilen,

For the tests performed at TU Delft a 2-3 mm thick epoxy adhesive Sikadur 30 from Sika with 10 mm thick steel plates was used. It was expected that with this glue line thickness the peak stresses could be reduced. Half of the specimens were tested with a taper and half of the specimens were tested without a taper, in order to investigate the effect of the taper. The steel plates of 10 mm thickness had a steel quality S235. For the Sikadur 30, no pressure has to be applied during the hardening. Sikadur 30 was also used for the 11 spruce specimens tested at TU Delft.

The experience with massaranduba and the first tests with azobé was that the failure would occur in the interface steel-timber, very close to this interface or partly in the interface. After this observation, the remaining azobé specimens were adjusted in thickness to 20 mm, to be able to create a larger surface for the adhesive-timber connection. This is shown in figure 5. For most of the specimens according to the right, leftovers from the first series were used, that had previously failed near the interface. As a consequence, the width of the specimens had to be reduced from 55

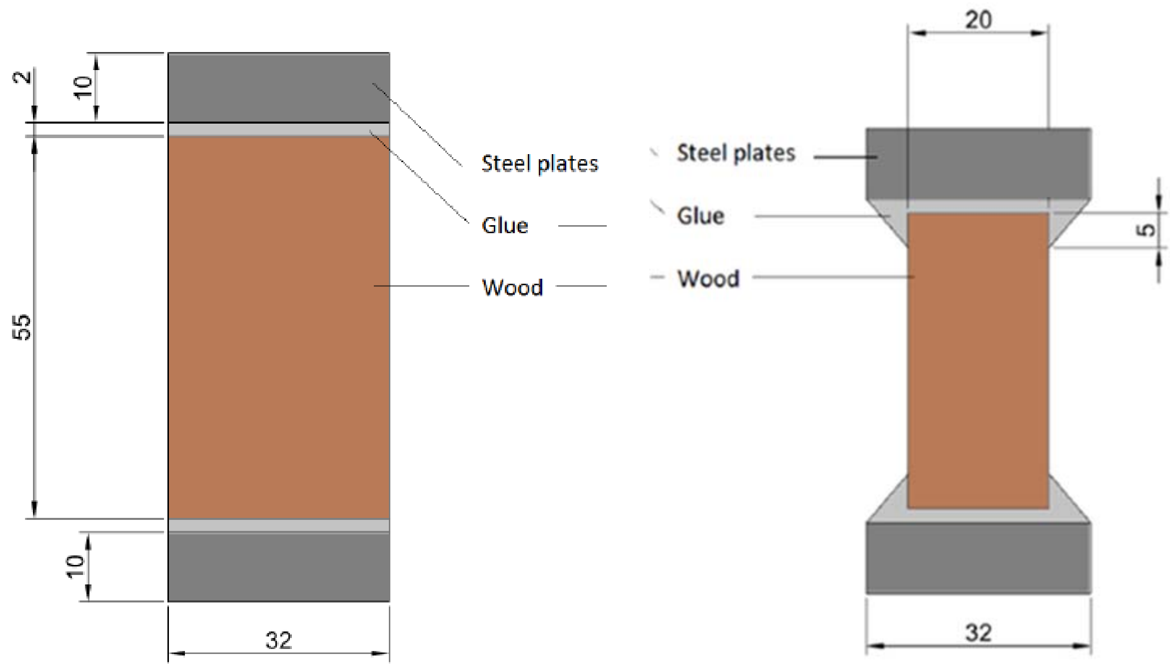

Figure 5: Adjustment of the test specimens to create a larger glue-timber surface (right).

mm to 42 mm. Because of the thickness of the glue and the reduction in width of every specimen, the loading angle was measured and used in the equation (4).

4 Test results

4.1 Mechanical properties

Table 3 and 4 give the test results according to method A (EN 408) and method B respectively. The test results are adjusted to a moisture content of 12% for method A. The density is adjusted according to EN 384. For the shear strength no guidance is given in EN 384. For compression parallel to the grain EN 384 states a change in strength value of 3% for every 1 % moisture content change. In this research was chosen to use a change in shear strength value of 2% for every 1% moisture content change below 18% m.c.. For the control species spruce, similar values are found for the specimens tested in TU Munich and TU Delft. In addition, the values of method B are also corrected for the fact that each test specimen has two spans and will fail at the weakest spot. Thus, the actual shear strength distribution is slightly higher than based on the pure test results. A method for the correction is given in Van de Kuilen and Blass (2005).

Table 3. Test results for the wood species tested according to EN 408 (method A).

Wood species	Spruce A	Spruce B	azobé	massara nduba	bilinga	oak	ash	beech
N	11	26	46	62	26	24	73	85
Mean shear strength (N/mm^2)	5.5	5.1	16.2	13.9	11.3	8.7	12.4	13.4
Standard deviation shear strength (N/mm^2)	0.5	0.9	3.1	2.4	1.08	0.6	1.8	1.6
Mean density (kg/m^3)	413	414	1074	1071	760	701	671	705
Standard deviation density (kg/m^3)	20.2	49.1	21.5	65.4	21.6	25.2	65.9	30.5
Mean moisture content (%)	13.4	9.8	15.8	14.6	14.6	17.5	12.4	13.4
Ratio mean density / mean shear strength	75	82	66	77	67	81	54	53

Table 4 Test results for the wood species tested according to a 5 point bending test (method B).

Wood species	Karri	massara nduba	angelim vermelho	uchi torrada	piquia	azobé	spruce
N	7	25	22	23	22	18	20
Mean shear strength at 12% (N/mm^2)	18.3	20.7	17.4	20.8	17.2	19.8	8.4
Standard deviation shear strength (N/mm^2)	2.1	2.8	2.4	2.4	2.5	2.4	0.9
Mean density (kg/m^3)	1047	946	1006	1071	1102	1225	482
Standard deviation density (kg/m^3)	68	46	46	142	25	32	48
Mean moisture content at test (%)	27	19	23	24	>30	>30	8
Ratio mean density / mean shear strength	64	51	65	58	72	69	53

4.2 Failure observations

In the standard tests (method A), it was observed that the different wood species show different failure patterns. According to their anatomical structure, the specimens failed in the radial direction or in a tangential line along the growth rings or showed a mix of both. Three groups can be distinguished, namely: ringporous hardwoods, diffuse prous hardwoods and softwoods (figure 6).

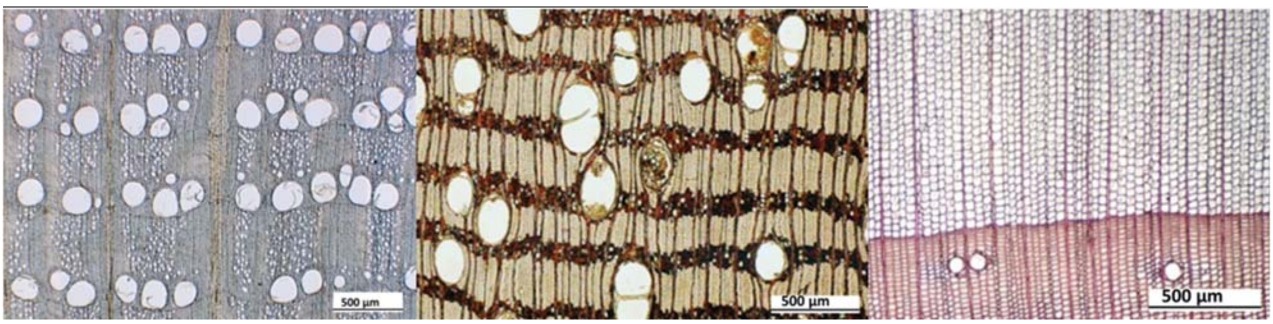

(A): e.g. oak, ash (B) e.g. azobé, beech (C) e.g. spruce

Figure 6 Microscopic cross-section of wood: ring porous (A), diffuse porous (B), softwood (C)

The ring-porous wood species failed in the rays in radial direction and the diffuse-porous in the rays and / or along the growth rings (figure 7). The softwoods failed along the growth rings on the border between early- and latewood (figure 7).

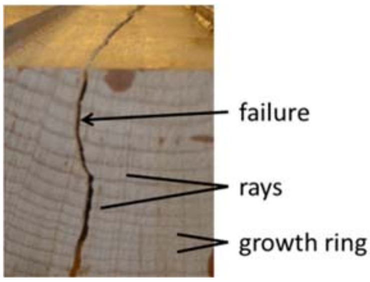

(A) Failure in ash (cross-section)

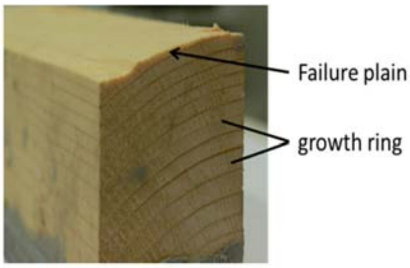

(B) Failure in spruce (cross-section)

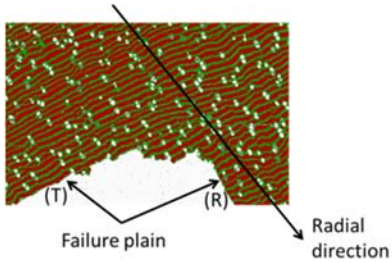

(c) Failure in azobé (cross-section)

Figure 7 Failure pattern in ring-porous wood (A), softwood (B), diffuse-porous wood (c)

Considering the proportion (table 5) and distribution of the anatomical elements (such as rays, fibres), it is found that the wood species with many and at the same time wide rays (such as oak, ash) generally fail in the rays. Diffuse-porous wood species with narrow rays (1-2 cells wide) such as azobé fail differently, partly in the radial and / or tangential direction. The wood species bilinga with a high ray portion fails in in rays.

Table 5 Proportion of cell types in different wood species (Wagenführ, 1980)

	Vessels (%)	Fibres (%)	Rays (%)	Parenchyma (%)
Spruce	-	95	5	
White Oak	8	58	29	5
Ash	12	62	15	11
Beech	39	40	16	5
Azobé	9	58	13	20
Bilinga	18	54	22	6

4.3 Method A versus Method B

From the mean strength values of method A and method B for species massaranduba, azobè and spruce (corrected to 12% moisture content, it can be noted that Method B gives higher strength values. The increase is 1.22 for azobé, 1.49 for massaranduba and around 1.6 for spruce. An important reason for the increased strength is related to the test set-up. Because of high stresses perpendicular to the grain at the supports in Method B, shear stress capacity increases, see also Steiger and Gehri [2011]. In order to estimate by how much, a comparison has been made between a standard engineering design and a linear elastic finite element model [Van de Kuilen and Leijten, 2002]. In standard engineering design, the test set-up for Method B would be modelled as shown in figure 8.

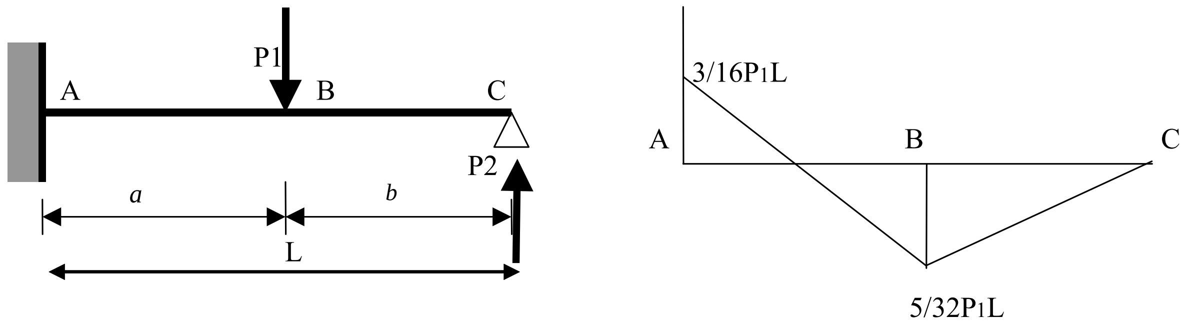

Figure 8 Mechanical model and bending moment distribution for Method B

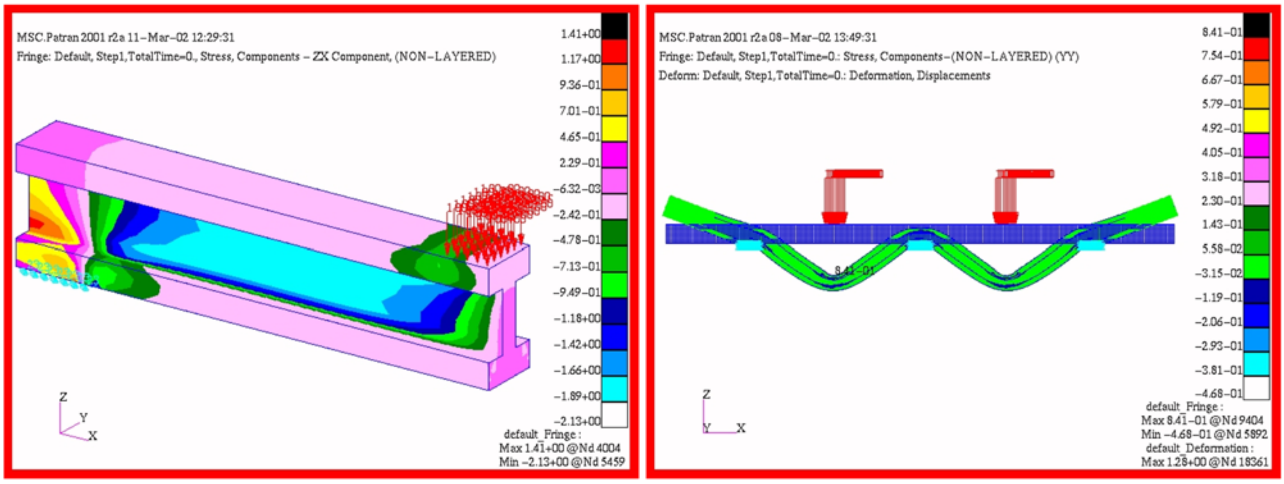

Figure 9 Model and shear stress flow (Left), Support, Load and Deformation view (Right)

From a comparison between the FEM model and the static model of Figure 8 it follows that the shear stresses according to the FEM model are about 20% less, depending on the width of the loads (distributed of perfect point loads) as well as the support model (perfectly hinged point supports at beam axis versus rotationally semi-rigid distributed supports below the beam). Consequently, the shear strength values as presented in table 4, calculated with the method of figure 8, are overestimated by about 20%. This indicates that in the case of azobé, the shear strength of method A, is almost the same as method B, but for massaranduba and spruce there is still an important difference to be noticed. Clearly, also with method A of EN 408, a normal compression perpendicular to the grain stress is exerted on the shear plane when loaded under an angle 14°.

5 Characteristic values

Characteristic values have been determined in accordance with EN 14358, assuming a lognormal distribution for the shear strength and a normal distribution for the density. Based on the test results, characteristic values have been determined for each species and test results matching the requirements of EN 408 in most cases. An analysis of the influence of the taper of the steel plates did not find any influences.

The requirement with respect to wood failure percentage may however have had an influence. It was found that shear strength values of azobé specimens with the modified geometry (figure 5 right) had consistent higher shear strength than with the standard geometry. For the calculation of the 5th-percentile value for azobé the adjusted type specimens have been used. For massaranduba the specimens with a percentage failure in the interface up to 40% have been used in the strength analysis to have a sufficient number of datapoints, even though no decrease in shear strength was found for specimens with higher failure percentages. It is remarkable however, that shear values are relatively low for massaranduba in comparison with azobé. However, for the derivation of characteristic values the result seems to be that a safe value for dense hardwoods is obtained when keeping the massaranduba values in.

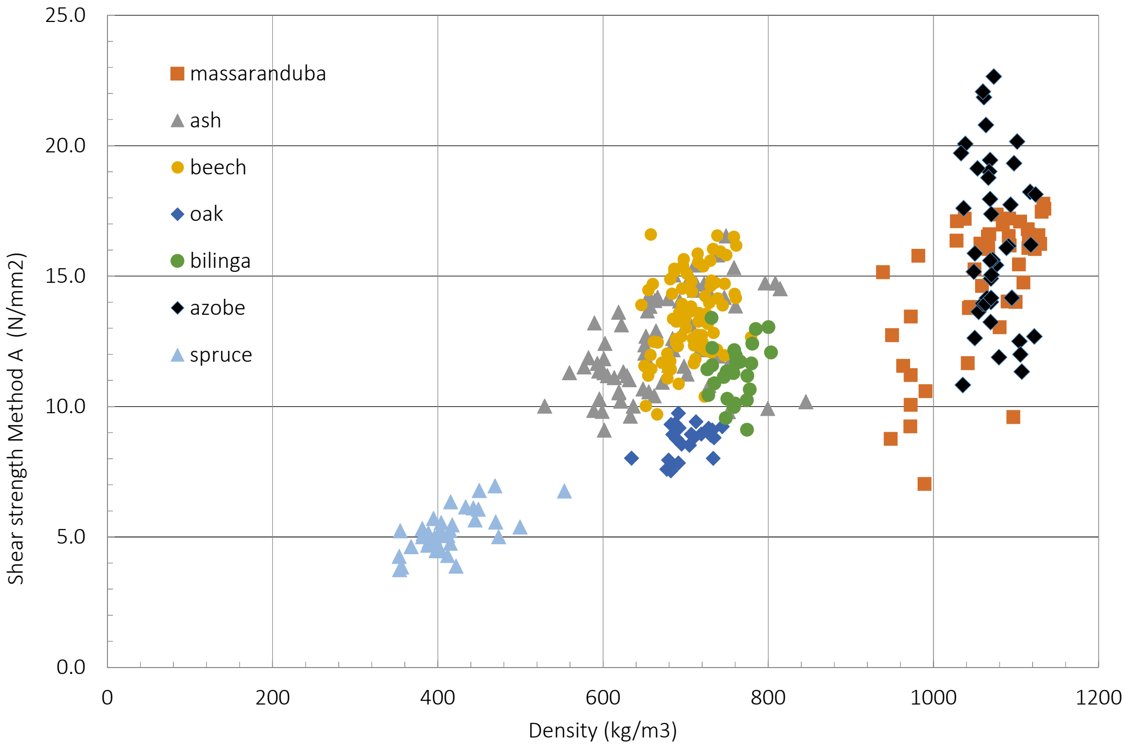

Figure 10 Shear strength data for test results of method A.

The differences in test results between standard size specimens and the modified ones may be caused by the difference in tested wood volume.

In Kovryga et al (2017) a non-linear regression analysis has been performed on the dataset at the 5-th percentile load-density level, which are given in table 6. On this basis, table 7 is derived as a proposal for a modified D-class table for EN 338, see also figure 11. The proposed values are below the medium dense hardwood data (ash, beech, oak, bilinga) and fit the 5-th percentile of the dense hardwoods well, especially considering the difficulties with the tests. For the medium dense hardwoods, some clear differences can be seen from figure 10, with species oak well below ash and beech. This may be caused by the sample size or origin, but also because of the different anatomical structure. The rays in the wood composition could be a weak anatomical element when shear load is applied. Depending on the distribution in wood and the geometry of the rays, they clearly influence the failure load and mechanism. However, the shear strength of the various wood species is essentially determined by the strength of the wood fibres in which the rays are embedded. The strength of the fibres depends above all on the microstructure of the cell wall, with the microfibrillar angle as one of the key components for shear and perpendicular to the grain strength. This might explain the different shear strengths of the various wood species, which do not have a close correlation with the density or have a large distribution in a density range such as oak and beech.

Table 6 Characteristic values of density and shear strength for method A (EN 408).

Species	spruce A	spruce B	azobé	massa-randuba	bilinga	oak	ash	beech
N	11	26	20	44	26	24	73	85
Characteristic shear strength $f_{v,k}$ (N/mm^2)	4.5	3.7	15.7	9.6	9.4	7.5	9.4	10.7
Characteristic density ρ_k (kg/m^3)	371	324	1022	948	719	654	553	650
Ratio ρ_k / $f_{v,k}$	82	87	65	100	76	87	59	61

Table 7 Proposal for new shear strength values for D-classes of EN 338

Class	D18	D24	D27	D30	D35	D40	D45	D50	D55	D60	D65	D70	D75	D80
ρ_k	475	485	510	530	540	550	580	620	660	700	750	800	850	900
f_v EN-338	3.5	3.7	3.8	3.9	4.1	4.2	4.4	4.5	4.7	4.8	5	5	5	5
f_v-proposed	5.5	5.6	5.9	6.1	6.2	6.4	6.7	7.1	7.5	7.9	8.3	8.8	9.2	9.6

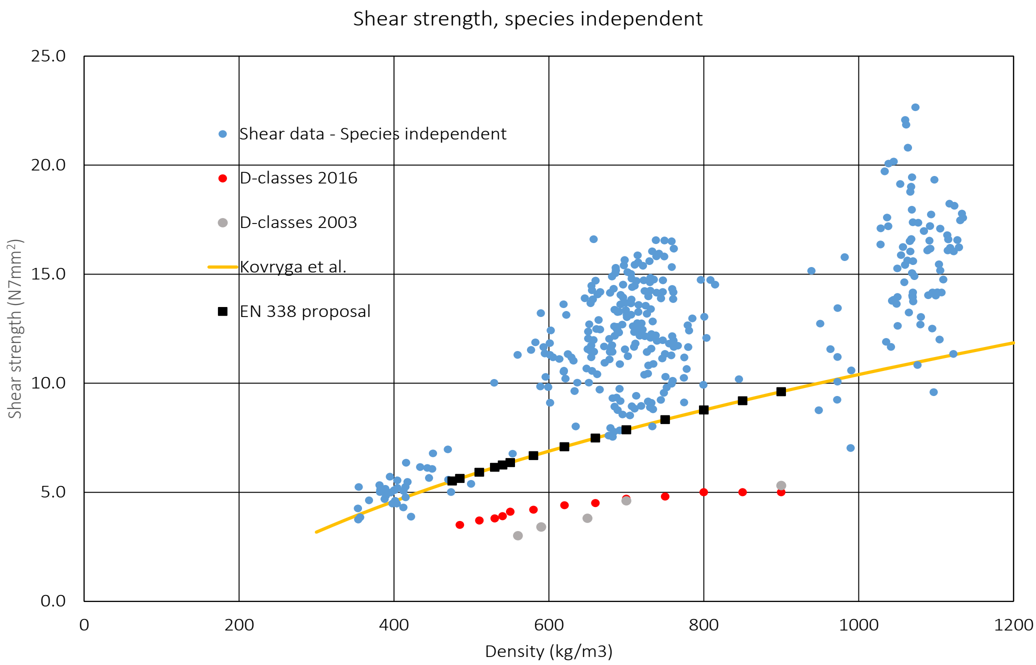

Figure 11 Shear strength in relation to strength class values of EN 338 Standard

6 Conclusions

In this study, it has been shown that:

Shear strength values for hardwoods as published in EN 338 are too low and may be raised. Published values for softwoods seem to fit well with the data.

The test procedure for shear strength as given in EN 408 can be applied on medium dense hardwoods, with some modifications on the steel plates. For dense hardwoodthe adhesion between steel and timber causes problems. A modified test specimen is presented, or 5-point bending tests can be used as an alternative. Further optimisation is needed though, as volume-effects may play a role.

Five point-bending testing using an I-profile is suited as well, but calculated values need to be adjusted for the geometry of the test set-up (loads and supports). This method is more in line with practical applications and shear verification by structural designers.

The proposed shear values are species independent. In case of medium dense hardwoods, anatomical features may lead to different strength values for different species. Some species might be underutilised because of this. Corresponding (characteristic) density values in EN 338:2016 for the higher strength classes (D60 and higher) seem to be low with respect to the modulus of elasticity and strength values for species assigned to these classes.

7 Acknowledgments

The VVNH - Netherlands Timber Trade Association and company Wijma Kampen BV are greatly acknowledged for their continued financial and in-kind support of the timber engineering research group at Delft University of Technology.

The Bavarian Forest Administration is greatly acknowledged for the support of this research project (Project X40 – Strength profiles of hardwoods) in their effort to promote the use of hardwoods in construction.

8 References

Denzler,J.K., Glos, P., Determination of shear strength values according to EN 408. Materials and Structures, 40(1):79-86, 2007

EN 338 Structural Timber- Strength classes. Brussels. CEN, 2016

EN 384 Structural Timber- Determination of characteristic values of mechanical properties and density. Brussels. CEN, 2016

EN 408 Structural Timber- Structural Timber and Glued Laminated Timber- Determination of some physical and mechanical properties. Brussels. CEN, 2012

Hunger, F., van de Kuilen, J.W.G. Festigkeitsprofile von heimischen Laubhölzern. Projekt 13508 / X40, TU Munich, 2015 (in Gernan)

Kovryga, A., Stapel, P., Van de Kuilen, J.W.G., Analysis of mechanical properties and their interrelationships for medium-dense European hardwoods. Submitted to Wood Science and Engineering, 2017.

Lam, F., Yee, H. Barrett, J.D. Shear Strength of Canadian Softwood Structural Lumber, CIB/W18/28-6-1

Ravenshorst G.J.P., Gamper, N., De Vries, P., Van de Kuilen, J.W.G., Determination of the shear strength of tropical hardwood timber, WCTE 2016, Vienna, Austria

Schickhofer, G. Determination of shear strength values for GLT using visual and machine graded spruce lamination, CIB-W18/34-12-6.

Steiger, R., Gehri, E. Interaction of Shear Stresses and Stresses Perpendicular to the Grain CIB/W18/44-6-2

van de Kuilen, J.W.G., Blass, H-J., Mechanical properties of azobé (*lophira alata*). Holz als Roh- und Werkstoff, 2005. 63: 1-10.

van de Kuilen, J.W.G., Leijten, A.J.M., Schuifsterkte bepaling van zeven houtsoorten voor de toepassing in verkeersbruggen. TU Delft report 2001-4/HE43 (in Dutch).

van de Kuilen, J.W.G., van Otterloo, J., Ravenshorst, G.J.P., de Vries, P.A., Load carrying capacity of large mortise and tenon joints in wooden mitre gates, WCTE 2014, Quebec, Canada:

Wagenführ,R. (1980) Anatomie des Holzes. VEB Verlag Leipzig 1980.

Discussion

The paper was presented by J W G van de Kuilen

H Blass commented that the long overhang in the 5 point bending tests would influence the results. JWG van de Kuilen responded that he did not take this into consideration but this was more similar to the case of an application in a Dutch bridge. H Blass also commented that the FEM calculation showing beam curvature over the end support was not reasonable. JWG van de Kuilen agreed and would look into it.

F Lam commented UBC and USFPL also worked with the 5 point bending tests in the 1990's. Even though shear failures were observed, the influence of combined shear and compression perpendicular grain stresses would lead to the higher shear capacity. This was difficult to quantify for general application. As a result 5 point bending was not accepted as standard test method in timber. Instead centre point bending with I cross sec-tion at a short span to depth ratio 7:1 to 10:1 worked well. JWG van de Kuilen agreed.

P Quenneville asked how to explain the formula limiting shear strength at 5 MPa. JWG van de Kuilen stated that this was conservative with limited knowledge. Also D class shear strength values of tropical hardwood and European hardwood were very different.

K Crews commented in Australia the 5 point bending test method is no longer used. Centre point loading at span to depth ratio of 6:1 would give very good results compared to the 5 point test.

A Salenikovich stated that N. American hardwood shear strengths are also low because of lack of data.

BJ Yeh asked for comments on volume effects in shear. JWG van de Kuilen stated that the volume difference between two groups was so small that it would not be possible to make a comment.

H Blass stated that the notched beam equation used in the first slide was not appropriate. JWG van de Kuilen agreed.

T Ehrhart and JWG van de Kuilen discussed failure mechanism as influenced by growth ring orientation and plane.

Steel-to-timber connections: Failure of laterally loaded dowel-type fasteners

Hans Joachim Blaß, Carmen Sandhaas and Nico Meyer
Timber Structures and Building Construction, Karlsruhe Institute of Technology

Keywords: timber, dowel-type fasteners, steel failure, MNV interaction, rope effect

1 Introduction

In many countries, timber connections with laterally loaded dowel-type fasteners are designed using the European Yield Model (EYM) based on Johansen's work (Johansen 1949). Johansen only considered timber-to-timber connections where bending is the only fastener failure mode. In bolted shear connections in steel structures instead, bolts fail in shear (Fig. 1 left). The extended EYM for steel-to-timber connections also considers bending as the fastener failure mode. If the rope effect is considered, a fastener tensile failure is taken into account. A moment-normal force interaction is not included in the design; both moment and tensile capacity may be exploited independently of each other. During testing of steel-to-timber connections especially with high density timber, however, combined bending and shear failure of the fasteners can be observed (Choquette 2016, Kobel et al. 2014, Misconel et al. 2016, Sandhaas 2012), see Fig. 1 right.

Figure 1: Fastener shear failure in a bolted steel plate connection (left) and in a steel-to-timber connection with central steel plate and beech glulam outer members (right).

In the design of timber connections with dowel-type fasteners, the governing failure mode should be identified in order to control the resistance. To date, a fastener failure due to combined moment, shear and normal forces in the fastener as shown in Fig. 1 (right) is not considered in the design of timber connections. The paper identifies cases where additionally to a bending moment also shear and normal forces in the fastener should be considered. Cases are identified where the adverse effect of moment, normal force and shear force interaction on the plastic fastener capacity and ultimately on the capacity of steel-to-timber connections should be taken into account.

2 Analytical model

Fig. 2 shows as an example the EYM failure mode with two plastic hinges for a fastener in single shear in steel-to-timber connections with an outer thick steel plate. Unlike in timber-to-timber connections, where the fastener shear force always reaches zero at the position of the plastic hinge, in steel-to-timber connections the shear force reaches its maximum in the shear plane between steel and timber, see position A in Fig. 2. For the plastic hinge inside the timber member, position B in Fig. 2, the shear force in the fastener is zero as in timber-to-timber connections. Since a normal force may develop in the inclined part of the fastener, the moment capacity of the plastic hinge within the timber member, position B in Fig. 2, might be reduced by a moment-normal force interaction, while the moment capacity of the plastic hinge in the steel-to-timber shear plane is additionally reduced by a shear force (see Fig. 3 left).

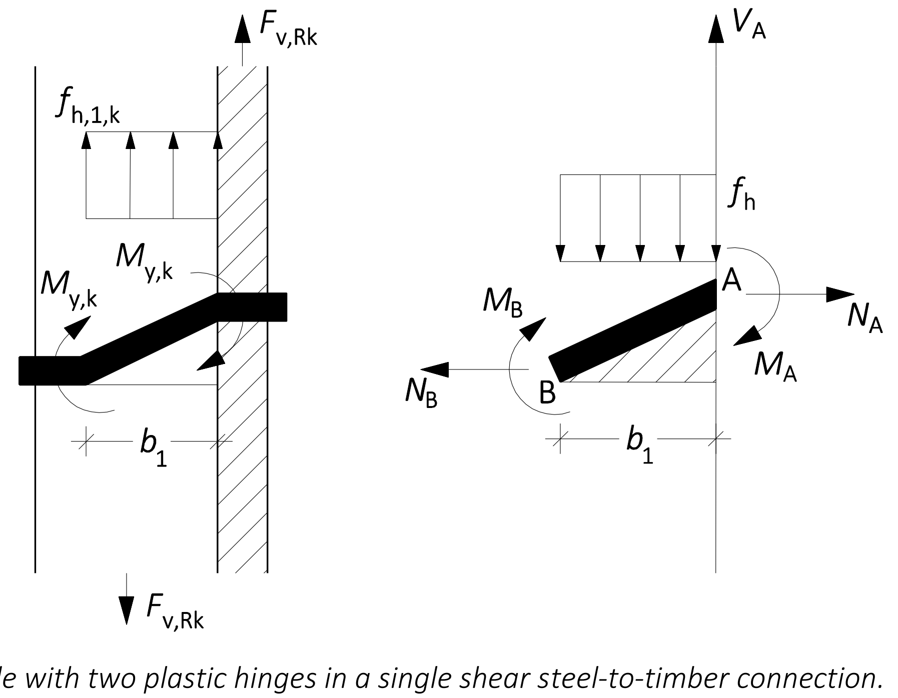

Figure 2: Failure mode with two plastic hinges in a single shear steel-to-timber connection.

The shear force V_A in Fig. 2 represents the Johansen part of the load-carrying capacity according to Eurocode 5, the additional capacity due to the rope effect is not transferred by fastener shear but by friction between steel plate and timber. According to the lower bound theorem in plastic steel design, the simultaneous occurrence of bending moment, shear force and normal force is taken into account by arbitrarily subdividing the circular fastener cross-section into three areas A_M, A_N and A_V, transferring a moment M, a normal force N or a shear force V (see Fig. 3 right) and satisfying the equilibrium und yield conditions. For simplicity, a linear elastic-perfectly plastic stress strain diagram without strengthening is assumed.

In position B in Fig. 2 the shear force is zero and the normal force N_B is smaller than N_A. Consequently, the ultimate moment M_B exceeds the ultimate moment M_A and with the friction coefficient μ between steel plate and timber member the load-carrying capacity results:

$$F_{v,R} = \sqrt{2 \cdot (M_{y,A} + M_{y,B}) \cdot f_h \cdot d} + \mu \cdot N_A = V_A + \mu \cdot N_A \tag{1}$$

Since any subdivision of the circular fastener cross-section fulfilling equilibrium leads to a lower bound of the real load-carrying capacity, the subdivision leading to a calculated maximum value of $F_{v,R}$ is determined and considered as load-carrying capacity per fastener. In order to identify the maximum value of $F_{v,R}$, the cross-sectional parts transferring the fastener moment (areas A_M in Fig. 3 right) are varied between zero (no moment transfer) and two half cycles (full plastic moment capacity).

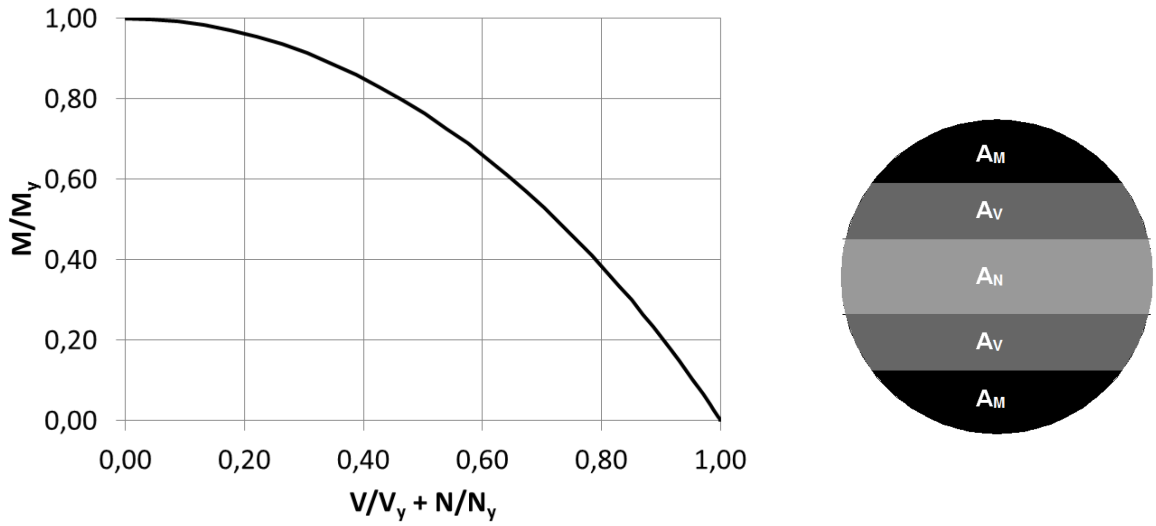

Figure 3: Bending moment-normal force-shear force (MNV) interaction for circular cross-section with elastic-plastic stress-strain curve (left) and fastener cross-section with assigned areas for M, N and V (right).

The plastic moment capacity depending on A_M results as:

$$M_{y,A} = 2 \cdot A_M \cdot x_s \cdot f_y \tag{2}$$

Where:

$M_{y,A}$ Yield moment based on two areas A_M

A_M Partial area for moment transfer in Fig. 3 right

x_s Distance of the centre of gravity of A_M from the circle centre

f_y Fastener yield strength

Disregarding the influence of the normal force N_B on the plastic moment capacity in position B, the fastener yield moment results as:

$$M_{y,B} = f_y \cdot \frac{d^3}{6} \tag{3}$$

The Johansen part of the load-carrying capacity V_A for any value of $M_{y,A}$ consequently is:

$$V_A = \sqrt{2 \cdot (M_{y,A} + M_{y,B}) \cdot f_h \cdot d} \tag{4}$$

The force V_A according to equation (4) represents the fastener shear force in position A depending on $M_{y,A}$. With the plastic steel shear strength the required cross-section A_V for the shear force V_A approximately is:

$$A_{V,req} = \frac{V_A \cdot \sqrt{3}}{2 \cdot f_y} \tag{5}$$

The remaining cross-sectional area A_N is available to transfer the fastener's normal force N_A:

$$A_N = \frac{\pi \cdot d^2}{4} - 2 \cdot (A_M + A_V) \tag{6}$$

The fastener's axial capacity is the lower value of the withdrawal capacity and the tensile capacity using the cross-sectional area A_N:

$$F_{ax,R} = \min\left\{f_{ax} \cdot d \cdot \ell_{ef} ; A_N \cdot f_y\right\} \tag{7}$$

Where:

f_{ax} Withdrawal parameter

d Fastener diameter

ℓ_{ef} Threaded or profiled penetration length

A_N Partial area for normal force transfer in Fig. 3 right

Since the MNV interaction not only reduces the Johansen part of the load-carrying capacity but also the fastener's axial capacity, the contribution from the rope effect is also affected.

3 Parameter study

In order to verify the influence of the MNV interaction on the load-carrying capacity of connections with dowel-type fasteners, the following parameters are varied:

- type of fastener: nail, screw, dowel, bolt
- fastener yield strength for dowels and bolts
- fastener diameter
- fastener penetration length
- timber density
- Johansen failure mode

For dowels and bolts the nominal yield strength f_y and the nominal tensile strength f_u of the steel are known from the fastener specification or directly from tensile tests, respectively. For nails and screws however, the fastener specifications do not provide yield strength f_y [N/mm²] and tensile strength f_u [N/mm²] but the tensile and bending capacities f_{tens} [N] and M_y [Nmm]. In order to apply the analytical model, effective yield strength $f_{y,ef}$ is determined from the tensile and bending capacities f_{tens} and M_y using the nominal diameter and a full circle cross section.

Fig. 4 exemplarily shows the influence of the timber strength class and hence the density on the characteristic load-carrying capacity of connections with ringed shank nails according to ETA-13/0523 loaded in single shear in steel-to-timber connections. The assumed failure mode is two plastic hinges per shear plane and the characteristic load-carrying capacities were calculated using the MNV-model (black diamonds in Fig. 4) and the EYM-model described in ETA-13/0523 (circles in Fig. 4).

The different curves in Fig. 4 all follow a similar trend: assuming $M_{y,A} = 0$, the load-carrying capacity corresponds to the load-carrying capacity of a nailed steel-to-timber connection with thin steel plate and one plastic hinge per shear plane. Increasing $M_{y,A}$ leads to increasing load-carrying capacities $F_{v,Rk}$ until a maximum is reached. Before reaching the maximum, the fastener's circular cross-section is loaded by a bending moment $M_{y,A}$, a shear force V_A and a normal force N_A. Until then, the combination of M, N and V does not cause yielding in the complete cross-section.

When the maximum is achieved, the yield strength is reached in the complete cross-section (see Fig. 3 right). A further increase of $M_{y,A}$ leads to an increase of V_A (see equation (4)) and the remaining area for N_A decreases. This decrease then leads to a decrease in rope effect and consequently to a decrease in the calculated load-carrying capacity $F_{v,Rk}$. Since any combination of A_M, A_V and A_N leads to a lower bound of the plastic load-carrying capacity, the curve's maximum is considered the connection's load-carrying capacity $F_{v,Rk}$ (black diamonds). The circles in Fig. 4 show for comparison the characteristic load-carrying capacities according to ETA-13/0523 (EYM) without limiting the rope effect and disregarding the MNV interaction. For the example in Fig. 4, the load-carrying capacity according to ETA is overestimated by 3 % for C14 to 11 % for Beech LVL.

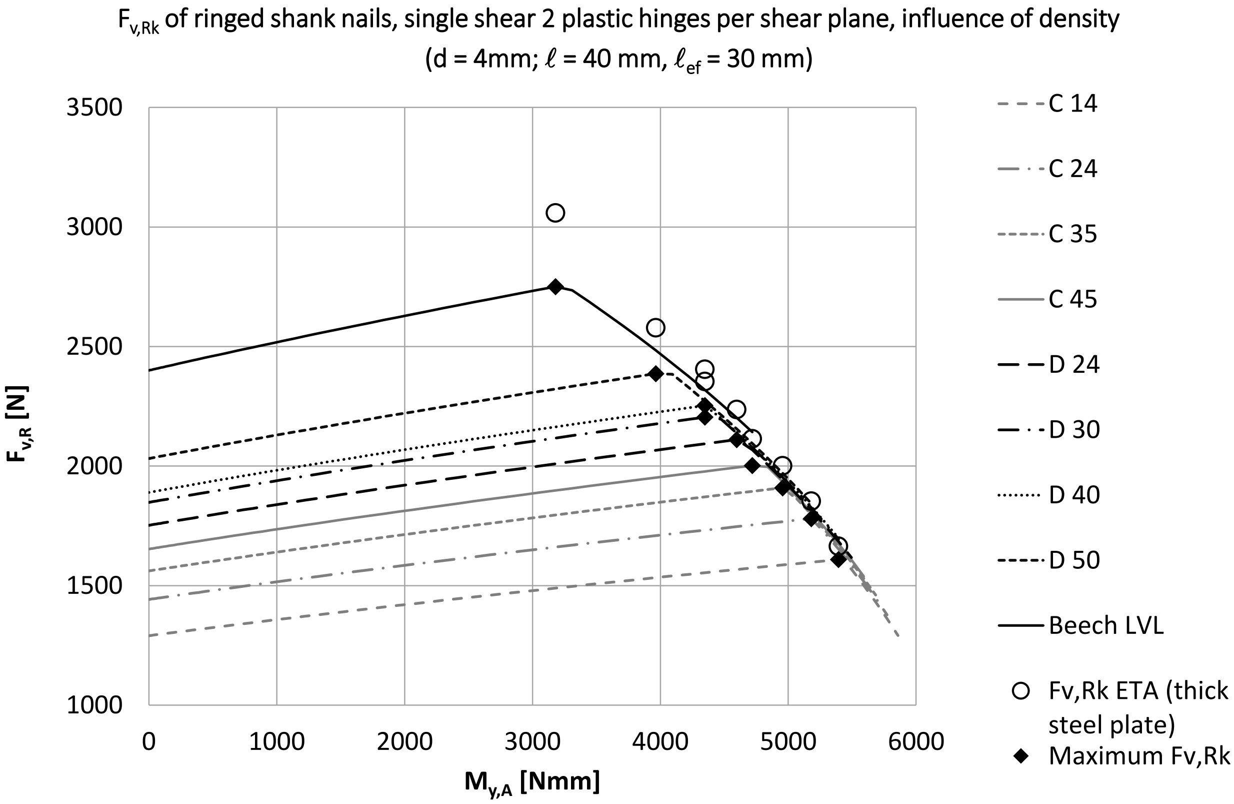

Figure 4: Influence of timber density on the load-carrying capacity of ringed shank nails loaded in single shear in steel-to-timber connections (Goossens 2017).

The calculated load-carrying capacities in Fig. 4 are based on the failure mode with two plastic hinges per shear plane. Since the failure mode is not known a priori, all possible failure modes need to be checked. Fig. 5 shows the result: only for very low densities below 320 kg/m³ the failure mode with one plastic hinge governs.

The dashed line in Fig. 5 shows the resulting load-carrying capacity according to the model incorporating MNV interaction.

The ratio between load-carrying capacity according to ETA-13/0523 and the load-carrying capacity according to the analytical model increases for larger penetration lengths and larger densities. For ringed shank nails with a diameter of 4 mm, the overestimation according to ETA-13/0523 is up to 20 %, for 6 mm nails up to 27 % (see Table 1).

Table 1 exemplarily shows the ratios of the load-carrying capacity according to Euro-code 5 with unlimited rope effect and the load-carrying capacity of the model taking into account MNV interaction.

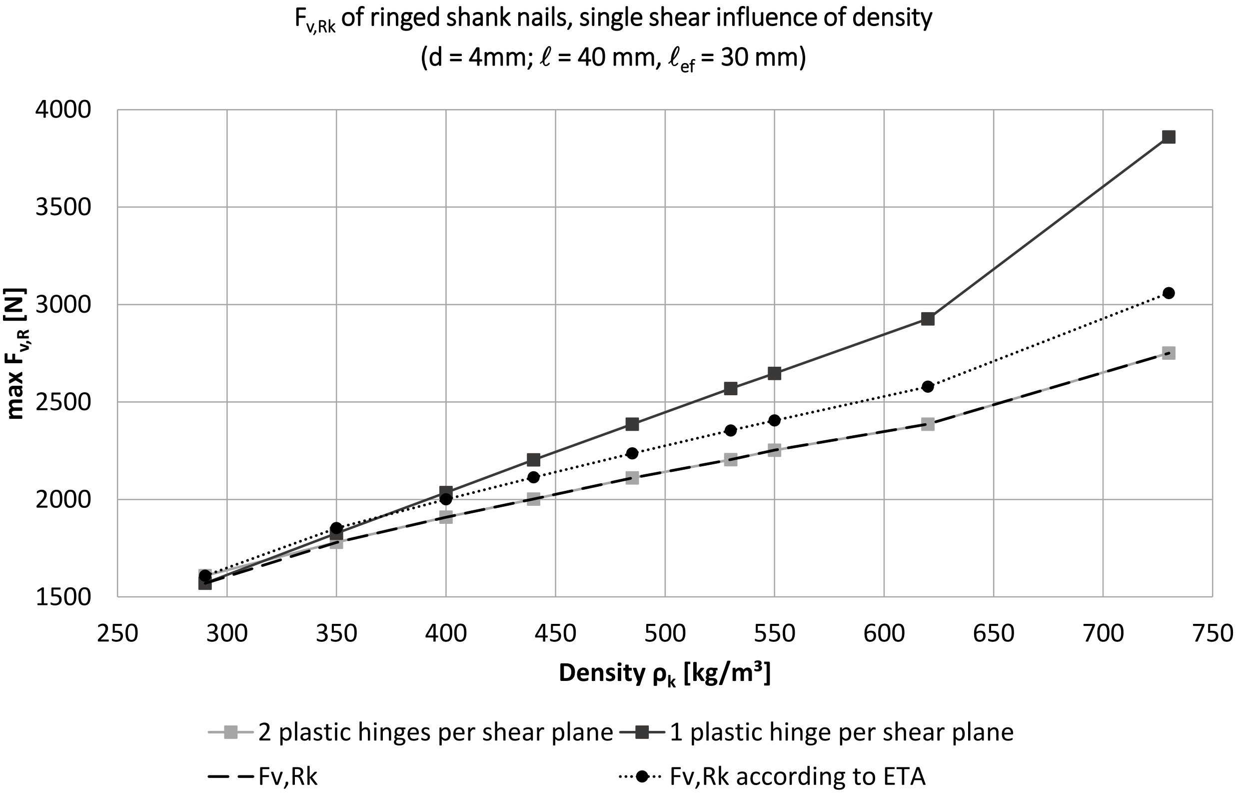

Figure 5: Influence of timber density on the load-carrying capacity of ringed shank nails loaded in single shear in steel-to-timber connections for different failure modes (Goossens 2017).

Table 1: Ratio of the characteristic load-carrying capacity according to Eurocode 5 to characteristic load-carrying capacity taking into account MNV interaction for selected fastener types, diameters and characteristic densities in steel-to-timber connections.

Fastener type, diameter and penetration length	Connection type	Characteristic density [kg/m³]		
		350	440	730
Ringed shank nail 4x80 mm	Single shear, thick outer steel plate	107 %	108 %	120 %
Ringed shank nail 6x80 mm		108 %	110 %	127 %
Full thread screw 5x70 mm		107 %	110 %	125 %
Full thread screw 8x130 mm		110 %	114 %	142 %
Full thread screw 10x180 mm		108 %	112 %	143 %
Full thread screw 12x200 mm		108 %	111 %	138 %
Dowel S355, 10 mm, t = 90 mm	Double shear, inner steel plate	104 %	105 %	108 %
Dowel S355, 12 mm, t = 90 mm		104 %	105 %	108 %
Dowel S355, 16 mm, t = 90 mm		103 %	103 %	108 %
Bolt 5.8, 12 mm, t = 90 mm		108 %	110 %	131 %
Bolt 5.8, 16 mm, t = 90 mm		106 %	107 %	132 %
Bolt 5.8, 20 mm, t = 90 mm		106 %	107 %	123 %

Overall, the following parameters have a distinct influence on the load-carrying capacity including the MNV interaction:

- type of fastener: fasteners displaying a distinct rope effect like profiled nails, screws or bolts show higher influence of MNV interaction than fasteners without rope effect as dowels
- fastener yield strength: increasing influence of MNV interaction with decreasing dowel or bolt grade
- fastener penetration length: increasing influence of MNV interaction with increasing nail or screw length
- timber density: increasing influence of MNV interaction with increasing characteristic density

4 Test results

4.1 Fastener tests

In the extended EYM including the rope effect, the yield moment M_y and the tensile capacity f_{tens} are the governing properties of metal dowel-type fasteners influencing the load-carrying capacity of timber connections. If the MNV interaction is taken into account, the fastener shear capacity is also required. While the shear capacity of dowels and bolts may be determined according to EN 1993-1-8, no information regarding the shear capacity of nails and screws is available yet.

In order to determine the fastener's shear capacity f_{shear}, a test setup with two steel plates was chosen where tensile forces and bending moments are avoided as far as possible (see Fig. 6).

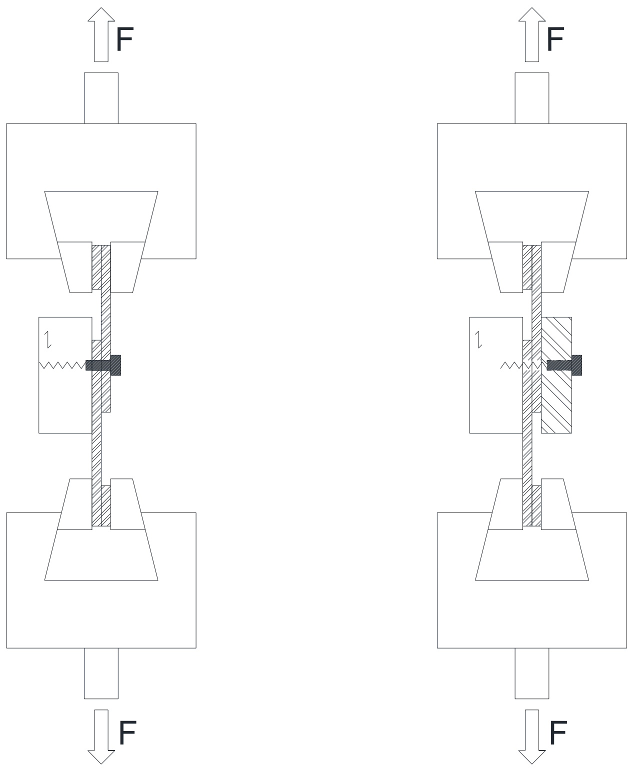

Figure 6: Fastener shear test setup for the smooth shank (left) and the threaded part (right) of a screw. (Goossens 2017).

For partially threaded screws, the shear capacity was determined both in the smooth shank and in the threaded part. An additional wood block on the side of the screw tip and a steel block on the side of the screw head allowed positioning the cross-section to be tested in the shear plane and prevented fastener rotation.

Table 2 shows the shear test results f_{shear} for the different fasteners as well as the yield moment M_y at 45° bending angle and the tensile capacity f_{tens}. Both mean values and characteristic values according to EN 14358 are given. The number of tests per series was mostly 10.

Table 2: Mean and characteristic values of the yield moment, the tensile capacity and the shear capacity for ringed shank nails and self-tapping screws.

Fastener type and diameter	$M_{y,mean}$ Nm	$f_{tens,mean}$ kN	$f_{shear,mean}$ kN	$f_{shear,mean}/f_{tens,mean}$	$M_{y,k}$ Nm	$f_{tens,k}$ kN	$f_{shear,k}$ kN	$f_{shear,k}/f_{tens,k}$
Nail 4 mm, thread	7.68	9.09	5.88	0.65	6.79	8.18	5.30	0.65
Screw 5 mm, thread	9.48	12.1	7.15	0.59	8.55	10.9	6.22	0.57
Screw 8 mm, thread	32.4	24.8	16.7	0.67	29.2	22.4	15.1	0.67
Screw 8 mm, shank	37.6	27.6	19.8	0.72	33.8	24.1	17.9	0.74
Screw 10 mm, thread	56.8	34.7	27.2	0.78	51.2	31.2	24.4	0.78
Screw 10 mm, shank	81.1	47.8	33.7	0.71	73.0	43.1	30.4	0.71
Screw 12 mm, thread	88.5	47.6	31.9	0.67	79.6	42.8	26.9	0.63
Screw 12 mm, shank	127	63.6	42.2	0.66	114	57.2	38.0	0.66

The ratio between shear and tensile capacity is between 0.59 and 0.78 for the mean values and between 0.57 and 0.78 for the characteristic values. The ratio between shear and tensile capacity for the shank of bolts or rivets according to Table 3.4 of EN 1993-1-8 is 0.6, for the thread either 0.6 (steel grades 4.6, 5.6 or 8.8) or 0.5 (steel grades 4.8, 5.8, 6.8 or 10.9). The corresponding ratios for ringed shank nails and self-tapping screws are obviously similar.

4.2 Connection tests

10 tests with laterally loaded ringed shank nails in single-shear steel-to-Beech LVL connections were performed. Apart from the connections, the nail properties M_y, f_{tens} and f_{shear} (see Table 2) as well as the nail's withdrawal capacity $F_{ax,R}$ and the embedding strength f_h were determined separately. The following parameters describe the connection:

- Ringed shank nails 4.0x35 in Beech LVL according to ETA-14/0354 or EN 14374
  $F_{ax,Rmean}$ = 3.99 kN - nails in wide face $F_{ax,Rmean}$ = 3.84 kN - in edge face
  $f_{h,mean}$ = 112 N/mm² - nails in wide face $f_{h,mean}$ = 98.6 N/mm² - in edge face
- Steel plate thickness: 2 mm
- Nailing without pre-drilling

- Angle between load and grain direction: 0°
- Angle between nail axis and grain direction: 90°

Steel-to-timber connections with 2 mm steel plates and softwood show a failure mode with two plastic hinges per shear plane, since the nail shank has a cone shape directly under the head and hence is clamped into the steel plate (Görlacher 1995).

Figure 7: Nail shear failure in steel-to-Beech LVL connection (left) and severed nail heads (right).

Five specimens with 8 nails each in the wide face and 5 specimens with 8 nails in the edge face of the LVL were tested to failure. The average failure load per nail was $F_{max,test}$ = 4.70 kN for the specimens with nails in the wide face and $F_{max,test}$ = 4.63 kN for the specimens with nails in the edge face. The failure of the nailed steel-to-Beech LVL connections was caused by nail failure in the shear plane between steel plate and LVL (see Fig. 7). The corresponding calculated load-carrying capacities taking into account the MNV interaction and assuming a friction coefficient μ = 0.5 between the steel plate and the Beech LVL are $F_{max,cal}$ = 4.81 kN for the specimens with nails in the wide face and $F_{max,cal}$ = 4.64 kN for the specimens with nails in the edge face. The calculated load-carrying capacities according to EYM considering the same input parameters result in $F_{max,cal}$ = 5.70 kN for the specimens with nails in the wide face and $F_{max,cal}$ = 5.40 kN for the specimens with nails in the edge face. For steel-to-timber connections with ringed shank nails in Beech LVL the model incorporating the MNV interaction obviously leads to more realistic load-carrying capacities.

A second comparison uses the test results in Sandhaas (2012). Sandhaas tested dowelled connections with inner steel plates and Beech glulam with different numbers of dowels in line with load and grain direction. Here, the connection tests with one dowel and two plastic hinges per shear plane as failure mode are considered (see Fig. 1 right). Again the results of two test series with five specimens each are compared with the calculation results of the model incorporating MNV interaction.

The following parameters describe the connection:

- Dowels with diameters of d = 12 mm and d = 24 mm in Beech glulam
  M_y = 177 Nm - 12 mm M_y = 1497 Nm - 24 mm

f_{tens} = 72,2 kN - 12 mm f_{tens} = 245 kN - 24 mm
$f_{h,mean}$ = 45.8 N/mm² - 12 mm $f_{h,mean}$ = 49.9 N/mm² - 24 mm

- Side member thickness: $t_1 = 6 \cdot d$
- Angle between load and grain direction: 0°

The dowel's shear capacity was assumed as 60 % of its tensile capacity.

The average failure load per 12 mm dowel was $F_{max,test}$ = 59.4 kN and $F_{max,test}$ = 208 kN per 24 mm dowel. Disregarding the rope effect, the corresponding calculated load-carrying-capacities taking into account the MNV interaction is $F_{max,cal}$ = 37.4 kN per 12 mm dowel and $F_{max,cal}$ = 157 kN per 24 mm dowel. The calculated load-carrying-capacity according to EYM considering the same input parameters results in $F_{max,cal}$ = 39.5 kN for the 12 mm dowel and $F_{max,cal}$ = 169 kN for the 24 mm dowel. For steel-to-timber connections with dowels in Beech glulam both the model incorporating the MNV interaction and the EYM obviously underestimate the real load-carrying-capacities at least for slender dowels showing a failure mode with two plastic hinges per shear plane. This statement is in agreement with findings in Blass and Colling (2015).

Even though dowels are not considered to have a withdrawal capacity, a rope effect could be one explanation for the ultimate test loads significantly exceeding the calculated maximum loads. Assuming a friction coefficient $\mu = 0.5$ between the steel plate and the Beech glulam, a withdrawal force of 26 kN for the 12 mm dowel and 60 kN for the 24 mm dowel would be required to achieve agreement between the ultimate test load and the calculated load-carrying capacity considering MNV interaction. Further research is required to clarify a possible rope effect on the load-carrying capacity of dowelled steel-to-timber connections.

5 Conclusions

Hardwoods are increasingly used in engineered timber structures. Because of their higher density and embedding strength, the load-carrying capacity of dowel-type fasteners is increased compared to softwoods. In the shear plane of steel-to-timber connections the dowel-type fastener is simultaneously loaded by bending moments and shear forces, in the case of fasteners displaying significant withdrawal capacity also by normal forces. The combined action of moment, shear and normal force may lead to metal fastener failure at loads below those predicted by the EYM.

An analytical model taking into account the MNV interaction on the load-carrying capacity of dowel-type fasteners in steel-to-timber connections was derived. The results of the model show a significant influence of the MNV interaction for fasteners in high density timber. The influence is more pronounced for higher fastener withdrawal capacity and lower fastener steel strength.

In order to verify the analytical model, ultimate test loads of nailed steel-to-timber connections with Beech LVL are compared with the results of the model. The ultimate loads from the tests agree very well with the model predictions. For the comparison, the model parameters embedding strength, withdrawal capacity, fastener tensile, and shear and bending strength were all determined separately by tests.

A similar comparison using test data with dowelled steel-to-Beech glulam connections showed higher load-carrying capacities in the tests compared with the model. However, the ultimate test loads also significantly exceeded the calculated load-carrying capacities predicted by the EYM. This discrepancy might be explained by a rope effect in steel-to-timber connections with dowels displaying a failure mode with two plastic hinges per shear plane.

6 References

Blass, H.J. and Colling F. (2015): Load-carrying capacity of dowelled connections. In: Proceedings. International Network on Timber Engineering Research, Meeting 48, Sibenik, Croatia. Paper 48-7-3.

Choquette, J. (2016): Évaluation d’une nouvelle méthode de calcul des assemblages de bois à l’aide de connecteurs de petits diamètres. Maîtrise en sciences du bois. Université Laval, Québec. www.theses.ulaval.ca/2016/32759/32759.pdf.

Goossens, K. (2017): M-N-V Interaktion in stiftförmigen Verbindungsmitteln für Stahlblech-Holzverbindungen. Master’s Thesis, Timber Structures and Building Construction, Karlsruhe Institute of Technology, Karlsruhe, Germany.

Görlacher, R. (1995): Load-carrying capacity of steel-to-timber joints with annular ring shanked nails. In: Proceedings. CIB-W18 Meeting 1995, Copenhagen, Denmark. Paper 28-7-3.

Johansen, K.W. (1949): Theory of Timber Connectors. Publications of the International Association of Bridge and Structural Engineering. No. 9: 249-262. Bern, General Secretariat.

Kobel, P., Steiger, R. and Frangi, A. (2014): Experimental analysis on the structural behaviour of connections with LVL made of Beech wood. In: Materials and Joints in Timber Structures, Springer.

Misconel, A., Ballerini, M. and van de Kuilen J.W. (2016): Steel-to-timber joints of Beech-LVL with very high strength steel dowels. 14th World Conference of Timber Engineering WCTE, Vienna, Austria.

Sandhaas, C. (2012): Mechanical behaviour of timber joints with slotted-in steel plates. Dissertation, Delft University of Technology, Delft, The Netherlands.

Discussion

The paper was presented by H Blass

S Winter asked about the appropriateness of calculations of screw using fu. H Blass replied there will be another paper discussing this point but the moment capacity from tests would have included strain hardening, so this would be appropriate.

P Quenneville asked about the assumption of no rope effect even though slide 4 seemed to show rope effect existed. H Blass agreed that slide 4 case did show rope effect; however, this was not yet considered because it would be difficult to tell practical engineers when to consider it and when not.

JWG van de Kuilen commented that although steel dowel shear failure was observed in single dowel connection one would not see this in a group of dowel in a row. H Blass agreed but this would depend on the connection layout.

P Quenneville asked about the observed failure of fasteners in the table. H Blass explained failures were a combined action of bending moment, shear and normal force.

F Lam received clarification of the concept of interaction of MNV.

A Salenikovich commented on their own work on screws and nails.

A Buchanan commented about seismic design on the issue of cyclic loading and capacity design principles. He asked if this could be used to look into the upper limit for capacity design as well as lower limits. H Blass stated yes.

R Jockwer received clarification on the effect of interaction between embedding stress and shear stress in wood on the connection. H Blass also commented that they did work in the past to investigate embedment influence on withdrawal capacity which was not significant.

The Embedbment Strength as a System Property

Yurrita, Miguel, Wood Chair. Department of Structural Analysis and Design. University of Navarra (Spain). myurrital@alumni.unav.es

Cabrero, J.M., Wood Chair. Department of Structural Analysis and Design. University of Navarra (Spain). jcabrero@unav.edu

Keywords: embedment strength, connections, timber, dowel, hardness, contact

1 Introduction

The calculation of the load capacity of timber joints is mostly based on the European Yield Model (EYM), originally proposed by Johansen (1949). In order to obtain the connection capacity, the model relies on the embedment strength.

It has usually been considered that the embedment strength is a property of the timber members in contact with the dowel. It is defined as the force that can be supported by the dowel area. For practical reasons the experimental obtained values are divided by a simplified area, given by the dowel diameter and the member thickness. And, therefore, the embedment strength is given by:

$$f_{h.0} = F_v\ t\ d \qquad (1)$$

where $f_{h,0}$ is the embedment strength parallel to the grain, F_v is the experimental capacity, t is the thickness of the timber member, and d is the dowel diameter.

However, as it will be presented in this contribution, and referring to a previous paper by Ehlbeck & Werner (1992) in the CIB W-18, “"*the embedding strength depends on the type of fastener, the joint configuration (such as member thickness, end and edge distances as well as spacing of the fasteners), the manufacturing of the joint (e.g. predrilled holes), and the wood species or the quality of the wood-based materials. Thus,* the embedding strength is not a special material property, but a system property."

2 State of the Art

2.1 Existing formulae

Several expressions have been proposed to estimate the embedment strength. They are experimentally based, and differ only in the parameters used. Timber density is always regarded as the primary parameter, and some of them include the dowel diameter as a secondary parameter.

However, early works by Fahlbusch (1949) and Norén (1974) were based on the experimental embedment strength of a dowel of 10 mm diameter:

Fahlbusch (1949)

$$f_{h,0}=f_{h,0,d10}(0.9+1/d) \quad (2)$$

Norén (1974)

$$f_{h,0}=f_{h,0,d10}[(66-d)/56] \quad (3)$$

where $f_{h,0}$ is the embedment strength, $f_{h,0,d10}$ is the reference embedment strength for the 10mm diameter dowel, and d is the dowel diameter in mm. In both cases, the embedment strength increases for diameters lower than 10mm, and diminishes for higher diameters.

The most usual proposals take both wood density and dowel diameter as the main parameters. Most of them are linear equations, being their difference only the value of the numerical coefficients. Below are some of the most known formulae:

Ehlbeck & Werner (1992)

$$f_{h,0}=0.102(1-0.01d)\rho, \quad (4)$$

Jumaat *et al.* (2006)

$$f_{h,0}=0.103(1-0.014d)\rho. \quad (5)$$

The proposal by Leijten and Köhler (2004) uses wood density and dowel diameter as parameters as well. However, it differs to the previous ones in two ways: there is a different expression for coniferous and deciduous, and it is not a linear equation:

$$f_{h,0}=0.097\rho^{1.07}d^{-0.25} \text{ for coniferous,} \quad (6)$$

$$f_{h,0}=0.087\rho^{1.09}d^{-0.25} \text{ for deciduous.} \quad (7)$$

It should be noticed that this latter proposal, on the contrary to the previous, was fitted to the characteristic value, and not to the mean value.

Other family of proposals only take the timber density as the primary and only parameter, like:

Sawata & Yasumura (2002)

$$f_{h,0}=0.08757\rho, \quad (8)$$

Sandhaas *et al.* (2013)

$f_{h,0}$=0.082ρ. (9)

2.2 Design standards

The formulae included in the current design standards are quite similar to the previously described, and they actually belong to each one of the previous families.

The formula from the Eurocode 5 includes both timber density and dowel diameter,

$f_{h,0}$=0.082(1-0.01d)ρ, (10)

while the formula in the American standard only takes timber density into account

$f_{h,0}$=0.07725ρ. (11)

The New Zealand draft (NZS 3603 revision, 2015) uses both approaches based on density and diameter for timber and glulam, and based only on density for timber and LVL from Radiata Pine.

3 Materials and Methods

3.1 Reference embedment tests

The comprehensive experimental campaign from Sandhaas (2012) is used throughout this work as the reference set of embedment tests. The wide range of timber densities considered by Sandhaas (2012) and the variation of both dowel diameter and steel grade, make this ensemble of tests one of the most representative and comprehensive available databases for embedment.

Two different dowel diameters (12 and 24 mm) were tested with a similar relative geometry of the tested specimen, there was a wide variety of wood species (spruce, beech, azobé, purpleheart, Brazilian and Peruvian cumaru) and wood densities (from 465 kg/m^3 up to over 1200 kg/m^3) and two steel grades (nominal S235 and 12.9). Therefore, any noticed difference should correspond to an actual influence, and not to a different experimental set-up, which might be the case if different embedment campaigns were used.

The tested material properties of the steel of the dowels are given in Table 1. Figure 1 depicts the obtained embedment strength, in relation to the timber density.

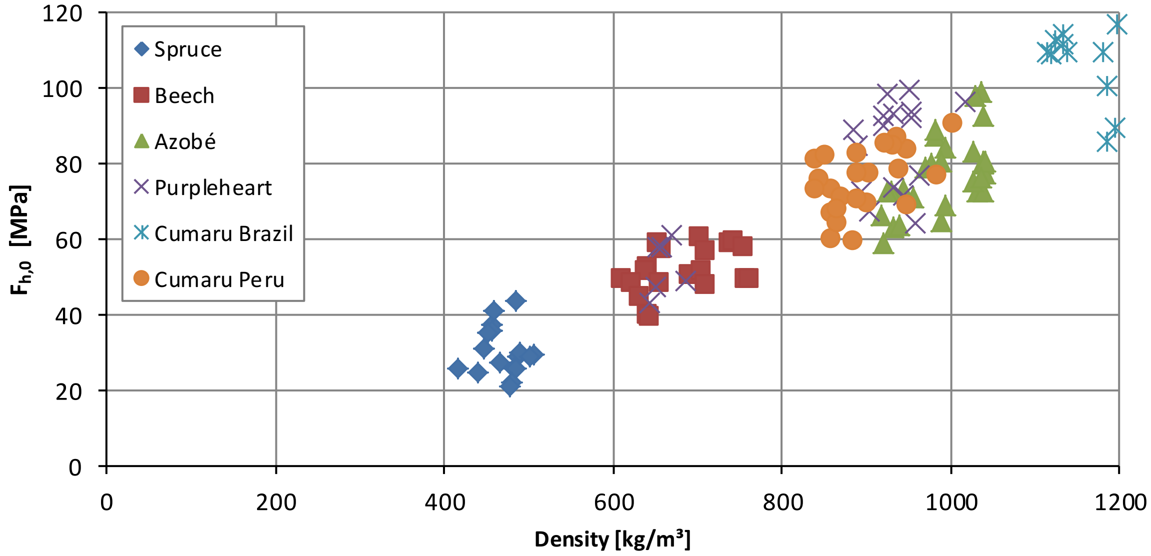

Figure 1. Experimental embedment strength in relation to the wood density and woodspecies (Sandhaas, 2012).

Table 1. Properties of the steel used for the dowels in the experimental tests (Sandhaas, 2012)

Steel grade	Diameter [mm]	Yield Strength [MPa]	Ultimate Str. [MPa]	Roughness [µm]	Vickers hardness [kp/mm^2]
S235	12	609	638	0.88	221
	24	517	541		
12.9	12	1324	1399	0.80	492
	24	1297	1379		

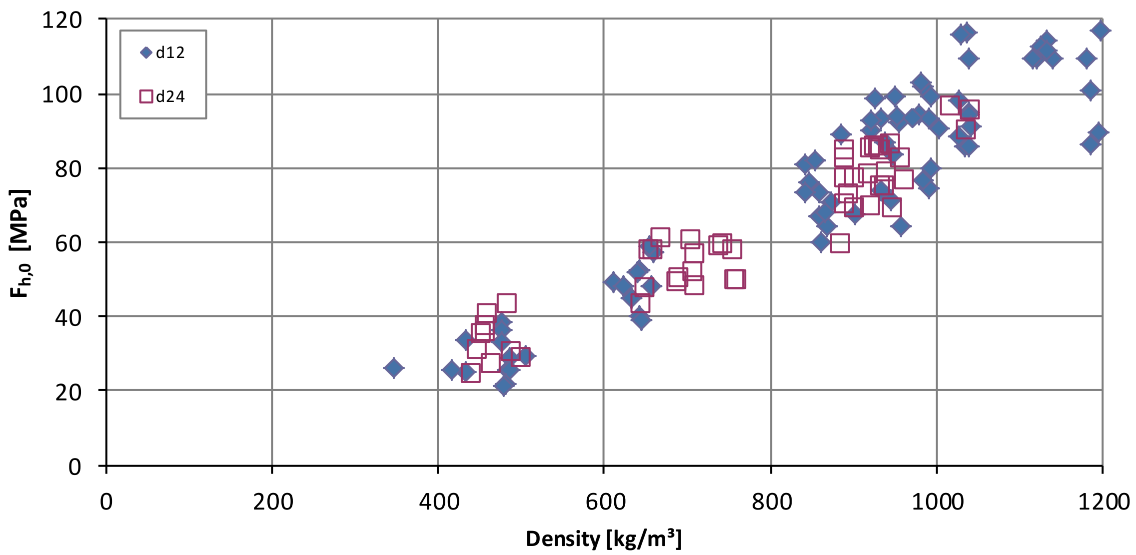

Figure 2. Experimental embedment strength classified by the dowel diameter, in relation to the wood density (Sandhaas, 2012).

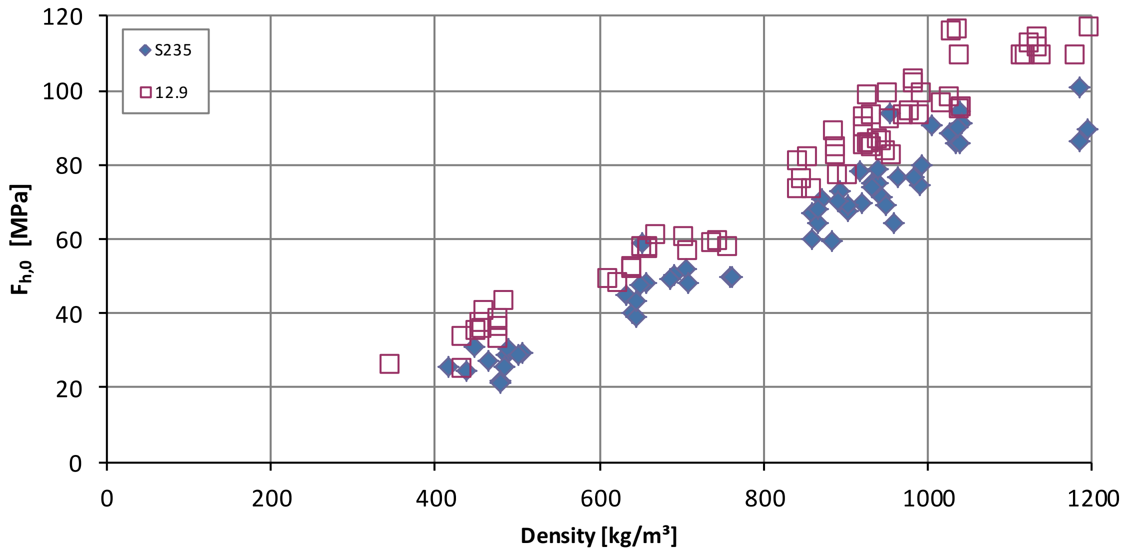

Figure 3. Experimental embedment strength classified by the steel grade of the dowel, in relation to the wood density (Sandhaas, 2012).

3.2 Analysis of test results

3.2.1 Influence of the wood density and wood species.

Figure 1 shows the embedment strength of all the tests classified by wood species. A clear correlation between density and embedment strength can be easily observed. No difference between the different wood species, apart from that derived from the density, can be noticed.

This is in line with the previously described proposals, which take density as a main parameter. Only the proposal by Leijten & Köhler (2004) proposes a different approach depending on the wood species.

3.2.2 Influence of the dowel diameter.

According to the formula in the Eurocode 5 (and to those which take dowel diameter as a secondary parameter), there should be a clear difference among the series with 12mm and 24 mm diameter dowels. The strength values of the 24 mm series should be around 13% lower than the 12 mm diameter tests.

However, if the experimental results by Sandhaas (2012) are plotted and classified according to the diameter of the fastener, as shown in Figure 2, no clear differences are seen between the two tested diameters.

This observation is in line with those proposals which do not consider the influence of the dowel diameter (Sandhaas *et al*., 2013; American standard). However, it should be proven if there is no diameter influence for other fasteners, such as nails.

3.2.3 Steel grade

One of the main features of the reference embedment tests by Sandhaas (2012) is the use of dowels with two different steel grades. And there is a clear difference when the embedment results are classified by steel grades, as shown in Figure 3. Sandhaas (2012) already noticed this trend in her work.

This result seems anyway to have little sense, since the embedment tests are specifically done only in the elastic range of the dowels. As it is well known, the elastic properties of the different steel grades are quite similar, and in any case, they do not differ to such an extent that could explain such a difference. Therefore, a different source explaining the different result should be found and explained.

4 Results and Discussion

4.1 Proposal

From the previous analyses, both the wood density and the steel grade have been found to be the primary parameters affecting the embedment strength. When analysing the measured material properties of the steel used by Sandhaas (2012) provided in Table 1, only their yield strength and hardness are significantly different.

Since the embedment test does not produce plastic behaviour in the dowel, and no plastic deformation was noticed by Sandhaas in her study, thinking on an influence of the yield strength is quite unreasonable.

In previous works, roughness has been described as a parameter modifying embedment strength. It was assumed that roughness could easily explain such difference by addressing contact phenomena. However, Sandhaas' results are not in line with previous results such as Sjödin *et al.* (2008). And moreover, the difference of the measured roughness between the two steel grades is not significant.

Hence, as a first approach, a fitted formula based on the timber density and the steel hardness is developed. However, the reason to use hardness is based on the measured (and therefore known) dowel properties on the original test campaign. A physical explanation for using hardness as a parameter is still to be found.

The following formula, which takes the Vickers hardness (measured in H_V) and the timber density (in kg/m^3) is proposed:

$$f_{h,0}=(0.012 + \rho\ 0.0088/1000)\ \rho\ H_v^{0.25} \quad (11)$$

The obtained formula is non-linear, and provides relatively higher embedment values for high wood densities. This proposal is in line with that from Leijten & Köhler

(2004), who proposed a linear equation with an higher slope for hardwood, and hence, for higher densities.

Since hardness is not usually known by the designer, and it is not an easy property to measure in cylindrical fasteners, a formula based on the yield strength would be more practical, although any possible underlying physical meaning would be lost. In the metallurgical literature, it has been proved that there is a relationship between hardness and the yield strength, as described by Cahoon *et al.* (1971)

$f_y = 0.1^n\ H_v/3,$ (12)

where the coefficient n depends on the type of material, being $n = 0.21$ for low-carbon steel. The obtained yield strength is not purely a yield strength, but the stress corresponding to a strain of 0.004 (Cahoon *et al.,*1971), although it is usually considered a good approach. By applying the previous equation (12) in (11), the following formula for the embedment strength, based on the yield strength, is derived:

$f_{h,0}=(0.0095+\rho\ \ 0.007/1000)\ \rho\ f_y^{\ 0.25}.$ (13)

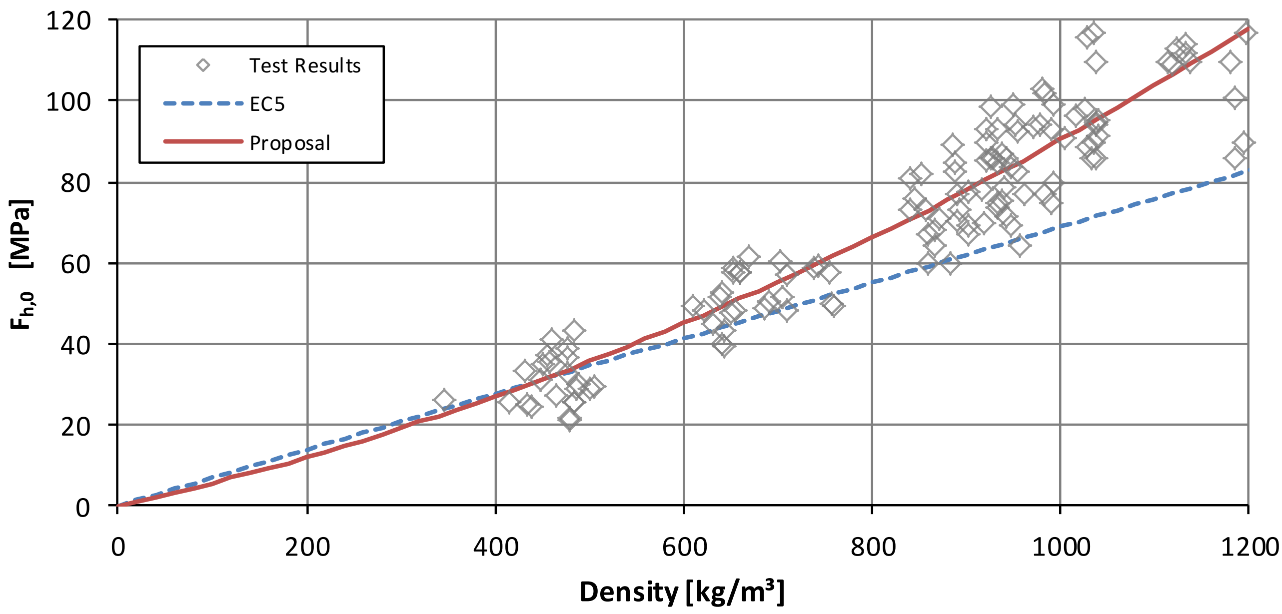

Figure 4. Proposal and Eurocode 5 formulae in comparison to the experimental results.

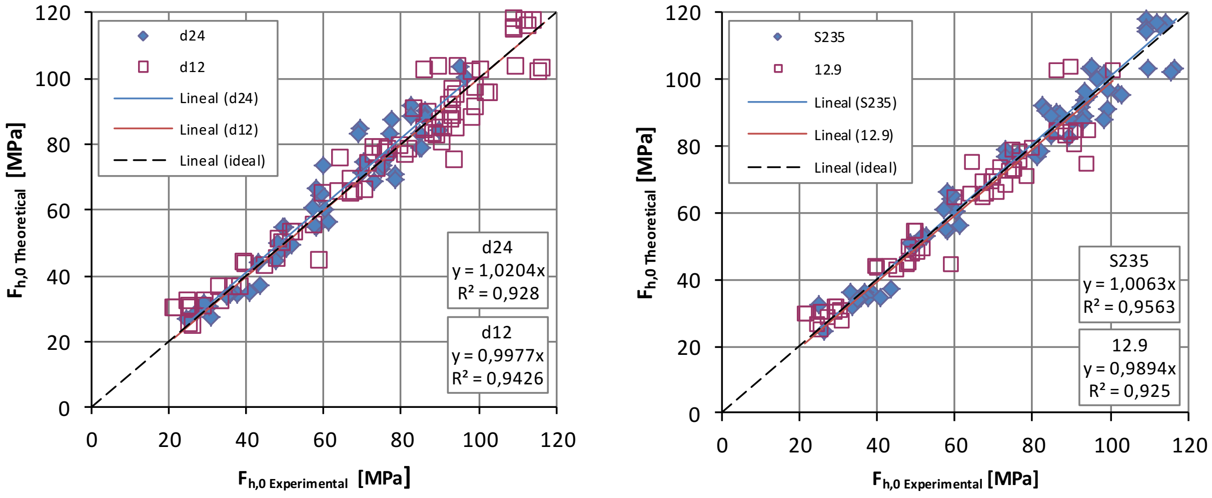

(a) Dowel diameter *(b) Steel grade*

Figure 5. Performance of the proposal against the experimental results. Results classified according to dowel diameter (left) and steel grade (right).

4.2 Validation

4.2.1 Results from Sandhaas (2012)

The correlation of the proposed formula with the experimental results by Sandhaas (2012) is shown in Fig. 4, in comparison to the Eurocode 5 proposal. It is revealed how, since it is a non-linear approach, it provides a better fit to the obtained results for high wood densities.

Figure 5 provides further insight into the performance of the proposal. Theoretical predictions are plotted distinguishing the dowel diameter (Fig. 5.a) and the steel grade (Fig. 5.b). It is shown that for both properties the formula behaves in a similar way, and that there is no significant difference among the different series.

The previously explained proposals in Sect. 2 have also been verified in comparison to the experimental results from Sandhaas (2012). The results for other different proposals are shown in Fig. 6.

Figure 6 shows the comparison between the predicted and the experimental values from Sandhaas (2012) for the proposed formula (11) and other proposals: Eurocode 5 (10), Leijten & Köhler (considering as an approach the average of (6) and (7)), Jumaat *et al.* (5), Sawata & Yasumura (8) and Sandhaas et al. (9). The equation of a linear fitted equation is given as a reference of the mean trend of the predictions.

The proposed formula provides the least mean error. Sawata & Yasumura obtain the lowest error from the remaining formulae, while the Eurocode 5 proposal is the most conservative, and obtains the highest error.Leitjen & Köhler, Jumaat et al. and Sandhaas et al. provide quite a similar mean error.

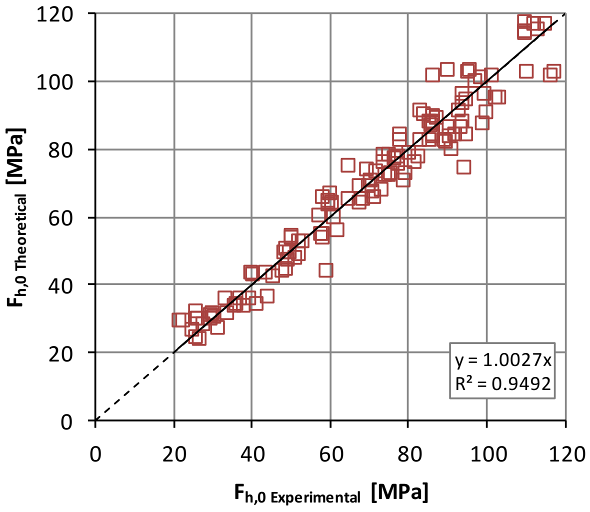

(a) Proposal

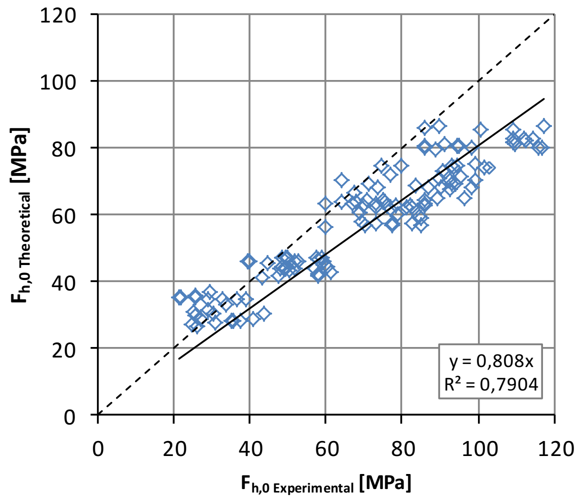

(b) Eurocode 5

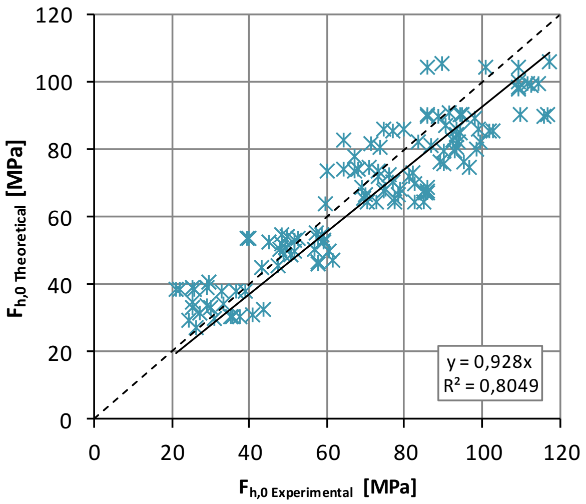

(c) Leijten & Köhler

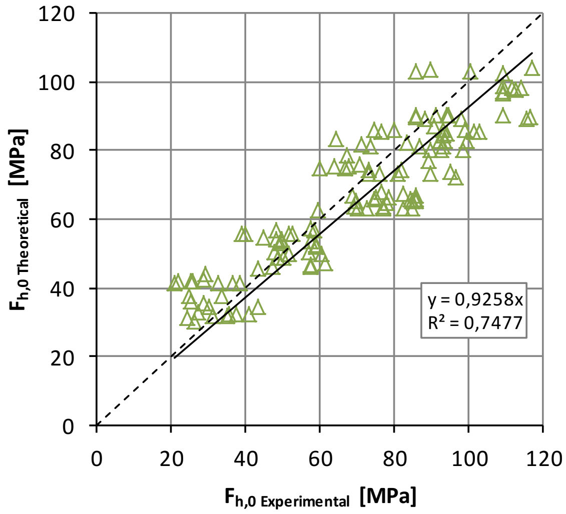

(d) Jumaat et al.

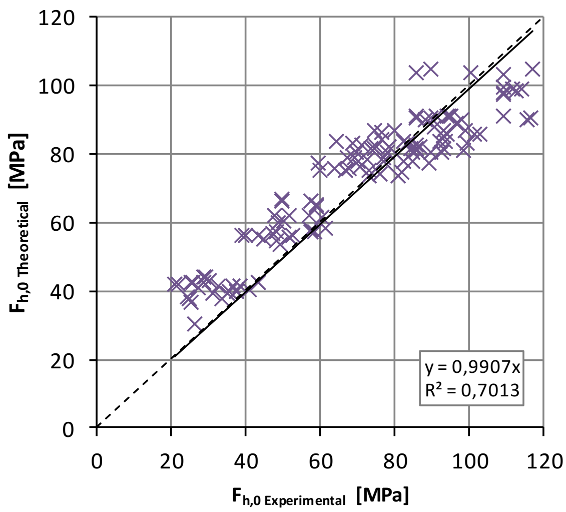

(e) Sawata & Yasumura

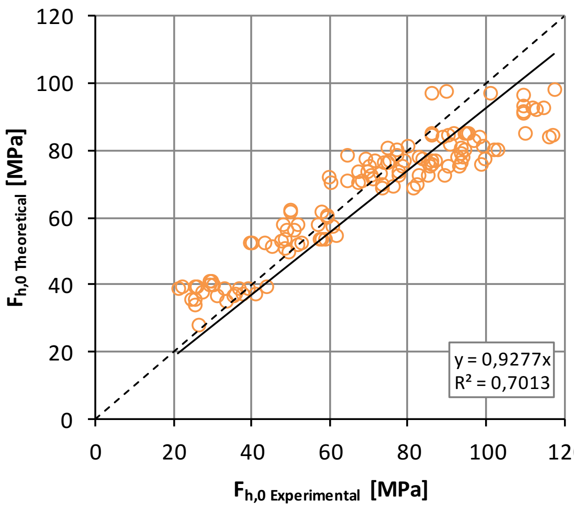

(f) Sandhaas et al.

Figure 6. Correlation of the different formulae against the experimental results by Sandhaas (2012).

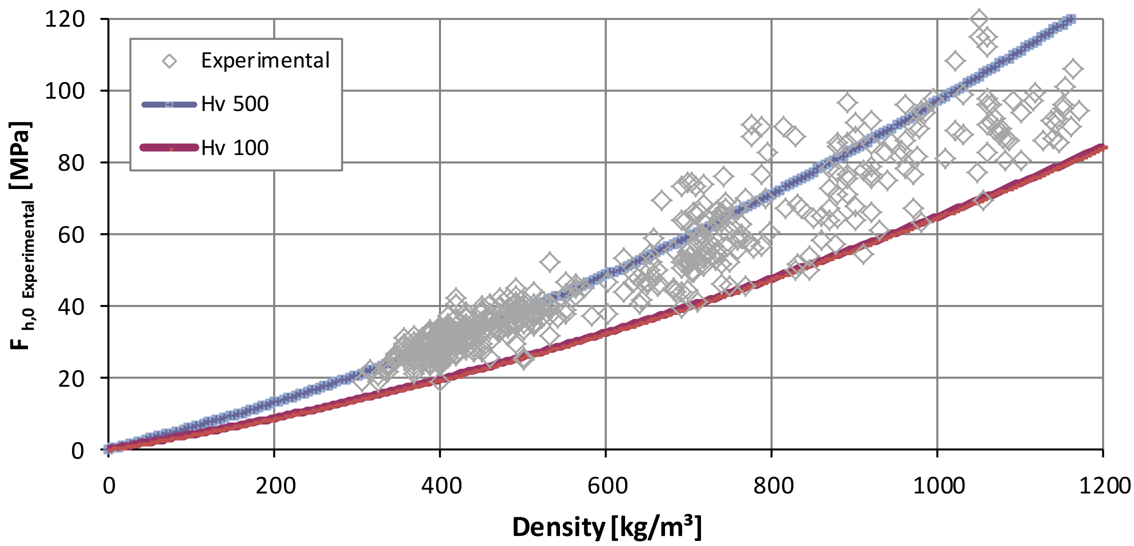

Figure 7. Prediction of the proposed formula (11) for two different limit hardness values: low (HV=100, fy=253 MPa), and high (HV=500, fy = 1264MPa).

4.2.2 Database from Leijten & Kohler (2004)

Having calibrated the proposed formula against the results from Sandhaas (2012), the formula was additionally validated (no fitting procedure was done in this second phase) against experimental embedment tests given in literature. To that mean, the comprehensive database compiled by Leijten & Köhler (2004) was used as reference. With exception of the tests from Whale & Smith (1986), all the remaining compiled test results (Ehlbeck & Werner, 1992; Vreeswijk, 2003; Sawata & Yasumura 2003) were from dowels.

The compiled tests do not provide information on the Vickers hardness of the dowel, and therefore, hypothetical hardness values are taken. As a proof of concept, two limit hardness values are shown in Figure 7: a low of HV = 100 (corresponding to f_y = 253 MPa), and a high boundary of HV=500 (f_y = 1264 MPa). The experimental results fall mostly within these two limit lines, proving the feasibility of the proposed approach. Moreover, the resulting non-linear prediction fits well into the experimental results.

5 Conclusions

Many different proposals have been made for the determination of the wood embedment strength. It has mainly been considered as a timber property, and therefore it is clear that timber density is a main parameter. Some authors proposed to take into account the dowel diameter as well, although recent proposals (Sandhaas *et al.*, 2013) and the herein presented proposal do not agree with such relationship.

But, actually, embedment strength is a quite complicated mechanism to understand, and it could be related to the contact phenomena arising in the contact surfaces of timber and the fastener, as proved in other works where a relationship with roughness (i.e. Sjödin *et al.,* 2008), or in the results (like the presented here) coming from the tests from Sandhaas (2012), where instead of roughness, hardness was found to possibly influence the resulting strength.

The herein presented proposal was calibrated against the experimental results from Sandhaas (2012), and further validated against the comprehensive database from Leijten & Köhler (2004), providing reliable predictions.

This work is yet to be finished, but it raises the attention to a crucial point. Although we do not necessarily think hardness is possibly the related parameter, it does point our attention towards the contact between timber and steel. As stated by Ehlbeck & Hemmer (1992), embedment strength should not be considered a timber property, but a *system property*. And it is necessary to provide insight into it in order to obtain a reliable formula.

Moreover, it would be advisable (although it seems not an easy task) to derive a proposal with some physical meaning, such as that already proposed by van der Put (2008) for particle boards.

Future works will aim to experimentally verify the observed trend with dowels made from materials of different hardness, and the possible influence of other usually dismissed parameters of the experimental setup, such as the geometrical configuration. On the other hand, it is intended to develop analytical and numerical models to provide further insight into the embedment process.

Acknowledgements

The first author is supported by a PhD fellowship from the Programa de Becas FPU del Ministerio de Educación y Ciencia (Spain) under the grant agreement FPU15/03413. The authors would like to acknowledge the contribution of the COST Action FP1402.

6 References

Cahoon, J. R.; Broughton, W. H. & Kutzak, A. R. (1971): The determination of yield strength from hardness measurements, Metallurgical Transactions 2 (7) 1979–1983.

Ehlbeck, J. & Werner, H. (1992): Softwood and Hardwood Embedding Strength for Dowel-type Fasteners. CIBW-18, 25-7-2.

Eurocode 5 (2004): Design of timber structures – Part 1-1: General and rules for buildings. CEN. (EN 1995-1-1).

Fahlbusch (1949): Ein Beitrag zur Frage der Tragfähigkeit von Bolzen. Holz bei statischer Belastung. Master's thesis, Braunschweig. Technische Hochschule Braunschweig, Promotionsarbeit.

Johansen, K. W. (1949): Theory of Timber Connections. International Association of Bridge and Structural Engineering, 9, 249-262.

Jumaat, M. Z.; Hazim, A. & Rahim, A. (2006): The Determination of the Embedment Strength of Malaysian Hardwood. *Proceedings of the 9th World Conference on Timber Engineering, WCTE Portland, USA,* 126.

Leijten, A. J. M. & Köhler, J. (2004): Evaluation of Embedment Strength Data for Reliability Analyses of connections. CIB W-37, 7–12.

NDS (2015): National Design Specification for Wood Construction. American Wood Council, ISBN 9781940383057.

NZS 3603 Revision (2105). Connections – Chapter 4.

Norén, B. (1974): Formulas indicating the strength of mechanical wood joints. Swedish Forest Products Research Laboratory, 226B.

Sandhaas, C. (2012) Mechanical Behaviour of Timber Joints with Slotted-in Steel Plates.Ph.D. Thesis, TU Delft.

Sandhaas, C.; Ravenshorst, G. J. P.; Blass, H. J. & Van De Kuilen, J. W. G. (2013): Embedment tests parallel-to-grain and ductility aspects using various wood species. European Journal of Wood and Wood Products 71 (5) 599–608.

Sawata, K. & Yasumura, M. (2002): Determination of embedding strength of wood for dowel-type fasteners. Journal of Wood Science 48, 138–146.

Sawata, K. & Yasumura, M. (2003): Estimation of yield and ultimate strengths of bolted timber joints by nonlinear analysis and yield theory. Journal of Wood Science 49 (5) 383-391.

Sjödin, J.; Serrano, E. & Enquist, B. (2008): Experimentelle und Rechnerische Untersuchung des Einflusses von Reibung in Verbindungen mit einem Stabdübel. Holz als Roh - und Werkstoff 66 (5) 363–372.

Van der Put, T.A.C.M. (2008) Explanation of the embedding strength of particle board, Holz als Roh- und Werkstoff 66, 259-265.

Vreeswijk, B. (2003): Verbindingen in Hardhout. Master Thesis, TU Delft.

Whale, L. R. J. & Smith, I. (1983): Mechanical timber joints, embedment tests. Report and Annex to Final report of DOE-project, TRADA.

Discussion

The paper was presented by J M Cabrero

R Jockwer asked about the embedment strength as a system parameter. How could one use this information as the parameter for the capacity of joints as there could be other non-linear effects in the joint. JM Cabrero stated that they were trying to verify the embedment strength and check the results against design provisions.

H Blass stated that it was unreasonable to use yield strength. He also commented on how would one test hardness influence on embedment strength. It would be difficult to accept this as it was not a parameter that could physically explain the differences.

S Aicher agreed with H Blass's comment. He stated however that the results seemed to indicate hardness as a parameter provided the best fit; hence, there could be some indication that hardness might be important.

JWG van de Kuilen discussed some of the past test results of hardwood where achieving the target moisture content was difficult. The decision to ignore dowel diameter in estimating embedment strength was an engineering decision. JM Cabrero agreed and stated they might consider such issues in the future.

A Salenikovich received clarification about the smallest diameter of dowel considered was 8 mm. He questioned also what was measured, for example in the perpendicular to grain case was it the maximum load?

JWG van de Kuilen commented that the quality of hole surface could have strong influence on the results.

P Quenneville asked why some of the data was ignored. JM Cabrero stated they did not fit. JWG van de Kuilen said that some of the data might be based on ½ hole tests and some on full hole tests; therefore, some of the data would not fit.

Nailed joints: Investigation on parameters for Johansen model

Carmen Sandhaas, Karlsruhe Institute of Technology

Rainer Görlacher, Karlsruhe Institute of Technology

Keywords: nail, Johansen model, yield moment, tension strength, withdrawal, head pull-through

1 Introduction

In Eurocode 5, nailed joints are designed using the Johansen model extended with the rope effect, the so-called European Yield Model (EYM). Necessary input parameters are hence, apart from geometrical data, embedment strength f_h, yield moment M_y and withdrawal and head pull-through capacity F_{ax} resp. F_{head}. Generally, empirical equations based on regression analyses have been derived for all four parameters f_h, M_y, F_{ax} and F_{head}. However, especially for ring shank nails, no consistent rules are given in the current version of Eurocode 5. Values for yield moments or withdrawal parameters, for instance, must be taken from technical documents of the single nails. This is not only cumbersome for practitioners, it also requires a considerable testing effort from producers.

The aim of this contribution is to propose more straightforward equations regarding the parameters wire tension strength f_u, nail tension capacity F_t, yield moment M_y, withdrawal parameter f_{ax} and head pull-through parameter f_{head}, which have to be experimentally established in current certification practice. Based on an extensive database comprising more than 8000 test results carried out for certification purposes, regression analyses have been carried out. Potential benefits are more robust design models covering a large range of nails, reduced testing and simplified design equations. Prerequisite to all derived equations are sufficient spacings and end and edge distances to avoid splitting.

2 State of the art

Joint design in the current Eurocode 5 is based on Johansen's model [1] that firstly had been applied to nailed joints by Moeller [2]. Since then, considerable research effort has been put into further development of methods to establish the ultimate characteristic load and deformation behaviour as discussed in Ehlbeck [3], who gives a concise and comprehensive summary of the state of the art in the late seventies. Ehlbeck already discussed input parameters necessary for the design of nailed joints such as embedment strength and yield moment as well as the contribution of the rope effect to the joint capacity and hence the withdrawal performance of non-smooth shank nails. The background discussed by Ehlbeck is still representative today as research efforts concerning bolted and screwed joints have been and still are in the focus whereas nailed joints are less represented in current research. An exception to this is the work done by Whale and Smith in the eighties concerning embedment strength [4, 5] and investigations by Blaß in the early nineties concerning group effects in nailed joints [6, 7].

In current certification practice, all five parameters, f_u, M_y, F_t, f_{ax} and f_{head}, are tested according to EN 14592 where a minimum value for the wire strength of f_u = 600 MPa is required. The evaluated values on the characteristic level are then declared in technical documents. For smooth shank nails however, the characteristic yield moment $M_{y,Rk}$ can also be calculated. For round nails for instance, Eurocode 5 gives the following Eq. (1):

$$M_{y,Rk} = 0.3 \cdot f_u \cdot d^{2.6} \tag{1}$$

where f_u is the wire tension strength and d is the nominal nail diameter.

Eq. (1) is based on work done by Werner and Siebert [8] and it is valid only when a tension strength of the wire of 600 MPa is inserted. This value of 600 MPa is mandatory even if the actual value is higher which is the case for diameters less than 4 mm. The exponent of 2.6 in Eq. (1) reflects an observed increase of yield strength (up to 1000 MPa for 2 mm nails) with decreasing nail diameter which can be explained with work hardening due to cold drawing.

Also for the parameters f_{ax} and f_{head}, regression equations are given in Eurocode 5 for short term loaded smooth shank nails:

$$f_{ax,k} = 20 \cdot 10^{-6} \cdot \rho_k^2 \quad \text{and} \quad f_{head,k} = 70 \cdot 10^{-6} \cdot \rho_k^2 \tag{2}$$

The withdrawal and head pull-through parameters for non-smooth shank nails are, analogously to M_y and F_t, defined in the individual declarations of performance of the producers. Considering the head pull-through parameter, this applies although the head shape may be the same for non-smooth and smooth shank nails.

3 Database

The global database consists of in total 8416 tests taken from 96 reports on mostly ring shank nails (rings 77%, threads 5%) and wires (11%). Special ring shank nails with smooth intermediate shanks as shown in Figure 1 on the left constituted 5.3% of the overall database, whereas smooth shank nails constituted only 1% of the database and square nails only 0.3%. For smooth shank nails, only wire strength was tested and no other parameters are available. Nails from 33 different producers were considered and the tests were carried out between 1997 and 2013. It is not considered useful to enlarge the database with older results as both steel grades and production technologies may have changed since then and any analyses would not be representative of modern nails. The geometrical properties given in Figure 1 on the right are also recorded in the database. The number of tests per parameter is given in Table 1. As properties of nails made from stainless steel do not differ significantly from all other nails, see for example Figure 2, no difference will be made in analyses.

With regards to the individual parameters, wire strength f_u, calculated with the wire diameter, and nail tension capacity F_t are measured maximum values. The given yield moment M_y is the value at a measured deformation angle of 45° or the reached maximum bending angle before rupture of the nails. It has to be reminded here that issues around test execution and preciseness of measured angles lead to uncertainties about the measured values as for instance, machine slip as well as elastic bending is included in the measurement during testing [9]. Withdrawal capacity F_{ax} and head pull-through capacity F_{head} were evaluated using softwood (*Picea abies*), stored at 65/20 and with the recorded densities. F_{ax} again is the measured maximum value whereas F_{head} is the maximum value or the value at a deformation of the testing machine of 15 mm.

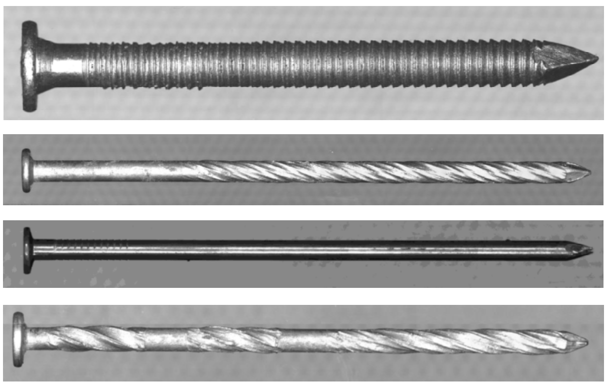

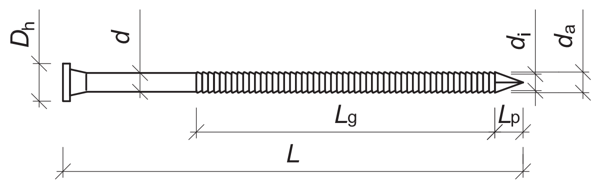

Figure 1. Left: Nail shapes in database. From top to bottom: ring shank nail, spiral nail, smooth shank nail, special spiral nail. Right: Geometrical properties with d = nominal nail diameter, d_i = inner diameter, d_a = outer diameter, D_h = head diameter, L_g = length of non-smooth shank, L_p = tip length.

Table 1. *Composition of database.*

	Wire tension strength f_u	Yield moment M_y^+	Nail tension capacity F_t	Withdrawal capacity F_{ax}	Head pull-through capacity $F_{head}^{\#}$
No. of tests	1076	2844	1160	2316	1020
Of which stainless steel	203	369	195	300	60
Of which hdg*	-	265	178	310	220

* hdg = hot-dip galvanised, + M_y measured at $\alpha = 45°$, # F_{head} at maximum value or value at a slip of 15 mm (slip of testing machine), whichever comes first.

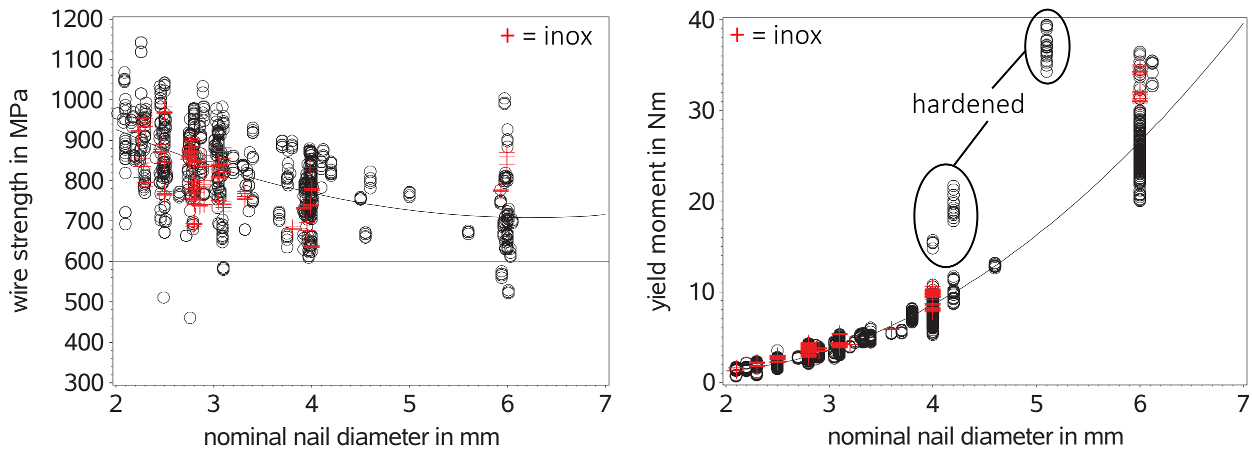

Figure 2. *Influence of stainless steel on wire strength (left) and on yield moment (right). Experimental values are shown and on the right, hardened nails are identified.*

4 Analysis and discussion

4.1 Wire strength and tension capacity

Similar to Werner and Siebert [8], a decrease of wire and nail strength with increasing diameter can be found back in Figure 3 where the nail strength $f_{u,nail}$ has been calculated using the tension capacity F_t and the nominal diameter d. The nail tension strength calculated with the nominal diameter d (and not with the inner diameter d_i) is slightly lower than the original wire strength. The decrease of tension strength with increasing diameter can be explained with work hardening due to cold drawing. As multiple passes are needed for smaller diameter nails, strength values are increasing with decreasing diameter.

For design purposes, wire strength tests are not needed. Tension tests on nails are sufficient to guarantee tension properties, calculated with the nominal diameter d. Producers may need wire tests however in order to control delivered steel grades. Furthermore, the significant difference between bright wire tension strength and subsequent tension strength of hot-dip galvanised (hdg) nails, the crosses in Figure 3, is obvious, especially for small diameter nails where a major part of the diameter is affected by heat. For hot-dip galvanised nails, it is indispensable to carry out tension tests on finished nails as wire strength has no significance. The same applies to hardened nails (special nails) where the wire strength is not correlated to the nail strength.

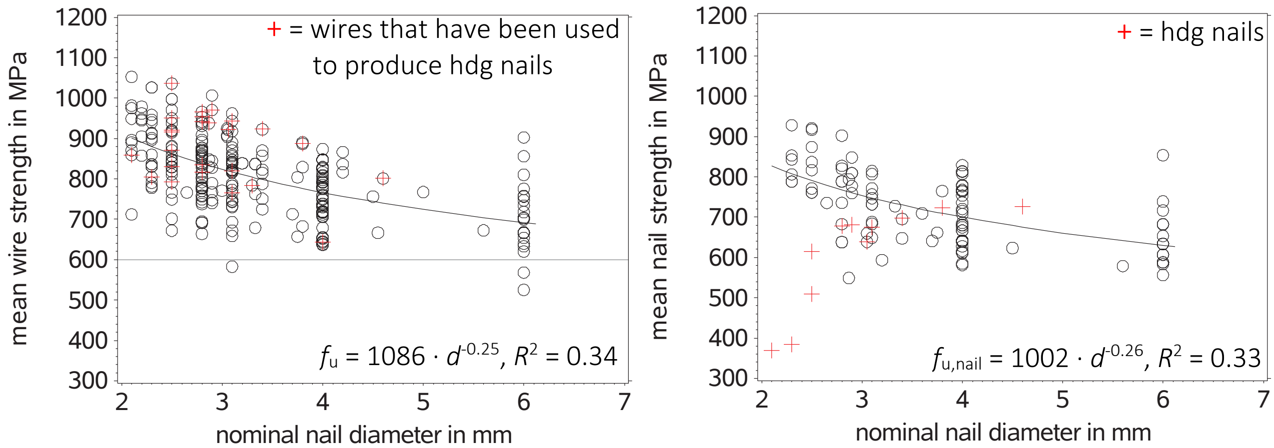

Figure 3. Left: Mean tension strength of wire versus nominal nail diameter d. Right: Mean tension strength of nail calculated with F_t and nominal diameter d. Data from 78 test series (403 single tests f_u, 916 single tests F_t). Regression excludes hdg nails.

4.2 Yield moment

A nonlinear regression analysis to derive an expression for M_y has been carried out. The dependent variables have been the nominal diameter d and $f_{u,nail}$ which is the tension strength calculated from the nail tension capacity F_t and the nominal diameter d. Only such a procedure is realistic as both inner diameter d_i and yield strength f_y are unknown values in practice. As an assignment of single M_y values to single F_t values within one testing series is not possible, mean values of both M_y and $f_{u,nail}$ form the basis of the regression analysis. The influence of nail types and steel qualities on the resulting regression equation has been investigated where no significant differences were observed (differences in independent variables of max 1.6%). Therefore, no differentiation has been made within the database, e. g. with respect to different nail types or normal and stainless steel. The hardened nails highlighted in Figure 2 on the right could not be included in the analysis as on these nails, only M_y has been tested and no data was available to calculate $f_{u,nail}$. It is expected that they would fit in the following equations if their actual tension strength would be used, which could be experimentally determined very easily. The nonlinear regression based on mean values of 105 test series resulted to (with R^2 = 0.995):

$$M_y = 0.185 \cdot f_{u,nail} \cdot d^{2.99} \tag{3}$$

Figure 4 on the left shows the experimental versus the predicted values. The very good agreement between tests and model resulting in a bisect line with small scatter can be seen. Eq. (3) is similar to the mechanical equation for a full plastic moment of a round section, Eq. (4):

$$M_{pl} = \frac{1}{6} \cdot f_y \cdot d^3 \tag{4}$$

Blaß and Colling [10] proposed Eq. (4) to calculate the yield moment of dowels considering an effective yield strength $f_{y,ef}$. Analogously, the following Eq. (5) is proposed for nails:

$$M_y = \frac{1}{6} \cdot f_{y,ef} \cdot d^3 \quad \text{with} \quad f_{y,ef} = f_{u,nail} \tag{5}$$

Figure 4 on the right shows the ratio between the individual experimental results and the calculated values using Eq. (5) and the mean nail tension strength $f_{u,nail,\ mean}$ per series. The observed 5-percentile of the ratio is 0.995 (64 of 1034 ratios are smaller than 1) and therefore, the 5-percentile is slightly exceeded.

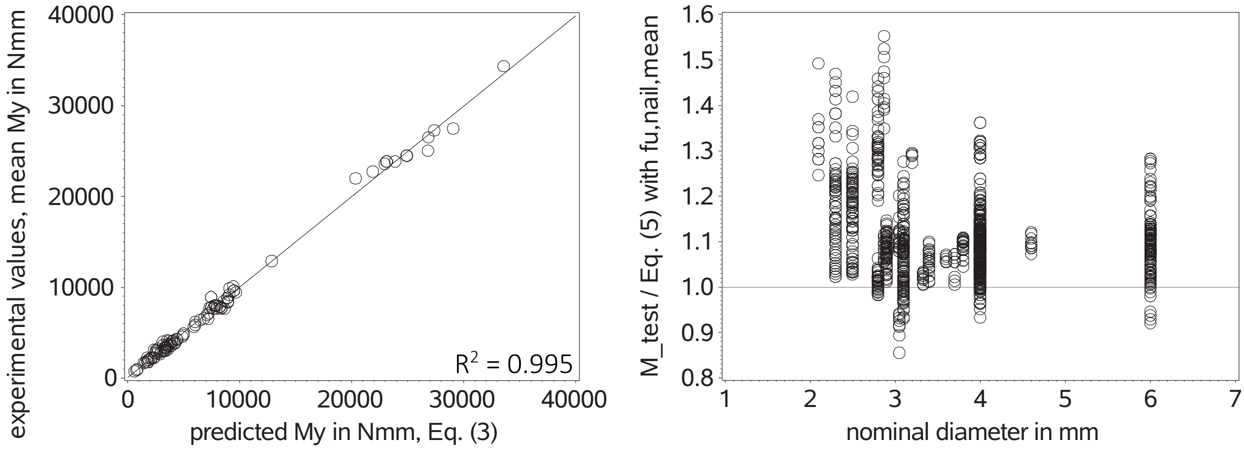

Figure 4. *Left: Experimental and predicted values (Eq. (3)) for the yield moment M_y.*
Right: The y-axis shows the ratio of individual experimentally determined yield moments over calculated yield moments using Eq. (5) and the mean nail tension strength values $f_{u,nail,mean}$ per series. The x-axis shows the nominal nail diameter.
Data from 105 test series (1034 single tests M_y, 1035 single tests F_t).

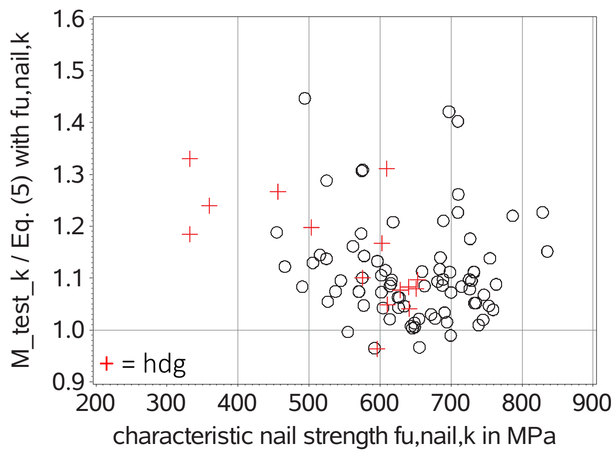

Figure 5. *Ratio between characteristic experimental and characteristic calculated yield moments (Eq. (5)) in dependence of the characteristic nail tension strength $f_{u,nail,k}$. Data from 105 test series (1034 single tests M_y, 1035 single tests F_t).*

Based on the procedure prescribed in EN 14358 [11], 5-percentile values have been estimated. The characteristic values were calculated from the test values assuming a lognormal distribution and a standard deviation of $s_y = 0.05$ for both the yield moment and the tension strength. This makes sense because both values are describing the same steel property and the differences in the variation are random. Figure 5 shows the ratio between experimental and calculated yield moments using Eq. (5) versus the characteristic nail tension strength $f_{u,nail,k}$. The ratio is based on characteristic values $M_{y,k}$ per test series and Eq. (5) with $f_{u,nail,k}$. The 5-percentile of the ratio is 1.00. Eq. (5) is therefore reflecting accurately the relationship between tension strength, nail diameter and yield moment and it is able to predict the characteristic yield moment $M_{y,k}$ using $f_{u,nail,k}$ as characteristic effective yield strength.

Figure 5 also shows that the characteristic tension strength of the nails varies in a wide range and it would hence not be economically efficient to define a minimum tension strength for all nails. It would rather be reasonable to define technical classes to calculate the characteristic yield moment with a characteristic effective yield strength $f_{y,ef,k}$ which is based on characteristic tension strength values, see vertical lines in Figure 5.

Concerning Eurocode 5, three options to regulate the yield moment of nails exist:

- No equation is given and the practitioners have to take the characteristic yield moments from the individual declarations of performance.
- Eq. (5) is inserted in Eurocode 5 where the characteristic tension strength $f_{u,nail,k}$ has to be taken from the declarations of performance.
- Technical classes are defined prescribing different characteristic tension strength values, where however, additional notes need to be given similar to prEN 14592 [12]. For instance, it must be clearly stated that small diameter nails may have significantly higher tension strength values than 6 mm nails (see also Figure 3 on the right). Table 2 gives some examples on how such classes could be defined.

Table 2. Possible definition of technical yield strength classes (YSC) for effective yield strength $f_{y,ef}$ (in MPa) of dowel-type fasteners.

YSC1	**YSC2**	**YSC3**	**YSC4**	**YSC5**	**YSC6**	**YSC7**
300	400	500	600	700	800	900
Mild steel dowels						
hdg nails	-	d = 6 mm →			d = 2 mm	
						Staples

4.3 Withdrawal parameter

For dowel type fasteners, the withdrawal parameter f_{ax} is calculated from the withdrawal capacity F_{ax} by the following equation:

$$f_{ax} = \frac{F_{ax}}{d \cdot L_{ef}} \tag{6}$$

where d is the nominal diameter and L_{ef} is defined as the length of the threaded part in the pointside member ($L_{ef} = t_{pen}$ (acc. EC 5 [13]) $= l_d$ (acc. EN 1382 [14])). That means that the tip of the nails has to be subtracted from the penetration length. Figure 6 shows the tip length L_p versus the nail diameter d of all test data. The tip length is between d and $2 \cdot d$ with a mean value of $1.4 \cdot d$.

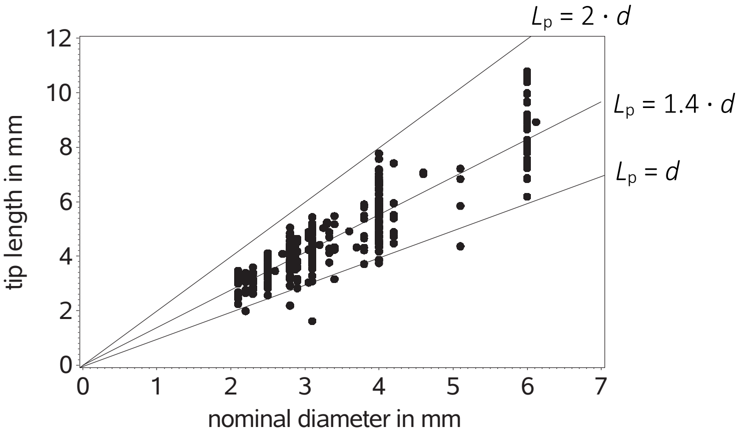

Figure 6. Tip length L_p versus nominal diameter d, 5483 values (L_p has not always been recorded).

Pearson's correlation coefficients of f_{ax} are given in Table 3. The influence of L_{ef}, L_p and d is weak and also the ring depth, which is expressed as the ratio between inner (d_i) and outer (d_a) diameter, shows no correlation (R = -0.00) with f_{ax}. Only the density correlates with f_{ax} (R = 0.33). For most types of fasteners, the withdrawal parameter is indeed a function of the wood density, as can be seen in Eq. (2). Figure 7 shows f_{ax} in dependence of ρ_{ax}. It can be seen that the range of tested densities is not fully representative for all softwood strength classes according to EN 338 [15] where classes with densities below 300 kg/m³ and higher than 500 kg/m³ exist, while the test values are between 329 and 472 kg/m³.

In order to give a closer look to the relationship between f_{ax} and ρ_{ax}, a nonlinear regression has been carried out (R^2 = 0.11) which is shown in Figure 7 and which corresponds to prEN 14592 [12]:

$$f_{ax} = 3.6 \cdot 10^{-3} \cdot \rho^{1.38} \tag{7}$$

Table 3. Correlation matrix for withdrawal parameter.

	ρ_{ax}	L_{ef}	d	ratio d_i/d_a	L_p
f_{ax}	**0.33**	-0.02	-0.18	-0.00	-0.20

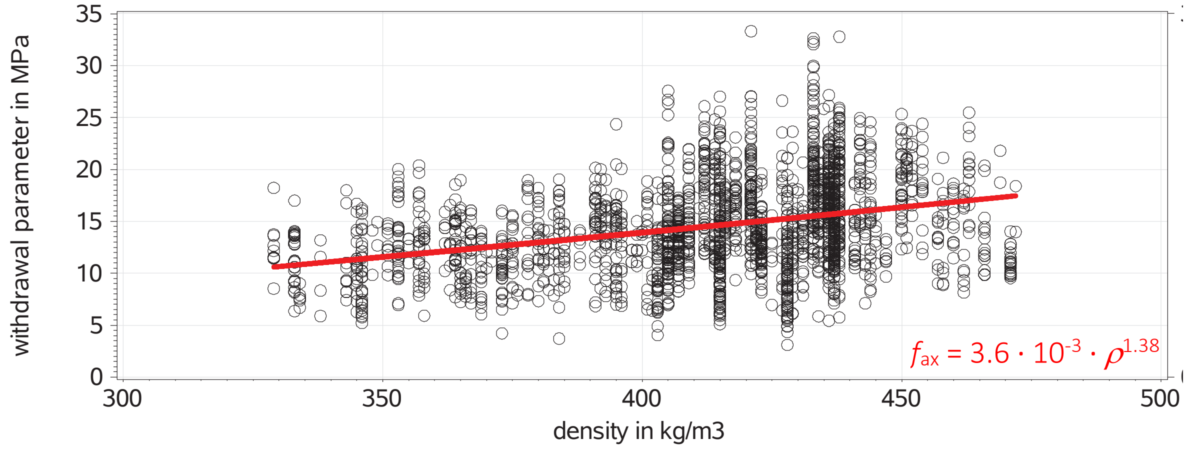

Figure 7. Withdrawal parameter versus density, 2316 tests.

Still, with a correlation coefficient of 0.33 and a R^2-value of 0.11, the scatter is rather high and the relationship between f_{ax} and ρ_{ax} is not very strong. One reason for this is that the differences between the nails of different producers are much higher than the differences caused by the density. This is visualised in Figure 8 were the withdrawal parameters are given per test series with increasing nominal diameters. In Figure 8, it can be also seen that the scatter within one test series is smaller for 4 to 6 mm nails than for smaller diameter nails. Additional influence effects were observed during testing. For instance, it has been observed that rather non-measurable factors guarantee good withdrawal parameters. Above all, the sharpness of the rings that can be felt when passing the nails through the fingers defines good performance. In the database, no information is available concerning the quality and sharpness of the rings or threads, and measuring it would increase testing efforts considerably.

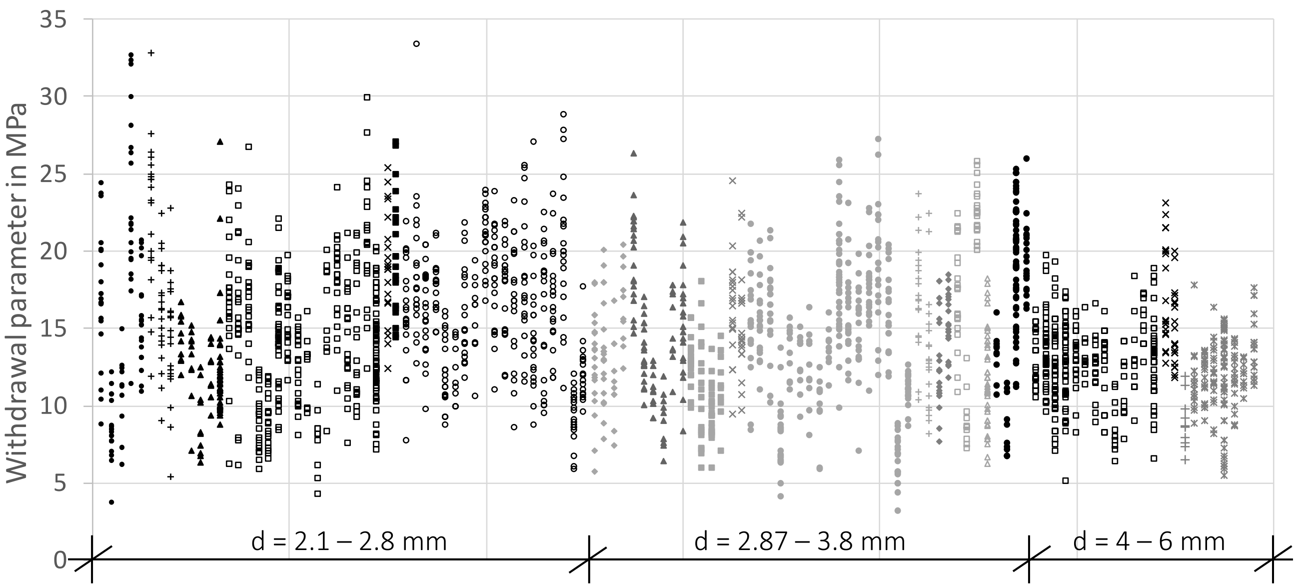

Figure 8. 2316 withdrawal parameters are shown per test series and with increasing diameters.

Based on the procedure prescribed in EN 14358 [11], 5-percentile values have been estimated assuming a lognormal distribution. The individual withdrawal parameters have been adjusted to a reference density of ρ_{ref} = 350 kg/m^3 using Eq. (7):

$$f_{\mathrm{ax,corr}} = f_{\mathrm{ax}} \cdot \left(\frac{350}{\rho_{\mathrm{ax}}} \right)^{1.38} \tag{8}$$

Figure 9 shows the characteristic withdrawal parameter $f_{ax,k}$ per test series versus the nominal diameter and the five nail types are identified. Spiral, special spiral and square nails did not reach characteristic values larger than 8 MPa. Furthermore, the scatter is higher for smaller diameter nails which has already been seen in Figure 8.

Based on the actual database and the analyses shown, it can be concluded that also in future, tests have to be carried out and values for f_{ax} have to be taken from technical documents. At the moment, no test results are available where one nail type has been tested using a large range of wood densities or where the detailed nail geometry including information on the ring sharpness has been measured. Consequently, no thorough analyses can be carried out concerning these influence parameters.

With regard to code implementation, technical classes could be introduced so that designers do not need to consult declarations of performance to get withdrawal parameters. The horizontal lines in Figure 9 correspond to the withdrawal classes for all fastener types in accordance with prEN 14592 [12], where values of 4.5, 6, 7, 8, 10 and 12 MPa are given. The decrease of variation with increasing diameter is observed also on the 5-percentile level. Considering the still persistent high scatter in Figs. 7 to 9, the necessity of determining f_{ax} with the effective penetration depth (i. e. subtracting the tip length) for joint design purposes remains worth discussing. If a nonlinear regression is carried out where f_{ax} is calculated with the full penetration depth, differences of 10% to 20% to Eq. (7) are evaluated which disappear in the scatter within one diameter or density range.

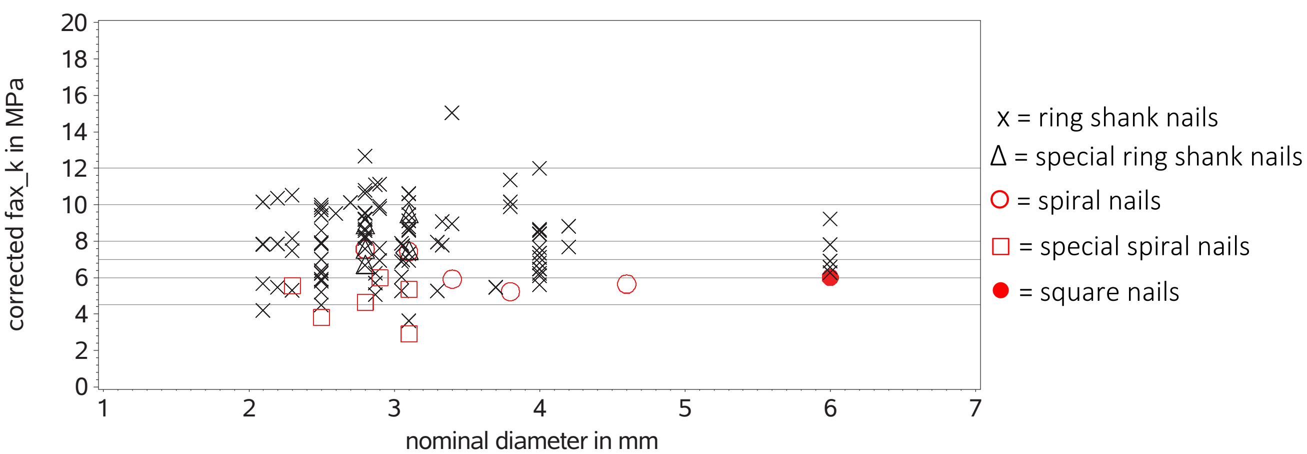

Figure 9. Characteristic withdrawal parameter f_{ax} versus nominal diameter. f_{ax} has been corrected with $(350/\rho_{ax})^{1.38}$. Withdrawal classes from prEN 14592 [12] are shown, see horizontal lines at 4.5, 6, 7, 8, 10 and 12 MPa. Data from 118 test series (2316 single tests f_{ax}).

4.4 Head pull-through parameter

Similar to the withdrawal parameter, also the head pull-through parameter is considered to be a function of the wood density, Eq. (2). Therefore, again a correlation between head pull-through parameter f_{head} and density ρ_{head}, Table 4 and Figure 10, has been carried out, where f_{head} has been calculated as follows with D_h = head diameter:

$$f_{head} = \frac{F_{head}}{D_h^2} \tag{9}$$

Table 4. Correlation matrix for head pull-through.

	ρ_{head}	D_h	d	D_h/d
f_{head}	**0.52**	-0.27	-0.27	0.08

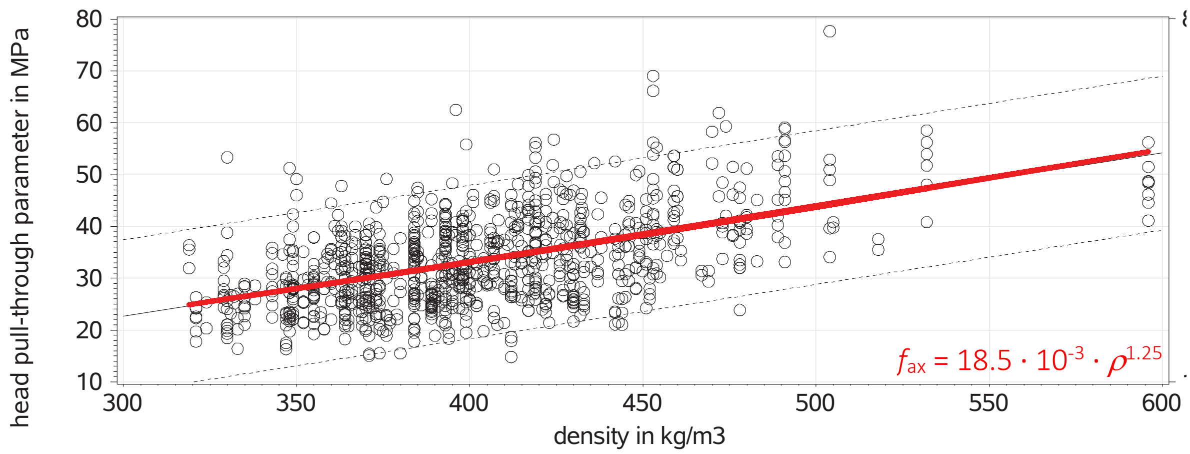

Figure 10. Head pull-through parameter versus density, 1020 single tests.

Considering Table 4, the ratio of head diameter D_h over nominal diameter d (where D_h is approximately 2 · d) shows no influence on f_{head}. The head shape however may have an influence, but this parameter has not been recorded. No head pull-through tests were carried out using standard ring shank nails with trumpet heads that are used to fasten steel plates. Table 4 gives a Pearson's correlation coefficient for the density of R = 0.52 and Eq. (10) gives the result of a nonlinear regression considering the complete database of 1020 results (with R^2 = 0.28). Eq. (10) is shown in Figure 10.

$$f_{head} = 18.5 \cdot 10^{-3} \cdot \rho^{1.25} \tag{10}$$

If the same regression is carried out excluding the few results for high densities > 550 kg/m³, Eq. (10) does not change significantly and gives slightly lower values of f_{head} for higher densities (difference at 500 kg/m³ is 6%). These slight differences are included in the 95%-confidence interval shown in Figure 10.

Again, based on the procedure prescribed in EN 14358 [11], 5-percentile values have been estimated assuming a lognormal distribution. The individual head pull-through parameters have been adjusted to a reference density of ρ_{ref} = 350 kg/m^3 using Eq. (10):

$$f_{\text{head,corr}} = f_{\text{head}} \cdot \left(\frac{350}{\rho_{\text{head}}} \right)^{1.25} \tag{11}$$

Figure 11 shows the characteristic head pull-through parameter $f_{head,k}$ per test series versus the nominal diameter and the four nail types are identified. Again, the scatter is higher for smaller diameter nails. Figure 11 also shows a decrease of f_{head} with increasing nail diameter which can be also concluded from Table 4 where the correlation coefficient for d (and its related parameter D_h) is -0.27 indicating a relationship between f_{head} and diameter.

Similar to the withdrawal parameter and based on the actual database and the analyses shown, it can be concluded that also in future, tests have to be carried out and values for f_{head} have to be taken from technical documents. With regard to code implementation, technical classes could be introduced also for head pull-through. The horizontal lines in Figure 11 correspond to the withdrawal classes for all fastener types in accordance with prEN 14592 [12], where values of 10, 12.5, 15, 18, 20, 25 and 30 MPa are given. Considering the persistent scatter of f_{head} in Figure 11 although head shapes do not differ significantly (round and flat shape and D_h approx. $2 \cdot d$), the random selection of the used timber seems to have a significant influence. Parameters such as annual ring widths and orientation of tangential and radial directions may impact on the experimental values and the question remains if high f_{head} values above 20 MPa are reliable. A lower bound value of 15 MPa seems to be possible which could be used, without further testing, for all nails with non-smooth shanks as long as $D_h/d > 1.8$.

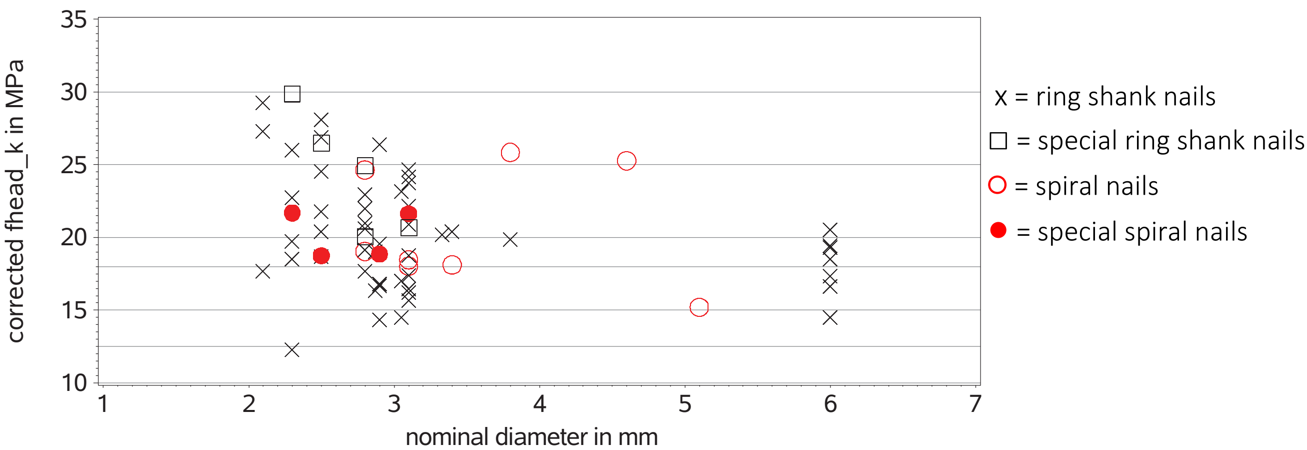

Figure 11. Characteristic head pull-through parameter f_{head} versus nominal diameter. f_{head} has been corrected with $(350/\rho_{head})^{1.25}$. Head pull-through classes from prEN 14592 [12] are shown, see horizontal lines at 10, 12.5, 15, 18, 20, 25 and 30 MPa. Data from 67 test series (1020 single tests f_{ax}).

5 Conclusions

A comprehensive database containing test results on mainly ring shank nails has been analysed. The following recommendations can be given concerning input parameters for joint design in accordance with the European Yield Model:

- Wire tension strength: These tests are not needed. However, producers may still require wire tests to control delivered steel grades.
- Nail tension capacity F_t: Tension tests on finalised nails need to be carried out and subsequently, a nail tension strength $f_{u,nail}$ can be calculated using the nominal diameter. This tension strength corresponds to an "effective yield strength $f_{y,ef}$"
- Yield moment M_y: The equation defining the theoretical full plastic bending capacity of a round section using an effective yield strength, Eq. (5), can be inserted in Eurocode 5 for all nail types except square nails where no tests were available. The nominal diameter and the nail tension strength is needed to calculate the yield moment in accordance with Eq. (5). The nail tension strength must be taken from individual DoPs. Additionally, yield strength classes could be defined giving different nail tension strength values.
- Withdrawal parameter: Considering the analysed database with its limitations, it is proposed to include technical classes in Eurocode 5 to facilitate design of nailed joints. Additionally, individual values can be taken from DoPs.
- Head pull-through parameter: The conclusions are analogous to those for the withdrawal parameter. Also here, the insertion of technical classes is proposed.

6 Acknowledgements

This work has been carried out within COST Action FP1402 and the authors would like to thank Elke Mergny, who started to assemble the database in the framework of a Short Term Scientific Mission which was paid by the same COST Action.

7 References

[1] Johansen KW (1949) *Theory of timber connections.* Publication 9, International Association of Bridge and Structural Engineering (IABSE), Basel, Switzerland.

[2] Moeller T (1951) *En ny metod foer beraekning av spikfoerband.* Handlingar no. 117, Chalmers Tekniska Hoegskola, Göteborg, Sweden.

[3] Ehlbeck J (1979) *Nailed joints in wood structures.* Bulletin no. 166, Wood Research and Wood Construction Laboratory, Virginia Polytechnic Institute and State University, USA.

[4] Whale LRJ, Smith I (1986) *Mechanical timber joints.* Report 18/86, TRADA, High Wycombe, UK.

[5] Whale LRJ, Smith I (1986) The derivation of design clauses for nailed and bolted joints in Eurocode 5. Paper 19-7-6. *CIB-W18 Meeting 19,* Florence, Italy.

[6] Blaß HJ (1990) Load distribution in nailed joints. Paper 23-7-2. *CIB-W18 Meeting 23,* Lisbon, Portugal.

[7] Blaß HJ (1991) Traglastberechnung von Nagelverbindungen. *Holz als Roh- und Werkstoff* **49**(3):91-98. doi:10.1007/BF02614345.

[8] Werner H, Siebert W (1991) Neue Untersuchungen mit Nägeln für den Holzbau. *Holz als Roh- und Werkstoff* **49**(5):191-198.

[9] Steilner M, Blaß HJ (2014) *A method to determine the plastic bending angle of dowel-type fasteners*. In: Aicher S, Reinhardt HW, Garrecht, H (eds) RILEM bookseries. Materials and joints in timber structures. Recent developments in technology. Stuttgart, Germany, pp. 603-613.

[10] Blaß, H. J., Colling, F. (2015) Load-carrying capacity of dowelled connections. Paper 48-7-3, pp. 115-129. *INTER Meeting 48,* Sibenik, Croatia.

[11] EN 14358 (2007) *Timber structures – Calculation of characteristic 5-percentile values and acceptance criteria for a sample*. Comité Européen de Normalisation (CEN), Brussels, Belgium.

[12] prEN 14592 (2017) *Timber structures - Dowel-type fasteners - Requirements*. Comité Européen de Normalisation (CEN), Brussels, Belgium.

[13] EN 1995 1-1 (2010) *Eurocode 5. Design of timber structures - Part 1-1: General -Common rules and rules for buildings*. Comité Européen de Normalisation (CEN), Brussels, Belgium.

[14] EN 1382 (2016) *Timber structures – Test methods – Withdrawal capacity of timber fasteners*. Comité Européen de Normalisation (CEN), Brussels, Belgium.

[15] EN 338 (2009) *Structural timber - Strength classes*. Comité Européen de Normalisation (CEN), Brussels, Belgium.

Discussion

The paper was presented by C Sandhaas

M Li asked about the diameter of nails as larger nails could split the wood. C Sandhaas responded that wood splitting was not recorded in the database.

P Quenneville asked about the issue related to quality of nail production. He said this would be seldom checked and asked how one would propose to check this. C Sandhaas said that this could be considered via careful choice of the maximum value and strict external quality control measurements.

A Salenikovich and C Sandhaas discussed about density control. C Sandhaas said that each nail test had an associated density measurement.

A Buchanan commented on engineered wood products such as LVL when density of the product might not reflect on the quality as the product would be densified during production. C Sandhaas responded in such cases one should conduct tests.

R Jockwer and C Sandhaas discussed in the last slide the COV of each test series that was used. There were test results with high COV. It would be interesting to see the real COV for the proper evaluation of the capacity. C Sandhaas said only if this reflects material property which was however not the case.

Cyclic bending fatigue properties of dowel type fasteners

Kenji Kobayashi, Shizuoka University, Japan

Motoi Yasumura, Shizuoka University, Japan

Keywords: Dowel type fasteners, Cyclic loading, Low cycle fatigue failure

1 Introduction

Joints with dowel type fasteners can realize high ductility with using slender shape fasteners and creating plastic hinges in timber members. Ductility of the joint is especially important regarding seismic performance. Joints have to resist random actions including cyclic loading.

Fasteners like screws have high strength to enable driving in without pre-drilling. But some screws are brittle because of heat treatments. In this case, joints with such screws will be also brittle especially in cyclic loading. It is classified as low cycle fatigue failure. Nails, dowels and bolts are generally more ductile than hardened screws. But they also show fatigue failure by large deformations or many repetitions. Li et al. (2012) and Kobayashi et al. (2016) reported about fatigue failure of the fastener at the joints. EN14592 (2012) and other standards have the requirements about bending angle such as $45/d^{0.7}$ deg., but the angle is introduced for reducing M_y and it is not suitable to evaluate cyclic bending performance.

In this study, we propose fatigue properties evaluated by constant angle cyclic bending tests.

2 Determination of fatigue properties

2.1 Manson-Coffin relationship

Fatigue failure is a weakening of a material caused by the stresses under cyclic loading. Even if the stress is lower than yield stress, high repetition enables the material to failure. This type of failure is called high-cycle fatigue failure. On the other hand, if the stress is higher than yield stress, repetitive plastic strain is applied to the material and it reaches to failure in relatively low number of cycles. This type of failure is called low-cycle fatigue failure.

Low-cycle fatigue failure is expressed by the Manson-Coffin relation;

$$\frac{\Delta\epsilon_p}{2} = \epsilon'_f \cdot (2N)^c \quad (1)$$

where:

$\Delta\epsilon_p/2$: plastic strain amplitude, ϵ'_f: fatigue ductility coefficient, $2N$: number of cycles to failure, *C*: fatigue ductility exponent.

ϵ'_f and *C* are determined empirically. There are derived from the relationship between logarithmic scales of N and $\Delta\epsilon_p$.

Here we assumed that the plastic strain $\epsilon_p$could be simply replaced by a plastic deformation angle γ_p. Equation (1) is changed by replacing ϵ_p to γ_p as follows;

$$\frac{\Delta\gamma_\mathrm{p}}{2} = \gamma_\mathrm{f} \cdot (2N_\mathrm{f})^C \quad (2)$$

where:

$\Delta\gamma_p/2$: plastic deformation angle, $2N_f$: number of cycles to failure, γ_f, *C*: regression coefficients.

Plastic deformation angle was determined by two crossing points to X-axis (point “b” and “d”, see Figure 2.1).

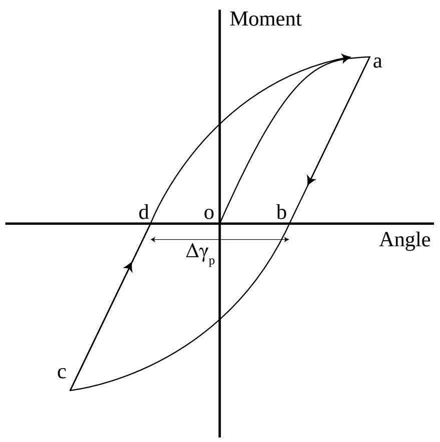

Figure 2.1. Definition of plastic deformation angle.

2.2 Cyclic bending test

2.2.1 Cyclic bending test method

Cyclic bending test was conducted to determine regression coefficients γ_f and *C*. Cyclic bending test method is shown in Figure 2.2. Clamp B has a rotation axis and it can apply reversal cyclic bending deformation to the specimen.

Cyclic bending test apparatus is shown in Figure 2.3. This apparatus is based on the annex A of ISO 10984-1 (2009). Since only monotonic loading is supposed in ISO 10984-1, we modified it to work under reversed loading. An above side of a loading arm is connected to a universal test machine and it can move up and down. Clamp B are connected to the rotation axis and the loading arm. It can apply bending moment to the specimen. Clamp A is connected to one edge of a lever. A load cell is connected to another side of the lever. A hinge and a linear guide enable to move Clamp A freely except rotation, and bending moment from Clamp B is transferred to the load cell as an axial force. Since a self-weight of the lever and Clamp A causes different loading conditions during cyclic tests, a weight is located at the edge of the lever to cancel the self-weight of the lever and Clamp A.

Bending moment at the fastener can be calculated from equation (3);

$$M = (l_6 + l_2)P \tag{3}$$

where:

M: bending moment at the fastener (Nmm), l_6: horizontal distance between the load cell and the tip of Clamp A (mm), l_2: distance between the Clamps A and B (mm), P: measured load by the load cell (N).

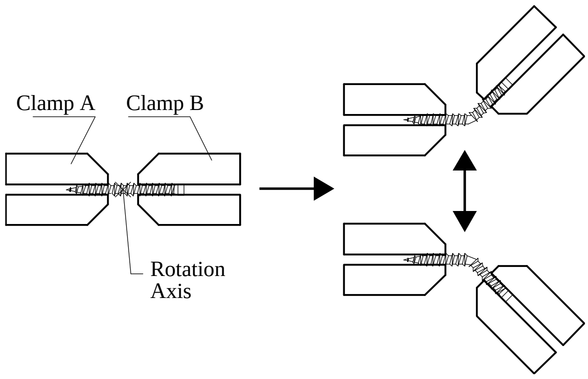

Figure 2.2. An image of cyclic bending test.

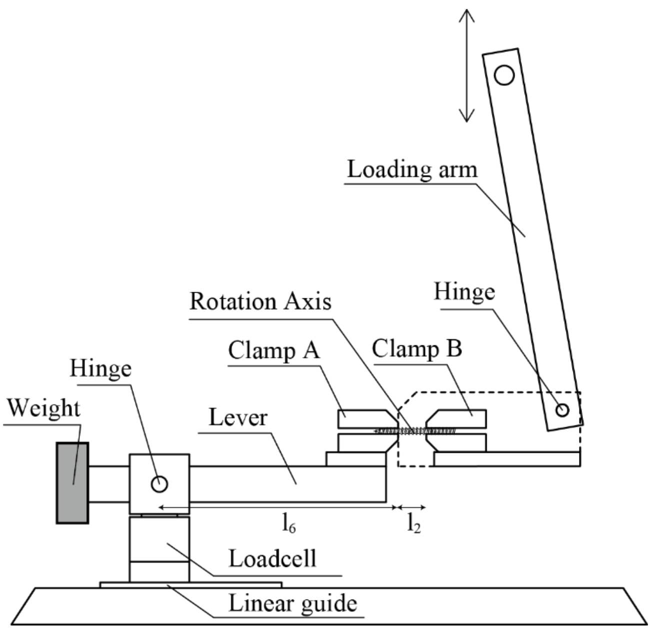

Figure 2.3. Cyclic bending test apparatus.

2.2.2 TEST SPECIMENS

Test specimens are shown in Table 2.1. Self-tapping screws with nominal diameter between 6mm and 8mm and two common nails for light-frame construction were used for the test. The head of the fastener was cut off and both side of the fastener were fixed by Clamps A and B. The distance between the clamps l_2 was two times of screw outer diameter or shank diameter.

Table 2.1. Test specimen.

Test specimen	Outer diameter(mm)	Root diameter(mm)	Bending angles (deg.)
Screw1	6	4	10, 15, 22.5, 30
Screw2	6.8	4.2	15, 22.5, 30
Screw3	6	3.8	15, 22.5, 30
Screw4	6	3.7	15, 22.5, 30
Screw5 thread	8	5.3	22.5, 30, 45
Screw5 shank	5.8	-	22.5, 30, 45
CN65 Nail	3.3	-	30
CN90 Nail	4.1	-	22.5, 30, 37.5, 45

2.2.3 TEST SCHEDULE

Test specimen was bent to both directions at constant angles until the fracture of the specimen occurred. Constant angles were shown in Table 2.1. From bending moment - deformation angle relationship, bending moment at maximum bending angle in each cycle (moment at point “a” and “c” in Figure 2.1, call “peak moment” hereafter) was obtained. Number of cycles to failure $2N_f$ (N_f: half cycle) was defined as the cycles when the peak moment becomes less than 80% of maximum moment.

2.2.4 TEST RESULTS

Representative moment - angle curve was shown in Figure 2.4. In case the deformation angle of 15 degrees, screw1 was failed at 20th negative cycle. Peak moment decreased as the number of cycle increase, and the number of cycle was determined as $2N_f$=18. In almost of all test specimens, the values of peak moment decreased as the number of cycles increased.

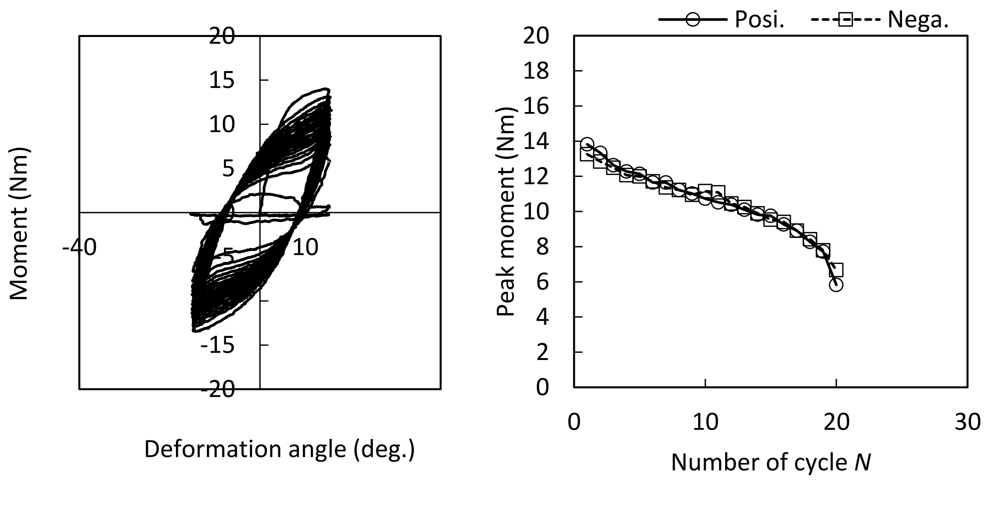

Figure 2.4. Representative moment - angle curve and relationship between number of cycle and peak moment (Screw1, 15deg.).

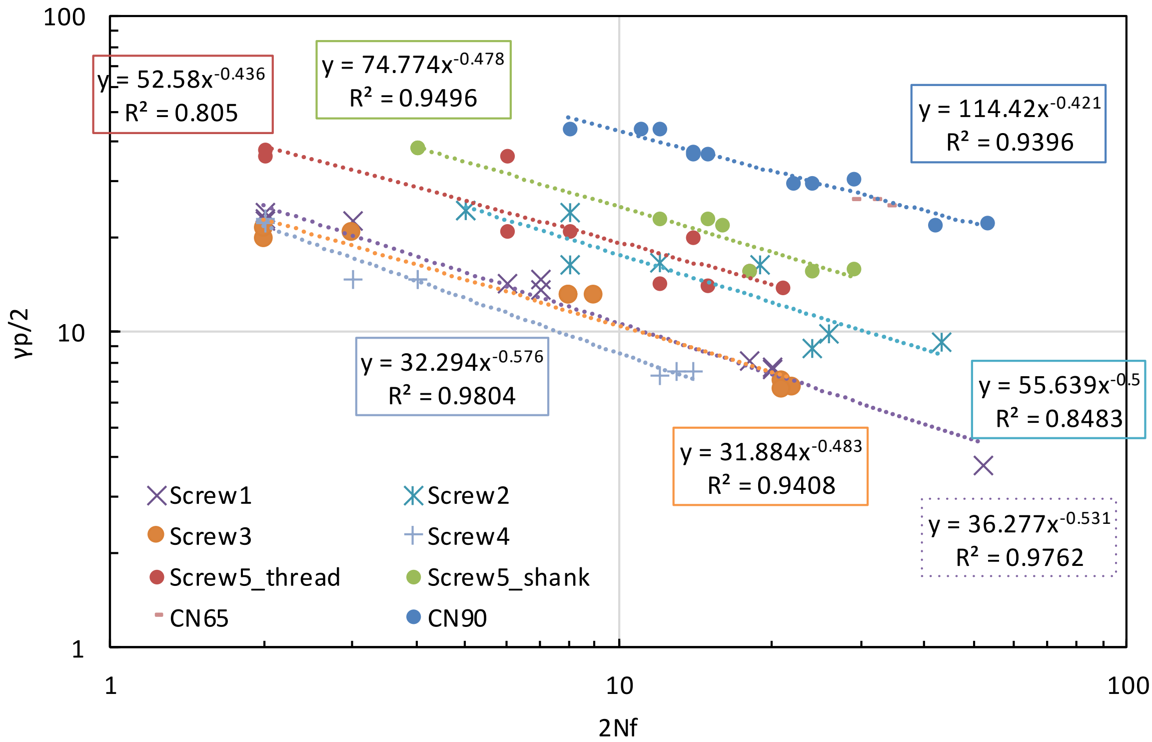

Figure 2.5. Relationship between plastic deformation angle and number of cycles to failure.

Relationship between plastic deformation angle and number of cycles to failure was shown in Figure 2.5. They showed linear relationship on double logarithmic plot and power rule was applicable. Therefore, it was found that the Manson-coffin rule is applicable by using plastic deformation angle. The value of γ_f was different between fasteners. Fasteners made from mild steel such as common nails showed high performance against cyclic loading. The value of *C* was in the range of -0.421 and -0.576. The absolute value was smaller than the value of *C* in 29 materials subjected to axial strain (C=-0.6, according to Manson (1965)).

3 MONOTONIC AND CYCLIC SHEAR TEST OF THE JOINT WITH DOWEL TYPE FASTENER

3.1 TEST MATERIALS

Two types of the joints were prepared to the test. CLT panels were prepared for main member of screw joints. Two kinds of wood species were selected for CLT- Sugi (*Cryptomeria japonica*, density: 410kg/m^3, moisture content: 10.0%) and Hinoki (*Chamaecyparis obtusa*, density: 490kg/m^3, moisture content: 10.3%). The thickness of CLT was 90mm (30mm×3ply). Each lamina in the same layer is not glued and there are no gaps between them. LVL was selected for main and side member of nailed joints. LVL were made from Hinoki (*Chamaecyparis obtusa*, density: 542kg/m^3, moisture content: 11.9%). The thickness of LVL was 40mm (13ply). Steel plates with thickness of 4.5mm were selected for side member of CLT joints. A diameter of a predrilled hole for the steel plate was 6.5mm. Screw1 in bending test was used for CLT joints, and CN90 nail for LVL joints.

3.2 TEST SETUP

Figure 3.1 shows test specimens of single shearing test of CLT and LVL joints. Grain direction of main member was arranged to 0° to the loading direction.

Monotonic and reversed cyclic loads were applied at each member by a universal test machine (Shimadzu Autograph AG-I). Applied load was measured by electronic loadcell with a capacity of 50kN. Relative displacements between main member and each side member were measured with electronic transducers with a capacity of 100mm. Six specimens were subjected to monotonic loading and reversed cyclic loading. The loading protocol is determined by ISO 16670 (2003), shown in Figure 3.2. D_u is determined as 25mm for cyclic loading.

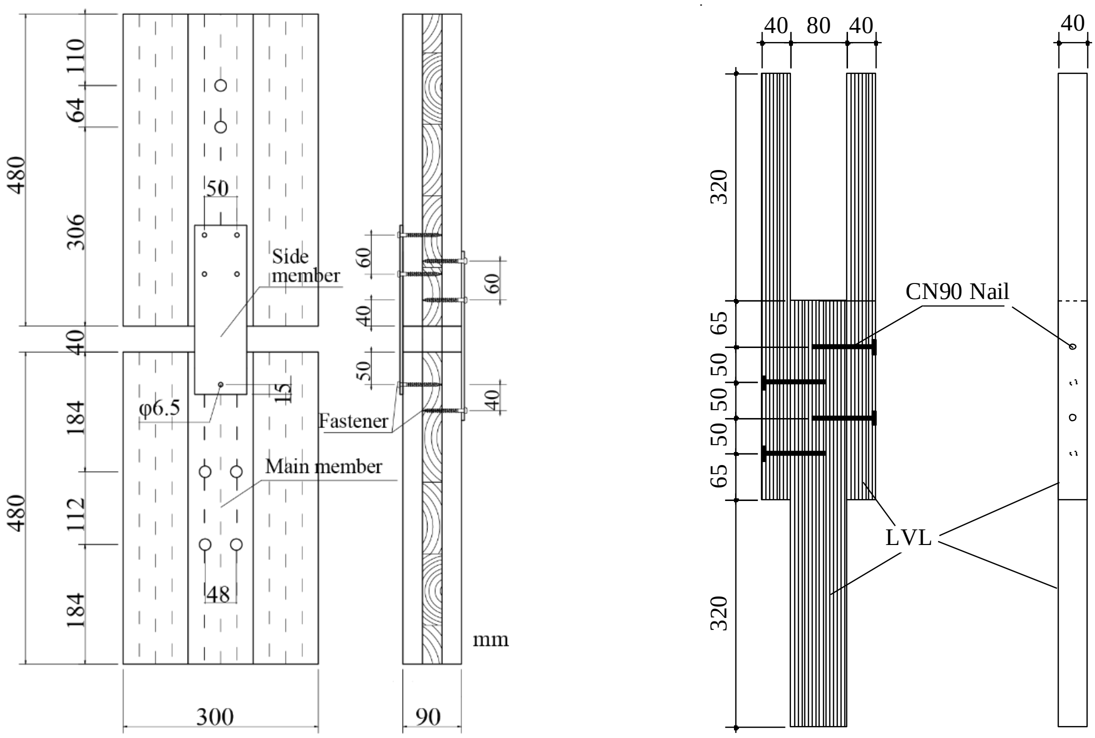

(a)CLT-screw joint (b)LVL-nail joint

Figure 3.1. Joint shear test specimens.

3.3 TEST RESULTS

Representative load – displacement curves of monotonic and cyclic tests were shown in Figure 3.3.

In CLT-scerw joints, specimens with main member of Hinoki showed high shear capacity than that of Sugi. Both series showed high ductility in monotonic loading. On the other hand, almost of all specimens were failed by the fracture of the screw in cyclic loading. Hinoki specimens showed lower ultimate displacements than that of Sugi specimens. Hinoki species have high density and embedding strength, and it makes the distance between plastic hinge and shear plane smaller. Therefore, deformation angle of the fastener becomes larger even if shear displacement is the same.

In LVL-nail joints, they showed similar tendency to CLT-screw joints between monotonic and cyclic loading. Almost of all specimens were failed by the fracture of the nail in cyclic loading. Even though the nail was made from mild steel, ultimate displacement cyclic loading was not so high (about 20mm).

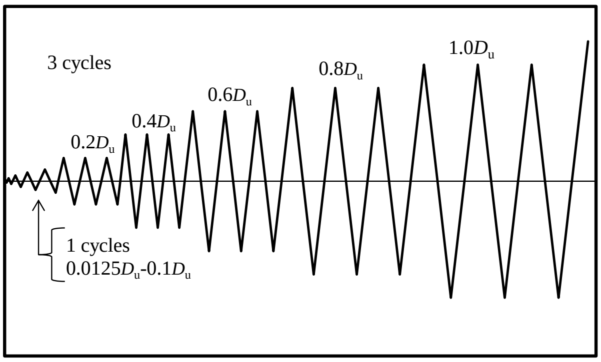

Figure 3.2. Loading protocol of ISO 16670.

3.4 Estimation of fatigue life

3.4.1 LINEAR CUMULATIVE DAMAGE RULE

Manson-coffin relation is derived based on several results of individual constant cyclic loading tests. When we think about a failure of a material exposed to continuous loading with different strain levels, the Miner's rule based on linear cumulative damage hypothesis will be applicable. The linear cumulative damage is determined as equation (4).

$$D = \frac{n_1}{N_1} + \frac{n_2}{N_2} + \cdots + \frac{n_i}{N_i} = \sum \frac{n_i}{N_i} \quad (4)$$

where:

D: linear cumulative damage, n_i: Cumulative cycles at *i*-th plastic deformation angle, N_i: Number of cycles to failure at *i*-th plastic deformation angle.

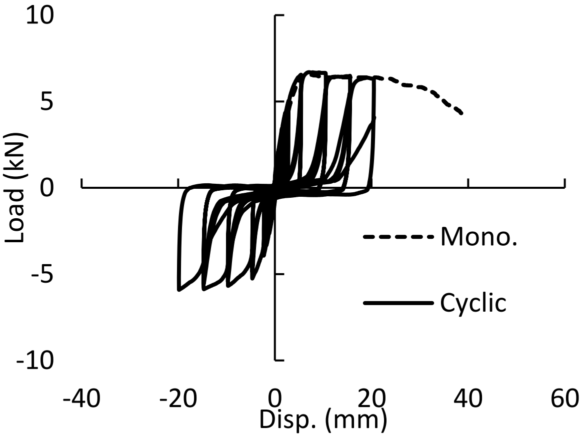

(a) Sugi CLT-Screw1

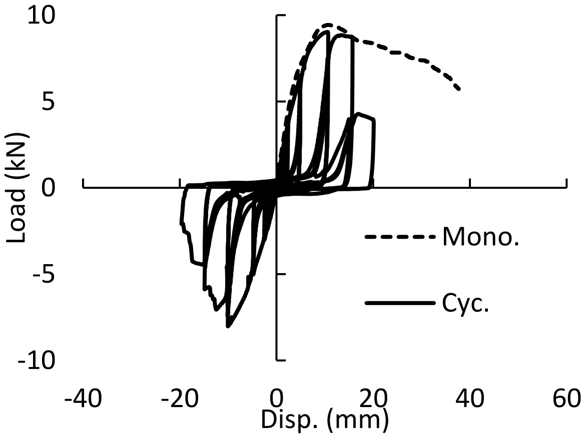

(b) Hinoki CLT-Screw1

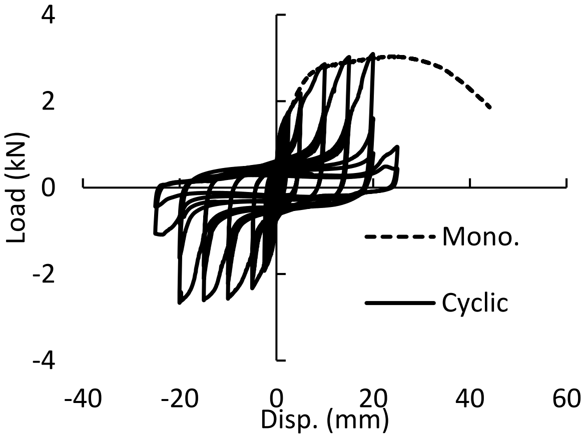

(c) LVL-CN90

Figure 3.3. Load-displacement curves of monotonic and cyclic joint shear test.

When *D* reached to 1, it is considered to be failure. This rule is generally used to predict fatigue failure lifetime.

3.5 Relationship between displacement and bending angle

Bending angle θ is determined from following equation:

$$\vartheta = \arctan(\delta / l) \quad (5)$$

where δ: joint displacement, l: length between plastic hinges or rotational center (see Figure 3.4).

Bending of the fasteners occur in modes III and IV. The length l can be calculated theoretically (e. g. Blass et al (2000), Kobayashi et al (2008, 2010)), which is expressed as equations (6) - (7).

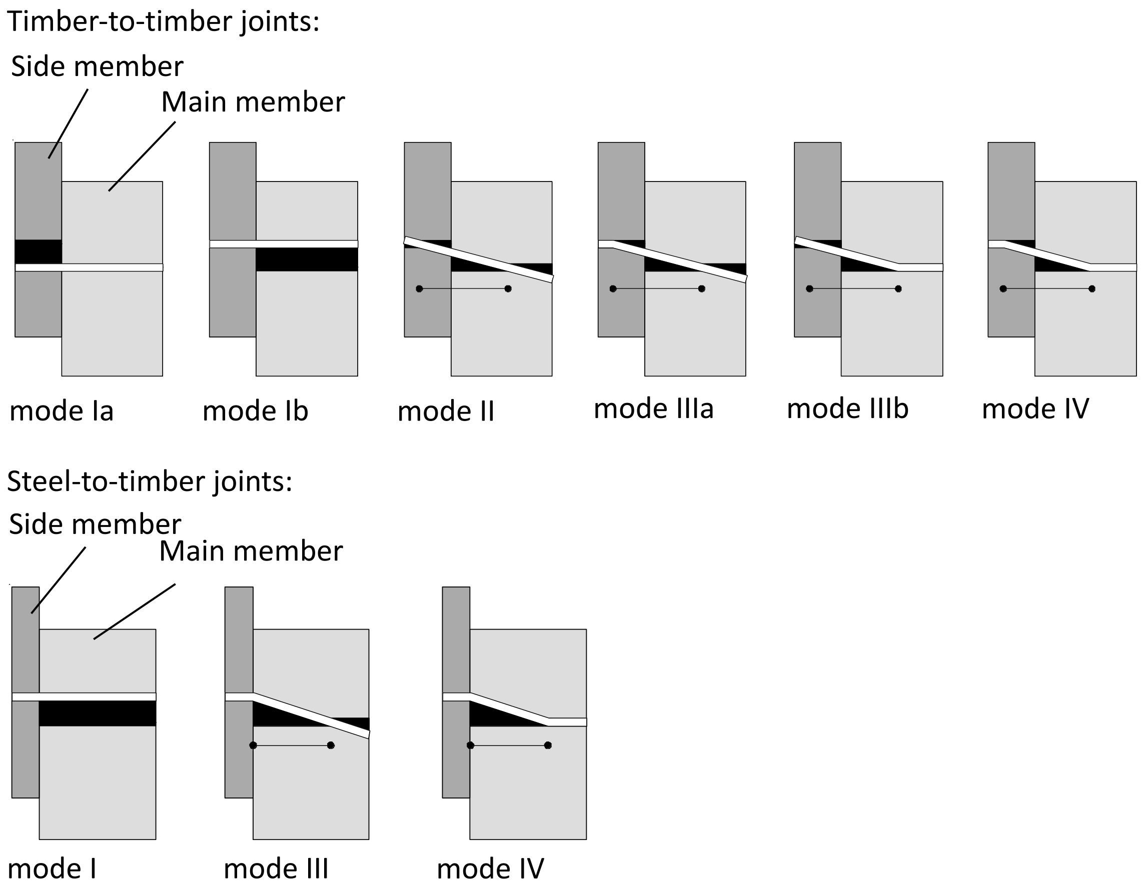

Figure 3.4. Failure modes and lengths between plastic hinges or rotational center.

For timber-to-timber joints:

$$l = \begin{cases} \frac{t_1}{2\beta}\sqrt{\alpha^2\beta^2 + 2\beta^2(\alpha^2+\alpha+1)+\beta} & \text{(II)} \\ \frac{t_1}{2\beta}\sqrt{\frac{4M_y\beta(\beta+2)}{f_{e1}dt_1^2} + 2\beta(\beta+1)} & \text{(IIIa)} \\ \frac{t_1}{2\beta}\sqrt{\frac{4M_y\beta(2\beta+1)}{f_{e1}dt_1^2} + 2\alpha^2\beta^2(\beta+1)} & \text{(IIIb)} \\ \frac{1}{\beta}\sqrt{\frac{4M_y\beta(\beta+1)}{f_{e1}d}} & \text{(IV)} \end{cases} \quad (6)$$

For steel-to-timber joints:

$$l = \begin{cases} \sqrt{\frac{4M_y}{f_e d} + \frac{t^2}{2}} & \text{(IIIa)} \\ \sqrt{\frac{4M_y}{f_e d}} & \text{(IV)} \end{cases} \quad (7)$$

Where t: thickness of the member, f_e: embedding strength of a member, α: ratio of the embedding strengths ($\alpha = t_2 / t_1$), β: ratio of the embedding strengths ($\beta = f_{e2} / f_{e1}$), M_y: bending moment of a fastener, subscript numbers 1, 2: number of the member (1: main member, 2: side member) at timber-to-timber joint.

Predicted and experimental steps to failure at joint shear tests were shown in Figure 3.5. Vertical line shows predicted failure lifetime. Black dot shows the experimental values of the steps which the load was finally exceeded 80% of maximum load in joint shear test.

Experimental values were varied because of the variation of embedding strength. Predicted value showed average or safety side against experimental results. Predicted failure lifetime showed average or safety side against experimental results.

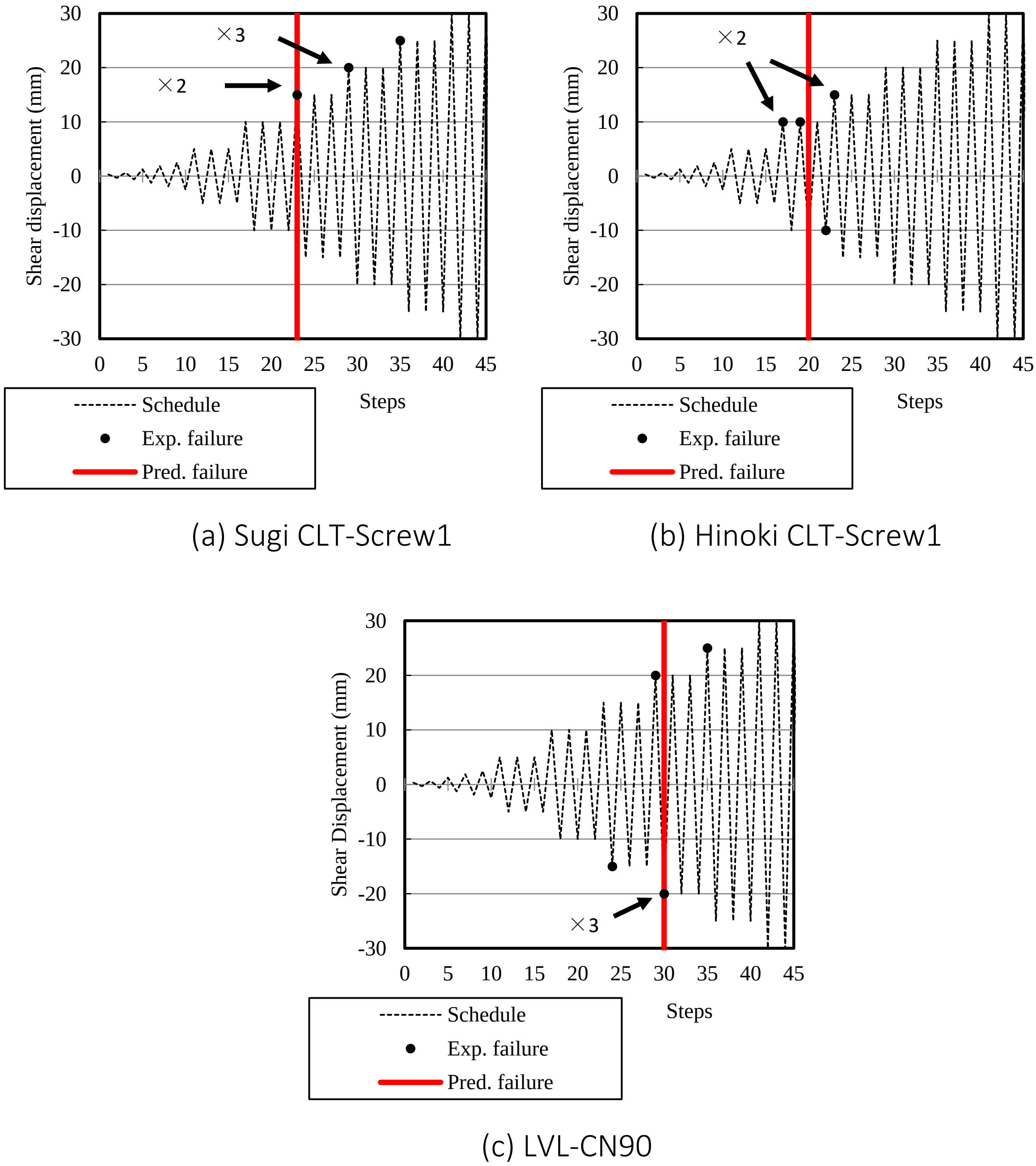

Figure 3.5. Prediction of steps to failure at joint shear test according to ISO16670.

4 Proposal for bending fatigue performance

4.1 Required cyclic bending performance

Regression coefficients are effective to evaluate fatigue performance of a fastener. Bending angle which the fastener just resists 3 cycles bending can be determined from regression curves in Figure 4.1. The value can be compared to theoretical bending angle in the joint.

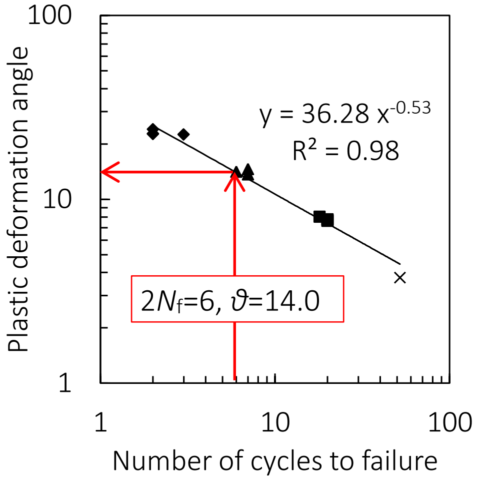

Figure 4.1.Determination of required deformation angle from cyclic bending test.

Figure 4.2 shows bending angles at displacement of 15mm. Embedment strength f_e and fastener tensile strength f_t are assumed to (a) f_e=25N/mm^2, f_t=1000 N/mm^2 or (b) f_e=40 N/mm^2, f_t =400 N/mm^2. Combination of high f_t and low f_e derives similar tendency to $45/d^{0.7}$ at timber-to-timber joint. On the other hand, combination of low f_t and high f_e derives much higher bending angle. For example, steel-slotted dowel joints with diameter of 16mm are required to survive over 40 deg. cyclic bending.

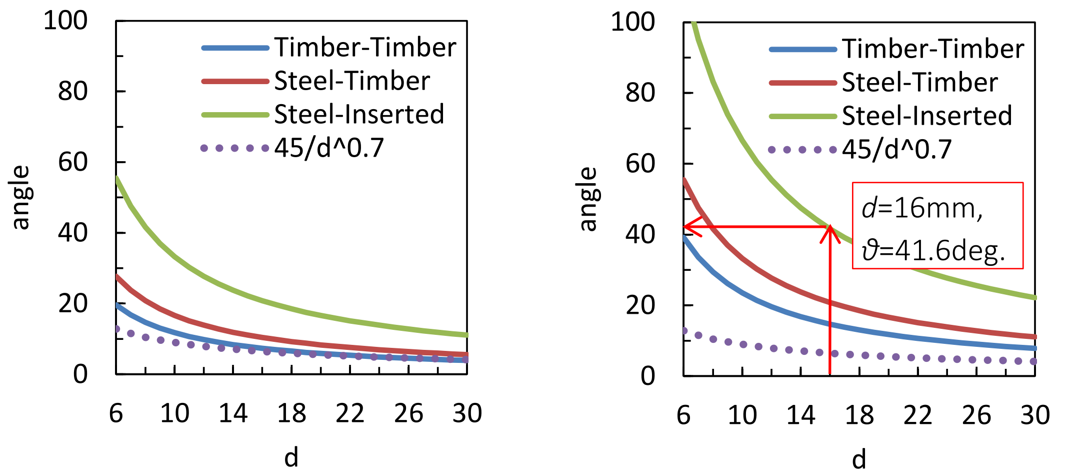

(a) f_e=25 N/mm^2, f_t =1000 N/mm^2 (b) f_e=40 N/mm^2, f_t =400 N/mm^2

Figure 4.2. Relationship between bending angle and fastener diameter.

5 Conclusion

We conducted constant angle cyclic bending test to evaluate bending fatigue properties. As a result, Number of cycles to failure and plastic bending angle showed linear relationship on double logarithmic plot. Bending fatigue properties γ_f and *C* could be determined from constant angle cyclic bending test. The value of γ_f varied depending on the fasteners. Mild steel showed high γ_f value. The value of *C* was between -0.421 and -0.576 in cyclic bending test.

We estimated fatigue life of the joint and compared to cyclic loading test results of the joints. Fatigue life in joint shear test could be estimated using bending fatigue properties and linear cumulative damage hypothesis.

It was clarified that required bending deformation depends on the combination of material properties. Large bending deformation are required at a joint with high embedment strength of the member and low bending moment of the fastener.

6 ACKNOWLEDGEMENT

This work was supported by JSPS KAKENHI Grant Number 15K18721.

7 References

Blass, H., J. et al. (2000): Effective bending capacity of dowel-type fasteners. CIB-W18 33-7-5, Delft, The Netherlands.

EN 14592+A1 (2012): Timber Structures - Dowel type fasteners - Requirements. European Committee for Standardization, Brussels, Belgium.

ISO 10984-1 (2009): Timber structures – Dowel type fasteners – Part 1: Determination of yield moment. International Organization for Standardization, Geneva, Switzerland.

ISO 16670 (2003): Timber structures - Joints made with mechanical fasteners - Quasi-static reversed-cyclic test method. International Organization for Standardization, Geneva, Switzerland.

Kobayashi K, et al. (2008): New Estimation method on stiffness and strength of single shear screw joints with structural panels. Journal of structural and construction engineering (Transactions of AIJ), No.622, pp. 121-128 (in Japanese).

Kobayashi K, et al. (2010): Estimation method on stiffness and strength of single shearing screw joints with steel side plates. 11th World Conference on Timber Engineering, Session 19-4, pp.725-732, Italy.

Kobayashi, K et al. (2016): Cyclic bending properties of screws for prediction of fracture lifetime of the fasteners and joints. 14th World conference on timber engineering, PS1-02: 5, Vienna, Austria.

Li, L et al. (2012): Exploratory study on fatigue behaviour of laterally loaded, nailed timber joints, based on a dissipated energy criterion. Holzforschung, Vol. 66, pp. 863–869.

Manson SS (1965): Fatigue: a complex subject – some simple approximations. Experimental Mechanics, pp. 193–226.

 INTER / 50 - 07 - 4

Discussion

The paper was presented by K Kobayashi

H Blass received clarification of the term "severe combination".

A Ceccotti asked about the speed of the cyclic test. K Kobayashi responded 1 to 2 mm/s.

C Sandhaas received clarification that the clamping distance was 2d.

A Buchanan commented that the quality of the material was important. For example higher quality screws from Europe would be very different from lower quality products from other parts of the world. Kobayashi explained the influence of screw quality.

P Quenneville received confirmation that some of the screws were Japanese and some were European.

V Rajcic received clarification that both screw and joint tests were performed.

Z Li commented that boundary conditions might be different from the real case. H Blass pointed out again that joint tests were done.

M Gershfeld asked whether CLT was edge glued. K Kobayashi said that the CLT was not edge glued.

Design Equations to Predict Losses in Post-Tensioned Timber Frames

Granello, Gabriele[1]; Leyder, Claude[2]; Palermo, Alessandro[1]; Frangi, Andrea[2]; Pampanin, Stefano[1,3]

[1]: University of Canterbury, New Zealand

[2]: ETH Zurich, Switzerland

[3]: University of Rome La Sapienza, Italy

Keywords: Long-Term Timber, PresLam, Post-tensioned timber

1 Introduction

In 2005 post-tensioned timber frames (Figure 1) were firstly proposed at the University of Canterbury (Palermo et al. 2005) also known as "Pres-Lam" system. The construction technique takes advantage of unbonded post-tensioned steel tendons passing through internal ducts in timber box beams, frames or walls, to create a moment resisting connection.

Figure 1: Post tensioned timber frames a) Massey University (c/o Andy Bunchanan), b) Trimble Navigation Office (c/o Paul Drummond), c) ETH House of Natural Resource (Copyright ETH Zurich/Marco Carocari) d) Merrit Building (c/o Andy Buchanan)

The idea is to accommodate the seismic demand through controlled rocking between structural elements and tendon elongation, which also ensures re-centring capability. Supplemental energy dissipation can be provided by introducing replaceable mild steel or other types of energy dissipation devices (Sarti et al. 2016), if necessary. As timber is subjected to creep with time passing (Ranta-Maunus 1975), post-tensioning tendons are enforced to shorten producing post-tensioning losses. Furthermore, the rate at which creep occurs can be increased by the moisture exchange between the material and the environment commonly known as "mechano-sorptive" creep (Armstrong and Kingston 1960).

The aim of this paper is to provide all the necessary design tools to calculate by hand the post-tensioning loss expected in a Pres-Lam frames. Although the procedure is generally applicable, the material parameters presented refer to the available creep test results for LVL (Radiata Pine) (Davies and Fragiacomo 2011) and Glulam (Spruce and Ash) (Wanninger et al. 2014).

2 Design Equations

The design equations to calculate the amount of losses are based on the analytical model developed by Fragiacomo and Davies (2011). This last considers Toratti (Toratti 1992) and Svensson and Toratti (Svensson and Toratti 2002) constitutive laws to describe the creep behaviour of timber parallel and perpendicular to the grain, respectively. The application of this model showed good agreement with experimental results for both LVL and glulam specimens (Fragiacomo and Davies 2011; Wanninger et al. 2014), and therefore it is considered the starting point of this work. However, its application for design purposes is not straightforward: it requires knowledge about the moisture content variation inside the timber members over the building's service life. This information will be provided by design tables which were built by solving the diffusion process for several environmental conditions and geometrical properties.

2.1 Post-tensioning Loss

The amount of post-tensioning loss at time t can be calculated as follows:

$$-\Delta P = \frac{-P_0\{\frac{l_\parallel \phi_\parallel(t)}{E_\parallel A_\parallel} + \frac{l_\perp \phi_\perp(t)}{E_\perp A_\perp} + \frac{l r_p(t)}{E_p A_p[1-\chi(t)_p r_p(t)]}\} + \Delta\epsilon_{\parallel,in}(t) l_\parallel + \Delta\epsilon_{\perp,in}(t) l_\perp - \Delta\epsilon_{p,in}(t) l}{\frac{l_\parallel[1+\chi(t)_\parallel \phi_\parallel(t)]}{E_\parallel A_\parallel} + \frac{l_\perp[1+\chi(t)_\perp \phi_\perp(t)]}{E_\perp A_\perp} + \frac{l}{E_p A_p[1-\chi(t)_p r_p(t)]}} \quad (1)$$

where the indices *//,⊥* refer to the correspondent timber properties parallel and perpendicular to the grain, respectively. The index *p* instead refers to the post-tensioning steel properties; *l, A, E* respectively represent the length of timber under load, the cross-sectional area and the elastic modulus; $\phi(t)$, $r_p(t)$ represent the timber creep function and the steel relaxation function. The terms ε_{in} represents the inelastic deformation due to changes in environmental conditions. The functions χ takes into account that the analytical solution is approximated by correcting the creep or relaxation function (Chiorino and Napoli 1984).

2.2 Long-term behaviour of timber

Timber exhibits creep behaviour when under permanent loads (Morlier 2004). The timber function is made of two different contributions, namely pure creep and mechano-sorptive creep (Fragiacomo and Davies 2011) . It can be expressed as Equation 2:

$$\phi(t,U,\hat{U}) = \phi(t)_c + \phi(t,U,\hat{U})_{ms} \tag{2}$$

where the first term is the pure creep contribution, and the second term is the mechano-sorptive contribution.

2.2.1 Pure Creep

The pure creep function is usually evaluated by performing a creep test in a controlled environment i.e. temperature and relative humidity are kept constant during the experiment. The deformation over time is expressed over the elastic deformation and the results are normally fitted with an exponential law as reported in Equation 3:

$$\phi(t)_c = at^b \tag{3}$$

Creep tests in a controlled environment were performed for LVL loaded parallel and perpendicular to the grain (Davies and Fragiacomo 2011), spruce glulam loaded parallel to the grain (Wanninger et al. 2014), and ash glulam loaded perpendicular to the grain(Wanninger et al. 2014) .The fitting parameters *a* and *b* are reported in Table 1 (*t* expressed in days).

Table 1 Pure creep parameters.

	LVL ∥	**LVL ⊥**	**Spruce ∥**	**Ash ⊥**
a	0.0071	0.0031	0.088	0.151
b	0.38	0.72	0.173	0.305

2.2.2 Mechano-sorptive

Mechano-sorptive creep depends on the moisture content variation inside the timber member during its loading period (Toratti 1992) . Its contribution can be split between a recoverable part (index *r*) and irrecoverable part (index *i*) :

$$\phi(t,U,\Delta\hat{U})_{ms} = \phi(t,U)_{ms,r} + \phi(t,\Delta\hat{U})_{ms,i} \tag{4}$$

The recoverable part can be calculated by using Equation 5:

$$\phi(t,U)_{ms,r} = \phi^{\infty}[1 - e^{-cUt/(\Delta t)}] \tag{5}$$

Where *c*, ϕ^{∞} are material parameters and U represents the accumulation of moisture variations over a period Δt. Suitable values for U can be obtained from the tables presented in the following sections depending on the environmental conditions.

The irrecoverable contribution can be calculated by using Equation 6:

$$\phi(t,\Delta\hat{U})_{ms,i} = m_{ms}(\Delta\hat{U}) \qquad (6)$$

Where m_{ms} is a material parameter and $\Delta\hat{U}$ are moisture levels that were not attained during the previous load history. Suitable values for $\Delta\hat{U}$ can be obtained from the tables presented in the following sections depending on the environmental conditions. Material parameters are reported in Table 2:

Table 2 Mechano-sorptive parameters.

	LVL ∥	**LVL ⊥**	**Spruce ∥**	**Ash ⊥**
$\boldsymbol{\phi^{\infty}}$	0.63	0.5	0.9	0.6
c	6.3	1	0.5	1
$\mathbf{m}_{ms}$	0	0	0	0.005

2.2.3 Inelastic deformation

The inelastic deformation of timber can be calculated according to Equation 7:

$$\epsilon_{in} = \alpha_u[u(t) - u(t_0)] \qquad (7)$$

Where *u* the average moisture content. The values of α_u are presented in Table 3.

Table 3 Inelastic deformation parameters.

	LVL ∥	**LVL ⊥**	**Spruce ∥**	**Ash ⊥**
$\boldsymbol{\alpha_u}$	0.00625	0.0165	0.00625	0.2

2.3 Long-term behaviour of steel

2.3.1 Relaxation

The steel relaxation function is available in the Eurocode 2 Part 1-1 Section 3.3.2:

$$r_p(t,\tau) = 10^{-5}k_1\rho_{1000}e^{k_2\sigma_p(\tau)/f_{pk}}\left(\frac{t-\tau}{1000}\right)^{0.75(1-\sigma_p(\tau)/f_{pk})} \qquad (8)$$

where $\sigma_p(\tau)$ is the stress on the tendon at time τ, f_{pk} is the characteristic strength of the pre-stressing steel, t- τ is the time since the post-tensioning in hours, ρ_{1000} is the percentage of loss after 1000 hours in a pure relaxation test and k_1, k_2 are material parameters. As the phenomenon of relaxation occurs more rapidly than creep (Soliman and Kennedy 1986) ,the non-linearity can be removed by considering $\sigma_p(\tau)= \sigma_p(t_0)$ as proposed by Fragiacomo and Davies (2011).

2.3.2 Inelastic deformation

The inelastic deformation of steel due to thermal variations can be computed according to Equation 9:

$$\epsilon_{p,i}(t) = \alpha_p[T(t) - T(t_0)] \qquad (9)$$

Where α_p is the steel dilatation coefficient equal to 10^{-5} C^{-1}.

3 Design Tables

The moisture content variation over time can be computed at different grades of detailing. A simplified approach is based on considering 2D Fick's law to estimate the moisture content within a beam's cross-section by assuming a constant value with respect to the member axes (e.g. (Schanzlin 2010; Khorsandnia et al. 2015)).

Even if this simplified assumption can be avoided by considering multi-Fickian models (Frandsen 2007; Fortino et al. 2013), the simpler approach, based on 2D equations appear to be sufficiently accurate for describing the behaviour of timber with a considerable grade of detailing and a reasonable computational effort. A recent application for LVL can be found in (Granello et al. 2016).

The 2D moisture problem over time was solved for different environmental conditions, geometry and material properties in order to cover the most common design applications.

3.1 Service Class

Eurocode 5 Part 1-1 Section 2.3.1.3 proposes three different Service Classes according to the environmental conditions the building will be subjected to. They are defined as:

- Service Class I: *characterized by a moisture content in the material corresponding to a temperature of 20C and the relative humidity of the surrounding air only exceeding 65% for a few weeks per year.*
- Service Class II: *characterized by a moisture content in the material corresponding to a temperature of 20C and the relative humidity of the surrounding air only exceeding 85% for a few weeks per year.*
- Service Class III: *characterized by climatic conditions leading to higher moisture contents than in Service Class II.*

The reported definitions were quantified by considering the following yearly average environmental conditions (refer to Figure) simulated by a sinusoidal curve:

- Service Class I: Relative humidity annually cycles between 40% and 70% (c.a. 14 weeks above 65%); Temperature equal to 20 C).
- Service Class II: Relative humidity annually cycles between 40% and 90% (c.a. 14 weeks above 85%); Temperature equal to 20 C.

- Service Class III: complete saturation of moisture content. Every year the moisture content varies between 8% and 30%.

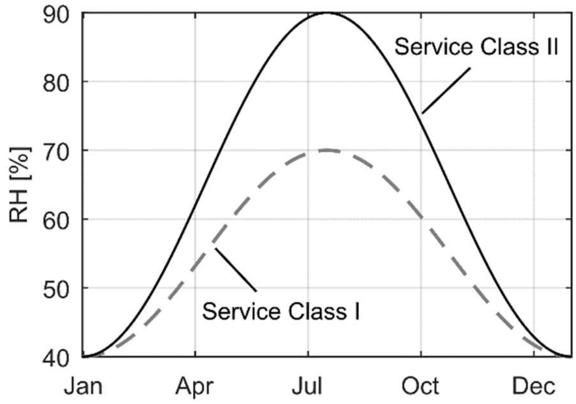

Figure 2 Humidity demand for Service Class I and II

3.2 Wet Perimeter

Normally larger sections (Schanzlin 2010) are less sensitive to the environmental humidity cycles because humidity takes more time to penetrate toward the inner part of the cross section. This quite complex phenomenon present some similarities with the problem of evaluating shrinkage in concrete. As Eurocode 2 deals with the size effect by providing simplified tables based on the concept of the wet perimeter, the same approach was adopted.

A parametric diffusion analysis was performed on 496 rectangular cross sections by considering the cyclic environmental conditions previously described, for a period of 50 years. The cross section dimensions range between 100x100 mm and 700x700 mm, considering a variation of 20 mm in every direction. Results are expressed with respect to the wet perimeter varying between 25 mm (section 100x100 mm, lower bound) and 175 mm (section 700x700 mm, upper bound).

3.3 Yearly moisture accumulation

The yearly moisture accumulation was evaluated by performing a diffusion analysis over 50 years. Results are presented in Figure 3.

Both glulam and LVL were considered at different levels of initial moisture content i.e. 8%, 16% and 24%. Results show that the wood specie has very little influence on the yearly moisture accumulation. The reason is because the humidity variation demand is seasonal i.e. low frequency, therefore the transitory parameters (i.e. diffusivity) do not significantly affect the overall response. The initial value of moisture content was found affecting the response in the first cycles. However, over 50 years this initial boundary condition becomes negligible.

Results were fitted with an exponential function $A\,e^{Bx} + C\,e^{Dx}$, which parameters are reported in Table 4.

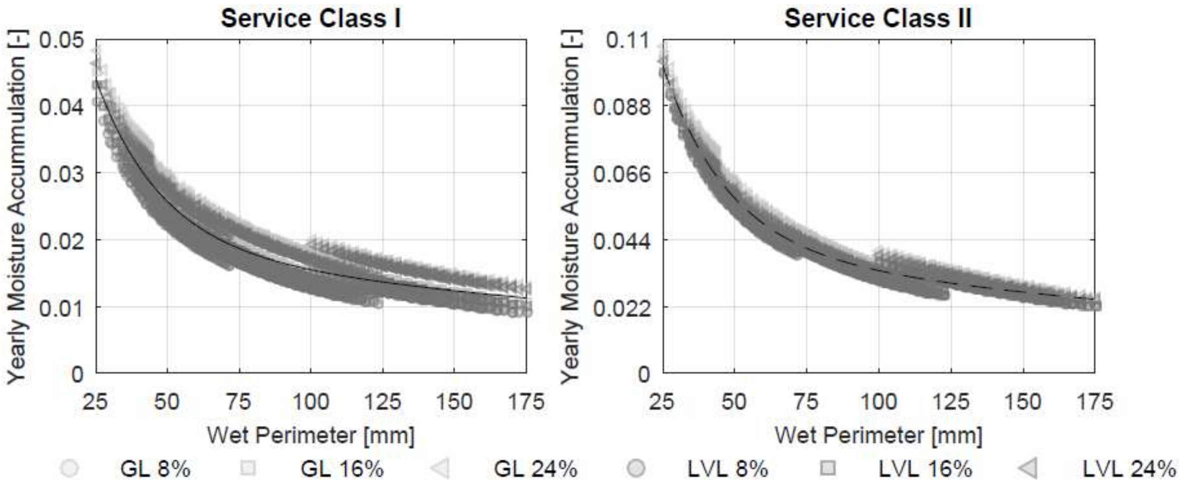

Figure 3: Yearly moisture accumulation for Service Class I and Service Class II.

Table 4 Yearly moisture accumulation fitting parameters

	A	B	C	D
Service Class I	0.0749	-0.0439	0.0205	-0.00345
Service Class II	0.1811	-0.0442	0.0451	-0.00355

As the assumption of complete saturation cycles every year was made for Service Class III, results are independent on the wet perimeter. The yearly accumulation of moisture content $U_{y,acc}$ can be easily obtained by $U_{y,acc}=2(U_{y,max}-U_{y,min})=0.44$;

3.4 Maximum moisture content attained

The maximum moisture content attained over 50 years is presented in Figure 4for different Service Class, wet perimeter values and initial moisture content.

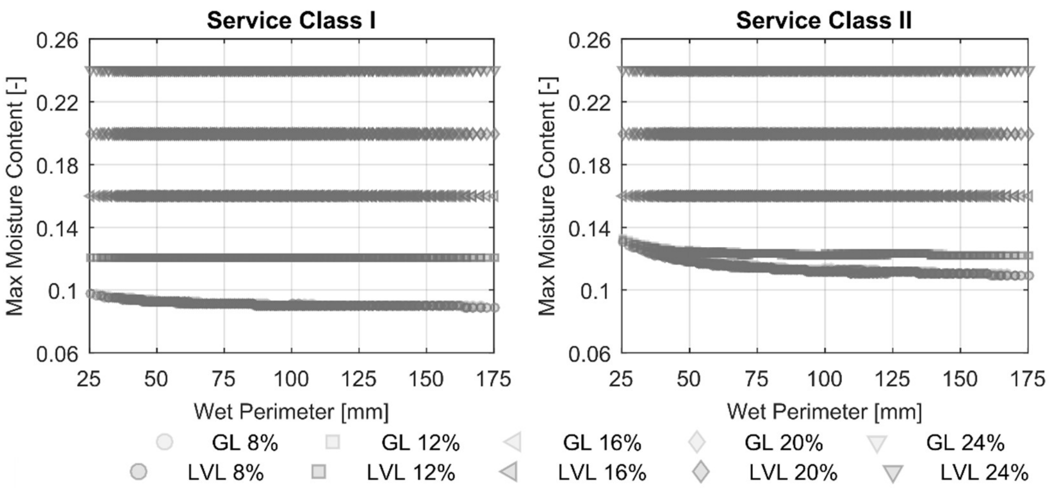

Figure 4: Maximum moisture content attained for different initial moisture contents.

To compute the mechano-sorptive irrecoverable contribution it is necessary to calculate the difference between the initial moisture content and the maximum value attained over the building life (e.g. 50 years).

It can be noticed that for a high value of initial moisture content (i.e. greater than 14%), the maximum moisture content attained is similar to the initial one. This happens since within Service Classes I and II the sections with a high initial moisture content mostly release moisture to the surrounding environment. On the other hand, a section with low initial moisture content (e.g. 8%) experiences a humidity uptake from the surrounding environment.

Figure 4 that glulam and LVL have similar results. Again, this happens because the diffusion process is subjected to seasonal cycles i.e. very low frequency. Regarding Service Class III, Û can be assumed equal to 0.3 i.e. 30%.

3.5 Equilibrium moisture content

As the moisture content varies with time, the inelastic deformation contribution (Equation 7) is also time-dependent. An estimation can be given by considering the average moisture content of the section for a period of 50 years. This value can be calculated by considering the average environmental condition that the member is subjected to and then estimating the equilibrium moisture content u_{eq}. A validated estimation is given by Rasmussens' formula (Rasmussen 1961), which provides the timber moisture content given environmental temperature and relative humidity. The formula is omitted due to space limitations, however the standard cases related to this work are presented in Table 5:

Table 5 Equilibrium moisture content for different Service Classes

	Service Class I	Service Class II
T [C]	20	20
RH [%]	55	65
u_{eq}	0.1	0.12

4 Integration Functions

For a linear viscoelastic problem, the stress strain relationship can be expressed by using Equation 10:

$$\epsilon(t) - \epsilon_{in}(t) = \frac{\sigma_0}{E}[1 + \phi(t)] + \int_0^t \frac{1+\phi(t,\tau)}{E} d\sigma(\tau) \tag{10}$$

The final deformation depends therefore on integrating the stress variation over time, and can be solved only by a step-by-step numerical integration. A simplified method known as Age Adjusted Method and historically applied for concrete (Chiorino and Napoli 1984), consists of introducing a χ function that allows to transform Equation 10 in Equation 11:

$$\epsilon(t) - \epsilon_{in}(t) = \frac{\sigma_0}{E}[1 + \phi(t)] + \frac{1+\chi(t,t_0)\phi(t,t_0)}{E}\Delta\sigma(t) \tag{11}$$

Equation 11 has the advantage of being algebraic, and it can be easily solved without numeric integration schemes. The function χ therefore represents a sort of weight applied to the different stress variations over time and can be calculated by imposing Equation 10 equal to Equation 11.

The variation of stress Δσ can be obtained by considering displacement compatibility at the anchorage. In case of straight barycentric tendon profiles (Fragiacomo and Davies 2011) the variation of stress is:

$$\Delta\sigma = \frac{E_p A_p}{A}\Delta\varepsilon \qquad (12)$$

Where A_p, E_p, A are the tendon area, tendon elastic modulus and timber cross section area, respectively. Δε represents the shortening in the tendons.

The χ function was numerically calculated for the most common design situations. With time passing it tends to a constant value, which is necessary to evaluate the losses at 50 years. Its range is reported in Table 6:

Table 6: χ function values at 50 years.

	LVL ∥	**LVL ⊥**	**Spruce ∥**	**Ash ⊥**
χ	[0.9-1]	[0.7-0.8]	[0.8-1]	[0.9-1]

The lowest should be used for Service Class I and the highest for Service Class III.

5 Case studies

The proposed equations are here applied to evaluate the post-tensioning force in two post-tensioned timber frames under monitoring: the ETH House of Natural Resources (HoNR) and the Trimble Navigation Offices.

5.1 The House of Natural Resources

The House of Natural Resources is an innovative timber building constructed in the ETH campus in Zürich (Figure5a). Among the different innovative technologies implanted (Leyder et al. 2015), the building's lateral loads resisting system is a two-story post-tensioned timber frame. This last is made of ash glulam columns and hybrid ash-spruce glulam beams (mainly spruce lamellae, except for the four bottom lamellae, which are made of ash cf. Figure 5) carrying both gravity and horizontal loads.

The construction of the fisrt story post-tensioned timber frame started in January 2014. The second story was built in July 2014, followed by the construction of the roof structure and installation of the façade. In June 2015 the building was inaugurated and since then operates as an office building for the laboratory of hydraulics, hydrology and glaciology of ETH Zürich.

Figure 5 House of Natural Resources: a) External view (copyright ETH Zurich/Marco Carocari) and b) beam column detailing (copyright ETH Zurich/Marco Carocari).

The frame is made up of eight three-bay frames which span roughly 6.5m each. Four frames span in one direction, and the remaining four frames span in the perpendicular direction. The beam cross-sections are 280 x 720 mm, while the column cross-section dimensions are 380 x 380 mm.

The post-tensioning cables are made of 4 strands each (total cross sectional area of A_p =600 mm^2) and were initially stressed to 700 KN. In terms of the relaxation function the following parameters were set according to Eurocode 2: k_1 =0.66, k_2 =9.1 and ρ_{1000} =2.5. The obtained function (Figure 6a) shows a total loss of pre-stressing equal to 3.15 % in 50 years (18250 days).

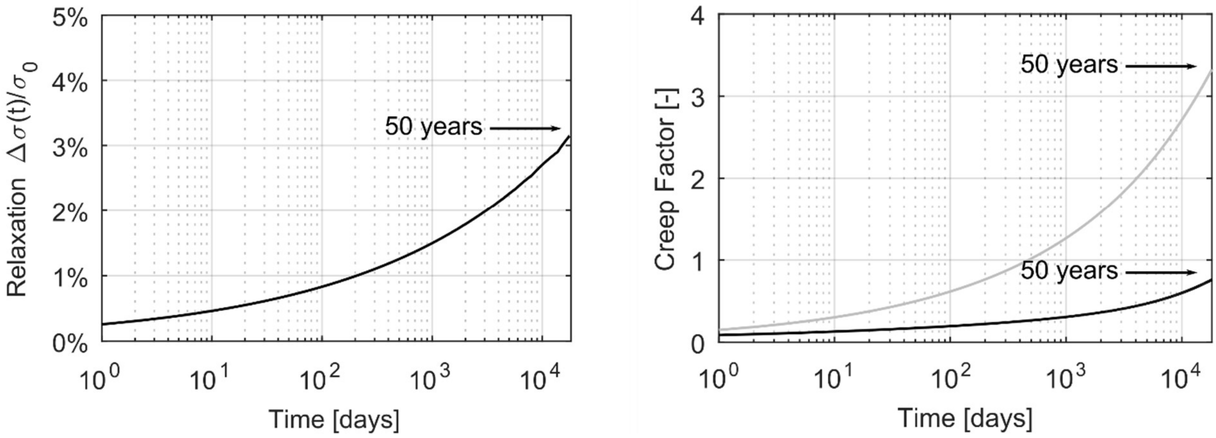

Figure 6 a) Relaxation function and b) creep function for beams (black line) and columns (grey line).

It is assumed that the buildings indoor environment corresponds to Service Class I. Based on a wet perimeter equal to 95 mm and 100 mm for the columns and beams, respectively, the yearly moisture accumulation can be estimated equal to 0.015. The resulting creep functions for the beams and columns are reported in Figure 6b. The initial moisture content in timber was measured equal to 11-12%, therefore no irrecoverable contribution from mechano-sorptive creep is expected.

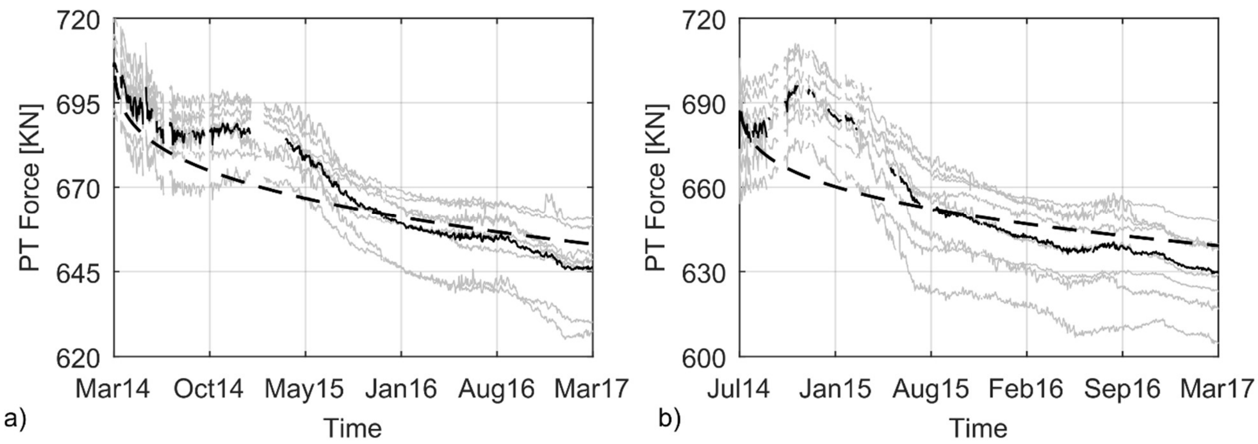

Figure 7 Post-tensioning trend at a) first and b) second floor: different frames (grey line), average (black line) and model (black dotted line).

The comparison between the analytical and the measured post-tensioning trend over time is presented in Figure7 for the first and second storey. It can be noted that the trend is described with reasonable accuracy by the analytical equations. There are some fluctuations which however are not captured by the model: the effect of the inelastic deformation due to temperature and moisture content is in fact not considered time dependent within this application. The response over 50 years is presented in Figure 8. It can be noticed that a loss equal to 17-18% is expected.

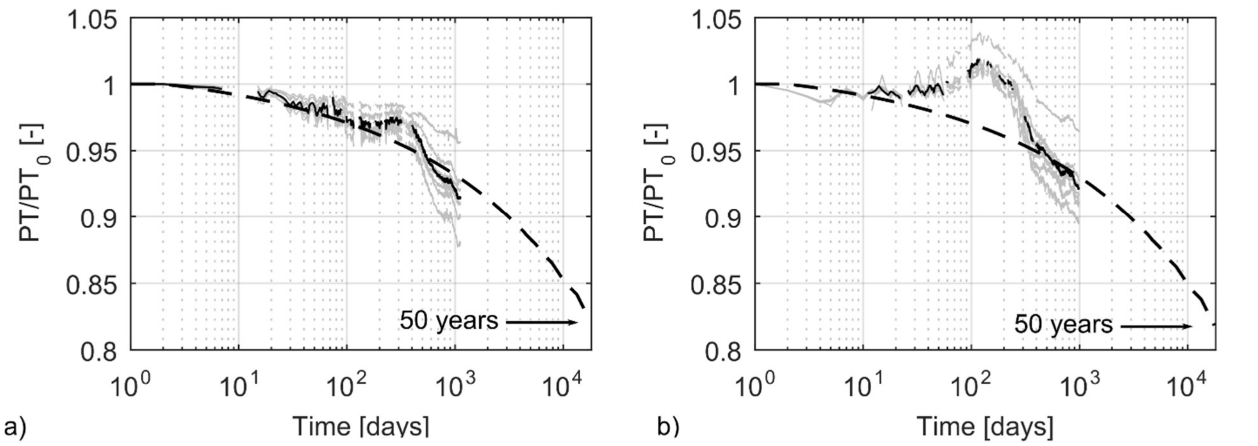

Figure 8 Response of the House of Natural resources over 50 years according to the model proposed.

5.2 The Trimble Navigation Offices

The Trimble Navigation Offices (Figure 9a) were built after the Canterbury Earthquakes of 2010 and 2011 (Brown et al. 2012) The structure was constructed with Pres-Lam walls in one direction and Pres-Lam frames in the other.

The two story frame is horizontally post-tensioned at the first floor while external energy dissipaters (Sarti et al. 2016)are installed at both levels. The frame is composed by seven spans 6.4 m long, while beams and columns present a cross-section of 315 x 600 mm. The elements were made up of Radiata Pine LVL. To protect the column and to provide an anchorage for the dissipaters, an external steel armor was placed at the rocking interface (cf. Figure 9b).

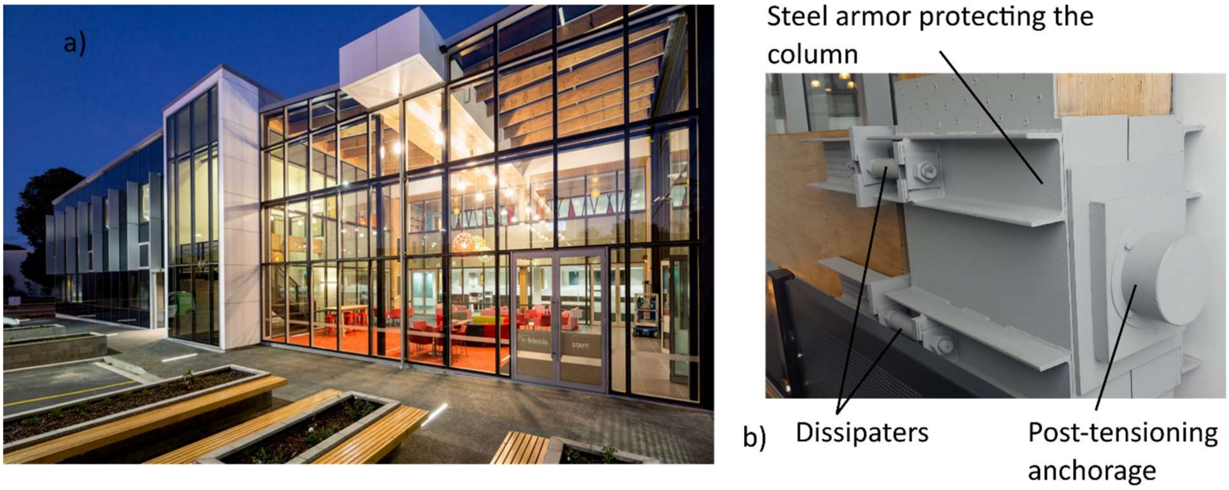

Figure 9: Trimble navigation Offices: a) overview of the building (www.opus.co.nz) and b) beam-column detailing.

Post-tensioning was applied by using six 15.7 mm diameter strands (A_p =1162 mm^2) for a total post-tensioning force of circa 910 KN. The tendon properties and the respective relaxation functions are the same as for the House of Natural Resources (Figure 6a).

The building is assumed to belong to Service Class I. By considering a wet perimeter of 103 mm for both columns and beams, the yearly moisture accumulation was estimated equal to 0.015. Creep functions were evaluated by considering LVL properties parallel and perpendicular to the grain. The initial moisture content of wood was assumed equal to 11% i.e. no post-tensioning loss due to inelastic deformation are considered. The temperature of the tendons during the post-tensioning phase was also assumed equal to 20C which leads to no thermal variations respect to the operational conditions.

The presence of steel plates has a beneficial effect on reducing the amount of losses as they reduce the portion of timber loaded perpendicular to the grain. Part of the post-tensioning force is in fact directly transmitted through the steel armor and therefore the column is only partially engaged: in order to take this positive effect into account, a global factor of 0.5 is applied to the ratios for considering the creep perpendicular to the grain (index $\perp$)in Equation 1. Further research considering the actual plate to timber stiffness ratio is necessary to better understand the stress path and to propose ad example more refined functions taking into account the armoring detailing.

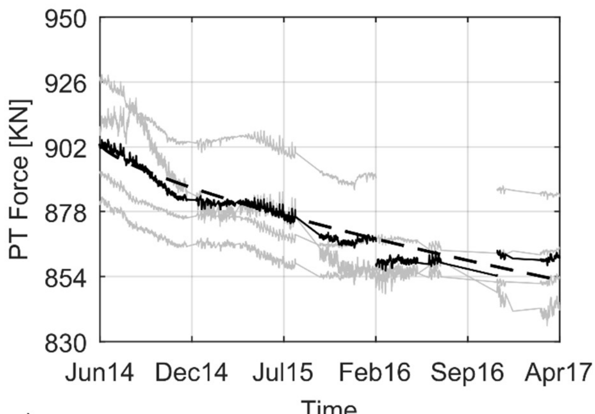

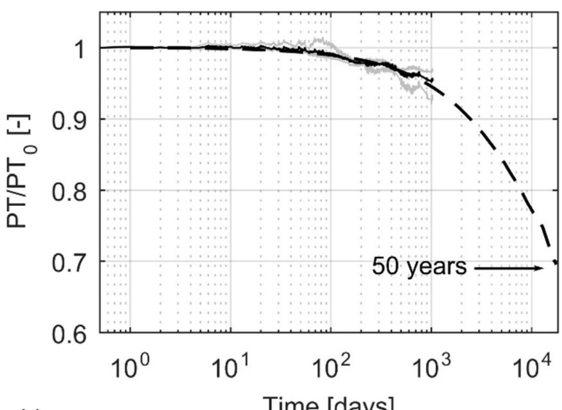

Figure 10 a) Post-tensioning trend in the Trimble frames: frames data (grey lines), average (black line), model (black dotted line); b) response over 50 years according to the model proposed.

Results are presented in Figure 10a while the response over 50 years in presented in Figure 10b. It can be notice that the model seems able to describe the data with reasonable accuracy. A loss equal to 30% is expected in 50 years.

6 Conclusion

This paper presents a design procedure to estimate by hand the amount of post-tensioning loss expected in a post-tensioned timber frame building. The procedure is based on a well-known analytical model available in literature and on supporting complementary design graphs: these last were obtained by simulating the humidity diffusion process within the timber members for different geometrical and environmental conditions.

The quantities related to the moisture content changes (e.g. mechano-sorptive creep effects) were calculated with respect to the concepts of "Service Class" and “wet perimeter” to be compatible with Eurocode’s procedures. Appropriate integration functions were also calibrated by comparing the numerical and analytical solution of the visco-elastic model.

Finally, the procedure was applied to describe the tendon force trends of two post-tensioned timber buildings under monitoring: the HoNR (ash and spruce glulam) and the Trimble Navigation Offices (Radiate Pine LVL). A loss equal to 17% and 30% in 50 years is predicted for the House of Natural Resources and for the Trimble Navigation Offices, respectively.

Regarding this last building, a factor of 0.5 is proposed to take into account the beneficial effect of the steel plates externally armoring the beam-column joint. Further research however is necessary to exhaustively investigate the stress path across the joint detailing, in order to consider different armoring solutions within the procedure. In both cases, the analytical results are in good agreement with the monitored data from the first 2 years of operation.

7 Acknowledgements

The authors would like to thank Mr. Paul Drummond for providing the data regarding the Trimble Navigation Offices.

8 References

Armstrong, L. D., and Kingston, R. S. T. (1960). "Effect of Moisture Changes on Creep in Wood." *Nature*, 185(4716), 862-863.

Brown, A., Lester, J., Pampanin, S., and Pietra, D. (2012). "Pres-Lam in practice—A damage-limiting rebuild project." *Proc., SESOC Conference,* Auckland, New Zealand.

Chiorino, M. A., and Napoli, P. (1984). *CEB design manual on structural effects of time-dependent behaviour of concrete*, Georgi.

Davies, M., and Fragiacomo, M. (2011). "Long-Term Behavior of Prestressed LVL Members. I: Experimental Tests." Journal of Structural Engineering, 137(12), 1553-1561.

Fortino, S., Genoese, A., Genoese, A., Nunes, L., and Palma, P. (2013). "Numerical modelling of the hygro-thermal response of timber bridges during their service life: a monitoring case-study." *Construction and Building Materials*, 47, 1225-1234.

Fragiacomo, M., and Davies, M. (2011). "Long-Term Behavior of Prestressed LVL Members. II: Analytical Approach." *Journal of Structural Engineering*, 137(12), 1562-1572.

Frandsen, H. L. (2007). "Selected constitutive models for simulating the hygromechanical response of wood." Department of Civil Engineering, Aalborg University, Denmark.

Granello, G., Giorgini, S., Palermo, A., and Pampanin, S. (2016). "Post-Tensioned LVL Beams : Experimental Results and Numerical Modelling." *World Conference on Timber Engineering*, Vienna, Austria.

Khorsandnia, N., Schänzlin, J., Valipour, H., and Crews, K. (2015). "Coupled finite element-finite difference formulation for long-term analysis of timber–concrete composite structures." *Engineering Structures*, 96, 139-152.

Leyder, C., Wanninger, F., Frangi, A., and Chatzi, E. (2015). "Dynamic response of an innovative hybrid structure in hardwood." *Proceedings of the Institution of Civil Engineers-Construction Materials*, 168(3), 132-143.

Morlier, P. (2004). *Creep in timber structures*, CRC Press.

Palermo, A., Pampanin, S., Buchanan, A., and Newcombe, M. (2005). "Seismic design of multi-storey buildings using laminated veneer lumber (LVL)." *New Zealand Society for Earthquake Engineering Conference*, Wairakei, New Zealand.

Ranta-Maunus, A. (1975). "The viscoelasticity of wood at varying moisture content." *Wood Science and Technology*, 9, 189-205.

Rasmussen, E. F. (1961). *Dry Kiln: Operator's Manual*, US Department of Agriculture.

Sarti, F., Palermo, A., and Pampanin, S. (2016). "Fuse-Type External Replaceable Dissipaters: Experimental Program and Numerical Modeling." *Journal of Structural Engineering*, 04016134.

Schanzlin, J. (2010). "Modeling the long-term behavior of structural timber for typical serviceclass-II-conditions in South-West Germany." *Habilitation Thesis*, University of Stuttgart, Germany.

Soliman, M. H., and Kennedy, J. B. (1986). "Prestress losses in continuous composite bridges." *PCI Journal*, 85.

Svensson, S., and Toratti, T. (2002). "Mechanical response of wood perpendicular to grain when subjected to changes of humidity." *Wood Science and Technology*, 36(2), 145-156.

Toratti, T. (1992). "Creep of Timber Beams in Variable Environment.", *PhD Thesis*, Helsinki University, Finland.

Wanninger, F., Frangi, A., and Fragiacomo, M. (2014). "Long Term Behavior of Post Tensioned Timber Connections." *Journal of Structural Engineering*, 141(6), 04014155.

Discussion

The paper was presented by A Palermo

P Dietsch commented about humidity demand over one year period as they had monitored many service class 1 buildings over the years. He stated the assumption for service class II is incorrect and should be checked against real data.

JW Van de Kuilen asked about pure creep and why there would be such a large variability in parameter "a" for the creep function. A Palermo said that they were based on test results. JW Van de Kuilen stated that the findings might be influenced by the time frame of the experiments. A Palermo agreed.

A Ceccotti asked about the situation of 90% loss. A Palermo said that it was an extreme case where almost all post tension was lost and it would be unlikely to happen.

JW Van de Kuilen discussed the consideration of starting date would be important as large moisture variation in the start dates would have a strong influence on the result. A Palermo explained that the plates were not stiff enough in the building. The influence might be reduced if the right size of plates were used. Also one could include a factor for the construction phase. A Palermo also stated that a 10% loss in 3 years would be expected.

K Crews stated that on-going monitoring and building maintenance would be important.

P Quenneville discussed whether the building was truly closed.

Glued thin-webbed beams – amendments to EC 5 for safe ULS design

Simon Aicher, Materials Testing Institute, University of Stuttgart

Cyrill Stritzke, Materials Testing Institute, University of Stuttgart

Keywords: glued thin-webbed beams, shear buckling, resistance to transverse forces, effect of bearing length and overhang

1 Introduction

The ultimate limit state (ULS) design of a glued thin-webbed beam, which may be an I-, box-, or multiple box-beam has to guarantee sufficient capacity versus bending moment, shear force, transverse or support forces as in case of any other structural building member. Furthermore, the necessary bond shear transfer between web(s) and flanges has to be verified. The bending stress design of the stated group of structural elements is straightforward and is represented correctly by Eurocode 5, part 1-1 (EC 5-1-1 or EC 5), section 9 [1].

The design equations for verification of bond shear stresses between flanges and web are rather correct, too, despite some possible amendments in case of very thick flanges where todays strength modifications are owed to Foschi [2].

Regarding the effect of the bending moment and especially of the shear force on the web resistance it is obvious that the design of the thin-webbed beams has to account for web buckling. Also for this aspect EC5 provides (rather) correct construction limitations and design equations, based essentially on work by Halasz and Cziesielski [3], Dekker et al. [4], Aune [5] and Solli [6].

The shear force design is a simple strength of materials approach (shear strength x modified web cross-section area) with linearly increasing shear force capacity along with increasing web depth up to a limit web slenderness ratio. Beyond the limit slenderness shear buckling is accounted for, what leads to a rather constant, slightly linearly decreasing shear force plateau. Contrary to the pure, not stability affected web slenderness range, the capacity in the stability range is influenced by an eventual stiffness orthotropy of the web plate, so far not accounted for in the EC 5 equations.

Finally, there is the transverse support force action resulting in compressive stresses in the support contact area on both, flanges and web. The compression forces furthermore result in a stability issue of the web when no or insufficient end stiffeners are present. The buckling load is strongly influenced by the web slenderness ratio and the support conditions, being bearing length and overhang. The design issue of bearing stresses in the contact area is not directly mentioned, but can / could be easily solved according to the general EC 5 provisions for compression perpendicular to grain taking into consideration the eventually considerable stiffness differences of the flange and web materials in the support area. The applicability of the bearing capacity increase options offered in EC 5, section 6, for structural wood products of constant cross-section nevertheless remains unclear.

Finally, however, there exists a widespread misunderstanding that the so determined resultant bearing force represents in any case the transverse force resistance on the 5%-quantile or design load level. In order to verify the latter, the stability issue of the web subject to transverse force has to be analyzed. With regard hereto, however, no design provisions accounting for a possible compression buckling are specified in EC 5. Contrary, this issue is addressed profoundly in the European steel structure design code EN 1993-1-5 [7] for plated structural elements, and hereby especially for I- and box- beams with unstiffened and stiffened end and intermediate load bearings, resembling apart from the material entirely the here regarded wood-based thin-webbed beams.

The fact that the present provisions in EC 5 do not lead in all cases to a safe assessment of the ultimate load capacity of thin-webbed elements is underlined by a look at European ETA-certified I-beams, for instance the beams with LVL-flanges and hardwood or OSB webs specified in ETA-06/0238 [8] and ETA-02/0026 [9]. The characteristic shear and vertical force capacities of these wide-spread products were derived test-based within the frame of ETAG (Guideline for European Technical Approval) 011 [10]. The herein [10] addressed test methods (EOTA TR 002) [11] however enable rather different alternative test procedures for determination of transverse force resistance. A comparison of the ETA-specified values with calculations according to EC 5 reveals for a wide range of configurations considerable mismatches, in the extreme case up to a factor of 3.

In acknowledgement of the above, theoretical investigations and experimental verifications were undertaken to clarify and amend the present EC 5-1-1 design procedure for thin-webbed beams. The experimental part aimed at the confirmation of ETA-specified shear and transverse force capacities for different support conditions, as well as the here reported calculations.

In the theoretical part of the work, the web resistance versus transverse forces at unstiffened beam ends was addressed in a first step. Thereby an attempt was made to adopt the provisions of EC 3-1-5 with modifications necessarily required by the different material behaviors and geometry conditions of thin-webbed wood-based beams with rather thick wooden flanges versus steel I-beams with thin webs and flanges.

2 Design of glued thin-webbed beams according to Eurocode 5-1-1

The strength of materials design, regarding bending and axial stresses, as given in EC 5-1-1, section 9, is correct and not regarded any further. The effect of web buckling due to bending stresses, and to some extent due to shear stresses, is controlled by the constructive detailing rule for web slenderness

$$\lambda_w = \frac{h_w}{b_w} \leq 70\,, \qquad (1)$$

where h_w and b_w are depth and width of the web, respectively. Web buckling due to shear stresses is further "actually primarily" accounted for by limitation of the design or characteristic shear force within the slenderness ratio range

$$35 \leq \lambda_w \leq 70$$

to a maximum design shear force capacity

$$F_{v,w,Ed} \leq F_{v,w,max,Rd}$$

with

$$\begin{aligned} F_{v,w,max,Rd} &= 35\, b_w^2 \cdot \left[1 + \frac{0.5\,(h_{f,t} + h_{f,c})}{h_w}\right] \cdot f_{v,0,d} \\ &= 35\, b_w^2 \cdot \eta_{hw} \cdot f_{v,0,d} \qquad (35 \leq \lambda_w \leq 70) \end{aligned} \qquad (2)$$

where

$$\eta_{hw} = 1 + \frac{0.5(h_{f,t}+h_{f,c})}{h_w} \qquad (3)$$

and $h_{f,t}$ and $h_{f,c}$ are depths of tensile and compressive flange, and $f_{v,0,d}$ is the design panel shear strength. Actually $F_{v,w,max,Rd} \neq const.$, as η_{hw} reduces slightly with increasing web slenderness λ_w, unless η_{hw} is kept constant by increasing the flange depths $h_{f,t/c}$ accordingly.

Below the web slenderness ratio $\lambda_w \leq 35$, where shear buckling can be disregarded, the design shear force resistance $F_{v,w,Rd}$ is linearly increasing with the relevant shear area, so

$$F_{v,w,Ed} \leq F_{v,w,Rd}$$

with

$$F_{v,w,Rd} = b_w \cdot h_w \cdot \eta_{hw} \cdot f_{v,0,d} \leq F_{v,w,max,Rd} \qquad (\lambda_w \leq 35) \qquad (4)$$

The design for the bearing compressive stresses (stiff supported length: l; overhang: a, see Fig.5) is performed as usual by

$$F_{v,w,Ed} \leq R_{90,d} \qquad (5)$$

with

$$R_{90,d} = [l + (l_l + l_r)] \cdot b_f \cdot k_{c,90} \cdot f_{c,90,d} \tag{6}$$

and

$$l_l = \min(a; l; 30\,mm)\,, l_r = \min\left(l; \frac{l1}{2}; 30\,mm\right). \tag{7}$$

$f_{c,90,d}$ design compressive strength perpendicular to flange bearing area and fiber direction

$k_{c,90}$ $k_{c,90}$ = 1 for $l_1 < 2H = 2[h_w + h_{f,t} + h_{f,c}]$, $k_{c,90}$ = 1,5 (solid wood) for $l_1 \geq 2H$, for l_1 (see Fig. 5)

3 Finite element analysis

The finite element results given below serve in this paper exclusively for a qualitative understanding and assessment of the regarded problem. Detailed quantitative comparisons with analytical solutions are provided separately. Figure 1a depicts the FE-model of a thin-webbed I-beam in a 4 point bending situation, with short bearing length at support A and, most important, no overhang. The plot in Figure 1b reveals the contours of the in-plane web compressive stress σ_y parallel to beam depth in the elastic state at a rather low load level. The limited spread of the stress beyond bearing length is clearly visible. Figure 1c finally shows the out-of-plane deflection contour of the buckled web due to vertical force/stress action being unrestrained by the free web edge.

In a comparison, Figure 2a shows the FE model of the same I-beam as in Fig. 1a now however, with distinct overhangs at both supports; Fig. 2b visualizes the beam in the buckling state at support A. The overhangs act as quasi-stiffeners, stabilizing the web and hereby leading to two facts. First, the vertical force buckling load level is considerably increased and, in the specific configuration at crucial support location A is already in a load range, where web buckling due to shear stresses, denoted by the typical inclined shear buckling fields, is interacting with the pure compressive force buckling phenomenon. In most cases the critical shear buckling load, i.e. shear force, is considerably higher as compared to the compression buckling force level. There can be an overlap of both buckling modes, and in case of long bearing lengths, combined with an overhang or distinct stiffnesses, shear buckling may become decisive. In this sense, shear and transverse force actions are considered independently and superpositioned in EN 1993-5-1 (EC 3-5-1) [7].

Here, for the purpose of this paper, it shall be assumed that the pure shear buckling phenomenon is sufficiently taken into consideration by the EC 5 rules specified above, i.e. by limiting the shear force resistance to a limit web slenderness value of λ = 35. So, the focus is exclusively on the vertical force resistance/buckling issue, where applicability of the EC3 design rules, given for thin-webbed steel beams, is investigated.

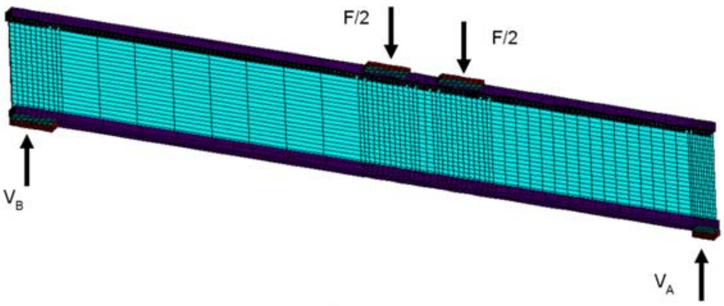

Fig. 1a: FE model of thin-webbed I-beam, with short bearing length at support A and no overhangs, subject to asymmetric 4-point bending loading

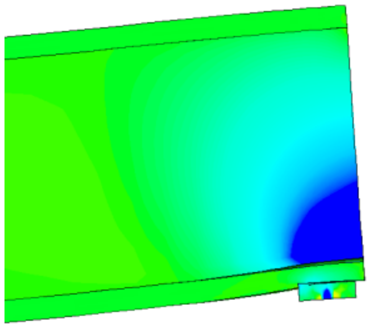

Fig. 1b: Vertical compressive stresses in the web in elastic range at support A

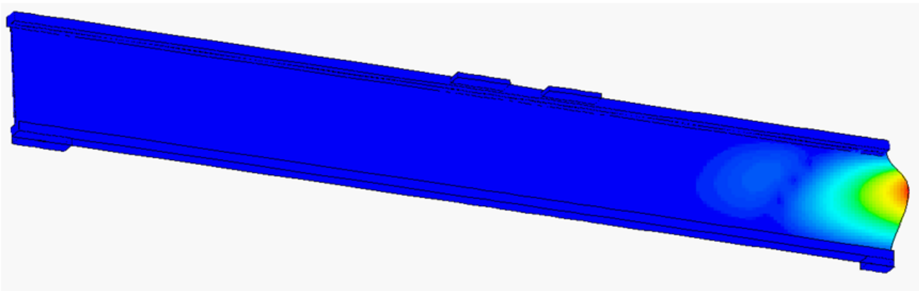

Fig. 1c: Buckling field/deformations, primarily due to transverse compressive stresses at support A

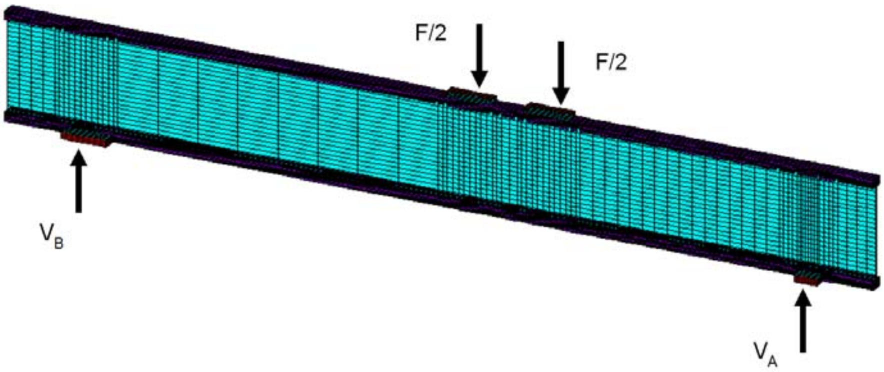

Fig. 2a: FE model of thin-webbed I-beam (same as in Fig. 1a, b),now with large (stiffening) overhangs at both supports

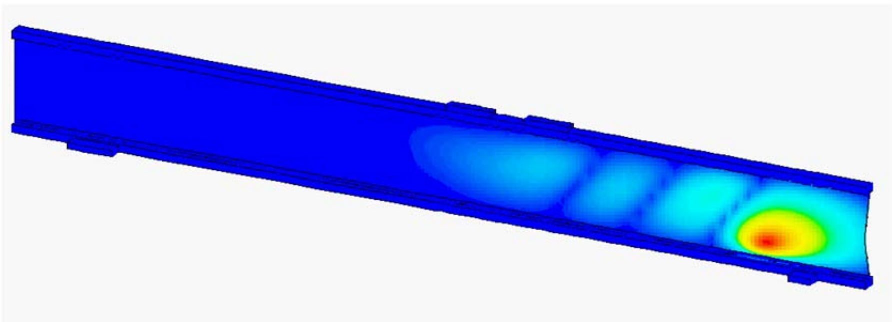

Fig. 2b: Buckling fields/deformations, primarily due to transverse compressive and shear stresses at support A

4 Vertical force design according to Eurocode 3-1-5

4.1 General

The design rules in EC 3-1-5 for resistance to transverse forces are given here adequately modified with regard to wooden components. Specifically the case, where the load/force is applied through one flange adjacent to an unstiffened beam and web end, as shown in Figure 3, type (c), is regarded.

Due to several material and geometry differences between steel versus timber and wood based materials, the rules specified in [7] cannot be transposed identically to timber I- or box beam situations, but have to be modified at several points. Nevertheless, the below stated approach remains fully consistent with the EC 3-1-5 steel construction design method. It should be emphasized, that there exists a strong necessity to harmonize, wherever possible, the design approaches for rather identical construction elements even though the materials and hence some detailing aspects may be rather different. Apart from material and geometry differences, a further prime concern should be laid on the task to implement same notations for identical geometric and, where possible, material properties.

Following, the bearing length, denoted by 's_s' (stiff support length) in EC 3-1-5, is denoted by 'l', as in EC 5-1-1; similarly, dimension of overhang, denoted by 'c' in [7], is written as 'a' according to EC 5-1-1.

4.2 Resistance to transverse force action

For an unstiffened web end, taking into consideration local buckling due to the transverse support force, the characteristic load resistance is specified in [7] as

$$F_{R,k} = f_{c,w,k} \cdot L_{eff} \cdot b_w \tag{8}$$

and

$$L_{eff} = \chi_F \cdot l_y \,, \tag{9}$$

where:

$f_{c,w,k}$	characteristic value of in-plane web compression strength in direction 'y' parallel to applied transverse force ,
L_{eff}	effective length to resist transverse forces,
l_y	effective loaded length, appropriate to the length of stiff bearing length, and
χ_F	reduction factor due to local buckling, resulting from transverse end force.

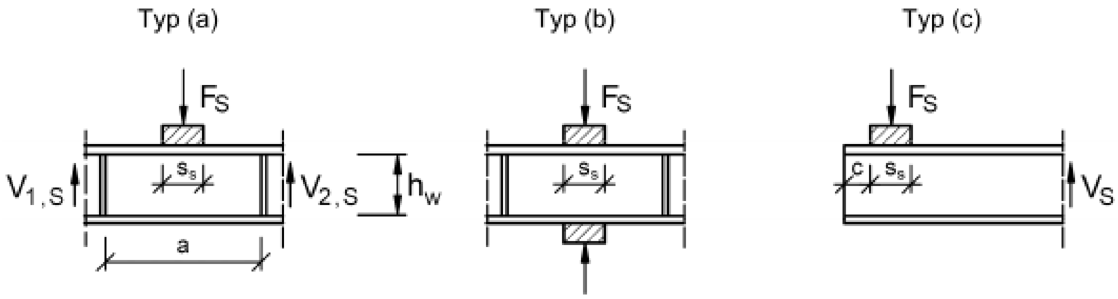

Fig. 3: Different types of vertical force actions on stiffened and unstiffened webs, according to [7]. Here, type (c) representing a transverse force action at the unstiffened beam end is regarded.

The reduction factor $\chi_F = f(\lambda_{F,rel})$, depending on relative web slenderness ratio $\lambda_{F,rel}$, is

$$\chi_F = \frac{0{,}5}{\lambda_{F,rel}} \leq 1{,}0 \tag{10}$$

where

$$\lambda_{F,rel} = \sqrt{\frac{F_{c,w,k}}{F_{cr,k}}}$$ relative web slenderness ratio, (11)

and

$$F_{c,w,k} = f_{c,w,k} \cdot l_y \cdot b_w$$ characteristic compressive web resistance force (12)

$$F_{cr,k} = \frac{\pi^2}{h_w} \cdot k_F \cdot \sqrt[4]{N_{x,w,05} \cdot N_{y,w,05}^3}$$ characteristic critical transverse buckling load (13)

with

$$N_{x,w,05} = \frac{E_{x,w,05} \cdot b_w^3}{12(1-\nu_{xy}\nu_{yx})}$$ web bending stiffness in direction x (14a)

$$N_{y,w,05} = \frac{E_{y,w,05} \cdot b_w^3}{12(1-\nu_{xy}\nu_{yx})}\,.$$ web bending stiffness in direction y. (14b)

In case of an isotropic web material (steel, hard fiberboard) the equation for the critical buckling load simplifies to ($E_{w,05} = E_{x,w,05} = E_{y,w,05}$, $\nu = \nu_{xy} = \nu_{yx}$):

$$F_{cr,k} = \frac{\pi^2}{12\,(1-\nu^2)}\, k_F\, E_{w,05} \frac{b_w^3}{h_w}\,, \tag{15}$$

In the case of steel ($\nu = 0{,}3$, $E = E_{w,05}$) one obtains

$$F_{cr,k} = F_{cr,05} = 0{,}9\, k_F\, E \frac{b_w^3}{h_w} \tag{16}$$

representing the critical buckling load expression given in [7]. Finally, the buckling factor k_F is

$k_F = 2 + 6\left(\frac{\ell + a}{h_w}\right) < k_{Fmax}$ buckling factor for transverse force action according to [7] for transverse force at unstiffened end (type (c) in Figure 3) (17a)

$k_{Fmax} = 6$ limit value of compression buckling acc. to [7]; note: for $k_F > k_{Fmax}$ shear buckling occurs (17b)

By equating the expressions for web shear buckling (not given here) and transverse compressive force buckling, it can be shown that k_{Fmax} should be better reduced to maximally 5 in case of wood based web materials such as hard fiberboard, OSB and plywood.

4.3 Determination of effective loaded length

The effective loaded length ℓ_y for the unstiffened end force condition should be calculated according to [7] as

$$\ell_y = \min\left[\ell_e + h_f \cdot \sqrt{\frac{m_1}{2} + \left(\frac{\ell_e}{h_f}\right)^2 + m_2} \quad ; \quad \ell_e + h_f\sqrt{m_1 + m_2}\right] \qquad (18)$$

where

$$\ell_e = \frac{k_F \cdot E_{w,05} \cdot b_w^2}{2 \cdot f_{c,w,k} \cdot h_w} \leq \ell + a \qquad (19)$$

and

$$m_1 = \frac{f_{c,90,f,k}}{f_{c,w,k}} \cdot \frac{b_f}{b_w}, \qquad (20)$$

$$m_2 = 0{,}02\left(\frac{h_w}{h_f}\right)^2. \qquad (21)$$

Quantity ℓ_y is not subject to restrictions in [7], but for wooden I-beams the condition

$\ell_y \leq 1{,}7\,(\ell + a)$

should be considered.

5 Experimental campaign

5.1 Test program

In order to verify theoretical considerations and possible adoption of new design approaches on shear and vertical force capacities of thin-webbed wood-based beams empirically, an experimental campaign was conducted with differently sized commercially available I-beams. A light composite wood-based I-beam, with trade name

STEICO joist, employed structurally in works on the basis of the European Technical Assessment [8], was used. In specific, the chosen symmetric I-shaped cross-section of the joists/beams is built up for different depths from equally sized LVL flanges (grade 2.0E LVL) with width and depth of b_f = 60 mm and $h_f = h_{f,c} = h_{f,t}$ = 39 mm, respectively. The web consists of hard fiberboard with a thickness of b_w = 8 mm. Figure 4 shows the cross-sectional build-up visualizing the bonded groove and tongue-type connection of the web to the flanges, too. The specific cross-sectional build-up, termed SJ_L60 in [8], has been investigated for three very different sizes, i.e. total depths being H = 200 mm, 350 mm and 500 mm. These beam depths represent significantly different web slenderness ratios $\lambda = h_w / b_w$ of 15,3, 34,0 and 52,8, respectively. The chosen beam depths represent the (almost) smallest, intermediate and largest produced sizes.

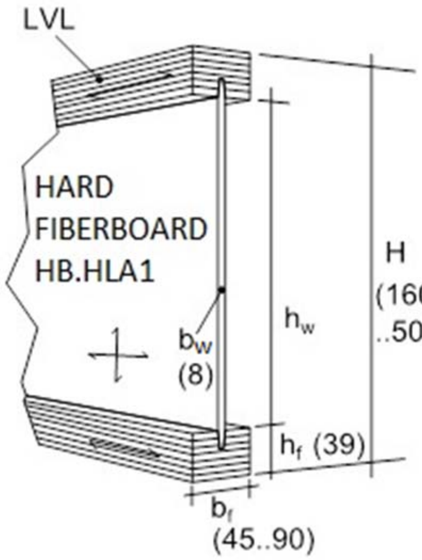

Fig. 4: Cross-sectional build-up of the experimentally investigated STEICO joists [8]

Table 1 gives a comparison of some relevant mechanical properties of the components.

Each beam size was tested with six configurations comprising three different support lengths l = 50 mm, 100 mm and 150 mm, and each of the support lengths was investigated with either no overhang (a = 0) or a large overhang of a = H / 2. In each of the configurations (only) 3 specimens were tested, so in total 54 specimens. All web ends were not equipped with stiffeners.

characteristic stiffness and strength properties in N/mm²	web hard fibreboard HB.HL A1 acc. to EN 622-2 [12]		flanges LVL (class 2.0E [8]) acc. to EN 14374 [13]	
bending strength	$f_{m,90,k}$ 1)	31	$f_{m,k}$	48
tensile strength	$f_{t,90,k}$ 1)	20	$f_{t,0,k}$	36
compressive strength II and ⊥	$f_{c,90,k}$ 1)	21	$f_{c,0,k}$ $f_{c,90,flat,k}$	36 3,8 2)
shear strength	$f_{v,k}$ (in plane)	14	$f_{v,flat,k}$	3,2 2)
modulus of elasticity	E_{mean} (in plane) 3) $E_{0,05}$	5300 $5300 \cdot 0{,}9 = 4770$ 5)	E_{mean} $E_{0,05}$	13800 4) 11600

1) subscript 90 used in [8] to denote diection parallel to beam for web material

2) according to DoP [14] for LVL R and R^s

3) here assumed also for bending out of plane as in [15]

4) 13789,5 ≈ 13800 N/mm² $= 2 \cdot 10^6$ psi

5) see chap. 6

Tab. 1: Stiffness and strength properties of the components of the I-beams according to [8] and [12]

Figure 5 shows the chosen 4 point bending test scheme. In order to provoke failure predetermined at one support, the loads were not applied at mid-length, but shifted significantly towards one support, here denoted as support A. Figure 6a shows the realized test set-up for the small and medium sized beams. In order to avoid any global flange/beam buckling, the higher beams had to be braced increasingly (see Figure 6b) For all beam configurations the horizontal out-of-plane web deflection was measured, see Figure 7.

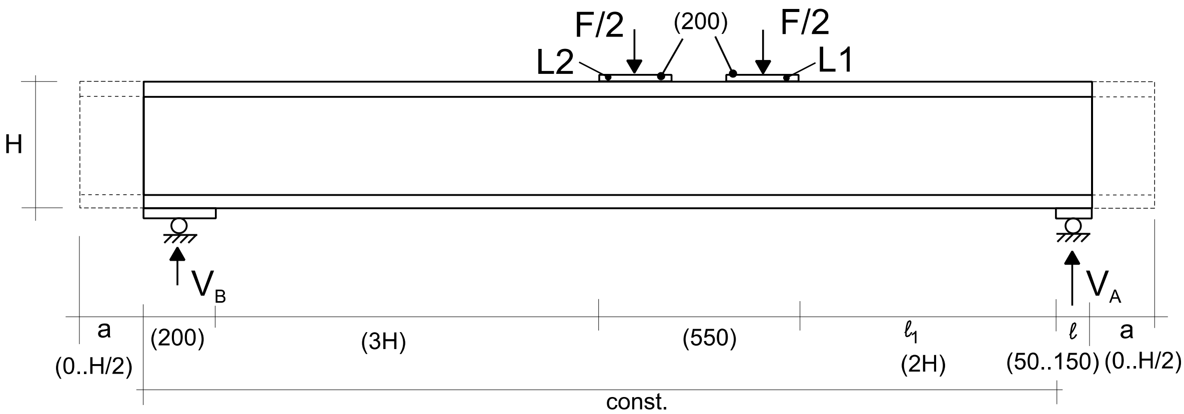

Fig. 5: Scheme of conducted I-beam 4-point bending test set-up and dimensions

:

a)

b)

Figure 6a,b: Views of realized test set-ups with I-beams of different depths

a) H = 200 mm; sparce bracing, b) H = 500 mm; extensive bracing

Fig. 7: View of deformation measurement at the beam support end A with short bearing length (horizontal displacement out of web plane; vertical beam/web displacement)

5.2 Test results

As the focus of this paper is to highlight the transverse force capacity of unstiffened, end-supported I-beams, here exclusively the results of the beams without overhang are regarded. In brief it should be mentioned that highly consistent with the finite element computations, presented qualitatively above, an overhang acts as a quasi-web stiffener, leading to a very significant increase (here, roughly by a factor 2) of the transverse force capacity. As the paper focuses further on the load capacity effect of an increased web slenderness ratio h_w / b_w, for each beam height and web slenderness ratio only results of one specific support length is regarded.

The failure behavior of the three configurations with significantly different beam depths and web slender ratios was, as expected, rather different. Hereby primarily web/flange bond line and pure web failures occurred in case of slenderness ratios λ_w = 15 and 34, whereas throughout bending/buckling failures out of plane were obtained at web slenderness ratio λ = 53. For the latter case, Figures 8a and 8b show two load-deformation stages. Figure 8a depicts the significant web deflection at a higher, non-linear load level (> 0,75 F_u) and Figure 8b shows the state of the final bending failure with an extremely out-of-plane deformed web.

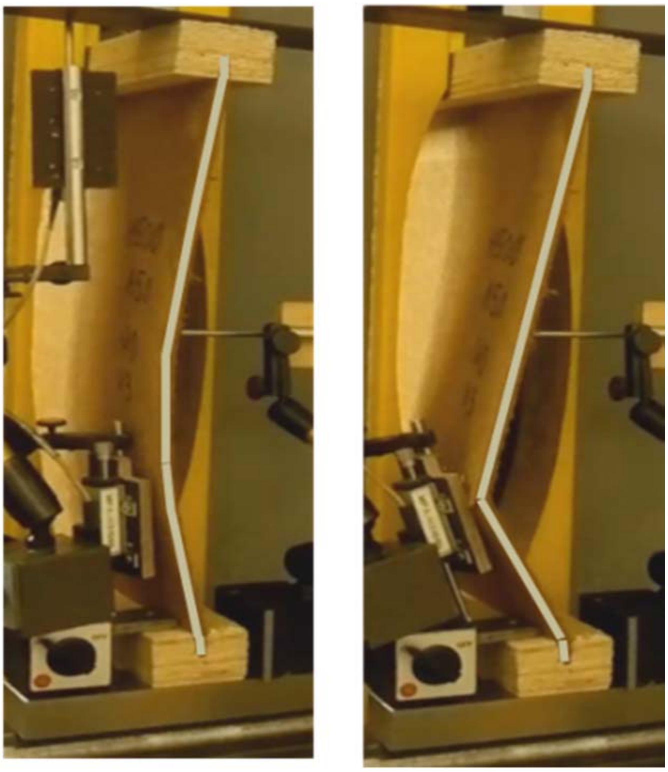

a) b)

Fig. 8a,b: Typical web bending and buckling failure of the investigated I-beams with a total depth of 500 mm; web slenderness ratio λ = 53

a) higher load level (> 0,75 F_u), b) failure state

total beam height H	bearing length ℓ	web slender-ness ratio $\lambda = h_w/b_w$	characteristic bearing capacity $R_{90,k}$		characteristic (web)shear force capacity $F_{v,w,Rk}$			characteristic vertical end support force resistance acc. to modified EC3 calculation	test results for vertical support(A) capacities $F_{R,u}$	
			ETA1)	EC52)	ETA3)	EC54)	EC5/ ETA	$F_{R,k}$	min	mean
mm	mm	-	kN	kN	kN	kN	-	kN	kN	kN
200	50	15,25	13,5	a)11,4 b)18,2 c)27,4	12,64	18,03	1,43	15,9	10,7	11,1
350	100	34	16,2	a)22,8 b)29,6 c)44,5	18,52	34,82	1,88	15,0	14,1	15,1
500	150	52,75	24,3	a)34,2 b)41,0 c)61,6	21,62	34,26	1,58	11,4	13,1	13,9

1), 2) for details of numerical values see chap. 6

3) ETA [8], Annex C, Table C2

4) acc. to Eqs. (2) to (4) and $f_{v,w,k}$ = 14 N/mm²

Table 2: Load capacities for differently sized wood-based I-beams (STEICO joists) without overhang (a = 0) and web stiffeners and different bearing lengths. Given are characteristic bearing, shear and total resistance forces, according to different EC 5 and EC 3 calculation models, according to product ETA [8] and according to test results.

The test results, regarding minimum and mean values of each configuration, are given in Table 2 altogether with calculated / tabulated characteristic bearing and shear force capacities according to ETA [8] and EC 5 [1]. Further Table 2 specifies the characteristic vertical end support force resistances according to the modified EC 3 approach.

6 Bearing capacities according to product ETA and EC 5

Following some explanations regarding the characteristic bearing and (web) shear force capacities specified in Table 2 with relation to ETA [8] and EC 5 [1] calculations are given.

ETA [8], Annex C, Table C4, specifies exclusively characteristic end bearing capacities for bearing lengths l = 35 mm, 45 mm and 89 mm. Based on the given capacities for l = 35 mm and 45 mm expressions $R_{90,k} = l \cdot b_w \cdot f_{c,90,eff,k}$ and $f_{c,90,eff,k} = f_{c,90,k} \cdot 1{,}2$ forward a characteristic compressive strength value perpendicular to fiber of $f_{c,90,k}$ = 3,8 N/mm² which conforms to the value specified in DoP [14] and Technical approval [16]. The compressive strength increase factor of 1,2 and hence $f_{c,90,eff,k}$ = 4,5 N/mm² is suggested in [16] for use in service class 1 only, and applied in [8]. For l = 89 mm recalculation from ETA [8] delivers a significantly smaller effective compressive strength of $f_{c,90,eff,k}$ = 2,7 N/mm^2. Here, for l = 50 mm and 100 mm the values $f_{c,90,eff,k}$ = 4,5 N/mm^2 and 2,7 N/mm^2, respectively, were used. For l = 150 mm a further reduced value of $f_{c,90,\ eff,k}$ = 2,0 N/mm^2 was chosen.

Regarding the characteristic bearing capacities specified in Table 2 for the EC 5 approach the following remarks apply to the three alternative values a) to c) given for each configuration. The bearing force specified under a) represents the most conservative approach perceivable, i.e. $R_{90,k} = l \cdot b_w \cdot f_{c,90,k}$ with $f_{c,90,k}$ = 3,8 N/mm^2 acc. to DoP [14]. The value specified under b) takes into account the one-sided fictive elongation of the bearing length by 30 mm. The value given under c) applies to the loading configuration where the clear distance l_1 between inner bearing length end and start of applied load conforms to $l_1 \geq 2H$, hereby employing additionally to the bearing length increase (b) the compressive strength increase factor $k_{c,90}$ =1,5 (see also [17]).

7 Numerical example for vertical end force resistance according to modified EC 3 approach

Following, exemplarily the characteristic end support force resistance of a specific configuration of the experimentally investigated thin-webbed STEICO-I-joist beams (H = 350 mm, l = 100 mm, a = 0) is evaluated with the modified EC 3-1-5 approach using the equations given in chap. 4. Results for other configurations are given in Table 2.

The stiffness and strength parameters employed in the calculations are specified in Table 1. A comment should be made with regard to the employed characteristic value for modulus of elasticity in bending out-of-plane of the regarded hard fiberboard. The characteristic 5%-quantile values of stiffness properties are in general not specified in Declarations of Performance (DoPs) of panel products and hence are also not specified in [8]. According to the German national Annex to EC 5-1-1 (DIN EN 1995-1-1/NA [15]), the 5%-quantile values of hard fiberboard panels shall be calculated as 80 % of the respective mean value (note: the rule $E_{05} = 0{,}8 \cdot E_{mean}$ applies strictly only to board type HB.HLA2 whereas here HB.HLA1 is employed). In case of the specifically regarded hard fiberboard and the smearing effect of a large area, it is considered sensible to calculate the characteristic value of MOE, used primarily to determine the critical buckling load, on the basis of $0.9 \cdot E_{mean}$.

The Poisson ratios of the quasi-isotropic web material hard fiberboard were taken as $\nu = \nu_{xy} = \nu_{yx}$ = 0,24, as specified in [18], [19] and [20].

From Eq. (17a) with k_{Fmax} = 5 and Eq. (15):

$$k_F = 2 + 6\left(\frac{100}{272}\right) = 4{,}21 < 5\,,$$

$$F_{cr,k} = \frac{\pi^2}{12\,(1-0{,}24^2)}\, 4{,}21 \cdot\, 4770\,\frac{8^3}{272} = 32{,}99\; kN\;.$$

From Eqs. (19), (20) and (21):

$$\ell_e = \frac{4{,}21 \cdot 4770 \cdot 8^2}{2 \cdot 21 \cdot 272} = 112{,}5\; mm\;\; > 100\; mm\,,$$

so: $\ell_e = 100\; mm$.

$m_1 = \frac{4{,}5}{21} \cdot \frac{60}{8} = 1{,}61$, note: here $f_{c90,f,k}$ = $f_{c,90,f,eff,k}$ = 4,5 N/mm^2 (see chap. 6),

$$m_2 = 0{,}02\,\left(\frac{272}{39}\right)^2 = 0{,}97\;.$$

From Eq. (18):

$$\ell_y = \min\left[+39 \cdot \sqrt{\frac{1{,}61}{2} + \left(\frac{100}{39}\right)^2 + 0{,}97}\;\;;\quad 100 + 39\sqrt{1{,}61 + 0{,}97}\right]$$
$$= \min[212{,}6\,;162{,}6] = 162{,}6\; mm\; < 1{,}7\;\cdot 100\; mm = 170\; mm.$$

From Eq. (12):

$$F_{c,w,k} = 21 \cdot 162{,}6 \cdot 8 = 27{,}32\; kN\;.$$

From Eqs. (11) and (10):

$$\lambda_{f,rel} = \sqrt{\frac{27{,}32}{32{,}99}} = 0{,}91\;\;,\;\; \chi_F = \frac{0{,}5}{0{,}91} = 0{,}55 < 1{,}0\;.$$

From Eqs. (9) and (8):

$$L_{eff} = 0{,}55 \cdot 162{,}6 = 89\; mm,$$

$$F_{R,k} = 21 \cdot 89 \cdot 8 = 15{,}0\; kN\;.$$

8 Comparison of test results vs. product ETA, EC 5 and modified EC 3 load capacity predictions

A comparison of the characteristic vertical end support force capacities based on the modified EC 3-1-5 calculations with the minimum and mean test results forwards for the beam configuration with medium web slenderness ratio 34 a very good agreement.

Regarding the most slender beam configuration ($\lambda = 53$), the modified EC 3 - result is on the conservative (safe) side and hereby 13% lower vs. the experimental minimum value. For the most stout configuration the calculated vertical end support force considerably overestimates the test results. However, this is irrelevant, as for that configuration the bearing resistance is the limiting factor in the tests and in calculation when employing the most conservative EC 5 approach, here denoted by method a), i.e. no fictive elongation of bearing length l and no $k_{c,90} > 1$.

When comparing the test results with the ETA [8] load capacities roughly sufficient agreements can be stated for the stout and medium slender web configurations although the test results are in any case well 10% lower than the design relevant characteristic capacities. For the very slender web configuration the ETA does not enable a true critical assessment of the test result as tabulated bearing resistances are limited to a maximum bearing length of 89 mm. The respective specified capacity (11,8 kN) is 10% lower than the experimental minimum value. However, no indication is given how to prevent an extreme unsafe calculation result by the approach revealed in chap. 6.

The extreme discrepancies between the test results and the EC 5 solutions are apparent. An extreme unsafe overestimation of the test results has to be stated for both, calculated bearing and shear force capacities (note: for the assessment of the EC 5 calculated bearing capacities the results obtained with method b) i.e. 30 mm increased bearing length and $k_{c,90} = 1$ are used.). In case of the most stout beam/web configuration the EC 5 results for bearing and shear forces are 70% higher as compared to the test results. In case of web slenderness 34 and 53 the calculations exceed the respective minimum test values by factors of minimally 2,1 to maximally 3,1.

9 Conclusions

It was revealed that the present calculation procedure in EC 5 for the web shear and transverse end support force capacity leads, at least for the regarded build-up configuration, to extremely too high, unsafe load capacities. This is especially true when an end support situation with an unstiffened web and no overhang is regarded. The values predicted by EC 5 exceed the the test results by factors of 1.7 to 3.1 and the load capacities given in a relevant product ETA by factors of 1,4 – 1,9.

The reason for the non-conservative EC 5 load prediction results from the fact that the transverse force buckling at the unstiffened end support leads to a significant reduction of the load capacity, so far not addressed in the European timber design code. This issue becomes obviously more severe with increasing web slenderness. Contrary to EC 5, several international steel construction codes, so EN 1993-1-5 (EC 3) on plated structural steel elements account very stringently for the transverse force design of unstiffened and stiffened end and intermediate supports. This aspect is tackled separately from the shear force (buckling) issue, however both actions can be addressed as interacting.

Although the EC 3 design equations for steel I-beams can obviously not be transferred identically to wood-based beams, an attempt was made to modify the relevant equations accordingly. The derived set of equations fit the ETA load capacities and the tests performed for verification in a considerably better manner. Irrespective hereof some factors could still be amended.

Apart from the primarily addressed transverse web force issue, it is noticeable that the bearing capacities, calculated for the specific product on the basis of EC 5 are significantly too high, especially when employing a $k_{c,90}$ value larger than 1 and making use of the permissible fictive bearing length increases.

The empirical verification of today´s EC5 shear and bearing force design approach of unstiffened end supports of thin-webbed I-beams was performed with I-beams generally brought on the market with tabulated design values derived by test assisted ETA approval procedures (here [10], [11]).These I-beams show throughout a specific tongue-groove connection of the web with the flanges which is not mirrored in the relevant EC 5 drawings for thin-webbed cross-section build-ups, yet not excluded. The mentioned specific flange-web connection is considered however being irrelevant for the obtained mismatch of the test and EC 5 calculations which necessarily need to be amended.

10 References

[1] EN 1995-1-1 (2004 + A1) Eurocode 5: Design of timber structures – Part 1 – 1: General – Common rules and rules for buildings. EN 1995-1-1:2004 +AC:2006 + A1:2008, CEN, Brussels

[2] Foschi, R.O. (1970): Rolling shear failure of plywood in structural components, Forest Products Lab, Information Report VP-x-67

[3] v. Halász, R., Cziesielski, E. (1966): Berechnung und Konstruktion geleimter Träger mit Stegen aus Furnierplatten. Berichte aus der Bauforschung. No. 47

[4] Dekker, J., Knipers, J., Ploos van Amstel, H. (1978): Buckling strength of plywood. Results of tests and design recommendations. Heron (23), No. 4, Delft, The Netherlands

[5] Aune, P. (1992): Trekonstruksjoner – del 1, Tapir Forlag, Norway

[6] Solli, K.H. (1995): Geleimte, dünnstegige Träger. Step B9, Step 1, Ed. Arbeitsgemeinschaft Holz e.V., Düsseldorf

[7] EN 1993-1-5 (2006): Eurocode 3: Design of steel structures – Part 1 – 5: Plated structural elements, EN 1993-1-5:2006 + AC:2009, CEN

[8] European Technical Assessment ETA-06/0238 (2014): STEICOjoist and STEICOwall (5th edition). Holder of assessment: STEICO SE, Feldkirchen, Germany

[9] European Technical Approval ETA-02/0026 (2006-2011): iLevel Trus Joist TJI Joists, Holder of Approval: Weyerhaeuser Products Ltd, Hopwood, Great Britain

[10] ETAG 011 (2002): Guideline for European Technical Approval of “Light composite wood-based beams and columns”, EOTA, Brussels

[11] EOTA Technical Report TR002 (2000): Test methods for light composite wood-based beams and columns

[12] EN 622-2 (2004): Fibreboards – Specifications – Part 2: Requirements for hardboards

[13] EN 14374 (2004): Timber structures – Structural laminated veneer lumber - Requirements

[14] Declaration of Performance (DoP) No. 03-0002-3 (2013): STEICO LVL, STEICO SE, Feldkirchen

[15] DIN EN 1995-1-1/NA (2013): National Annex – Nationally determined parameters – Eurocode 5: Design of timber structures – Part 1-1: General – Common rules and rules for buildings, CEN, Brussels

[16] Technical building approval Z-9.1-842 by DIBt (2014): Laminated veneer lumber “STEICOLVL R”, “STEICOLVL RS”, “STEICOLVLX”, approval holder: STEICO SE, Feldkirchen

[17] Blaß, H. J., Ehlbeck, J., Kreuzinger, H., Steck, G. (2004): Erläuterungen zu DIN 1052:2004-08. Ed. DGfH Innovations-und Service GmbH, München

[18] Lundgren, S. A. (1969): Wood-based panel products as building materials. Part I. Swedish Fibreboard Information 2.11

[19] Albers, K. (1970): Querdehnungs- und Gleitzahlen sowie Schub- und Scherfestigkeiten von Holzwerkstoffen. PhD thesis, University of Hamburg

[20] Möhler, K., Steck, G. (1979): Näherungsformeln zur Berechnung von Verbundbauteilen aus Vollholz und Holzwerkstoffen. Holz Roh-Werkstoff (37): 221 – 225

Discussion

The paper was presented by S Aicher

E Serrano commented about the slender web and the splitting of flange failure mode.

S Aicher agreed that this type of beam could result in many types of failure modes including splitting of flange. E Serrano asked how common this type of beam design would be needed. S Aicher said that the work was done in the framework of another testing project where they did the testing. He was not sure who would produce such product regularly. He commented that even though they would not be used commonly the design method should be correct. He also stated that this type of beams could have high bearing loads.

In-Grade Evaluation of U.S. Glulam Beams, End Joints, and Tension Laminations

Borjen Yeh, Ph.D., P.E.; Jessie Chen, Ph.D., P.E.; and Tom Skaggs, Ph.D., P.E.

APA – The Engineered Wood Association, Tacoma, Washington, U.S.A.

Keywords: Structural Glued Laminated Timber, Glulam, End Joints, Tension Laminations, In-Grade, Full-Scale

1 Introduction

Structural glued laminated timber (glulam) has been in commercial production in the U.S. since 1934 [Rhude, 1996]. There are about 30 glulam plants in the U.S., producing a total volume of 606000 m^3 (257 million board feet) of glulam in 2016 for a variety of construction applications [APA, 2016]. Today, the glulam manufacturing in the U.S. has been standardized in ANSI A190.1, *American National Standard for Structural Glued Laminated Timber* [ANSI/APA, 2017]. In the meantime, an analytical methodology, known as the "I_K/I_G" model established in 1954 through extensive research conducted by the U.S. Forest Products Laboratory in Madison, Wisconsin, has also been standardized in ASTM D3737, *Standard Practice for Establishing Allowable Properties for Structural Glued Laminated Timber* [ASTM, 2012]. The ASTM D3737 methodology was previously reviewed in the CIB W18 paper 40-12-4 [Williamson and Yeh, 2007].

ASTM D3737 provides a basis for glulam design properties published in ANSI 117, *American National Standard for Structural Glued Laminated Timber of Softwood Species* [ANSI/APA, 2015] for a variety (86 in total) of glulam layup combinations, including mixed-grade ("combined") and single-grade ("homogeneous") glulams. For hardwood species, the glulam industry generally adopts AITC 119, *Standard Specifications for Structural Glued Laminated Timber of Hardwood Species* [AITC, 1996], which has not been updated since 1996 due in part to the dissolution of American Institute of Timber Construction (AITC) in 2012 and an insignificant production volume for hardwood glulams in the U.S.

As compared to the European practice, ASTM D3737 and ANSI 117 adopt a different assumption in assigning glulam design values, i.e., the end joint strength is assumed to perform at a level that will support the assigned glulam properties and does not reduce the glulam structural performance through in-plant quality assurance on an on-going basis. In other words, the published glulam design values are predicated on the performance of end joints, as defined in ANSI A190.1. Therefore, the quality of end joints remains critical to the glulam beam performance. However, there are no requirements in ANSI A190.1 for full-scale glulam beam tests as part of the quality assurance program on a regular basis. It is assumed that if the glulam components – laminating lumber, adhesive, end joints, and face joints are properly quality-controlled at the plant, the finished glulams will perform well without full-scale glulam beam tests. This practice has apparently stood the test of time as there have been no major glulam performance issues reported in the U.S.

For these reasons, full-scale glulam beam test data are quite limited. However, as other engineered wood products, such as structural composite lumber (SCL) and prefabricated wood I-joists, are regularly tested in full size, it is considered desirable to obtain glulam performance data from "in-grade" productions sampled over multiple years from representative production facilities to re-evaluate or reaffirm the current glulam design values that have been in use for decades in the U.S.

As a result, a 4-year in-grade glulam program was initiated in 2012 by APA – The Engineered Wood Association, which trademarks about 92% of glulam production currently in the U.S. and Canada. With the support of the glulam industry, the in-grade program sampled and tested full-scale glulam beams, and matched end joints and tension laminations from regular productions. This paper provides an analysis of the glulam beam bending strength (MOR) and modulus of elasticity (MOE), the tensile strength of end joints, and the tensile strength and long-span E (LSE) of tension laminations. The results are compared to the published design values based on the ASTM D3737 analytical model for glulams used in the U.S.

2 Objectives

The main objectives of this multiple-year in-grade glulam evaluation program were to determine the overall quality of glulam beams manufactured from multiple manufacturing facilities in the U.S. using regular productions and to re-evaluate or reaffirm the published glulam design values based on the ASTM D3737 analytical model.

3 Materials and Methods

3.1 Materials

Although there are 86 softwood glulam layup combinations that are prescribed in ANSI 117, the vast majority (75% or more) of current glulam productions in the U.S. are manufactured in accordance with 4 primary glulam layup combinations: 24F-V4 Douglas-fir (DF), 24F-V3 Southern Pine (SP), 24F-V8/DF, and 24F-V5/SP. These layup combinations use mostly visually graded lumber except that mechanically graded lumber may be substituted on an equivalent performance basis in accordance with ANSI A190.1 and ANSI 117. This substitution occurs mostly on special tension laminations ("302-24"). The first 2 layup combinations are unbalanced layups for DF and SP, meaning the layups are asymmetrical for the lamination grades used on top and bottom portions of the glulam beam. On the other hand, the latter 2 layup combinations are balanced layups for DF and SP, meaning the layups are symmetrical. In reality, the unbalanced layups are significantly more popular than the balanced layups in the U.S. Therefore, the in-grade program focused on the unbalanced glulam layup combinations of 24F-V4/DF and 24F-V3/SP.

To ensure the tension lamination and its end joints are stressed more like a tension member (vs. a bending member), a beam depth of 12 and 13 laminations, i.e., 457 mm (18 inches) and 454 mm (17-7/8 inches) was chosen for 24F-V4/DF and 24F-V3/SP, respectively, based on the standard lamination thickness of 38 mm (1-1/2 inches) and 35 mm (1-3/8 inches) for DF and SP. The actual glulam beam layups are shown in Table 1.

Table 1. Glulam Layups Used for In-Grade Testing.

Layup Details and Predicted Properties	Lamination #	24F-V4/DF	24F-V3/SP
		Lamination Thickness and Grade[(a)]	
Layup Details	13	—	35-mm N1D10
	12	38-mm L2D	35-mm N1D10
	11	38-mm L2D	35-mm N2D8
	10	38-mm L2	35-mm N2M8
	9	38-mm L3	35-mm N2M8
	8	38-mm L3	35-mm N2M8
	7	38-mm L3	35-mm N2M8
	6	38-mm L3	35-mm N2M8
	5	38-mm L3	35-mm N2M8
	4	38-mm L3	35-mm N2D8
	3	38-mm L2	35-mm N2D8
	2	38-mm L1	35-mm N1D12
	Special Tension Lam	38-mm 302-24	35-mm 302-24
MOR[(b)], MPa (psi)		34.7 (5040)	34.7 (5040)
MOE[(c)], MPa (10^6 psi)		12600 (1.83)	12500 (1.82)

(a) Lamination grades are defined in ANSI 117. "302-24" is a special tension lamination grade.

(b) Predicted modulus of rupture (MOR) values are the characteristic values (5^{th} percentile with 75% confidence) adjusted to the standard beam volume of 130 mm x 305 mm x 6400 mm (5-1/8 inches x 12 inches x 21 feet) at the standard moisture content of 12%. The predicted MOR values are limited by the characteristic end joint strength. Without end joints, the predicted MOR value is 35.2 MPa (5109 psi) and 38.5 MPa (5586 psi) for 24F-V4/DF and 24F-V3/SP, respectively.

(c) Predicted modulus of elasticity (MOE) values are the mean apparent MOE values adjusted to the standard moisture content of 12%. The MOE values are assumed to be 95% of the true MOE values in accordance with ASTM D3737.

3.2 Sampling

At least 30 full-size glulam beams of about 130 mm x 457 mm x 10 m (5-1/8 inches x 18 inches x 33 feet) were sampled each year from 3 or more glulam plants (i.e., 10 beams per plant). This sampling continued in 4 consecutive years (2012 through 2015). As the beams were sampled from each glulam plant, at least 30 matched end joints of 38 mm x 140 mm x 2100 mm (1-1/2 inches x 5-1/2 inches x 7 feet) and 30 matched tension laminations of 38 mm x 140 mm x 4000 mm (1-1/2 inches x 5-1/2 inches x 13 feet) were also sampled from the same production so that the component performance could be correlated to the glulam beam performance. Since it is a common practice to combine Coastal and Inland Douglas-fir for the 24F-V4/DF layup combination, efforts were made to sample these 2 sub-wood species separately so as to ensure that the published design values could be evaluated for both. The DF and SP glulam layup combinations have the same published stress class of 24F-1.8E, which has a characteristic bending strength of 34.7 MPa (5040 psi) and mean apparent modulus of elasticity of 12400 MPa (1.8 x 10^6 psi).

At the end of this in-grade program, a total of 130 beams (50 Coastal Douglas-fir, 40 Inland Douglas-fir, and 40 Southern Pine), 397 matched end joints (150 Coastal Douglas-fir, 122 Inland Douglas-fir, and 125 Southern Pine), and 370 matched tension laminations (125 Coastal Douglas-fir, 120 Inland Douglas-fir, and 125 Southern Pine) were sampled from 13 different glulam plants (5 Coastal Douglas-fir, 4 Inland Douglas-fir, and 4 Southern Pine).

3.3 Test Methods

All materials were tested at the APA Research Center in Tacoma, Washington, which has an ISO/IEC 17025-accredited independent test laboratory for the tests covered in this program.

Lamination Tests: The long-span E of tension laminations was tested flatwise in accordance with AITC T116, *Modulus of Elasticity for E-Rated Lumber by Static Loading* [AITC, 2007], using a center-point load method with an on-center span of 3810 mm (150 inches), resulting in a span-to-depth ratio of 100:1. This long-span E is essentially the true E due to minimal shear deflection at this large span-to-depth ratio. The tensile strength of the tension laminations was tested in accordance with AITC T123, *Sampling, Testing and Data Analysis to Determine Tensile Properties of Lumber* [AITC, 2007], using a 2440 mm (8-foot) gauge length, which is a standard in the U.S. for structural lumber tests.

End Joint Tests: The tensile strength of end joints was tested in accordance with AITC T119, *Full Size End Joint Tension Test* [AITC, 2007], using a 610-mm (2-foot) gauge length, which is a standard in the U.S. for structural end joint tests.

Glulam Beam Tests: A two-point load method, as shown in Figure 1, was applied to test each glulam beam using a span-to-depth ratio of approximately 21. The test apparatus, including rocker-type reaction supports, reaction bearing plates and rollers, load bearing block, and load bearing rollers was set up following ASTM D198, *Standard Test Methods of Static Tests of Lumber in Structural Sizes* [ASTM, 2015]. The position of end joints in each beam was random and not specifically excluded from the center one-half (high tensile stress) portion of the glulam beam.

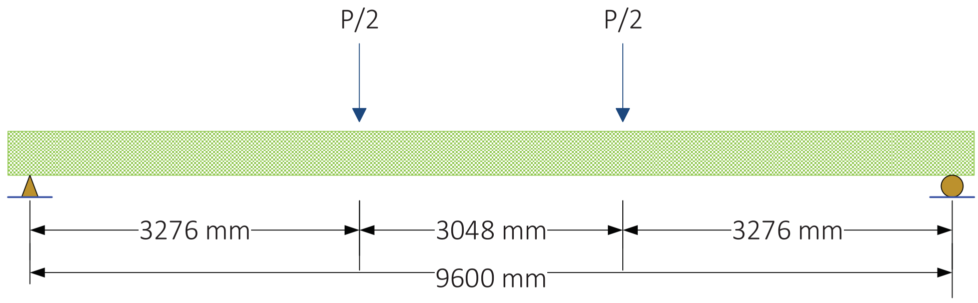

Figure 1. Loading configuration for glulam beam bending tests

For determining the glulam bending strength, the MOR value obtained from bending testing was adjusted by a volume factor, C_v, (Equation 1) based on the 2015 *National Design Specification for Wood Construction,* NDS [ANSI/AWC, 2015].

$$C_v = \left(\frac{130}{b}\right)^{\alpha} \left(\frac{305}{h}\right)^{\alpha} \left(\frac{6400}{\ell}\right)^{\alpha} \qquad (1)$$

where: C_v = volume factor,
α = 1/10 for Douglas-fir glulam and 1/20 for Southern Pine glulam, and
b, h, ℓ = beam width and depth, and test span in mm, respectively.

In addition, the MOR and apparent MOE values were adjusted to the standard 12% moisture content based on ASTM D1990, *Standard Practice for Establishing Allowable Properties for Visually-Graded Dimension Lumber from In-Grade Tests of Full-Size Specimens* [ASTM, 2014].

4 Results and Discussion

4.1 Tension Lamination Properties

Based on the sample of 370 tension laminations (125 Coastal Douglas-fir, 120 Inland Douglas-fir, and 125 Southern Pine) from 13 different glulam plants, results of tension lamination tensile strength and long-span E are summarized in Table 2.

Table 2. Tension lamination properties.

Species	N	Tension Lamination Tensile Strength			Long-Span E	
		Mean, MPa (psi)	COV	Characteristic Value [(a)], MPa (psi)	Mean, MPa (10^6 psi)	COV
Douglas-fir	245[(b)]	49.4 (7164)	0.30	27.7 (4024)	15830 (2.30)	0.13
Southern Pine	125	57.6 (8359)	0.26	35.2 (5103)	14931 (2.17)	0.15
Combined	370	52.2 (7568)	0.29	29.7 (4307)	15525 (2.25)	0.14

(a) 5th percentile with 75% confidence based on an assumed lognormal distribution function.
(b) For long-span E, the number of observations (N) is 244.

The published characteristic tensile strength for the 302-24 tension laminations regardless of the wood species is 27.6 MPa (4008 psi). As shown in Figure 2 and Table 2, the industry-wide data met the published characteristic tensile strength. At the lower tail of the data distribution, the lognormal distribution fits better than the normal distribution. In reviewing individual test results, there were 14 out of 370 tested tension laminations that were lower than the published tensile strength of 27.6 MPa (4008 psi). This represents about 3.8% of probability, which is within the expected probability in practice.

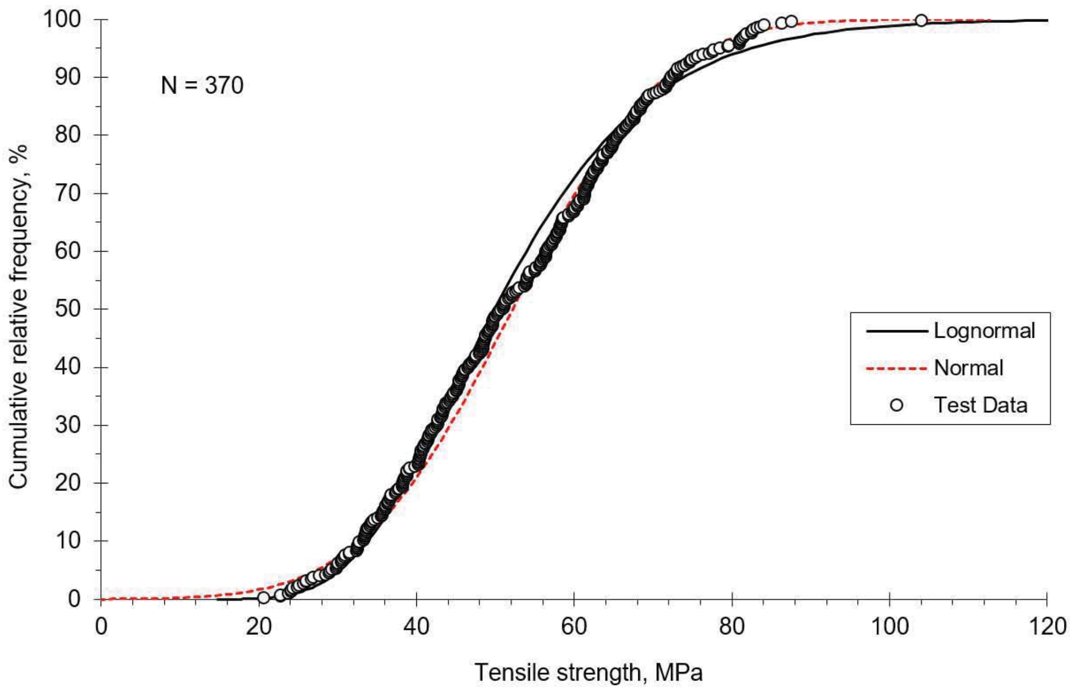

Figure 2. Tensile strength of tension laminations

Table 2 also shows the long-span E for the 302-24 tension laminations. The published LSE is 14500 MPa (2.1 x 10^6 psi) and 13800 MPa (2.0 x 10^6 psi), respectively, for Douglas-fir and Southern Pine 302-24 tension laminations. As shown in Table 2, the tested LSE values exceeded the published LSE values by about 10%.

4.2 End Joint Properties

Based on the sample of 397 end joints (150 Coastal Douglas-fir, 122 Inland Douglas-fir, and 125 Southern Pine) from 13 different glulam plants, results of end joint tensile strength are summarized in Table 3.

Table 3. End joint tensile strength.

Species	N	End Joint Tensile Strength		
		Mean, MPa (psi)	COV	Characteristic Value [(a)], MPa (psi)
Douglas-fir	272	39.6 (5740)	0.18	27.9 (4042)
Southern Pine	125	40.5 (5873)	0.16	30.2 (4376)
Combined	397	39.9 (5782)	0.17	28.6 (4153)

(a) 5th percentile with 75% confidence based on an assumed lognormal distribution function.

As previously mentioned, end joints are required to be quality-controlled in accordance with ANSI A190.1 based on the glulam performance level. Since end joints are required to be tested in full-scale tension (instead of bending), for glulam bending members, the end joint must be quality-controlled at 80% of the characteristic bending strength of the glulam beam by taking into account the difference between tensile and bending strengths. As a result, since the characteristic bending strength of 24F glulam beams is at least 34.7 MPa (5040 psi), the end joints must be quality-controlled at the characteristic tensile strength of 27.6 MPa (4008 psi) in accordance with ANSI A190.1.

As shown in Figure 3 and Table 3, the characteristic end joint tensile strengths met the required value of 27.6 MPa (4008 psi) for 24F glulam beams. It should be noted that the coefficient of variation (COV) for the tensile strength of end joints is significantly lower than that of tension laminations shown in Table 2. In reviewing individual test results, there were 11 out of 397 tested end joints that were lower than 27.6 MPa (4008 psi). This represents about 2.8% of probability. While this level of probability is considered acceptable in practice, the use of an in-line proof loader in production (note that not all end joints tested in this program were proof-loaded, which reflects the current industry practice) may help to eliminate the low performer in production.

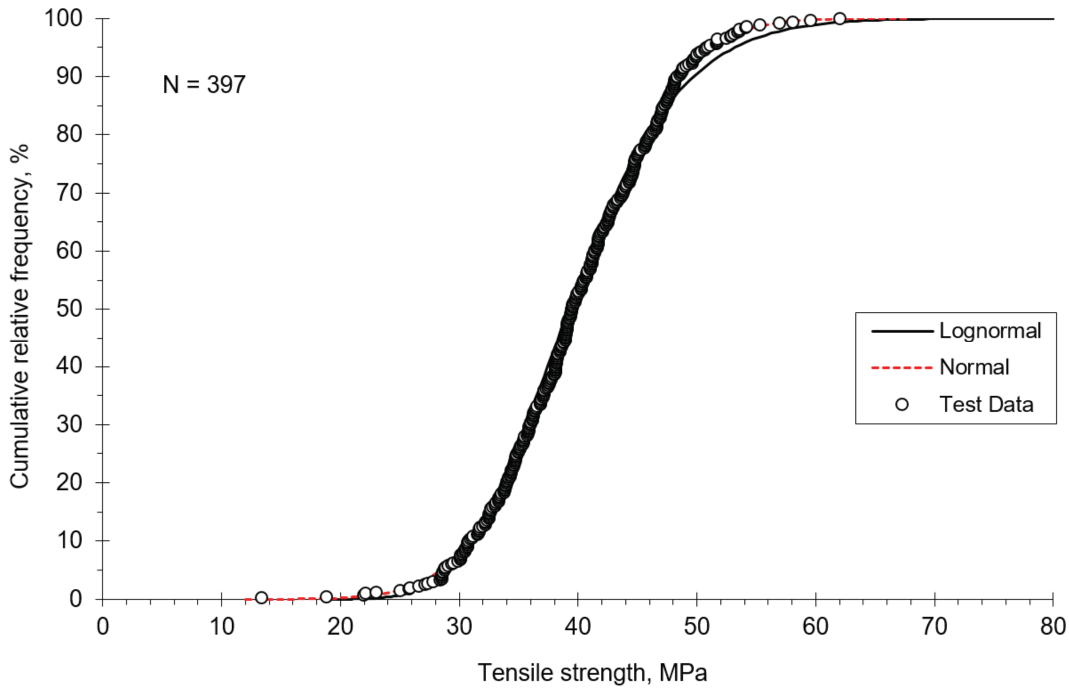

Figure 3. Tensile strength of end joints

4.3 Glulam Beam Performance

Based on the sample of 130 glulam beams (50 Coastal Douglas-fir, 40 Inland Douglas-fir, and 40 Southern Pine) from 13 different glulam plants, results of glulam beam bending properties are summarized in Table 4. As previously noted, the bending strength values have been adjusted for the volume effect. In addition, both MOR and MOE values have been adjusted for the standard moisture content of 12%.

Table 4. Glulam beam bending properties.

Species	N	Glulam Beam Bending Strength (MOR)			Glulam Beam Modulus of Elasticity (MOE)	
		Mean, MPa (psi)	COV	Characteristic Value [(a)], MPa (psi)	Mean, MPa (10^6 psi)	COV
Douglas-fir	90	46.7 (6767)	0.16	34.2 (4965)	14055 (2.04)	0.10
Southern Pine	40	50.4 (7307)	0.17	36.6 (5312)	14179 (2.06)	0.07
Combined	130	47.8 (6933)	0.17	35.0 (5078)	14093 (2.04)	0.09

(a) 5th percentile with 75% confidence based on an assumed lognormal distribution function.

Most glulam beams failed in bending due to finger joint tension failure at the ultimate load, while there were some beams failed as a result of tension lamination failure due to edge knots or slope of grain, as shown in Figure 4. Note that the edge knot shown in Figure 4 was noticed to be off-grade for the 302-24 tension laminations, which is limited to 1/6 of the lamination width. Since this was uncommon in occurrence, its test results were not removed from the database reported in Table 4 for added conservatism.

Figure 4. Glulam beam failure modes

The published MOR for 24F glulams, as predicted by the ASTM D3737 analytical model (see Table 1) is 34.7 MPa (5040 psi), which is governed by the end joint strength. Based on the characteristic tensile strengths of tension laminations (Table 2) and end joints (Table 3), a combination of tension lamination and end joint tension failures are to be expected for these tested glulam beams. As noted from Table 4, the characteristic glulam MOR is 35.0 MPa (5078 psi) based on the combined test data, which matches well with the predicted MOR of 34.7 MPa (5040 psi). While the characteristic glulam MOR for Douglas-fir glulam beams is about 1.5% below the targeted value, it is within the standard rounding tolerance (2%) for the design bending value of 24F glulam beams. Figure 5 shows the bending strength (MOR) data distribution for all glulam beams tested in this program.

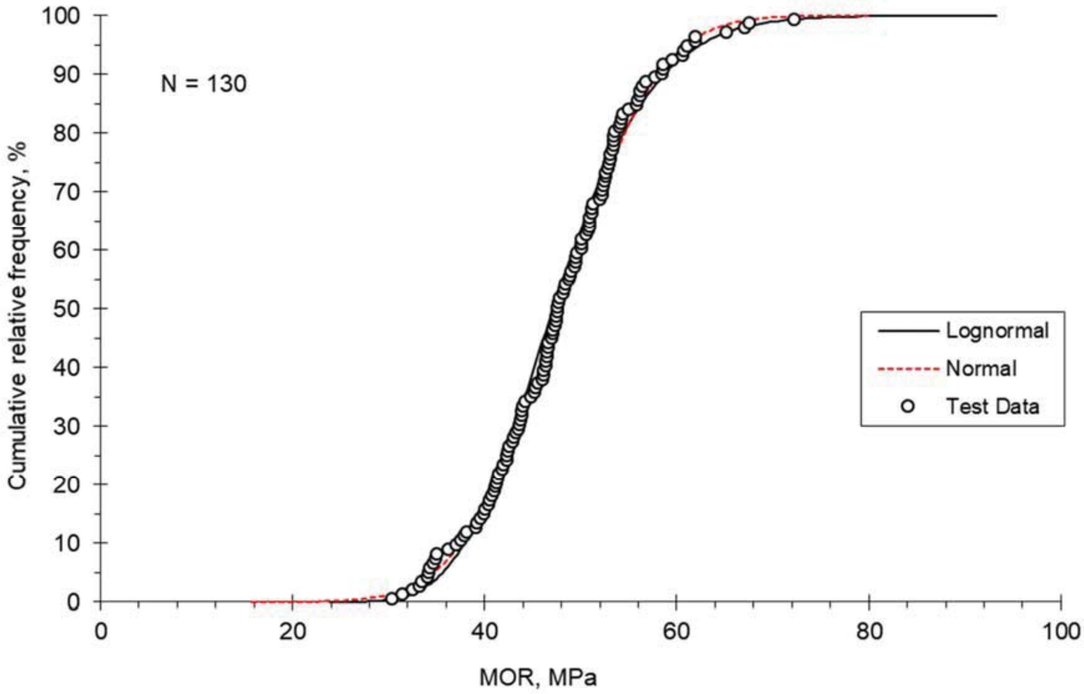

Figure 5. Bending strength (MOR) of glulam beams

In reviewing individual test results, there were 5 out of 130 beams with an MOR that was lower than the expected MOR for 24F glulam beams. This represents about 3.8% of probability, which correlates well with the 3.8% and 2.8% probabilities reported above for tension laminations and end joints, respectively. While this level of probability is considered acceptable in practice, the continuing attention to lumber grading and end joint quality control techniques should be helpful to the improvement of glulam beam performance.

When comparing the characteristic end joint tensile strength shown in Table 3 and the glulam beam bending strength shown in Table 4, the ratio of end joint tensile strength and glulam beam bending strength is 4042 psi/4965 psi or 0.814 for Douglas-fir glulams, 4376 psi/5312 psi or 0.824 for Southern Pine glulams, and 4153 psi/5078 psi or 0.818 for the combined data. These results are similar and confirm the aforementioned ratio of 0.80 that has been adopted by the U.S. glulam industry in the last 30 years.

The data distribution for the combined glulam beam MOE results is shown in Figure 6. Table 4 also shows the mean glulam beam MOE values, which are significantly (about 13%) higher than the predicted value of 12600 MPa (1.83 x 10^6 psi) for 24F-V4

Douglas-fir glulams and 12500 MPa (1.82 x 10^6 psi) for 24F-V3 Southern Pine glulams. This should not be a surprise based on the 10% higher LSE values from the tension laminations, as shown in Table 2. As the ASTM D3737 analytical model adopts the transformed-section method in predicting the glulam beam MOE, the glulam beam MOE is directly affected by the lamination LSE. In fact, when the lamination LSE values are increased by 10%, the predicted beam MOE would be 13860 MPa (2.01 x 10^6 psi) for the 457 mm (18 inches) deep 24F-V4 Douglas-fir beams and 13790 MPa (2.00 x 10^6 psi) for the 454 mm (17-7/8 inches) deep 24F-V3 Southern Pine beams. These predicted glulam MOE values are within 3% of the tested glulam MOE values shown in Table 4. This confirms that the transformed section method is a reasonable model for predicting glulam beam MOE. Therefore, a continuing quality control of the lamination LSE should be adequate to ensure the glulam stiffness performance.

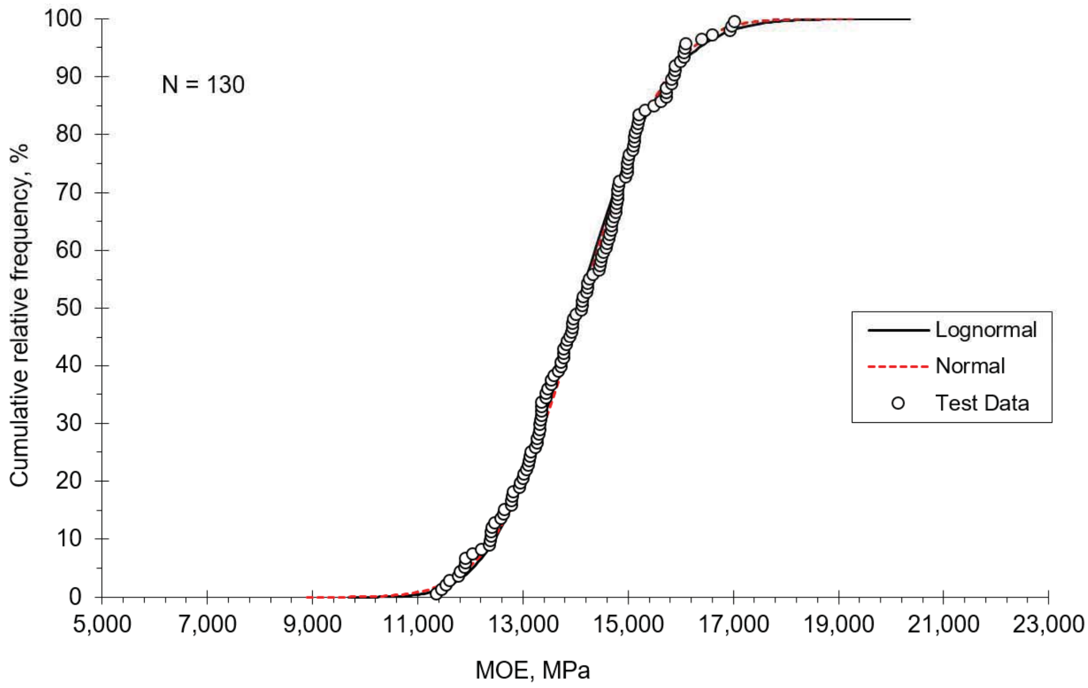

Figure 6. Bending modulus of elasticity (MOE) of glulam beams

The relatively high glulam beam MOE obtained from this in-grade program, as compared to the currently published glulam MOE, was discussed by glulam manufacturers for a possible revision to the current design values. However, due to a concern over consistent supplies of high quality lumber laminations in the long run, a conscious decision was made by the glulam industry to not pursue this option at this point. The industry will continue to monitor the lamination LSE.

5 Conclusions

Results obtained from this 4-year in-grade program, which included the tensile strength of end joints, tensile strength and long-span E of tension laminations, and bending strength and modulus of elasticity of glulam beams, are representative of the state of glulam production quality in the U.S. Overall, a total of 130 glulam beams, 370 tension laminations, and 397 end joints were evaluated.

Overall, the following conclusions can be drawn based on the results obtained from this program:

1. The tensile strength of tension laminations met the published value. On the other hand, the long-span E of tension laminations exceeded the published value by about 10%. This has a positive and direct impact to the glulam beam MOE. Since the tension lamination performance is critical to the glulam beam performance, the lumber grading for laminations in glulam production should continue to be a priority for glulam manufacturers.
2. The tensile strength of end joints met the value established by the glulam standard, ANSI A190.1, for the 24F glulam beams. Since the end joint performance is critical to the glulam beam performance, the daily quality control of end joints in glulam production should remain vigilant by glulam manufacturers.
3. The ratio of 0.8 for the characteristic tensile strength of end joints and the characteristic bending strength of glulam beams, as established by ANSI A190.1 is confirmed by the results of this program.
4. The bending strength of glulam beams met the design value published in the glulam design specification, ANSI 117, while the bending modulus of elasticity exceeded the published value by about 13%, which is attributed in part by the higher LSE of tension laminations.
5. The ASTM D3737 analytical model remains adequate for predicting glulam design values and no immediate revisions to the model are suggested by the results obtained from this program.

6 References

American Institute of Timber Construction. 1996. *Standard Specifications for Structural Glued Laminated Timber of Hardwood Species*. AITC 119. Englewood, CO.

American Institute of Timber Construction. 2007. *Modulus of Elasticity for E-Rated Lumber by Static Loading*. AITC T116 (in Test Methods for Structural Glued Laminated Timber). Centennial, CO.

American Institute of Timber Construction. 2007. *Full Size End Joint Tension Test*. AITC T119 (in Test Methods for Structural Glued Laminated Timber). Centennial, CO.

American Institute of Timber Construction. 2007. *Sampling, Testing and Data Analysis to Determine Tensile Properties of Lumber*. AITC T123 (in Test Methods for Structural Glued Laminated Timber). Centennial, CO.

ANSI/APA. 2015. *American National Standard Specification for Structural Glued Laminated Timber of Softwood Species*. ANSI 117 (published by APA – The Engineered Wood Association). Tacoma, WA.

ANSI/APA. 2017. *American National Standard for Structural Glued Laminated Timber*. ANSI A190.1 (published by APA – The Engineered Wood Association). Tacoma, WA.

ANSI/AWC. 2015. *National Design Specification for Wood Construction*. NDS (published by American Wood Council). Leesburg, VA.

APA – The Engineered Wood Association. 2016. *Market outlook and regional production 2016 - 2020*. APA Economics Report E82. Tacoma, WA.

ASTM International. 2012. *Standard Practice for Establishing Allowable Properties for Structural Glued Laminated Timber*. ASTM D3737. West Conshohocken, PA.

ASTM International. 2014. *Standard Practice for Establishing Allowable Properties for Visually-Graded Dimension Lumber from In-Grade Tests of Full-Size Specimens*. ASTM D1990. West Conshohocken, PA.

ASTM International. 2015. *Standard Test Methods of Static Tests of Lumber in Structural Sizes*. ASTM D198. West Conshohocken, PA.

Rhude, A.J. 1996. *Structural glued laminated timber: history of its origins and early development*. Forest Products Journal 46(1): 15-22.

Williamson, T.G. and B.J. Yeh. 2007. *Standard practice for the derivation of design properties of structural glued laminated timber in the United States.* In Proceedings of CIB W18: Paper 40-12-4. Bled, Slovenia.

Discussion

The paper was presented by BJ Yeh

A Buchanan asked do you have limitation on end-joint spacing in US. BJ Yeh responded that end-joints within a lamination must be at least 6 feet apart. End-joints distance between adjacent lamination must be greater than 6 inches. Proof loading of end-joints would allow the longitudinal requirements to be waived.

F Lam commented that there was a large difference between the DF and SYP species with the SYP having higher values. If DF were taken alone they would be slightly below the target level. Statistical analysis could probably show that there was no difference. BJ Yeh agreed and he said that the DF values were only slightly lower than target which could be attributed to the inclusion of off grade beams in the database. F Lam stated that although inclusion of the off grade data was conservative but this would be against in-grade testing philosophy.

JWG van de Kuilen questioned whether there would be any difference between vertical and horizontal finger joints. BJ Yeh said that in N. America there is no distinction between the types of finger joints unless wider width lamina was considered.

JWG van de Kuilen and BJ Yeh agreed that machine rated lamina would make a difference.

S Winter asked about proof loading experience in N. American glulam production. BJ Yeh said end joint proof loading is available in 1/3 of the plants and there is a standard for proof loading.

In-plane loaded CLT beams – Tests and analysis of element lay-up

Henrik Danielsson, Division of Structural Mechanics, Lund University, Sweden

Erik Serrano, Division of Structural Mechanics, Lund University, Sweden

Mario Jeleč, Department of Materials and Structures, University of Osijek, Croatia

Vlatka Rajčić, Department of Structures, University of Zagreb, Croatia

Keywords: CLT, testing, in-plane loading, beam, hole, notch

1 Background, aim and objectives

This work concerns in-plane loaded CLT beams, including beams with a hole or a notch. Using CLT for such structural elements is very relevant from a practical engineering point of view since the transversal layers have a reinforcing effect with respect to stress perpendicular to the beam axis.

Due to the general composition of CLT, the stress state is however very complex and many failure modes need to be considered in design. The beam strength is furthermore affected not only by the basic material strength and the gross cross sections dimensions, but also affected by the ratio of the longitudinal and transversal layer widths and by the dimensions of the cross sections of the individual laminations. Many of the geometry parameters are defined by the producer, e.g. the widths t_0 and t_{90} of the longitudinal and transversal layers respectively. Other parameters, such as dimensions of individual laminations and lamination placement with respect to element edges, are often not known to the engineer in an actual design situation since the beams in general are cut from larger elements. In this cutting, no consideration of the location of the beam element edges in relation to the edges of the individual laminations is made.

Experimental tests on CLT beams are for example reported by Bejtka (2011) and Andreolli et al (2012). Comprehensive experimental tests and a composite beam model for stress analysis and strength verification have further been presented by Flaig (2013, 2014, 2015a, 2015b) and by Flaig and Blass (2013), including stress based failure criteria for relevant failure modes. A basic assumption for that model is that the CLT lay-up for 5-layer elements consists of an interior longitudinal layer of twice the width as compared to the width of the surface layers (e.g. an interior longitudinal layer composed of two, flatwise glued, longitudinal laminations). The tests were also mostly carried out on beam specimens having this type of lay-up, which is relevant from an academic point of view but less relevant from a practical point of view since this type of lay-up very seldom is used in practice. Most specimens were furthermore produced with a regular lamination pattern having m number of laminations of equal width b in the longitudinal layers, i.e. total beam height $h = mb$.

The aim of this paper is to present a base for verification of the model for stress and strength analysis suggested by Flaig (2015a, 2015b). Of the many lay-up parameters influencing CLT-beam behaviour, this paper focuses on the effect of interior longitudinal layer width and the resulting magnitude and distribution of internal forces in the beam and the torsional moments acting in the crossing areas.

2 Tests of in-plane loaded CLT beam elements

Tests on in-plane loaded CLT beams have been carried out at Lund University and a detailed description of the tests and results are presented in Danielsson et al (2017).

Five different test setups A-E according to Figure 2.1 were used. Each test series consisted of four nominally equal tests giving a total of 20 individual tests. The beams were produced from symmetrical 5-layer CLT and had a height of h = 600 mm and a gross cross section width of 160 mm (40-20-40-20-40). Each of the three longitudinal layers had a layer thickness of 40 mm and both transversal layers had a thickness of 20 mm. The laminations used for the longitudinal and transversal layers were of 172 mm and 146 mm width, respectively.

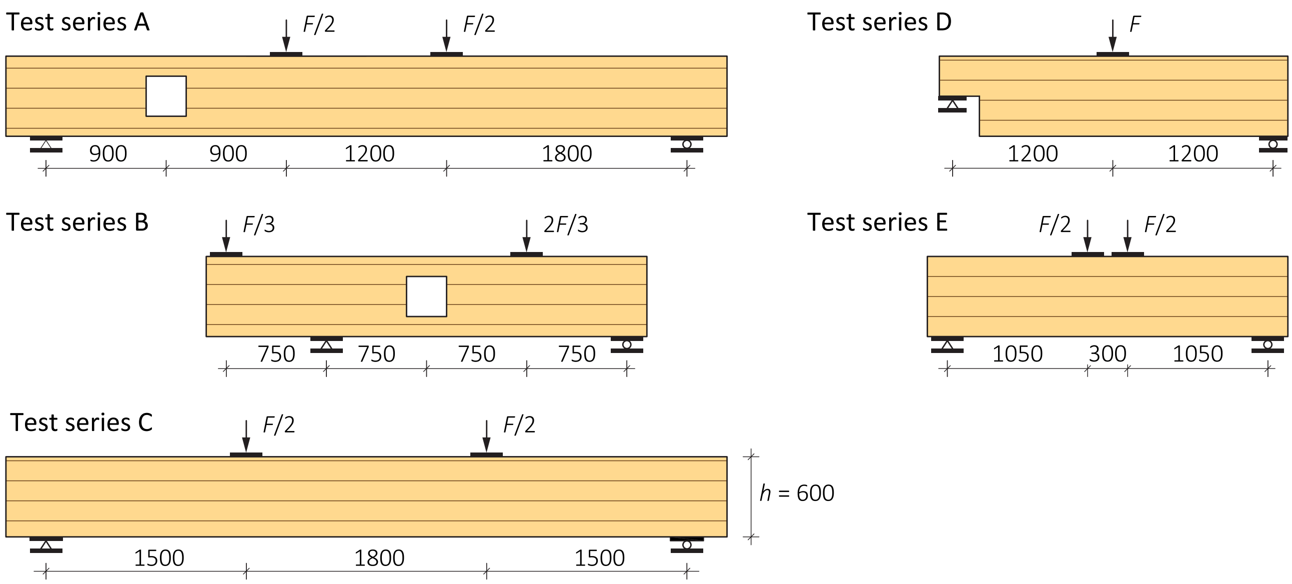

Figure 2.1. Overview of test series for in-plane loaded CLT beams, dimensions in mm.

For test series A and B, a square hole of side length 300 mm was placed centrically with respect to the beam height direction. For the test series D, a notch of depth 300 mm was used and the centreline of the support was placed at a distance of 200 mm from the notched corner. Holes and notches were cut by the manufacturer without corner radius.

All beams were produced by Cross Timber Systems Ltd according to the European Technical Assessment ETA-15/0906 (2016). The wood species used is stated as being European spruce or equivalent softwood. The mean density of the test specimens was 456 kg/m^3 and the moisture content at the time of testing was 10-11 %. It is in the ETA stated that the narrow faces of the laminations belonging to the same layer need not to be bonded together. At the time of testing, there were no visible gaps between the laminations in the elements and there appear not to have been any (or very little) edge-bonding between the laminations.

Compared to the experimental tests presented by Flaig (2013), the present tests concern elements of more conventional CLT lay-up: equal width of all longitudinal layers. The specimens were furthermore cut from larger CLT panels, meaning that the widths of the upper- and lower-most longitudinal laminations were random in the range 5 mm < b < $b_{max,}$ where b_{max} = 172 mm. Also the placement of holes and notches was random with respect to the position of the longitudinal and transversal laminations.

3 Analytical beam models

Models for stress analysis and beam strength verification for in-plane loading of CLT elements are for example presented by Flaig (2013, 2014, 2015a, 2015b) and by Flaig and Blass (2013). These models are in general based on conventional beam theory considerations with addition of certain assumptions and simplifications to account for the orthogonal layered composition.

3.1 Prismatic beams

A brief review of the model for calculation of stresses relating to the relevant failure modes is presented below. The equations presented are based on models by Flaig (2013, 2014, 2015a, 2015b) and by Flaig and Blass (2013). The equations are based on notation for geometry and load parameters according to Figures 3.1 and 3.2 and relate to prismatic CLT beams without edge-bonding and composed of laminations having identical stiffness properties. A more detailed review of the considered model is presented in Danielsson et al (2017).

The maximum normal stress in the longitudinal layers, due to bending, is given by

$$\sigma_{\mathrm{x}} = \frac{M}{W_{\mathrm{net}}} \qquad \text{where} \quad W_{\mathrm{net}} = \frac{t_{\mathrm{net,0}} h^2}{6} \tag{1}$$

where M is the bending moment, $t_{net,0} = \Sigma t_{0,k}$ and h is the beam height.

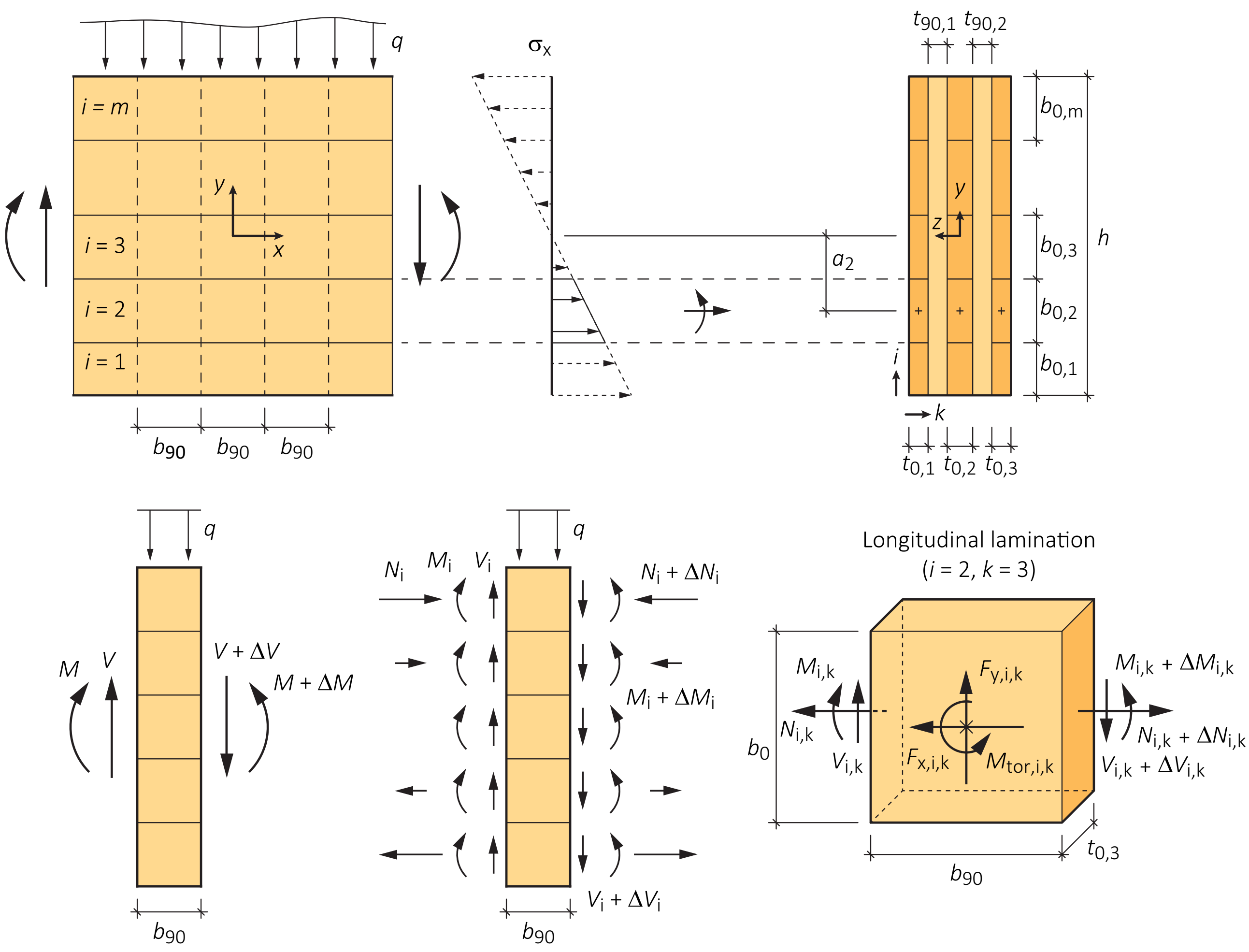

Figure 3.1. Illustration of beam model and definition of load and geometry parameters.

The maximum value of the gross shear stress (shear failure mode I) is given by

$$\tau_{\text{xy,gross}} = \frac{3}{2}\frac{V}{t_{\text{gross}}h} \tag{2}$$

where V is the shear force and $t_{\text{gross}} = \Sigma t_{0,\text{k}} + \Sigma t_{90,\text{k}}$ is the gross cross section width.

The maximum value of the net shear stress in the longitudinal and transversal layers (shear failure mode II) are given by

$$\tau_{\text{xy,net,0}} = \frac{3}{2}\frac{V}{t_{\text{net,0}}h} \quad \text{and} \quad \tau_{\text{xy,net,90}} = \frac{3}{2}\frac{V}{t_{\text{net,90}}h} \tag{3, 4}$$

where $t_{\text{net,0}} = \Sigma t_{0,\text{k}}$ and $t_{\text{net,90}} = \Sigma t_{90,\text{k}}$ refer to the net cross section width of the longitudinal and transversal layers, respectively.

In addition to the shear stress τ_{xy}, which are present in both longitudinal and transversal laminations, shear stresses τ_{xz} and τ_{yz} acting in the crossing areas between the longitudinal and transversal laminations are also present. Using the model as suggested by Flaig, the shear stresses acting in the crossing area can be categorized as (a) shear stress parallel to the beam axis τ_{xz}, (b) shear stress perpendicular to the beam axis τ_{yz} and (c) torsional shear stress τ_{tor}.

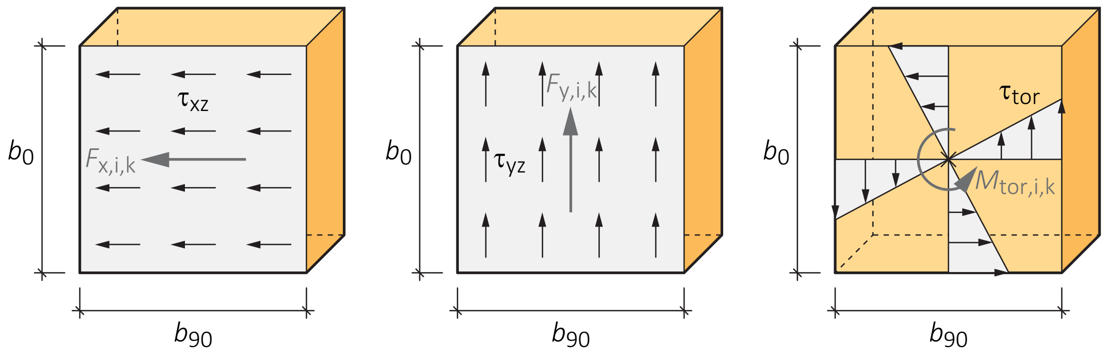

Figure 3.2. Illustration of assumed shear stress distributions in the crossing areas.

The distributions of the shear stresses over the crossing areas are assumed according to the illustration in Figure 3.2 and the derivation of maximum stress values are based on calculation of the forces $F_{x,i,k}$ and $F_{y,i,k}$ and the torsional moment $M_{tor,i,k}$ acting in the crossing area *i,k* according to Figure 3.1.

The shear stress τ_{xz} in the crossing area/areas belonging to lamination *i,k* is given by

$$\tau_{xz,i,k} = \frac{F_{x,i,k}}{b_{0,i}b_{90}} \qquad \text{where} \qquad F_{x,i,k} = \frac{\Delta N_{i,k}}{n_{CA,k}} \tag{5}$$

where $\Delta N_{i,k}$ is the differential normal force in longitudinal lamination *i* of layer *k*, $n_{CA,k}$ is the number of crossing areas that longitudinal lamination *i,k* shares with adjacent transversal laminations and $b_{0,i}$ and b_{90} are the widths of the longitudinal and transversal laminations, respectively. The differential normal force $\Delta N_{i,k}$ can be expressed as

$$\Delta N_{i,k} = \frac{\Delta M}{I_{net}} t_{0,k} b_{0,i} a_i \tag{6}$$

where $\Delta M = Vb_{90}$. Assuming equal width of the transversal and longitudinal laminations (i.e. $b_0 = b_{90} = b$) and constant ratio between the longitudinal layer widths and the number of crossing areas for each layer (i.e. constant value of $t_{0,k}/n_{CA,k}$), the maximum value of the shear stress parallel to the beam axis may then be expressed as

$$\tau_{xz} = \frac{6V}{b^2 n_{CA}}\left(\frac{1}{m^2} - \frac{1}{m^3}\right) \tag{7}$$

where n_{CA} is the total number of crossing areas in the beam width direction and *m* is the number on longitudinal laminations in the beam height direction (i.e. $m = h/b$).

The shear stress perpendicular to the beam axis, from a distributed load *q* [N/m] caused by e.g. a distributed support reaction force, may be expressed as

$$\tau_{yz} = \frac{q}{hn_{CA}} \tag{8}$$

The torsional shear stress distribution illustrated in Figure 3.2, and corresponding to relative rigid body rotation over a shear compliant medium, gives a maximum torsional shear stress of the middle points of the four sides according to

$$\tau_{tor,i,k} = \frac{M_{tor,i,k}}{I_{P,CA,i,k}}\frac{b_{max}}{2} \qquad \text{where} \qquad I_{P,CA,i,k} = \frac{b_{0,i}b_{90}}{12}\left(b_{0,i}^2 + b_{90}^2\right) \tag{9}$$

where b_{max} = max($b_{0,i}$, b_{90}). Assuming $b_0 = b_{90} = b$, constant value of $t_{0,k}/n_{CA,k}$ and equal torsional moments for all crossing areas in the beam height direction, the maximum torsional shear stress may then be expressed as

$$\tau_{\mathrm{tor}} = \frac{3V}{b^2 n_{\mathrm{CA}}}\left(\frac{1}{m} - \frac{1}{m^3}\right) \qquad (10)$$

3.2 Beams with a hole or an end-notch

For CLT beams with a hole or an end-notch, failure modes relating to bending at the hole/notch and tension perpendicular to the beam axis are also relevant, in addition to the failure modes mentioned in Section 3.1. Proposals for design equations are presented by Flaig (2015b), see also Jeleč et al (2016).

3.3 Shear strengths and stress interaction criteria for failure in crossing areas

For verification with respect to gross shear failure (mode I), characteristic shear strength according to the strength class of the laminations according to EN 338 and use of k_{cr} = 1.0 is proposed by Flaig (2015a). For net shear failure (mode II), a characteristic shear strength of 8.0 MPa is suggested.

Regarding shear failure in the crossing areas (shear failure mode III), the three stress components reviewed above (τ_{xz}, τ_{yz} and τ_{tor}) represent for a specific point either longitudinal shear, rolling shear or a combination of both. A shear stress component giving pure longitudinal shear in the longitudinal lamination represents pure rolling shear in the transversal laminations, and vice versa. Thus, for failure in the crossing areas, and based on experimental tests on crossing areas loaded in either uniaxial shear, pure torsion, or a combination of both, failure criteria according to

$$\frac{\tau_{\mathrm{tor}}}{f_{\mathrm{v,tor}}} + \frac{\tau_{\mathrm{xz}}}{f_{\mathrm{R}}} \leq 1.0 \qquad \frac{\tau_{\mathrm{tor}}}{f_{\mathrm{v,tor}}} + \frac{\tau_{\mathrm{yz}}}{f_{\mathrm{R}}} \leq 1.0 \qquad (11a, 11b)$$

are proposed by Flaig (2015a). The test results indicate a mean value of the torsional strength of about $f_{v,tor}$ = 3.5 MPa and a mean value of the rolling shear strength of about f_R = 1.5 MPa. The corresponding characteristic values are $f_{v,tor,k}$ = 2.75 MPa and $f_{R,k}$ = 1.1 MPa.

3.4 Influence of element lay-up on shear stresses in crossing areas

The parallel to beam axis shear stress τ_{xz} according to Equation (7) and the torsional shear stress τ_{tor} according to Equation (10) are both strongly dependent of the element lay-up in terms of the longitudinal lamination width b and the number m of longitudinal laminations in the beam height direction ($m = h/b$).

According to Flaig (2015a), Equations (7) and (10) give good approximations for the range of lay-ups that are used in practice, also when the ratio $t_{0,k}/n_{CA,k}$ is not constant. Lay-ups with constant value of $t_{0,k}/n_{CA,k}$ for all longitudinal layers are not very common on the market. On the contrary, CLT elements have more often greater longitudinal layer widths in the external layers than in the internal layers. Equations (7) and (10) then underestimate the maximum value of the shear stress parallel to the beam axis and the torsional shear stress.

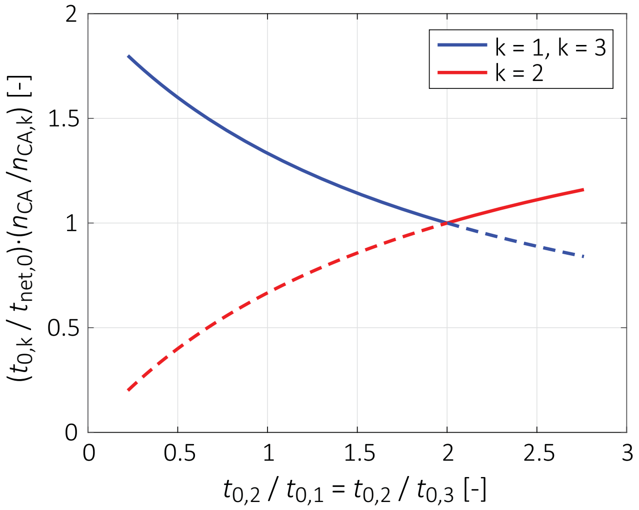

Figure 3.3. Factor for prediction of shear stress vs. relative width of longitudinal layers.

Accounting for varying ratio $t_{0,k}/n_{CA,k}$ between the k layers of longitudinal laminations, the maximum shear stress parallel to the beam axis τ_{xz} and the maximum torsional shear stress τ_{tor} are given by Flaig (2013)

$$\tau_{\mathrm{xz}} = \frac{6V}{b^2 n_{\mathrm{CA,k}}} \frac{t_{\mathrm{0,k}}}{t_{\mathrm{net,0}}} \left(\frac{1}{m^2} - \frac{1}{m^3}\right) \tag{12}$$

$$\tau_{\mathrm{tor}} = \frac{3V}{b^2 n_{\mathrm{CA,k}}} \frac{t_{\mathrm{0,k}}}{t_{\mathrm{net,0}}} \left(\frac{1}{m} - \frac{1}{m^3}\right) \tag{13}$$

and the difference in predicted stress in the crossing areas belonging to longitudinal lamination k, compared to Equations (7) and (10), may hence be expressed by the factor $(t_{0,k}/t_{net,0})\cdot(n_{CA}/n_{CA,k})$. The relationship between the relative widths of the internal and external layers and the predicted stress for the respective layers is illustrated in Figure 3.3 for a 5-layer CLT element. Assuming a fixed net cross section width $t_{net,0}$, the maximum stress increases by 33 % for the case of equal width of all longitudinal layers and by 60 % for the case of external layers having twice the width of the internal layer, compared to the reference case of $t_{0,2}/t_{0,1} = t_{0,2}/t_{0,3} = 2.0$. Despite this, it is stated in Flaig (2013, 2015a) that for commonly used lay-ups, this influence can be neglected.

4 Test results

The results from the tests, in terms of failure load (maximum load) and maximum values of stress components at the maximum load, are given in Tables 4.1-4.5. The stress values are based on the assumption of equal widths of the longitudinal and transversal laminations according to approximate mean values as $b_0 = b_{90} = b = 150$ mm and of constant ratio $t_{0,k}/n_{CA,k} = t_{net,0}/n_{CA} = 30$ mm for all longitudinal layers. Thus, the influence of the actually varying ratio $t_{0,k}/n_{CA,k}$ has not been taken into account, following the statement of Flaig (Flaig 2013, 2015a) that for commonly used lay-ups this influence is negligible. The stress components corresponding to the dominating mode of failure, based on observations during testing, are indicated by being underlined.

Stress components for test series of beams with a hole (test series A and B) and beams with an end-notch (test series D) are based on models presented by Flaig (2015b). For test series C and E, the respective equation used for calculation of stresses is indicated in the tables by a number in parenthesis. Graphs of applied load *F* vs. beam deflection for the four individual tests of test series A-E are shown in Figure 4.1.

For all tests in series C and E, the load bearing capacity in terms of maximum load is related to bending failure and cracking due to a combination of bending and tension in the longitudinal laminations. Before reaching maximum load, a gradual decrease in stiffness can however be noted from the load vs. deflection graphs for test series E in Figure 4.1. Although the modes of failure are categorized as bending failures, the final failures were for test series E probably preceded by at least partial failure in the crossing areas between longitudinal and transversal laminations before maximum load.

Table 4.1. Failure load (maximum load) and corresponding stress values for test series A.

	F_{max} [kN]	σ_x [MPa]	$\sigma_{x,h}$ [MPa]	$\sigma_{t,0,h}$ [MPa]	$\tau_{xy,gross,h}$ [MPa]	$\tau_{xy,net,90,h}$ [MPa]	$\tau_{xz,h}$ [MPa]	$\tau_{yz,h}$ [MPa]	$\tau_{tor,h}$ [MPa]
A1	277.1	34.6	$\underline{42.9}$	18.5	4.33	14.6	0.73	0.62	2.21
A2	295.0	$\underline{36.9}$	45.6	19.7	4.61	15.5	0.78	0.66	2.36
A3	293.5	$\underline{36.7}$	45.4	19.6	4.59	15.4	0.77	0.65	2.34
A4	304.3	38.0	$\underline{47.1}$	20.3	4.76	16.0	0.80	0.68	2.43
Mean	292.5	36.6	45.3	19.5	4.57	15.4	0.77	0.65	2.34

Table 4.2. Failure load (maximum load) and corresponding stress values for test series B.

	F_{max} [kN]	σ_x [MPa]	$\sigma_{x,h}$ [MPa]	$\sigma_{t,0,h}$ [MPa]	$\tau_{xy,gross,h}$ [MPa]	$\tau_{xy,net,90,h}$ [MPa]	$\tau_{xz,h}$ [MPa]	$\tau_{yz,h}$ [MPa]	$\tau_{tor,h}$ [MPa]
B1	523.9	18.2	29.1	20.5	5.46	18.4	0.92	$\underline{0.68}$	$\underline{2.79}$
B2	475.6	16.5	26.4	18.6	4.95	16.7	0.83	$\underline{0.62}$	$\underline{2.53}$
B3	491.9	17.1	27.3	19.2	5.12	17.2	0.86	$\underline{0.64}$	$\underline{2.62}$
B4	502.0	17.4	27.9	19.6	5.23	17.6	0.88	$\underline{0.65}$	$\underline{2.67}$
Mean	498.3	17.3	27.7	19.5	5.19	17.5	0.87	0.65	2.65

Table 4.3. Failure load (maximum load) and corresponding stress values for test series C.

	F_{max} [kN]	σ_x (1) [MPa]	$\tau_{xy,gross}$ (2) [MPa]	$\tau_{xy,net,0}$ (3) [MPa]	$\tau_{xy,net,90}$ (4) [MPa]	τ_{xz} (7) [MPa]	τ_{yz} (8) [MPa]	τ_{tor} (10) [MPa]
C1	413.2	$\underline{43.0}$	3.23	4.30	12.9	0.65	0.37	1.61
C2	363.2	$\underline{37.8}$	2.84	3.78	11.3	0.57	0.33	1.42
C3	335.6	$\underline{35.0}$	2.62	3.50	10.5	0.52	0.30	1.31
C4	412.9	$\underline{43.0}$	3.23	4.30	12.9	0.65	0.37	1.61
Mean	381.2	39.7	2.98	3.97	11.9	0.60	0.35	1.49

Table 4.4. Failure load (maximum load) and corresponding stress values for test seris D.

	F_{max} [kN]	σ_x [MPa]	$\sigma_{x,n}$ [MPa]	$\sigma_{t,0,n}$ [MPa]	$\tau_{xy,gross,n}$ [MPa]	$\tau_{xy,net,90,n}$ [MPa]	$\tau_{yz,n}$ [MPa]	$\tau_{tor,n}$ [MPa]
D1	350.9	29.2	19.5	38.0	5.48	19.6	0.63	2.45
D2	349.3	29.1	19.4	37.8	5.46	19.5	0.63	2.44
D3	361.6	30.1	20.1	39.2	5.65	20.2	0.65	2.53
D4	345.5	28.8	19.2	37.4	5.40	19.3	0.62	2.42
Mean	351.8	29.3	19.5	38.1	5.50	19.7	0.64	2.46

Table 4.5. Failure load (maximum load) and corresponding stress values for test series E.

	F_{max} [kN]	σ_x (1) [MPa]	$\tau_{xy,gross}$ (2) [MPa]	$\tau_{xy,net,0}$ (3) [MPa]	$\tau_{xy,net,90}$ (4) [MPa]	τ_{xz} (7) [MPa]	τ_{yz} (8) [MPa]	τ_{tor} (10) [MPa]
E1	491.3	35.8	3.84	5.12	15.4	0.77	0.44	1.92
E2	519.5	37.9	4.06	5.41	16.2	0.81	0.47	2.03
E3	513.0	37.4	4.01	5.34	16.0	0.80	0.46	2.00
E4	476.3	34.7	3.72	4.96	14.9	0.74	0.43	1.86
Mean	500.0	36.5	3.91	5.21	15.6	0.78	0.45	1.95

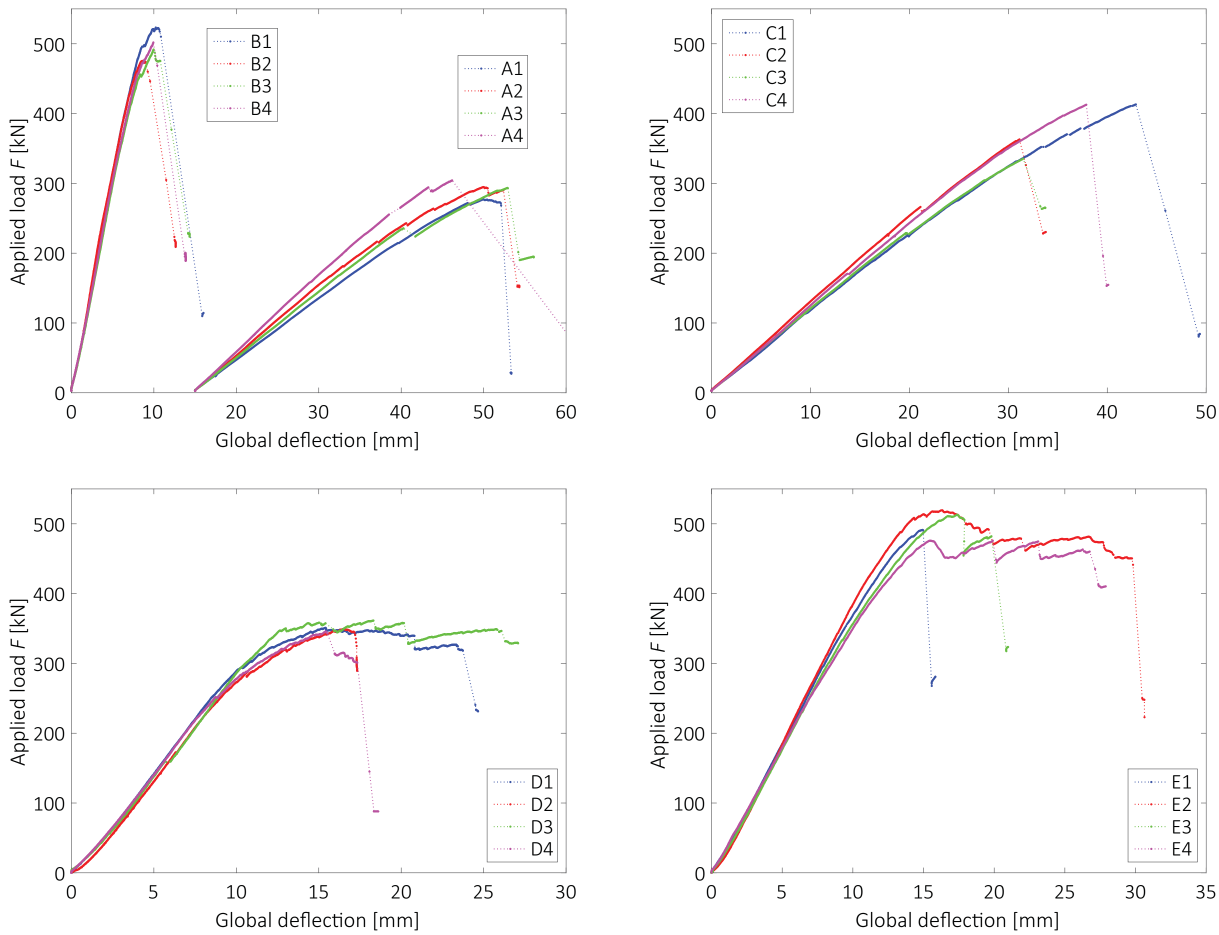

Figure 4.1. Applied load F vs. global beam deflection for test series A, B, C, D and E.

5 FE-analysis

3D FE-analyses were carried out in order to investigate the influence of the relative width of the longitudinal layers $t_{0,k}$ on the shear stresses in the crossing areas as discussed in Section 3.4. Also the distribution of $M_{tor,i,k}$ with respect to the beam height direction was investigated, this being relevant in relation to Equations (10) and (13).

The FE-analyses were performed using Abaqus 2017. The laminations were modelled as linear elastic and orthotropic with stiffness parameters according to Table 5.1. The rectilinear material directions are denoted by L in the lamination length direction, T in the width direction and R in the thickness direction. Adjacent laminations within the same layer were modelled with a 0.1 mm gap. The flatwise bonding between the laminations was modelled using a combination of hard contact in compression and elastic response in tension perpendicular to the crossing areas and in the two shear directions. The linear elastic traction-separation model used a single stiffness value for all three directions, $K_{nn} = K_{tt} = K_{ss} = 1000$ N/mm^3, for tension and the two shear directions, respectively. The contact stiffness parameters were chosen based on comparison of calculated global beam stiffness according to the FE-model and the experimentally found beam stiffness (values in the range of 10-1000 N/mm^3 were tested, showing negligible influence on the force distribution and minor influence on global stiffness).

A gross beam geometry and loading situation according to test series C, see Figure 2.1, was used considering symmetry in two directions. 8-node linear brick elements (C3D8 in Abaqus) was used and the FE-meshes consisted of cubically, or close to cubically, shaped elements having a side length of about 10 mm. Longitudinal and transversal laminations widths were assigned as $b_0 = b_{90} = 150$ mm and the applied load corresponds to $V = 0.5F = 100$ kN. Three beam lay-ups were considered, according to:

- Lay-up 30-20-60-20-30 ($t_{net,0} = \Sigma t_{0,k} = 120$ mm, $t_{0,2}/t_{0,1} = t_{0,2}/t_{0,3} = 2.0$)
- Lay-up 40-20-40-20-40 ($t_{net,0} = \Sigma t_{0,k} = 120$ mm, $t_{0,2}/t_{0,1} = t_{0,2}/t_{0,3} = 1.0$)
- Lay-up 48-20-24-20-48 ($t_{net,0} = \Sigma t_{0,k} = 120$ mm, $t_{0,2}/t_{0,1} = t_{0,2}/t_{0,3} = 0.5$)

Internal forces and moments found from the FE-analyses and according to the analytical model presented by Flaig and Blass are presented in Tables 5.2-5.4, considering forces and moments as illustrated in Figure 5.1. The forces from the FE-analyses are determined by integration of stresses in the longitudinal laminations and in the crossing areas, respectively. The forces from the analytical model are determined based on the actual ratio $t_{0,k}/n_{CA,k}$. The influence of element size was tested for one beam lay-up, showing negligible influence on force distributions even with element size of 5 mm.

Table 5.1 Lamination stiffness parameters used for FE-analyses.

E_L [MPa]	E_T [MPa]	E_R [MPa]	G_{LT} [MPa]	G_{LR} [MPa]	G_{TR} [MPa]	ν_{LT} [-]	ν_{LR} [-]	ν_{TR} [-]
12000	400	600	750	600	75	0.50	0.50	0.33

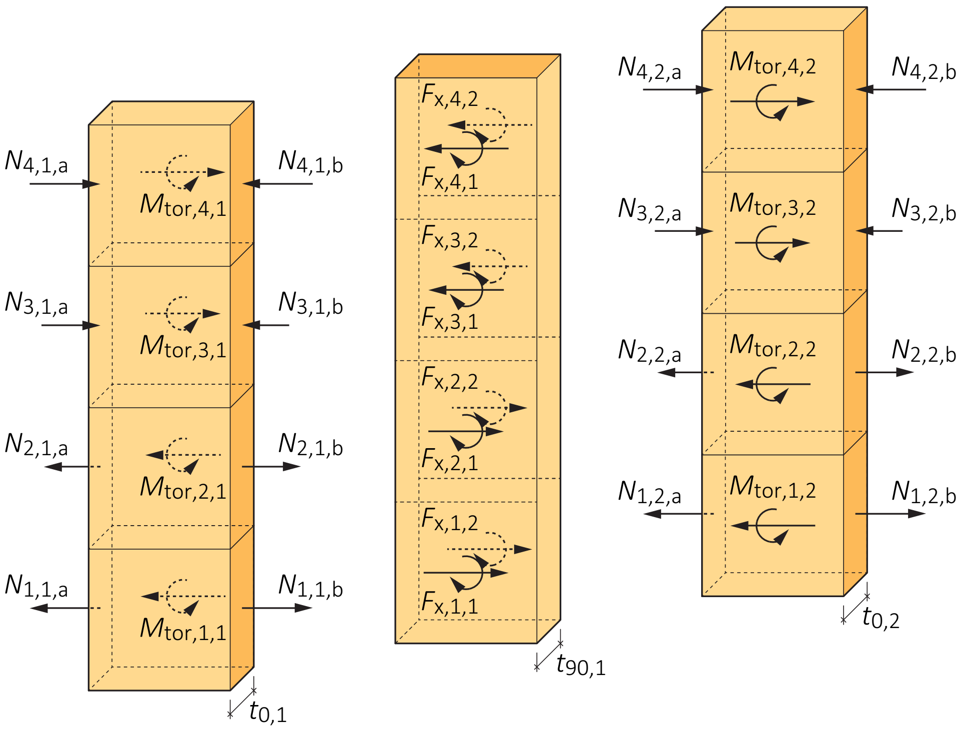

Figure 5.1. Internal forces/moments $N_{i,k}$, $F_{x,i,k}$ and $M_{tor,i,k}$ in longitudinal/transversal laminations.

The internal forces $N_{i,k}$ and $F_{x,i,k}$ as calculated by the analytical model and by FE-analyses agree well in general, however showing slightly larger discrepancies for $F_{x,i,k}$ compared to $N_{i,k}$. Regarding the torsional moments $M_{tor,i,k}$, the agreement between the analytical model and the FE-results is less good with differences being in the range of ± 50 % and even more. The absolute values of $F_{x,i,k}$ and $M_{tor,i,k}$ from the FE-analyses were found to be sensitive to the method of evaluation, i.e. the post-processing approach used for integration of stresses. The relative magnitude between the layers (i.e. the relative load sharing between layers) was however not much affected.

Table 5.2. Internal forces, in N, and torsional moments, in Nmm, for lay-up 30-20-60-20-30.

	$N_{i,1,a}$		$N_{i,1,b}$		$F_{x,i,1}$		$M_{tor,i,1}$	
i	FE	Analytical	FE	Analytical	FE	Analytical	FE	Analytical
4	28200	28100	34800	35100	7140	7030	607000	879000
3	9490	9360	11300	11700	1920	2340	1220000	879000
2	9580	9360	11500	11700	2060	2340	1180000	879000
1	28100	28100	34500	35100	7000	7030	489000	879000
	$0.5\ N_{i,2,a}$		$0.5\ N_{i,2,b}$		$F_{x,i,2}$		$M_{tor,i,2}$	
i	FE	Analytical	FE	Analytical	FE	Analytical	FE	Analytical
4	28200	28100	34800	35100	7150	7030	604000	879000
3	9480	9360	11200	11700	1930	2340	1220000	879000
2	9590	9360	11500	11700	2060	2340	1180000	879000
1	28100	28100	34500	35100	7010	7030	487000	879000

Table 5.3. Internal forces, in N, and torsional moments, in Nmm, for lay-up 40-20-40-20-40.

	$N_{i,1,a}$		$N_{i,1,b}$		$F_{x,i,1}$		$M_{tor,i,1}$	
i	FE	Analytical	FE	Analytical	FE	Analytical	FE	Analytical
4	37600	37400	46300	46800	9370	9380	693000	1170000
3	12600	12500	14900	15600	2510	3130	1380000	1170000
2	12800	12500	15300	15600	2690	3130	1330000	1170000
1	37500	37400	46000	46800	9200	9380	540000	1170000
	0.5 $N_{i,2,a}$		0.5 $N_{i,2,b}$		$F_{x,i,2}$		$M_{tor,i,2}$	
i	FE	Analytical	FE	Analytical	FE	Analytical	FE	Analytical
4	18800	18700	23300	23400	4880	4690	517000	586000
3	6350	6240	7560	7800	1330	1560	1050000	586000
2	6370	6240	7670	7800	1420	1560	1020000	586000
1	18700	18700	23100	23400	4790	4690	435000	586000

Table 5.4. Internal forces, in N, and torsional moments, in Nmm, for lay-up 48-20-24-20-48.

	$N_{i,1,a}$		$N_{i,1,b}$		$F_{x,i,1}$		$M_{tor,i,1}$	
i	FE	Analytical	FE	Analytical	FE	Analytical	FE	Analytical
4	45200	44900	55500	56200	11200	11300	782000	1410000
3	15100	15000	17800	18700	2980	3750	1540000	1410000
2	15400	15000	18300	18700	3190	3750	1480000	1410000
1	45000	44900	55100	56200	11000	11300	599000	1410000
	0.5 $N_{i,2,a}$		0.5 $N_{i,2,b}$		$F_{x,i,2}$		$M_{tor,i,2}$	
i	FE	Analytical	FE	Analytical	FE	Analytical	FE	Analytical
4	11300	11200	14000	14000	3000	2810	427000	352000
3	3830	3740	4570	4680	825	938	870000	352000
2	3810	3740	4610	4680	885	938	849000	352000
1	11300	11200	13900	14000	2950	2810	373000	352000

6 Discussion and conclusions

Based on the present tests of prismatic beams and beams with a hole or an end-notch, considering the results in terms of stress components as presented in Tables 4.1-4-5, and strength values according to Section 3.3, the model suggested by Flaig (2015a, 2015b) seems to yield reasonable or conservative predictions for the beam strength.

As regards shear failure in the crossing areas (shear mode III) and Equations (5)-(10), the considered model is derived based on assumptions of constant ratio $t_{0,k}/n_{CA,k}$ for all longitudinal layers and is hence for 5- and 7-layer CLT elements (strictly) valid only when having internal longitudinal layer/layers of twice the width as the external longitudinal layers. Furthermore, equal width of the longitudinal and transversal laminations according to $b_0 = b_{90} = b$ is assumed. The present specimens were composed of elements with varying ratio $t_{0,k}/n_{CA,k}$ and different laminations widths for the longitudinal and transversal layers. Also the width of the individual longitudinal laminations differed within the specimens, with the widths of the upper- and lower-most longitudinal laminations being in the range 5 mm < b_0 < 172 mm. Despite the discrepancies between model assumptions and present specimen geometries, reasonable or conservative predictions for the beam strength were found.

The comparison of results according to the FE-analyses and the analytical expressions, in terms of the lamination forces $F_{x,i,k}$ and $N_{i,k}$ according to Tables 5.2-5.4, show overall a reasonable agreement. Comparing lay-ups 40-20-40-20-40 and 48-20-24-20-48 to the lay-up 30-20-60-20-30, the results of the FE-analyses for $F_{x,i,k}$ agree well with the influence of the ratio $t_{0,k}/n_{CA,k}$ as predicted by Equation (12) and shown in Figure 3.3. Thus, it seems that, at least for the cases investigated here, the approach used by Flaig to determine these lamination *forces* is adequate, *taking into account the influence of the lamination width ratio* $t_{0,k}/n_{CA,k}$, which cannot be neglected.

The FE-analyses also showed that the torsional moments $M_{tor,i,k}$ are influenced by the ratio $t_{0,k}/n_{CA,k}$, although not to the full extent as predicted by Equation (13) and shown in Figure 3.3. Comparing lay-ups 40-20-40-20-40 and 48-20-24-20-48 to the lay-up 30-20-60-20-30, the FE-analyses give about 13 % and 26 % increase in torsional moments. The assumption that the torsional moments are equal for all crossing areas in the beam height direction is clearly not supported by the FE-analyses, see Tables 5.2-5.4, which show significantly higher torsional moments close to the beam central axis.

Table 6.1 shows the mean values of estimated shear stresses from test series C and E assuming either a constant, or the actual, ratio $t_{0,k}/n_{CA,k}$ and evaluation of Equation (11a) based on proposed mean values of $f_{v,tor}$ = 3.5 MPa and f_R = 1.5 MPa. The final failure for all tests of both test series C and E was categorized as bending failure. From this comparison, it appears as is if the mean shear strengths $f_{v,tor}$ and f_R of the beams tested are greater than the assumed mean values. For test series E, the gradual decrease in stiffness prior to reaching maximum load may however be due to partial failure/damage in the crossing areas. Another possible reason for the comparatively high stress interaction ratios, without obvious shear mode III failure, may be that the assumption of equal torsional moments for all crossing areas in the beam height direction is inaccurate, as suggested by the FE-analyses.

Table 6.1. Estimated mean shear stress at failure (shear mode III) and evaluation of Equation (11a).

	$t_{0,k}/n_{CA,k} = t_{net,0}/n_{CA}$ = 30 mm			$t_{0,k}/n_{CA,k}$ = 40 mm		
	τ_{xz}	τ_{tor}	Interaction	τ_{xz}	τ_{tor}	Interaction
	(7)	(10)	(11a)	(12)	(13)	(11a)
	[MPa]	[MPa]	[-]	[MPa]	[MPa]	[-]
Test series C	0.60	1.49	0.83	0.79	1.99	1.10
Test series E	0.78	1.95	1.08	1.04	2.60	1.44

It should be noted that, from a theoretical point of view, the origin of the in-plane shear stress components acting in the crossing areas is irrelevant. The "torsional shear strength", $f_{v,tor}$, can thus only be understood as a fictitious strength parameter strongly related to the structural properties of the test conditions used to determine it.

7 Acknowledgments

The financial support from the Swedish Research Council Formas through grant 2016-01090 and from COST Action FP1402 (for the Short Term Scientific Mission (STSM) of Mario Jeleč to Lund University during the fall of 2016) is gratefully acknowledged.

8 References

Abaqus 2017 (2016), Dassault Systèmes.

Andreolli M, Tomasi R, Polastri A (2012): Experimental investigation on in-plane behaviour of cross-laminated timber elements. In: Proc. CIB-W18, CIB-W18/45-12-4, Växjö, Sweden.

Bejtka I (2011): Cross (CLT) and diagonal (DLT) laminated timber as innovative material for beam elements. KIT, Karlsruhe, Germany.

Danielsson H, Jeleč M, Serrano E (2017): Strength and stiffness of cross laminated timber at in-plane beam loading. Report TVSM-7164, Division of Structural Mechanics, Lund University, Sweden.

European Technical Assessment ETA-15/0906 from 24.02.2016. Cross Timber Systems – CLT, Solid wood slab elements to be used as structural elements in buildings. Austrian Institute for Construction Engineering, Vienna, Austria.

Flaig M (2013): Biegeträger aus Brettsperrholz bei Beanspruch in Plattebene. PhD thesis, KIT, Karlsruhe, Germany.

Flaig M, Blass HJ (2013): Shear strength and shear stiffness of CLT-beams loaded in plane. In: Proc. CIB-W18, CIB-W18/46-12-3, Vancouver, Canada.

Flaig M (2014): Design of CLT beams with rectangular holes or notches. In: Proc. INTER, INTER/47-12-4, Bath, United Kingdom.

Flaig M (2015a): In Plattenebene beanspruchte Biegeträger aus Brettsperrholz – Teil 1: Effektive Festigkeits- und Steifigkeitskennwerte für die Schubbemessung. Bautechnik 92:741-749.

Flaig M (2015b): In Plattenebene beanspruchte Biegeträger aus Brettsperrholz – Teil 2: Brettsperrholzträger mit angeschnittenen Rändern, Durchbrüchen oder Ausklinkungen. Bautechnik 92:750-758.

Jeleč M, Rajčić V, Danielsson H, Serrano E (2016): Structural analysis of in-plane loaded CLT beam with holes: FE-analysis and parameter studies. In: Proc. INTER, INTER/49-12-2, Graz, Austria.

Discussion

The paper was presented by H Danielsson

BJ Yeh commented that in the C and E test series bending fracture occurred which would not be not a surprise. H. Danielsson said that this was what the results show. BJ Yeh asked about the difference in the strength between the vertical and horizontal layers assumed in the finite element analysis. H. Danielsson said that they did not consider the strengths in the finite element analysis and they only obtained the stress estimates.

P Dietsch asked whether there was an influence from the random location of the laminae within the beam. H Danielsson said that the coefficient of variation was very small. H Blass commented that the layup and the consequent homogenisation must have an influence.

S Aicher and H Danielsson discussed the strength values assumed for the beams. He asked whether these were board values or CLT values. H Danielsson said that they were values of the CLT beam and not a single board. S Aicher said that these values would still be high.

Experimental investigations on the mechanical behaviour of glued laminated beams made of oak

Carole Faye, Technological Institute FCBA, France

Guillaume Legrand, Technological Institute FCBA

Didier Reuling, Technological Institute FCBA

Jean-Denis Lanvin, Technological Institute FCBA

Keywords: Hardwood glulam beams, oak, mechanical and bonding performances.

1 Introduction

By comparison with softwood species, hardwood species are of little use in the construction sector, although the available resource is important [1]. For example, in Germany, France, Austria and Slovenia, standing stocks are: 1 117 millions m^3 (Mm^3) of beech, 1 108 Mm^3 of oak, 197 Mm^3 of ash and 135 Mm^3 of sweet chestnut. For comparison, in Germany and France, the softwood resource is: 1 618 Mm^3 of Norway spruce, 1 049 Mm^3 of Pines and 185 Mm^3 of Douglas fir.

In order to develop the use of hardwood species in construction, research projects [1], [2], [3], [4] have been recently carried out on:

- assessment of strength properties in order to determine visual grading rules,
- bonding performance with the aim to develop hardwood glued laminated products made of hardwoods.

In France, oak has, by far, the highest share of hardwood standing stocks. Oak has aesthetic characteristics, good mechanical performance and natural durability.

In this context, this paper presents experimental investigations on the mechanical behaviour of glulam made of European oak (Quercus robur and /or Quercus petraea) grown in France.

This work is part of a European project EU-Hardwood [1]. Firstly, the impact of the sampling method on the mechanical properties of oak planks is presented. Secondly, experimental results on glulam made of oak is presented. In addition, the relationship between the strength of laminations and finger-joints and the strength of glulam is investigated.

This work will contribute to elaborate a European standard on hardwood glued laminated products under discussion in CEN TC 124 / WG3. This working group is in charge of European standard EN 14 080 [5] which deals, until now, only with softwoods glued laminated beams.

2 Impact of the sampling method on the mechanical properties of oak boards

Two different scenarii of timber samplings (corresponding to different supply chains) were tested, involving a low degree of change for the first one (named sawmill based sampling) and a strong degree of change for the second one (named specific sampling).

2.1 First sampling: Sawmill based sampling

The objective of this sampling was to investigate the feasibility of producing Oak glued laminated beams with square edged timber traditionally proposed by French oak sawmills. So, sampling has been performed directly in the sawmill from their usual production. The characteristics of the boards were as follows:

- processed from large diameter logs, excluding butt logs,
- cross section of 27 ×160 mm^2 and moisture content between 10 and 12%.

The boards were visually graded according to the French standard NFB52-001-1 [6] in which each visual grade is assigned to a strength class (D_{xx}) of EN338 (see table 1) [7]. It was therefore possible to evaluate yields within these D_{xx} strength classes. Results are reported in table 2. Most of the specimens are assigned to D24 strength class.

We can specify that, in the next version of the European Standard EN 1912 [8], correspondence between visual mechanical grading and strength grades will be included.

Table 1. Mechanical and physical properties according EN 338 [7] for Dxx hardwood boards.

Strength classes acc. To EN 338	D40 */(C40)**	D30 / *(C30)*	D24/ *(C24)*	D18/ *(C18)*
$f_{m,0,k}$ (characteristic bending strength)N/mm^2	40 / *(40)*	30 / *30*	24 /*24*	18 / *18*
$f_{t,0,k}$ (characteristic tensile strength) N/mm^2	24 / *(26)*	18 / *(19)*	14 / *(14,5)*	11 / *(10)*
$E_{m,0,mean}$ (average bending modulus of elasticity) N/mm^2	13 OOO *(14 000)*	11 OOO *(12 000)*	10 000 *(11 000)*	9 500 *(9 000)*
ρ_k (characteristic density) [kg/m³]	550 / *(400)*	530/ *(380)*	485/ *(350)*	475/ *(320)*

**Values for softwood strength classes (C_{xx}) are also presented.*

Table 2. Oak grading results for boards issued from sawmill based sampling.

Strength classes acc. to EN 338 obtained by visual grading	D40	D30	D24	D18	Reject
Yields	**0%**	**24%**	**70%**	**4%**	**2%**

2.2 Second sampling : Specific sampling

The objective of this specific sampling was to produce glulam made from oak with higher mechanical performance while remaining at production costs similar to the previous sampling. In order to satisfy these criteria, young trees were selected (less than 80 years old) with a DBH (Diameter Breast Height) between 25 cm and 40 cm [9].

After visual grading, the yields were derived (see Table 3): 81% of the boards are classified into D30 or higher. The cross section of the boards (at seasoned stage) was 31×200 mm^2.

Currently, D40 visually grade is not offered for French oak resource, because it was not possible to identify relations between visual criteria and grade determining properties for grades higher than D30 due to high variability of strength, stiffness and density.

Pre-sorting oak logs from trees with a DBH of 25-40 cm allows to reduce the mechanical variability of oak wood resource and in consequence, this allows to visually grade D40.

So, in order to obtain pieces graded D40 for the glulam production, we calibrated visual criteria according to NF B 52 001 methodology adapted for pre-sorted logs.

Table 3. Oak grading results for boards issued from specific sampling.

Strength classes acc. to EN 338 obtained by visual grading	D40	D30	D24	D18	Reject
Yields	**37%**	**44%**	**13%**	**5%**	**1%**

3 Experimental investigations on oak laminations and glulam

3.1 Materials and methods

For each sampling method (see § 2.1 and 2.2) and each strength class (Dxx), two subsamples (A&B) of boards, having the same modulus of elasticity determined by vibration (MTG device use), were constituted:

- Subsamples A: boards and finger joints to perform tensile and flatwise bending tests according to respectively EN 408 [10] and EN 14 080 Annex E. Unfortunately, for D24 and D40 strength classes, no tensile tests on boards were performed due to a lack of boards. The finger joints profile (which is usual for softwood glued laminated beams) is described in Figure 1 (left).

- Subsamples B: boards to produce oak glued laminated beams and to perform mechanical and bonding tests according to EN 14 080. Oak glued laminated beam height was between 160 and 300 mm. The thickness of laminations was 20 mm. The same MUF glue was used to produce finger joints and to bond the laminations.

Experimental results concerning the sawmill based sampling (see § 2.1) and the specific sampling (see § 2.2) are respectively presented in sections 3.2 and 3.3.

3.2 Experimental results on oak boards, finger-joints, glued laminated beams for the first sampling

Statistical values of mechanical properties and density of oak boards and finger joints are reported respectively in tables 4.1 and 4.2.

The main observations are the following:

- boards visually graded to D30 have a lower tensile strength than expected (17 instead of 18 N/mm^2),
- density values for D24 and D30 are similar and higher than given in EN 338 (see table 1),
- modulus of elasticity of D30 is very similar to the required value (cf. table 1),
- characteristic values of finger joints strength are similar for D24 and D30. This unexpected result may be explained by a higher variability for D30 boards which induces a lower calculated characteristic value.

Table 4.1. Results of tensile tests on oak visually graded boards issued from sawmill based sampling (see § 2.1).

Visual grading	Properties	Mean value	Coefficient of variation	5% -value ****	MC (%)	Nb of tests
D30 (h=160×b=23,5) mm^2	Local $E_{t,0}$ [N/mm^2]*	**11 100**	27%		12	26
	$f_{t,0}$ [N/mm^2]**	42,9	46%	**17**	8,9	26
	ρ [kg/m^3]***	687	8%	**593**	12	26
D24	No tensile tests					
	*ρ [kg/m^3]****	*688*	*10%*	***571***	*12*	*40*
D18	No tensile tests					

* local modulus of elasticity in tension determined according to EN 408 adjusted to 12% Moisture Content.
** tensile strength determined according to EN 384 [12] adjusted to b=150 mm.
*** density adjusted to 12% Moisture Content.
**** characteristic values (5%) calculated according to EN 14 358 [11].

Table 4.2. Results of flatwise bending tests on oak finger joints issued from first sampling (see § 2.1).

Visual grades	Section mm²	Properties	Mean value	Coefficient of variation	5% -value ****	MC (%)	Nb of tests
D30	(h=24×b=160)	$f_{m,j}$ [N/mm²]*	57,8	32%	**29,6**	11,6	32
D24		$f_{m,j}$ [N/mm²]*	52,6	26%	**30,1**	12	41
		*ρ [kg/m³]****	*684*	*8%*	***588***	*12*	*41*

* flatwise bending strength of finger joints, at nominal dimensions, determined according to EN 14 080 Annex E.
*** density adjusted to 12% Moisture Content.
**** characteristic values (5%) calculated according to EN 14 358 [11].

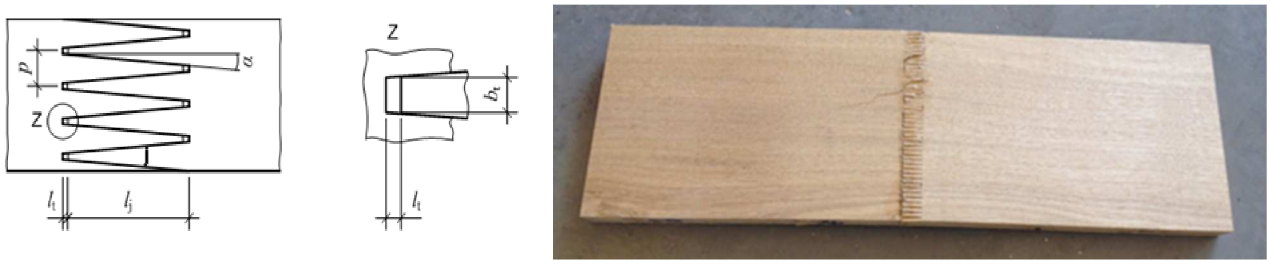

l_j, finger length = 15 mm

p, pitch = 3,8 m b_t, tip width= 0,42mm.

Figure 1. description of the finger joints (left) and finger joints after failure in flatwise bending (right).

Statistical values of mechanical properties of oak glued laminated beams are presented in tables 4.3 and 4.4 for beams produced respectively with:

- D30 boards for homogeneous beams and with D30/D18 for combined beams,
- D24 boards for homogenous beams with two heights.

For each oak beam configuration, comparison with the requirements of softwoods strength classes produced according to EN 14 080 is presented.

From table 4.3, we can observe that:

- mechanical properties as well as density of homogenous and combined oak glued laminated beams are similar even for density values. Lower bending strengths for combined beams can be explained by a higher coefficient of variation.
- in comparison with EN 14 080 requirements : density of oak beams are higher and modulus of elasticity are lower (as for softwood and hardwood solid boards for a same strength class higher than D18, see table 1). Experimental values of oak beams strength are higher than minimum requirements of standard softwood glued laminated beams values.

From table 4.4, by comparing characteristic bending strength values for H_{glulam}=180 mm and H_{glulam}=300 mm, a height effect coefficient can be estimated at 0,062. This value can be considered under-estimated due to the fact that bending strength coefficient of variation is higher for H_b=300 mm than for H_b =180 mmm. Comparison with EN 14 080 requirements cannot be easily made since tensile tests were not performed on D24 boards to verify the actual strength. However, we can notice that parallel and perpendicular to grain compression strength values are significantly higher for oaks beams in comparison with softwood beams.

Table 4.3. Experimental results on 20 homogeneous beams produced from D30 boards and 20 combined beams from D30/D18 boards- comparison with the requirements for softwoods glued laminated beams.

Properties of glued laminated beams	GL beams produced with visually graded D30 oak and D30&D18 H_{glulam}=180 mm /b=160 mm		Requirements for softwoods according to EN 14 080 adjusted for H_{glulam}=180 mm and $thickness_{lam}$=20 mm	
	20 homogenous beams with 9 **D30** laminations	20 combined beams with 9 laminations: **3 D30/ 3D18/3D30**	GL28h with **C30** laminations, **$f_{m,j,k}$=36 N/mm²**	GL28C with **C30&C18** laminations
Mean bending strength $f_{m,g,mean}$ [N/mm²]*	46,3 (13%)	52,6 (18%)	/	
Characteristic bending strength $f_{m,g,k}$ [N/mm²]	**35,7**	**34,2**	32,3	32,3
Mean modulus of elasticity $E_{0,g,mean}$ [N/mm²]	11 400 (12%)	11 200 (7%)	12 600	12 500
Characteristic modulus of elasticity $E_{0,g,05}$ [N/mm²]	9 000	9 600	10 500	10 400
Mean density $\rho_{g,mean}$ [kg/m³]	655 (3%)	662(2%)	460	420
Characteristic density $\rho_{g,k}$ [kg/m³]	**622**	**638**	425	390


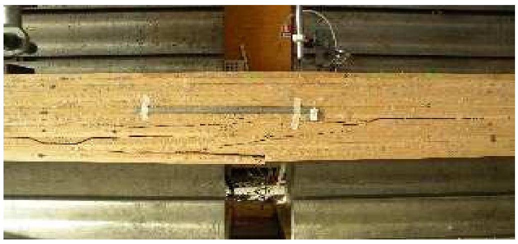

Figures 2. A bending test on oak glued laminated beam and specimen after failure.

Table 4.4. Experimental results on 40 glued laminated beams produced from D24 boards (for two heights) - comparison with the requirements for softwoods glued laminated beams.

Properties of glued laminated beams	**Homogenous GL beams** produced with visually **graded D24** b=160 mm		Requirements for softwoods GL24h according to EN 14 080 adjusted to H_{glulam}=300 mm and thikness$_{lam}$=20 mm
	20 beams H_{glulam} =160 mm 8 laminations	20 beams H_{glulam} =300 mm 15 laminations	GL24h with **C24** laminations, $\mathbf{f_{m,j,k}=30}$ **N/mm²**
BENDING			
Mean bending strength $f_{m,g,mean}$ [N/mm²]	47,6 (17%)	40,8 (11%)	/
Characteristic bending strength $f_{m,g,k}$ [N/mm²]	34	32,7	27
Mean modulus of elasticity in bending $E_{0,g,mean}$ [N/mm²]	11 900 (9%)	11 400 (4%)	11 500
Characteristic modulus of elasticity in bending $E_{0,g,05}$ [N/mm²]	10 000	10 500	9 600
COMPRESSION	parallel	Perp. to grain	Parallel/ Perp. to grain
Mean compression strength $f_{c,\ g,mean}$ [N/mm²]	47,7 (6%)	8,6 (6%)	/
Characteristic compression strength $f_{c,\ g,k}$ [N/mm²]	42	7,65	24 / 2,5
Mean modulus of elasticity In compression $E_{c,g,mean}$ [N/mm²]	12 000 (14%)	479 (8%)	/
Characteristic modulus of elasticity In compression $E_{c,g,k}$ [N/mm²]	9 100	335	/
Mean density $\rho_{g,mean}$ [kg/m³]	653 (2%)	652 (2%)	420
Characteristic density $\rho_{g,k}$ [kg/m³]	**624**	**628**	385

Figures 3. A failure example of oak glued laminated beam tested in compression parallel to grain (left) and perpendicular to grain (right).

The bonding quality (inter-laminations) was also controlled for each configuration by means of delamination tests and shear tests of the glue-joints.

Experimental results concerning the configuration of glulam produced with visually graded D24 of the cross section 160×160 mm^2 are presented in tables 4.5 and 4.6 respectively for shear and delamination tests. They indicate that the bonding quality satisfies the requirements by means of suitable adhesive and bonding parameters production.

Table 4.5. Experimental results on 40 shear tests on square edge specimens from glued laminated beams produced with D24 oak boards.

Shear tests on square edge specimens from glue laminated beams acc. to EN 14080, annex D		
Shear strength (f_v) (MPa)		
	Mean values based on individual glue lines shear strength	Min 12,3
		Max 15,3
		Mean 13,8
	Wood failure percentage (WFP) (%)	
	Mean values based on individual glue lines wood failure percentages	Min 71
		Max 99
		Mean 91
Requirement : If Mean values of fv ≥ 11, then WFP ≥ 45		
Conformity		**40 / 40**

Table 4.6. Experimental results on 20 delamination tests (1 specimen /beam) on full glued laminated beams produced with D24 oak boards.

Delamination tests on full glued laminated beams cross section acc. to EN 14080 annex C method B		
Total delamination (Dtot) after 1 cycle (%)		
	Quantity of test samples	20
	Min	0,6
	Max	15,7
	Mean	3,9
	Requirement : Dtot Mean ≤ 4, 1 additional cycle if 4 < Dtot Mean ≤ 8	
	Compliant samples after 1 cycle	14 / 20
	Accepted samples for 1 additional cycle	4 / 20
	Non compliant samples	2 / 20

Total delamination (Dtot) after 1 additional cycle (%)	
Quantity of test samples	4 / 20
Min	5,6
Max	8,6
Mean	7,1
Requirement : Dtot Mean ≤ 8	
Compliant samples after the additional cycle	3 / 4
Non compliant samples	1 / 4
Conformity (compliant samples after the all procedure)	**17 / 20**

3.3 Experimental results on oak laminations, finger-joints, glued laminated beams **for the second sampling**

Statistical values of mechanical properties and density of oak boards and finger joints are presented respectively in tables 5.1 and 5.2.

The main observations are the following:

- Visually D30 graded boards fulfill EN 338 requirements, even for tensile strength. Modulus of elasticity and density values are significatly higher than required values (see Table 1), and even than for the first sampling (see Table 4.1);
- Finger joints strength is much higher than for the first sampling (see table 4.2). This cannot be explained by quality production since finger joints of both samplings were produced at the same time. The lower coefficient of variation observed for the second sampling may explain the increase of strength values.

Table 5.1. Results of tensile tests on oak visually graded boards issued from specific sampling (see § 2.2).

Visual grading	Properties	Mean value	Coefficient of variation	5% - value ****	MC (%)	Nb of tests
D30 (h=160×b=23,1) mm^2	Local $E_{t,0}$ [N/mm^2]*	**13 900**	14%		12	21
	$f_{t,0}$ [N/mm^2]**	40,2	32%	**18,5**	9,1	21
	ρ [kg/m^3]***	713	7%	**663**	12	21

* local modulus of elasticity in tension determined according to EN 408 adjusted to 12% Moisture Content
** tensile strength determined according to EN 384 [12] adjusted to b=150 mm.
*** density adjusted at 12% MC.
**** characteristic values calculated according to EN 14 358.

Table 5.2. Results of flatwise bending tests on oak finger joints issued from specific sampling (see § 2.2).

Visual grading	Section mm²	Properties	Mean value	Coefficient of variation	5% -value (4)	MC (%)	Nb of tests
D40	h=24 mm b=16 mm	$f_{m,j}$ [N/mm²]*	85,1	16%	**59,8**	9,4	26
D30		$f_{m,j}$ [N/mm²]*	77	17%	**54,5**	9,4	30

* flatwise bending strength, at nominal dimensions, determined according to EN 14 080 Annex E.

Statistical values of mechanical properties of glued laminated beams are presented in tables 5.3 and 5.4 for beams produced respectively with:

- D40 boards for homogenous beams,
- D30 boards for homogeneous beams and with D30/D18 for combined beams.

For each beam configuration, comparison with the requirements of softwoods strength classes produced according to EN 14 080 is presented.

From table 5.3, comparison with EN 14 080 requirements cannot be directly made since tensile tests were not performed on D40 oak boards to verify the actual strength. However, we can imagine that, as for D30 class, visually D40 oaks boards for the second sampling have higher properties than required by EN 338.

From table 5.4, we can notice that oak beams produced with D30 boards have higher properties than required by EN 14 080 and than glued laminated beams produced with D30 boards of the first sampling. It is explained by the fact that both boards and finger joints properties are higher than for the first sampling.

Table 5.3. Experimental results on 15 glued laminated beams produced with D40 oak boards-comparison with the requirements for softwood glued laminated beams.

Properties of glued laminated beams	GL beams produced with visually graded D40 oak H_{glulam} =180 mm / b=160 mm	Requirements for softwoods according to EN 14 080 adjusted for H_{glulam}=180 mm and $thickness_{lam}$=20 mm
	15 Homogeneous beams with 9 D40 laminations	GL32h with **C40** laminations, $\mathbf{f_{m,j,k}}$**=41 N/mm²**
Mean bending strength $f_{m,g,mean}$ [N/mm²]*	81,2 (13%)	/
Characteristic bending strength $f_{m,g,k}$ [N/mm²]	**61,7**	37
Mean modulus of elasticity $E_{0,g,mean}$ [N/mm²]	16 300 (4 %)	14 200
Characteristic mod. of elasticity $E_{0,g,05}$ [N/mm²]	14 900	11 800
Mean density $\rho_{g,mean}$ [kg/m³]	726(2%)	490
Characteristic density $\rho_{g,k}$ [kg/m³]	**709**	440

Table 5.4. Experimental results on 30 glued laminated beams produced with D30 and with D30/D18 oak boards- comparison with the requirements for softwood glued laminated beams.

Properties of glued laminated beams	GL beams produced with visually graded D30 oak and D30&D18 H_{glulam} =180 mm /b=160 mm		Requirements for softwoods according to EN 14 080 adjusted for H_{glulam}=180 mm and $thickness_{lam}$=20 mm	
	25 homogeneous beams with 9 **D30** laminations	5 combined beams with 3 **D30/ 3D18/3D30**	GL28h with **C30** laminations, $f_{m,j,k}$=36 N/mm²	GL28C with **C30&C18** laminations
Mean bending strength $f_{m,g,mean}$ [N/mm²]*	63,8 (16%)	56,3 (13%)	/	
Characteristic bending strength $f_{m,g,k}$ [N/mm²]	**46,5**	/	32,3	32,3
Mean modulus of elasticity $E_{0,g,mean}$ [N/mm²]	15 800 (5%)	15 000 (4%)	12 600	12 500
Characteristic modulus of elasticity $E_{0,g,05}$ [N/mm²]	14 400	/	10 500	10 400
Mean density $\rho_{g,mean}$ [kg/m³]	725(3%)	729 (2%)	460	420
Characteristic density $\rho_{g,k}$ [kg/m³]	**703**	/	425	390

3.4 Experimental relationship between laminations and glued laminated beams

With the aim of deriving relation between boards and glued laminated beams modulus of elasticity, "modulus fractile fractile curve'' was established. For this purpose, experimental results on boards and beams concerning visually D30 class oak for the two samplings were used.

The following relation (illustrated in Figure 4) was obtained: $E_{0,g,mean}$ = 1,08 × $E_{0,l}$.

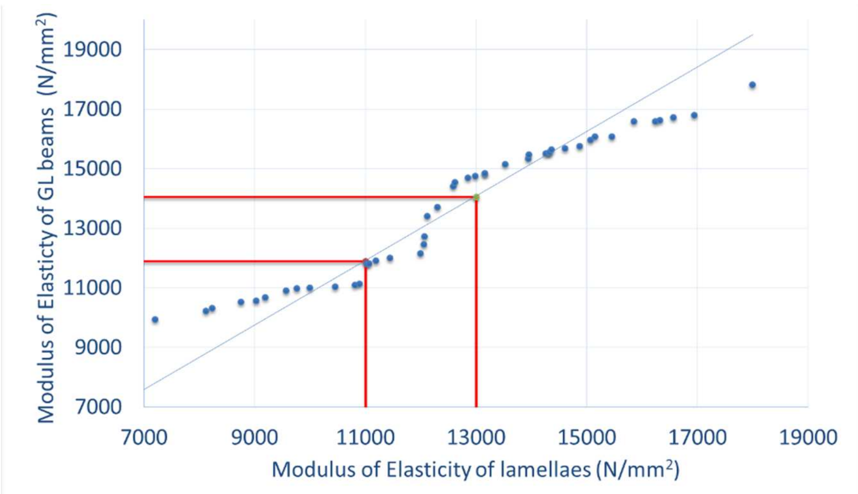

Figure 4. Relation between glued laminated beam modulus of elasticity, $E_{0,g,mean}$ and boards modulus of elasticity $E_{0,l}$ established from experimetal fractile fractile curve. $E_{0,g,mean}$ = 1,083 × $E_{0,l}$ (R^2= 0,8).

The same approach was conducted on the strength values on experimental results on boards and beams made of D30 class oak for the two samplings, to establish the *"strength fractile fractile curve''.*

The following relations (illustrated in Figure 5) were obtained respectively for average values and with 95% confidence interval:

- with average values : $f_{m,g,k} = 20,89 + 0,3909\ f_{t,0,l,k} + 0,2715\ f_{m,j,k}$
- with 99% confidence interval : $f_{m,g,k} = 17,24 + 0,3909\ f_{t,0,l,k} + 0,2715\ f_{m,j,k}$.

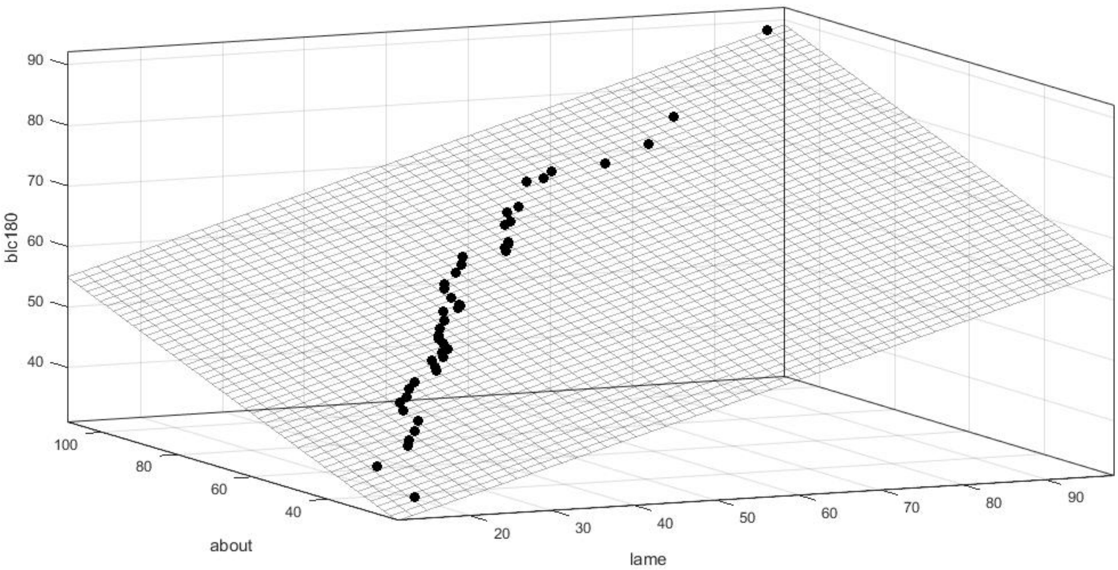

Figure 5. Relation between glued laminated beam bending strength $f_{m,g,k}$ and (boards tensile strength $f_{t,0,l,k}$ and finger joints flatwise bending strength $f_{m,j,k}$) established from experimental fractile curve (R^2=0,986).

A comparison of these ''strength fractile fractile curves'' and the relation given in EN 14 080 is presented in Table 6 when these formula are applied to D30 boards.

We can notice that the relation given in EN 14 080 provides safe estimation of oak glued laminated beams produced with D30.

The determination of an optimized relation between oak laminations and glued laminated beams can be established by developing a finite element modelling of the mechanical behavior of the beams which takes into account the actual behaviour of boards. This model should be validated, partly, from the data presented in this paper.

Table 6. Relation between glued laminated beam bending strength $f_{m,g,k}$ and (boards tensile strength $f_{t,0,l,k}$ and finger joints flatwise bending strength $f_{m,j,k}$) established from several approchaes.

	Boards and finger joints strength		Calculated glulam strength with different approaches			
	$f_{t,0,l,k}$ [N/mm²]	$f_{m,j,k}$ [N/mm²]	$f_{m,g,k}$ [N/mm²]			
			According EN 14 080 with H_{glulam} = 600 mm	According EN 14 080* With H_{glulam}=180 mm and thickness-$_{lam}$=20mm	According fractile curve with average values H_{glulam} = 180	According fractile curve with a 99% confident interval H_{glulam} =180 mm thickness-$_{lam}$=20mm
D30, EN 338	18	36	27,9	**32,3**	37,7	34
D30, sawmill based sampling (§ 3.1)	17	29,6	25,5	**29,4**	35,6	32
D30, specific sampling (§ 3.2)	18,5	54,5**	32,7	**36,7**	42,9	39

*relation according EN 14 080: $f_{m,g,k} = -2,2 + 2,5\, f_{t,0,l,k}^{0,75} + 1,5\, (f_{m,j,k} / 1,4 - f_{t,0,l,k} + 6)^{0,65}$

**relation according EN 14 080 is also calculated in this case although its application is limited to $f_{m,j,k} \leq 1,4\, f_{t,0,l,k} + 12$.

4 Conclusions

Based on an experimental study carried on 120 oak glued laminated beams, strength and stiffness properties and density were evaluated and compared with the requirements of EN 14 080 for softwoods. The impact of the sampling was also investigated: first sampling was essentially constituted with D24 , second one was carried out in order to identify D40.

The main conclusions are the following:

- For both oak samplings, density of oak is higher than required values according to EN 338 for hardwoods,
- For D30 boards, finger joints strength for the second sampling is much higher than for the first sampling. This may be partly due to a lower coefficient of variation of strength values.
- Based on experimental values of D30, relations between boards and glued laminated beams bending properties were established: we can conclude that the relation given in EN 14 080 provides a safe estimation of oak glued laminated

beams produced with D30. The determination of an optimized relation between boards and glued laminated beams properties can be established by developing a finite element modelling.

- Strength values of oak glued laminated beams exceed the strength values of softwood glued laminated beams by a factor of about 2 and 3 respectively in parallel and perpendicular to the grain compression.

Aknowledgment : The study was supported by the Agricutlture Minitry, the French asssociation France Bois Forêt, ADEME (French Environment & Energy Management Agency) and CODIFAB (French Federation of Wood Industry).

5 References

[1] EU-Hardwoods project (March 2014- December 2016): European project coordinated by Austria in collaboration with Germany, Slovenia and France, funded by the WoodWisdom-Net research program under the ERA-NET Plus Scheme of the Seventh Framework Program (FP7) of the European Commission.

[2] Aicher S, Zachary C and Dill-Langer G 201 (August 2014), Hardwood glulams – emerging timber products of superior mechanical properties. Proceedings of World Conference on Timber Engineering 2014, Quebec, Canada.

[3] Lanvin JD et al. (September 2015), Strength assessment and potential for use as glulam of French chsetnut lumber. Proceedings of 5th International Scientific Conference on Hardwood Processing, Quebec, Canada.

[4] Tran VD et al. (August 2014), Experimental study of multi-layered beams made of beech timber glued with different adhesives, Proceedings of World Conference on Timber Engineering 2014, Quebec, Canada.

[5] EN 14 080 (August 2013): Timber Structures – Glued laminated Timber and glued solid timber- Requirements.

[6] NF B 52-001-1 (August 2011): Regulations governing the use of timber in structure — Visual classification for the use of French softwood and hardwood species in structures — Part 1: Massive wood.

[7] EN 338 (July 2016): Structural timber – strength classes.

[8] EN1912 (June 2012): Structural Timber — Strength classes — Assignment of visual grades and species.

[9] Lanvin JD, Reuling D (January 2012), « Caractérisation du chêne sessile et pédonculé de France en vue de son utilisation en structure », Revue Forestière française Volume LXIV, pp 151 – 165.

[10] EN 408 (September 2012): Timber structures – structural timber and glued laminated timber – determination of some physical and mechanical properties.

[11] EN 14 358 (2006): Timber structures – calculation and verification of characteristics values.

[12] EN 384 (June 2010): Structural timber- Determination of characteristic values of mechanical properties and density.

Discussion

The paper was presented by C Faye

H Blass commented that the compression strength values with moisture content of 10 to 12 % were high. If this product would also be used in service class 2, you would need to decrease the value by 1/3 to account for the lower compression strength in service class 2.

H Blass asked about the difference in MOE of laminae and finish glulam being different from 1:1. It was clarified that the MOE of the laminae was based on localized tension MOE.

P Stapel and C Faye further discussed the relationship between local and glulam MOE in that all data was used.

JWG van de Kuilen questioned about the scatter in the data as it would be too low to cover the usual grade. C Faye said that it might be low but all the data was used.

P Stapel said that the 5th percentile value for tension strength of laminae was too low. How was it possible to get such high bending strength? C Faye said that they used more data in the statistical analysis. P Stapel suggested one should use an adjusted value in the model to account for the low sample size.

T Ehrhart said that the height of the beams was not too large. If one wanted the information to apply to large beams then size effect would be an issue. C Faye agreed as they planned to work on large beams and as such there would be lots of finger joints in such beams.

Effective Flange Width of a CLT Slab in Timber Composite Beams

Reza Masoudnia[*], Ashkan Hashemi, Pierre Quenneville

Department of Civil and Environmental Engineering, Faculty of Engineering, University of Auckland, Auckland, New Zealand
* Corresponding author: e-mail: rmas551@aucklanduni.ac.nz

Abstract

A timber composite beam consists of a Cross Laminated Timber (CLT) panel attached to a girder such as a Laminated Veneer Lumber (LVL) beam. Under positive bending moment, part of the CLT panel acts as the flange of the LVL girder and resists compression. When the spacing between the LVL girders becomes large, simple beam theory is not applicable because the compressive stresses in the flange vary with the distance from the LVL girder web and the flange area over the web is more highly stressed than the extremities; this phenomenon is termed shear lag. For the design of steel-concrete composite sections, the effective flange width concept has been introduced into national and international design specifications. Despite the large number of studies regarding steel and concrete composite structures, comparative, comprehensive research has not been conducted on timber composite structures. In this study, a numerical model was developed and experimentally validated for analyzing different configurations of timber composite beams. Based on a parametric study, a formula is proposed for determining the effective flange width of timber composite beams.

Keywords: CLT, Timber Composite Beams, Effective Flange Width, LVL, shear lag

1 Introduction and literature review

Shear lag is a confirmed phenomenon in T-section beams and occurs when the in-plane shear strain in the flange of a girder under loading and bending causes smaller longitudinal displacements of the areas of the flange far from the web compared with areas near the web. This phenomenon can lead to imprecise estimates of the displacements and stresses at the extreme fibers of composite sections using Euler bending theory (Amadio et al 2002; Aref et al. 2007; Zou et al. 2011; Chiewanichakorn et al. 2004; Timoshenko et al. 2009). For the design of composite steel-concrete sections, the concept of an effective flange width has been introduced into national and international design specifications. Based on this concept, various simplified effective flange width formulas have been derived from analytical and experimental results. For example, Table 1 shows the requirements for determining the effective flange width from various sources. For practical reasons, the code provisions simplify these requirements. In most cases, the provisions have remained unaltered for a long time (Castro et al 2007; Salama et al 2011).

Table 1. Effective flange width (be) formulas in various design codes (AISC 2001; CSA 2001; DD ENV 1994-2 2001; Chiewanichakorn et al. 2007; ACI 2001).

Source	Formulas
AISC-LRFD:13.1	be is the smallest of: (1) Beam span/4 (2) bs (3) 2 times the distance to the slab edge
CANADIAN CSA: S16-01 & Euro-Code (2000)	be is the smallest of: (1) Beam span/4 (2) bs
ACI	be is the smallest f: (1) Beam span/4 (2) bw+16hf (3) Center-to-center beam spacing

b_e: effective flange width of concrete flange for composite beam
b_s: width of concrete flange for composite beam
h_f: flange thickness
b_w: web breadth

Only limited studies have investigated timber composite T-beams, including timber double skin panels and stress-laminated timber bridges. The research on the former is a case study on stress-laminated timber bridges consisting of laminated deck sections combined with glued-laminated timber beams compressed transversely with high-strength steel rods. The research on the latter focuses on double skin panel floors made of oriented strand board (OSB) or plywood; this study presented a formula for predicting the effective flange width for timber box sections (Porteous et al 2013; Ozelton et al 2008; Davalos et al 1993). A basic analytical study on the effective flange width of timber composite beams with a CLT slab showed that the non-uniform distribution of normal stresses along the flange width in a timber composite T-beam is the result of shear deformation in the CLT panel (Thiel et al 2016).Despite the large number of studies regarding steel and concrete composite structures, comparative, comprehensive research has not been conducted on timber structures (Salama et al 2011; Davalos et al 1993; Adekola et al 1968; Elkelish et al 1986; Timoshenko et al 2009; Nassif et al 2005; Adekola et al 1974). Recognizing the lack of research on the effective flange width in timber structures, this study seeks to investigate the effective flange width in a CLT slab in timber composite beam under positive bending. The concept of effective flange width is important for a simplified structural analysis, especially for computing stresses and displacements (Chen et al 2007). These data assist more efficient and effective design of timber structural members, such as timber flooring systems, therefore encouraging more economical building designs (Masoudnia et al 2013; Masoudnia et al 2016; Masoudnia et al 2017).

2 Test Setup and Numerical Modelling

A timber composite beam was experimentally tested in the University of Auckland test hall, and the obtained results were used to verify a numerical model. As shown in Figure 1, the timber composite beam consisted of a seven meter long planed LVL beam with a width of 300 mm and a depth of 600 mm and a top flange of a 5 layer CLT panel with a width of 2000 mm, a depth of 200 mm and a length of 6000 mm. The panel was mechanically fastened to the LVL beam by forty-eight 550 mm self-tapping screws with a diameter of 11 mm. The screws were set at a 45° angle to provide additional composite action between the panel and the beam. A bending test was conducted using a Material Testing Systems (MTS) actuator testing machine with sufficient load capacity to apply a service load on the test specimen. To monitor the vertical deflection, 3 linear variable differential transducers (LVDTs) were attached at the mid-span of the beam and at the supports (Masoudnia et al 2017).

The finite element package ABAQUS version 6.13-3 was used to determine the exact stress distributions in the longitudinal layers of the CLT panels for the simply supported timber composite beam. The accuracy of the numerical technique used in this study has been previously validated by comparing the mid-span deflection of the T-section and the associated components (CLT panel and LVL beam), comparing the slip between the panel and the LVL beam every 1m along the span of the timber composite beam and finally the effective flange width of the timber composite beam from the numerical models with experimental data (Table 2 to Table 4 and Figure 2). The close agreement shown by these results confirms that the model is sufficiently precise to determine the effective flange width of the timber composite beam (Masoudnia et al 2017; ABAQUS 2014).

Table 2. Comparison of the experimental and numerical results for mid-span deflection

Test Specimen	W×T×L (mm)×(mm)×(mm)	Deflection	
		Experimental (mm)	Numerical (mm)
CLT	2030×200×6000	17.9 *	17.9
LVL	300×605×6000	3.1 *	3.1
Timber Composite Beam	CLT+LVL (connected by screws)	1.8 **	1.7

W: Width (mm), T: Thickness (mm), L: Length (mm)
* Deflection for the 50-kN four-point loading test,
** Deflection for the 50-kN single-point loading test.

Table 3. Comparison of the experimental and the numerical slip results

LVDT	Position of the LVDT	Slip (mm) (Experimental)*	Slip (mm) (Numerical)*
1	At mid-span	0	0
2	1 m from mid-span	0.056	0.055
3	2 m from mid-span	0.084	0.085
4	3 m from mid-span	0.121	0.122

* Deflection for the 50-kN single-point loading test

Table 4. Comparison of the experimental and numerical results of effective flange width

Specimen	Effective flange width (Experimental)	Effective flange width (Numerical)	$\frac{\text{Experimental result}}{\text{Numerical result}}$
CLT composite beam	980 mm	995 mm	0.98

3 Numerical Parametric Study

This study focuses on the CLT panel configurations and their effect on the effective flange width. The experimentally validated numerical model was used to study the effects of varying the characteristics of the longitudinal and transverse layers of the CLT panel in combination with the LVL beam on the effective flange width of timber composite beams. Various thicknesses of CLT panels constructed of boards with a modulus of elasticity of 6 GPa, 8 GPa or 10 GPa were investigated. Table 5 summarizes the specifications and the obtained effective flange widths for the timber composite beams.

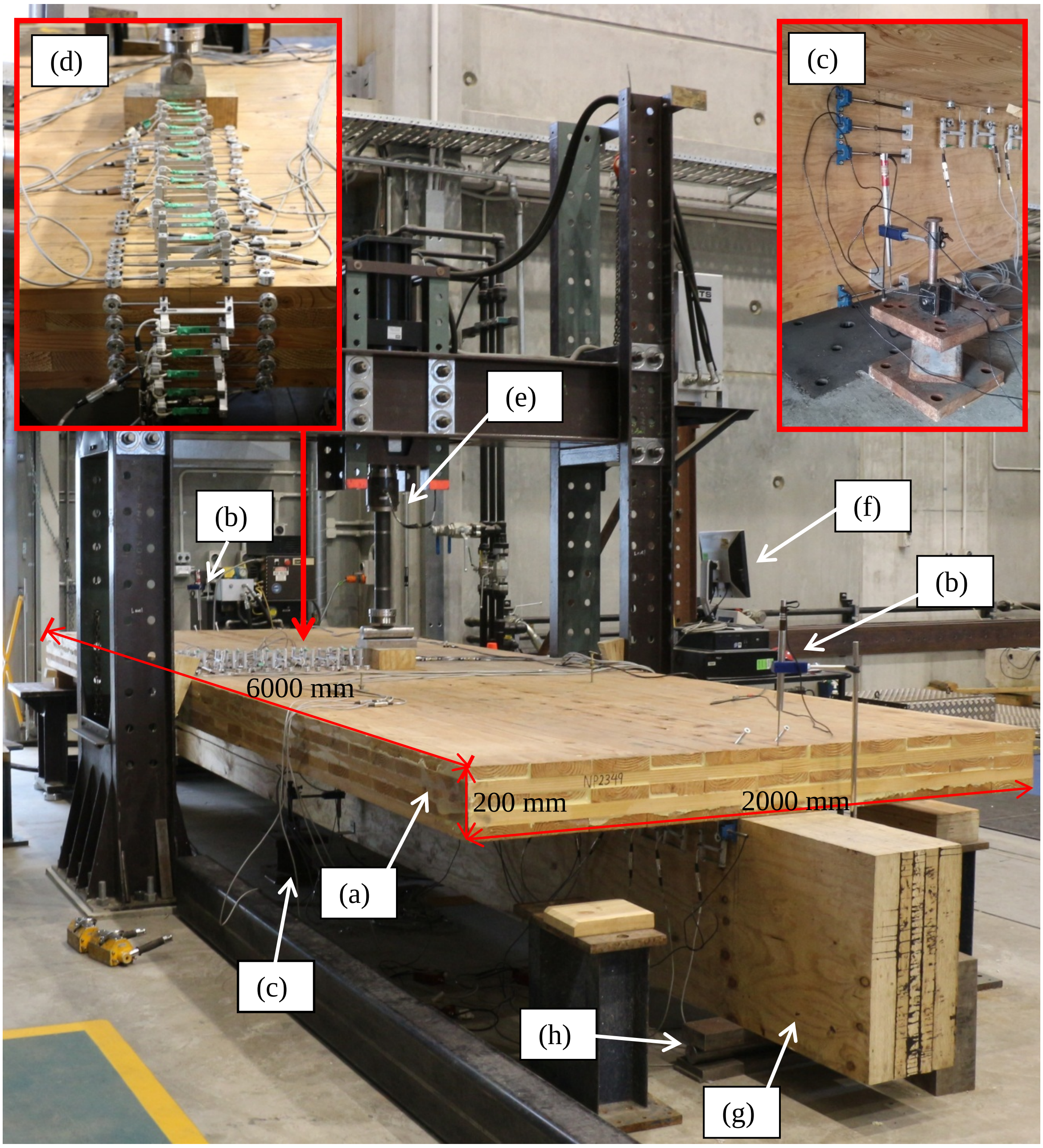

Figure 1. General test setup of the timber composite beam during the bending test.
(a) CLT panel; (b) LVDT at the supports; (c) LVDT at the mid-span; (d) Arrangement of the portal gauges on the surface of the CLT panel; (e) MTS machine; (f) Data acquisition system; (g) LVL beam; (h) Roller support.

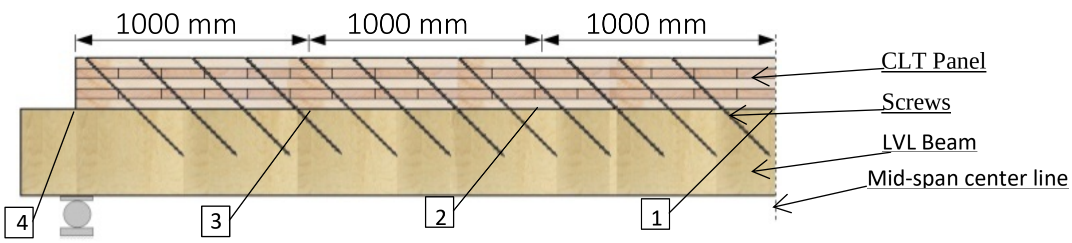

Figure 2. Slip monument for every 1m along the span of the timber composite beam (Elevation).

Table 5. Specifications and effective flange width (mm) of the timber composite beams

Configuration	CLT (mm) W×T[1]×L	CLT (GPa) $E_{L1}, E_{L2}, E_{L3}, E_{L4}, E_{L5}$[2]	LVL (mm) W×T×L	LVL (GPa) MoE	Predicted effective width flange (mm)
1	2000×200×6000 $2000\times(40_b+40_b+40_b+40_b+40_b)$[1]$\times6000$	8, 8, 8, 8, 8[2]	300×600×6000	11	790
2	2000×160×6000 $2000\times(40_b+20_b+40_b+20_b+40_b)\times6000$	8, 8, 8, 8, 8	300×600×6000	11	460
3	2000×100×6000 $2000\times(20_b+20_b+20_b+20_b+20_b)\times6000$	8, 8, 8, 8, 8	300×600×6000	11	1055
4	2000×140×6000 $2000\times(20_b+40_b+20_b+40_b+20_b)\times6000$	8, 8, 8, 8, 8	300×600×6000	11	1950
5	2000×200×6000 $2000\times(40_b+40_b+40_b+40_b+40_b)\times6000$	6, 6, 6, 6, 6	300×600×6000	11	760
6	2000×160×6000 $2000\times(40_b+20_b+40_b+20_b+40_b)\times6000$	6, 6, 6, 6, 6	300×600×6000	11	440
7	2000×100×6000 $2000\times(20_b+20_b+20_b+20_b+20_b)\times6000$	6, 6, 6, 6, 6	300×600×6000	11	1015
8	2000×140×6000 $2000\times(20_b+40_b+20_b+40_b+20_b)\times6000$	6, 6, 6, 6, 6	300×600×6000	11	1880
9	2000×200×6000 $2000\times(40_s+40_s+40_s+40_s+40_s)\times6000$	8, 8, 8, 8, 8	300×600×6000	11	710
10	2000×160×6000 $2000\times(40_s+20_s+40_s+20_s+40_s)\times6000$	8, 8, 8, 8, 8	300×600×6000	11	410
11	2000×100×6000 $2000\times(20_s+20_s+20_s+20_s+20_s)\times6000$	8, 8, 8, 8, 8	300×600×6000	11	945
12	2000×140×6000 $2000\times(20_s+40_s+20_s+40_s+20_s)\times6000$	8, 8, 8, 8, 8	300×600×6000	11	1755
13	2000×200×6000 $2000\times(40_s+40_s+40_s+40_s+40_s)\times6000$	6, 6, 6, 6, 6	300×600×6000	11	680
14	2000×160×6000 $2000\times(40_s+20_s+40_s+20_s+40_s)\times6000$	6, 6, 6, 6, 6	300×600×6000	11	390
15	2000×100×6000 $2000\times(20_s+20_s+20_s+20_s+20_s)\times6000$	6, 6, 6, 6, 6	300×600×6000	11	905
16	2000×140×6000 $2000\times(20_s+40_s+20_s+40_s+20_s)\times6000$	6, 6, 6, 6, 6	300×600×6000	11	1690
17	2000×200×6000 $2000\times(40_b+40_b+40_b+40_b+40_b)\times6000$	10, 10, 10, 10, 10	300×600×6000	11	985
18	2000×160×6000 $2000\times(40_b+20_b+40_b+20_b+40_b)\times6000$	10, 10, 10, 10, 10	300×600×6000	11	575
19	2000×100×6000 $2000\times(20_b+20_b+20_b+20_b+20_b)\times6000$	10, 10, 10, 10, 10	300×600×6000	11	1315
20	2000×140×6000 $2000\times(20_b+40_b+20_b+40_b+20_b)\times6000$	10, 10, 10, 10, 10	300×600×6000	11	2440
21	2000×200×6000 $2000\times(40_s+40_s+40_s+40_s+40_s)\times6000$	10, 10, 10, 10, 10	300×600×6000	11	885
22	2000×160×6000 $2000\times(40_s+20_s+40_s+20_s+40_s)\times6000$	10, 10, 10, 10, 10	300×600×6000	11	365
23	2000×100×6000 $2000\times(20_s+20_s+20_s+20_s+20_s)\times6000$	10, 10, 10, 10, 10	300×600×6000	11	1180
24	2000×140×6000 $2000\times(20_s+40_s+20_s+40_s+20_s)\times6000$	10, 10, 10, 10, 10	300×600×6000	11	2185

1 The numbers in the parentheses are the thicknesses of the individual CLT layers.
2 The 5 numbers are the modulus of elasticity of each CLT layer.
b This index next to the numbers in parentheses indicates that the width of the wood plank is 180mm.
s This index next to the numbers in parentheses indicates that the width of the wood plank is 90 mm.
MoE & E indicate the modulus of elasticity (units are GPa).

3.1 The Effect of the Transverse Layer Thickness on the Effective Flange Width

Figure 3 illustrates the effect of different thicknesses of transverse layers on the effective flange widths in simply supported 6 m long beams under a single vertical load. The thickness variation of the transverse layers was considered for CLT panels with an elastic modulus of 6 GPa, 8 GPa and 10 GPa. This figure shows that increasing the depth of the transverse layer to greater than the depth of the longitudinal layer significantly increases the effective flange width. For instance, when 40 mm thick longitudinal layers are replaced by 20 mm thick layers, the effective flange width increases by approximately 2.5 times, from 790 mm to 1880 mm (specimens No. 1 and No. 4 in Table 5). Furthermore, the effect of the modulus of elasticity of the CLT timber boards is presented in Figure 3 and Table 5. Figure 3 shows that the effective flange width generally increases by approximately 5 % when the modulus of elasticity of the boards increases from 6 GPa to 8 GPa. For instance, when the modulus of elasticity of the CLT panel increases from 6 GPa (specimen No. 8 in Table 5) to 8 GPa (specimen No. 4 in Table 5), the effective flange width increases from 1880 mm to 1950 mm.

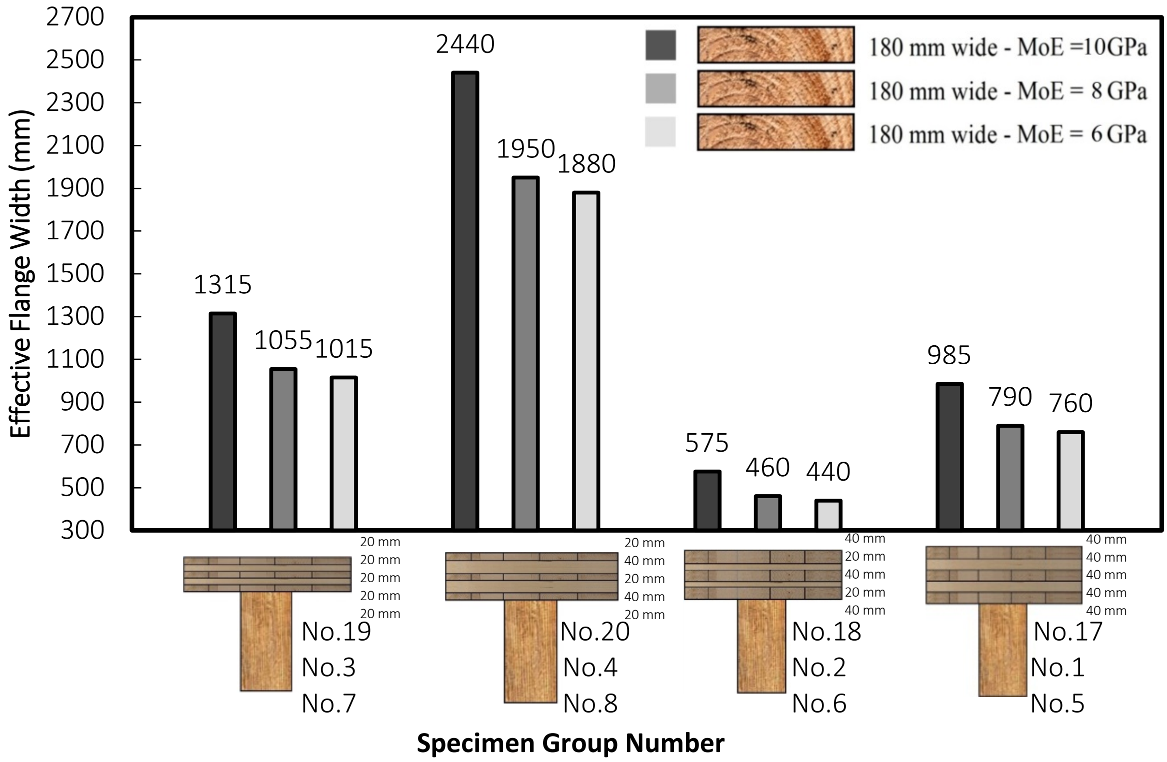

Figure 3. Effect of the layers configuration and CLT material properties on the effective flange width.

3.2 Effect of Wood Plank Characteristics on the Effective Flange Width

To consider the effect of the CLT panel wood plank widths on the effective flange width of the timber composite beams, two beam configurations were modeled using a 5-layer CLT with 90-mm or 180-mm wide boards with a modulus of elasticity of 6 GPa, 8 GPa or 10 GPa. Various combinations of 40-

mm-thick and 20-mm-thick layers were modeled to study the effect of the two wood plank widths on the effective flange width. Figure 4 shows that the effective flange width increased when a CLT panel with 90-mm-wide boards was replaced by a CLT panel with 180-mm-wide boards.

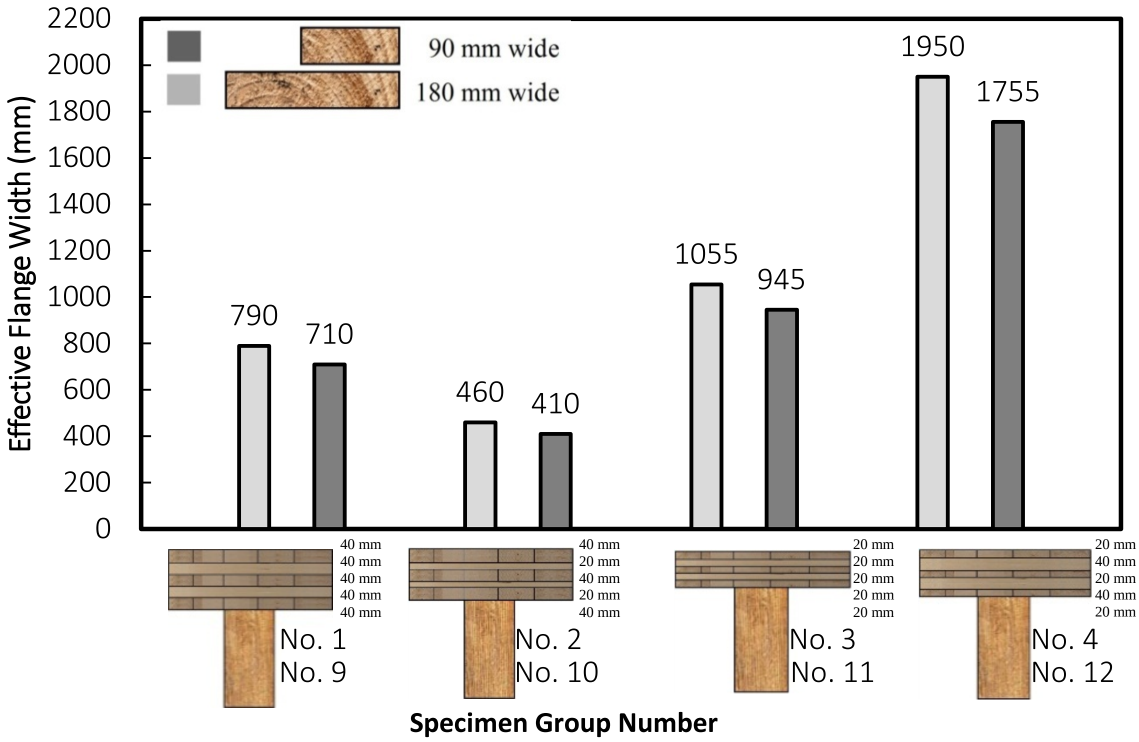

Figure 4. Effect of the CLT wood plank width on the effective flange width of timber composite beams.

The maximum difference in the effective flange width among all twenty-four numerical analysis results was observed between configurations 14 and 20 (Table 5). This significant change was due to two factors: the lower ratio of the transverse layer depth to the longitudinal layer depth in the CLT panel combined with the higher modulus of elasticity in configuration 20 and the use of smaller width boards in the CLT panel in configuration 14. These changes led to a 560% difference in the effective flange width of these two specimens.
The presented results in Figure 3 and Figure 4 show that increasing the CLT thickness has a positive effect on the effective flange width only when the increase is the result of increasing the thickness of the transverse layers.
Figure 5 compares the effective flange width, CLT cost and bending stiffness (EI) of three timber composite beams. A 33 cm and a 149 cm increase in the effective flange width was observed between configuration 2 and configurations 1 and 4, respectively; these increases led to 42% and 14% reductions in CLT cost, respectively. Moreover, the CLT layer arrangement in configuration 4 increased the EI of the section by 8% and 7% compared to configurations 2 and 1, respectively.

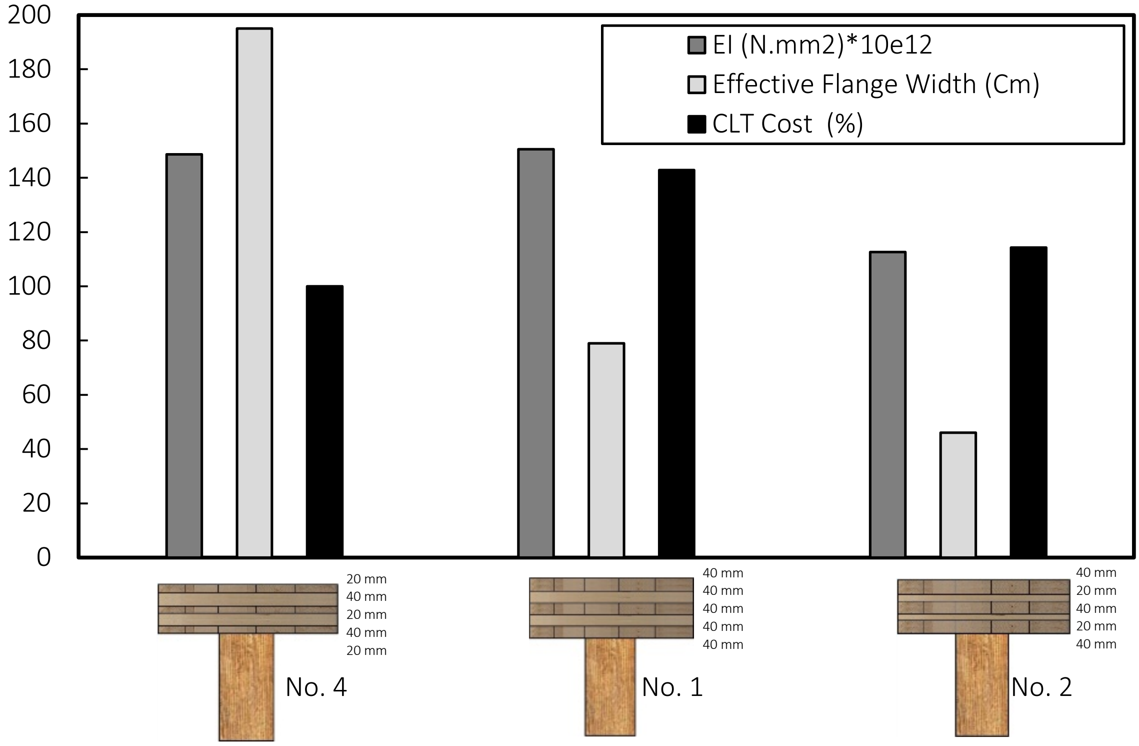

Figure 5. Comparison of the effective flange width, CLT cost and EI of timber composite beams.

4 Proposed Formula for the Effective Flange Width of Timber Composite Beams

A formula for calculating the effective flange width (b_{eff}) of timber composite beams is proposed based on the results of the parametric numerical study. The formula can be used to predict the effective flange width of timber composite beams constructed with CLT panels of various layer configurations, material properties and plank widths and varying span lengths under an applied service load. All materials are assumed to remain in the elastic phase.

Figure 6a and Figure 6b compare the effective flange widths calculated using equation 1 and equation 2 and their corresponding results obtained from numerical analyses for timber composite beams constructed of 6-GPa, 8-GPa or 10-GPa CLT panels with two different board widths. The comparison shows a maximum difference of 9.8% between the calculations and the numerical results, which confirms that the formula is sufficiently precise for predicting the effective flange width.

b_{eff} = minimum ($b_{eff\ (single\ beam)}$, width of CLT panel) in mm Eq. 1

$$b_{eff\ (single\ beam)} = \alpha \times \beta \times 23400 \left(\frac{(\sum \text{Longitudinal layer thickness})^2}{(\sum \text{Transferse layer thickness})}\right)^{-0.67} \quad \text{Eq. 2}$$

$$\alpha \text{ (coefficient of material properties)} = \begin{cases} 0.95 & \text{if MoE} = 6 \text{ GPa} \\ 1.00 & \text{if MoE} = 8 \text{ GPa} \\ 1.30 & \text{if MoE} = 10 \text{ GPa} \end{cases}$$

$$\beta \text{ (coefficient of plank width)} = \begin{cases} 0.915 & \text{if plank width} = 90 \text{ mm} \\ 1.000 & \text{if plank width} = 180 \text{ mm} \end{cases}$$

** Interpolate if modulus of elasticity is between the values given.*
*** Interpolate if width is between 90 mm and 180 mm.*

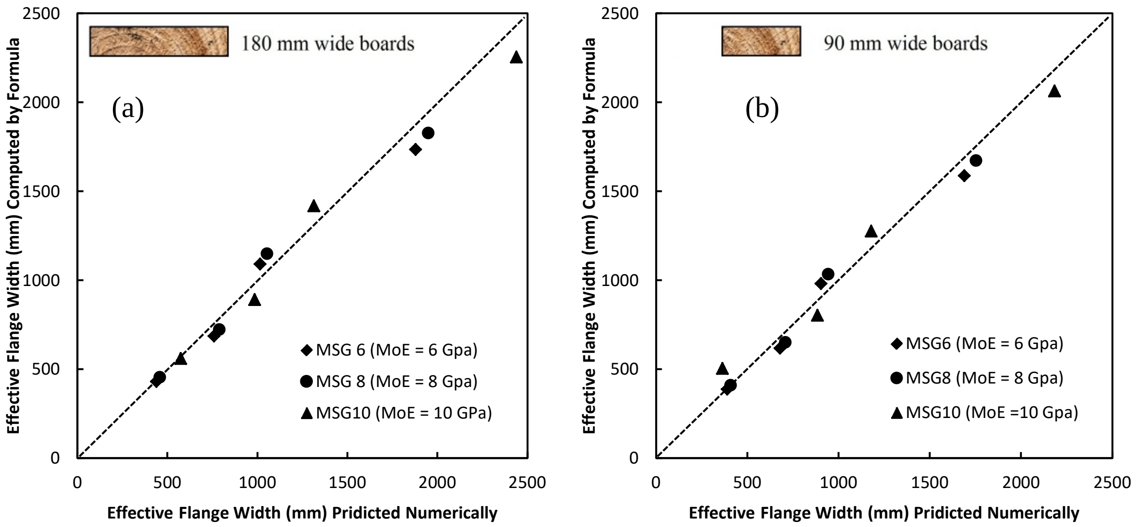

Figure 6. Comparison of the results from the proposed formula and numerical model for 6-m-long timber composite beams: (a) CLT panel with 180-mm-wide boards, (b) CLT panel with 90-mm-wide boards.

5 The Effect of the Shear Stiffness of the Connector on the Effective Flange Width

To investigate the effect of the shear stiffness on the effective flange width, a series of screws was removed, and the effective width flange was measured experimentally. The obtained result was then compared with the corresponding numerical model. The slip variation measurement shows that 40 is the minimum number of screws that can provide fully composite action between the CLT panel and LVL beam. Therefore, the effective flange width was measured experimentally when the CLT panel and LVL beam were connected with 30, 20 and 10 screws to simulate 75%, 50% and 25% composite action in the timber composite beam. The summarized results in Table 3 show that the number of screw shear connectors significantly affected the effective flange width of the timber composite beams. A reduction of screw shear connectors by 20%, 50% and 70% decreased the effective flange width by 20%, 30% and 48%, respectively.

Table 3. Effect of screw shear connectors on the effective flange width

Composite action	Number of screws	Effective flange width Experimental Result (mm)	Effective flange width Numerical Result (mm)

100%	40	980	995
80%*	32	862	878
50%	20	685	702
30%**	12	510	523

* Close to 25% reduction

** Close to 75% reduction

In addition, the calculated effective bending stiffness (EI) with the effective flange width results from the numerical analysis and recommended formula were compared with the calculated effective bending stiffness with the gamma method, as shown in Figure 7. The comparison shows that the bending stiffness obtained by the gamma method is overdesigned compare with the obtained results based on the numerical analysis and formula.

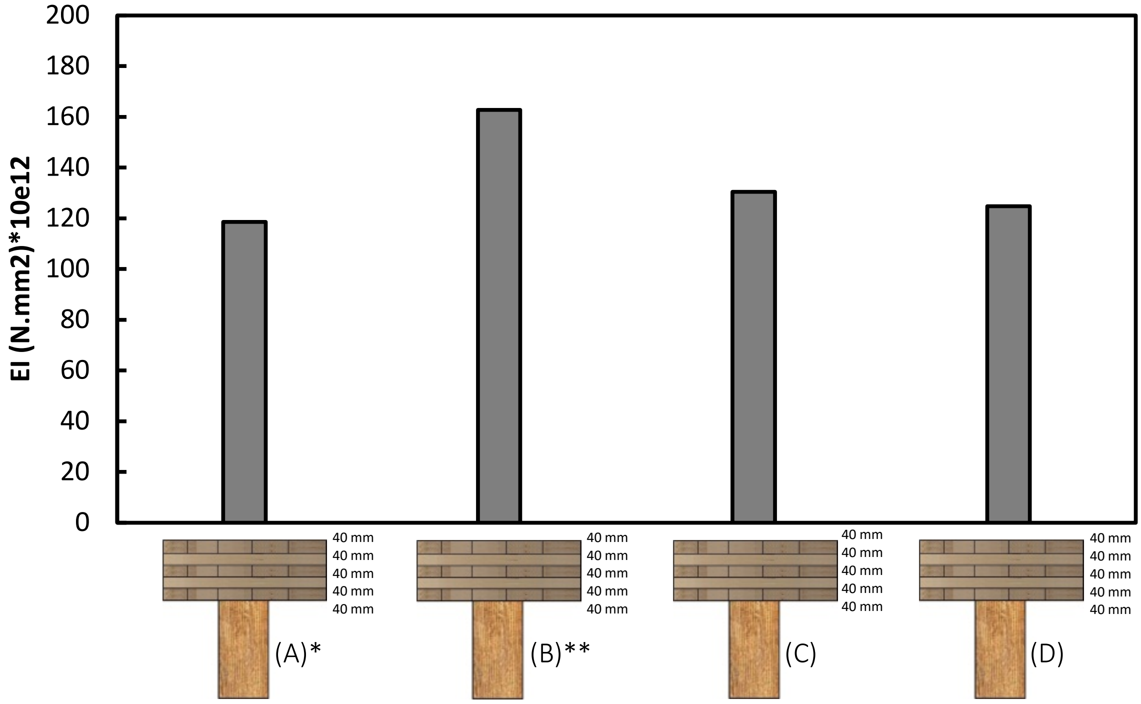

Figure 7. Comparison of the calculated bending stiffness (EI) of timber composite beam (specimen No.5) based on Gamma method (A), Gamma method (B), numerical analysis (C) and recommended formula (D).

** Only Three longitudinal layers in CLT was used to calculate the moment of inertial*

*** Whole section consider in moment of inertia calculation*

6 The Effect of the CLT Layers configuration on the Effective Flange Width of timber composite beams with equal CLT thickness

The effect of the layers configuration has been investigated for two timber composite beams which are comprised of a CLT panel with equal overall thickness but with different configurations of longitudinal and transverse layers (Figure 8a and Figure 8b). Figure 8a shows a comparison of specimen No.6 and specimen E. Both are 160 mm thick. In specimen No.6, the panel is comprised of 40 mm longitudinal layers and 20 mm transverse layer and specimen E CLT panel is constructed of 20 mm longitudinal layer and 50 mm transverse layers. The comparison shows that using thicker longitudinal layer in specimen No.6 leads to a 75 % decrease in effective flange width compare to the specimen E effective width, although the overall CLT thickness remain similar.

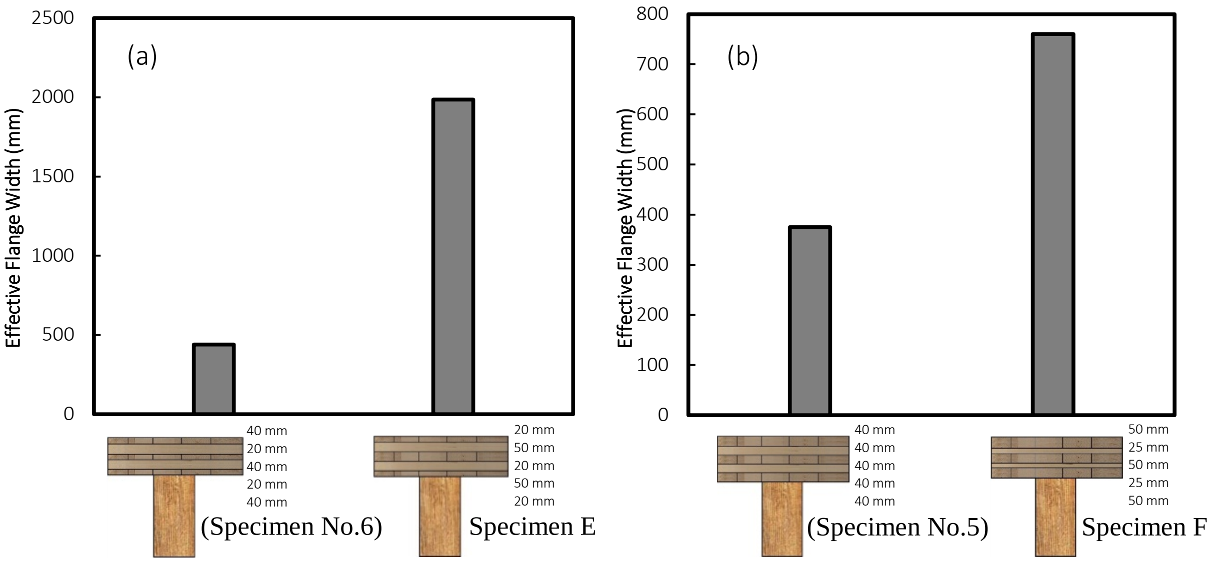

Figure 8. Effect of the CLT layers configuration on the effective flange width of timber composite beams for MoE of 6 GPa and with equal CLT thickness (a) CLT thickness at 160 mm, (b) CLT thickness at 200 mm.

7 Conclusions

The objective of this study was to understand the parameters that affect the effective width of a CLT slab in a timber composite beam. A full-scale timber composite beam was tested experimentally, and a numerical model of the timber composite beam with actual geometric and material properties was developed to estimate the effective flange width. The accuracy of the proposed 3D numerical model of the timber composite beam was verified considering mid-span deflection, the effective flange width and the slip between the CLT panel and the LVL beam. The close agreement between the numerical results and the corresponding experimental tests confirmed that the numerical model is sufficiently accurate for determining the CLT effective flange width. The numerical model was then used to conduct a parametric analysis of the timber composite beams. The effective flange widths of various timber composite beams were extensively studied considering various arrangements, widths, thicknesses and modulus of elasticity values for the CLT boards. The effective flange width increased with any changes that increased the ratio of the transverse layer depth to the longitudinal layer depth. Moreover, using thicker longitudinal layers in similar thickness of the CLT slab decreases the effective flange width. Furthermore, stiffer transverse layers in CLT panels with a higher modulus of elasticity slightly improved the effective flange width. The maximum improvement in the effective flange width in timber composite beams was the result of using CLT panels with wider and thicker boards, with higher modulus of elasticity values, and with the maximum ratio of the transverse layer thickness to the longitudinal layer thickness. In addition, the results showed that an ideal layer arrangement in timber composite beams can notably increase the strength of the section and can significantly reduce the materials consumed and associated costs. Finally, a formula was proposed for predicting the effective flange width of timber composite beams and validated for a span varying between 6 m and 10 m, a Young's modulus between 6 GPa and 10 GPa and a plank width between 90 mm and 180 mm. In addition, the formula is only applicable when the transverse and longitudinal layers have the same material properties. Therefore, additional parametric studies are required to consider the effect of boards with different mechanical and geometrical properties.

Acknowledgments

The authors would like to thank the laboratory technicians, Mark Byrami and Andrew Virtue, for their contribution in preparing the test setup. Gratitude is extended to Prof. Hans Joachim Blass for providing ideas and support with ABAQUS.

References

Amadio, C., and Fragiacomo, M. (2002). “Effective width evaluation for steel-concrete composite beams.” J. Constr. Steel Res., 58(3), 373–388.

Aref, A. J., Chiewanichakorn, M., Chen, S. S., and Ahn, I. S. (2007). “Effective slab width definition for negative moment regions of composite bridges.” J. Bridge Eng., 10.1061/(ASCE)1084-0702(2007)12:3(339), 339–349.

Zou, B., Chen, A., Davalos, J. F., and Salim, H. A. (2011). “Evaluation of effective flange width by shear lag model for orthotropic FRP bridge decks.” Comp. Struct., 93(2), 474–482.

Castro, J. M., Elghazouli, A. Y., and Izzuddin, B. A. (2007). “Assessment of effective slab widths in composite beams.” J. Constr. Steel Res., 63(10), 1317–1327.

Salama, T., and Nassifb, H. (2011). "Effective flange width for composite steel beams." J. Eng. Res., 8(1), 28–43.

AISC. (2001). Manual of steel construction: Load and resistance factor design, American Institute of Steel Construction, Inc., Chicago, IL.

CSA (Canadian Standards Association). (2001). Limit state design of steel structures-CAN/CSA-S16-01, CSA, Rexdale, Ont., Canada.

DD ENV 1994-2:2001, Eurocode 4. (1994). Design of composite steel and concrete structures. Part 2: Composite bridges and Part 1.1, general rules and rules for buildings, British Standard Institution, London.

Porteous, J., and Kermani, A. (2013). Structural timber design to Eurocode 5, John Wiley & Sons, Chichester, UK.

Ozelton, E., and Baird, J. (2008). Timber designers' manual, C. L. Staples, London, UK.

Thiel, A., Brandner, R. (2016). "ULS design of CLT Elements-basics and some Special Topics", Proceeding of the joint conference of COST actions FP1402 & FP1404 KTH building materials.

Chen, S. S., Aref, A. J., Chiewanichakorn, M., and Ahn, I. S. (2007). "Proposed effective width criteria for composite bridge girders." J. Bridge Eng., 10.1061/(ASCE)1084-0702(2007)12:3(325), 325–338.

Chiewanichakorn, M., Aref, A. J., Chen, S. S., and Ahn, I. S. (2004). "Effective flange width definition for steel-concrete composite bridge girder." J. Struct. Eng., 10.1061/(ASCE)0733-9445(2004)130:12(2016), 2016–2031.

Davalos, J. F., and Salim, H. A. (1993). "Effective flange width for stress-laminated T-system timber bridges." J. Struct. Eng., 10.1061/(ASCE)0733-9445(1993)119:3(938), 938–953.

Adekola, A. O. (1968). "Effective widths of composite beams of steel and concrete." Struct. Eng., 46(9), 285–289.

Elkelish, M. S., and Robinson, H. (1986). "Longitudinal cracking of composite beams with ribbed metal deck." Can. J. Civ. Eng., 13(6), 733–740.

Timoshenko, S., and Gere, J. (2009). "Theory of elastic stability". Courier Dover Publications, Mineola, NY.

Nassif, H., Abu-Amra, T., and El-Tawil, S. (2005). "Effective flange width criteria for composite steel girder bridges." Proc., Transportation Research Board 84th Annual Meeting. Paper No. 05-2477.

Masoudnia, R. (2013). Stub girder flooring system for timber construction, Provisional Report, The University of Auckland, Auckland, New Zealand.

Masoudnia, R., Hashemi, A., and Quenneville, P. (2016). "Evaluation of effective flange width in the CLT composite T-beams." Proc., World Conf. on Timber Engineering, Vienna, Austria.

Masoudnia, R., Hashemi, A., and Quenneville, P. (2017). “Predicting the effective flange width of a CLT slab in timber composite beams.” Journal of Structural Engineering (Under Review).

Masoudnia, and Quenneville, P. (2017). “Improvements to timber composite beams.” Provisional patent number 731716.

Adekola, A. O. (1974). “The dependence of shear lag on partial interaction in composite beams.” Int. J. Solids Struct., 10(4), 389–400.

ACI (American Concrete Institute). (2002). “Building code requirements for reinforced concrete.” AISC, 318-02 2001, Manual of steel construction: Load and resistance factor design, American Institute of Steel Construction, Inc., Chicago, IL.

ABAQUS. (2014). Theory manual, version 6.13. Hibbitt, Karlsson & Sorensen, Inc., Pawtucket, RI.

Discussion

The paper was presented by P Quenneville

A Buchanan questioned if you try to develop a long span floor system for say a 9 m x 9m grid you would be strengthening the case in one direction and weakening it for the other direction. P Quenneville disagreed and provided an explanation.

K Crews stated this type of system would be limited by what one could transport. Furthermore secondary effects such as vibration would be more important.

S Aicher asked what was assumed when calculating the shear resistance of the lowest cross layer. If they were edge bonded this would be a different issue. P Quenneville stated that the model assumed elastic behaviour only and did not consider failures.

P Dietsch stated that rolling shear modulus would be important and asked what value was used and what would be the influence of the number of screws in terms of composite action. P Quenneville said that the rolling strength properties of the material were assumed and the influence of number of screws would be dealt with in a future paper.

S Winter asked what would be the practical implication of this model. P Quenneville responded that the effective width can be up to 2.5 m.

S. Winter and P Quenneville discussed the support conditions and shear lag effect at the end of the beam. H Blass commented that the laminae were not edge glued so one would have a low shear modulus within the plane and the cantilever action would also have shear deformation. They also discussed putting high transverse stiffness at the beginning of the span.

A Buchanan queried the possibility of putting the panel in the opposite direction. H Blass and P Quenneville agreed that this would not work because one would not have composite action.

Improved Design Equations for the Resultant Tensile Forces in Glulam Beams with Holes

Cristóbal Tapia Camú, Materials Testing Institute, University of Stuttgart

Simon Aicher, Materials Testing Institute, University of Stuttgart

Keywords: glulam, holes, reinforcement forces, design equations, Eurocode 5, parametric analysis

1 Introduction

The use of holes in beams made of glued laminated beams (glulam) is often necessary in constructions, as they are required for the passing-through of plumbing, electrical and other service relevant infrastructure systems. These apertures represent a significantly weak region in the beam, leading to noticeable decreases in maximum loading capacities. The failure mechanism is well known and is manifested by the propagation of cracks in the direction of the grain and beam length axis, starting from two zones with high tensile stresses perpendicular to the grain located diagonally opposite on the periphery of the hole.

The European Timber Design Code, EN 1995-1-1 (2010), hereby EC5, contains no provisions for either unreinforced or reinforced holes. The current version of the German National Annex to EC5 (2013) regulates external hole reinforcements by wood panels (plywood, LVL), as well as the usage of internal, glued-in rods or screws reinforcements to improve the mechanical response of the glulam/LVL in the region surrounding a given aperture. In order to correctly dimension them, design equations are provided to compute the acting forces, which can deviate significatnly from results obtained by means of finite element simulations (*Aicher*, 2011). This study aims at improved design equations for the tensile forces perpendicular to the grain at the periphery of holes for implementation in the future EC5 version.

Firstly, the paper compares the design forces obtained acc. to EC5/NA (2013) vs. the results of a FE model. Then, a modified set of design equations fitted to the numerical results is presented for holes of different shapes placed symmetrically at mid-depth. Further, the effect of vertical eccentricities of holes on the design force is investigated. Finally, the presented design equations are assessed with regard to an inhomogeneous build-up.

2 Design of holes in DIN EN 1995-1-1/NA

The present design of holes and hole reinforcements according to DIN EN 1995-1-1/NA (2013) is based on a fictive resultant tensile force, $F_{t,90}$, representing the integral of the stresses perpendicular to the grain in the hole periphery in the crack relevant sections. This force is composed of two additive parts: one, $F_{t,V}$, accounting for the shear force, which cannot be transferred in the hole area, and a second part, $F_{t,M}$, related to the bending moment present in the cross-section:

$$F_{t,90} = F_{t,V} + F_{t,M} \tag{1}$$

$$F_{t,V} = \frac{V \cdot h_d}{4 \cdot h}\left(3 - \frac{h_d^2}{h^2}\right) \tag{2}$$

$$F_{t,M} = 0.008 \cdot \frac{M}{h_r}. \tag{3}$$

The shear force part, $F_{t,V}$, conforms sensibly to half of the integral of the parabolically distributed shear stresses along the full hole depth (rectangular hole) or 0.7 times of the hole depth for the case of the round holes regarded here (*Blaß et al.*, 2004; *Aicher & Höfflin,* 2001). The moment related part, $F_{t,M}$, is in contrast rather diffuse and needs amendment, as has been discussed previously by *Aicher & Höfflin* (2001). The dimensional notations of (reinforced) holes according to DIN EN 1995-1-1/NA (2013) are shown in Fig. 1.

The vertical force acc. to Eq. (1) is used for the design of unreinforced and reinforced holes, where it is compared either against a fictive resulting resistance force based on the size-dependent tensile strength of the glulam perpendicular to the grain, or for the design of reinforcement elements (screws, rods, plates).

3 Methodology

3.1 Studied configurations

In this study a variety of holes of different sizes relative to the depth of a rectangular beam cross-section and shapes, all allowed acc. to DIN EN 1995-1-1/NA (2013), were simulated under two different loading situations: one comprising a hole placed in a pure bending moment region, denoted as configuration *A* (see Fig. 1a), and a second, general case, where the holes are subjected to both shear and moment, here referred to as configuration *B* (see Fig. 1b). For the latter, different ratios of moment to shear force (M/V) were analyzed at the periphery of the hole; this was achieved by varying the length of the distance l_A between 1.5 and 5 times the depth of the beam

h. The relative sizes of the apertures ranged from h_d/h = 0.1 to h_d/h = 0.4 in increments of 0.05. Regarding the shapes of the holes, round, square and rectangular (side aspect a:h_d = 2.5) openings were regarded. For the rectangular shapes a corner radius r = 20 mm was used throughout. In the first major part of the presented investigations the holes were placed at mid-depth of the glulam beam, whilst in the second part eccentricities were considered, as well.

The eccentricities used in the second part of the study were taken such that each hole would fulfill the current requirements in DIN EN 1995-1-1/NA (2013) where a minimum depth of 0.25h is specified for the reduced cross-sections (h_{ru} and h_{ro}, see Fig. 1) above and below the hole. For each hole depth, h_d, the maximum eccentricity e_{max} was computed and used to create models with ratios e/h ranging from -e_{max} to +e_{max} in steps of 0.05h.

A third part of the study was dedicated to the influence of the inhomogeneity of the build-up, which was studied for a particular, however practically very representative, case of a classified inhomogeneous GL24c build-up given in EN 14080 (2013) with a stiffness ratio E_{outer}/E_{inner} = 11 000/7 500 = 1.47. Regarding the assessment of the stiffness inhomogeneity, exclusively a square hole of depth h_d/h = 0.3 and eccentricities of e/h= ± 0.1 were simulated. The ratio l_A/h was chosen as 3.

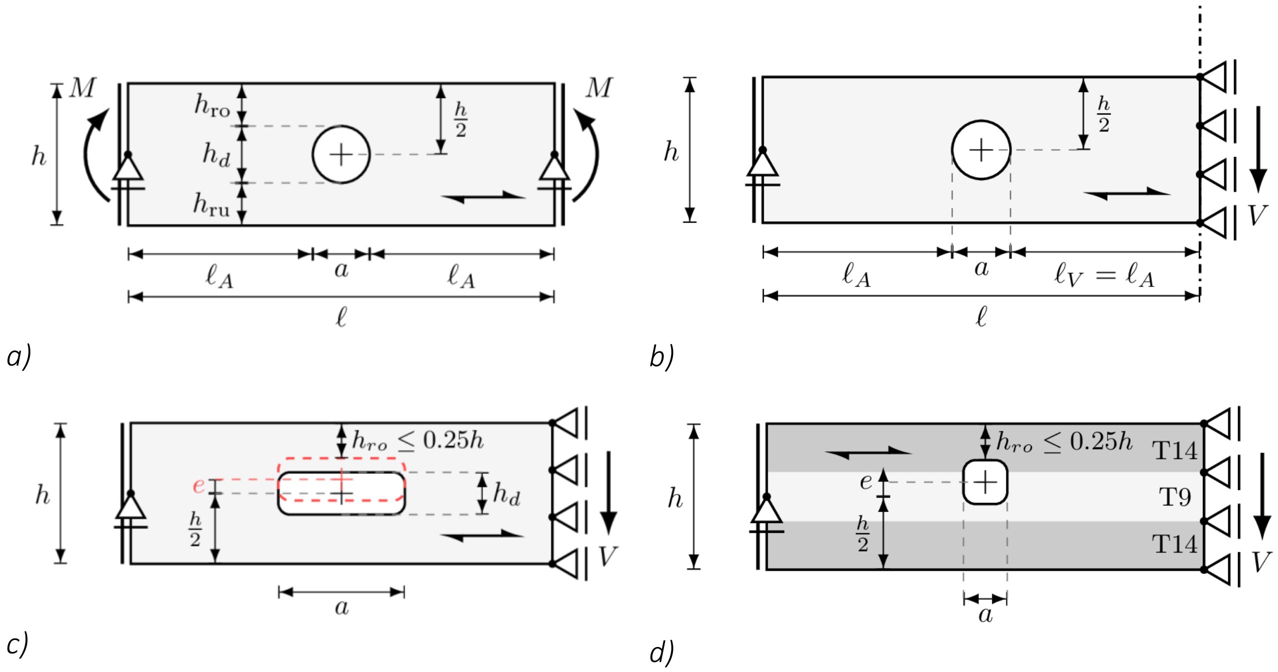

Figure 1: Hole arrangements (examples), geometry and section forces in the study. a) configuration A; b) configuration B; c) definition of eccentricity and minimum value $h_{ro/ru}$; d) positioning of rectangular hole in an inhomogeneous build-up.

3.2 Finite Element Model

A two-dimensional parametric FE-model was programmed in Abaqus V2016 using its python scripting interface. The mesh comprised eight-node, quadratic plain-stress elements with reduced integration (CPS8R) with a side size of approximately 1 mm directly at the perimeter of the hole, increasing up to 5 mm in the region influenced by the hole (≈*h* away from the perimeter) and reaching about 20 mm at the regions far away from the aperture. Note: the absolute depth of the beam in the FE-analysis, however irrelevant for all below stated results and conclusions, was h = 450 mm.

Under the assumption that the end sections remain plain during deformation, the free nodes at both vertical edges of the beams of configuration *A* were constrained to move as a rigid body. This was implemented by bonding the nodes at the free ends with two-dimensional rigid elements (R2D2) placed vertically at both ends of the beam, as symbolized by the thick black lines in Fig. 1a. In order to couple the movement of the rigid elements and of the associated beam nodes so-called "tight constraints" were applied. The bending moment was applied at mid-depth of the free ends at both sides.

Similarly, rigid elements were applied to the left end of the configuration *B*, whilst the nodes of the right end (symmetry condition) were restrained in the horizontal direction. The load *P* was applied as a line load at the right edge, in order to distribute the shear force along the entire depth.

The linear solver of Abaqus was used, taking care that no geometrical nonlinearities were considered in the computations, which allows for a better comparison with analytical equations that do not account for nonlinear effects.

3.3 Analysis of the obtained results

The analysis of the data focuses mainly on the computation of the forces perpendicular to the grain occurring in the vicinity of the hole. A direct method to do this is described by *Aicher & Höfflin* (2001), where the stresses perpendicular to the grain direction are integrated along a horizontal path starting from the point of maximum stresses perpendicular to the grain at the perimeter of the hole (ϑ_1 and ϑ_2) until their values reach zero (see Fig. 2).

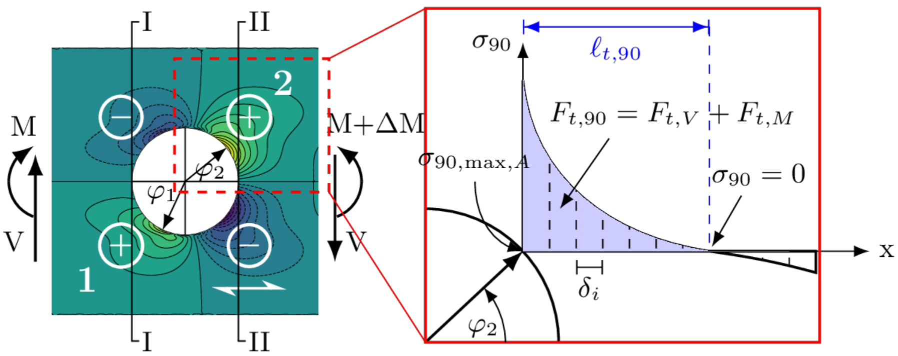

Figure 2: Description of the integration path used to compute the vertical force $F_{t,90}$

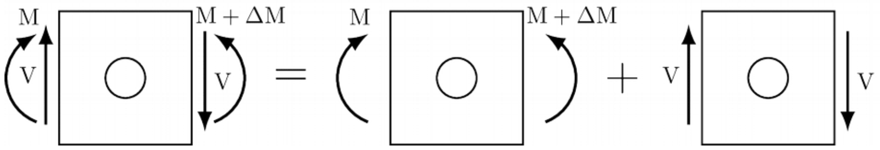

Figure 3: Separation of the regarded bending loading condition into a pure linearly varying moment and a pure constant shear-force component

This procedure can be applied at both sides of the hole (I and II) but generally only side II of Fig. 2 is considered, since it leads to the largest values for the computed vertical force $F_{t,90}$.

The current design approach for holes in the German Annex to EN 1995-1-1 (2013) consists in a decomposition of the total force $F_{t,90}$ in two components, attributed to a pure moment and a pure shear force contribution (see Eqs. (1) to (3)). In order to assess the accuracy of each one of the terms specified in Eq. (1) to (3) the problem is separated into its two parts, so that they can be analyzed independently. Unfortunately, this separation is not trivial, as mechanically trivial pure moment action is possible, however, constant or variable shear force is always associated with superimposed bending moment action (see Fig. 3).

The methodology used in this study to separate the pure moment and fictive pure shear force effect is based on the approach used by *Aicher & Höfflin* (2001), where the field of stresses perpendicular to the grain, resulting exclusively from the shear force component, is obtained by subtracting the results of the pure moment configuration from the general configuration where shear force and moment are present. This requires both meshes *A* (pure moment) and *B* (moment + shear) to perfectly match with each other, in order to allow the computation of the stress difference at each node.

However, the method, as implemented by *Aicher & Höfflin* (2001), still represents a small inaccuracy, emanating from the fact that the results from the pure bending moment configuration do not account for the variation of the moment along the hole length, ΔM, but uses a constant moment related to the center of the hole. Although the error resulting from this simplification is rather small, this study considers an improvement to accounts for the variation of the pure bending moment by means of a simple scale factor, individually calculated for the results at each node. In essence, for each node i of the pure bending moment model the obtained stresses are scaled by a factor μ_i, as shown in Fig. 4.

The factor μ_i takes into account the magnitude of the moment at each point in the configuration *B* (shear + moment) and scales the stresses obtained in configuration *A* (pure moment) accordingly, which can then be subtracted from the results of configuration *B* to obtain the influence of a "pure shear-force" loading configuration. The illustrations Fig. 5 show the results of this process for the case of a round hole with

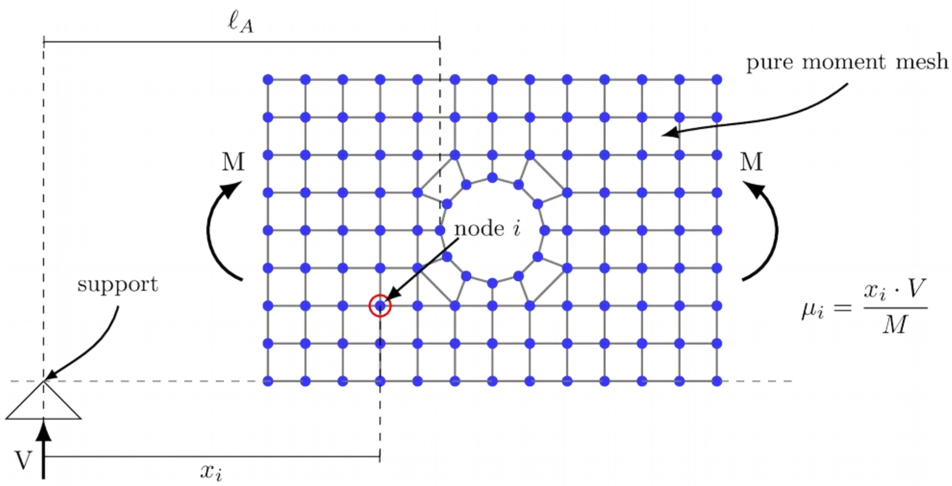

Figure 4: Graphical illustrationof the methodolgy used to scale the stresses perpendicular to the grain at each node of the mesh corresponding to the pure bending moment.

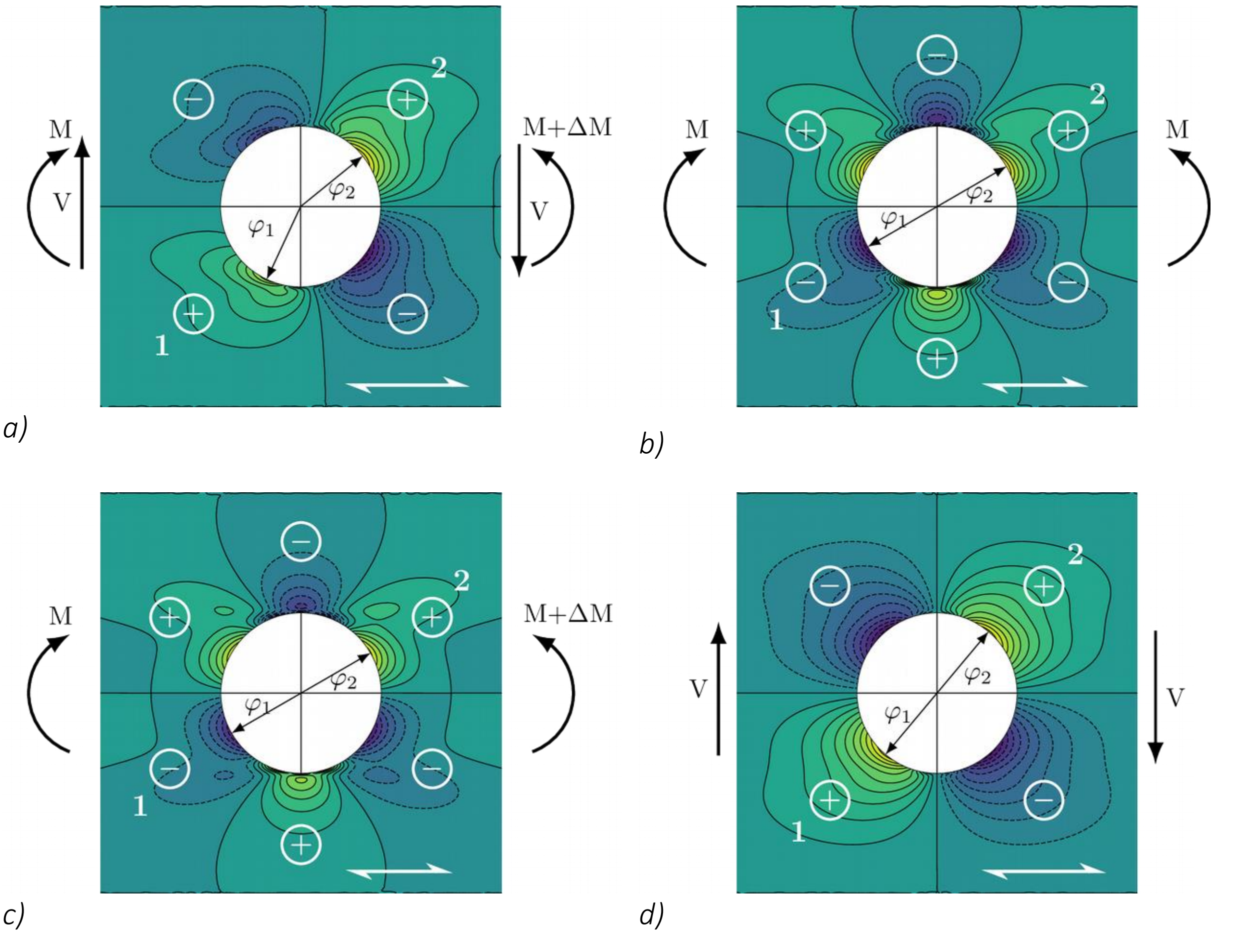

Figure 5: Distribution of stresses perpendicular to the grain and beam axis for different real and fictive load configurations. a) real load configuration with shear force and a linearly varying moment; b) real pure bending moment load configuration (moment at hole center); c) fictive pure linearly varying moment load configuration, obtained according to Fig. 4; d) fictive pure shear for loading configuration, obtained by subtracting (c) from (a).

ratio h_d/h = 0.3 and l_A/h = 5. Here, Fig. 5a shows a clear distortion of the stresses perpendicular to the grain due to the moment and shear action. Figs. 5b and c give the results for constant and linearly varying moment, and Fig. 5d presents the results for the pure shear case. In this way, each component of the vertical force $F_{t,90}$ can be integrated independently and later used to compare with the Eqs. (1) to (3) and calibrate new equations.

4 Results

4.1 Comparison between FE results and current design equations

In the first stage of the analysis the results obtained in the finite element simulations for the vertical force ($F_{t,90,FE}$) were compared with the forces $F_{t,90,eq}$ obtained from applying the NA standard Eqs. (1) to (3). This was done for all simulated configurations, as explained in section 3.1. Figures 6a, 6b and 7a show the ratio $F_{t,90,FE}/F_{t,90,eq}$, for all relevant hole size and shape configurations, revealing how conservative or non-conservative the standard equations are.

Fig. 6a shows the results for the round holes, where the values denote a rather conservative force prediction of Eqs. (1) to (3). It can be seen that for larger holes (h_d/h) the design equation gets less conservative, and even some values on the unsafe side are obtained for combinations of large holes and low *M/V* ratio.

It is important to mention that somewhat larger forces are obtained on the "left", i.e. closer to the support side as compared to the "right" side of the hole configurations (zones 1 and 2 of Fig. 2). Here, values up to 5% higher as the ones obtained with Eqs. (1) to (3) are found. This is mainly due to the fact that the point of maximum stress perpendicular to the grain is found at a larger angle ϑ as compared to the one observed on the side 2, thus, taking a larger portion of the shear stresses of the cross-section. However, since the focus in this study is placed on verifying the accuracy of Eq. (1), where both terms $F_{t,M}$ and $F_{t,V}$ are positive —whilst integration of the pure moment configuration in the zone 1 yields negative values—, a comparison with the vertical force computed at the zone 2 (see Fig. 2) seems more adequate in a first step. Furthermore, this behavior (larger vertical forces on the left side) is only observed for round holes, being due to the above described effect.

Fig. 6b shows the results for a quadratic hole, i.e. rectangular hole with a side aspect ratio a:h_d = 1:1. Similarly as for round holes, the ratios of FE-computations vs. code-predicted values lay on the conservative side for practically all the studied configurations. The most notable difference is the rather smaller variation of the ratios within a same hole size (h_d/h ratio), which in the case of round holes is larger.

Finally, Figs. 7a and 7b show the results obtained for the rectangular holes with side aspect ratio $a:h_d$ = 2.5:1 (the largest side aspect ratio allowed acc. to DIN EN 1995-1-1/NA (2013)). It can be seen, that the vertical forces calculated from Eqs. (1) to (3) tend to underestimate the FE results, especially for larger holes with low M/V ratio.

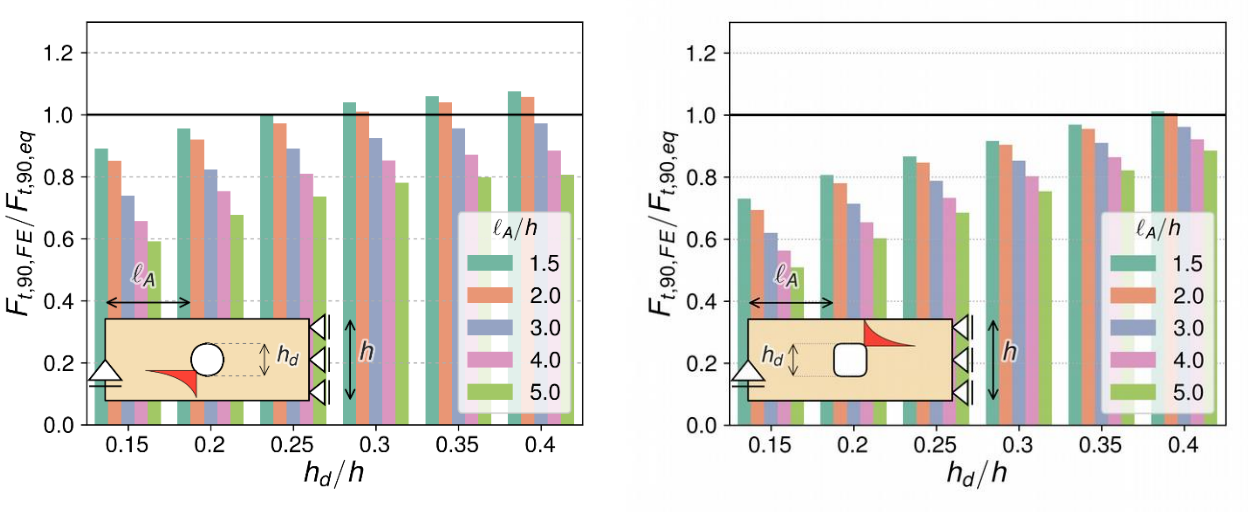

a) b)

Figure 6: Relation of forces $F_{t,90,FE}$ acc. to finite element analysis vs. the NA results $F_{t,90,eq}$ (Eqs. (1) to (3)); a) round hole (left side of the hole); b) quadratic hole (right side of the hole)

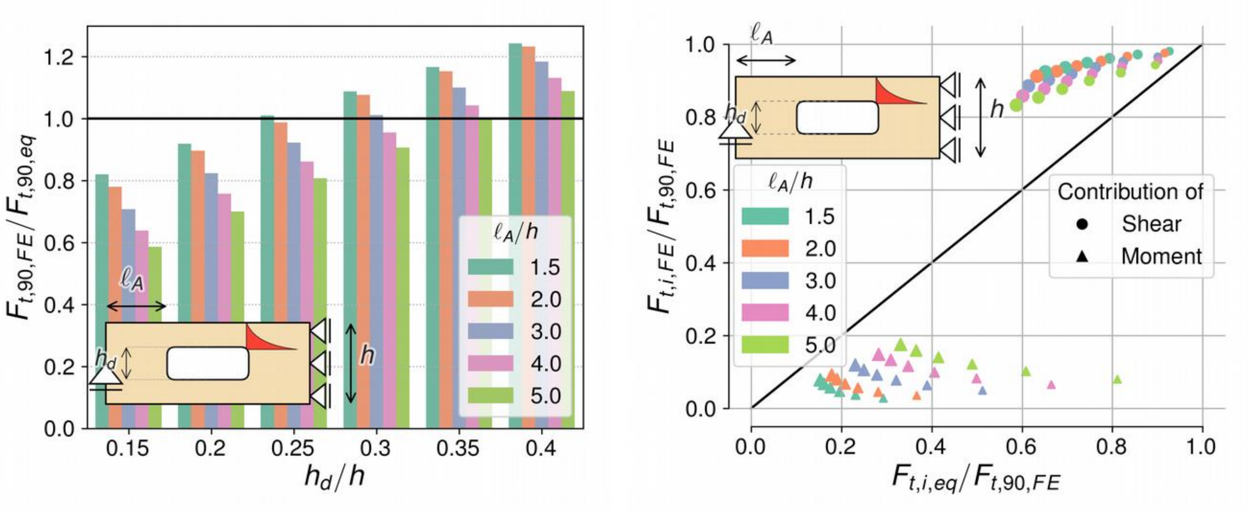

a) b)

Figure 7: Relation of forces $F_{t,90,FE}$ acc. to finite element analysis vs. the NA results $F_{t,90,eq}$ (Eqs. (1) to (3)); a) rectangular hole (right side of the hole); b) Independent analysis of moment and shear components

Fig. 9b gives further insight into how each of the two components of the total vertical force relate when calculated with either Eqs. (1) to (3) or by FEM, then normalized by the total vertical force $F_{t,90}$ computed with the FE model. Values above the line with unitary slope in Fig. 9b mean that the results obtained with the design equations are smaller with respect to the "real" (FE-computed) values, i.e. the design is non-conservative. On the other hand, values below the line suggest conservative design forces.

It can be observed, that the moment component tends to be conservative or extremely conservative, depending on the size of the hole, while the vertical shear component is predicted in an unsafe manner by Eq. (2). This is why the total force computed acc. to Eq. (1) shows non-conservative results for small ratios *M/V* but conservative values once the moment component turns more relevant.

4.2 Derivation of improved design equations

4.2.1 Modifications for the shear force component

Regarding the equation related to the computation of the shear force related component, the approach used is basically the same as the one applied to derive the current design equation (Eq. (1)), with the addition of an extra multiplication term. This yields the relation

$$F_{t,V} = \frac{\xi V h_d}{4h} \cdot \left(3 - \left(\frac{\xi h_d}{h}\right)^2\right) \cdot \left(1 + \alpha \left(\frac{\xi h_d}{h}\right)\right), \tag{4}$$

where V is the shear force present at the analyzed side of the hole, h and h_d are depth of the beam and of the hole, respectively. The coefficients α and ξ are factors that need to be fitted to the results from the simulations.

4.2.2 Modifications for the bending moment component

The modification proposed to capture the influence of the bending moment on the total force $F_{t,90}$ is based on the solution given by *Aicher & Höfflin* (2001) for round holes. Hereby the bending stresses are integrated over half of the depth of the hole, since these are the stresses that need to be redirected in the region of the hole (the first two products terms in Eq. (5)). In order to take into account the effects produced by the different geometries, the result of the integration is then multiplied by a third term:

$$F_{t,M} = \frac{\eta M}{h} \cdot \left(\frac{\xi h_d}{h}\right)^2 \cdot \left(1 + \kappa \frac{\xi h_d}{h}\right) \tag{5}$$

In Eq. (5), M, as usual, represents the bending moment at the analyzed side of the hole. The coefficients η and κ factors are determined from fitting to the results from the simulations; whereby coefficient ξ has been obtained within the phase of parameter determination of Eq. (4).

4.3 Fitting of proposed equations

The fitting process of the coefficients α, ξ, η and κ for the proposed design equations was performed in two consecutive steps for each one of the three different hole geometries studied. For this, the least-squares algorithm was used, where, in detail, the sum of all the differences between the simulated forces $F_{t,i,FE}$ and the forces $F_{t,i,eq}$ obtained with Eqs. (4) and (5) was minimized as

$$\min \sum \left(F_{t,i,eq} - F_{t,i,FE}\right)^2 \qquad \text{,for } i = V, M. \tag{6}$$

The values $F_{t,i,FE}$ were calculated at an angle ϑ = 50° for the round holes, while for the rectangular shapes a slightly different angle ϑ = 45° was used. The forces integrated on the basis of these angles were proven to give always equal or higher values than the ones computed at the angle where the maximum stress perpendicular to the grain is found, thus assuring that the fitted equations predict the maximum force analyzed.

Interestingly, the coefficient η evolved equally as 0.1 for any of the regarded geometries. This means that η = 0.1 can be included directly in Eq. (5) for simplification. Similarly, the values for the factors ξ are very close to each other and it is well perceivable within the frame of a simplification to use the largest value ξ = 0.86 for all the cases.

Table 1: Fitted parameters for each geometry studied to be used in the Eqs. (4) and (5) accordingly

shape	ξ	α	η	κ
○	0.81	0.43	0.1	0.40
□	0.84	1.1	0.1	0.16
▭	0.86	1.9	0.1	0.33

On the other side, it can be clearly seen, that the coefficient that captures most of the differences between geometries is the factor α, where a great variation can be observed. Further, in case of not negligible moment contributions the coefficient κ becomes more decisively in accounting for geometry-caused differences.

In the first step, the shear force component $F_{t,V}$ was analyzed, a process through which the coefficients ξ and α were obtained. After this, the moment component $F_{t,M}$ of the vertical force was fitted, whereby the coefficient ξ, obtained in the $F_{t,V}$-determination-step, was used to compute the factors η and κ. Table 1 shows the coefficients found for each studied configurations. The results of this process can be seen in Figs. 8 to 9, where the total forces $F_{t,90}$ are calculated with the modified equations and compared with the forces integrated at the angle of maximum stress at the perimeter, $\vartheta_{max,}$ (see Fig. 2).

The goodness of the fit throughout the entirety of the configurations becomes even more evident, when comparing the results to those obtained with the existing equations (1–3). This is even truer for the below discussed rectangular shape with a high aspect ratio.

Fig. 8a shows the comparison for the round holes, where slightly conservative values are obtained for the forces at the bending tension region closer to the support (zone 1, see Fig. 2). The solution tends to get progressively more conservative, which is due to the fact that Fig. 8a analyses the force $F_{t,90}$ at the zone 2, where the moment component $F_{t,M}$ has a negative value, hence rendering the total force smaller as *M/V* increase. The solutions on the upper side (zone 2, see Fig. 2) (not presented here) lay on the safe side and looks analogous to the solution for quadratic holes in Fig. 8b, but

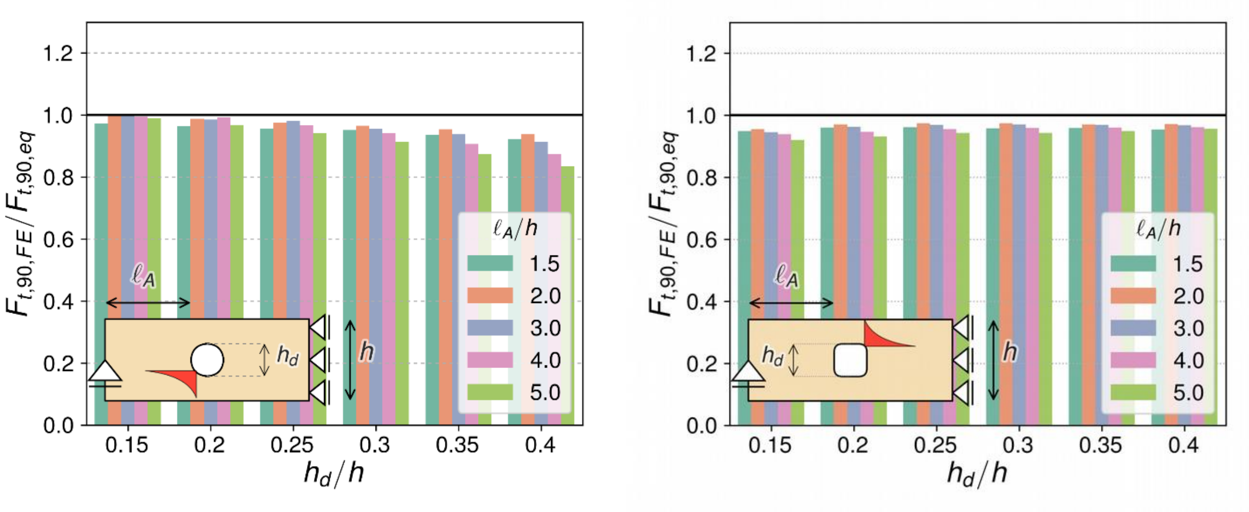

a) b)

Figure 8: comparison between forces $F_{t,90}$ computed with fitted Eqs. (4) and (5) and the ones obtained with the finite element model

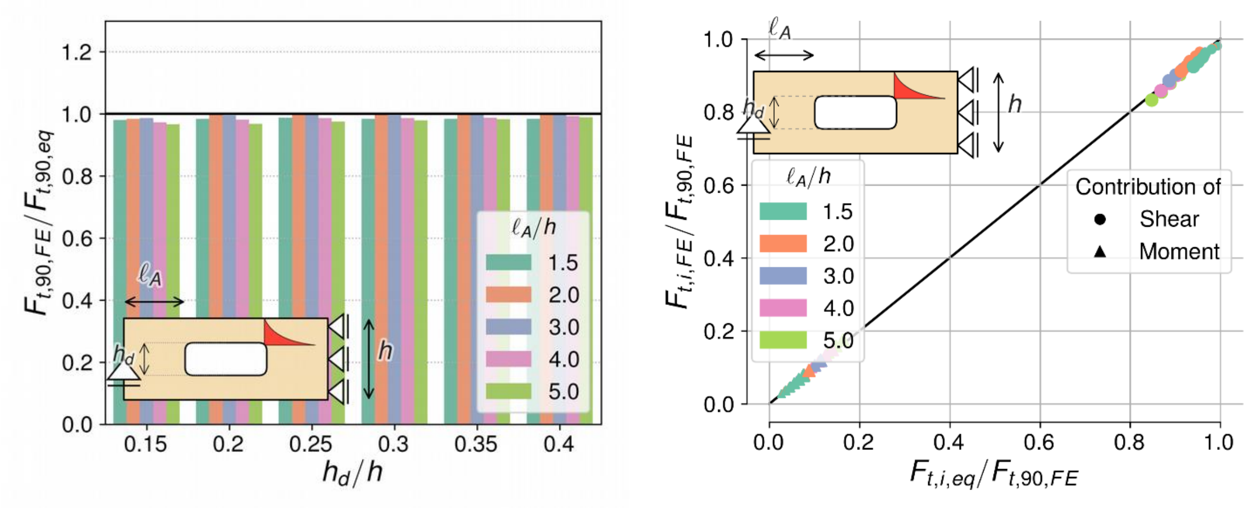

a) b)

Figure 9: comparison between forces $F_{t,90}$ computed with fitted Eqs. (4) and (5) and the ones obtained with the finite element model

slightly more conservative, which is bound to the fact that an angle ϑ = 50° was used to fit the results, which for this case returns rather conservative values in comparison with the ones computed at ϑ_{max}.

Fig. 8b shows the $F_{t,90,FE}/F_{t,90,eq}$-results for the rectangular holes with a side aspect ratio a:h_d=1:1. The fitted results lay slightly below the unity line throughout all the relevant hole and load configurations h_d/h and l_A/h = M/V. In both cases of round and rectangular holes a very small tendency to get higher forces with the modified equations is observed when the ratio M/V increases. This renders the solution be more conservative, but the accuracy is still by far better than it is with the Eq. (1) to (3) (see Figs. 6 and 7).

For the large rectangular holes with a side aspect ratio $a:h_d$ = 2.5:1 depicted in Fig. 9a actually the best agreement of throughout almost unity between the FE-computed forces and the new design equations is obtained. Similarly as for the other two cases the values lay slightly below the unity line. In addition, Fig. 9b reveals that each of the components $F_{t,V}$ and $F_{t,M}$ of the total force $F_{t,90}$ coincide almost exactly with the FE simulations.

It is further interesting to note that the derived coefficients comply well with the solutions for the moment contribution $F_{t,M}$ given by *Aicher & Höfflin* (2001) for round holes via a different evaluation approach. In the cited literature $F_{t,M}$ is given by

$$F_{t,M} = 0.084 \cdot \frac{M}{h} \cdot \left(\frac{h_d}{h}\right)^2. \tag{7}$$

Evaluating the first two terms of the new equation and their derived coefficients one obtains

$$F_{t,M} = 0.07 \cdot \frac{M}{h} \cdot \left(\frac{h_d}{h}\right)^2. \tag{8}$$

and the third term ($1 + \kappa\xi\, h_d/h$) results for hole sizes of h_d/h = 0.2,…,0.4 in 1.07 to 1.13, i.e. roughly 1.1. This results in a total factor of roughly 0.077, being very close to the former studies.

For the case of rectangular holes, it should be stated that the presented coefficients and hereby the very good approximation of the FE-results are bound to the employed corner radius. In case of larger corner radii the derived coefficients will deliver conservative results, as long as the corner radius used complies with the relation $r_{corn}/h \geq 20/450 \approx 0.044$. In any case, corner radii ≤ 20 mm should not be used, as the magnitude of the stress concentration increases exponentially and premature crack formation at low loads becomes more likely.

4.4 Effect of hole eccentricity

Although a mid-depth placement of holes is most desirable, in many cases an eccentricity has to be introduced, i.a. due to fixed positions of sewage, heating and ventilation pipes. The offset from mid-depth leads to slightly different stress distributions around the holes, which in turn affects the value of the force $F_{t,90}$. The adjective "slightly" refers, however, exclusively to holes which are not placed too close to the beam edges. The eccentricity e, or its normalized value e/h, is defined as the (relative) shift of the hole center vs. mid-depth, whereby e is counted positively when the hole is shifted towards the bending compression edge. The maximum shift regarded in this investigation is restricted, so that the remaining beam depths above and below the hole are minimally 0.25h, what conforms to the present provisions in DIN EN 1995-1-1/NA (2013).

In this section the effect of an eccentricity of the hole, as described in section 2.1, is studied, whereby the equations calibrated in the previous section are used.

Fig. 10 presents the results obtained for the vertical forces of round holes at sections I (closer to the support) and II (farther from the support, see Fig. 2) for eccentricity ratios in the range of *e/h* = ± 0.15. Although no special consideration regarding the eccentricity is made in the Eqs. (4) and (5), the Figs. 10a and 10b reveal that the vertical forces are still captured very well and almost throughout in a conservative/safe manner. Nevertheless, a positive eccentricity (hole towards the compression bending edge) produces the worst case in terms of an increase of the force $F_{t,90}$, whereby an increase of up to 12% is observed for *e/h* = 0.1 at the section I of the hole, closer to the support. Starting from this point, and dependent on the hole size, the vertical force diminishes.

This behavior matches the experimental findings for unreinforced round holes shown by *Danzer et al.* (2016), in the sense that the lowest ultimate loads observed correspond to holes with an eccentricity *e/h* = 0.1. This agrees with the observation of the maximum tensile forces, $F_{t,90}$, being numerically found at the same eccentricity *e/h* = 0.1. *Ardalany et al.* (2012) showed similar results regarding the ultimate loads of eccentrically placed holes.

A similar behavior is observed for rectangular holes with a side aspect ratio $a{:}h_d$ = 1:1, shown in Fig. 11. Again, the peak value for the vertical force is located around *e/h* = 0.1 whereby the proposed equations forward results about 10% lower as obtained with the FE model. But again, the overall behavior of the modified equations is still fairly good.

The results for the rectangular holes with a side aspect of $a{:}h_d$ = 2.5:1, not presented graphically, are similar to the ones shown for the other geometries, whereby the error observed on *e/h* = 0.1 now is about 20%, when compared to the numerical solutions. Furthermore, similar as observed in Fig. 11b, a peak of the force $F_{t,90}$ is observed for *e/h* = -0.05, here resulting in an error of 8%.

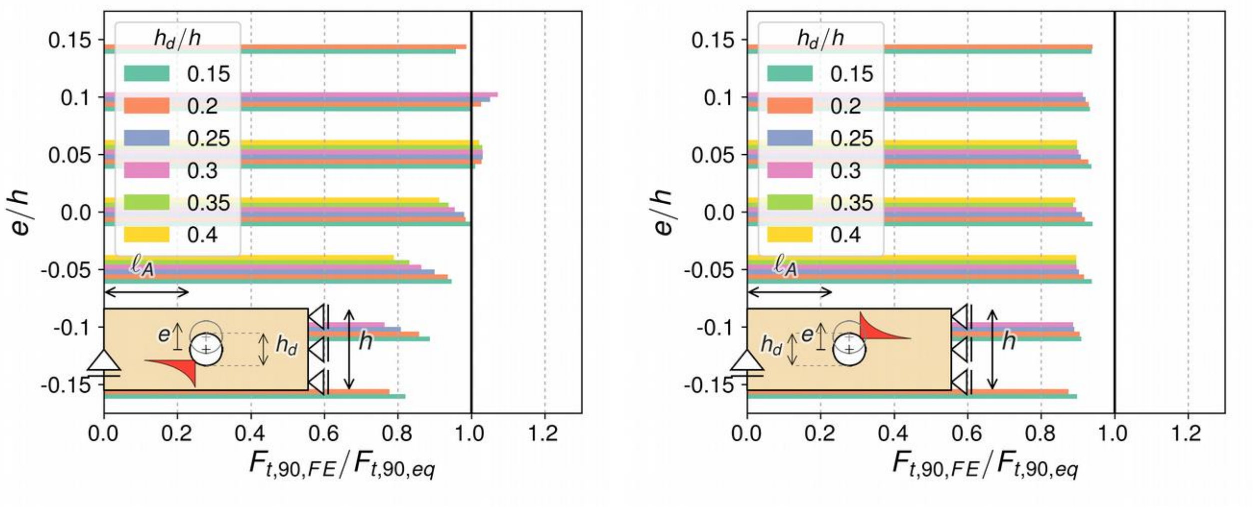

a) *b)*

Figure 10: Ratio of FE-computed forces $F_{t,90}$ vs. new design Eqs. (4) and (5) for different hole sizes and eccentricities of round holes

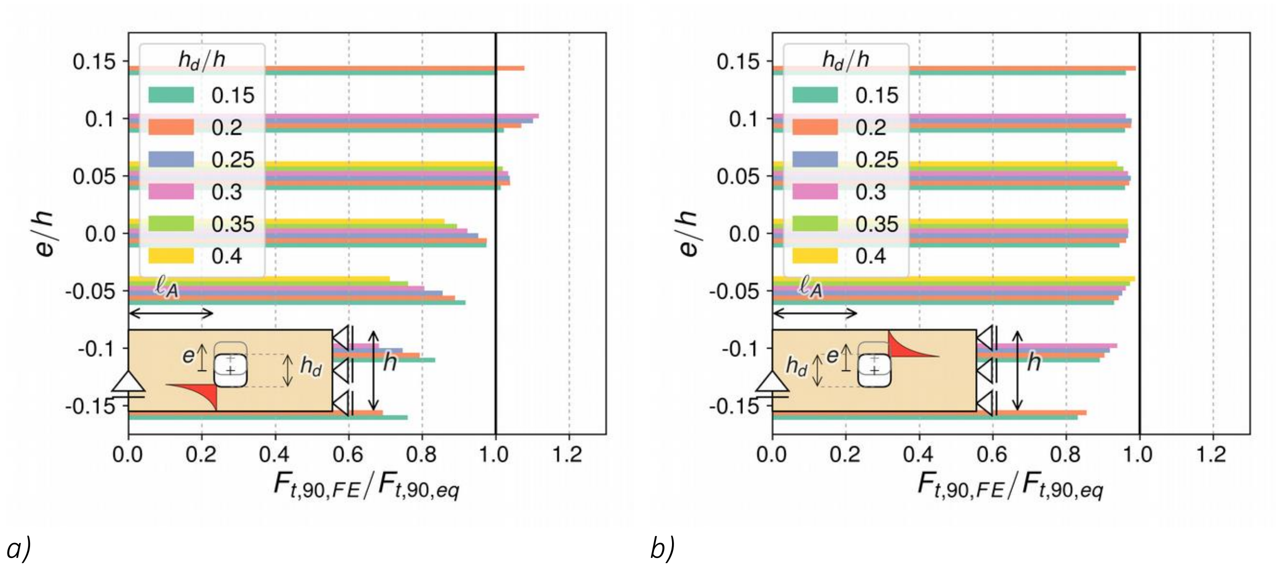

Figure 11: Ratio of FE-computed forces $F_{t,90}$ vs. new design Eqs. (4) and (5) for different hole sizes and eccentricities of quadratic holes

In the context of this paper no further eccentricity-adapted equations were derived. Nevertheless, with the existing equations derived for holes placed at mid-depth, in general, a rather good agreement of the force $F_{t,90}$ is possible

4.5 Effect of inhomogeneously build-up glulam beams

In all above presented results and their underlying Finite Element computations a homogeneous build-up of the beams, together with an equal orthotropic constitutive law, has been assumed for the plane-stress analysis. However, in most cases glulam beams are built-up inhomogeneously with stiffer and hence, stronger laminations in the outer parts as compared to the inner part of the beam depth. Although the effect of an inhomogeneous build-up was considered not having too much influence, a computational verification has been performed with an inhomogeneous build-up of rather strongly differing moduli of elasticity parallel to the grain.

In detail, the simulations were performed for the constitutive ratios present in a specific classified GL24c build-up, given in Table 2 of EN 14080 (2013), where both outer thirds of the cross-sectional depth consist of T14 laminations ($E_{t,0,l,mean,T14}$ = 11 000 N/mm^2), whereas the inner third is composed of T9 laminations ($E_{t,0,l,mean,T9}$ = 7 500 N/mm^2). As a consequence, the ratio of both MOE's is 1.47, being rather significant. The same stiffness ratio was used for the modulus of elasticity perpendicular to the grain (EN 338 (2016): $E_{t,90,l,mean,T14}/E_{t,90,l,mean,T9}$ = 370/250 = 1.48).

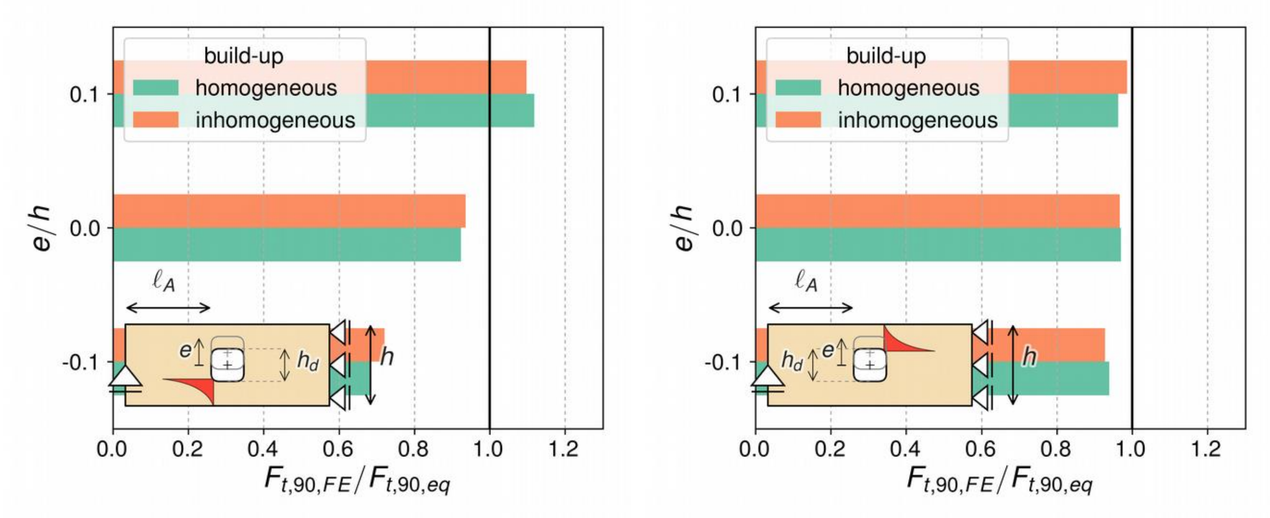

a) b)

Figure 12: comparison between forces $F_{t,90}$ computed with fitted Eqs. (4) and (5) and the ones obtained with the finite element model for different eccentricities in inhomogeneous build-ups

In order to assess the effect of the inhomogeneous build-up on stresses and forces $F_{t,90}$ perpendicular to the grain two eccentric hole positions e/h = ± 0.1 were analyzed in comparison with a similar-shaped and sized hole placed at mid-depth.

The results of the ratios of the FE-analysis vs. the solutions of the new design equations, derived for homogeneous build-ups, are presented in Figs. 12a,b.

It can be seen that the difference of the integrated forces perpendicular to the grain and their throughout very good approximations by the new design equations are affected only marginally by the inhomogeneous build-up. Hereby it is further rather unimportant whether the hole corners are in the lesser stiff or in the stiffer glulam cross-section part. Marginally higher forces as compared to the homogeneous FE simulations and the derived new design equations are obtained in sections I and II when the hole is moved towards negative and positive eccentricities, respectively.

5 Conclusions

The design of holes in glulam beams, and hereby of the forces perpendicular to the grain, especially needed for dimensioning and detailing of reinforcements is given world-wide in just a few codes, including a major contribution in the German National Annex NA to Eurocode 5 (EC5). The latter solutions are rather conservative for round and quadratic holes, but are partially on the unsafe side in case of larger rectangular holes.

The paper presents new analytical design equations with the same format for round and rectangular holes, which enable a significantly improved prediction of the hole (reinforcement) design-relevant force perpendicular to the grain. The equation format is based, where possible on the existing NA provisions extended by a few coefficients calibrated with extensive finite element parameter studies.

The present pronouncedly incorrectly specified force contribution by the bending moment in the NA document inevitably needs to be changed. As derivation of the new equations is essentially based on the FE analysis of holes placed at mid-depth of homogeneously built-up glulam beams, the effect of hole eccentricities and of inhomogeneous beam build-ups has been checked exemplarily. It was found that the basic design equations apply well within the addressed realistic construction boundaries and eccentricities, as well as to inhomogeneous build-ups and, hence, are proposed for implementation in the new Eurocode 5.

6 References

Aicher, S. (2011): Glulam Beams with Internally and Externally Reinforced Holes - Test Detailing and Design. In: International Council For Research And Innovation In Building And Construction, Working Commission W18 - Timber Structures, Alghero, Italy.

Aicher, S. & Höfflin, L. (2001): Round holes in glulam members. Part 1: Analysis (in German), Bautechnik 78 :706-715.

Ardalany, M.; Fragiacomo, M.; Deam, B. & Carradine, D. (2012): Effect of Hole Location on the Load-Carrying Capacity of Laminated Veneer Lumber Beams, Australian Journal of Structural Engineering 13 :231-242.

Blaß, H.J., Ehlbeck, J., Kreuzinger, H. & Steck, G. (2004): Erläuterungen zu DIN 1052: 2004-08, Entwurf, Berechnung und Bemessung von Holzbauwerken, Deutsche Gesellschaft für Holzforschung, München

Danzer, M., Dietsch, P. & Winter, S. (2016): Reinforcement of round holes in glulam beams arranged eccentrically or in groups. In: CD-ROM Proceedings of the World Conference on Timber Engineering (WCTE 2016).

Eurocode 5 (2010): Design of timber structures - Part 1-1: General - Common rules and rules for buildings. CEN. (EN 1995-1-1).

EN 14080 (2013): Timber structures – Glued laminated timber and glued solid timber – Requirements; CEN.

EN 338 (2016): Structural timber – Strengths classes, CEN

German National Annex to EC5 (2013): German National Annex – Nationally determined parameters – Eurocode 5: Design of timber structures – Part 1-1: General – Common rules and rules for buildings, DIN. (DIN EN 1995-1-1/NA)

Discussion

The paper was presented by C Tapia Camú

S Winter received clarification of the meaning of conservative results in this paper.

P Dietsch commented about the eccentricity creating shear and moments. He questioned about be the influence of moving the hole along the length of the beam towards the middle. Also the recommendation of corner radius seemed to require a large diameter drill which would be impractical.

F Lam asked about the case of interaction between tensile perpendicular to grain stress and shear stress. C Tapia said that this was not considered as the aim was to get a more accurate equation for estimating tensile perpendicular to grain stress.

H Danielsson asked if the inclusion of normal forces were considered as well. C Tapia denied.

R Jockwer asked about the influence of stressed volume on reduction of strength. C Tapia said that the equation allowed calculation of internal forces needed for reinforcement. Size effect on strength exists but was not under consideration. S Aicher added the work aimed to quantify the forces needed for reinforcement calculations. Material properties were separate issues.

Round holes in glulam beams arranged eccentrically or in groups

Martin Danzer, Philipp Dietsch and Stefan Winter

Chair of Timber Structures and Building Construction

Technical University of Munich

Keywords: timber, glulam beams, holes, holes arranged eccentrically, groups of holes, reinforcement

1 Introduction

The current edition of the European Timber Design Code EN 1995-1-1 (2004) does not contain design provisions for holes in beams. The German National Annex DIN EN 1995-1-1/NA (2013) provides such design and construction rules, which are, however, restrictive with regard to the positioning of holes in the beam. Experimental investigations in the form of small- and large-scale tests and numerical investigations on round holes in glulam beams were realized considering the unreinforced as well as the reinforced state in the form of fully threaded screws and threaded rods. The objective was to generate an experimental basis for deriving a design format and to study the general structural behaviour as well as the influence of parameters like eccentricity over the beam height, clear distance between two holes and effect of reinforcement.

2 Experimental investigations

Basis of the experimental investigations were two test series in the form of small-scale tests ($b \times h$ = 120 mm x 400 mm) and large-scale tests ($b \times h$ = 200 mm x 1000 mm).

2.1 Test program

In Figure 1 the main configurations of the small-scale tests are shown. With respect to eccentric arrangements of individual holes the location was varied in four steps (e/h = ±0.175; ±0.100), regarding groups of holes arranged in horizontal direction the clear distance was varied in three steps (l_z = 1.05h; 0.70h; 0.35h). To enable a comparison between the aforementioned configurations a consistent hole diameter d/h = 0.35 was chosen. Groups of holes arranged in vertical direction were tested in only one configuration with a smaller hole diameter d/h = 0.25 due to fewer possibilities in variation given by the geometry. The configuration for comparative tests on individual holes is not shown separately in Figure 1. For these tests, only two new specimens were available. All other configurations consisted of three specimens. The material used was glulam GL 28h. For the reinforced specimens two fully threaded screws d = 10mm arranged over the beam width were used. The inclination between screw axis and fibre direction was set to α = 60° in most cases, except α = 90° in case of the vertical group. For further information see Danzer et al. (2017).

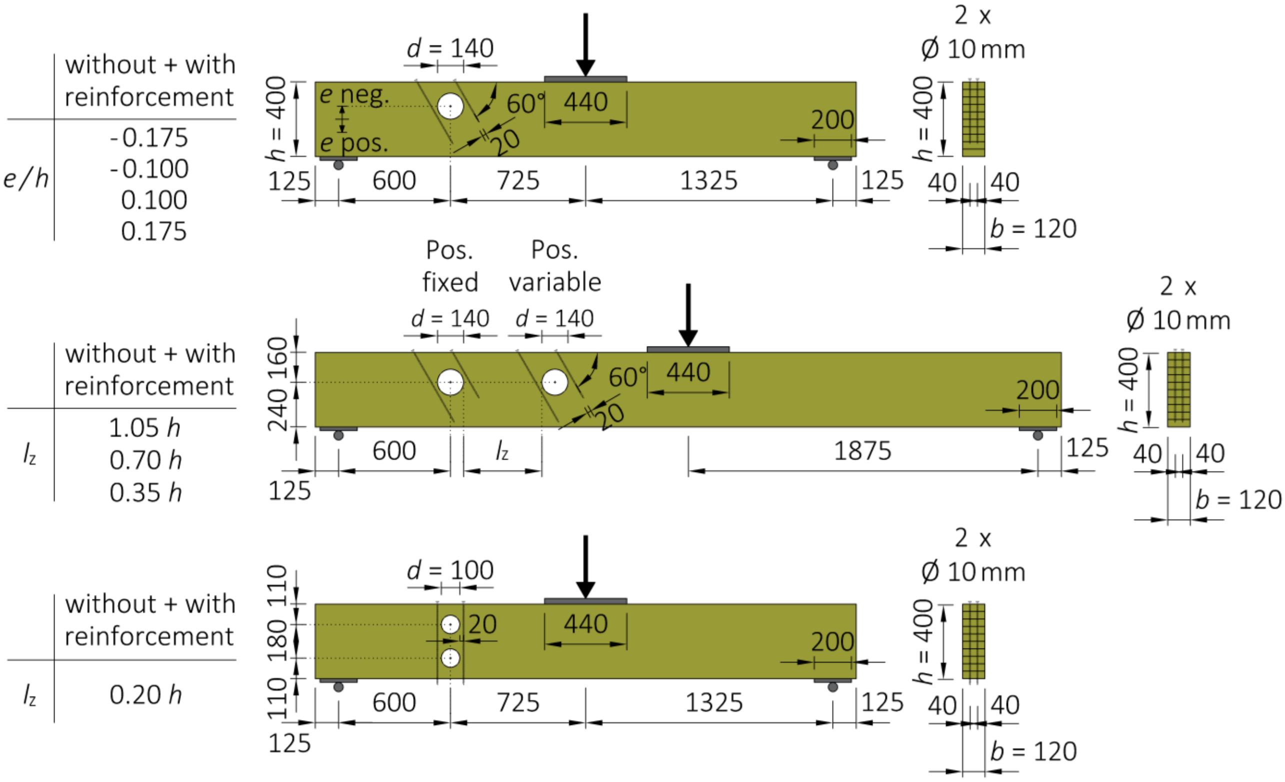

Figure 1: Configurations of the small-scale tests

In the large-scale tests two configurations of individual holes arranged eccentrically (e/h = ±0.175), one configuration of a horizontal group (l_z = 0.35h) and one configuration of a vertical group (l_z = 0.20h) were tested, see Figure 2. All configurations were reinforced by two screwed-in threaded rods d = 16mm arranged over the beam width. Based on results of numerical investigations the inclination of the reinforcing elements in the configurations *individual hole (e/h = 0.175)* and *vertical group* was adapted to α = 45°. In addition, two configurations of individual holes (d/h = 0.40; e/h = ±0.100) were tested without reinforcement under pure bending moment. Each configuration consisted of four specimens. Two out of the four specimens corresponded to strength class GL 24h and two corresponded to strength class GL 28h, respectively.

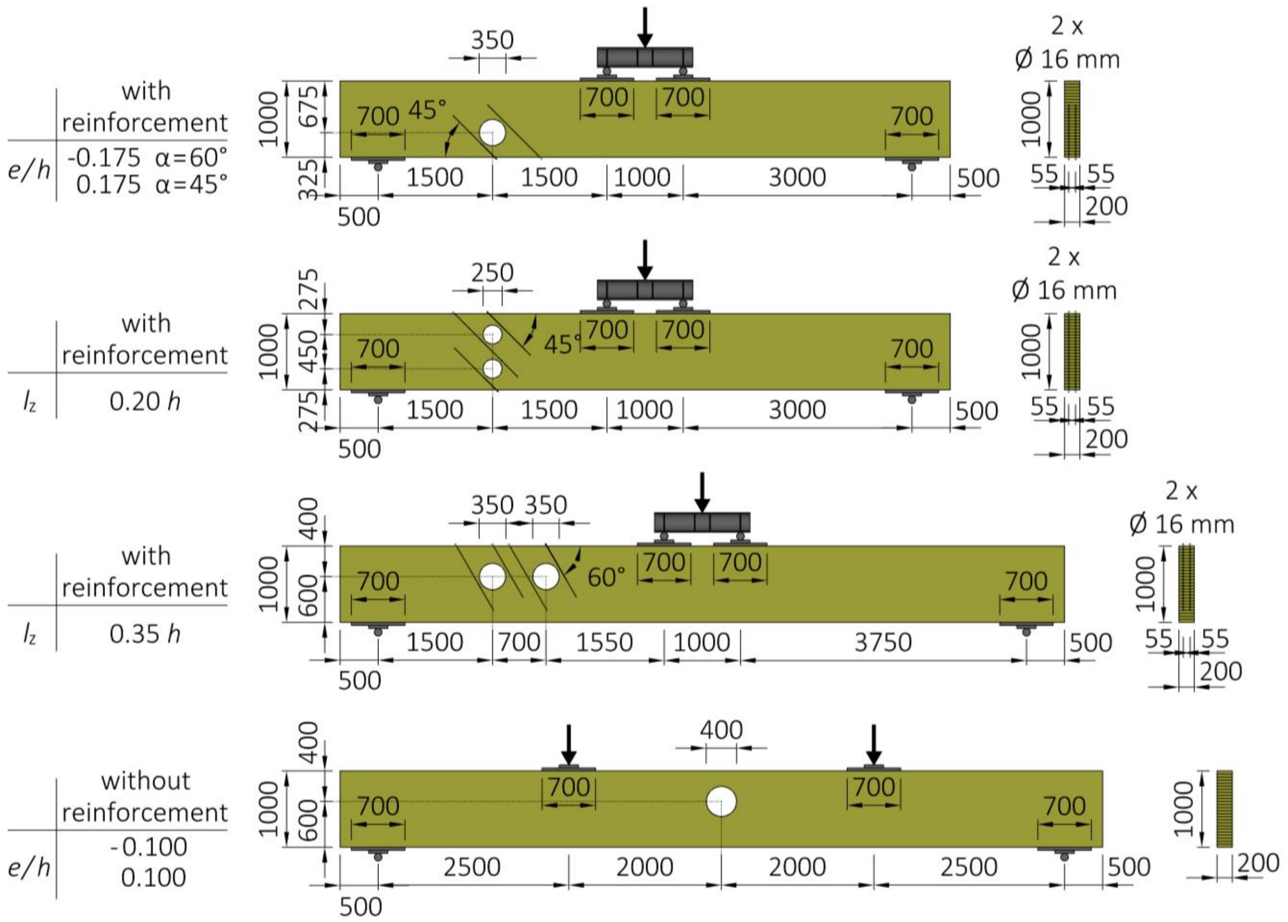

Figure 2: Configurations of the large-scale tests

2.2 Results

Due to the failure characteristics the tests results given in the following were differentiated according to the three steps *crack initiation in the middle of the cross sectional width*, *full crack over the whole beam width* and *ultimate load*.

- Individual holes arranged eccentrically (d/h = 0.35)

In case of the small-scale tests in the unreinforced state only a marginal influence of the eccentricity can be stated for all three levels of failure, see Figure 3. In the reinforced state the influence of the eccentricity at the load levels *full crack* and *ultimate load* was more pronounced in the form of decreasing load-bearing capacities when grouping the eccentricity from the edge under compressive bending stresses to the edge under tensile bending stresses. In comparison to the unreinforced state load increases of up to 98% could be observed, depending on the eccentricity.

In the large-scale tests a similar structural behaviour when compared to the small-scale tests could be observed. Comparing the ratios of the ultimate loads reached for the two extreme eccentricities in both test series reveals a marginally higher value in case of the large-scale tests (0.77 instead of 0.72). This means that the adapted inclination of reinforcement (α = 45°) resulted in a slightly better performance.

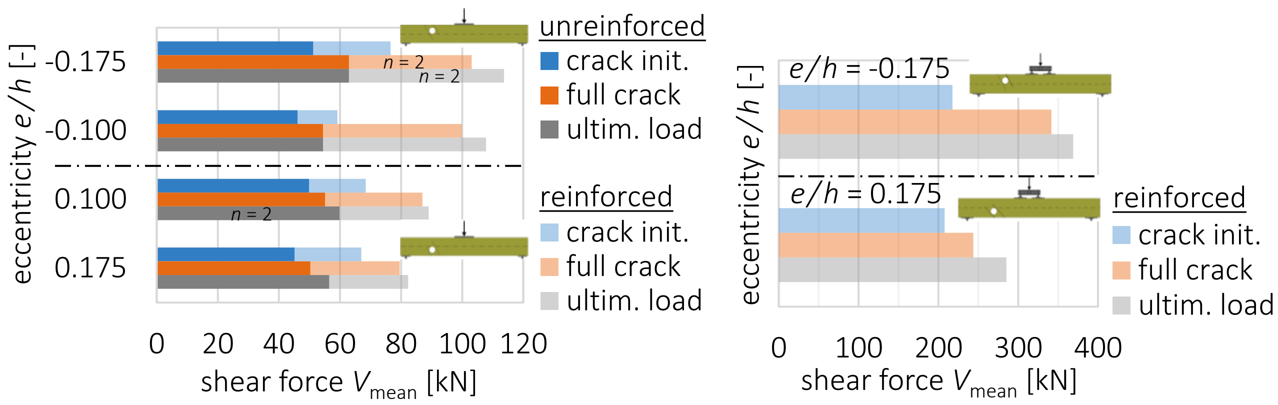

Figure 3: Test results for individual holes arranged eccentrically (d/h = 0.35); left: small-scale tests; right: large-scale tests

- Groups of holes arranged in horizontal direction (d/h = 0.35)

In case of the small-scale tests in the unreinforced state a decreasing clear distance resulted in decreasing load-bearing capacities to a minimum level of about 73% in case of the smallest clear distance, see Figure 4. The group arrangement with the largest clear distance failed at only negligibly lower loads when compared to the results for the individual holes. In the reinforced state neither in the small-scale tests nor in the large-scale tests a clear statement is possible at the load level *ultimate load* due to premature beam failure in global bending/shear distant to the holes.

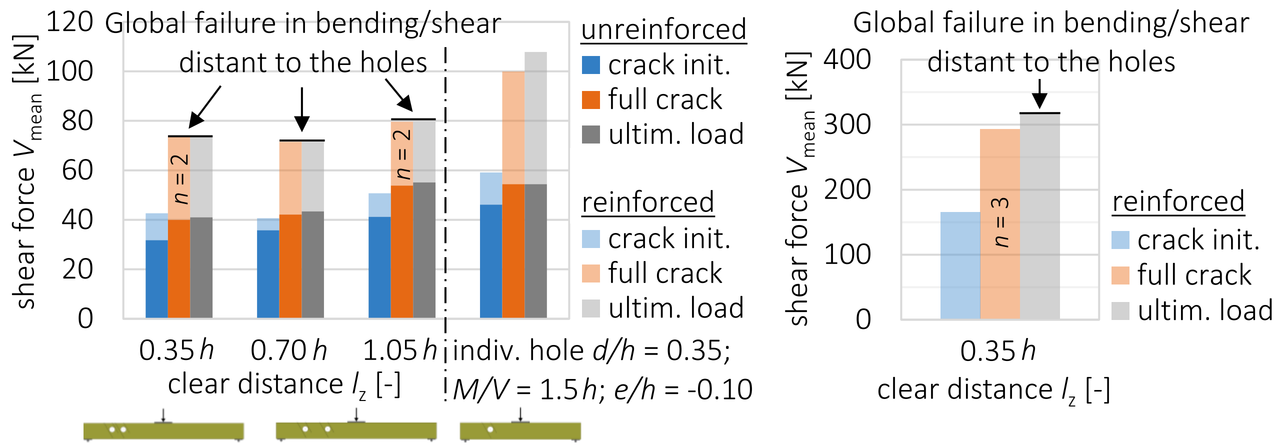

Figure 4: Test results for groups of holes arranged in horizontal direction (d/h = 0.35); left: small-scale tests; right: large-scale tests

- Groups of holes arranged in vertical direction (d/h = 0.25)

In case of the small-scale tests in the unreinforced state only a small mutual influence of the group arrangement could be observed compared to the individual holes, see Figure 5. However, the percentage load increases in the reinforced state are small in comparison to those of the individual holes with inclined applications of the reinforcement. Reasons are different failure modes but also a small reinforcing effect as a result of an application under α = 90°.

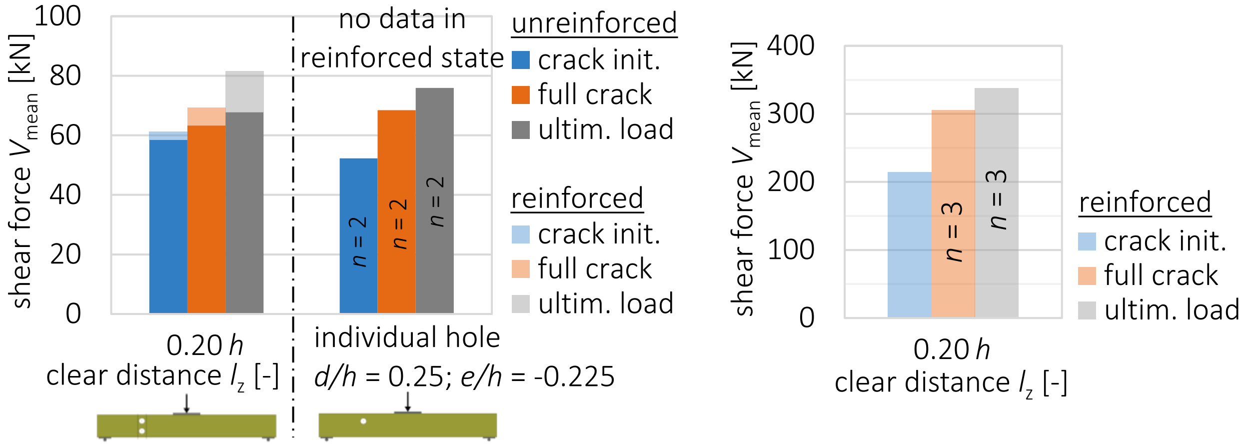

Figure 5: Test results for groups of holes arranged in vertical direction (d/h = 0.25); left: small-scale tests; right: large-scale tests

At ultimate load levels calculated load-bearing capacities in shear based on the gross cross-sections reveal similar values for small- and large-scale tests. The larger area exposed to shear in case of the large-scale tests, resulting in smaller estimated shear strength, indicate the higher reinforcing effect of the application under α = 45°.

- Individual holes arranged eccentrically under pure bending moment (d/h = 0.40)

The observed failure of both configurations at the ultimate load level was a bending tension failure in the region of the hole. At the levels of crack initiation and full crack almost no difference in load level can be seen for the two configurations, see Figure 6. At the ultimate load level the influence of the hole located in the bending tension zone was more pronounced.

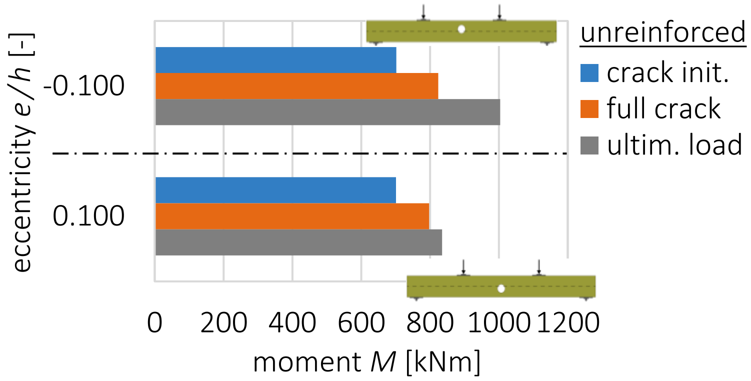

Figure 6: Test results for individual holes arranged eccentrically under pure bending moment (d/h = 0.40)

In addition to stresses in tension perpendicular to the grain and shear also concentrated stresses in grain direction occur close to the hole edges above and below the hole. According to numerical simulations the magnitude of these stress concentrations can be several times higher than the bending stresses at the beam edge, see Figure 7 for an exemplary location of the hole in the area of compressive bending stresses. To further investigate that behaviour strain gauges were placed on some specimens at the hole edge inside the hole and in the direct vicinity of the hole edge as well as the beam edge.

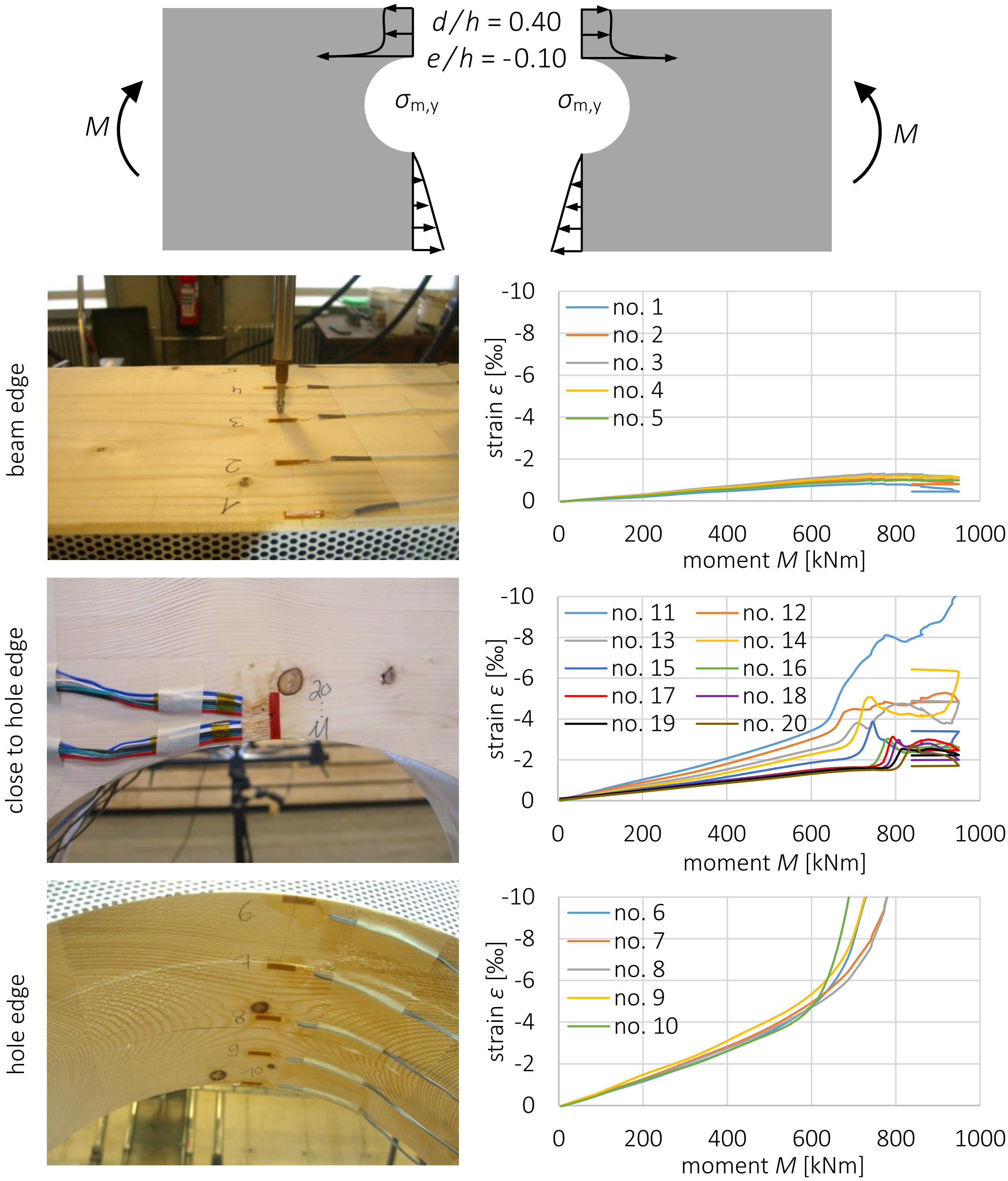

Figure 7: Strain measurements to investigate the concentration of stresses in direction of the grain around the hole (specimen no. 1, GL 28h, e/h = -0.10)

A comparison of the results at the hole edge and the beam edge confirms the results of the numerical investigations in the form of significantly higher values at the hole edge. Up to a moment M = 600 kNm an approximately linear elastic behaviour can be observed at the hole edge. Further load increase results in a disproportionate strain increase, i.e. a plastic behaviour. Analysing the strain gauges at the side face it can be seen that the stress concentration decreases rapidly with increasing distance to the hole edge and that the extension of the plastic zone increases with further load increase.

For the configuration with the hole in the area under bending tension also significantly higher strains were measured at the hole edge. In contrast to the arrangement in the area of compressive bending stresses a linear elastic behaviour was observed until failure at ultimate load.

3 Numerical investigations

3.1 Influence of eccentricity

In general, placing a hole in a timber beam has an effect on all three stress components, σ_m, σ_{90} and τ. The structural behaviour can always be derived from the shares of the stress distributions σ_m and τ of the gross cross-section, which cannot be transferred through the hole and thus have to be redistributed around the hole, see Figure 8.

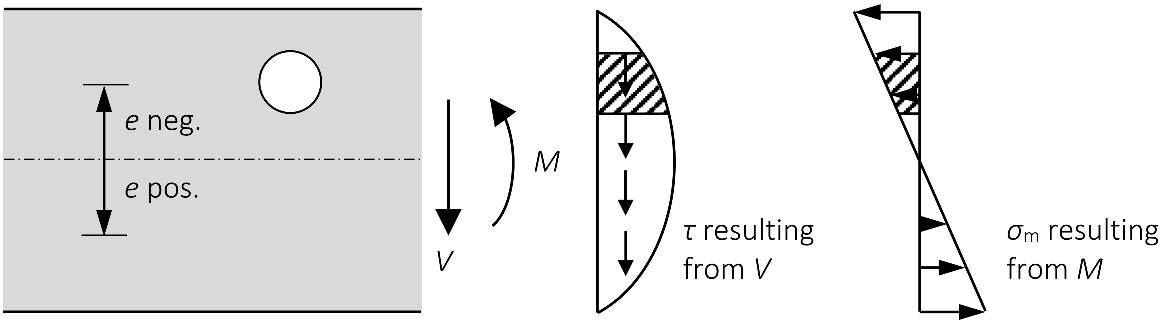

Figure 8: Shares of the stress distributions which have to be redistributed around the hole

In case of the distribution of shear stresses τ the magnitude of this share slightly decreases with increasing eccentricity. In case of the distribution of bending stresses σ_m the magnitude of this share significantly increases. Thus an increasing eccentricity has a positive effect on the structural behaviour in case of a shear force V and a negative effect in case of a moment M. For each consideration of the influence of a hole a superposition of these contrary effects of different magnitude is necessary. Thus, the location of the hole in the beam (e/h, M/V) is decisive to determine its entire effect.

Exemplarily this behaviour can be illustrated by means of resulting load-bearing capacities in tension perpendicular to the grain in the unreinforced state. Load-bearing capacities were determined by numerical simulations, that were combined to a Weibull based design approach, investigated by Höfflin (2005) for centrically located holes. In Figure 9 the resulting load-bearing capacities are shown for two different hole diameters in dependence of the location in the beam ($b x h$ = 120 mm x 400 mm). The assumed strength in tension perpendicular to the grain for a reference volume V_0 = 0.01 m³ was $f_{t,90,mean}$ = 0.83 N/mm². For very small ratios of M/V (marginal influence of M) the influence of the eccentricity is slightly positive but becomes more negative with increasing ratio M/V (increasing influence of M).

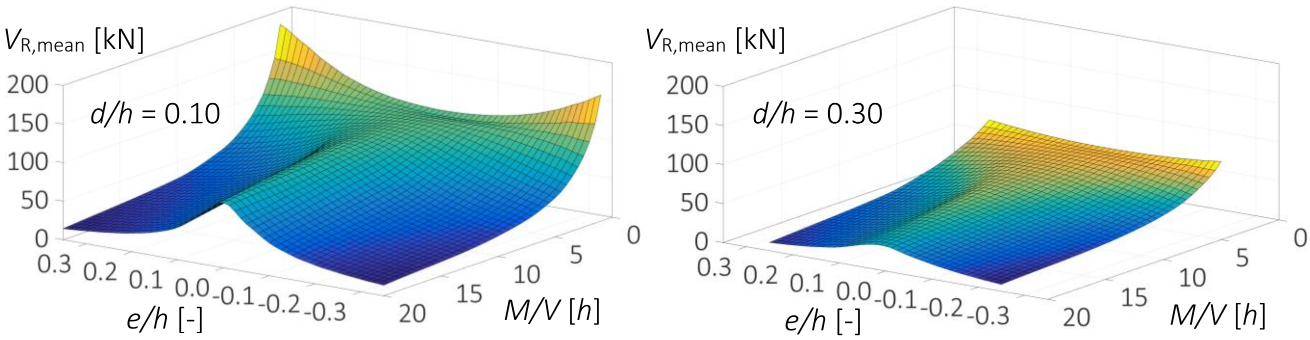

Figure 9: Load-bearing capacities in tension perpendicular to the grain (bxh = 120mmx400mm)

3.2 Effect of reinforcement

To quantifiy the effect of the reinforcement, the configurations of the eccentrically located holes of the small-scale tests were investigated in numerical simulations, separating between tension perpendicular to the grain and shear. Reinforcement by two fully threaded screws $d = 10$mm over the beam width with different inclinations but constant distance between screw axis and hole edge was considered. For general modelling of the reinforced state, experiments to determine the axial stiffness between screw and timber and validation of the numerical model it is referred to Danzer et al. (2016) and Danzer et al. (2017).

- Effect of reinforcement regarding tension perpendicular to the grain

In Figure 10 the effect of different inclinations of the reinforcing elements regarding tension perpendicular to the grain is displayed. In analogy to the unreinforced state the Weibull-based design approach also was used for the reinforced state. Clearly visible are the higher load-bearing capacities in the cases of an inclined application. For locations of the holes in the area under compressive bending stresses $\alpha = 60°$ reveals the highest values, for locations of the holes in the area under tensile bending stresses $\alpha = 45°$ reveals the highest values.

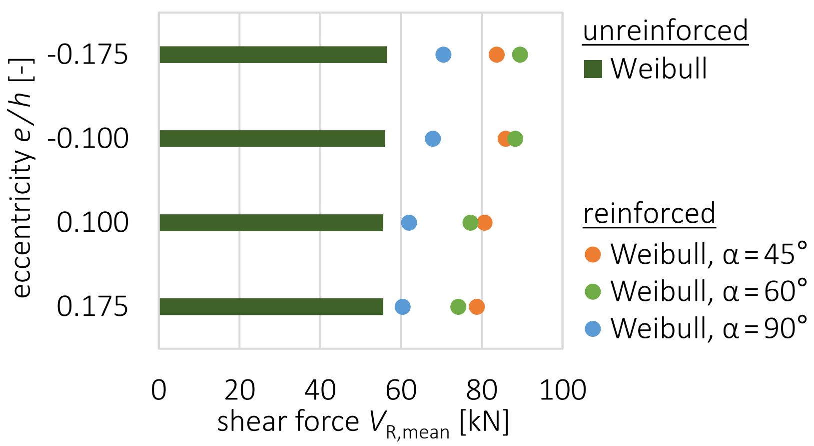

Figure 10: Load-bearing capacities in tension perpendicular to the grain without/with reinforcement

The numerical results determined for the unreinforced state show good agreement with the experimental results, the results determined for the reinforced state tend to underestimate the experimental results, see Danzer et al. (2016) and Danzer et al. (2017) for an in-depth comparison.

- Effect of reinforcement regarding shear

To quantify the effect regarding shear, distributions of shear stresses were determined along two paths representing planes of potential crack formation, extended from the middle of the hole towards the beam end/midspan. In addition, the axial forces in the reinforcing elements were determined and displayed at the side of the diagrams. Figure 11 exemplarily shows the results for the eccentricity e/h = -0.175 in the uncracked state.

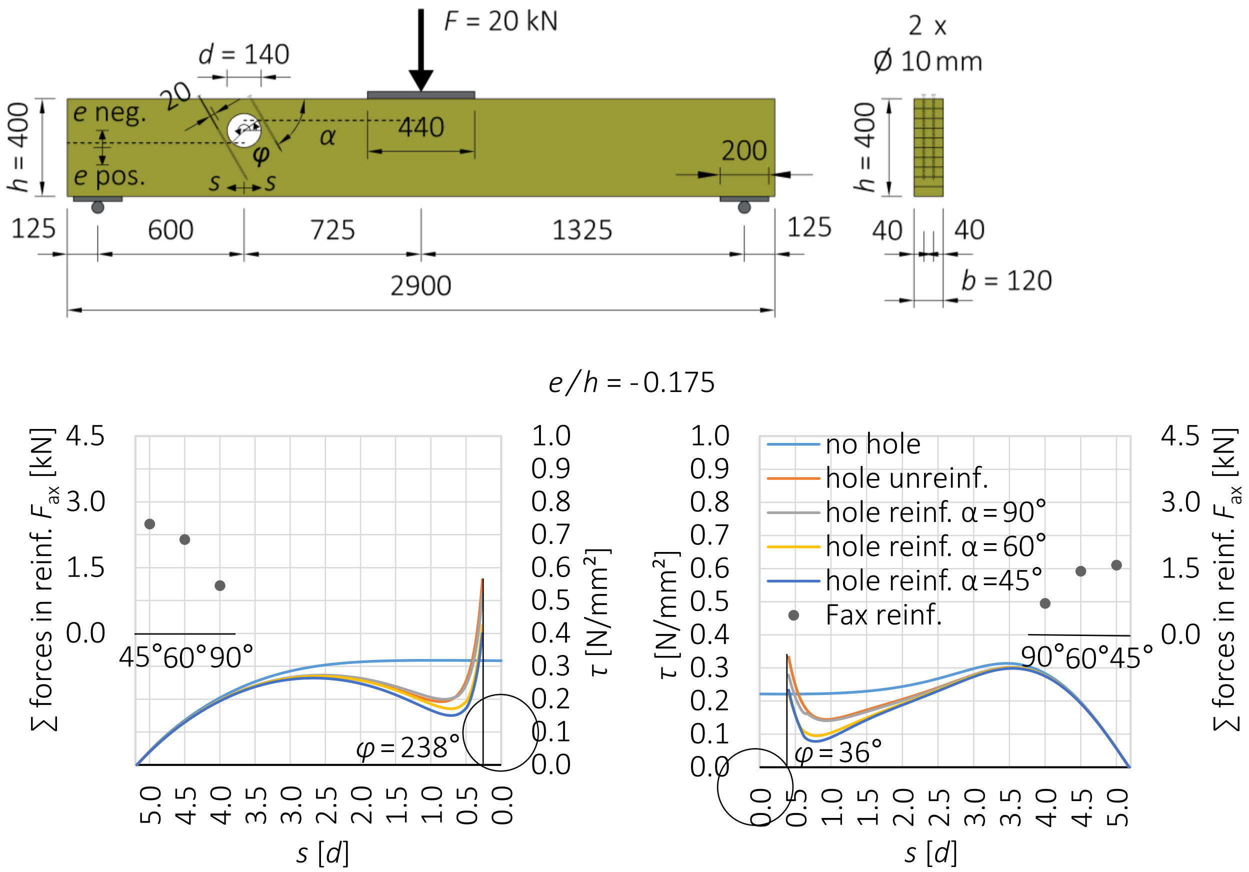

Figure 11: Distributions of shear stresses along two paths representing planes of potential crack formations

Regarding the reduction of shear stresses in dependence of the inclination of the reinforcing elements an inclination of α = 90° shows almost no effect due to the low stiffness perpendicular to the screw axis. Inclined applications result in a more pronounced reduction whereby the largest effect is obtained for an inclination of α = 45°.

4 Design approach

4.1 Individual holes arranged eccentrically

Basis of the following design approach is a parametric study within the context of numerical simulations (*b/h* = 120 mm/400 mm; *V* = 10 kN; *M* = 16 kNm). The results received therein were benchmarked against the experimental results. A comparison of test results and estimated load-bearing capacities based on Weibull theory showed good agreement (see Danzer et al. (2016) and Danzer et al. (2017) for more information), hence it was decided to transfer this approach into the existing design format of the German National Annex DIN EN 1995-1-1/NA (2013), see equations (1) to (9).

$$\frac{\frac{F_{t,90,V}}{l_{t,90,V}}+\frac{F_{t,90,M}}{l_{t,90,M}}}{0.5\cdot b\cdot k_{vol}\cdot f_{t,90}}\leq 1.0 \tag{1}$$

with $$F_{t,90,V,I/III}=\frac{V\cdot 0.7\cdot d}{4\cdot h}\cdot\left[3-\left(\frac{0.7\cdot d}{h}\right)^2\right]\cdot k_{ecc} \tag{2}$$

$$k_{ecc}=0.1+\frac{d}{h}+4.5\cdot\frac{h_{ro/ru}}{h}+0.2\cdot\frac{d}{h}\cdot\frac{h_{ro/ru}}{h}-4.9\cdot\left(\frac{h_{ro/ru}}{h}\right)^2 \tag{3}$$

$$l_{t,90,V,I/III}=1.3\cdot d \tag{4}$$

and $$F_{t,90,M,I}=M\cdot\frac{d}{h^3}\cdot Max\begin{Bmatrix}-0.62\cdot(e-0.13\cdot d)\\ -0.2\cdot(e-0.45\cdot d)\\ 0.3\cdot(e-0.08\cdot d)\end{Bmatrix} \tag{5}$$

$$l_{t,90,M,I}=0.8\cdot d\cdot\left(1-\frac{e}{d}\right)\qquad with\;0.6\cdot d\leq l_{t,90,M,I}\leq 1.0\cdot d \tag{6}$$

$$F_{t,90,M,III}=M\cdot\frac{d}{h^3}\cdot 0.22\cdot(e+0.19\cdot d) \tag{7}$$

$$l_{t,90,M,III}=0.4\cdot d \tag{8}$$

$$k_{vol}=\left(\frac{V_0}{0.072\cdot b\cdot d^2\cdot\pi}\right)^{0.2}\qquad with\;V_0=0.01m^3 \tag{9}$$

According to equation (1) the load cases shear force *V* and moment *M* are considered with individual distribution lengths $l_{t,90}$ in the form of a simplified addition regardless the differing locations of the individual maxima. In contrast to the existing design format two possible locations of maximum stresses (quadrant I and III) have to be taken into account for eccentric arrangements, see Figure 12. In case of the shear force *V* the established equation to determine the resultant force perpendicular to the grain of a hole located centrically was extended by a factor k_{ecc} to account for the eccentricity of the hole, see equations (2) and (3). If quadrant I is considered, the distance to the upper edge h_{ro} has to be used, in case of quadrant III the distance to the lower edge h_{ru}.

In case of the moment M the resultant forces in the two different quadrants were approximated by sectionally linear functions, see equations (5) and (7).

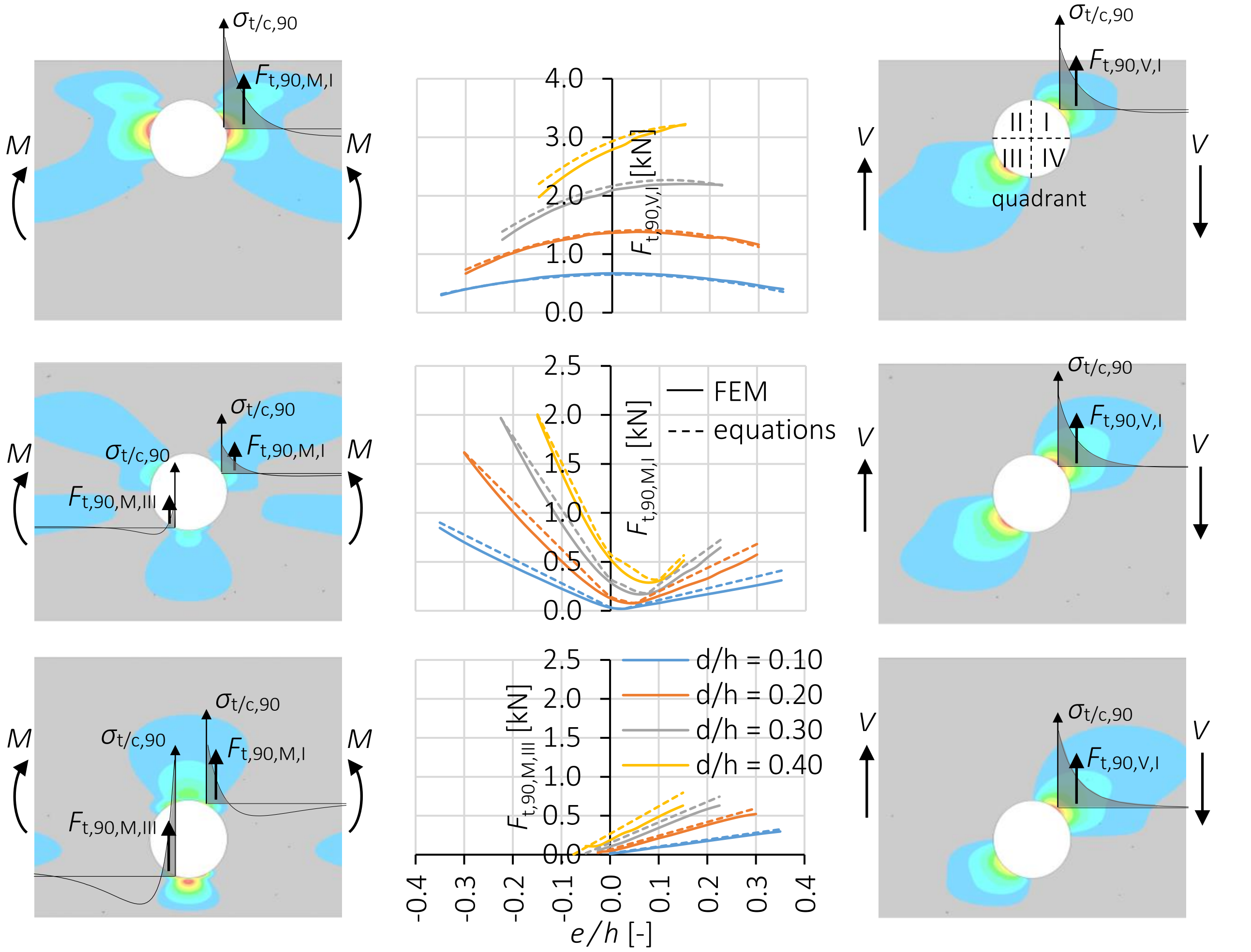

Figure 12: Comparison of resultant forces perpendicular to grain (FEM vs. equations (2), (3), (5) and (7))

In order to obtain the best possible agreement to experimental results the individual distribution lengths $l_{t,90}$ based on numerical investigations were slightly adapted, resulting in equations (4), (6) and (8). The volume defined by the expression in the denominator of equation (9) has the geometry of a segment of a ring with an aperture angle $\vartheta = 50°$, a radial extension of $\Delta r = 3/8 \cdot d$ and a thickness of the beam width b. A variation of these geometrical parameters had only a negligible effect on the results, hence the definition mentioned above is assessed sufficient and insensitive with respect to small changes of its parameters.

For assessment of the safety level a comparison of test results and the presented design approach at the level of characteristic values is shown in Figure 13. In addition to own test results of holes arranged eccentrically also test results of holes arranged centrically, based on investigations of Aicher & Höfflin (2006), were used. The characteristic values of the test series were determined based on a logarithmic normal distribution according to EN 14358 (2016) in combination with a global coefficient of variation

(COV_g = 15,8%) according to EN 14545 (2008), determined by considering all test results shown in Figure 13. The characteristic strength in tension perpendicular to the grain used in the design approach was $f_{t,90,k}$ = 0.5 N/mm².

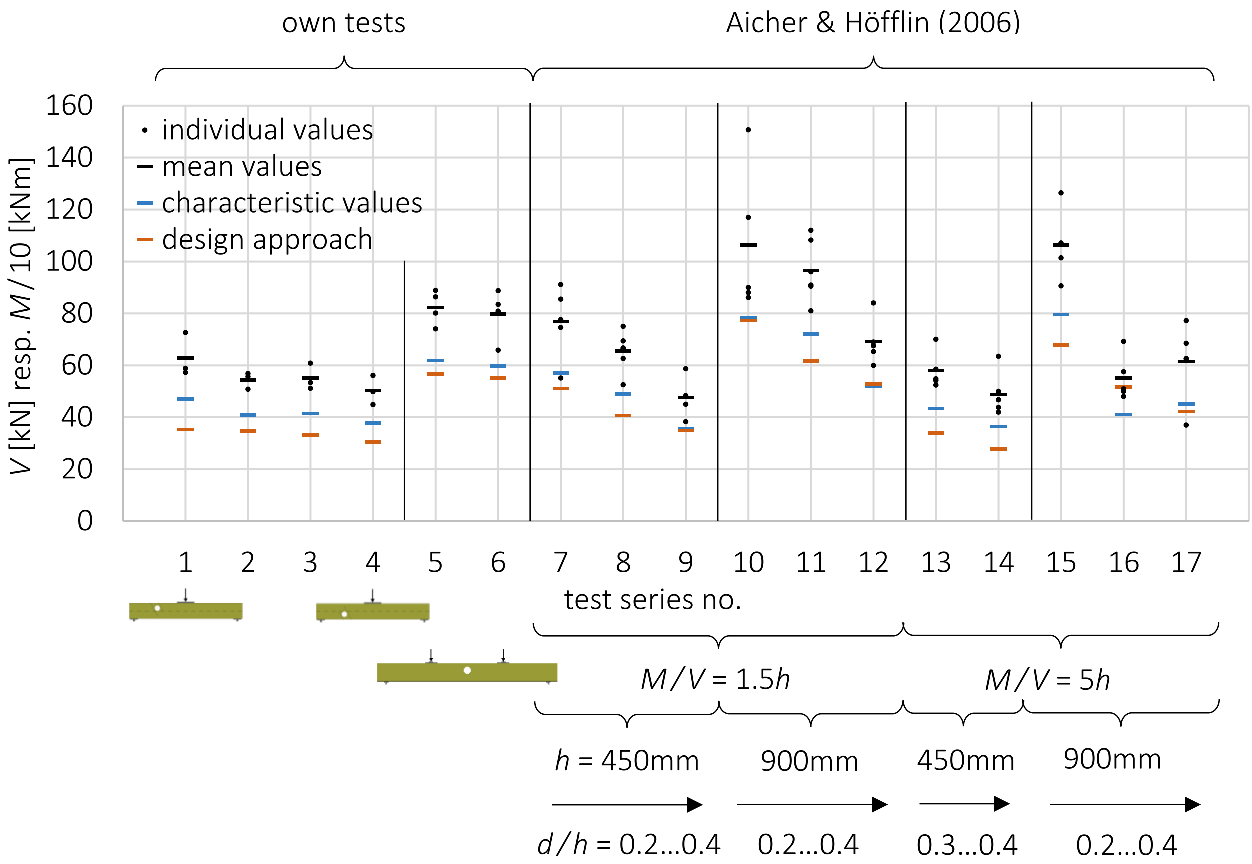

Figure 13: Comparison of test results vs. design approach at the level of characteristic values (load level: full crack over the whole beam width)

With the exception of test series no. 16 the design approach does not exceed the characteristic values of the experimental results. The results of test series no. 16 is assumed less relevant because of several reasons. Test series 15 – 17 show no clear trend although the diameter is increasing continuously whereas the other parameters remain constant. A comparison of test series 13 and 16 indicates a lower load-bearing capacity for the configuration featuring a beam height twice as large. A comparison of different ratios *M/V* (test series 10 – 12 with 15 – 17) shows only a marginal influence in cases of *d/h* = 0.20 and 0.40 but a pronounced one in case of *d/h* = 0.30.

4.2 Design of inclined reinforcement

With regard to designing inclined reinforcing elements, two different approaches were pursued to obtain the axial forces in the reinforcement. Towards this aim simplified numerical simulations of the partially cracked state in the form of a specified crack length *d*/2 were done.

The first approach is based on forces resulting from the stress distribution in tension perpendicular to the grain (uncracked state), which are converted by trigonometric functions in dependence of the angle of the inclined reinforcing elements, see Figure 14. A comparison of this procedure with axial forces in the reinforcing elements obtained with the numerical model mostly resulted in conservative results but also in non-conservative results.

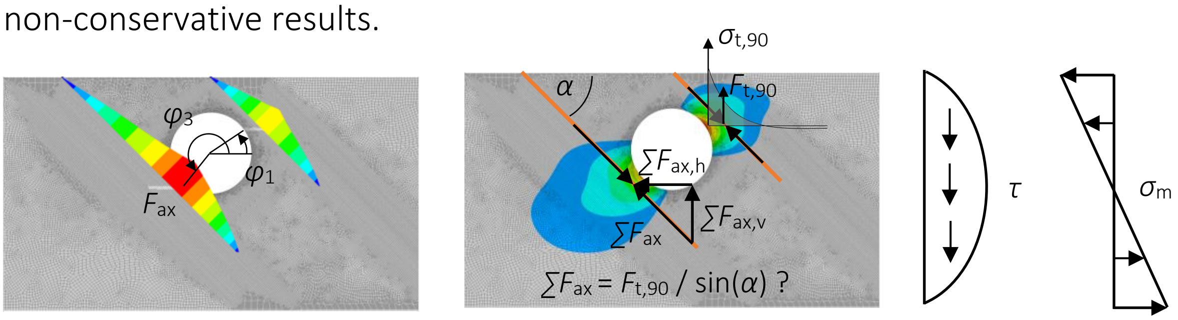

Figure 14: Scheme showing the determination of the axial forces in the reinforcement based on resultant forces in tension perpendicular to the grain

The second approach is based on shares of the horizontal shear flow due to a shear force *V* at the expected levels of crack formation, see Figure 15. Here, the fact that shear stresses at a hole also occur because of a moment *M,* is neglected for reason of simplification. Based on the horizontal components of the axial forces in the reinforcing elements obtained in the numerical model a length of about 0.3*d* was determined for an inclination α = 60° and a length of about 0.55*d* was determined for α = 45° (*d* hole diameter). Strain measurements inside the threaded rods realized during the large-scale tests confirm the order of magnitude but reveal slightly lower values compared to the simulations which were based on the small-scale tests reinforced by fully threaded screws.

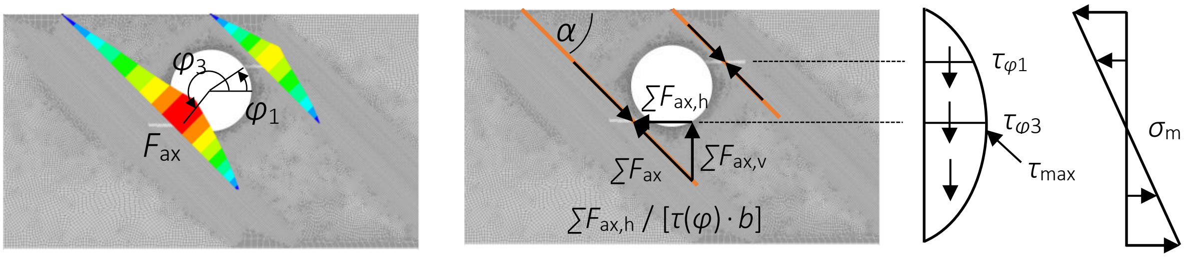

Figure 15: Schematically figure of determining the axial forces of the reinforcement based on resultant shares of the horizontal shear flow

Due to the simplified nature of the numerical considerations and the limited variation of parameters no general design concept can be given at this stage. Towards this aim, further investigations are necessary.

4.3 Groups of holes

4.3.1 Arrangement in horizontal direction

With regard to groups of holes arranged in horizontal direction the mutual influence in dependence of the clear distance l_z was also quantified in numerical parametric studies. Considering the unreinforced state, load-bearing capacities (determined using Weibull theory, see chapter 3.1) of groups of holes were compared to those of the respective individual holes. In this context load-bearing capacities describe a failure in tension perpendicular to the grain in the form of a crack over the whole beam width. In Figure 16 the general procedure as well as the varied parameters are shown.

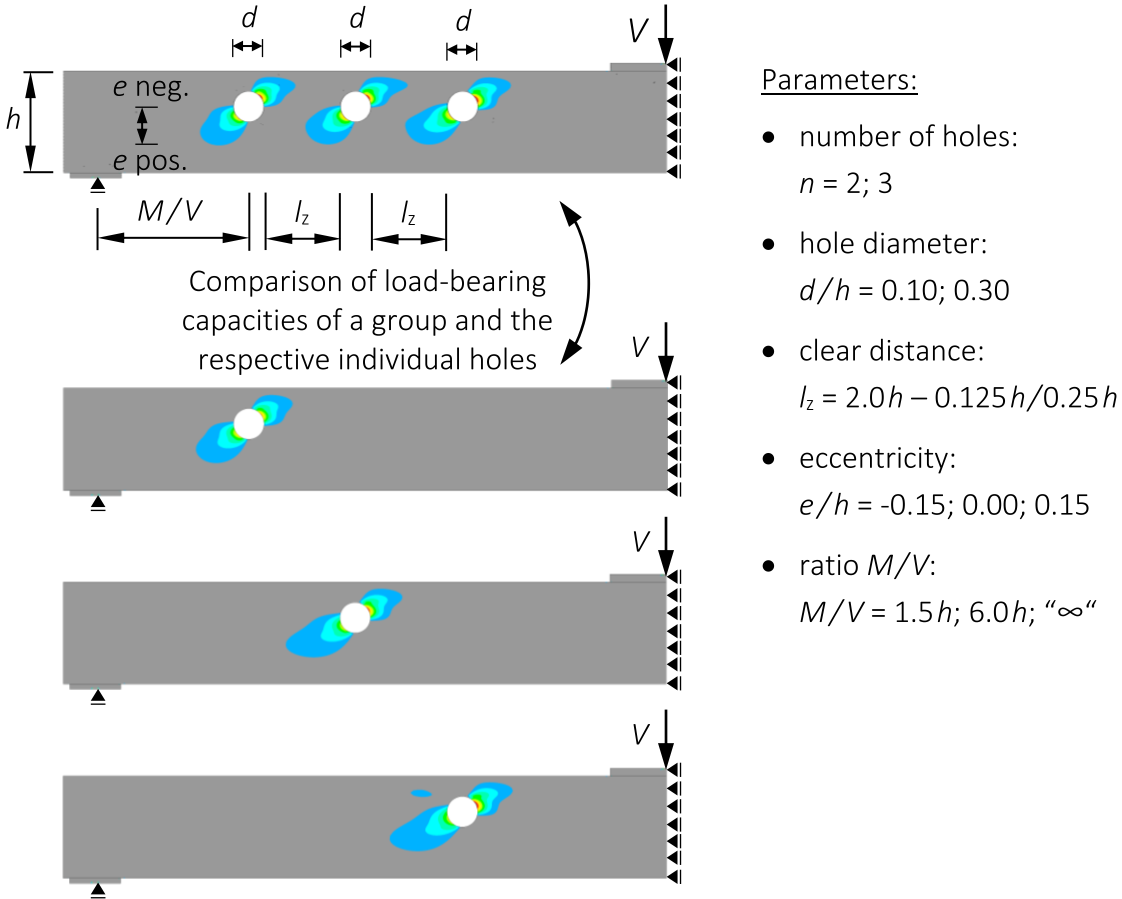

Figure 16: Procedure and varied parameters for determining the influence of the clear distance l_z

The numerical parameter study shows that the mutual influence is not only dependent on the clear distance l_z but also on the location in the beam, i.e. in general on the situation of loading. Thereby an increasing ratio M/V has a positive effect, i.e. the most critical location is the region near the supports, dominated by shear forces. The mutual influence also is affected by the number of holes in the form of a slightly more pronounced influence in case of three holes.

Regardless the number of holes and the location in the beam the following reduction factor for the load-bearing capacity of a group was derived for the most critical situation (n = 3; M/V = 1.5h):

$$k_{space,hor} = Min\begin{Bmatrix} 1 \\ 1 - 0.2 \cdot \dfrac{1.5 \cdot h - l_z}{1.5 \cdot h} \\ 1 - 0.4 \cdot \dfrac{5 \cdot d - l_z}{5 \cdot d} \end{Bmatrix} \quad (10)$$

limitations:

- $n \leq 3$
- $d/h \leq 0.30$
- $l_z \geq 1d$

In Figure 17 this reduction factor is compared to the numerical results.

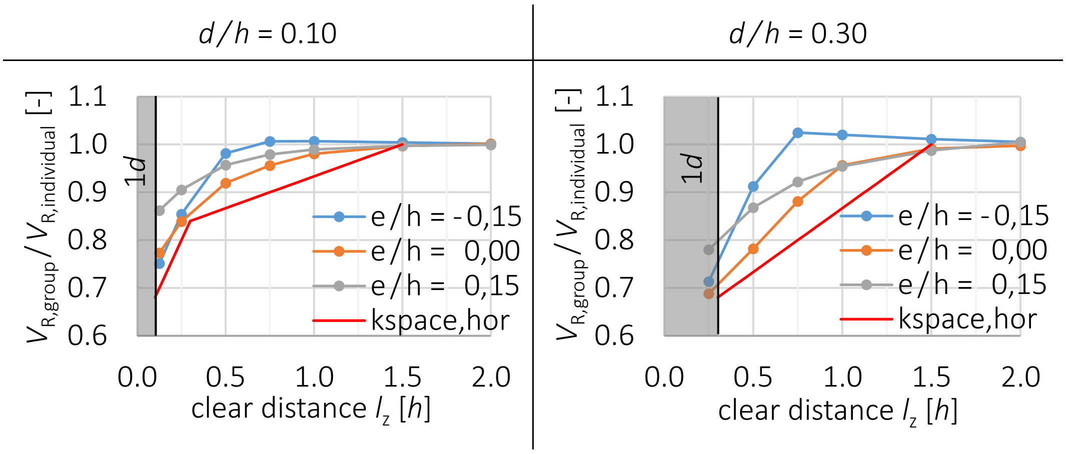

Figure 17: Comparison between the derived reduction factor and results from simulations for horizontal groups of three holes (M/V = 1.5h)

A comparison between equation (10) and the test results of the small-scale tests is debatable due to the violated limitations (d/h = 0.35). However, an extrapolation of equation (10) would result in a conservative reduction compared to the test results.

4.3.2 Arrangement in vertical direction

The structural behaviour of groups of holes arranged in vertical direction was investigated in a similar way to those arranged in horizontal direction. Due to geometrical limitations the hole diameter was limited to d/h = 0.15. By means of these investigations the following reduction factor could be derived:

$$k_{space,vert} = Min\begin{Bmatrix} 1 \\ 1 - 0.15 \cdot \dfrac{5 \cdot d - l_z}{5 \cdot d} \end{Bmatrix} \quad (11)$$

limitations:

- $n \leq 3$
- $d/h \leq 0.15$
- $l_z \geq 1d$
- symmetric arrangement

In Figure 18 a comparison of this reduction factor and the numerical results is shown for the most critical case.

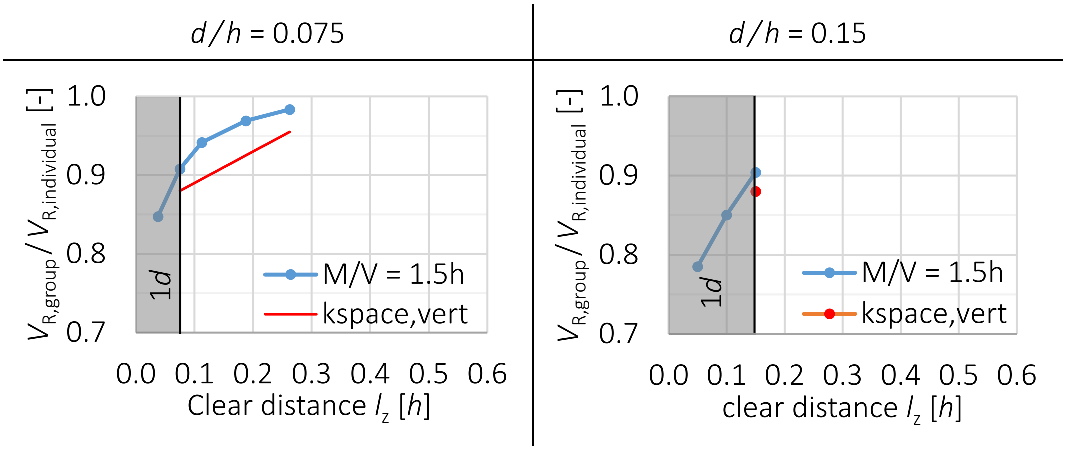

Figure 18: Comparison between the derived reduction factor and results from simulations for vertical groups of three holes (M/V = 1.5h)

A comparison between equation (11) and test results of the small-scale tests is also debatable due to the violated limitations. However, an extrapolation of equation (11) would be on the safe side compared to the test results.

5 References

Aicher, S., Höfflin, L. (2006): Tragfähigkeit und Bemessung von Brettschichtholzträgern mit runden Durchbrüchen – Sicherheitsrelevante Modifikationen der Bemessungsverfahren nach Eurocode 5 und DIN 1052. Forschungsbericht. MPA Stuttgart.

Danzer, M., Dietsch, P., Winter, S. (2016): Reinforcement of round holes in glulam beams arranged eccentrically or in groups. World Conference on Timber Engineering 2016, Conference Proceedings. Vienna, Austria.

Danzer, M., Dietsch, P., Winter, S. (2017): Einfluss exzentrisch positionierter Einzeldurchbrüche und Gruppen von Durchbrüchen auf die Tragfähigkeit von Brettschichtholzträgern – Entwicklung von Bemessungsverfahren und Konstruktionsregeln für Verstärkungsmaßnahmen. Schlussbericht zu IGF-Vorhaben 18048N. Lehrstuhl für Holzbau und Baukonstruktion, TU München.

EN 1995-1-1 (2004): Design of timber structures – Part 1-1: General – Common rules and rules for buildings. CEN. Brussels.

DIN EN 1995-1-1/NA (2013): National Annex – Nationally determined parameters – Eurocode 5: Design of timber structures – Part 1-1: General – Common rules and rules for buildings. DIN. Berlin.

EN 14358 (2016): Timber structures – Calculation and verification of characteristic values. CEN. Brussels.

EN 14545 (2008): Timber structures – Connectors – Requirements. CEN. Brussels.

Höfflin, L. (2005): Runde Durchbrüche in Brettschichtholzträgern – Experimentelle und theoretische Untersuchungen. Dissertation. Schriftenreihe Heft 90. MPA Universität Stuttgart.

Discussion

The paper was presented by M Danzer

S Aicher received clarification that in Figure 17 effect of multiple holes in horizontal direction the minimum clear distance used was 1d.

Two-way Spanning CLT-Concrete-Composite-Slabs

Stefan Loebus, Chair for Timber Structures and Building Construction, TUM

Philipp Dietsch, Chair of Timber Structures and Building Construction, TUM

Stefan Winter, Chair for Timber Structures and Building Construction, TUM

Keywords: Timber-concrete-composite, cross-laminated timber, two-way spanning slab, shear connection, notch, fully threaded screw, plate load-bearing behaviour, force-fitting element joint

1 Introduction

This contribution deals with investigations on the load-bearing behaviour of two-way spanning cross-laminated-timber-concrete-composite slabs (CLTCC). To this aim, different examinations on shear connectors, slabs and slab sections, as well as on force-fitting element joints were realized. The examination contains experimental tests of different scale, FEM-simulations and static spring-models.

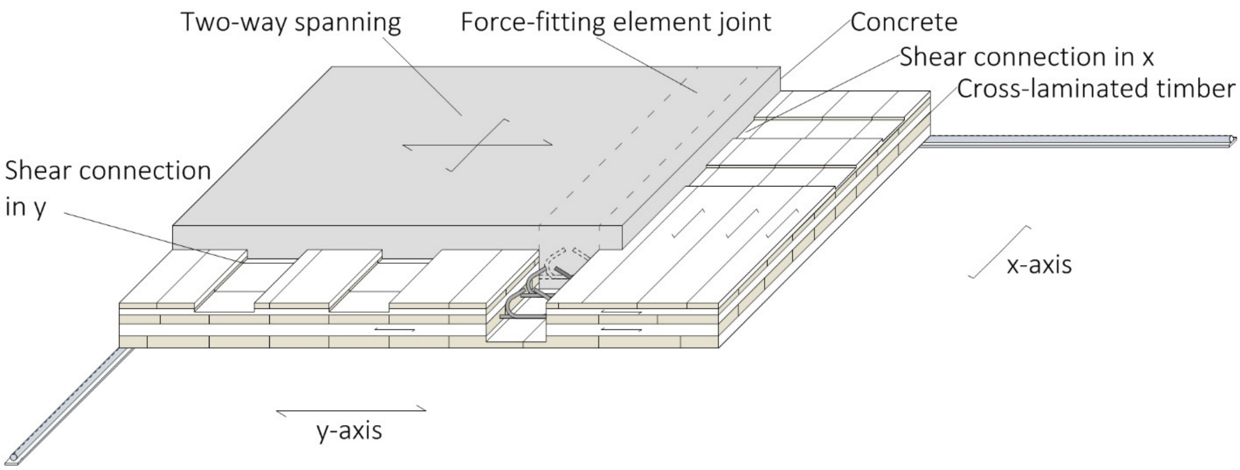

Figure 1. Two-way spanning cross-laminated-timber-concrete-composite slab.

Cross-laminated timber (CLT) was selected for the timber layer, as it is capable of bearing load biaxially. Two shear connectors, for which the load bearing behaviour in uniaxial timber-concrete-composite (TCC) systems is well known, were examined in a two-way spanning system: Fully threaded screws applied at an angle of 45° to the grain and rectangular notches. For both connections adequate construction guidelines in the given biaxial stress field and in combination with cross-laminated-timber will be presented.

As transportation and production limit the element size of cross-laminated timber, a force-fitting element joint is necessary to activate the biaxial load-bearing capacity. With glued-in reinforcement bars, a connection will be shown, which meets both requirements of stiffness and practical buildability.

Prior to the investigations, the following boundary conditions were specified, see Table 1:

Table 1. Overview of parameters and boundary conditions.

Parameter	Value
Concrete	Strength class C20/25; very pourable (>F5); min. reinforcement A_{min} = 1.88 cm²/m in each direction; Layer thickness $t_{concrete}$ = 60 - 80 mm
Cross-laminated timber	Strength class C24; Individual Layer thickness t_{layer} = 20 / 30 / 40 mm; Maximum 5 layers; t_{CLT} = 120 - 160 mm
Shear connection	Notch – rectangular, not reinforced; in different sizes; Fully-threaded screw with 45° to the grain, d = 8.0 mm, l = 160 mm, $l_{ef,timber}$ = 110 mm
Separation layer between concrete and timber	None
Supports	All-side hinged; No hold against lifting
Side length ratio	L_y / L_x = 1
Element joint	Glued-in reinforcement bars

In addition, the effect of torsion and the interaction of the principal span directions in x- and y- axis are examined.

For a better understanding of the plate load-bearing behaviour, the slab is examined in real tests and a solid FE-model with individual layer and connection detailing. Simplified solutions for a continuous and homogenous distributed shear stiffness and a representation of the element joint are given and are meant as the foundation for a further simplified plate model.

Within the FEM simulations, the given two-spanning system is compared to common one-way spanning timber-concrete-composite systems.

It was attempted to describe the most important aspects of the research results to the given topic. Due to the length of this paper, some simplifications in the description had to be made. For detailed information, see [Loebus, 2017].

2 Shear connection

2.1 Alignment in plane

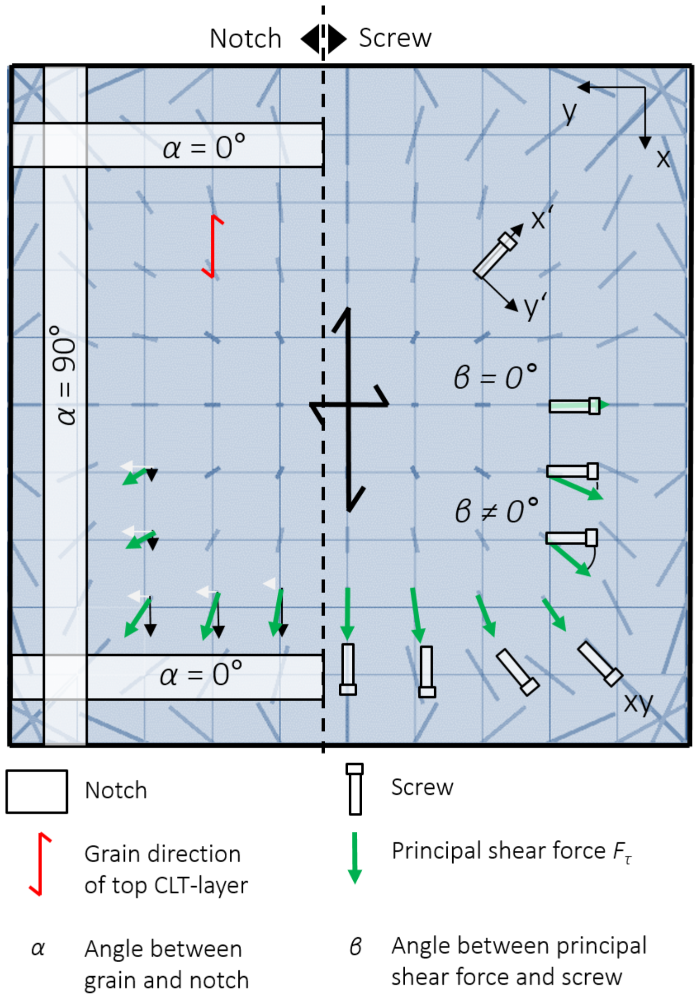

Figure 2. Alignment of shear connection in plane (for plane definition compare also Figure 6).

The load bearing behaviour of the given shear connectors, fully threaded screws applied at an angle of 45° to the grain and rectangular notches, is well known for uniaxial timber-concrete-composite systems, e.g. [Blaß et al., 1995] and [Michelfelder, 2006]. In the following, the connectors are examined in a two-way spanning system. In a stress field of a plate, the alignment of the connectors in plane becomes relevant. The connector follows either the alignment of principal stress or the given orthogonal alignment of the CLT. In fabrication, the notch cutting procedure fits an orthogonal alignment and an alignment to wood grain direction, while the screw can be placed freely in plane without a bigger effort and is independent from the grain direction, when neglecting the embedment. Therefore, the screw can be aligned along the direction of principal shear forces. The alignment of shear connections is schematically shown in Figure 2.

2.2 Notch

2.2.1 General

The load-bearing behaviour of notches in a one-way spanning system and in solid wood was recently summarized in [Kudla, 2015]. The slip modulus K_{ser} varies between 800 to 1,800 kN/mm/m, the load bearing capacity F_u between 520 and 730 kN/m. Regarding the two-way spanning CLT-concrete-composite system, two issues have to be dealt with: (1) The rolling shear perpendicular to grain in the CLT as an additional semi-rigidity in the cross-section in both load-bearing axis. (2) The obligatory activation of the y-axis (see Figure 1) with an effective smaller static height than the x-axis.

To develop a notch connection that works in both axis of the CLT, FEM-simulations, two-sided push out tests and parametric studies were performed. The derived construction guidelines and load-bearing characteristics are given in the following. Three major issues were identified, given in Figure 3.

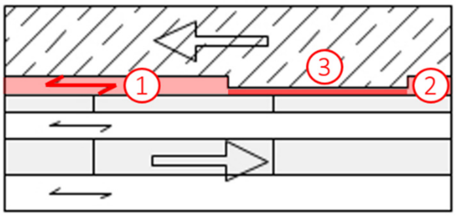

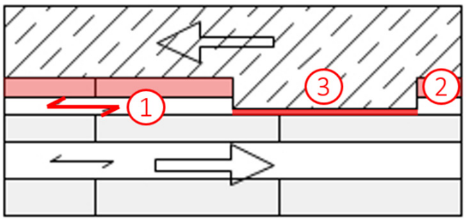

a) Notch parallel to grain (α = 0°) *b) Notch perpenticular to grain (α = 90°)*

Figure 3. Notch construction overview with (1) Load application into timber (2) Top layer thickness (3) Activating a larger area for transmitting shear stress into the next layer by hanging back the timber in front of the notch below the notch.

2.2.2 Shear load application into CLT

The evaluation of the push-out shear test as shown in Figure 4 and Table 2 show, that a notch connection perpendicular to grain reaches only a fraction of load-bearing capacity and shear stiffness compared to a notch parallel to grain. Even if there is barrier effect of the next CLT-layer, the notch design in y-axis cannot be the same as in x-axis. To activate both axis equally from the perspective of shear stiffness, it is necessary to ensure a load application parallel to grain in both axis, as shown in Figure 3 no. 1.

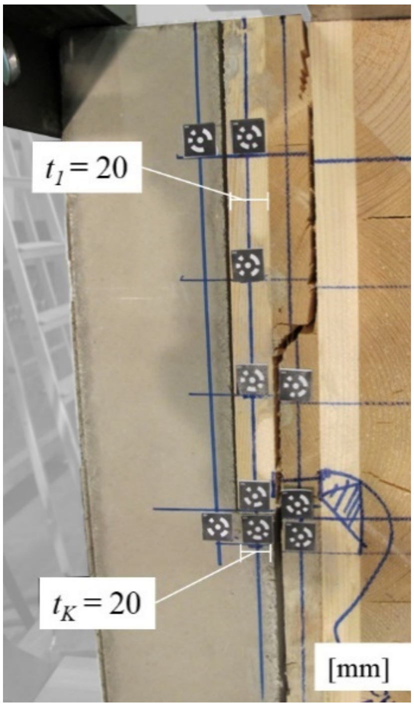

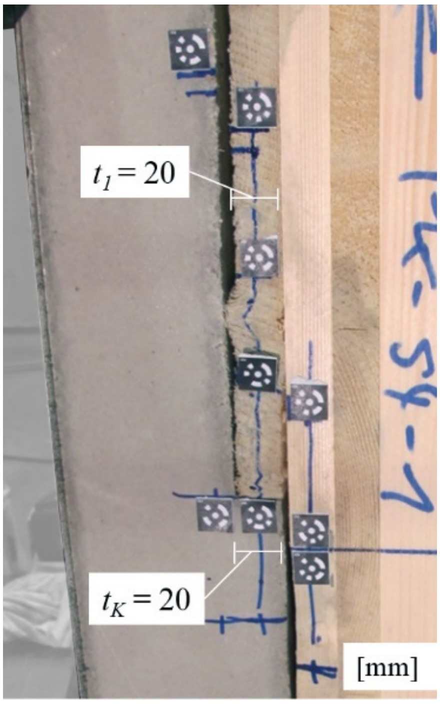

a) Notch parallel to grain (α = 0°) *b) Notch perpenticular to grain (α = 90°)*

Figure 4. Failure mechanisms from push-out tests – Material according to Table 1. Notch depth t_k = 20 mm; Top and second CLT-layer $t_1 = t_2$ = 20 mm; Notch length l_N = 200 mm; Timber length in front of the notch l_v = 250 mm.

Table 2. Test results: Push-out tests according to Figure 4 and [EN 26891].

α	$t_{concrete}$*	$F_{u,mean}$	F_k	CV(F)	$k_{s,mean}$	CV(k_s)	N
[°]	[days]	[kN/m]	[kN/m]	[%]	[kN/mm/m]	[%]	[Piece]
0	17	344.7	295.9	6.5	676.5	30.1	3
0	120	370.5	322.0	1.6	759.5	25.3	2
90	17	97.4	86.5	3.5	134.0	15.6	3
90	120	124.7	106.5	4.8	83.1	5.1	2

** The first series was tested after reaching the minimum concrete strength C20/25 after $t_{concrete}$=17 days. The top CLT-layer had relatively high humidity (~25%). After $t_{concrete}$ = 120 days a second series was tested with reduced humidity.*

2.2.3 Influence of the top CLT-layers

In consequence of the necessity to apply the shear load parallel to grain in each plate axis and respecting the fact that with increasing total notch depth the size of tension stress in the concrete console increases, the top layers should be kept relatively thin, see Figure 3 no. 2. As the element-joint requires a certain thickness in the bottom CLT-layers, later shown in Section 3, this leads to an asymmetric CLT-layer setup.

2.2.4 Depth of notch in load-bearing CLT-layer

Regarding the characteristics of a notch in CLT, the dominant parameter is the rolling shear stiffness of CLT-layers perpendicular to grain, as seen in the failure pictures of Figure 4. The transfer of shear stress from the notch to the next soft shear layer can be improved by enlarging the effective contact length between both layers. Therefore, to enlarge the shear transmission area between the layers, the timber in front of the notch should be hanged back beneath the notch, see Figure 3 no. 3 and the comparison in Figure 5. In addition, gaps in CLT without edgewise bonding are bypassed more effectively, if the transmission area is larger.

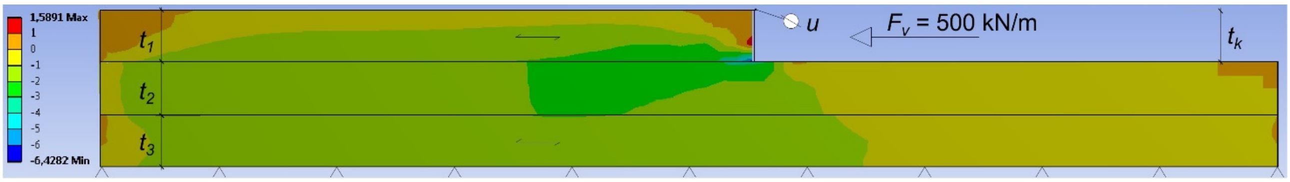

a) Notch depth t_k = 20 mm, without hanger for timber in front of the notch; $K_{ser} = F_v/u$ = 584 kN/mm/m

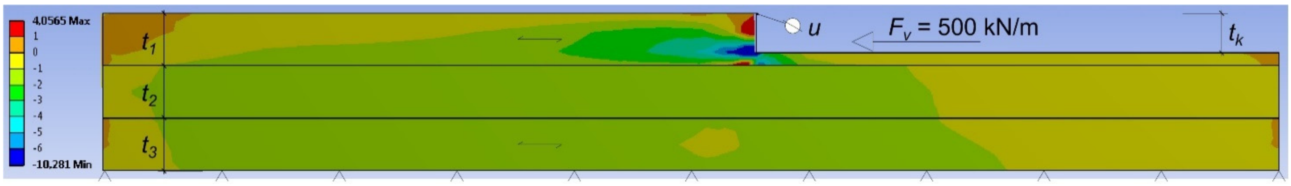

b) Notch depth t_k = 15 mm, hanger thickniss $\Delta t = t_1 - t_k$ = 5 mm beneath the notch; K_{ser} = 707 kN/mm/m

Figure 5. Comparing the effect of a hanger for the timber in front of the notch by a shear stress distribution τ_{xz} [N/mm²] with CLT-layer thickness $t_1 = t_2 = t_3$ = 20 mm [ANSYS 17.1].

2.3 Screw

2.3.1 General

The load-bearing behaviour of screwed shear connections is examined exemplarily with the fully-thread screw ASSY Plus, because it has a German and a European Technical Approval, [Z-9.1-648] and [ETA-13/0029], for CLT-concrete-composites. The slip moduli in those approvals differ. Therefore, they are both taken into consideration. The examinations on the biaxial load-bearing behaviour can be transferred to other screw-types as long as the according slip moduli are given.

2.3.2 Differentiation in axial and lateral load application

From the perspective of the screw, it is differentiated between axial (x’) and lateral (y’) load application in plane, see Figure 6. Both load directions feature an individual load bearing capacity and slip modulus, see Table 3.

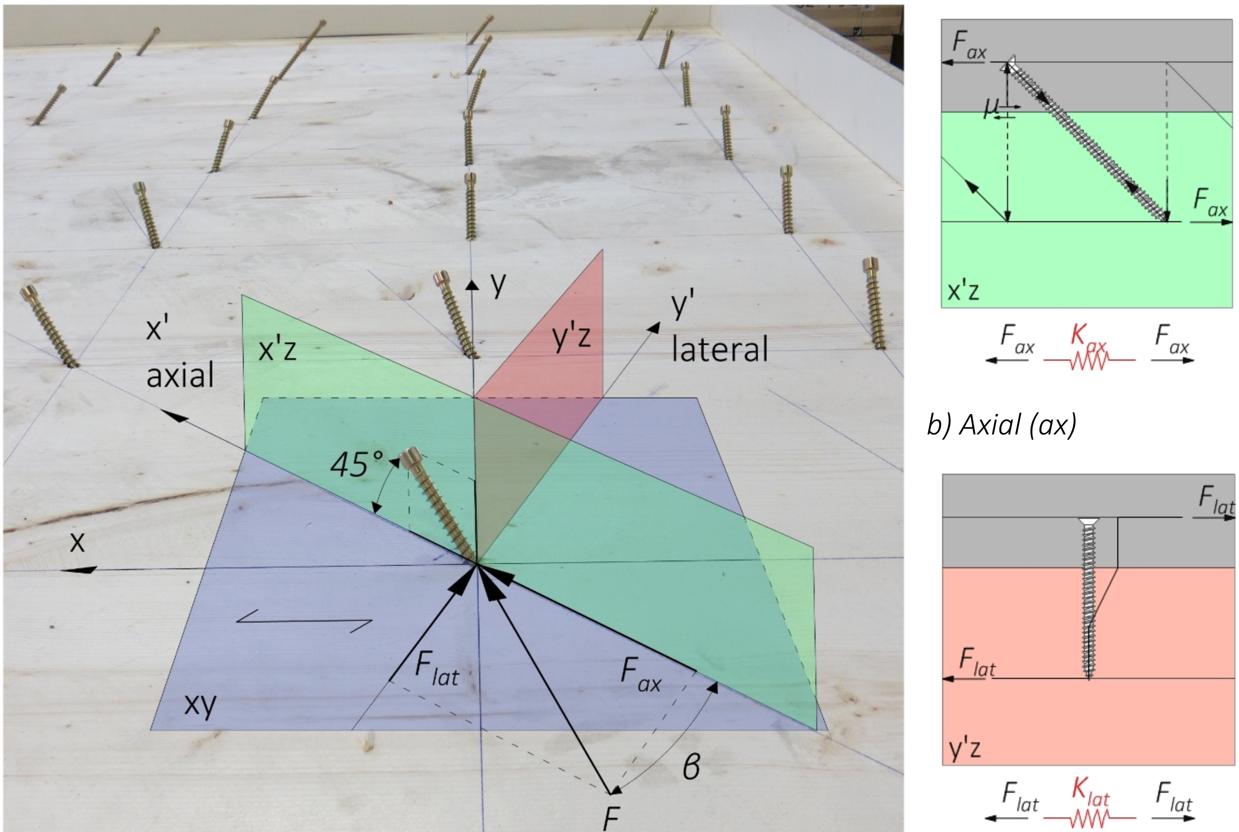

b) Axial (ax)

a) Photo of the screw connection and the CLT of a plate test specimen, described in detail in Section 4. For an exemplary screw plane, sections, and force distribution are visualised.

c) Lateral (lat)

Figure 6. Load application on a screw shear connection. Dimensions according to Table 1.

Table 3. Load-bearing capacity and slip modulus of a fully-threaded screw timber-concrete-composite connection with screws according to [ETA-13/0029] and [Z-9.1.-648]; ρ_k = 350 kg/m³

	Axial (β = 0°)		Lateral (β = 90°)			Ratio axial / lateral		
	ETA (μ* = 0.25/0)	abZ	ETA	abZ		ETA (μ = 0.25/0)	abZ	
F_{Rk}	7.8 / 6.2	6.2	3.1	3.6	[kN]	2.5 / 2.0	1.7	[-]
K_{ser}	11.0	11.0	2.0	1.5	[kN/mm]	5.5	7.3	[-]

** μ = friction coefficient concrete-timber*

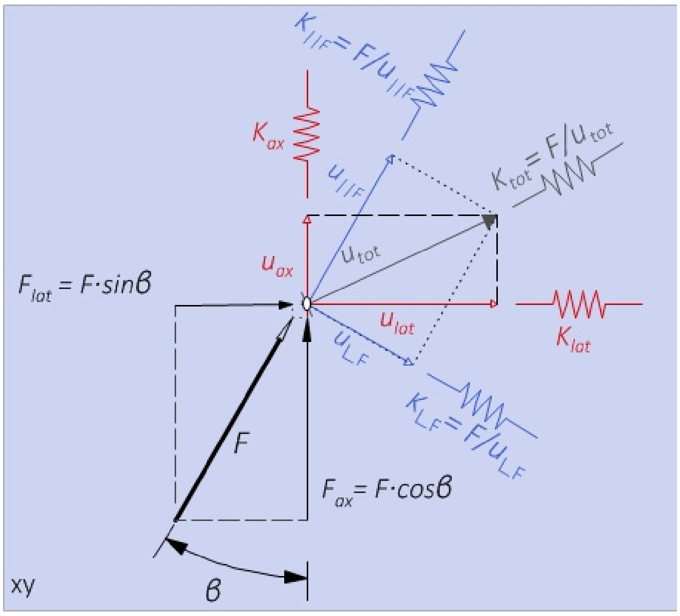

Figure 7 Slip behaviour due to an orthotropic slip modulus (K_{ax}; K_{lat})

According to Figure 7, the principal shear force F can be distributed on the equivalent slip moduli K_{ax} and K_{lat}, represented as vectorised springs. From the resulting slip u_{ax} and u_{lat} the total slip u_{tot} and together with F, the total slip modulus K_{tot} can be derived. In practice the application of K_{tot} as relevant slip modulus is difficult in use, because the spring vector of K_{tot} is not in direction of $F(\beta)$. For 0° < β < 90° the orthotropic slip moduli lead to a deviating slip $u_{|\_F}$ perpendicular to the force F. As the screws are applied in a bundle, it is assumed that the potential slip $u_{|\_F}$ is braced by a force redistribution on surrounding screws in other directions. Consequently, $K_{//F}$ is used as relevant slip modulus.

The slip modulus in direction of the principal shear force $K_{//F}$ can be calculated according to Equation 1:

$$K_{\parallel F} = \left[\frac{\cos^2\beta}{K_{ax}} + \frac{\sin^2\beta}{K_{lat}}\right]^{-1} \tag{1}$$

Combining the load-bearing capacity according to [DIN EN 1995-1-1] Equation 8.28 the maximum value depending on the angle β according to Figure 6 and Figure 7 is given in Equation 2:

$$F_{Rd} = \left[\left(\frac{\cos\beta}{F_{Rd,ax}}\right)^2 + \left(\frac{\sin\beta}{F_{Rd,lat}}\right)^2\right]^{-0,5} \tag{2}$$

A distribution of $K_{//F}$ and F_{Rd} is given in Figure 8. It shows a logarithmic reduction in dependence on *β.*

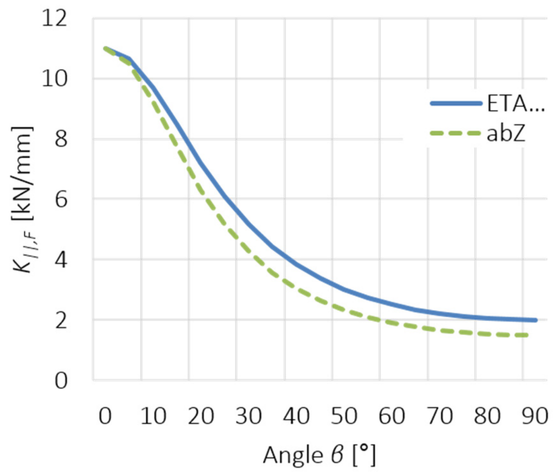

a) Slip modulus $K_{//F}$

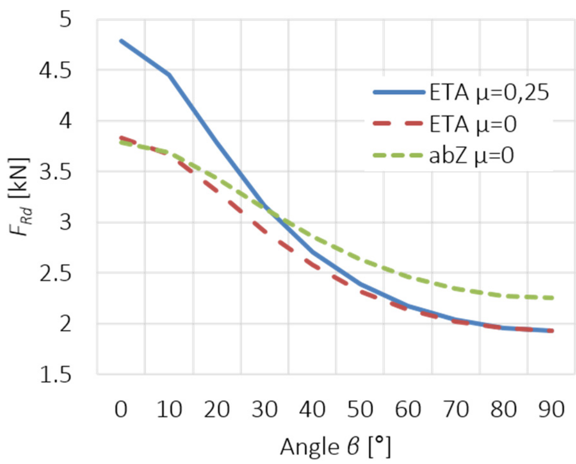

b) Load-bearing capacity F_{Rd}

Figure 8. Slip modulus and load-bearing capacity in dependence on β for a shear connection with screws according to Table 3.

The load-bearing behaviour of the connection under a deviating angle of application β was subject to push-out shear tests, Figure 9. Results and testing parameter are summarized in Table 4.

Table 4. Test results: Push-out test on timber-concrete-composite connections with fully-threaded screw according to Table 1, Table 3, Figure 9 and [EN 26891].

β	$t_{concrete}$*	$F_{u,mean}$	F_k	CV(F)	$k_{s,mean}$	CV(k_s)	N
[°]	[days]	[kN/m]	[kN/m]	[%]	[kN/mm/m]	[%]	[Piece]
0	17	21.1	18.7	2.0	80.3	15.5	3
0	120	21.8	15.3	10.8	41.9	7.2	2
30	17	19.1	17.0	4.6	54.8	30.3	3
30	120	20.1	17.4	1.9	18.9	17.7	2
60	17	14.7	11.7	9.2	47.1	38.6	3
60	120	15.4	13.4	1.4	7.1	16.4	2

** The first series was tested after reaching the minimum concrete strength C20/25 after $t_{concrete}$=17 days. The top CLT-layer had relatively high humidity (~25%). After $t_{concrete}$ = 120 days a second series was tested with reduced humidity.*

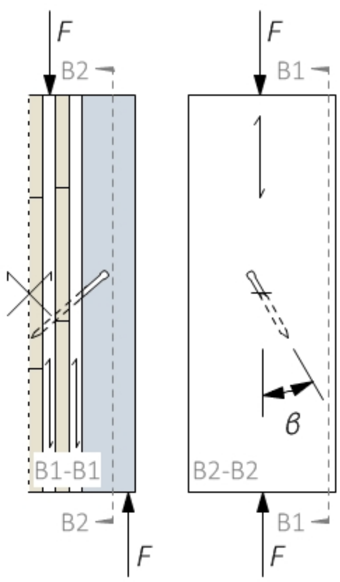

Figure 9. Testing scheme push-out test fully-threaded screw.

While the absolute values of the results deviate, the ratio β /0° for $t_{concrete}$ = 120 days shows good agreement with the slip moduli from the technical approvals, see Table 5.

Table 5. Comparison of the slip moduli from the approvals (ETA/abZ) and the push-out test results ($t_{concrete}$ = 17d / 120d) in dependence on β.

β	$K_{//F}$		$K_{//F,\beta} / K_{//F,0°}$		$k_{s,mean}$		$k_{s,\beta} / k_{s,0°}$	
[°]	[kN/mm]		[-]		[kN/mm]		[-]	
	ETA	abZ	ETA	abZ	17d	120d	17d	120d
0	11.0	11.0	1.00	1.00	80.3	41.9	1.00	1.00
30	5.2	4.3	0.47	0.39	54.8	18.9	0.68	0.45
60	2.5	1.9	0.23	0.17	47.1	7.1	0.59	0.17

A direction change of the force F due to the orthotropic slip modulus is neglected under the assumption that the screw is aligned to the principal shear force as close as possible. By aligning the screw to the principal shear force in plane, an isotropic slip modulus K_A may be assumed in plane of the shear connection. A deviating force application angle can occur however, if load situations, long-term behaviour or discretization in the screw alignment change, and therefore should be taken into account by applying $K_{//F}(\beta_{deviate})$, according to Equation 1 or Figure 8a.

3 Force-fitting element joint

As transportation and production limit the CLT-element size, a force-fitting element joint is necessary to activate the biaxial load-bearing capacity. Most important parameter is the effective bending stiffness of the joint connection. A reduction in stiffness reduces the stiffness of the respective axis orthogonal to the joint and therefore a balanced biaxial load-bearing behaviour. As the concrete layer can be realized in one piece, the focus lies on the element joint between the CLT-elements, in particular the lowest CLT-layer with the resulting tension force Z parallel to grain, compare Figure 10a.

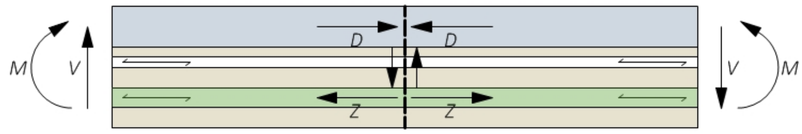

a)

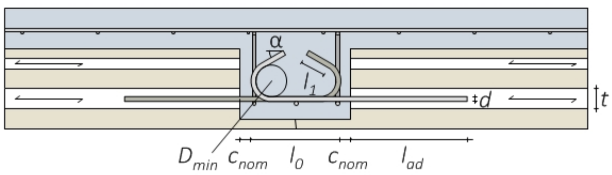

b)

Figure 10 Force-fitting element joint – a) forces to be transferred and b) joint connection with glued-in reinforcement bars

Different connection types, such as fully threaded screws applied crosswise under 45° and 135° or gluing, were compared. With glued-in reinforcement bars, Figure 1 and Figure 10b, a connection was developed, which meets the requirements of stiffness and practical buildability.

Glued-in steel bars are a very stiff connection-type in timber engineering. If reinforcement bars are used as steel bars, the connection can be applied in concrete as well. In the concrete, the bars of two CLT-elements can be overlapped and jointed force-fittingly. The bars are curved to reduce the overlapping length.

The concrete-part of the connection can be designed according to [EN 1992-1-1] Sec. 8. For the timber-part, information can be found in [Steiger, 2012] and requirements according to [DIN EN 1995-1-1/NA 11.2].

To minimise the loss in stiffness, the stiffness of the steel bars EA_{steel} should be equal to the stiffness of the corresponding CLT-layer (in green in Figure 10a) EA_{timber}. From the perspective of minimum spacing, this requirement complies with a layer thickness of 30 mm as shown in the results of a parametric study, see Table 6.

Table 6. Parametric study of the connection 'steel bars glued in CLT-layer'.

Geometry		Aim: EA_{steel} / EA_{timber} = 1.0			Limit: $a_{2,req}$ = 5d & $a_{2,c,req}$ = 2.5d	
$t_{CLT\text{-}layer}$ [mm]	d_{bar} [mm]	n_{bar} [Piece/m]	a_2 [mm]		$n_{bar,max}$ [Piece/m]	max EA_{steel} / EA_{timber}
30	8	31	32	4d	25	0.8
30	10	20	50	5d	20	1.0
30	12	14	72	6d	17	1.2
40	8	42	24	3d	25	0.6
40	10	27	37	3.7d	20	0.75
40	12	19	54	4.5d	17	0.9

With E_{timber} = 11,000 N/mm², E_{steel} = 210,000 N/mm², according to [DIN EN 1995-1-1/NA] Tab. NA.22

The performance of the connection was verified in a four-point bending test as shown in Figure 11. In addition to the specimen featuring the element-joint, reference specimens with a continuous CLT-element were tested. The connection was realised with nine reinforcement bars per metre, d = 10.0 mm, on each element side, which resembles 45% of the jointed timber layer stiffness. The reason to stay below the full stiffness of the timber layer was to provoke a ductile failure in the steel bars and to keep the connection in an economical format. Further specimen specifications are given in Table 8.

The test results show a similar deflection behaviour of the jointed elements in comparison to those without. The overall loss in stiffness is smaller than expected. The low stiffness of the effective steel cross section in comparison to the jointed timber layer is compensated by a stiffening effect of the concrete block. Further, the failure behaviour is ductile, because of the yielding of the steel bars. The elements can be joined with barely any loss in stiffness and failure load can be determined more precisely, compare Table 7.

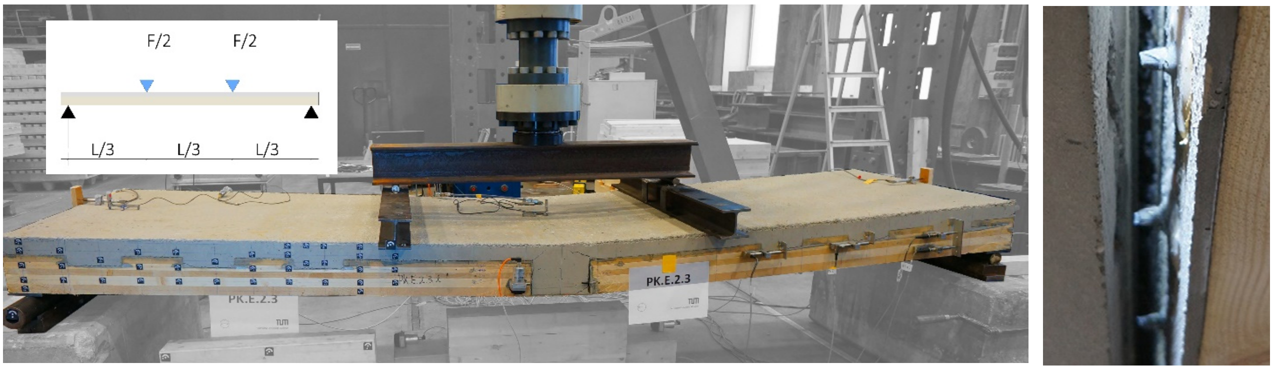

a) Four-point bending test scheme and test setup with L=3.4 m. In this picture the element-joint fails. *b) Steel bar failure*

Figure 11. Test on one-way spanning slab, 3.5 m x 1.0 m, with a force-fitting element joint analogous to the section in y-axis in Figure 1.

Table 7. Test results of the four-point bending test. For comparative reasons equivalent stiffness moduli k_s and k_u were calculated based on [EN 26891].

Element joint	$F_{u,mean}$	CV(F_u)	$k_{s,mean}$	CV(k_s)	$k_{u,mean}$	CV(k_u)	N
	[kN]	[%]	[kN/mm/m]	[%]	[kN/mm/m]	[%]	[Piece]
No	113.05	15.6	3.98	2.7	3.09	16.5	3
Yes	90.40	3.0	3.87	9.1	2.14	19.2	3
Ratio	$F_{u,mean}$		$k_{s,mean}$		$k_{u,mean}$		
Yes / No [%]	80.0		97.2		69.3		

4 Plate load-bearing behaviour

4.1 General

The plate load-bearing behaviour was examined in two plate test series and accompanying FEM-simulations. The tests included a torsion test on a plate section and full plate tests in analogy to a uniaxial four-point-bending test, Figure 12a. Apart from the individual failure mechanism and the maximum load-bearing capacity, the stiffness of the plate and potential improvement of the serviceability in comparison to existing one-way-spanning timber-concrete-composite slabs were objects of interest.

4.2 Experimental behaviour

The specimens match in the application of the shear connectors according to the proposed alignment in Section 2: Notches in an orthogonal alignment and screws following the direction of principal shear force in the plane of the slab, Figure 12b, c. Specimen parameters are given in Table 8. The results show a high load-bearing capacity and a constant deformation behaviour along a long range of the load level. The failure mechanism is successive and ductile. The specimens show a similar high level of stiffness up to a load of approximately 55 % F_u, independent from the shear connector, Figure 13. Both systems reached a similar level of maximum load, which is characterized by the final failure of the lowest layer of the CLT. This was preceded by a failure of the concrete layer.

Table 8. Specimen parameters to the plate and element joint tests.

Layer thickness		Screw	trajectorially aligned
Concrete	60 mm	Total length l - diameter d	160 mm - 8.0 mm
CLT	|20-20|20-30|30 mm	Effective length $l_{ef,timber}$	110 mm
Shear Connection		Angle in cross-section	45°
Notch (α = 0°)	orthogonally aligned	Distances a_x x a_y	250 mm x 250 mm
Length l_N x Depth t_N	140 mm x 15 mm	Discretisation angle in plane	22.5°
Length in front of notch l_v	200 mm	**Slab lengths**	
Notch (α = 90°)	orthogonally aligned	Total	3,500 mm
Length l_N x Depth t_N	160 mm x 35 mm	Support width	100 mm
Length in front of notch l_v	180 mm	Span L	3,400 mm

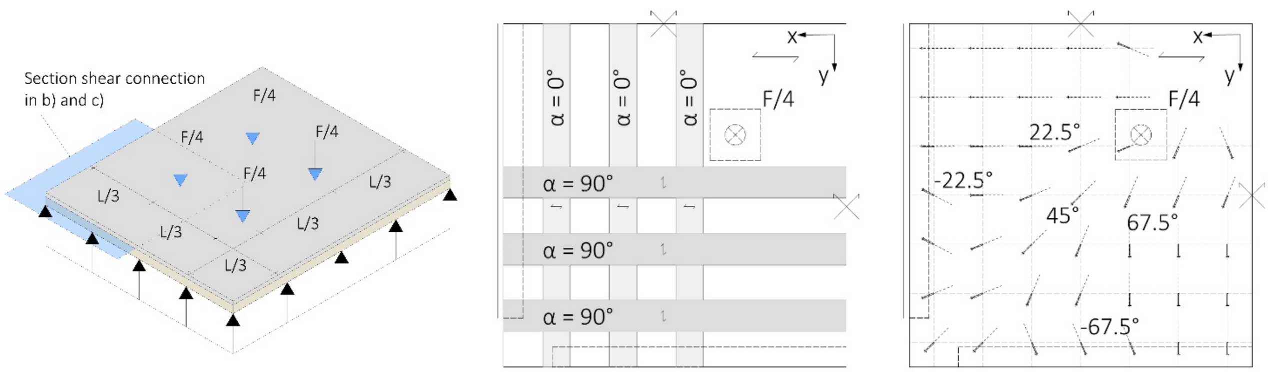

a) Test setup *b) Notch shear connection* *c) Screw shear connection*

Figure 12. Full plate test – Setup and specfic specimen design.

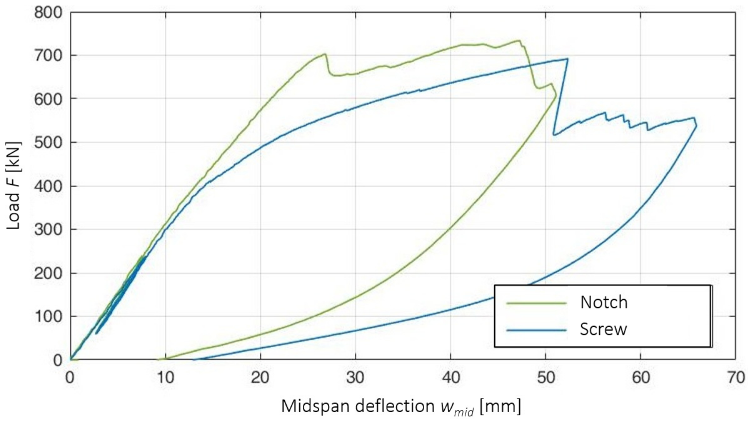

Figure 13. Load-deflection-curve to full plate test.

4.3 FEM-Model

The experimental examinations were accompanied by FEM-simulations. The slab with notches as shear connectors was simulated in a fully scaled solid model. For the screws a simplified model was developed. In the simplified model, the shear stiffness of the screw connection is distributed uniformly over the plane of the slab and is transferred into the top CLT-layer by calculating the slip modulus of the screws into the shear modulus. With this method, the modelling and processing effort was reduced a lot. Potential shear reinforcement effects of the inclined screws on the CLT-element are not covered. In comparison, the FEM-models behave softer than the plate test results. From the perspective of serviceability, this behaviour is on the safe side. The simplified model is applied on investigations in the next Sections 4.4 – 4.7.

4.4 Biaxial load-bearing behaviour

In the FEM-simulation following the full plate test setup, the effective biaxial load-bearing behaviour of the composite-slab was evaluated by comparing the vertical support reactions in principal and transverse direction. In a perfect isotropic plate, a uniformly distributed load would spread 50/50 into the supports of both axis. For the orthotropic CLT-concrete-composite-slab, the load distributes in a range of 55/45 to 58/42. This demonstrates a clear biaxial load-bearing behaviour.

4.5 Torsion

The torsional bending is an essential mechanism of the load bearing behaviour of a plate. In experimental examinations regarding the torsional bending stiffness, the influence of different construction parameters such as CLT-layer configuration or shear connectors was quantified. The composite-slab behaves very ductile when exposed to torsional bending, the ultimate force was not reached while the deflection exceeded the testing setup limits with w_{max} > L/30. The cracking of the concrete layer results in a considerable loss of torsional bending stiffness. The samples with $h_{concrete}/h_{CLT}$ = 0.5 und L/h = 8.5 showed a loss of 58% - 67%. The minimum reinforcement was not taken into account, as it was placed in middle height of the concrete layer. To quantify the share and the influence of the torsional behaviour on the plate load-bearing behaviour, the shear modulus in plane was compared for all materials in the FEM-simulation ($G_{xy,FEM} = G_{xy,material}$ vs. $G_{xy,FEM} = 0$). As a result, the deflection of a two-way spanning composite slab with torsional stiffness close to zero is about 25% higher in comparison to a slab with uncracked concrete (with L/h = 19).

4.6 Comparison

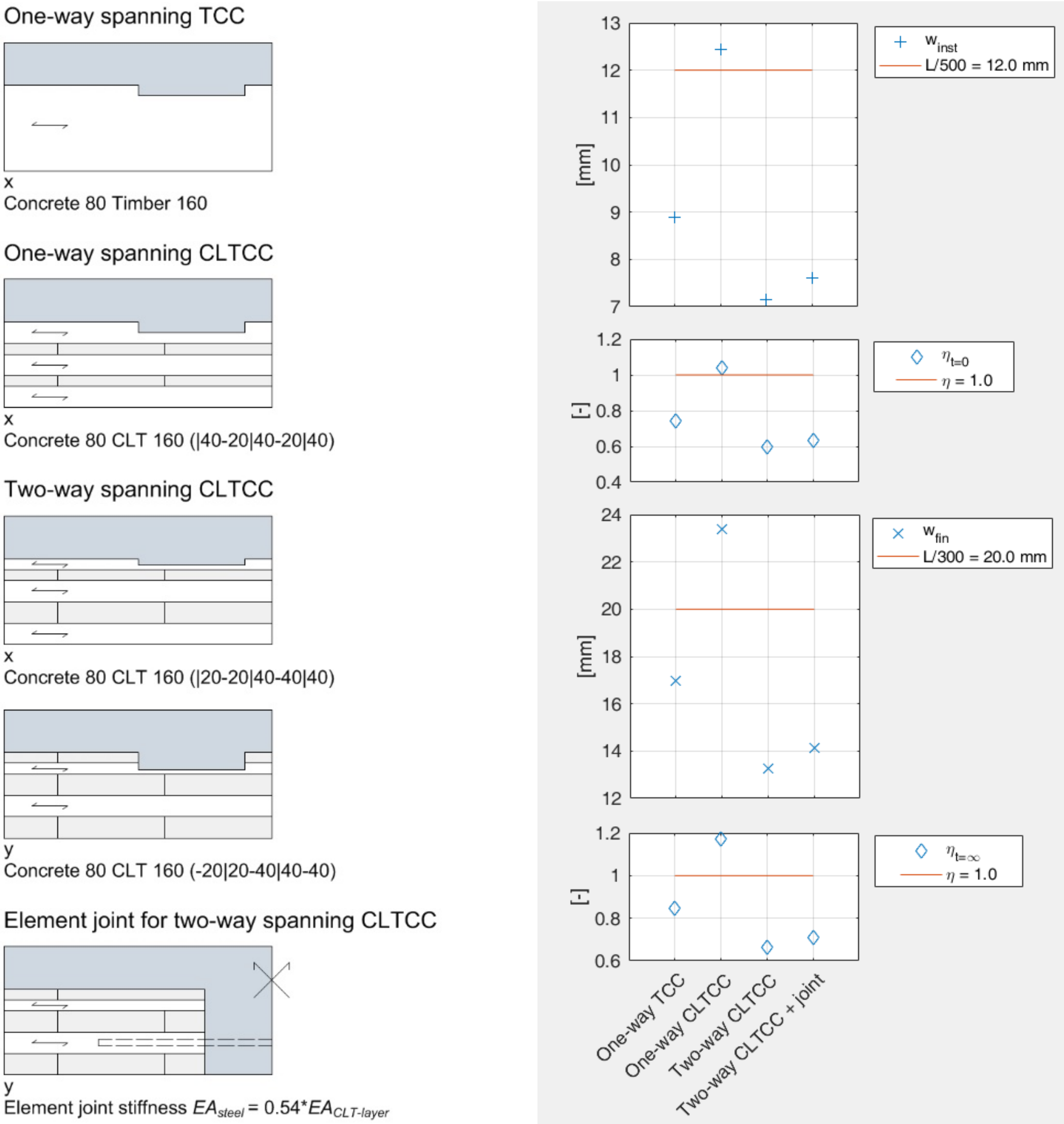

Figure 14 Comparison by deflection of different timber-concrete-composite slabs

Based on the earlier investigations, FEM-simulations on different slab assemblies in one-way and two-way spanning directions and side lengths L_x x L_y = 6.0 m were conducted, see Figure 14. Material properties accord with Table 1. For the shear connection a continuous distributed slip modulus in plane K_A = 1,778 kN/mm/m² was taken, which equates to a notch connection with K_{ser} = 800 kN/mm/m every 0.45 m. The applied element joint stiffness with $EA_{steel} = 0.54 \cdot EA_{CLT\text{-}layer}$ results from ten reinforcement bars per metre and side with d = 12.0 mm. The full load value was set to $p_{k,inst}$ = 7.9 kN/m² and $p_{k,q\text{-}p}$ = 6.7 kN/m². The benchmark of comparison was the serviceability limit state with the characteristic midspan deflection w_{inst} and final deflection w_{fin}. Having the same height, the deflection w_{inst} reduces by 38.8% from one-way spanning CLTCC to two-way CLTCC + joint and by 14.3% from one-way TCC to two-way CLTCC + joint.

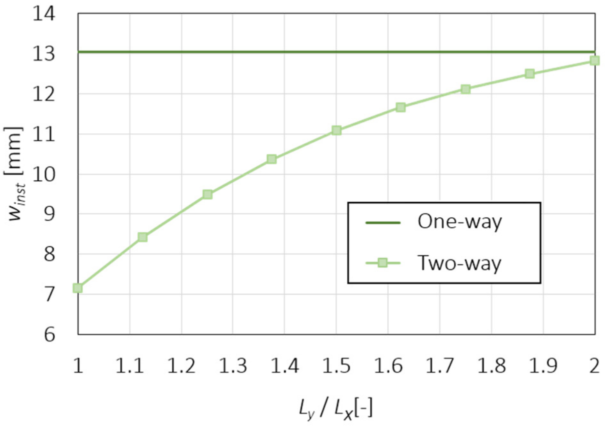

Figure 15 Influence of the side length ratio on the maximum deflection

4.7 Side length ratio

The influence of the side length ratio on the characteristic deflection w_{inst} was determined by FEM for the assembly two-way spanning CLTCC according to Section 4.6 and L_x = 6.0 m. The result is given in Figure 15. With a side length ratio L_y / L_x = 2.0 the deflection of the two-way spanning slab converges the one-way spanning.

5 Conclusion

The applicability of the TCC-construction method for two-way spanning systems was demonstrated. Solutions for the arrangement of shear connectors and CLT-layers within the slab were found. The influences of torsion on the plate load-bearing behaviour was determined. With glued-in reinforcement bars, a connection was developed, which meets the requirements of stiffness and practical buildability. A comparison with one-way spanning TCC-slabs shows distinct material reduction potentials.

The next step is to develop a calculation model for two-way spanning CLT-concrete-composites that can be applied with established instruments in practice.

6 References

ANSYS 17.1 (2016): Finite-element-software. Workbench, Release 17.1, Ansys Inc.

Blaß, H. J. et al. (1995): Trag- und Verformungsverhalten von Holz-Beton-Verbundkonstruktionen. Research report. Karlsruhe Institute of Technology.

Blaß, H. J. et al. (2006): Tragfähigkeit von Verbindungen mit selbstbohrenden Holzschrauben mit Vollgewinde: Karlsruher Berichte zum Ingenieurholzbau 4. Karlsruhe Institute of Technology.

DIN EN 1991-1-1/NA (2010): National Annex - Nationally determined parameters - Eurocode 1: Actions on structures - Part 1-1: General actions - Densities, self-weight, imposed loads for buildings. DIN.

DIN EN 1995-1-1/NA (2013): National Annex - Nationally determined parameters - Eurocode 5: Design of timber structures - Part 1-1: General - Common rules and rules for buildings. DIN.

EN 338 (2016): Structural timber - Strength classes. CEN. Brussels

EN 1991-1-1 (2010): Eurocode 1: Actions on structures - Part 1-1: General actions - Densities, self-weight, imposed loads for buildings. CEN. Brussels

EN 1992-1-1 (2011): Eurocode 2: Design of concrete structures - Part 1-1: General rules and rules for buildings. CEN. Brussels.

EN 1995-1-1 (2010): Eurocode 5: Design of timber structures - Part 1-1: General - Common rules and rules for buildings. CEN. Brussels.

EN 16351 (2015): Timber structures – Cross-laminated timber – Requirements. CEN. Brussels.

EN 26891 (1991): Timber structures; joints made with mechanical fasteners; general principles for the determination of strength and deformation characteristics. CEN. Brussels.

ETA-13/0029: Wuerth ASSY Plus VG: Self-tapping screws for use in wood-concrete slab kits. Valid from 01/2013 to 07/2017. ETA Denmark.

ETA-09/0036: MM-crosslam: Solid wood slab elements to be used as structural elements in buildings. Valid from 06/2013 to 06/2018.

Kudla, K. (2015): Notched Connections for TCC Structures as Part of the Standard: COST Action FP1402 - Short Term Scientific Mission. Report. University of Stuttgart.

Leonhardt, F. et al. (1973): versuche zur Ermittlung der Tragfähigkeit von Zugschlaufenstößen. In: Deutscher Ausschuss für Stahlbeton, Band 226.

Loebus, S. and Winter, S. (2017): Zweiachsige Tragwirkung bei Holz-Beton-Verbundkonstruktionen. Final report. Technical University of Munich.

Mestek, P. (2011): Punktgestützte Flächentragwerke aus Brettsperrholz (BSP) – Schubbemessung unter Berücksichtigung von Schubverstärkungen. Dissertation. Technical University of Munich.

Mestek, P. et al. (2011): TEILPROJEKT 15: TP 15 Flächen aus Brettstapeln, Brettsperrholz und Verbundkonstruktionen. Research report. Technical University of Munich.

Michelfelder, B. C. (2006): Trag- und Verformungsverhalten von Kerven bei Brettstapel-Beton-Verbunddecken. Dissertation. University of Stuttgart.

Steiger, R. (2012): In Brettschichtholz eingeklebte Gewindestangen: Stand des Wissens zu einer leistungsfähigen Verbindungstechnik. In: Tagungsband 18. Internationales Holzbau-Forum.

Z-9.1-648: Würth ASSYplus VG Schrauben als Verbindungsmittel für Holz-Beton-Verbundkonstruktionen. Valid from 11/2012 to 11/2017. DiBt.

Z-9.1-705: 2K-EP Klebstoff WEVO-Spezialharz EP 32 S mit WEVO-Härter B 22 TS zum Einkleben von Stahlstäben in Holzbaustoffe, WEVO Chemie GmbH.

Discussion

The paper was presented by S Loebus

H Blass asked what would be the typical application. S Loebus responded 6 m x 6 m or 7 m x 7 m rooms such as classroom in schools as well as cases with posts and concentrated supports.

H Blass asked what would be the advantage over a pure CLT plate. S Loebus responded that this system would be much stiffer and the concrete would be available for acoustic control already. A Ceccotti added that in this system control of floor vibration would be advantageous also. H Blass further asked would the same advantage be available for a pure CLT system of equal height. S Loebus agreed that CLT is a two way system. S Winter said that in this study they used weak concrete on purpose. Better results would be achieved if higher quality concrete was used.

A Palermo asked about the effect of shrinkage of the concrete. S Loebus discussed about shrinkage effects and stated that the study had not yet been extended to long term studies.

A Buchanan commented that the shrinkage in the concrete on top would lead to higher deformation. S Loebus said that minimum reinforcement for shrinkage crack control was used. Also fire performance for two way spanning system should be better because of more levels of redundancy. A Buchanan agreed as tensile membrane action would be available.

M Gershfeld and S Loebus discussed the efficiency of Ly/Lx ratio. S Loebus said that the reinforcing bar needed to be introduced in the second layer and Ly/Lx ratio of one would be more efficient. M Gershfeld said that no need for drop beam would be a great advantage.

R Jockwer asked whether changes in load sharing were observed when screws began to fail versus the notched case. S Loebus said that the distribution of load did not seem to change. When screws failed in one area, concrete uplifting was observed in the region with screw pull out of the CLT. Support loads were only obtained from linear elastic FEM and not from tests.

M Li asked about installation of screws as double incline installation in some locations could lead to confusion in practice. H Blass commented that putting two full grids of screws in the two main axes would be a practical solution. S Loebus said that the slip modulus of the screws not applied in the direction of the principle axis would be an issue. H Blass disagreed. S Winter said that too many screws would be too expensive and notches would be more cost effective.

Shake Table Tests on Large-Scale Hybrid Steel Frame and Timber Shear Wall System with Slotted-Bolted Friction Dampers

Hanlin Dong, Ph. D. student, Tongji University

Zheng Li, Assistant Professor, Tongji University

Qi Luo, Ph. D. student, Tongji University

Minjuan He, Professor, Tongji University

Keywords: Hybrid steel-timber structure, Slotted-bolted friction damper, Shake table test, Large-scale specimen

1 Introduction

Timber is a renowned building material for its sustainability. However, the height of pure timber construction is limited in most countries due to its combustibility. To make timber buildings taller, a kind of hybrid steel-timber structural system has been proposed by *He et al.(2014)*. Such system has two lateral force resisting subsystems, i.e. steel moment resisting frame, and light wood-frame shear walls. A number of research have been carried out on such system. *He et al.(2014)* carried out reversed cyclic tests on several 1-story-3-bay hybrid system specimens, confirming that the installation of the shear wall system had a significant increase on the initial lateral stiffness of the bare steel frame. The wood-frame shear wall was effective in the initial stages of loading, but the effectiveness began to lose after damage developed in the shear walls. Numerical simulations carried out by *Li et al.(2013, 2014)* have further proved that this system is less efficient if a high performance level is required.

As is mentioned by *He et al.(2014)*, the connections between the steel frame and the shear wall had a significant influence on the total lateral behavior. Thus, the connections are improved to achieve a higher stiffness and higher level industrialization utilizing slip-critical high-strength bolts and steel connectors. During a severe earthquake, the wood-frame shear walls in the conventional hybrid system suffered from large damage, which led to a great degradation in their lateral stiffness. To improve this, supplemental slotted-bolted frictional dampers are introduced to this system. These dampers served also as the connections between the steel frame and the timber shear walls. The dampers are supposed to prevent the walls from suffering large seismic force. Thus, the performance of the shear wall under large earthquake is improved.

In this paper, the new type of connection is firstly introduced. This connection can be easily modified into a slotted-bolted friction damper. The design concept and lateral load resisting mechanism of the damper connection is described. Then, a series of shake table tests on a 4-story hybrid structure with and without supplemental dampers are introduced, and some structural responses reflecting the seismic behavior is compared and discussed.

2 Steel-Timber Connection

The connection between steel frame and timber shear walls is the key part of hybrid steel-timber structure. The proper design of the connections makes the structure easy-to-assemble and robust. Nail and bolts are commonly used connections between wood and steel. However, pure nail or bolt connection are not highly industrialized, which takes more time and in-situ manual work to assemble. The hybrid steel frame – timber shear wall system is supposed to enjoy a high-level of industrialization. The shear walls are supposed to be pre-fabricated in factory, and assembled on site. Therefore, the connections must be suitable to this concept. A cross-slotted steel-timber connection with a high error-tolerance is proposed by the authors. This connection can be easily modified into a slotted-bolted damper connection. In the following subsections, these two connections are introduced.

2.1 Cross-Slot Connection

The steel-timber connection is a novel connection which can be widely used in prefabricated steel-timber connections. The schematic configuration of such connection is shown in Figure 1(a). The upper part is a steel plate welded or bolt-connected to the steel frame. In the steel plate, a long slot is drilled for bolt connection. The lower part is a steel connector. This connector has bolt or nail holes in the lower side, through which bolts or nails can connect the it to the timber shear wall. In its upper part, another long slot, whose axis is perpendicular to the slot in the afore-mentioned slot, forms a so-called cross-slot connection. Slip-critical high-strength bolt can be inserted into the cross-slot so that the steel structure and timber structure are connected.

The error-tolerance mechanism of the connection is illustrated in Figure 1(b). For the steel frame of hybrid steel-timber structure, the sections are usually relatively small. So the initial bending imperfection can be correspondingly significant. This may cause the steel frame suffer from a translation or rotation from the designed position relative to the timber structure. However, this initial imperfection will not cause any assembly problem to the cross-slot connection. Thick washers are used to distribute the normal force in the bolt, to ensure a slip-critical connection.

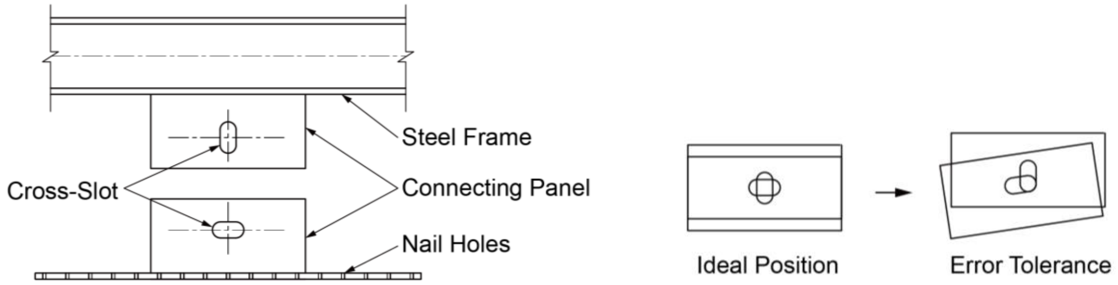

(a) Cross-slot connection *(b) Error-tolerence mechanism*

Figure 1. Schematic drawing of cross-slot connection

2.2 Slotted-bolted connection

The slotted-bolted connection is a steel-timber damper connection. The concept of this connection is illustrated schematically in Figure 2(a). This connection, based on the cross-slotted connection, utilizes the concept of frictional damper. Several friction pads are inserted to the recesses milled in the steel plates near the vertical slot to form a reliable friction surface. *Kim(2007)* has carried out several tests on the friction pads of different material, and convinced their stability and durability. The horizontal slot is lengthened to leave space for the high-strength bolt to slide. The prestress of the bolt and the slot length are especially designed for each connection to achieve a better overall performance for the building. *Guo(2012)* has proposed one solution to determine these values.

The concept of the slotted-bolted damper connection is described in Figure 2(b). When the lateral force exceeds the activation force (i.e. the maximum static friction force), the bolt, together with the lower part of the connection, begins to slide. The frictional force keeps nearly constant during the whole sliding procedure, so that a great deal of energy is dissipated by the work of the frictional force. At this time, the shear force in the damper, which equals to the kinematic frictional force, does not increase, so that the connected shear wall can be protected by the damper. This is the most important reason that the damper is used in the steel-timber connection in the hybrid steel-timber structure. It is worthy to mention that when the bolt reaches the edge of the horizontal slot, it cannot further move in that direction, so the damper is called to be locked by the slot. At this time, the force of shear wall in this direction can further increase.

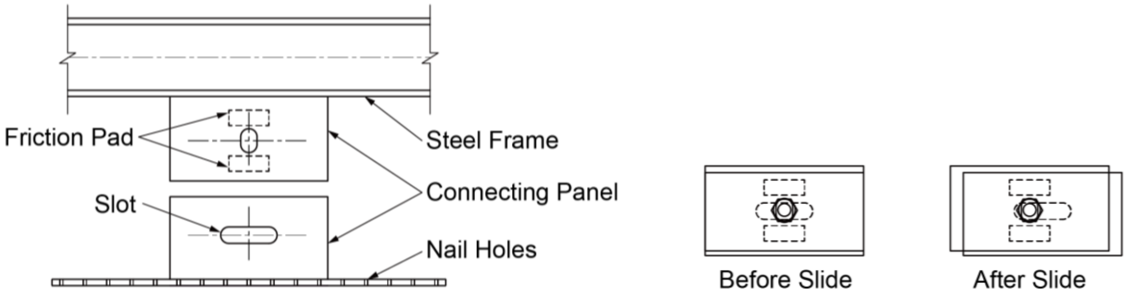

(a) Slotted-bolted connection *(b) Damper sliding mechanism*

Figure 2 Schematic drawing of slotted-bolted connection

In the perspective of the overall building, the advantages of employing such damper connections are shown in Figure 3. At low lateral loading levels (Figure 3a), the supplemental damper is not yet activated, and therefore acts as a connection element between the timber shear wall and the steel frame with large stiffness. The steel moment resisting frame and the timber shear walls deform together to resist lateral forces and provide a high stiffness for wind loading and low amplitude seismic loading (Figure 3b). As the applied lateral the force increases, when the timber shear wall reaches a specially designed load, the supplemental damper is activated, i.e. sliding initiates (Figure 3c). After this point, even though the inter story drift keeps increasing, the applied forces and deformations in the timber shear wall cease to increase, and remains in the elastic response range. The timber infill wall is therefore protected even under very severe seismic loading. In this system, the dampers dissipate earthquake energy instead of the timber infill walls. If the lateral deformation keeps on increasing to a point where the lateral stability of the system is threatened, the damper is designed to lock when the bolt reaches the end of pre-defined slots inside the damper. When this occurs, the timber shear wall is engaged again, increasing the stiffness and the strength of the structural system (Figure 3d) and further protecting against collapse as damage is induced in the shear wall. Only under such extreme loading conditions, would the timber shear walls have to be repaired or replaced.

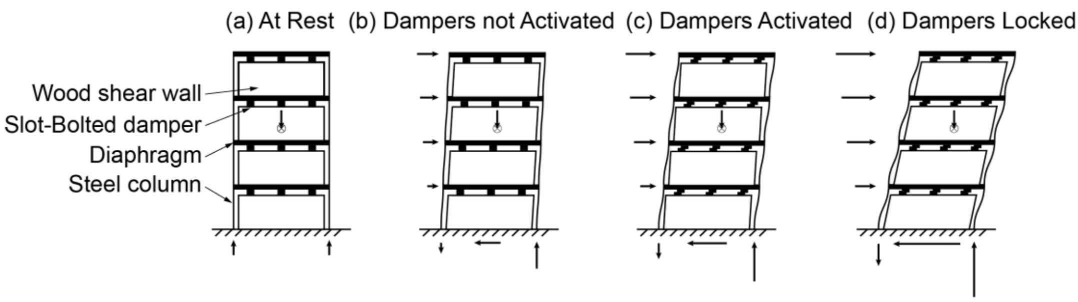

Figure 3. Concept of Damper in an Overall Structure

In the hybrid steel-timber structure, the connections can be either the cross-slotted connection, or the slotted-bolted connection. The arrangement of these connections should be based on engineering judgments or other advanced design theories like that proposed by *Guo*(2013).

3 Shake Table Tests

Large-scale shake table test is a desired way to obtain the real seismic behaviour of a new structural system. A handful of shake table tests on timber structures have been done recently (*Ceccotti* 2013, *Tomasi* 2015, *Lindt* 2016). The experimental observations and data collected were convincing in describing the overall behaviour of structure and the hysteresis behaviour of lateral force resisting components. To better understand the seismic behaviour of this hybrid system, a series of shake table tests have been carried out. The main objective was to observe and compare the inter-story drift and shear force response of damped and undamped system.

3.1 Test Specimen

3.1.1 Overview

The specimen was a scaled substructure of a prototype office building. The layout of the prototype is shown in Figure 4. In the figure, the black dotted lines represent timber shear walls. The red dotted rectangle region in the plan view represents the substructure tested.

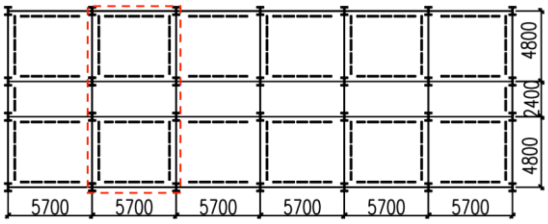

(a) Plan View

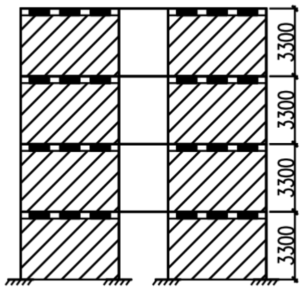

(b) Elevation View

Figure 4 Prototype Structure

The scaling factor in dimension was 2/3 (specimen over prototype). To meet the dimensional similitude law, another two scaling factors should be determined. Here, as the material of the specimen was the same as that of the prototype, the scaling factor of stress and modulus of elasticity was set to be 1. Considering the mass and overturning capacity of the shake table, the acceleration scaling factor was set to be 2. Other scaling factors was determined by these three values.

The test specimen was a 4-story, 3-span, 1-bay structure. The plan layout of the structure was 8m x 3.75m in axis. The three spans were 3.2m, 1.6m and 3.2m, respectively. The total height of the specimen was 8.8m. The height of each story was 2.2m. The elevation view of the specimen is shown in Figure 5.

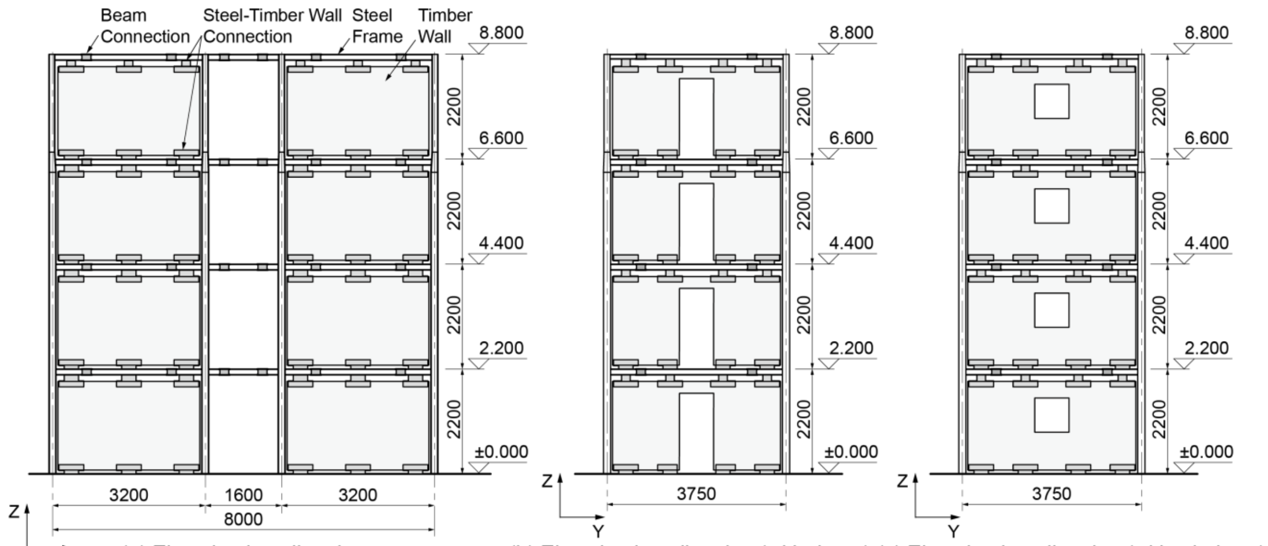

(a) Elevation in x direction (b) Elevation in y direction (with doors) (c) Elevation in y direction (with windows)

Figure 5 Elevation view of the specimen

3.1.2 Steel frame

The material of steel frame was Q235 defined in Chinese *Code for design of steel structures GB50017*(2003). The sections of the steel members are shown in Table 1. The steel beams were connected to the columns by splice connections with high-strength bolts. The end of the beam brackets was welded onto the column. 6mm Doubler plate was welded to the panel zone to improve stiffness. The configuration of the beam-to-column connection is shown in Figure 6(a). An 25mm-thick end plate was welded to the column foot. It was connected to the shake table via a steel foundation. The configuration of the steel column is shown in Figure 6(b).

Table 1 Steel frame sections

Item	Floor	Section
Beam in *x*-direction	L1~L3	HW125x125x6.5x9
	L4	HW100x100x6x8
Beam in *y*-direction	L1~L4	HW125x125x6.5x9
Column	L1~L3	HW150x150x7x10
	L4	HW125x125x6.5x9

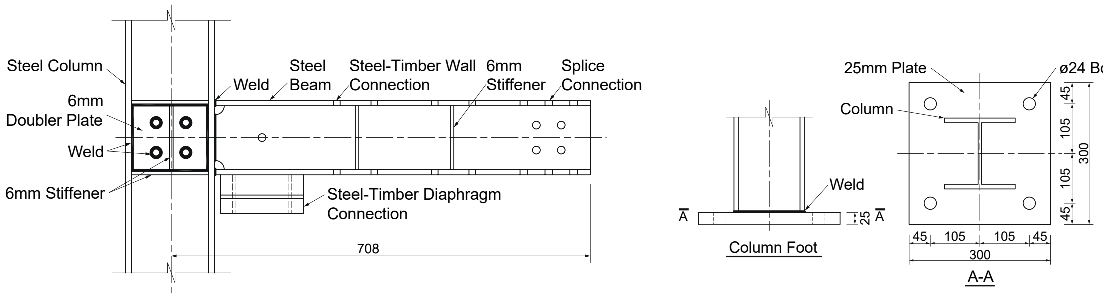

(a) Beam-to-column connection *(b) Column foot*

Figure 6 Steel frame configuration

3.1.3 Timber shear wall

The material of timber used in this specimen was SPF (Spruce-Pine-Fir) class B. The moisture content was 13%~17%. Timber shear wall utilized the shear walls of light frame timber construction. The timber frame was made of 38mm x 89mm dimension lumbers. Three layers of sill plate and wall plate were designed to make space for steel-timber connection. The timber frame was connected by 3.3mm pneumatic nails. The sheathing panels were 12mm OSB panels. The sheathing panels were connected to the frame by pneumatic nails. The configurations of the shear wall frames are shown in Figure 7. In *x* direction, the axial distance of the studs was 406mm. The sheathing OSB panel was divided into four parts. In *y* direction, openings were set to the shear walls representing the windows and doors in the prototype. The dimension of these openings and sheathing panel partition are shown in Figure 7(b). The nailing space of all the shear walls are listed in Table 2.

Table 2 Detailing of timber shear walls

Type	Story	Sheathing	Nailing Space (outer-inner, mm)
Wall in *x* direction	L1	Double	75-150
	L2	Double	100-200
	L3	Double	150-300
	L4	Single	125-250
Wall in *y* direction	L1	Double	75-150
	L2	Double	75-150
	L3	Double	100-200
	L4	Double	125-250

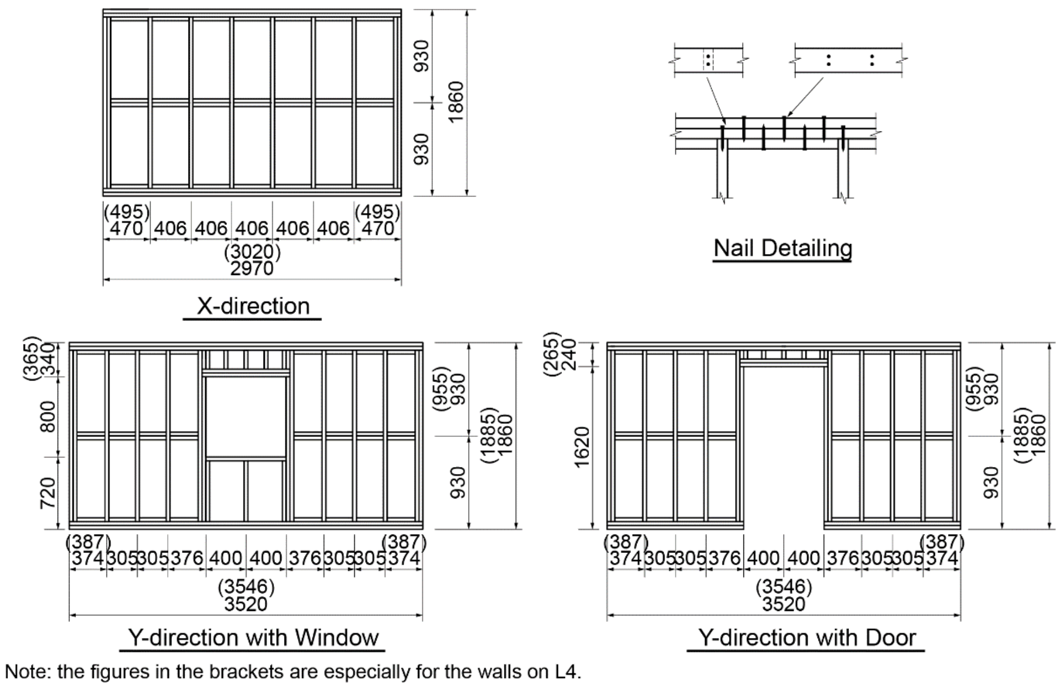

(a) Timber shear wall framing

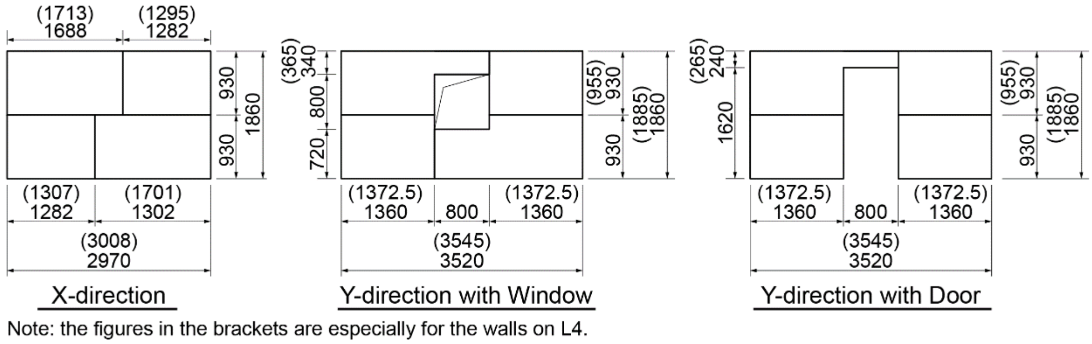

(b) Timber shear wall sheathing

Figure 7 Configuration of timber shear wall

The timber shear walls were connected to the steel frame utilizing the cross-slotted connection and the slotted-bolted damper connection. In *x* direction, in which was interested, slotted-bolted damper connections were set on the top of the shear walls on story 1 to 3. For story 4 in *x* direction and all the connections in *y* direction, the cross-slotted connection were set on the top of the shear walls. As for the bottom of the shear walls, they were connected right after the walls were lifted into position, so align adjustment in vertical direction was unnecessary. Therefore, another steel connector without bolt was used. These three kinds of connections are illustrated in Figure 8. Figure 8(a) is the cross-slotted connection on the top. Figure 8(b) is the steel connector on the bottom. Figure 8(c) is the slotted-bolted damper connection on the top.

For the slotted-bolted damper connection used in the test, an explosion figure (Figure 8d) better illustrates its configuration. It is slightly different from the schematic drawing in the former section. The upper steel panel is modified into two T-shape connectors that were connected to the beam flange with slip-critical high-strength bolts. Two recesses were milled in each T-shaped connector to hold the friction pads. The two connectors nipped the lower steel panel. The lower steel panel is part of a Y-shaped connector. The two arms of the connector hoop the timber shear wall, and connects to it by self-tapping screws. Two extra round holes are used in both the upper steel T-shaped connector and the lower Y-shaped steel connector. These holes are called disabling holes. If bolts are inserted into these holes, the bolts are no longer able to slide, so the dampers are disabled. The structure system without damper is formed by disabling all the dampers. The dampers can also be enabled again by removing the side bolts. In this way, two structure systems, the damped system and the undamped system can be switched to each other during the test to compare the different behavior.

The material of friction pad used in this specimen was NAO780. Before the test, a series of pilot tests were carried out to obtain the behavior of different friction pads and frictional surfaces. The NAO780 pad with mill steel surface and M16 bolt has been proved to be a better choice among all the combinations tested. The activation loads of the dampers were controlled by applying specified torque to the bolts using a torque wrench. The bolt torque used in the test were 120N•m, 90N•m and 60N•m for story 1 to 3, respectively. The corresponding activation load was expected to be 15kN, 10kN and 5kN for each damper, respectively.

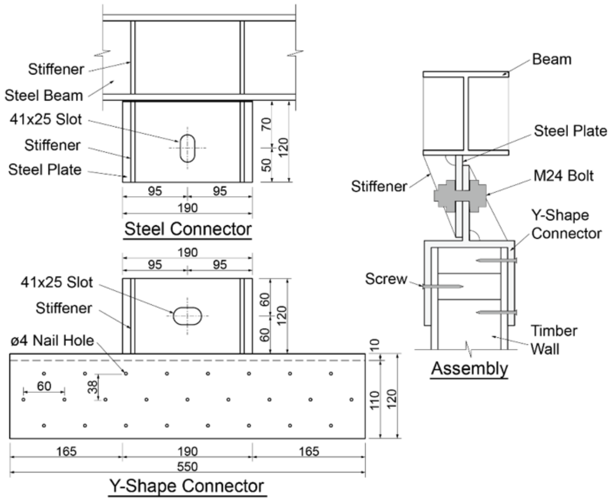

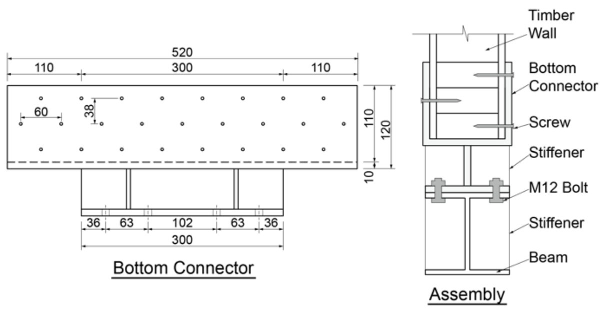

(a) Cross-slot connection on the top of the wall (b) Steel connector on the bottom of the wall

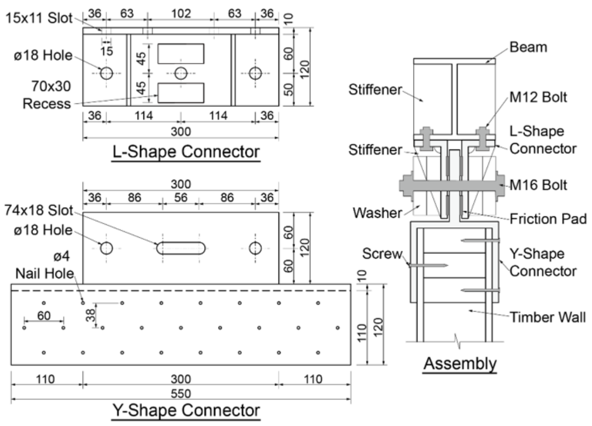

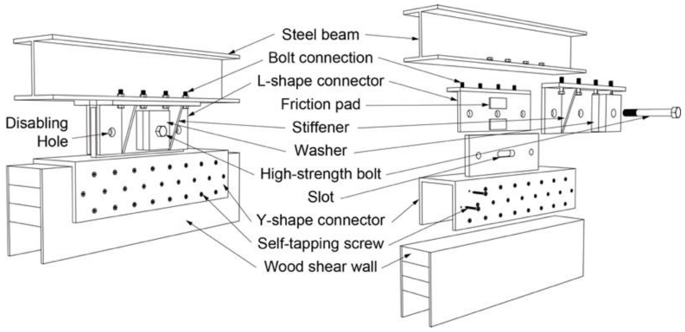

(c) Slot-bolted damper connection (d) Damper explosion view

Figure 8 Configurations of the steel-timber connections in the test

3.1.4 Timber diaphragm

The diaphragm was conventional timber diaphragm with dimension lumber joists and OSB panel decking. The joists were connected to the steel beams with steel plate supporters welded onto the bottom flanges of the beams or gusset plates on the splice connection in factory. They were fastened by masonry nails. The configurations of the connections are shown in Figure 9. Supplemental mass bricks were adhered to the decking with silicon gel. The total mass of the specimen for each story from 1 to 4(roof) were 13141kg, 13141kg, 13067kg, 8556kg, respectively.

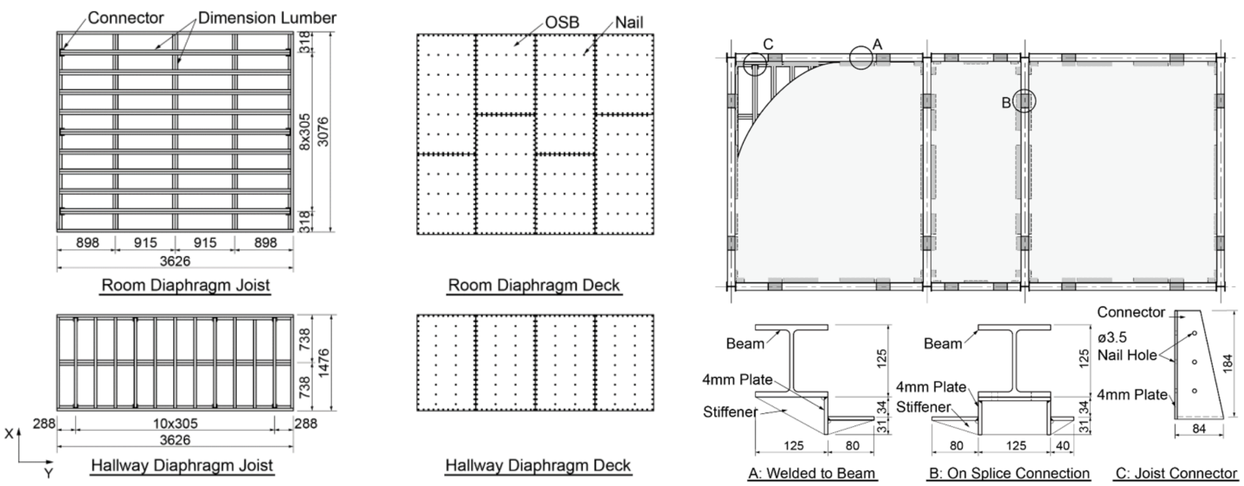

(a) *Diaphragm joists and decking* (b) *Diaphragm connections*

Figure 9 Configurations of timber diaphragm

3.2 Test Program

Four intensity of earthquakes were considered: minor, moderate, major and extreme earthquakes. The minor, moderate and major earthquakes were defined as the frequent, basic and rare earthquake whose design basic acceleration was 0.20g (seismic precautionary intensity VIII) according to Chinese *Code for seismic design of buildings GB50011* (2010). The extreme earthquake was defined as the rare earthquake whose design basic acceleration was 0.30g (seismic precautionary intensity VIII). The input excitations were based on historical earthquake acceleration records. They were Wenchuan earthquake (Wolong station, EW direction, 2008), El Centro Earthquake (NS direction, 1940), and KOBE earthquake (KJMA station, NS direction, 1995). These records were modified to the input excitations by a two-step procedure. Firstly, the records were amplified to meet the earthquake intensity. In *GB50011* (2005), the amplification procedure is based on PGA. The PGA of each earthquake intensity is specified. For minor, moderate, major and extreme earthquake, they are 0.07g, 0.20g, 0.40g and 0.51g. So only a simple amplification factor was used to meet this specification. The spectra of the amplified major earthquakes are shown in Figure 10. For the second step of the two-step procedure, the amplified record was scaled according to the similitude law. The acceleration was scaled by multiplying the acceleration scaling factor 2, and the time was scaled by multiplying the time scaling factor 0.577.

During the test, the system with enabled damper (damped system) and disabled damper (undamped system) was studied. So the structure was changed between adjacent phases. To change the damped system to the undamped system, the disabling bolts were used. Before inserting the disabling bolts, some thin steel plates were tightly inserted between the steel panels to prevent the friction pad from suffering large pressure. The disabling bolts were fastened by torque wrenches to form a slip-critical connection, so that the timber wall could deform together with the steel frame during the whole excitation. To change the undamped system back to the damped system, the disabling bolts and temporary steel plates were removed, and the high-strength bolts were released and re-tightened to the designed torque by torque wrench. At first, the damped system under minor and moderate earthquakes were tested. Then the undamped system under minor and moderate earthquakes were tested. After that, the damped and undamped system under major earthquake was tested. For each earthquake intensity in these phases, three excitations in the order of Wenchuan, El Centro and KOBE were applied. At last, the damped system under extreme El Centro earthquake was tested. The test program is listed in Table 3. To acquire the response of the structure, displacement sensors (LVDTs) and acceleration sensors were set on each story at the top of the beams.

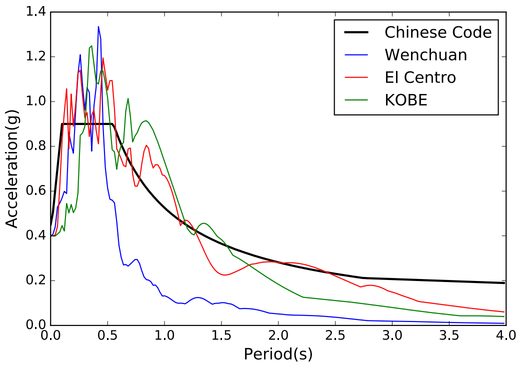

Figure 10 Earthquake spectra

Table 3 Loading program

No	System	Excitation	PGA(g)
1	Damped	3 minors	0.16
2	Damped	3 moderates	0.40
3	Undamped	3 minors	0.16
4	Undamped	3 moderates	0.40
5	Damped	3 majors	0.80
6	Undamped	3 majors	0.80
7	Damped	1 extreme	1.00

3.2.1 Test results

The photo of the test specimen is shown in Figure 11. The main test observations are shown in Figure 12. For minor, moderate earthquakes and major Wenchuan earthquake, little damage on the structure was observed. The damped system and the undamped system performed nearly identically. For major El Centro and KOBE earthquakes, the dampers were observed to slide as expected. Some corners of OSB panels were damaged due to bearing (Figure 12a). The commonly known nail pulling-out and embedment were observed in a limited range of positions. Some nails pierced the joists and studs (Figure 12bc). During major earthquake test, the upper and lower OSB panels of the shear wall were observed to have a relative displacement (Figure 12d). No severe damage was observed. The structure performed well under major, even extreme earthquake. The test ended up after PGA reached 1.0g for damped system, because the overturning moment was very close to the tolerance of shake table. It's important to mention that the overturning moment exceeded the tolerance of the shake table during major KOBE earthquake on the undamped system, so the PGA for this test was decreased to 0.75g (0.8g expected). Thus, in the following discussions, the major KOBE earthquake did not reach the expected intensity.

(a) OSB Corner Damage *(b) Joist Tearing*

(c) Nail Pierce Stud *(d) OSB relative displacement*

Figure 11 Specimen photo *Figure 12 Test observations*

The inter-story drifts and story shear forces were obtained. The inter-story drifts were calculated by dividing the relative displacement for each story by the story height. The absolute story displacement value was the average of the LVDTs results for a certain story. The story shear forces were calculated based on the story accelerations utilizing Newton's second law. The inter-story drifts and the story shear forces are plotted in Figure 13 and Figure 14, respectively.

The largest inter-story drift of the four stories occurred at story 2, though the inter-story drift of the first three stories varied not much. The drift response was quite small for Wenchuan earthquake, compared to that for the other two earthquakes. For minor earthquakes, the inter-story drift of damped and undamped systems were identical. For moderate earthquakes, some differences appeared. The global drift of the damped system under KOBE earthquake was a little smaller than that of the undamped system. This difference was more obvious under major earthquake. However, for El Centro earthquake, the drift was similar for the two systems even under major earthquake. After extreme earthquake excitation, the largest inter-story drift reached nearly 0.9%. This showed the great seismic behaviour of the hybrid steel-timber structure.

As for the story shear, structure under Wenchuan earthquake attracted less seismic load compared to the other two earthquakes. The story shear force of minor and moderate earthquakes of damped and undamped system were identical. For major earthquakes except Wenchuan earthquake, apparent difference was observed. The shear force of damped system of the first floor was 13% smaller than that of the undamped system for El Centro earthquake. Though the PGA of damped system under major KOBE earthquake was larger than that of undamped system, the story shear force was smaller. This result indicated that the damped system attracted less seismic force than the undamped system. The dampers were effective during the seismic excitations.

The shake table test further concluded that the hybrid steel-timber system with dampers had a good seismic behaviour. The largest inter story drift under extreme earthquake was limited to 1%. The dampers played an important role in reducing the seismic shear force in the structure.

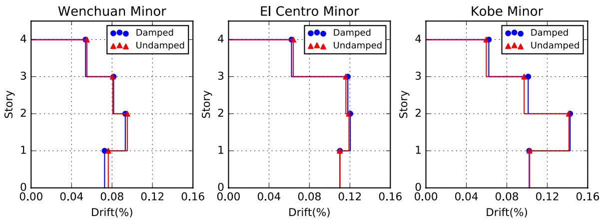

(a) Minor earthquake

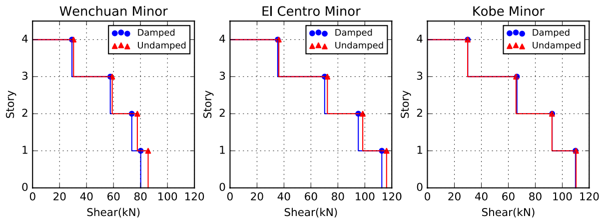

(a) Minor earthquake

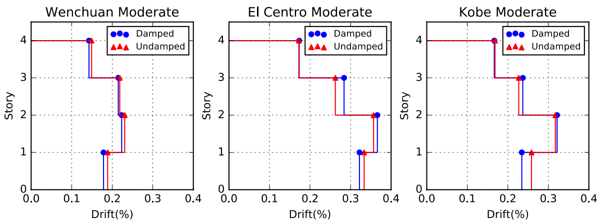

(b) Moderate earthquake

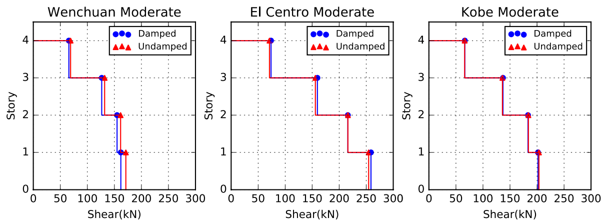

(b) Moderate earthquake

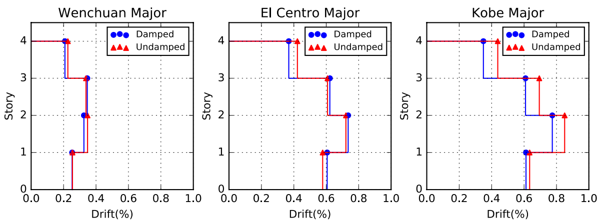

(c) Major earthquake

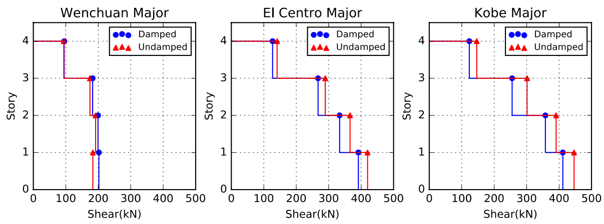

(c) Major earthquake

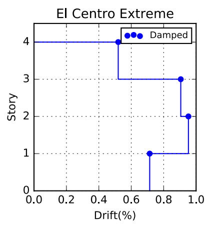

(d) Extreme earthquake

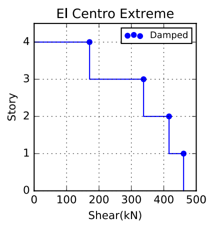

(d) Extreme earthquake

Figure 13 Inter-story drift response

Figure 14 Story shear force response

4 Conclusions

To make timber structure taller, a hybrid steel-timber lateral load resisting system has been proposed. This system utilizes steel moment resisting frame and timber shear wall to resist seismic shear force. The key design consideration of such system is the steel-timber connection. In this paper, two novel steel-timber connections, i.e. cross-slotted connection and slotted-bolted damper connection are proposed. The cross-slotted connection has a high tolerance of pre-fabrication error, so that a highly industrialized hybrid system can be realised. The slotted-bolted damper connection is supposed to improve the overall behaviour of the hybrid structure, and protect the timber shear wall from large damage.

To capture the behaviour of the system, a 2/3 scaled substructure is tested on the shake table. The damped system and undamped system were compared. The excitations were scaled to four intensities. The test results showed that the hybrid structural system had good seismic performance. Only a little damage was observed after all the earthquake excitations. The damped system attracted less seismic force.

In the future work, a numerical model will be developed based on the data obtained from the shake table tests as well as the corresponding planar frame tests, to capture the behaviour of the system. Then parametric studies will be carried out to propose guidelines of designing such structure.

Acknowledgement

The authors acknowledge support from *The National Natural Science Foundation of China: Seismic Performance and Design Method of Multi-Story Timber-Steel Hybrid Structures Grant No. 51378382*, as well as *the Foundation of World-Class International Research Collaboration on High-End Disciplines in Civil Engineering of Tongji University: Research on Seismic Damage Mechanism and Energy Dissipation Optimization of Multi-Story Hybrid Steel Frame – Timber Shear Wall Structure*.

Reference

Ceccotti, A., Sandhaas, C., Okabe, M., et al. (2013): Sofie project - 3d shaking table test on a seven-storey full-scale cross-laminated timber building. Earthquake Engineering & Structural Dynamics, 42(13): 2003-2021.

GB50017 (2003): Code for design of steel structures (in Chinese).

GB50011 (2010): Code for seismic design of buildings (in Chinese).

Guo, J. W. W., Christopoulos, C. (2012): Performance spectra based method for the seismic design of structures equipped with passive supplemental damping systems. Earthquake Engineering & Structural Dynamics, 42(6): 935–952.

He, M., Li, Z., Lam, F., et al. (2014): Experimental investigation on lateral performance of timber-steel hybrid shear wall systems. Journal of Structural Engineering, 140(6): 04014029.

Kim, H.J. (2007): Self-centering steel moment-resisting frames with energy dissipating systems. Doctoral thesis, University of Toronto, Ontario, Canada.

Li, Z., He, M., Lam, F., et al. (2013): Finite element modelling and parametric analysis of timber-steel hybrid structures. The Structural Design of Tall and Special Buildings, 23(14): 1045–1063.

Li, Z., He, M., Li, M., et al. (2014): Damage assessment and performance-based seismic design of timber-steel hybrid shear wall systems. Earthquakes and Structures, 7(1): 101–117.

Lindt, J. V. D., Bahmani, P., Mochizuki, G., et al. (2016): Experimental seismic behavior of a full-scale four-story soft-story wood-frame building with retrofits. II: shake table test results. Journal of Structural Engineering, 142(4): E4014004.

Tomasi, R., Sartori, T., Casagrande, D., et al. (2015): Shaking table testing of a full-scale prefabricated three-story timber-frame building. Journal of Earthquake Engineering, 19(3): 505-534.

Discussion

The paper was presented by Zheng Li

S Aicher asked how such system would re-center. Z Li said that they would need to un-tighten the bolts and rely on gravity to re-center the building. He said post tension tendon could be considered in a later study.

A Ceccotti received confirmation that Kobe JAM record with PGA of 0.8 g was considered and the amplification factor of 2 was found resulting in upper floor acceleration of 1.6 g.

A Palermo asked about the ductility for friction system and how would one design this. Z Li said that force based design was considered initially. A Palermo asked why it would be important to lock this device. Z Li said that it was needed to provide some robustness.

M Gershfeld asked if the test structure was the core of a building as there were few openings. Z Li said yes it was the core with a corridor between the two cores.

F Lam commented that the fundamental period of the structure was between 0.5 s to 1 sec and the various earthquake spectra were conditioned between these periods. He asked what the period of the higher mode for the building were as there were some high peaks in the conditioned spectra just below 0.5 sec. Z Li would check into this.

Dissipative joints for CLT shear walls

Tobias Schmidt, Hans Joachim Blass, Karlsruhe Institute of Technology, Germany

Keywords: cross laminated timber (CLT), ductile / dissipative connections, shear walls

1 Introduction

Plates or diaphragms made of cross laminated timber are ideal members to transfer vertical as well as horizontal loads in buildings. The excellent mechanical properties of CLT combined with a high degree of prefabrication enable CLT members to be used in residential as well as in other buildings, where steel and concrete are still the predominant building materials. Examples are industrial and commercial buildings, engineered timber structures in general and – in Europe – inner-city buildings up to about 10 storeys. However, the technical limit is far beyond 10 storeys. A recent example is the 18 storey Brock Commons Student Residence at the University of British Columbia in Vancouver, Canada. Here, a hybrid system is used with a first storey made of structural concrete and 17 storeys of mass timber construction with glulam columns and CLT floors. The vertical loads of the 53 m high building are transferred by the timber structure, while horizontal loads are transmitted by the CLT floor diaphragms to the two concrete cores. Since the building footprint is 15 m x 56 m, the floor diaphragms require a large number of joints between single panels. The accumulated length of these edge joints in the floor diaphragms is about 5 km.

Earthquake or wind loads on buildings cause diaphragm action in CLT members. CLT members are especially suited for in-plane loads due to their high shear strength and stiffness. However, the ductility and energy dissipation capacity of a CLT structure is mainly determined by the number and properties of the mechanical connections. Presently, the required energy dissipation capacity for earthquake loading is often achieved by metallic dowel-type fasteners loaded beyond their yield load. Both plastic embedding deformation of the timber as well as plastic bending deformation of the fastener contribute to energy dissipation. The load-slip curves for connections with laterally loaded dowel-type fasteners show pinched hysteresis loops under cyclic loads (FIGURE 1.1). Additionally, the achieved load at a certain displacement decreases under repeated loading – impairment of strength ΔF (FIGURE 1.1). Consequently, the connection properties change with the number of load cycles and the energy dissipation capacity decreases significantly (Ceccotti, 1995).

In order to achieve continued energy dissipation under the repeated cycles of a longer earthquake, the connection displacement needs to be continually increased. However, the displacement capacity in CLT shear walls is limited in practice e.g. due to the limited inter-storey drift especially for shorter wall sections.

The reason for the pinched hysteresis behaviour and the impairment of strength is the embedding deformation behaviour of wood: the wood is plastically compressed under the action of a dowel-type fastener leading to a cavity in the timber member (see FIGURE 1.1 (a)). When the load direction is reversed, the fastener has to bridge the gap between the two plastic hinges without being supported by wood until it touches the cavity surface at the opposite side (see FIGURE 1.1 (b)). Until then, the fastener mechanically acts as a fastener between two members with a gap in between (see FIGURE 1.1 (c)). Since the load-carrying-capacity of a laterally loaded fastener decreases with increasing gap width, the load at a given slip also decreases at repeated load cycles. Hereby, the contribution of plastic embedding deformation of the wood is reduced as well, mainly the plastic bending of the fastener remains. If the fastener is repeatedly bent without touching the rim of the cavity, the energy dissipation is predominantly based on plastic fastener bending. Due to the inclination of the fastener axis, tensile forces develop in nails or screws leading to partial withdrawal out of the timber members and a rope effect increasing the load-carrying-capacity.

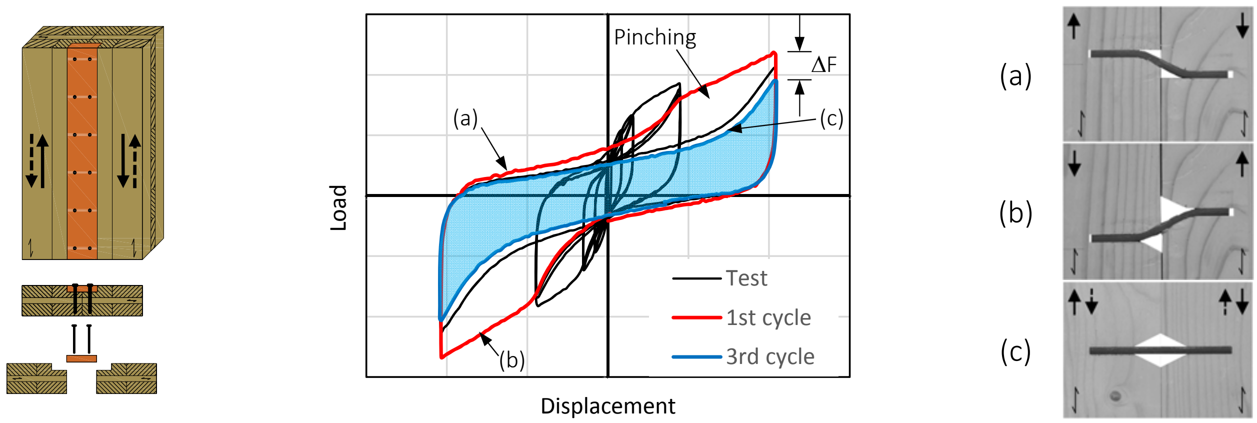

FIGURE 1.1. Pinched hysteresis loops and impairment of strength between the first load cycle and third load cycle at the same displacement of traditional lap joint with nails under cyclic loading. Cavities resulting from reversed load cycles in timber-to-timber connection with dowel-type fasteners (a, b and c) .

As a consequence of the observed behaviour of laterally loaded dowel-type fasteners in timber members, the portion of the energy dissipation caused by metallic fasteners bending' should be maximised while the contribution from plastic wood embedment deformation be minimised. This leads to less pinching and a reduced impairment of strength. Ideally, only plastic steel deformation should occur, while the timber embedding stresses remain in the elastic range.

A special device for timber structures, so called U-shaped Flexural Plates (UFPs), was proposed e.g. by Kelly et al. (1972) and Iqbal (2007), see FIGURE 1.2 (a, b). Especially for concrete structures, a practical solution, so-called »bending dampers« may be found in Pocanschi and Phocas (2003) and Dimitrov and Pocanschi (1985), see FIGURE 1.2 (c). Except the gap, bending dampers are quite similar to laterally loaded dowel type connections in timber members.

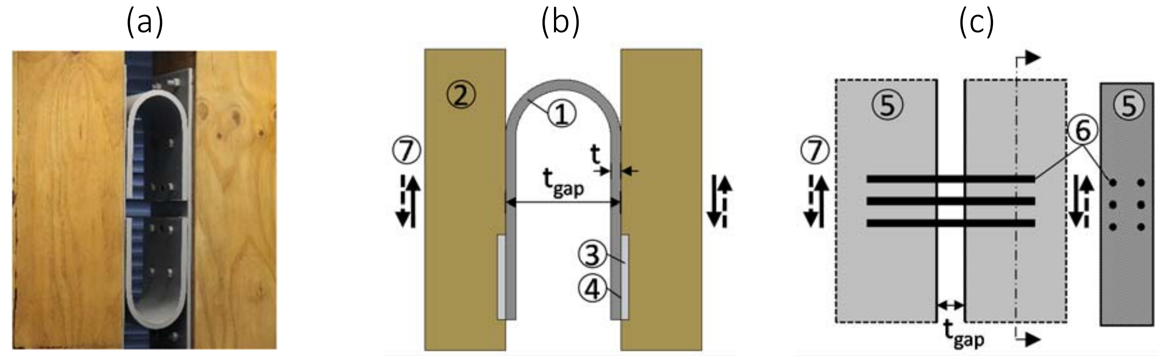

1	UFP	5	Concrete member
2	Timber member	6	Reinforcing steel
3	Embedded plate	7	Load direction
4	Site weld	t / t_{gap}	Steel plate thickness / Gap between two members

FIGURE 1.2 U–shaped flexural plate (UFP) after Kelly et al. (1972): bolted connection between UFP and embedded plate (left); UFP after Iqbal et al. (2007): welded connection between UFP and embedded plate (middle); Dimitrov and Pochanschi (2003): bending damper between two conrete members (right).

In a first step, the energy dissipated in a timber-to-timber connection by the timber members on the one hand side and the steel dowels on the other side was evaluated for different gap sizes (equations (1) - (3)). Both, the timber material under embedding stresses and the dowel under bending action are assumed to behave as rigid-plastic materials according to Johansen's theory (1949).

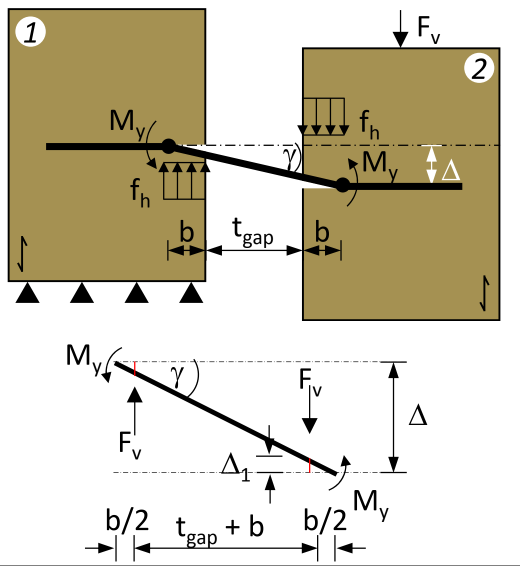

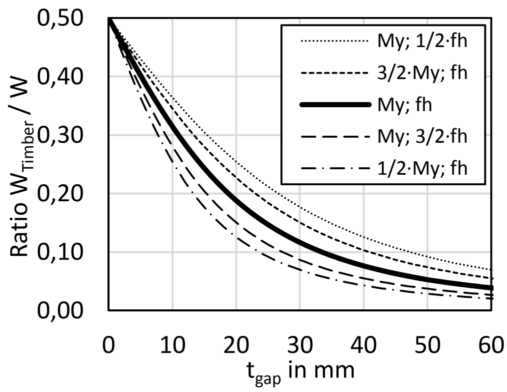

With: $M_y = 2{,}7 \cdot 10^5$ Nmm; $f_h = 43$ N/mm²

$$W = F_v \cdot \Delta = W_{Timber} + W_{Fastener} \tag{1}$$

$$W_{Timber} = F_v \cdot \frac{\Delta \cdot b}{t_{gap} + 2 \cdot b} \tag{2}$$

$$W_{Fastener} = 2 \cdot M_y \cdot \gamma = 2 \cdot M_y \cdot \frac{\Delta}{t_{gap} + 2 \cdot b} \tag{3}$$

f_h	Embedding strength
M_y	Yield moment

FIGURE 1.3 Failure mode for timber-to-timber joints with two plastic hinges per shear plane.

FIGURE 1.3 (right) shows the ratio of the energy dissipated by plastic embedding deformation of timber according to equation (2) and the entire energy dissipation according to equation (1) depending on the gap size. A gap between the two timber members significantly reduces the contribution of the plastic embedding deformation while the contribution of steel bending is reduced to a much lesser extent. The ratio is further minimised by increasing embedding strength and decreasing yield moment.

Another possibility to reduce the embedding stress and thus plastic embedding deformation and to increase plastic fastener bending moments is to increase the contact area between fastener and timber. This means increasing the width of the metallic fastener but not the thickness, ultimately leading to steel plates as fasteners (see FIGURE 1.4). In order to maximise the contribution from steel plate bending, a gap is arranged between the two timber members to be connected. First tests were performed using timber members made of Beech LVL with very high embedding strength or compression strength parallel to grain, respectively. The resulting energy dissipation of the tested connectors was very high compared to traditional timber connections with laterally loaded fasteners. Also the hysteresis loops were hardly pinched resulting in stable load-slip behaviour under repeated loading.

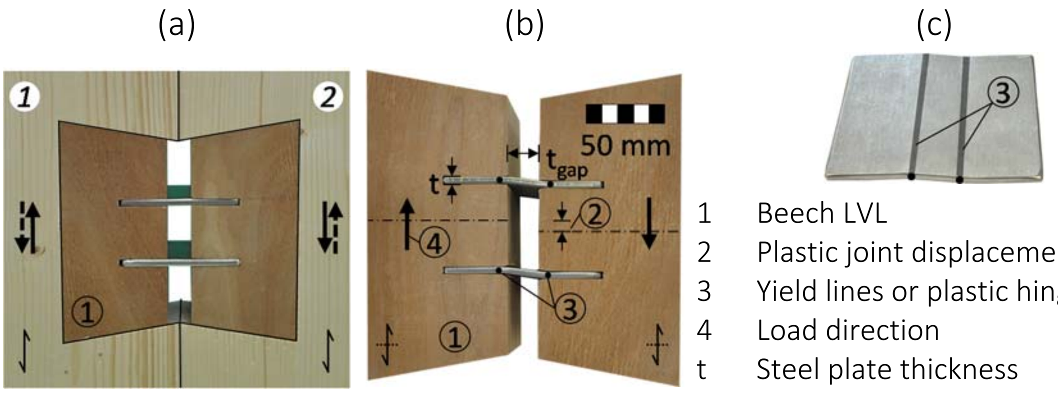

1 Beech LVL
2 Plastic joint displacement
3 Yield lines or plastic hinges
4 Load direction
t Steel plate thickness
t_{gap} Gap between timber members

FIGURE 1.4 Disspative connector according to Schmidt (2016).

The advantage of steel plate fasteners compared to the UFPs is the easier fabrication of the connections; the disadvantage is the still existing – even though small plastic embedding deformation of the timber. The reduction of the net cross section of the timber members is not relevant for shear wall panels since the remaining cross-section for vertical or out-of-plane loads is entirely sufficient.

In a next step, the steel plate fasteners were tested in CLT timber members made of spruce softwood with lower compression strength parallel to grain compared to Beech LVL.

2 Materials and methods

European softwood (Norway spruce) CLT according to European Technical Approval ETA-11/0210 was used for the specimens. The three-layer CLT had a symmetrical layup (40–20–40 mm) with a total thickness of 100 mm and a ratio of 4 between the sum of longitudinal and cross layer thickness. Due to aesthetic reasons, the edges between adjacent longitudinal layer boards are bonded. However, for the edge bonding a non-structural adhesive is used and hence the edge glue lines must not be used in the determination of the in-plane shear strength of the CLT. The cross layers are not edge bonded. The effective characteristic in-plane shear strength of the CLT according to ETA 11/0210 is hence only $f_{v,k}$ = 1.6 MPa for the full cross-section. The average gross density of the CLT specimens is 452 kg/m³ with a Coefficient of Variation (COV) of 4.6 %. Table 1 shows the properties of the longitudinal layers determined after the connection tests. The steel plate fasteners were made of 6 mm thick mild steel S235JR with average yield strength f_y = 318 MPa and average tensile strength f_u = 455 MPa.

Table 1 Longitudinal layer properties of spruce CLT

	Value	COV in %
Compression strength parallel to grain in MPa	43.0	12.9
Density in kg/m³	431	10.8
Moisture content in %	11.1	5.90

FIGURE 2.1 shows the connection principle. The steel plate precisely fits into the CLT slots. The gap size t_{gap} is defined by recesses in the CLT members. The penetration length t_e ensures a failure mode with two plastic hinges. Each specimen consists of three CLT elements connected by a steel plate in the joint lines. A small gap of 2 mm was left between the side and middle members of the connection in order to avoid friction. The middle member was loaded in both directions and the displacement was measured using four LVDTs. The evaluation of the test results is based on the load F parallel to the joint line and the average of four LVDT readings. Six test series with varying gap size t_{gap} between 0, 10, ..., 50 mm were performed with two fasteners in each series and two single tests in each series. The load-displacement behaviour was determined in cyclic tests according to EN 12512. Since the test program is based on the yield-deformation of the connection, after preliminary calculations the yield-deformation was estimated to 3 mm. The cyclic tests were performed until a permanent displacement Δ = 18 mm.

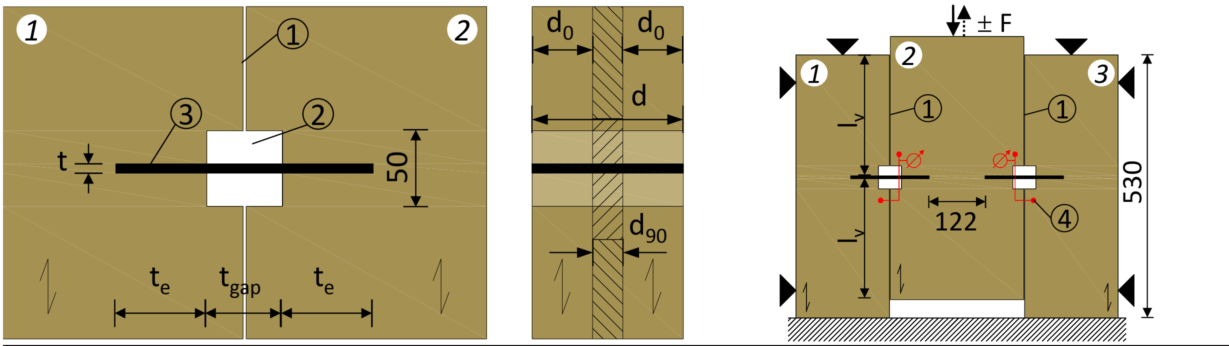

t	Steel plate thickness = 6 mm	1	Gap 2 mm
t_e	Penetration length = 60 mm	2	Recess
d	CLT thickness = 100 mm	3	Steel plate connection with gap
d_0	Longitudinal layer thickness = 40 mm	4	Four LVDTs on front and back side
d_{90}	Cross layer thickness = 20 mm	l_v	Loaded end distance ≥ 262 mm

FIGURE 2.1 Dissipative connector in CLT members (left) and test setup (right).

2.1 Results and discussion

FIGURE 2.2 left exemplarily shows a tested connection with two plastic hinges in the steel plate, the steel plate itself is shown in FIGURE 2.2 right. The yield lines are continuous over the width of the steel plate, the reduced embedding resistance of the cross layer does not influence the bending deformation of the steel plate. The length of the plastic embedment area (see FIGURE 2.2) decreases with increasing gap size t_{gap}. Consequently, the portion of energy dissipation contributed by plastic steel deformation also increases with increasing gap size t_{gap} while the connection's load-carrying-capacity decreases. The different load-slip behaviour of connections with different gap sizes t_{gap} is shown in FIGURE 2.3 for gap size t_{gap} = 0 mm (left) and t_{gap} = 50 mm (right). While pronounced pinching behaviour is observed for gap size t_{gap} = 0 mm, gap size t_{gap} = 50 mm leads to nearly constant energy dissipation with repeated load cycles (see FIGURE 2.3). A longitudinal shear failure of the CLT wasn't observed.

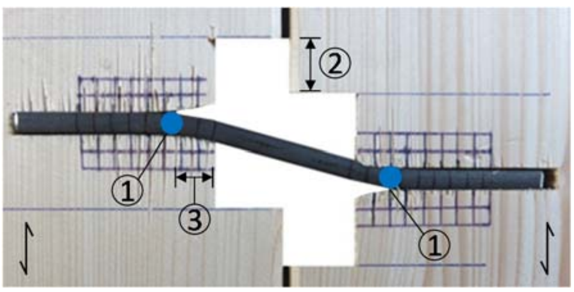

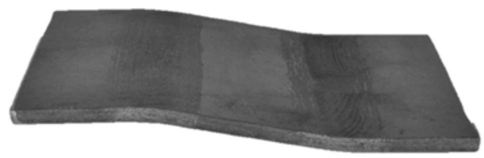

1 Plastic hinges
2 Plastic relative displacement Δ
3 Area with plastic embedding deformation

FIGURE 2.2 Loaded connection with dissipative connector in CLT members with t_{gap} = 40 mm (left) and deformed steel plate used in a connection (right).

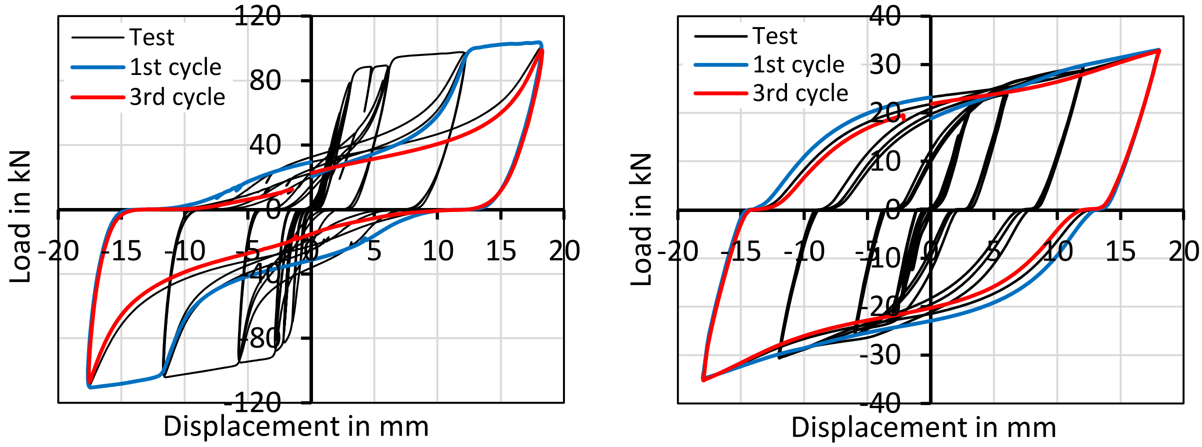

FIGURE 2.3 Hysteresis loops with t_{gap} = 0 mm (left) and t_{gap} = 50 mm (right).

Table 2 shows the test results for the different series. The decrease in load-carrying capacity but also impairment of strength with increasing gap size t_{gap} is obvious. FIGURE 2.4 shows that ΔF is about 0 % for larger gap sizes ($t_{gap} \geq 40$ mm). This is significantly lower than e.g. CLT-screw connections with ΔF about 20 % (Gavric et al., 2015). The equivalent hysteretic damping ratio increases with increasing gap size t_{gap} for both the first and the third load cycle. For larger gap sizes ($t_{gap} \geq 20$ mm) and Δ = 18 mm the damping ratio is in between 21.8 % to 28.7 %. In comparison, CLT-screw connections are reaching about 7 % to 8 % (Gavric et al., 2015). The decrease in load-carrying-capacity with increasing gap size may be compensated by a larger number of connectors thereby ensuring quasi stable energy dissipation behaviour for many load cycles.

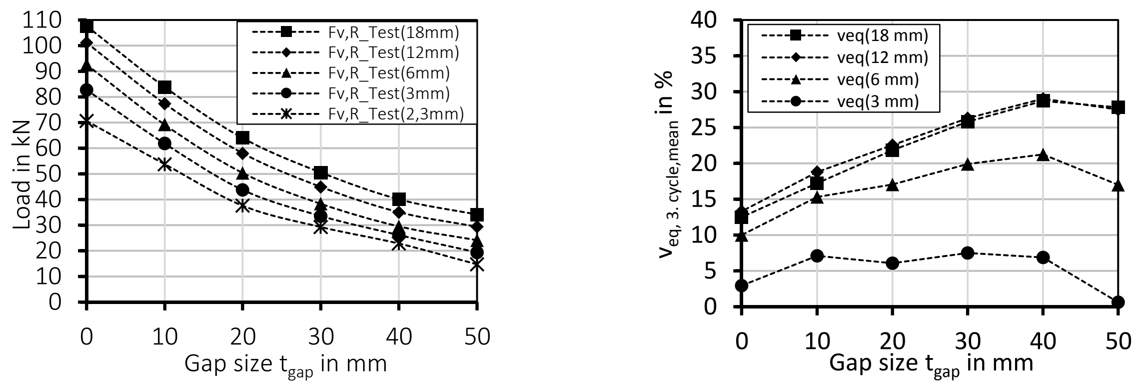

FIGURE 2.4 Load carrying-capacity (left) and damping ratio (right) depending on the gap size as mean values of two tests.

Table 2 Cyclic test results as average of two single tests

		Cycles at 18 mm slip				Cycles at 12 mm slip			
Series	t_{gap} mm	F_{max} kN	$\Delta F_{1\text{-}3,max}$ %	v_{eq} %	v_{eq} %	F_{max} kN	$\Delta F_{1\text{-}3,max}$ %	v_{eq} %	v_{eq} %
		1st cycle		1st cycle	3rd cycle	1st cycle		1st cycle	3rd cycle
1	0	108	4.07	20.4	12.5	101	3.54	24.4	13.3
2	10	83.9	2.38	24.7	17.3	77.3	1.13	28.2	18.8
3	20	63.9	1.32	28.0	21.8	58.0	-0.52	30.2	22.5
4	30	50.5	2.24	31.2	25.8	44.9	-2.06	32.5	26.3
5	40	40.0	0.78	33.0	28.7	35.0	-2.68	33.0	29.0
6	50	34.1	0.04	32.2	27.8	29.3	-3.53	31.1	27.5

		Cycles at 6 mm slip				Cycles at 3 mm slip			
Series	t_{gap} mm	F_{max} kN	$\Delta F_{1\text{-}3,max}$ %	v_{eq} %	v_{eq} %	F_{max} kN	$\Delta F_{1\text{-}3,max}$ %	v_{eq} %	v_{eq} %
		1st cycle		1st cycle	3rd cycle	1st cycle		1st cycle	3rd cycle
1	0	92.6	3.05	21.3	10.0	82.7	5.39	6.90	2.98
2	10	69.2	0.51	23.8	15.3	61.8	2.56	10.9	7.10
3	20	50.3	-3.25	23.6	17.1	43.7	-0.11	8.47	6.08
4	30	38.3	-4.58	25.3	19.9	33.5	-0.51	9.47	7.50
5	40	29.5	-5.70	25.0	21.3	26.1	-0.34	8.48	6.89
6	50	24.1	-6.98	19.1	17.0	19.3	-3.90	2.33	0.62

F_{max} Mean ultimate load at a certain displacement
$\Delta F_{1\text{-}3,max}$ Maximum impairment of strength
E_d Dissipated Energy in Nmm
E_p Available potential Energy in Nmm
v_{eq} Mean equivalent hysteretic damping ratio: $v_{eq} = E_d/(2\pi E_p)$

Additional compression shear tests were carried out to determine load-carrying capacity and slip modulus under monotonic loading. The average slip moduli k_{ser} out of 3 single tests depending on the gap size is given in Table 3.

Table 3 Slip modulus k_{ser} determined in compression shear tests for two steel plates in a joint line.

t_{gap} in mm:	0	1	20	30	40	50
K_{ser} in kN/mm:	68.6	55.9	38.4	27.4	17.0	13.0
COV in %	16.7	10.0	19.0	8.00	3.64	1.67

3 Analytical and numerical consideration

3.1 Design method

Using the principles of the EYM-European Yield Model for dowel-type fasteners, the load carrying-capacity of a connection with steel plates as fasteners may be derived based on the compression strength parallel to grain of the CLT longitudinal layers and the plastic bending moment capacity of the steel plate (Johansen, 1949 and Blaß, Laskewitz, 2013). Basically, there are 6 possible failure modes of the connection, see equations (6) - (9). The load-carrying capacity of the desired failure mode with two plastic hinges is expressed by equation (9). FIGURE 3.1 shows the mechanical model of the connection with two plastic hinges and a comparison with test results for different displacement levels. The calculated load-carrying-capacity according to equation (9) for connections with gap is reached in the tests already at displacement levels of 3 mm using f_y and at displacement levels of 12 mm using f_u. The plastic bending moment resistance of the steel plate is calculated according to equation (10).

$$F_{v,R} = \sum_i d_{0,i} \cdot f_{c,0,1} \cdot t_{e,1} \tag{4}$$

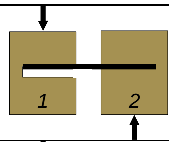

$$F_{v,R} = \sum_i d_{0,i} \cdot f_{c,0,2} \cdot t_{e,2} \tag{5}$$

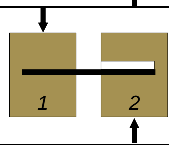

$$F_{v,R} = \sum_i d_{0,i} \cdot f_{c,0,1} \cdot \frac{\beta}{1+\beta} \cdot \left(-2 \cdot t_{gap} - t_{e,1} - t_{e,2} + \sqrt{\begin{array}{l} 4 \cdot t_{gap}^2 + \left(2 + \frac{1}{\beta}\right) \cdot t_{e,1}^2 + (2+\beta) \cdot t_{e,2}^2 \\ +4 \cdot t_{gap} \cdot t_{e,1} + 4 \cdot t_{gap} \cdot t_{e,2} + 2 \cdot t_{e,1} \cdot t_{e,2} \end{array}} \right) \tag{6}$$

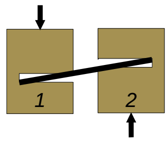

$$F_{v,R} = \sum_i d_{0,i} \cdot f_{c,0,1} \cdot \frac{2 \cdot \beta}{2+\beta} \left(-t_{gap} - \frac{t_{e,1}}{2} + \sqrt{\begin{array}{l} t_{gap}^2 + t_{gap} \cdot t_{e,1} + \frac{t_{e,1}^2}{2} + \frac{t_{e,1}^2}{2 \cdot \beta} \\ + \frac{2 \cdot M_y}{f_{c,0,1} \cdot \beta \cdot \sum_i d_{0,i}} + \frac{M_y}{f_{c,0,1} \cdot \sum_i d_{0,i}} \end{array}} \right) \tag{7}$$

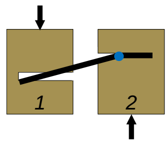

$$F_{v,R} = \sum_i d_{0,i} \cdot f_{c,0,1} \cdot \frac{\beta}{1/2+\beta} \left(-t_{gap} - \frac{t_{e,2}}{2} + \sqrt{\begin{array}{l} t_{gap}^2 + \left(\frac{1}{2} + \frac{1}{2} \cdot \beta\right) \cdot t_{e,2}^2 + t_{gap} \cdot t_{e,2} \\ + \frac{2 \cdot M_y}{f_{c,0,1} \cdot \sum_i d_{0,i}} + \frac{M_y}{f_{c,0,1} \cdot \beta \cdot \sum_i d_{0,i}} \end{array}} \right) \tag{8}$$

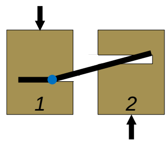

$$F_{V,R} = \sum_i d_{0,i} \cdot f_{c,0,1} \cdot \frac{1}{1+\beta} \left(\sqrt{\beta^2 \cdot t_{gap}^2 + 4\beta \cdot (\beta+1) \frac{M_y}{\sum_i d_{0,i} \cdot f_{c,0,1}}} - \beta \cdot t_{gap} \right) \tag{9}$$

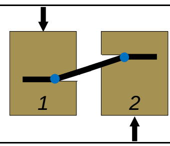

$$M_y = f_y \cdot W_{pl} = f_y \cdot \frac{b_{steel\ plate} \cdot t^2}{4} \quad \text{und} \quad M_u = f_u \cdot W_{pl} = f_u \cdot \frac{b_{steel\ plate} \cdot t^2}{4} \tag{10}$$

$d_{0,i}$	Thickness of the longitudinal layer i	M_y; M_u	Yield moment of steel plate
$f_{c,0}$	Compressive strength parallel to grain	t / $b_{steel\ plate}$	Thickness / width of the steel plate
β	$f_{c,0,2}$ / $f_{c,0,1}$	t_{gap}	Gap size

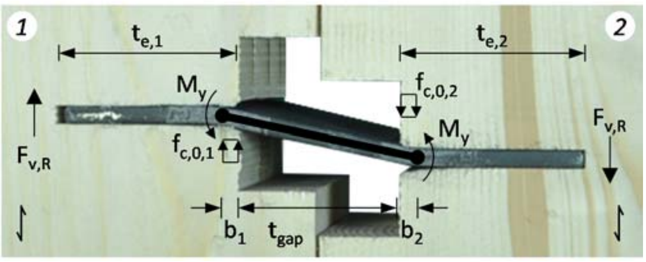

b Length of plastic compression deformation in the first load cycle

$b_{1st,cycle} = F_{v,R} / (\Sigma d_{0,i} \cdot f_{c,0})$ (11)

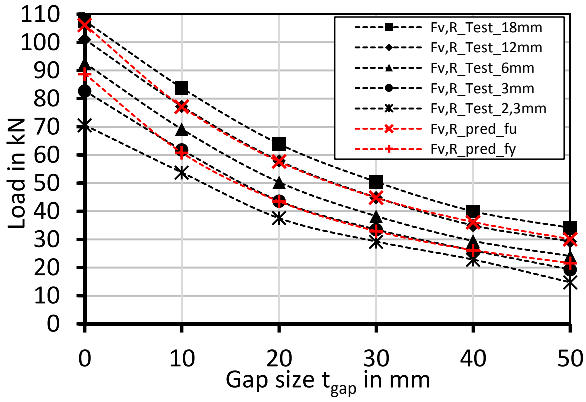

FIGURE 3.1 Mechanical model of the connection (left) and calculated load-carrying-capacity of two steel plates in comparison with test results (right).

In order to ensure the desired failure mode with two plastic hinges, a minimum value for the penetration length $t_{e,min}$ in each timber member 1 and 2 is required.

$$t_{e,\min,1} = \left(2\cdot\beta\cdot\sqrt{\frac{M_y}{\sum_i d_{0,i}\cdot f_{c,0,1}}} + \sqrt{\frac{\sum_i d_{0,i}\cdot f_{c,0,1}\cdot\beta^2\cdot t_{gap}^2 + 4\cdot M_y\cdot\beta^2 + 4\cdot M_y\cdot\beta}{\sum_i d_{0,i}\cdot f_{c,0,1}}} + 2\cdot\sqrt{\frac{M_y}{\sum_i d_{0,i}\cdot f_{c,0,1}}} - \beta\cdot t_{gap} \right)\cdot\frac{1}{\beta+1} \quad (12)$$

$$t_{e,\min,2} = \left(2\cdot\beta\cdot\sqrt{\frac{M_y}{\sum_i d_{0,i}\cdot\beta\cdot f_{c,0,1}}} + \sqrt{\frac{\sum_i d_{0,i}\cdot f_{c,0,1}\cdot\beta^2\cdot t_{gap}^2 + 4\cdot M_y\cdot\beta^2 + 4\cdot M_y\cdot\beta}{\sum_i d_{0,i}\cdot f_{c,0,1}}} + 2\cdot\beta^2\sqrt{\frac{M_y}{\sum_i d_{0,i}\cdot\beta\cdot f_{c,0,1}}} - \beta\cdot t_{gap} \right)\cdot\frac{1}{\beta^2+\beta} \quad (13)$$

However, varying strength values can influence the behaviour of the connection and lead to unexpected failure modes. FIGURE 3.2 shows the consequences of different strength values parallel to grain of both CLT members. Low compression strength values of CLT member 1 (FIGURE 3.2 right) led to the unexpected failure mode with only one plastic hinge and decreased load-carrying capacity and energy dissipation.

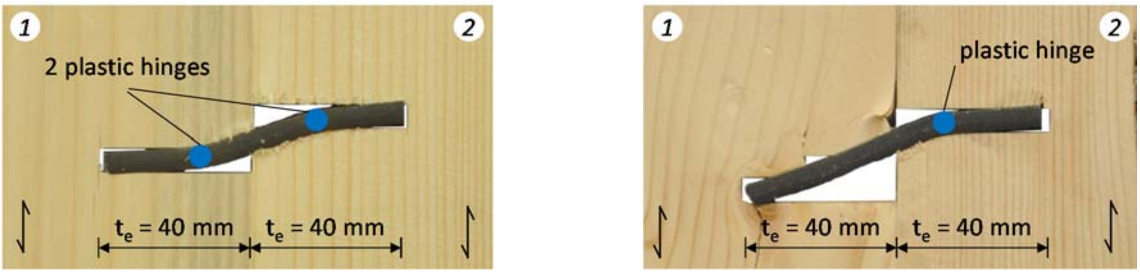

FIGURE 3.2 Same geometry – different strength values – different failure modes. Expected failure mode with 2 plastic hinges (left) and unexpected failure mode with one plastic hinge (right).

3.2 Required penetration length based on stochastic strength values

To verify the effect of varying timber compression and steel tensile strength values a Monte-Carlo-Simulation based on normally distributed strength values with 20000 realizations for each gap size was carried out. The generated data (see Table 3) is based on the strength values from tests (see materials and methods). To generate the data the software *Microsoft Excel 2013* was used. FIGURE 3.3 shows the simplification which was chosen to perform the simulation: Only two CLT longitudinal layers were considered and the CLT cross layer was neglected. To generate the results, simulated strength values were randomly chosen and equation (12) and (13) were evaluated. Since plastic strain in the steel plate connection was reached in all cases, only the ultimate yield moment M_u has to be considered.

Table 4 Generated strength values

	$f_{c,0,1}$ N/mm²	$f_{c,0,2}$ N/mm²	f_u 1) N/mm²	M_u N/mm²
min	20.8	20.8	218	97941
max	65.8	74.7	677	304426
mean	43.3	43.4	455	204559
s	5.91	5.81	59.9	26935
COV in %	13.6	13.4	13.2	13.2
median	43.3	43.4	455	204607
5%-quantile	**33.6**	**33.8**	355	159852
95%-quantile	53.1	52.9	552	**248610**
98%-quantile	55.4	55.1	580	260793
number	$n = 10^4$	$n = 10^4$	$n = 10^4$	$n = 10^4$
distribution	normal	normal	normal	normal

1) According to Sadowski et al. (2015)

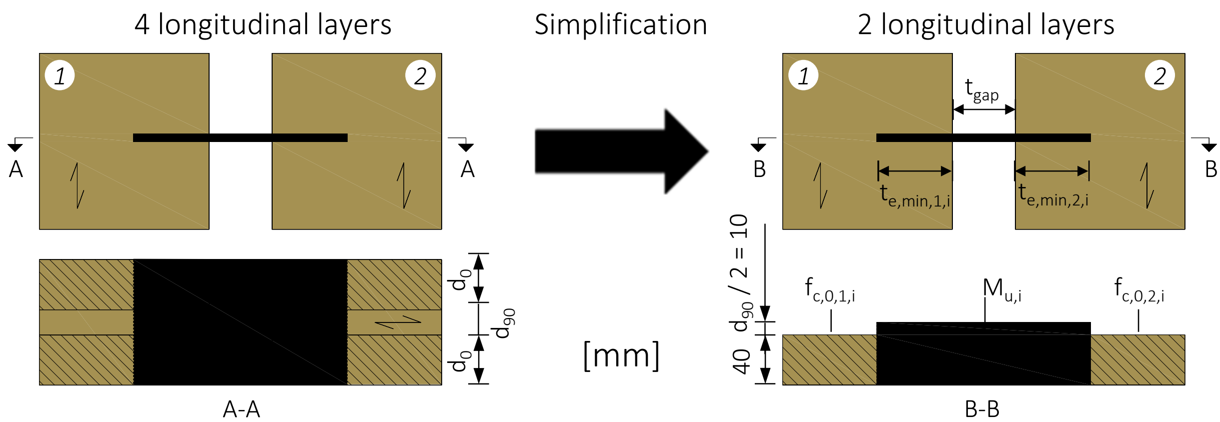

FIGURE 3.3 Connection principle (left) and simulation principle (right).

Results and discussion

The histogram in FIGURE 3.4 left exemplarily shows the distribution of the simulated required penetration length values to ensure two plastic hinges per shear plane. The distribution is close to a normal distribution. FIGURE 3.4 right shows relevant quantile-values for $t_{e,min}$ for all gap sizes. If $M_{u,95}$ and $f_{c,0,05}$ are used to determine $t_{e,min}$, the penetration length is close to the 98%-quantile of the simulation results (see FIGURE 3.4 right).

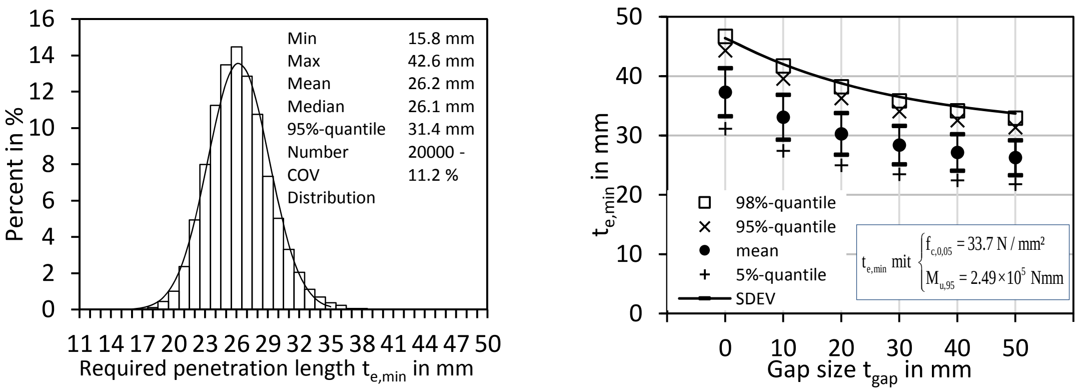

FIGURE 3.4 Simulated penetration length for M_u. Distribution for t_{gap} = 50 mm (left) and $t_{e,min}$ depending on the gap size (right).

The Software *IBM SPSS 24* was used to recheck the results. Therefore 10^6 realisations were generated and evaluated. A significant deviation wasn't observed.

The largest penetration length is required, when high yield moment and low compression strength parallel to grain coincide. Since the yield moment is generally larger than the lower 5%-quantile, an upper quantile of M_u, calculated with the tensile strength, should be used to calculate the minimum penetration length $t_{e,min}$. Similarly the 5%-quantile of the compression strength perpendicular to grain should be used. It is suggested to replace M_y with $M_{u,95}$ and $f_{c,0}$ with $f_{c,0,05}$ in equations (12) and (13).

After finishing the cyclic test program with several load cycles a kind of wear out effect was observed resulting in the length of plastic compression deformation being 2 to 4 times as high as the calculated value "b" according to equation (11). This might be explained with lower compression strength values of longitudinal layers parallel to grain under repeated loading up to the compression strength. Since the compression strength parallel to grain of longitudinal layers is determined under monotonic load, which means the stress is applied in only one load-cycle, the minimum penetration length according to equations (12) and (13) is only valid for the first load-cycle in such a connection. Future work will consider this problem and an experimental study is planned to determine reduced compression strength values ($f_{c,0,05,red}$) under repeated load. Currently, equations (12) and (13) can be used to determine the penetration length for static loads.

4 Conclusions

For the dissipative shear wall joints the typical pinching and impairment of strength of hysteresis loops at repeated loadings could nearly completely be avoided by arranging a gap between the CLT members around the steel plate. The behaviour of connections in shear walls will be studied in shear wall tests. Further research will answer particularly the following questions:

- Is the load-slip behaviour of the dissipative steel plate connection significantly influenced by the rope effect?
- How should the effective number of consecutive connectors in a joint line be calculated?
- What is the influence of cyclic loading on the compression strength parallel to grain of the CLT longitudinal layer in comparison to static loading?
- After a strong earthquake, the steel plate connections will be loaded beyond their elastic limit. In order to assess the remaining dissipation capacity needed to resist aftershocks or further earthquakes, the complete cyclic test program according to EN 12512 was performed 5 to 10 times with each specimen. Increasing the number of load-cycles leads to reduced load-carrying capacity and less energy dissipation. However, for larger gap sizes the reduction of the mechanical properties is comparatively low (see FIGURE 4.1). Based on finite element modelling of the connection, the plastic steel strain remains below 10 %. This confirms the assumption that low cycle fatigue of the steel plate will not be a governing failure mode even after repeated strong earthquakes.

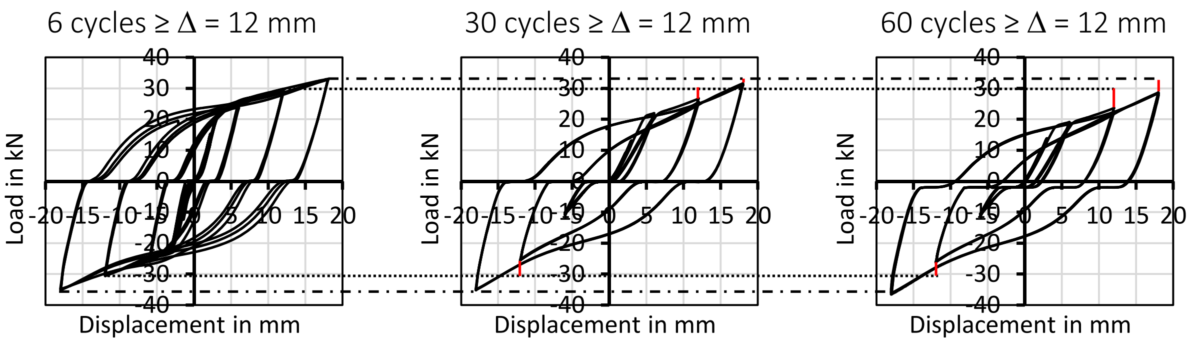

FIGURE 4.1 Load-Displacement curves for a steel plate connection with t_{gap} = 50 mm after multiple cyclic loads.

While steel plate connections without a gap are very suitable for floor diaphragms of buildings, where high stiffness and load-carrying-capacity but no energy dissipation are required, the steel plate fastener with gap is able to provide the necessary energy dissipation in CLT shear walls in earthquake prone regions. These steel plate connections are aiming at easy fabrication using automatic processing machines and quick assembly at the construction site. The simple and cost-effective connection provides high energy dissipation and is easy to design.

5 References

Blaß HJ; Laskewitz B (2003): Tragfähigkeit von Verbindungen mit stiftförmigen Verbindungsmitteln und Zwischenschichten. Bauen mit Holz 105 (2003), H. 1 P. 26-35, H. 2 P. 30-34.

Ceccotti A (1995): Timber connections under seismic actions. STEP lecture C17, Timber Engineering STEP 1, ISBN 90-5645-001-8, Centrum Hout, The Netherlands

Dimitrov, N; Pocanschi A (1985): Wandscheiben mit dynamischer Anpassungsfähigkeit für Bauten in Erdbebengebieten. Bauingenieur 60, S. 91-98.

Gavric I; Fragiacomo M; Ceccotti A (2015): Cyclic behavior of typical screwed connections for cross-laminated (CLT) structures. European Journal of Wood and Wood Products 73 (2015), S. 179–191.

Iqbal, A; Pampanin, S; Buchanan, A (2007): Improved Seismic Performance of LVL Post-tensioned Walls Coupled with UFP devices. 8th Pacific Conference on Earthquake Engineering. Singapore, 5-7 December.

Johansen KW (1949): Theory of timber connections. International Association for Bridge and Structural Engineering, Vol. 9 (1949), P. 249-262.

Kelly, J M; Skinner, R I; Heine, A J (1972): Mechanisms of Energy Absorption in Special Devices for use in Earthquake Resistant Structures. Bulletin of the New Zealand Society for Earthquake Engineering, 5 (3).

Pocanschi A; Phocas M C (2003): Kräfte in Bewegung – Die Techniken des erdbebensicheren Bauens. Teubner Verlag Juli.

Sadowski AJ; Rotter JM; Reinke T; Ummenhofer T (2015): Statistical analysis of the material properties of selected structural carbon steels. Structural Safety (2015), Vol. 53, P. 26-35.

Schmidt T (2016): Kontaktverbindungen zur Längsschubübertragung in den Schmalseiten von Brettsperrholzelementen. Doktorandenkolloquium Holzbau, P. 41–56. Stuttgart: Universität Stuttgart.

Discussion

The paper was presented by T Schmidt

P Quenneville commented whether the geometry of the plate would stay "as-is" if rope effect was mobilized.

P Dietsch commented that the test set up was intended to avoid friction between two components.

M Li commented about gaps from the test set up. Gaps might be produced by the system after a few cycles resulting different hold down forces. H Blass agreed but said that this would lead to much higher forces on the hold-downs.

A Buchanan commented that the CLT system activating the damping was important. He asked how to do this if two walls came together at 90 degrees. H Blass responded that the same connection could be used in a corner.

A Palermo commented that location of plastic hinge would move during loading which could lead to better performance for fatigue. H Blass agreed that this was observed.

M Gershfeld asked whether changes in steel cross section could improve the situation. For example changes the width towards the middle may enhance the performance. H Blass responded that this was considered already and might not be needed.

F Lam commented that UBC work with a different damper system indicated that damping might not be mobilized when higher capacity dampers were used and suggested that dynamic analysis could be used to optimize the approach. H Blass agreed.

Required Seismic Performance of CLT Panel Buildings from Japanese Standard

Tatsuya MIYAKE, Nihon System Sekkei Architects & Engineers

Motoi YASUMURA, Shizuoka University

Naohito KAWAI, Kougakuin University

Hiroshi ISODA, Kyoto University

Mikio KOSHIHARA, The University of Tokyo

Takahiro TSUCHIMOTO, Building Research Institute

Yasuhiro ARAKI, Building Research Institute

Takafumi NAKAGAWA, National Institute for Land and Infrastructure Management

Keywords: CLT panel, Seismic performance, Seismic design, Connection

1 Introduction

CLT panel is expected as a suitable material for middle-rise buildings also in Japan. Japanese government notifications on the structural design of CLT panel buildings ("GN" in the followings) were issued on Apr. 1, 2016. Following the issue of GN, the guidebook on the regulations of GN and the manual on design and construction of CLT panel buildings were published each on Jun. and Oct., 2016. However, structural possibility of CLT buildings in Japan is supposed to be smaller than that in the other countries because of high seismic risk.

In this paper, firstly, the outlines of the regulations of GN and the descriptions of the manual are introduced. Next, based on the regulations of GN and the descriptions of the manual, dealing the constructions with the standard composition as objectives, the required wall quantity (total wall length divided by floor area) as an index of structural possibility is examined based on the structural calculation method regulated in GN. As a result, it is confirmed that the required wall quantity for middle-rise CLT panel buildings is larger than the other constructions such as the reinforced concrete boxed wall-buildings. Therefore, the reduction of the required wall quantity is necessary for prevalence of middle-rise CLT buildings in Japan. Lastly, a high-performance connection system is proposed to reduce the required wall quantity, and outline of the static lateral loading test of the system are introduced.

2 Outline of the standard

2.1 Applicable structural materials

2.1.1 CLT panel

CLT panel is needed to satisfy either conditions below.

- It conforms to Japan Agricultural Standards of CLT ("JAS" in the followings), and its standard strength is ruled in Japanese government notification.

- It is given the ministerial materials approval and the designation of the standard strength based on Japanese government notification.

2 type of lamina compositions such as "symmetrical-different-grade composition" and "homogeneous-grade composition" are ruled in JAS. The grades of CLT panel are ruled as Mx60, Mx90 and Mx120 for the former, S30, S60, S90 and S120 for the latter. The numbers in these names of the grades mean 10 times of the lower limit value of average bending elastic modulus (GPa, "MOE" in the followings) of laminas which is ruled as 30 for inner layer of the symmetrical-different-grade composition. However, the applicable CLT panels are limited as Mx60, S30 and S60 because the other grades are not yet given the standard strength.

2.1.2 The other materials

The applicable wooden materials for columns and beams are lumbers, glued laminated lumbers and laminated veneer lumbers which are regulated in the government notifications on the applicable materials for the post-and-beam constructions.

The material for connections which conform to Japanese Industrial Standards or foreign standards is applicable. And the composition of connection has to be confirmed its structural performance from test.

2.2 Standard composition of constructions

2.2.1 The vertical and horizontal plane of structure

As shown in Figure 2.1, wall panels in 1^{st} story are set on the foundation or sills. In the upper story, wall panels are normally platformed on the floor slab. The vertical planes of structure are composed with rectangular narrow panels ("NP" in the followings), or with large width panels with rectangular opening(s) ("LP" in the followings). LP is classified into "LP1" or "LP2". In LP1, the settings of the connections are same as NP to allow vertical cracks at the corner of opening from horizontal deformation. The support members have to be set in both side of opening to prevent falling of the lintel so that seismic performance of LP1 is regarded similar to NP. In LP2, vertical cracks at the corner of opening are not allowed, and omission of tensile connections above and below corners of the opening is allowed. The support members also have to be set as fail-safe.

As shown in Figure 2.2, the horizontal planes of structure such as floor slab and roof slab are normally composed with rectangular CLT panels. As another method, they can be composed using conventional floor framing and roof framing with beams, plywood boards and so on.

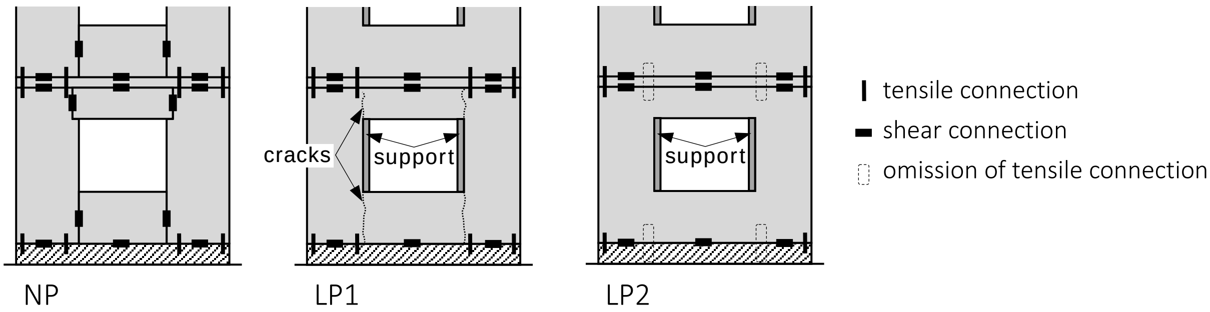

Figure 2.1. The standard compositions of the vertical planes of structure.

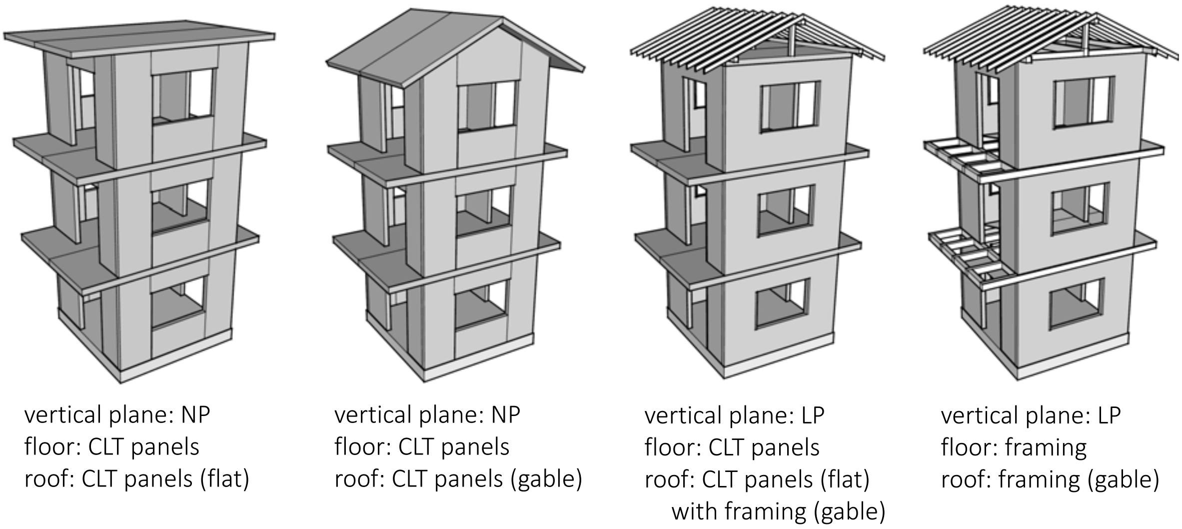

Figure 2.2. The standard compositions of the horizontal planes of structure.

2.2.2 The connections

In japan, the connections of CLT panel constructions are required higher strength than that in the other countries because of high seismic risk. And the tensile connections are required not only the strength but also the deformation capability to secure the ductility of the vertical plane of structure to lateral seismic force. Considering these requirements, the manual shows the connections in Figure 2.3 as the normal connections. The tensile connections at the top and the bottom of wall panels are the screwed steel plate with bolt as shown in “Composition #1” or the tensile bolt as shown in “Composition #2”. Steel materials ensured plastic deformation capability are applied to these bolts. The other connections are screwed steel plate or screwed plywood.

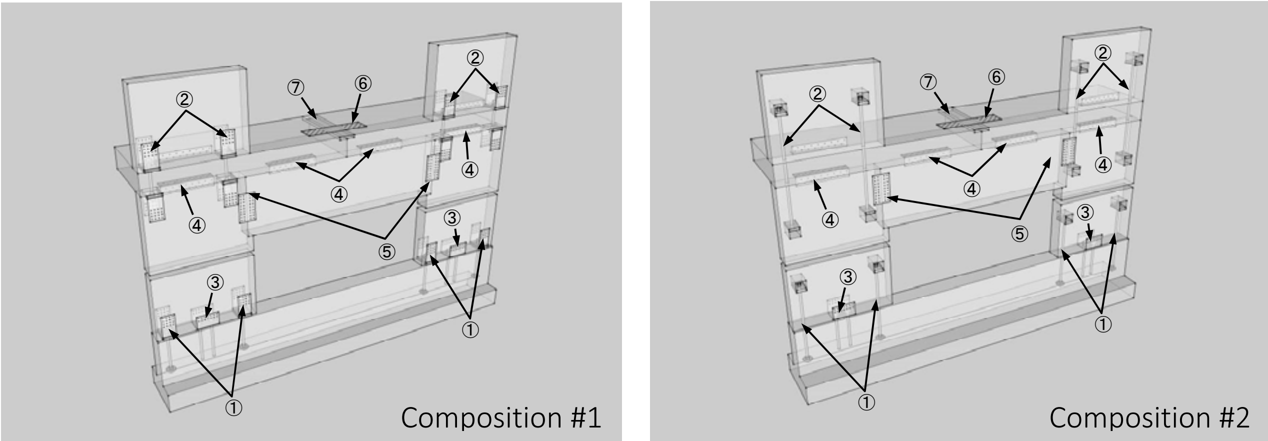

1: Wall – Foundation (tensile) 2: Wall – Wall (tensile) 3: Wall – Foundation (shear) 4: Wall – Floor (shear) 5: Lintel – Wall (shear) 6: Floor – Floor (tensile) 7: Floor – Floor (shear)

Figure 2.3. The normal composition of connections.

2.3 The procedure of seismic design

There are several structural calculation methods such as “Calculation of allowable strength”, “Calculation of horizontal load carrying capacity”, “Calculation of response and limit strength” (“CRLS” in the followings) and so on. Among these method, CRLS is most advanced where the maximum response from the prescribed earthquake is calculated to examine the seismic performance.

In CRLS, as Equation (1), (2), and as shown in Figure 2.4, relations of horizontal load and displacement of each story from static load incremental analysis are converted into the relation of acceleration, A and displacement, Δ of the equivalent single degree of freedom as the capacity curve.

$$\Delta = \frac{\sum_i m_i \cdot d_i^2}{\sum_i m_i \cdot d_i} \quad (1)$$

$$A = Q_B \cdot \frac{\sum_i m_i \cdot d_i^2}{\left(\sum_i m_i \cdot d_i\right)^2} \quad (2)$$

where m_i = mass of i floor, d_i = horizontal displacement from foundation of i floor.

The relation of acceleration response spectrum, S_a and displacement response spectrum, S_d is calculated as the demand curve. S_a-S_d relation of the large earthquake on 2nd class of soil when the equivalent damping factor, h_{eq} = 0.05 is set as shown in figure 2.5. For the large earthquake, S_a-S_d relation shown in Figure 2.5 are multiplied by F_h shown in Equation (3) to consider response reduction effect by damping.

$$F_h = \frac{1.5}{1+10h_{eq}} \tag{3}$$

For the moderate earthquake, S_a-S_d relation is calculated as 0.2 times of that shown in Figure 2.5.

A and Δ corresponding to the maximum response are obtained as intersection of the capacity and the demand curves.

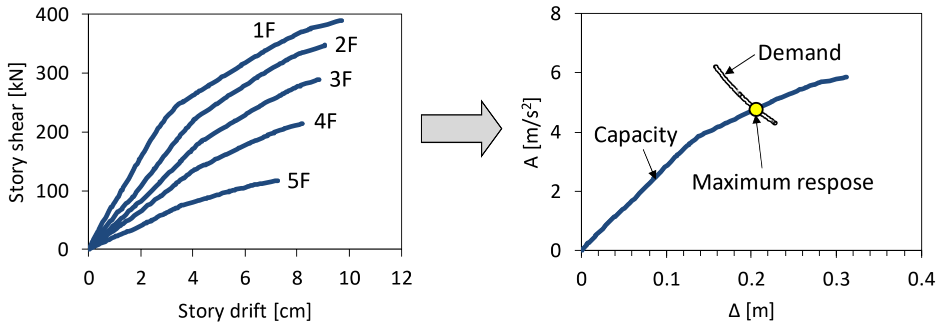

Figure 2.4. The process of CRLS

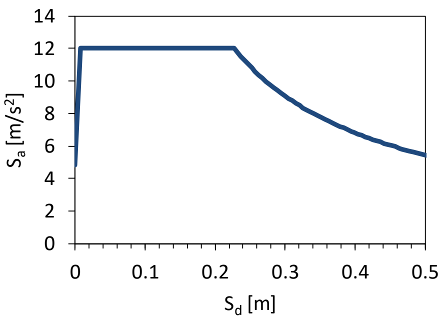

Figure 2.5. Sa-Sd relation of the large earthquake (h_{eq} = 0.05)

The maximum responses from the moderate earthquake and from the large earthquake are examined to satisfy the design criteria set as below.

Level 1: For the moderate earthquake,
- Stress of CLT panels ≦ Allowable stress
- Force of connections ≦ Allowable strength
- Story drift angle ≦ 1/120

Level 2: For the large earthquake,
- Stress of CLT panels ≦ Standard strength
- Deformation of connections ≦ Ultimate deformation
- Story drift angle ≦ 1/30

2.4 Standard structural model

2.4.1 The composition of the model

As the structural model used for the static load incremental analysis, FE (Finite Element) model where CLT panels and connections are converted into plane shell elements and spring elements, have been confirmed to have enough precision from comparative analyses with results of past shake table tests. However, FE model requires enough knowledge on modelling theory because the maximum stress of shell elements depends on division of elements, for example. Considering these difficulties, the manual regulates the frame model shown in Figure 2.6 as the standard structural model where CLT panels are converted into shear panels and beam elements

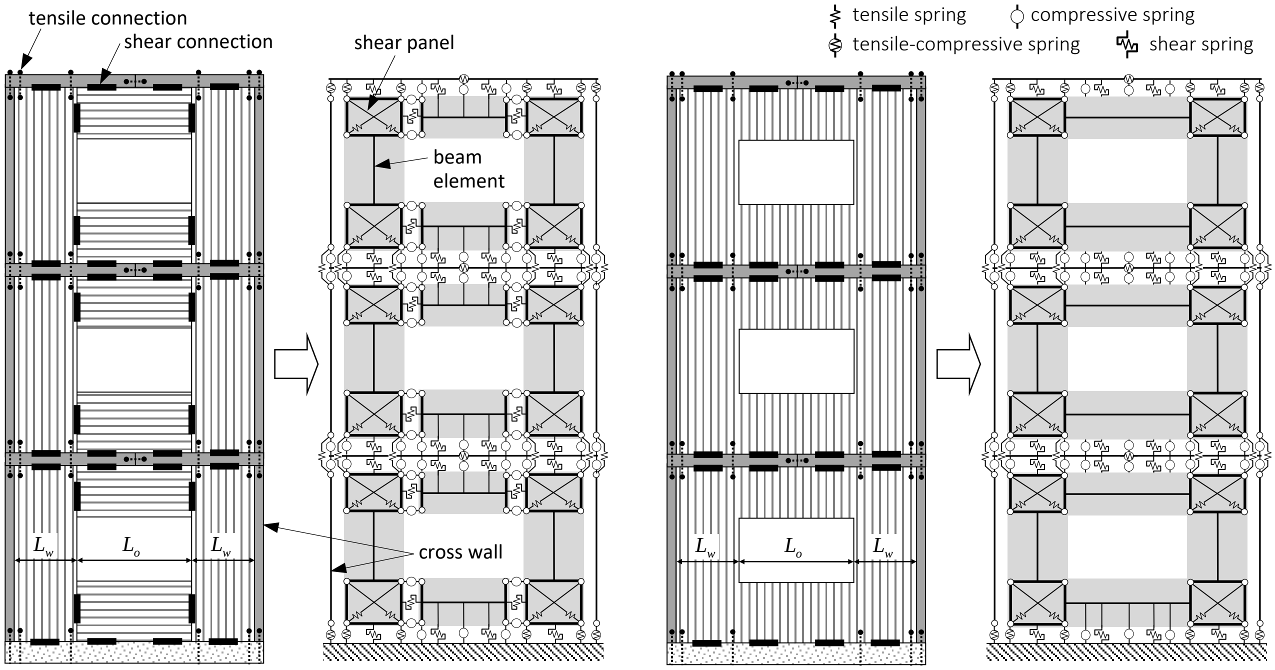

Vertical plane of NP *Vertical plane of LP*

Figure 2.6. Composition of the standard structural models

2.4.2 Standard strength and elastic modulus of CLT panel

The in-plane standard strength, F_c, F_b, F_t of CLT panel are calculated from Equation (4)-(6) as the allowable lower limit performance.

Compressive: $$F_c = \sigma_{c.oml} \cdot \frac{A_A}{A_0} \times 0.75 \quad (4)$$

Bending: $$F_b = \sigma_{b.oml} \cdot \frac{A_A}{A_0} \times 0.6 \quad (5)$$

Tensile: $$F_t = \sigma_{t.oml} \cdot \frac{A_A}{A_0} \times 0.75 \quad (6)$$

$$A_A = \frac{\sum E_i \cdot A_i}{E_0} \quad (7)$$

where $\sigma_{c.oml}, \sigma_{b.oml}, \sigma_{t.oml}$ = compressive, bending and tensile strength of laminas in surface layer, A_0 = whole cross section, A_A = effective cross section, E_i = MOE of laminas in i layer, A_i = cross section of i layer, E_0 = MOE of laminas in surface layer.

$\sigma_{c.oml}, \sigma_{b.oml}$ and $\sigma_{t.oml}$ are ruled each as 21.6MPa, 27.0MPa and 16.0MPa for laminas with 6.0GPa of MOE. And the standard strength of compressive perpendicular to grain, F_{cv} is ruled as 6.0MPa. The allowable stress is 2/3 times of these standard strength.

In the followings, the layer where the direction of grain of lamina is parallel or perpendicular to the direction of force are each called “parallel layer”, “cross layer”. And x-direction and y-direction are defined each perpendicular and parallel to the direction of surface laminas. Normal elastic modulus of CLT panels in x-direction and y-direction, E_x, E_y are calculated based on the assumption that only parallel layers are effective. Shear elastic modulus, G_{xy} is set as 0.5GPa based on static shear test of CLT panels. Based on these regulations, for example, F_c, F_b, F_t and E_x, E_y are set as shown in Table 1.

Table 1. In-plane standard strength and elastic modulus of CLT panels

Grade	Direction of lamina	E_S [GPa]	E_I [GPa]	F_c, F_b [MPa]	F_t [MPa]	E_x [GPa]	E_y [GPa]
Mx60-3-3	＝⊥＝	6.0	3.0	10.8	8.00	1.00	4.00
Mx60-5-5	＝⊥＝⊥＝	6.0	3.0	8.10	6.00	1.20	3.00
Mx60-7-7	＝⊥＝⊥＝⊥＝	6.0	3.0	6.94	5.14	1.29	2.57
S60-3-3	＝⊥＝	6.0	6.0	10.80	8.00	2.00	4.00
S60-5-5	＝⊥＝⊥＝	6.0	6.0	9.72	7.20	2.40	3.60
S60-7-7	＝⊥＝⊥＝⊥＝	6.0	6.0	9.25	6.85	2.57	3.43
S90-5-7	＝＝⊥＝⊥＝＝	9.0	9.0	14.57	10.98	5.14	6.43

* “Grade” is expressed as “g-m-n” where “g” means the grade mentioned in Section 2.1.1, “m, n” means the number of layer and ply. “m” is counted as one for adjacent laminas in same direction. “＝” = parallel layer, “⊥” = cross layer. E_S, E_I = MOE of surface laminas and inner laminas, F_c, F_b, F_t = value in y-direction.

* Strength and elastic modulus of “S90-5-7” are estimated based on structural characteristics of laminas ruled in JAS, because the standard strength is not yet given.

2.4.3 Structural performance of connections

As shown in Figure 2.6, connections are modelled as spring elements. In this paper, based on the results of past test, the load-deformation relations of the tensile spring and the shear spring are set as shown in Figure 2.7 for the connections of “Composition #1” in Figure 2.3. These relations are similar to that described in the manual. The strength at 1st yield point corresponds to the allowable strength. The standard on diameter of the bolt in the tensile connections is set “M16” for Wall-Foundation connections, “M20” for the other tensile connections. The length of the bolts is set 400mm for Wall-Foundation connections, 210mm for the other tensile connections. The number of screws in the shear connections is 14 for Wall-Foundation connections, 18 for the other shear connections. The diameter and the length of screws are each 4.0mm, 65mm.

Based on the description of the manual, the load-deformation relations of compressive spring elements are assumed as bi-linear as shown in Figure 2.7. Their yield strength, P_y, initial stiffness, k_1 and 2nd stiffness, k_2 are obtained as Equation (8)-(16). The allowable strength is 2/3 times of P_y. The ultimate deformation is not defined.

Wall-Foundation:
$$P_y = F_c \cdot t_w \cdot d_{eff} \tag{8}$$
$$k_1 = k_e \cdot t_w \cdot d_{eff} \tag{9}$$
$$k_2 = 0 \tag{10}$$

Wall-Floor:
$$P_y = F_{cv} \cdot t_w \cdot d_{eff} \tag{11}$$
$$k_1 = \frac{E_{cv} \cdot t_w \cdot d_{eff}}{t_f} \tag{12}$$
$$k_2 = k_1 / 8 \tag{13}$$

Wall-Wall:
$$P_y = F_{cv} \cdot t_w \cdot d_{eff} \tag{14}$$
$$k_1 = \frac{1.5E_{cv} \cdot t_w \cdot d_{eff}}{t_f} \tag{15}$$
$$k_2 = k_1 / 8 \tag{16}$$

where t_w = thickness of wall panel, d_{eff} = effective panel width assumed as 1/4 times of distance from tensile connection to opposite edge of panel, k_e = compressive stiffness of panel assumed as 15.6N/mm^3, t_f = thickness of floor panel, E_{cv} = elastic modules perpendicular to grain of the surface lamina assumed as 0.2GPa.

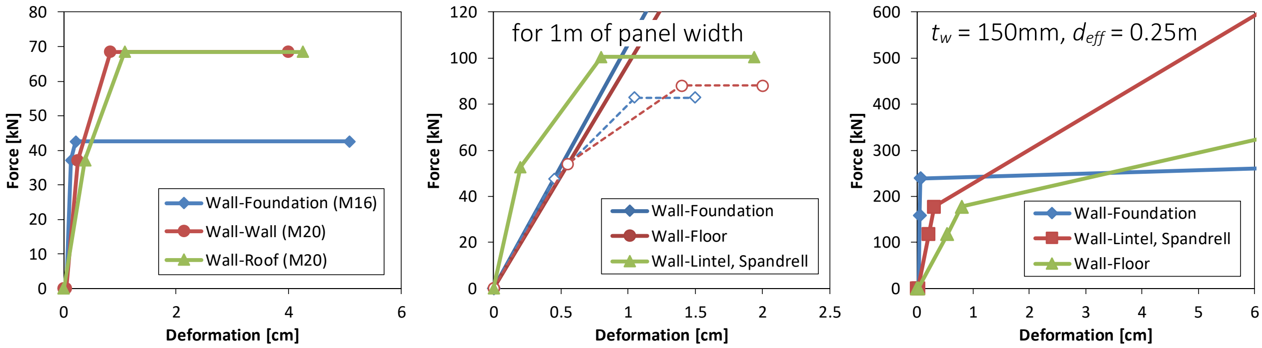

Tensile *Shear* *Compreesive*

Figure 2.7. Load-deformation relations of the spring ements for the connections

Considering that tensile and compressive spring elements are set at the corner of panels in the frame model, load-deformation relations of spring element corresponding to tensile and compressive connections are modified where deformation is divided by R and strength is multiplied by R that is the ratio of the distance between tension and compression resultant to the width of panel, D. R is obtained as Equation (17).

$$R = 0.83\frac{d}{D} \quad (17)$$

where d = distance from tensile connection to opposite edge of panel assumed as $d = D - 100$ mm in this paper, the coefficient “0.83” is led from the assumption that the distance between the neutral axis and the tensile connection is $d/2$.

3 Required wall quantity and practicability

3.1 Objectives of the estimation

Using 2D frame models corresponding to vertical planes of structure of NP shown in Figure 2.6, the required wall quantity, L_{req} was estimated from CRLS based on the structural performance of CLT panels and connections set in Section 2.4. In the estimation, parameters were set as below.

- Number of story: 3, 5
- Width of wall panels, L_w : 1.0m, 1.5m, 2.0m
- Width of openings, L_o : 1.0m, 2.0m, 3.0m, 4.0m
- Height of story: 3.0m, lintel: 0.6m, spandrel: 1.0m
- Cross wall: 1m of width, 2 of tensile connections
- Arrangement of spandrel walls
  - Case 1: Exist in all story as shown in Figure 2.6
  - Case 2: Not exist in all story

The distribution of story weights was 0.75 in the top story, 1.0 in the other stories. The grade of wall CLT panels was Mx60-3-3 and Mx60-5-5 for 3 story constructions, Mx60-5-5 and Mx60-7-7 for 5 story constructions. Thickness of laminas was 30mm for all CLT panels.

Diameter of bolts in the tensile connections of Wall-Foundation was M16 for Mx60-3-3, M20 for Mx60-5-5, M24 for Mx60-7-7. Strength of tensile spring elements shown in Figure 2.7 were multiplied by ratio of cross section of bolts in the Wall-Foundation connections to M16. The load-deformation relations shown in Figure 2.7 of the shear spring elements of wall, lintel and spandrel correspond to 1m of their width. And their strength was assumed as proportional to their width. Besides, the shear connections at top and bottom of wall panels were assumed to keep the initial stiffness considering the effect of friction.

The load-deformation relations of the compressive springs shown in Figure 2.7 were modified depending on the thickness and the width of CLT panels.

3.2 Weight carrying capacity and required wall quantity

From static load incremental analysis using the frame models, relations of story shear and story drift were obtained to calculate the capacity curve. Total weight of the frame model was adjusted so that the intersection of the capacity and the demand curve match with the limit point corresponding to the design criteria mentioned in Section 2.3 for both of Level 1 and 2. The demand curve was calculated assuming h_{eq} = 10% as the lower limit based on the results of past shake table tests. The adjusted total weight was divided by total width of wall CLT panels in 1st story of the frame model to obtain the weight carrying capacity, w_c of wall CLT panels as shown in Figure 3.1.

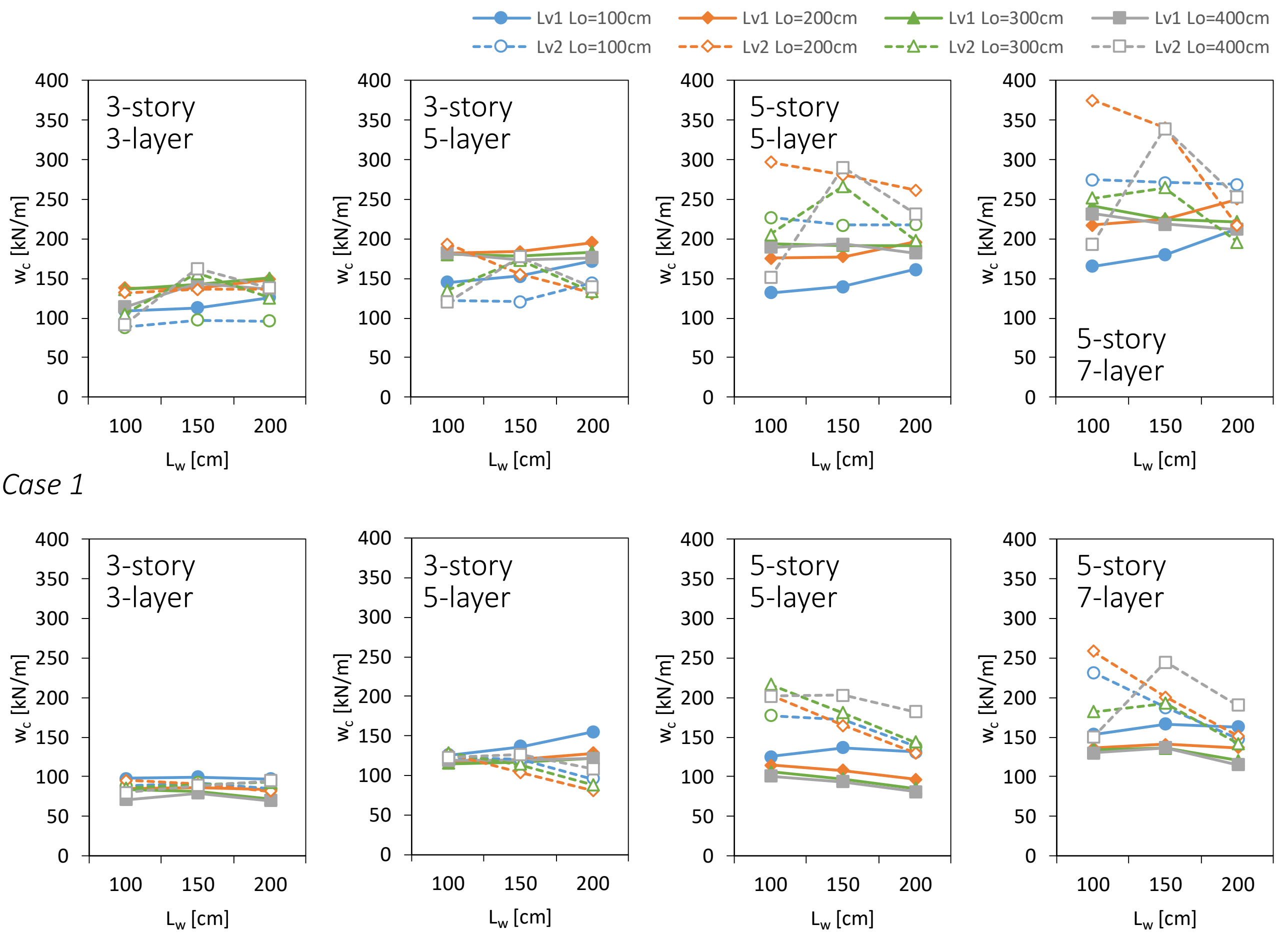

Figure 3.1. The relations of the weight carring capacity, w_c and wall width, L_w

Then the required wall quantity, L_{req} was obtained as Equation (18).

$$L_{req} = \frac{w_{ttl}}{w_c} \tag{18}$$

where w_{ttl} = total weight of building divided by floor area of 1st story.

The story weight was assumed as 3.5kN/m^2 for ordinary 3-story buildings, and as 6.0kN/m^2 for fire resistive 5-story buildings to set w_{ttl} as 9.63kN/m^2 and 28.5kN/m^2 each for both buildings based on the story weight distribution mentioned in Section 3.1. The general value of L_{req} was obtained as shown in Table 2.

Table 2. General value of required wall quantity, L_{req}

story	3	3	5	5
wall CLT	3-layer	5-layer	5-layer	7-layer
w_{ttl} [kN/m^2]	9.63	9.63	28.5	28.5
w_c [kN/m]	75	98	108	137
L_{req} [m/m^2]	0.128	0.098	0.264	0.208

L_{req} of 3-story buildings is generally less than the standard wall quantity of reinforced concrete boxed wall-buildings which is ruled as 0.12-0.15m/m^2 (*Architectural Institute of Japan*, 2003), proving practicability while L_{req} of 5-story buildings is approximately 2 times larger than the standard wall quantity. The practicability of 5-story CLT buildings with the standard connections mentioned in Section 2.2.2 has to be regarded as inadequate.

4 Development of high-performance connections

The reduction of L_{req} is necessary for prevalence of middle-rise CLT buildings in Japan. It will be achieved by improvement of the connections. In this Chapter, a high-performance connection system and outline of the static lateral loading test of the system are introduced.

4.1 Composition of the high-performance connection system

Drift-penned inserted steel plate connections are suitable for CLT panels because the split failure of the parallel layers is prevented by the cross layer, and it is comparatively easer to obtain high strength. Focusing this fact, the high-performance connections shown in Figure 4.1 are proposed.

The thickness of the inserted steel plates is 12mm, the diameter of drift-pins is 20mm in all of the connections. The vertical tensile connections between the wall panels and the foundation are composed with 4 of M20 anchor bolts which are installed to the base-plate welded to the inserted steel plate. The hardware of the shear connections of Wall-Foundation is installed to the foundation with anchor bolts. The vertical connections between the wall panels in the upper and the lower stories are composed with 4 of M20 bolts for the tensile force. These bolts are installed between the base-plates welded to the inserted steel plates. And for the compressive force, the steel bars are installed in the floor panel to reduce the embedding deformation. The hardware of the shear connections of Wall-Floor is fastened to the floor panel with bolts which are glued in the floor panel and screwed into the base-plate of the lower story. The end of lintel is also connected to the steel plate which is inserted into the top of wall panel.

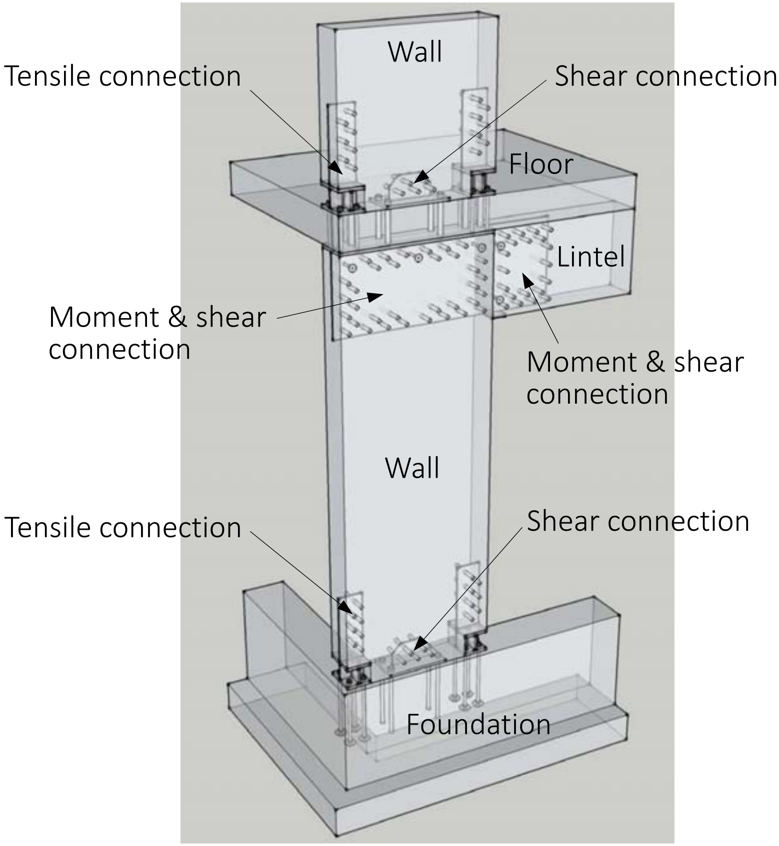

Figure 4.1. Proposed connection system

4.2 Static lateral loading test of the connection system

4.2.1 Composition of the test specimen

The test specimen is composed with wall in 1st and 2nd story, and with lintel as shown in Figure 4.2. The walls and the lintel are made from CLT panels of S90-5-7 grade, and they are fastened each other by the connection system mentioned in Section 4.1. The bottom of the wall in 1st story is fixed to the steel jig corresponding to the foundation. The width of the wall is 1m. The lintel is vertically supported at the position of 2m distance from wall edge. The specimen is subjected to the cyclic lateral load, P_H at the position corresponding to half height of 2nd story. The constant vertical load, P_V is acted on the top of the wall of 2nd story. P_V is set as 0kN and 500kN.

4.2.2 Test results

The relations of the lateral load, P_H and the story drift angle in 1st story are as shown in Figure 4.3. The allowable horizontal strength estimated from these relations based on the regulation of the manual is 76.9kN for P_V = 0, and 111.9kN for P_V = 500kN.

The structural model corresponding to the specimens were set to confirm that the analytical results agreed with the test results. Then the characteristics of the spring elements corresponding to the connections were applied to the structural model of 5-story vertical plane of structure dealt in Chapter 3 to obtain the weight carrying capacity, w_c. As a result, w_c of the 5-story vertical plane of structure in Case 2 (spandrel wall didn't exist in all story) was estimated as 375kN which was determined from the criteria shown in Section 2.3. And from Equation (18), the required wall quantity, L_{req} was obtained as 0.076m/m^2 proving enough practicability.

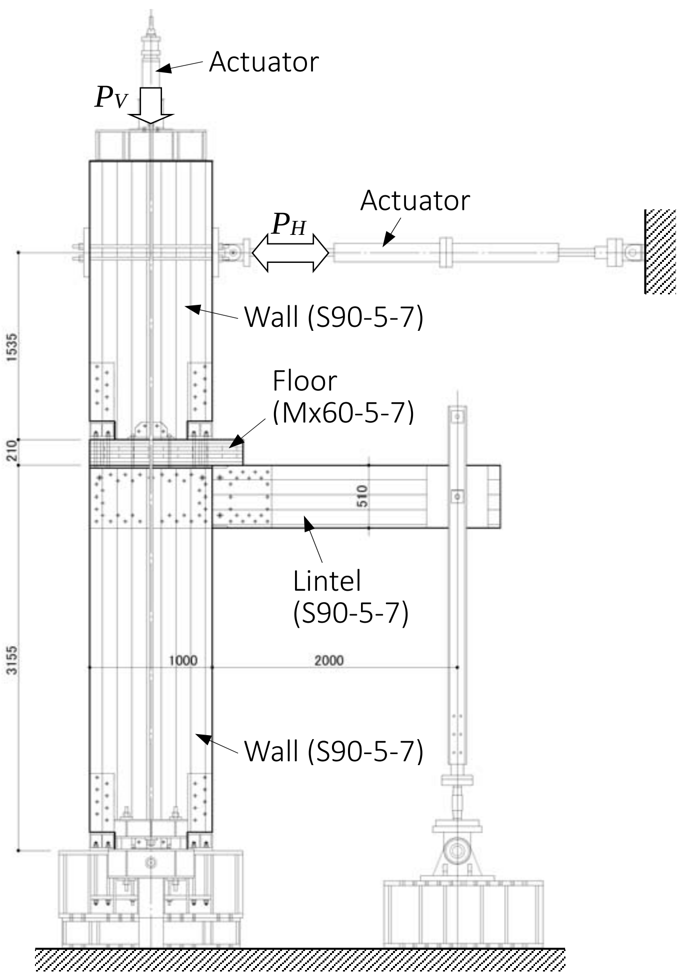

Figure 4.2. Test set up of the lateral loading test

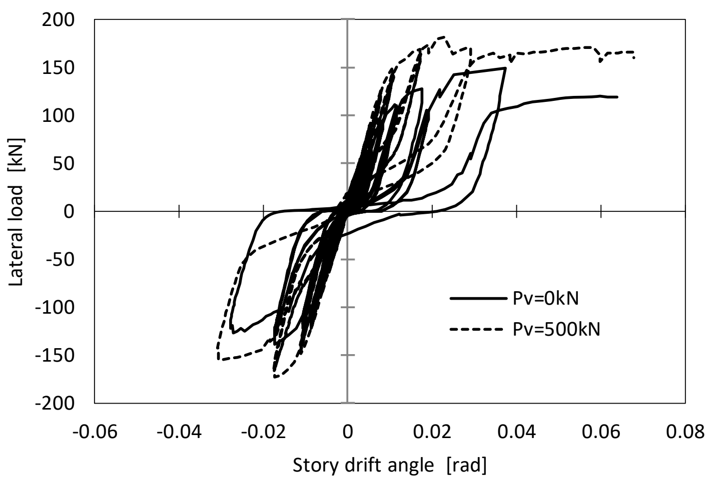

Figure 4.3. Relations of lateral load and story drift angle

5 Conclusions

In this paper, dealing the middle-rise CLT buildings with the standard composition and the standard connections described in the manual on the structural design of CLT buildings in Japan as the objectives, the required wall quantity, L_{req} was calculated based on the structural calculation method regulated in Japanese government notification to examine the practicability of the CLT buildings. As results, L_{req} of 3-story CLT buildings was generally less than the standard wall quantity of reinforced concrete boxed wall-buildings proving practicability while L_{req} of 5-story buildings was approximately 2 times larger than the standard wall quantity. Therefore, the practicability of 5-story CLT buildings with the standard connections had to be regarded as inadequate.

Succeedingly, the high-performance connection system using drift-pinned insert steel plates was introduced to reduce L_{req} of 5-story CLT buildings. As a result, it was confirmed that L_{req} of 5-story CLT buildings with the connection system was approximately half of the standard wall quantity of reinforced concrete boxed wall-buildings proving enough practicability. However, there was another condition to apply the hi-grade CLT panels which were not yet given the standard strength for the regal structural design

Besides introduced here, connection method has various possibility. The development and the proposal of the suitable connection methods for the middle-rise CLT buildings are expected. In addition, issuance of the standard strength of the hi-grade CLT panel is also expected in near future for prevalence of the middle-rise CLT buildings in Japan.

6 Acknowledgement

The study in Chapter 3 and 4 was carried out as the research project subsidized by Ministry of Land, Infrastructure and Transport and Forestry Agency of Japan. And most of the fruits shown in Chapter 4 was brought by Dr. Yoshiharu AZUMI as a colleague of Nihon System Sekkei Architects & Engineers.

7 References

Architectural Institute of Japan (2003): The design standard of reinforced concrete boxed wall-buildings.

Discussion

The paper was presented by T Miyake

A Buchanan asked why platform framing and not balloon framing was considered. T Miyake commented that construction with through walls would be allowed based on a different design method. 5 story buildings would also be possible under another method.

H Blass asked about LP1 and LP2. LP1 was expected to have cracks and LP2 was not expected to have cracks. How would one know this ahead of time? T Miyake said the CLT panels were first considered using structural models.

A Ceccotti asked if the CLT walls were compared with reinforced concrete walls what would be the thicknesses of the walls for this type of building. T Miyake said that the CLT walls would be 90 to 150 mm in thickness and reinforced concrete walls would be 150 to 200 mm in thickness.

R Jockwer commented that high performance connections with dowels and bolts were considered. Would the use of self tapping screw connections be possible? T Miyake responded that this was not within the scope of the study.

Shaking Table Tests for Verification of Seismic Design of CLT Panel Buildings

Hiroshi ISODA, Kyoto University

Naohito KAWAI, Kougakuin University

Tatsuya MIYAKE, Nihon System Sekkei Architects & Engineers

Motoi YASUMURA, Shizuoka University

Mikio KOSHIHARA, The University of Tokyo

Takahiro TSUCHIMOTO, Building Research Institute

Yasuhiro ARAKI, Building Research Institute

Takafumi NAKAGAWA, National Institute for Land and Infrastructure Management

Keywords: Shaking Table Test, CLT panel, Seismic design

1 Introduction

CLT panel is expected as suitable material for mid-rise buildings also in Japan. Japanese government notifications on the structural design of CLT panel buildings ("GN" in the followings) was issued on Apr. 1, 2016. Following the issue of GN, the guidebook on the regulations of GN and the manual on design and construction of CLT panel buildings were published

However, structural possibility of CLT buildings in Japan is supposed to be smaller than that in the other countries because of high seismic risk. In this paper, the outline of shaking table tests for CLT construction is summarized. The specimen are designed in accordance with numerical studies conducted at the stage of the regulation making process. Main specification and values in the regulations of GN are based on the numerical studies and some design values such as reduction factors are derived from the results of destruction mechanism of shaking table tests.

2 Concept of Structural Design for Specimens

Five specimens were prepared for three-dimensional shaking table tests in 2015 and 2016. The shaking table tests for three-story structure being loaded five-story seismic weight were conducted before these tests to evaluate story shear stiffness in 2014. In 2015, the final purpose of our research was to confirm numerical method for evaluating non-linear story shear and drift and in 2016, seismic design procedure was established and three specimens consisting of different structural system were prepared. Followings are design process in research team.

Various wall types of CLT panels, such as narrow shear walls without openings and wide shear walls with openings, were tested during the first stage of the project [1]. Especially, two types of shear wall with openings were tested: first, a composite wall with an opening consisting of narrow, hanging and spandrel walls; second, a shear wall with an opening hollowed out from a wide CLT panel. This is because structural performances of these shear walls are thought to be significantly different. Figure 1 shows the wall types by specimen and the load deformation relationship of these shear walls. All of the CLT panels are 150 mm in thickness, and 5-layer 5-plly and tensile bolts are used to connect the bottom of the CLT panels with the foundation, the side of the CLT and the hanging wall. Overall, the following two observations can be made:

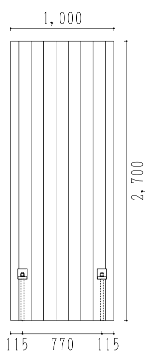

(1)Narrow shear wall

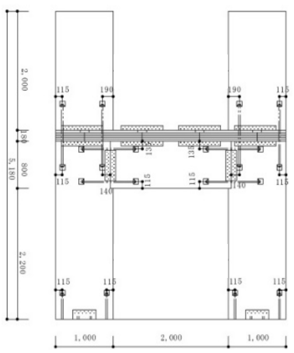

(2)Composite wall

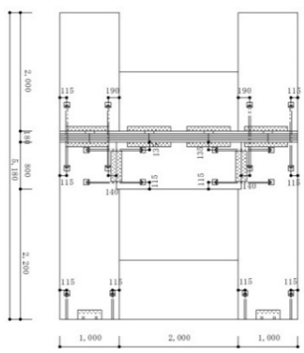

(3) Composite wall

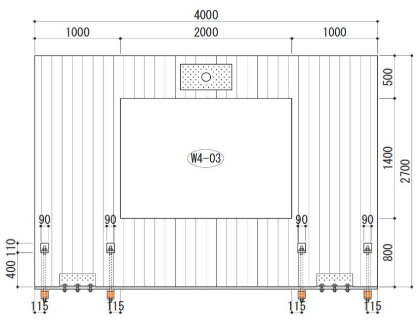

(4)Wide wall with opening

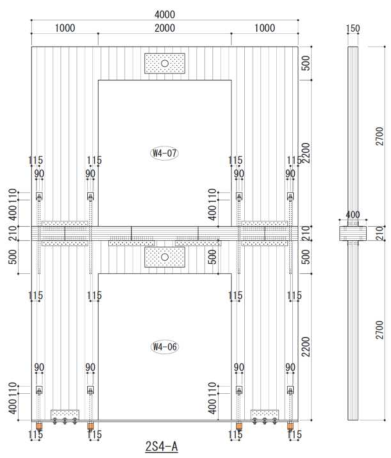

(5) Wide wall with opening

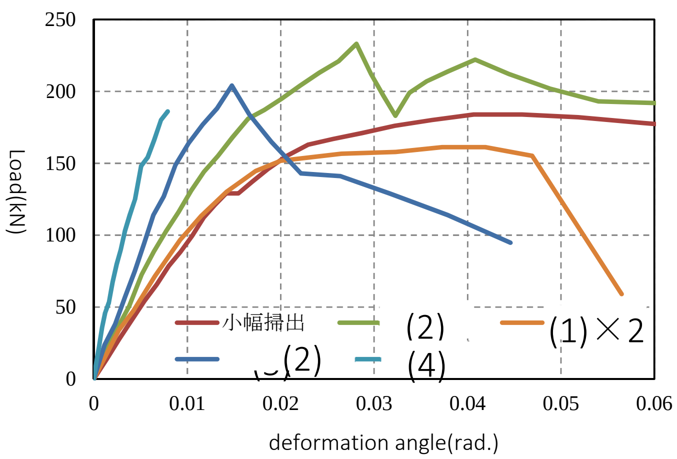

(6) Load deformation relationship

Figure 1 Static loading tests for shear walls

The composite wall composed of a narrow shear wall has high ductility compared to the wide wall with an opening.

The wide shear wall with an opening is twice the size of the composite wall but the same in strength.

When CLT building is composed with two types of wall system in one building, there is a possibility that the wide wall with an opening will be destroyed before the composite wall with an opening demonstrates their full performance. In other words, there is a possibility that the simple addition of wall performance is not satisfied.

At a stage of making structural design procedure in the project, two types of CLT building structure systems, one the assembly of narrow size panels and the other the use of large size panels with opening(s) are classified. The former is suitable for mid-rise building as it reveals ductile behaviour, while the latter is better for low-rise buildings as it has high capacity but is brittle. From the results of static loading tests, it was decided that the target buildings would be a five-story structure composed with a narrow shear wall as a mid-rise timber building and a three-story building composed with a wide shear wall as a low-rise CLT building. The wide shear wall systems are also divided into two systems. When connectors are put at the four corners of each shear wall of one wide panel and cracks occur at each corner of the openings, this wide panel is divided into narrow panels and the seismic behaviour of the structure corresponds to a building composed with narrow shear walls. A summary of their structural systems is shown in Figure 2.

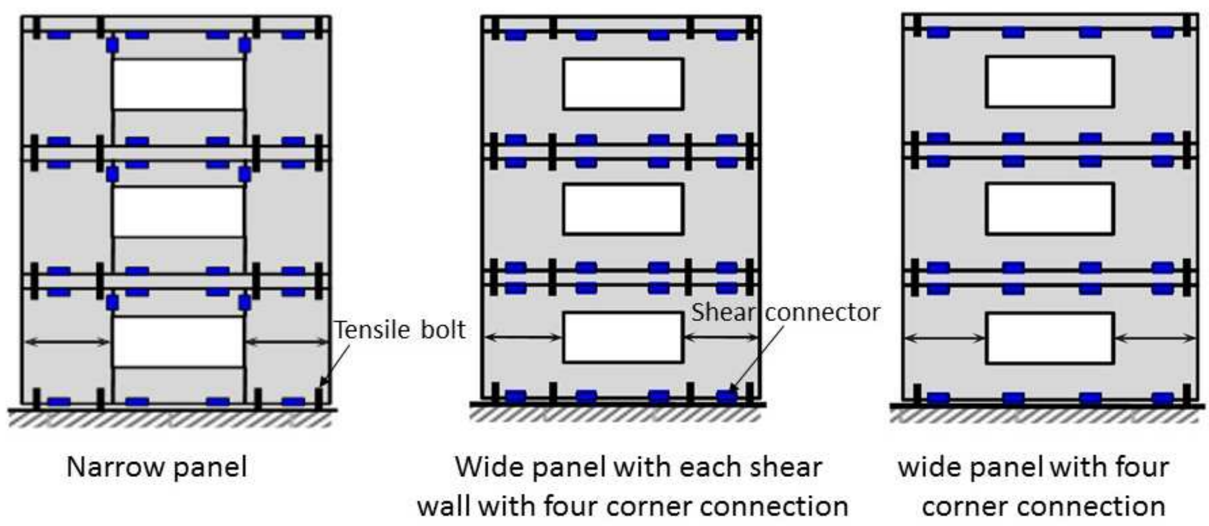

Figure 2 Three different structural system

As the results of test results and discussions, an appropriate structural system for med-rise structure was determined as the structure consisting of high ductile narrow wall and that for low rise structure was also determined as the structure of both wide and narrow shear wall system in high seismic region. When a high strength connection system is proposed to connect CLT and CLT/foundation and/or cracks are prevented in corners of opening of wide shear wall, the possibility of the med- and high-rise structure composing of wide shear wall increase despite in a high seismic region.

Structural design of three different specimen are obeyed the minimum requirement of proposed design procedure.

3 Detail of Specimen and Input Waves

Five-story and four types of three-story specimens are tested as shown in Figure 3.

Specimen C, D and E differ in construction method of the shear wall panels. The shear wall of specimen C and D is wide-wall with opening, and the shear wall of specimen E is composite wall with window opening. The difference between C and D is the part of the tensile joint of the shear wall panel. Specimen C has tensile joints at the corner of the wide wall with opening. On the other hand, specimen D and E have tensile joints at the corner of the wing wall.

Table 1 shows the outline of specification of the test specimen. Figure 4 shows the zoom-in photos of joints.

(1)Specimen A *(2)Specimen B*

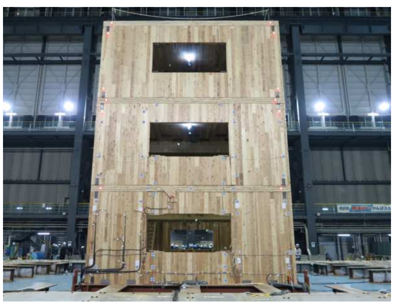

(3)Specimen C *(4)Specimen D(left) and E(right)*

Figure 3 Test specimen of full scale shaking table test

Table 1 Specification of the full scale shaking table test specimens

		Specimen A	Specimen B	Specimen C	Specimen D	Specimen E
		5story	3 story	3 story	3 story	3 story
Height(m)		14.5	8.7	8.7	8.7	8.7
Plan(m×m)		6×14.5	6×10	6×10	6×10	6×10
Specification of the wall and Length of the Panel		Mx60A 5Layer5Ply (t=150mm) 1,2,3m (Short side) 1,1.5,2m (Long side)	S60A 3Layer3Ply (t=90mm) 2m,3m (Short side) 1,1.5,3m (Long side)	S60A 3Layer3Ply (t=90mm) 1.75m (Short side) 1.75, 2m (Long side)	S60A 3Layer3Ply (t=90mm) 1m(Short side) 1, 0.825m (Long side)	S60A 3Layer3Ply (t=90mm) 1m(Short side) 1, 0.825m (Long side)
Specification of the floor panel		Mx60A 7Layer7Ply (t=210mm)				
Joint	Wall-Base Vertical	Tensile bolt M24	U-shape joint with screws and tensile bolt			
	Wall-Floor Vertical	Tensile bolt M24	U-shape joint with screws and tensile bolt			
	Wall-Base Horizontal	U-shape joint With screw	U-shape joint with screws			
	Wall-Floor Horizontal	L-shape joint With screw	L-shape joint with screws			
	Wall-Wall Vertical	-	-	-	-	-
	Wall-Hang-ing wall Shear	Steel plate with screw	(wide wall)	Steel plate with screws	(wide wall)	(wide wall)
	Wall-Hang-ing wall tensile	Tensile bolt M16×2	-	-	-	-
	Wall-span-drel wall Shear	-	-	-	-	-
	Wall-span-drel wall tensile	-	-	-	-	-
	Floor-Floor	Spline joint（Plywood and wood screw） Edge :Tensile resistant metal plate with screws				
Weight	5 story(t)	32	-	-	-	-
	4 story(t)	64	-	-	-	-
	3 story(t)	64	20	19.7	19.4	19.4
	2 story(t)	64	32	31.6	31	31
	1 story(t)	67	32	32	31	31

a) Wall-Base1

b) Wall-Base2

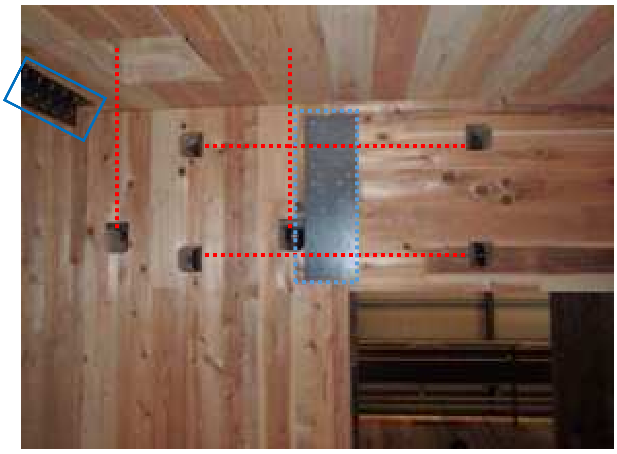

c) Wall-Floor

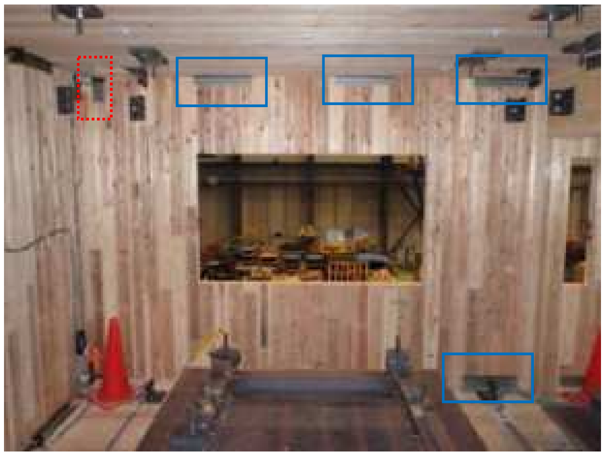

d) Wall-Hanging wall

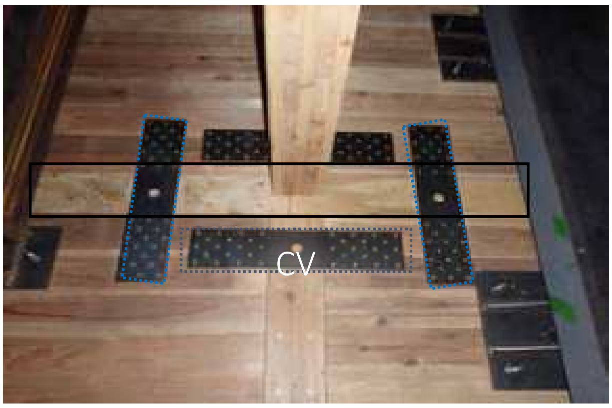

e) Floor-Floor

Tensile bolt	U-shape joint with screws and tensile bolt	Steel plate with screws
U-shape joint with screws	L-shape joint with screws	Spline joint

Figure 4 Photos of connections

The design weight of each floor was calculated in consideration of dead load and live load as shown in Table 1 as well , and steel weights were put on the floor panels so that the amount of the examination weight might reach the design seismic weight.

For input waves of strong ground motion, an artificial wave that was produced to suit the response spectrum on “ground type 2” provided under the Building Standard Law of Japan (BSL) and the strong ground motion recorded during the Kobe earthquake of 1995 (JMA Kobe) were used. Time history acceleration are shown in figure 5 ad the Sa-Sd curve (relationships of response spectrums of acceleration and displacement) of the input waves BSL and JMA Kobe in Figure 5 as well. BSL 20% as a moderate ground motion and BSL 100% as a severe ground motion were applied respectively in the x-direction and the y-direction, and JMA Kobe 100% was applied as the three-dimensional wave so that the component of larger acceleration (NS component) is applied to the long-span direction. Return periods for moderate and severe earthquakes are 50 and 200 years, respectively, in Japan.

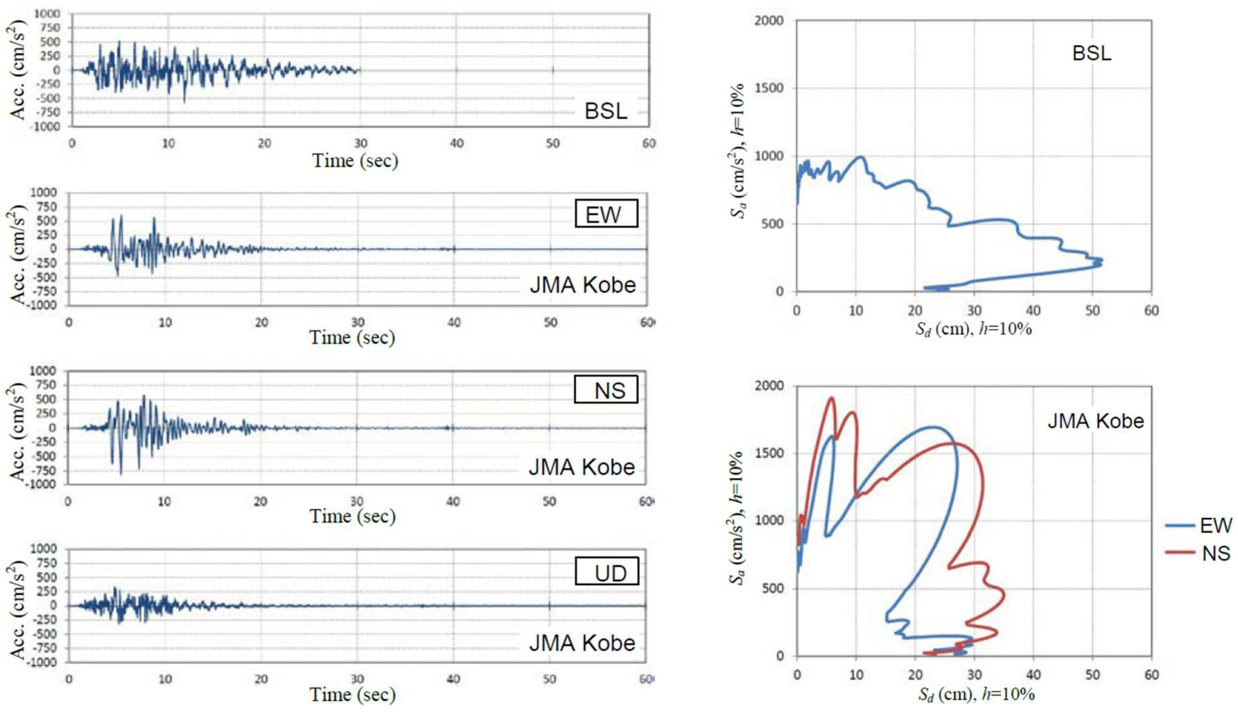

Figure 5 Time history acceleration of input waves and Sa-Sd Curve

4 Damages

Typical damages are shown in figure 6. Out-of-plane buckling by the compression force was occurred in five story specimen during 100% of Kobe ground motion. Compression destruction at the bottom of the CLT panel was also observed in the final stage of tests as shown in (2). Destruction of the shear wall panel was seen in specimen B during 140% of Kobe motion. Destruction of the boundary part of the hanging wall part and the wing wall part in wide shear wall were occurred as shown in (4) and (5). The applied shear force at the point of crack occurrence correspond to the shear force calculated by numerical model. Destruction in the boundary part of the hanging wall and narrow shear wall was observed the final stage of tests.

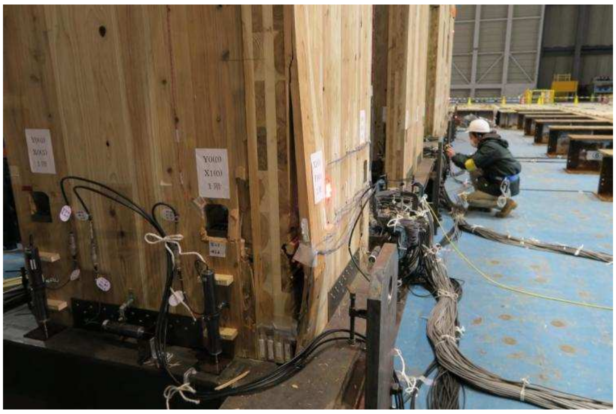

(1) Bucking

(2) Destruction in compression

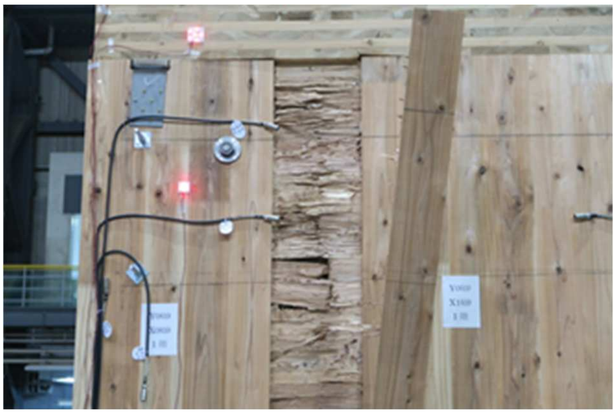

(3) Destruction in shear

(4) Destruction at the corner of opening

(5) Crack and separation

(6) Destruction in connection

Figure 6 Typical Damages

5 Discussion: Comparison of Test Result and Predictions by Numerical Model

Figure 7 shows an example of load-displacement curves in both numerical model and tests results. Two numerical models were considered to predict system level response in building and sectional stress. To predict sectional stress and failure in CLT, two dimensional finite elements (shell element) were used. This finite element is expressed as a linear and connections are expressed as nonlinear springs. Finite element model is so complicated in a practical design stage and bending bar with shear panel model was also proposed as shown in figure 8. The linear and nonlinear parameters defined by static and dynamic loading test has been introduced in the past studies.

The prediction curves correspond well to test results but high ductile performance was shown in the test result.

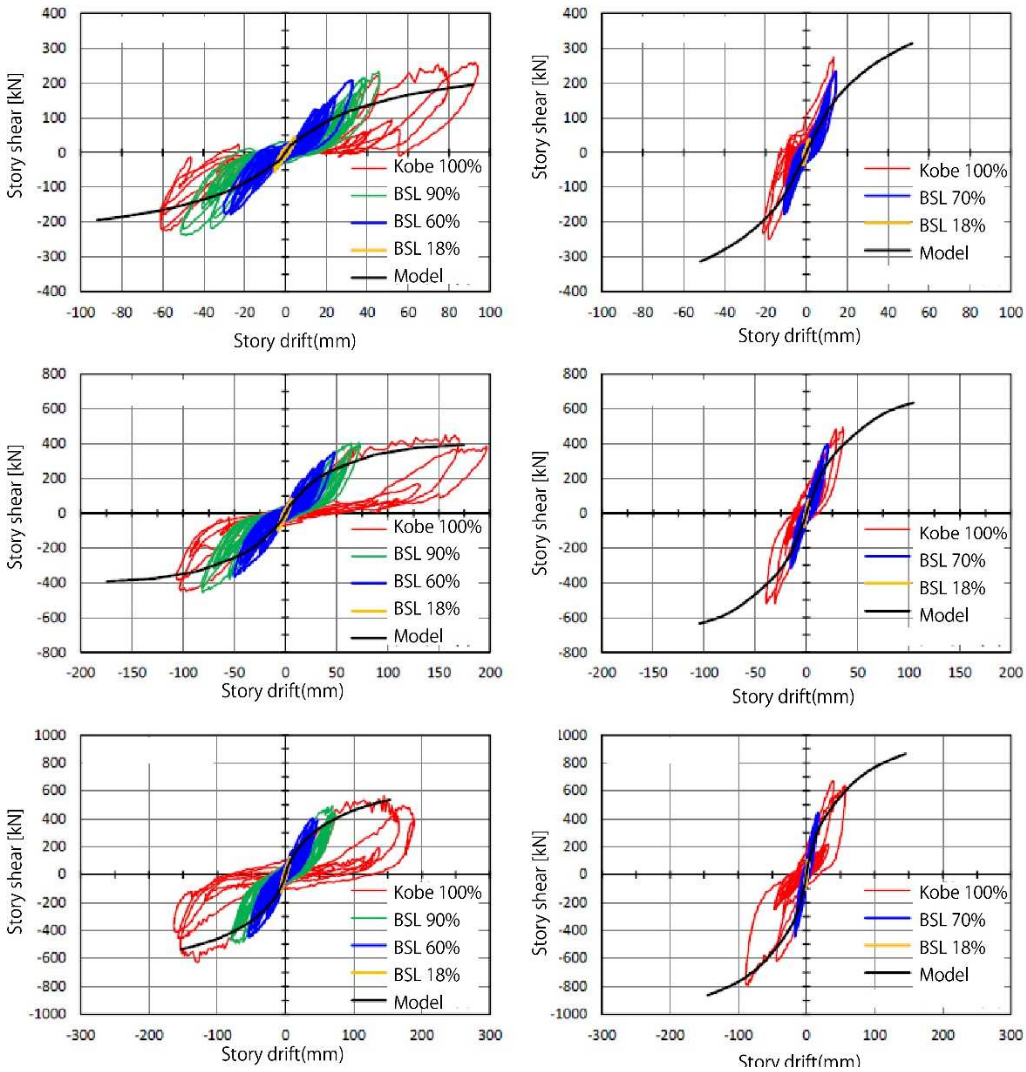

Figure 7 Comparison of test results and predictions in story shear and drift

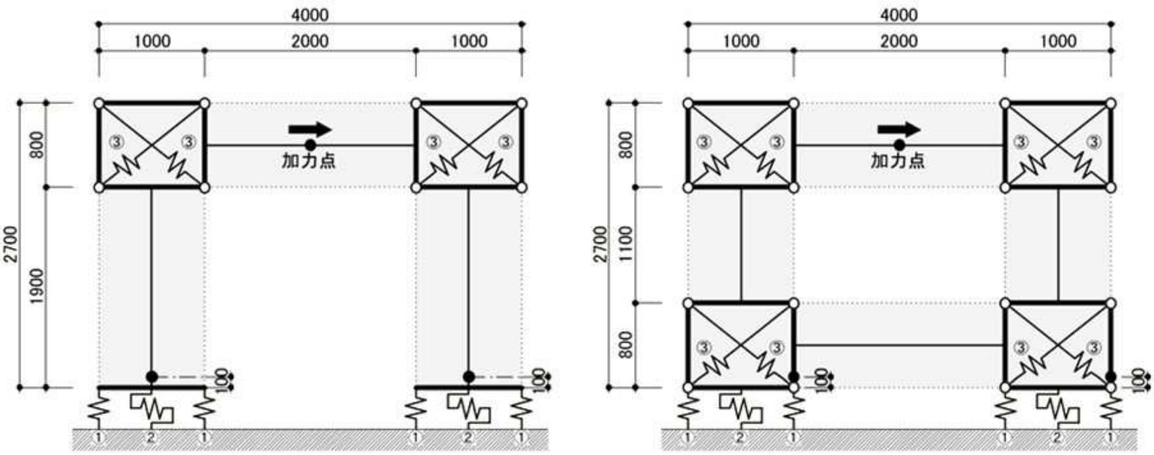

Figure8 Modelling of CLT shear wall （Left ：Door type opening、Right ：Window type opening）

6 Conclusions

In 2015, we conducted shaking table tests for evaluating seismic performance of CLT construction. At that time, our knowledge of structural performance for CLT members and their connection were limited. As the result of their limitations, story shear was underestimated in comparison with test results. In 2016, we summarized static and dynamic structural performance for members and their connections including friction resistance in CLT surface and foundation experimentally and numerically. We also proposed some numerical models which are FEM, and beam elements and shear panel with non-linear spring. Our prediction in the relationship between story shear and displacement correspond well with test results except the limit state of story drift.

7 References

Tatsuya Miyake, Kazuyuki Matsumoto, Takahiro Tsuchimoto, Hiroshi Isoda, Naohito Kawai and Motoi Yasumura(2014) "AN ANALYTICAL ESTIMATION ON SEISMIC PERFORMANCE OF 3 STORY CONSTRUCTION WITH JAPANESE "SUGI" CLT PANELS" Proceedings of the 2014 WCTE, Canada.

Naohito Kawai, Tatsuya Miyake, Motoi Yasumura, Hiroshi Isoda, Mikio Koshihara, Shiro Nakajima, Yasuhiro Araki, Takafumi Nakagawa, Motoshi Sato(2016) "FULL SCALE SHAKE TABLE TESTS ON FIVE STORY AND THREE STORY CLT BUILDING STRUCTURES" Proceedings of the 2016 WCTE, Vienna, Austria.

Motoshi Sato, Naohito Kawai, Tatsuya Miyake, Motoi Yasumura, Hiroshi Isoda, Mikio Koshihara, Shiro Nakajima, Yasuhiro Araki, Takafumi Nakagawa(2016) "STRUCTURAL DESIGN OF FIVE-STORY AND THREE-STORY SPECIMEN OF THE SHAKING TABLE TEST" Proceedings of the 2016 WCTE, Vienna, Austria.

Discussion

The paper was presented by H Isoda

M Gershfeld asked about the acceleration at the upper storey level. H Isoda said ~ 1.2 g. M Gershfeld received clarification that the deformations were based on inter-story drift and the weak story was designed to be the first story as the walls were the same in all levels.

A Ceccotti commented about the CLT failure and suggested that the weak SUGI material with low MOE might be an issue. He also received clarification that 3 ply CLT was used. He commented that 3 ply CLT only has one transverse layer and in Italy at least 5 ply CLT for walls for this type of building would be used.

A Buchanan commented that even if the material was not strong it could be possible to design the building with no damage. He asked if the Japanese standards would be interested in no damage philosophy. H Isoda said that the residents are interested. Performance based design principles are available for high performance buildings at say 1.5 times minimum requirements stipulated in Building standard law. H Isoda also stated that the high performance system would carry financial incentives with mortgages.

A Palermo stated that large acceleration could lead to failure of non-structural components. He queried with partial damages how would one do the repair and retrofit. H Isoda said that damage control systems could be used via using a stiffer system or base isolation system.

JW van de Kuilen commented about the extreme seismic event was based on large event occurred in the past. It might be better to define such event via Gamma function.

M Li and H Isoda discussed the return period and the level of the Kobe earthquake.

Capacity design of CLT structures with traditional or innovative seismic-resistant brackets

Roberto Scotta, Davide Trutalli, Luca Marchi - University of Padova, Italy

Luca Pozza - University of Bologna, Italy

Ario Ceccotti - University IUAV of Venezia, Italy

Keywords: CLT, capacity design, connections, seismic design

1 Introduction

The seismic response of cross-laminated timber (CLT) buildings is strongly dependent on the cyclic behaviour of connections between panels and to foundation, since CLT panels have a rigid and elastic behaviour in their plane. The standard connections used at foundation and in-between storeys are angle brackets and hold-downs (hereafter identified as *traditional connections*), which are manufactured to prevent respectively sliding and rocking of the shear wall. They are normally made of punched and cold-formed thin steel plates fastened to the panel generally with ring shank nails or screws. Ductility and energy dissipation capacities are entirely assigned to these dowel-type fasteners, whereas the steel plates should be over-resistant to prevent premature brittle failures. However, even if a ductile failure is assured, the wood embedment of fasteners leads to a marked pinching behaviour of the connection, limiting its dissipative capacity.

Diffusion of tall CLT buildings in high-seismicity areas claims an insight into their seismic design to ensure (1) increased ductility and dissipative capacities and (2) improved reliability of ductile parts of the structure.

(1) To the first purpose, two different strategies can be adopted. The first consists in the fragmentation of façades into narrow modular CLT panels, reciprocally jointed by means of ductile screws or nails, suitable to assure the formation of at least one plastic hinge in the fastener. The resulting increased dissipative capacity has been quantified by analysing full-scale tests of CLT shear walls (*Pozza et al.*, 2016), via parametric numerical analyses (*Pozza & Trutalli*, 2016) and also by comparison of shake-table tests

of different buildings (*Ceccotti*, 2008; *Flatscher & Schickhofer*, 2015). However, from the builders' viewpoint the fragmentation of the panels is unpopular due to the increased number of on-site joints and installation difficulties. A second strategy is the adoption of *innovative connections* with improved ductility and dissipative capacities. Various types of dissipative brackets have been developed in recent years (*Loo et al.*, 2014; *Baird et al.*, 2014; *Latour & Rizzano*, 2015; *Sarti et al.*, 2016; *Scotta et al.*, 2016) characterized by ample and stable hysteretic cycles. They exploit the hysteretic behaviour of steel or friction, so reducing or completely avoiding the pinching effect. To work properly, these connections must localize not only the failure but also the deformability in their ductile component, whereas the anchoring to the panel should guarantee limited and elastic deformations. This means that, as opposed to *traditional connections*, the fastening of the device to the panel must be over-resistant.

(2) To the second purpose, the improved reliability of ductile connections requires clear and comprehensive capacity-design rules, to guarantee that failures or incompatible deformations be not localized in the brittle parts of the connection. The capacity design approach was originally developed for RC structures (*Paulay & Priestley*, 1992). Its extension to timber and specifically to CLT structures has been formally defined and applied (*Jorissen & Fragiacomo*, 2011; *Fragiacomo et al.*, 2011; *Sustersic et al.*, 2011; *Gavric et al.*, 2013; *Izzi et al.*, 2016). Capacity design needs the definition of reliable overstrength factors γ_{Rd}, which are not provided in the current version of Eurocode 8 (2013) for timber structures. A proposal for revision of Chapter 8 of Eurocode 8 (2013) is available in literature (*Follesa et al.* 2015; *Follesa et al.* 2016). In these works, a γ_{Rd} for the CLT building technology and the formulations for its application in the capacity design are proposed.

The main obstacle to apply capacity design with *traditional connections* derives from the uncertainty in evaluating the actual strength of fasteners (i.e., the ductile component of *traditional connections*), which often largely exceeds the corresponding characteristic load-bearing capacity provided by Codes, e.g., Eurocode 5 (2009) or specific Technical Approvals (ETAs). This evidence and the high standard deviation values exhibited by the ductile part of such connections result in frequent events of brittle failures (*Gavric et al.*, 2013). Conversely, the use of *innovative connections*, characterized by low scattering of strength properties and well-predictable yielding and peak forces, makes capacity design more accessible. In this case, the underestimation of the actual strength of dowel-type fasteners (i.e., the brittle component of *innovative connections*) is on the safe side in the application of the capacity design.
This work aims to give a contribution towards the reliability of capacity design of CLT, and in general of timber buildings. A general procedure applicable to whatever connection for the robust evaluation of proper γ_{Rd} values is proposed.

The availability of results from cyclic-loading tests of an innovative connection allows the detailed application of such procedure. Reliability of the obtained γ_{Rd} for the capacity design of the fastening of the innovative bracket to a CLT panel is demonstrated through experimental evidences. The proposed procedure for γ_{Rd} evaluation is comparatively applied also to *traditional connections*, for which experimental data are available in literature (*Gavric et al.*, 2015; *Izzi et al.*, 2016).

Both the procedure for evaluation of overstrength factors and the γ_{Rd} values obtained in this work could be helpful in drafting the forthcoming release of Chapter 8 of Eurocode 8.

2 Capacity design

In this section, a conceptual model of capacity design is given, with the aim of discussing the definition of the overstrength factor to be used in designing the brittle components of a connection, based on strength properties of its ductile part.

Hereafter, the component of the connection which is desirable to deform plastically and fail before the others is identified as *ductile*, whereas all the other components, which are brittle or less ductile, are identified as *brittle*. Hence, the fastening of a connection to a CLT panel could be referred as the *ductile* part of a *traditional connection* or the *brittle* part of an *innovative connection,* independently from its actual ductility.

2.1 Conceptual model

Figure 1 shows a conceptual model according to (*Jorissen & Fragiacomo*, 2011) of the capacity design of the weakest brittle component, starting from the strength properties of the ductile element of the system. This approach is based on the scattering of peak strength of the ductile part and the analytical procedures applied to evaluate such strength (i.e., rules according to a Code). The main parameters in Figure 1 are:

d_y yielding displacement;
d_{peak} displacement corresponding to peak strength;
F_{code}^{-} characteristic load-bearing capacity estimated according to Code;
F_{peak}^{-} 5th percentile of the maximum strength obtained by tests;
F_{peak}^{mean} mean value of the maximum strength obtained by tests;
F_{peak}^{+} 95th percentile of the maximum strength obtained by tests;
F_{y}^{-} 5th percentile of the yielding strength obtained by tests;
F_{y}^{mean} mean value of the yielding strength obtained by tests;
F_{y}^{+} 95th percentile of the yielding strength obtained by tests;
γ_{Rd} overstrength factor;
γ_{an} analytical overstrength ($F_{peak}^{-} = \gamma_{an}\, F_{code}^{-}$);
γ_{sc} scattering of peak strength ($F_{peak}^{+} = \gamma_{sc}\, F_{peak}^{-}$).

Subscripts *B* or *D* identify brittle elements or the ductile element respectively.

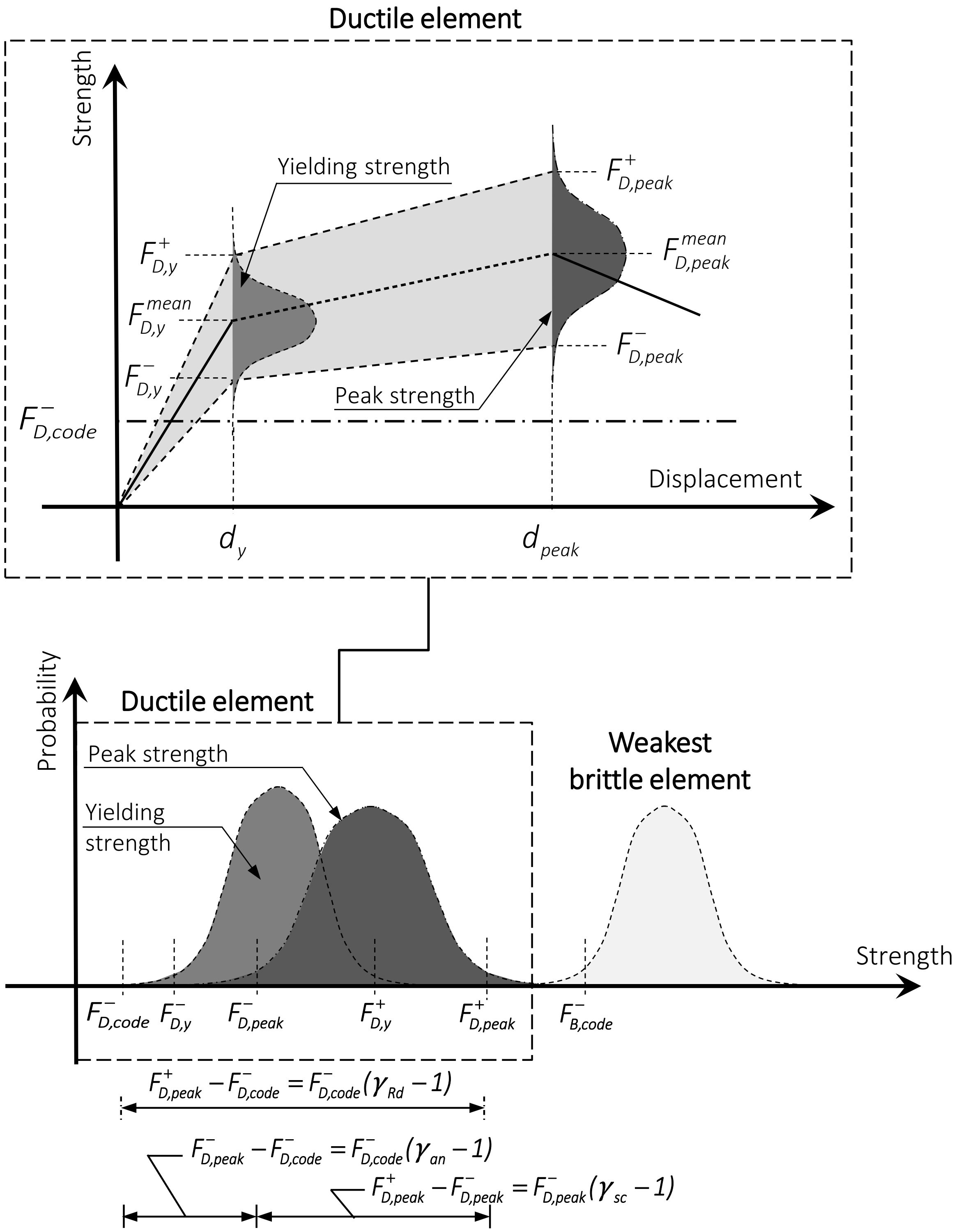

Figure 1. Conceptual model of the capacity design applied to a ductile connection

The capacity design consists in fulfilling inequality (1), i.e., the brittle parts of the system must assure a 5th-percentile load-bearing capacity higher or equal to the 95th-percentile peak strength of the ductile part, which is expressed as the product of the over-strength factor γ_{Rd} and the Code strength $F^{-}_{D,\,code}$:

$$F^{-}_{B,\,code} \geq F^{+}_{D,peak} = \gamma_{Rd} \cdot F^{-}_{D,\,code} \tag{1}$$

Hence, the overstrength factor γ_{Rd} can be defined directly as a unique term, according to Equation (2), or can be split into two parts as in Equation (3).

$$\gamma_{Rd} = F^{+}_{D,\,peak} / F^{-}_{D,\,code} \tag{2}$$

$$\gamma_{Rd} = \gamma_{sc} \cdot \gamma_{an} = F^{+}_{D,\,peak} / F^{-}_{D,\,peak} \cdot F^{-}_{D,\,peak} / F^{-}_{D,\,code} \tag{3}$$

The described conceptual model is based on the hypothesis that a set of experimental tests (at least three) is available to characterize the statistical distribution of the peak strength of the ductile component and then to compute directly $F^{+}_{D,\,peak}$. However, this experimental characterization is generally not available, and $F^{+}_{D,\,peak}$ is normally unknown by practitioners. Note that γ_{Rd} is code-dependent being strictly correlated to the analytical method used to compute $F^{-}_{D,\,code}$, which is the only value available to practitioners. This aspect is of utmost importance for timber connections, and specifically for CLT, for which $F^{-}_{D,\,code}$ is currently not univocally defined, depending on the chosen values of parameters in the calculation model. For instance, for a dowel-type fastener, $F^{-}_{D,\,code}$ is normally computed according to Eurocode 5 (2009), applying the Johansen's Theory (1949), but the resulting load-bearing capacity is not univocal, depending on the chosen values of parameters in the analytical formulations and on the special rules provided by product approvals (e.g., European Technical Approval, ETA). Therefore, γ_{Rd} values are affected not only by the statistical variability of the strength of the ductile element (γ_{sc}) but also by the analytical method to estimate its characteristic strength, according to a particular Code (γ_{an}). Therefore, it is fundamental that γ_{Rd} values proposed in a Code be consistent with the analytical methods and parameters available in the same Code.

It must be evidenced that, differently from the proposal in (*Follesa et al.* 2015; *Follesa et al.* 2016, *Izzi et al.*, 2016), the factor β_{Sd}, accounting for the strength degradation due to cyclic loading, does not appear in Equation (1). According to the cited works, factor β_{Sd} (≤ 1.0) should divide $F^{-}_{D,\,code}$ to estimate the first cycle strength starting from load-bearing capacity of the third loading cycle. However, according to the Johansen's Theory (1949) or specific ETAs, $F^{-}_{D,\,code}$ already represents the monotonic strength of metal fasteners. Therefore, the further division of $F^{-}_{D,\,code}$ by β_{Sd} would be conceptually not consistent with the theory used to estimate the load-bearing capacity of the connector. Otherwise, the strength $F^{-}_{B,\,code}$ could be reduced by β_{Sd} when the brittle component is subjected to strength degradation, but such provision results to be excessively conservative since the application of capacity design is intended to prevent the entering of brittle components into their inelastic field. It is worth noting that, in the seismic design of the connection system, the cyclic strength decay is considered in the definition of the behaviour q-factor, according to Eurocode 8 (2013), used to compute the design forces in the ductile components.

Finally, it is worth emphasizing that, the example provided in Figure 1 displays a typical connection characterized by an elastic-hardening skeleton curve with a final softening behaviour. According to standards for loading tests (e.g., EN 12512, 2006), the failure load F_u can be lower than the peak strength, when ultimate displacement d_u is higher than the displacement at maximum strength d_{peak}. Note that F_u is not needed for the application of the capacity design and has not to be confused with the peak strength.

2.2 Capacity design for CLT structures

As mentioned above, the application of capacity design to *traditional connections* is based on the evaluation of the strength properties of the ductile part, which is in most cases realized with small diameter nails or screws.

An exhaustive experimental research about steel-to-timber joints with ring shank nails for CLT is available in (*Izzi et al.*, 2016). According to these tests and depending on the chosen parameters to compute $F^{-}_{D,\,code}$ and on the angle of the force to the face lamination of the panel, the obtained γ_{Rd} values are in the range between about 1.6 and 2.6, thus demonstrating the strict correlation between γ_{Rd} and the analytical models and parameters to compute $F^{-}_{D,\,code}$. These values may be used to apply the capacity design at connection level, to design the steel plate of the connection or the anchoring to foundation or floor.

Gavric et al. (2015) evaluated γ_{Rd} from tests in shear or tension of angle brackets and hold-downs anchored to CLT floors or to foundation. Values of γ_{sc} and γ_{an} were given; γ_{Rd} can be obtained from their product, resulting in values in the range between about 2.0 and 3.4. These values may be useful to apply a capacity design at wall level, i.e., selected ductile connections should yield before others so assuring a rocking-type failure instead of a sliding one (*Pozza et al.*, 2016), or at the building level, where a "box" behaviour of the building should be assured, allowing an effective transmission of shear forces among adjacent panels (*Gavric et al.*, 2013).

The adoption of *innovative connections* developed to localise yielding in steel parts, and therefore with well-defined and predictable yielding and peak strength, undoubtedly would result in a more reliable application of the capacity design. No formulas are normally available to evaluate the load-bearing capacity of such connections. According to Eurocode 3 (2014), in steel structures $F^{-}_{D,\,code}$ is normally assumed coincident with nominal $F^{-}_{D,\,y}$: this assumption can be extended to innovative connections and, according to Equation 2, γ_{Rd} can be obtained directly as ratio between $F^{+}_{D,\,peak}$ and $F^{-}_{D,\,y}$. Testing of the ductile component can be conduced separately from tests of brittle components. It is worth noting that for these connections, if their strength and stiffness depend only on the property of steel and not on other phenomena (e.g., friction and wood embedment), $F^{-}_{D,\,y}$ might be computed with good accuracy also by means of detailed finite-element analyses if a robust non-linear constitutive law reproducing the actual elastoplastic behaviour of steel (e.g., the *Ramberg & Osgood* law, 1943) is adopted.

3 Application of capacity design

In this section, a practical application of the general concepts discussed above is reported and the γ_{Rd} suitable for a specific *innovative connection* is evaluated. The proposed procedure can be adopted for any generic connection.

3.1 Evaluation of the overstrength factor

An innovative steel bracket (*Scotta et al.*, 2016) was conceived and tested at the University of Padova. Details on conceiving, design and experimental validation of such ductile bracket, able to withstand both tensile and shear forces, can be found in *Scotta et al.* (2016) and *Marchi et al.* (2016).

Six mechanical tests (three in tension and three in shear) of the steel bracket have been performed according to the quasi-static cyclic-loading protocol of EN 12512 (2006), Figure 2. Results are plotted in Figure 3 in terms of force-displacement curve for all tests. With reference to the curves of the specimens loaded in shear, the projection of forces and displacements to the local axis x (see Figure 2b) is shown, to present the results in terms of lateral force and lateral displacements. All the reported force values are referred to a single bracket.

The tension tests of the bracket and the bi-linearization method (a) of EN 12512 (2006) returned $F^{-}_{D,y}$ and $F^{+}_{D,\,peak}$ values of 27.41kN and 48.17kN respectively, according to EN 1990 (2010). Therefore, the resulting overstrength factor γ_{Rd} for this bracket loaded in tension, according to the conceptual model presented in section 2.1 and assuming $F^{-}_{D,\,code} = F^{-}_{D,\,y}$ (see section 2.2), is equal to 1.76. In shear loading conditions, γ_{Rd} is equal to 1.15, resulting from the bi-linearization method EEEP (*Foliente*, 1996) and from $F^{-}_{D,\,y}$ and $F^{+}_{D,\,peak}$ values of 38.83kN and 44.83kN respectively. This lower value for the shear tests is mainly due to the perfectly plastic behaviour of the bracket.

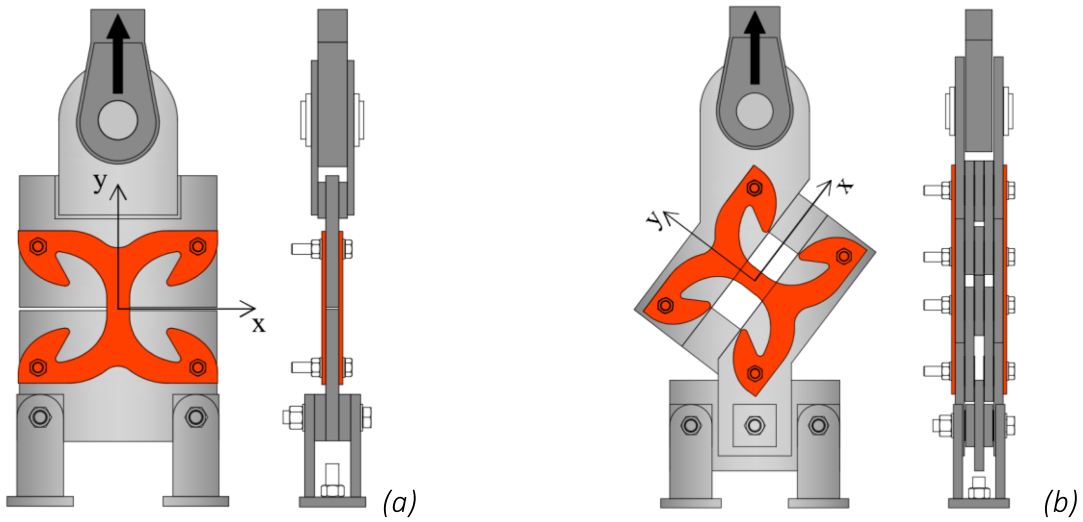

Figure 2. Test setup of the innovative bracket: (a) tests in tension; (b) tests in shear

Table 1 shows a comparison in terms of γ_{Rd} among the tested brackets in shear and tension, steel-to-timber joints with ring shank nails laterally loaded in parallel or perpendicular to face lamination of the CLT panel, and traditional hold-downs and angle brackets in shear and tension. The values for nails and *traditional connections* have been extrapolated from literature (*Izzi et al.*, 2016; *Gavric et al.*, 2015), assuming as $F_{D,\,code}^{-}$ the load-bearing capacities evaluated according to Eurocode 5 (2009), which are available in the same research works. This table lists also the overstrength sub-factors γ_{sc} and γ_{an}. It can be noted that the use of *innovative brackets*, which localize the ductility and energy dissipation capacity in a steel element, can strongly reduce the scattering of peak force and therefore the γ_{sc} value. On the contrary, a steel-to-timber connection with dowel-type fasteners has obviously a higher statistical dispersion.

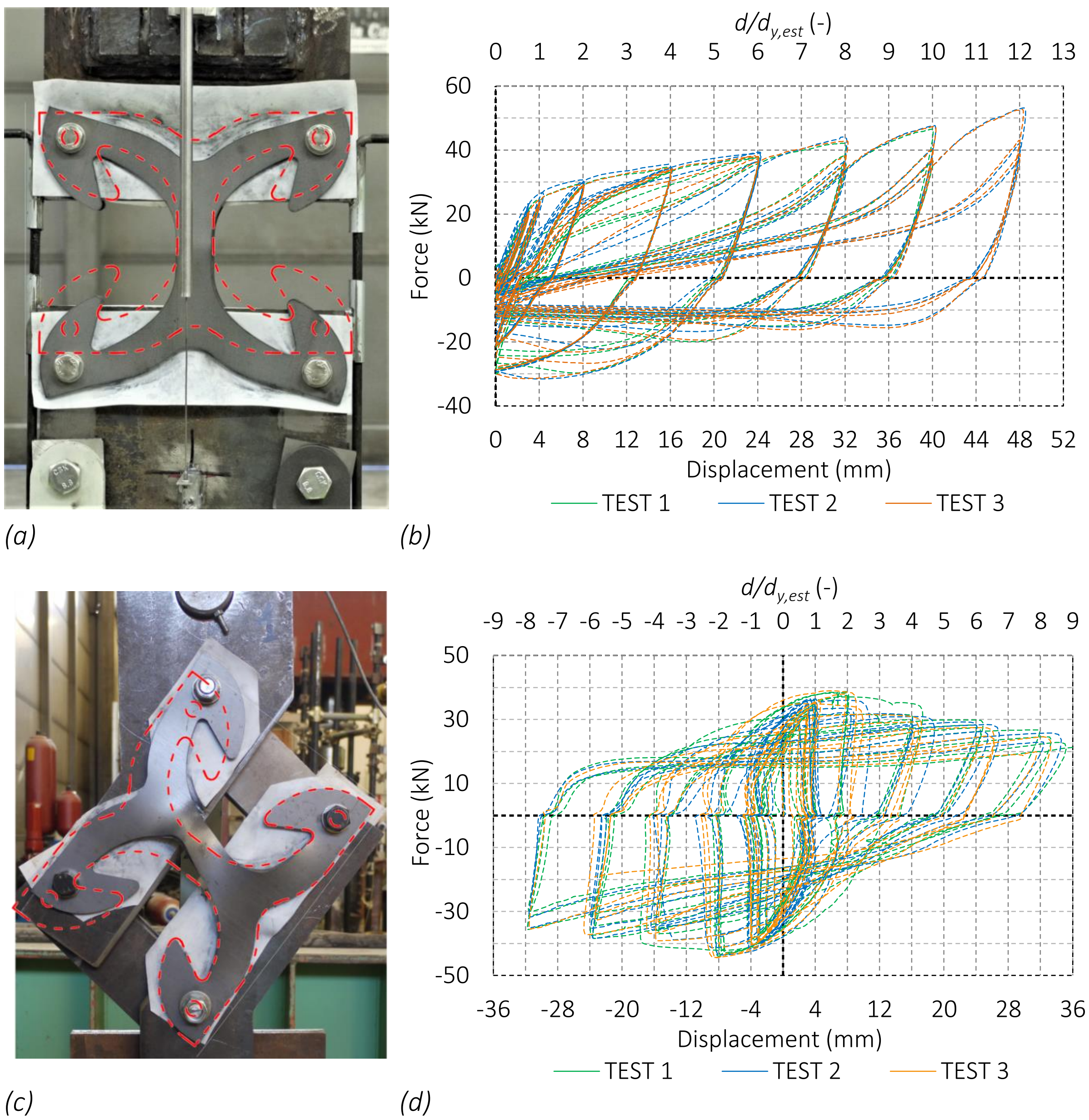

Figure 3. Axial (a, b) and shear (c, d) tests of the innovative bracket: photos of deformed specimens and force-displacement curves for a single bracket (estimated yielding displacement $d_{y,est}$ = 4.00mm)

Table 1. Comparison of overstrength factors for the innovative bracket, steel-to-timber nails and standard hold-downs and angle brackets

Connector/Fastener	γ_{sc}	γ_{an}	γ_{Rd}
Innovative bracket in tension	1.04	1.68	1.76
Innovative bracket in shear	1.04	1.11	1.15
Nails loaded parallel to face lamination*	1.27	1.61	2.04
Nails loaded perpendicular to face lamination*	1.53	1.69	2.59
Hold-down in tension**	1.30	2.60	3.38
Hold-down in shear**	1.38	-	-
Angle bracket in tension**	1.23	2.80	3.44
Angle bracket in shear**	1.16	1.70	1.97

*Values extrapolated from (*Izzi et al.*, 2016); **Values extrapolated from (*Gavric et al.*, 2015)

3.2 Application of capacity design to the connection of the innovative bracket

An applicative example of the conceptual model of capacity design given in Section 2.1, consisting in the design of the connection to the CLT panel of the innovative bracket, is here reported. Connection is designed to be more resistant than the bracket, avoiding plastic deformation of steel-to-timber fasteners and wood embedment.

The CLT element is a 120mm thick panel composed by 5 layers of C24 timber boards. The brackets are fastened to the panel with 16x200mm 8.8-class calibrated bolts passing through the 16 mm slots. Such hinge fixing allows the horizontal arms to rotate and to dissipate energy due to steel plasticization. These bolts introduce concentrated point forces in timber, which would result in prevalent wood embedment, compromising the dissipative properties of the connection. Several techniques are available to improve strength and stiffness of dowel-type joints and to reduce the pinching phenomenon (e.g., punched steel plates, toothed plate connectors, hollow steel tubes). In this application, a technique similar to punched metal plates (*Blass et al.*, 2000) has been chosen: a rectangular S275JR steel plate with dimensions of 330x200x3mm has been placed between the bracket and the panel. The thin steel plate is realized with two 16mm holes at the fixing points of the bracket. The plate was fastened to the panel with fourteen 8x100mm self-tapping partially threaded screws. The characteristic load-bearing capacity of the screws was computed according to Eurocode 5 (2009). In detail, a total shear strength $F^-_{B,\,code}$ = 52.86 kN was obtained for the effective number of screws n_{eff} = 12.64, assuming the characteristic embedment strength in the timber member $f_{h,k}$ according to Eurocode 5 (2009), the fastener yield moment $M_{y,Rk}$ and withdrawal capacity $f_{ax,k}$ according to ETA-11/0027 (2016) and the characteristic value of panel density ρ_k equal to 385 kg/m^3. Spacing and edge distance of fasteners were verified according to Eurocode 5 (2009). The value of $F^-_{B,\,code}$ is therefore higher than $F^+_{D,\,peak} = \gamma_{Rd} \cdot F^-_{D,\,code}$ = 48.24 kN (obtained assuming $F^-_{D,\,code} = F^-_{D,\,y}$), thus fulfilling Equation (1) and complying with the capacity design criterion.

Finally, a cyclic-loading test of the complete connection was conducted following the same cyclic-loading procedure and setup adopted for the bracket, in order to verify the reliability of the capacity design. The experimental test of the complete connection was conducted only in tension, Figure 4.

From the superimposition of the results recorded for the bracket and the test of the complete connection, a very similar hysteresis behaviour (Figure 5a) and a negligible decrease of strength and dissipative capacity have been proved (Figure 5b-c). The reduction of strength and viscous damping ratio ν_{eq} (EN 12512, 2006) for the complete connection with respect to the mean value from the three tests of the bracket can be quantified for all the loading cycles. It can be noted that the resulting values show the conservation of high dissipation capability of the innovative bracket also considering the slight reduction of performances due to the low elastic deformation of the complete fastening system.

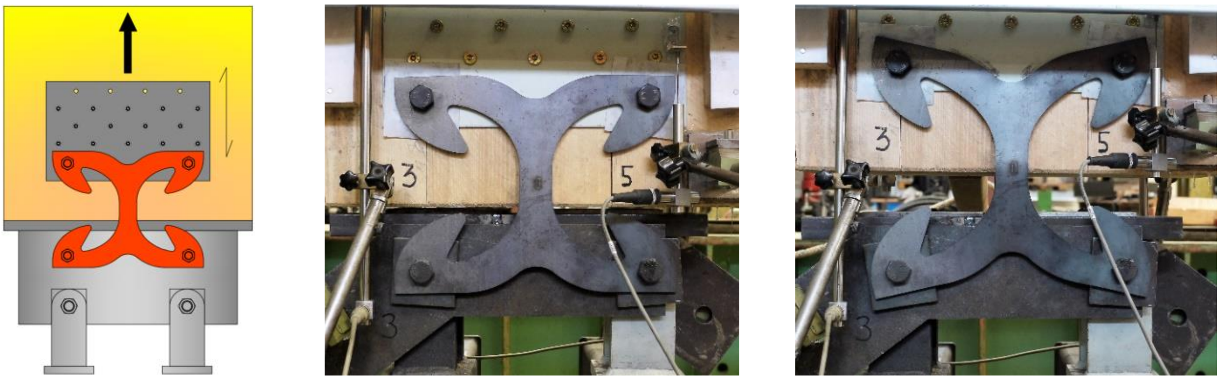

(a) (b) (c)

Figure 4. Test of the complete connection: (a) tested specimen; (b) photo of the undeformed specimen; (c) specimen at maximum vertical displacement of 48mm

4 Conclusions and implications in the seismic design according to Eurocodes

A conceptual model of capacity design has been presented and its application to the design of connections for CLT buildings has been discussed.

The overstrength factor γ_{Rd} has been defined as the minimum overstrength to be assured by the load-bearing capacity of all brittle (or less ductile) components with respect to the load-bearing capacity of the most ductile part of the connection. The load-bearing capacity of both ductile and brittle part is defined as the characteristic strength according to a specific Code.

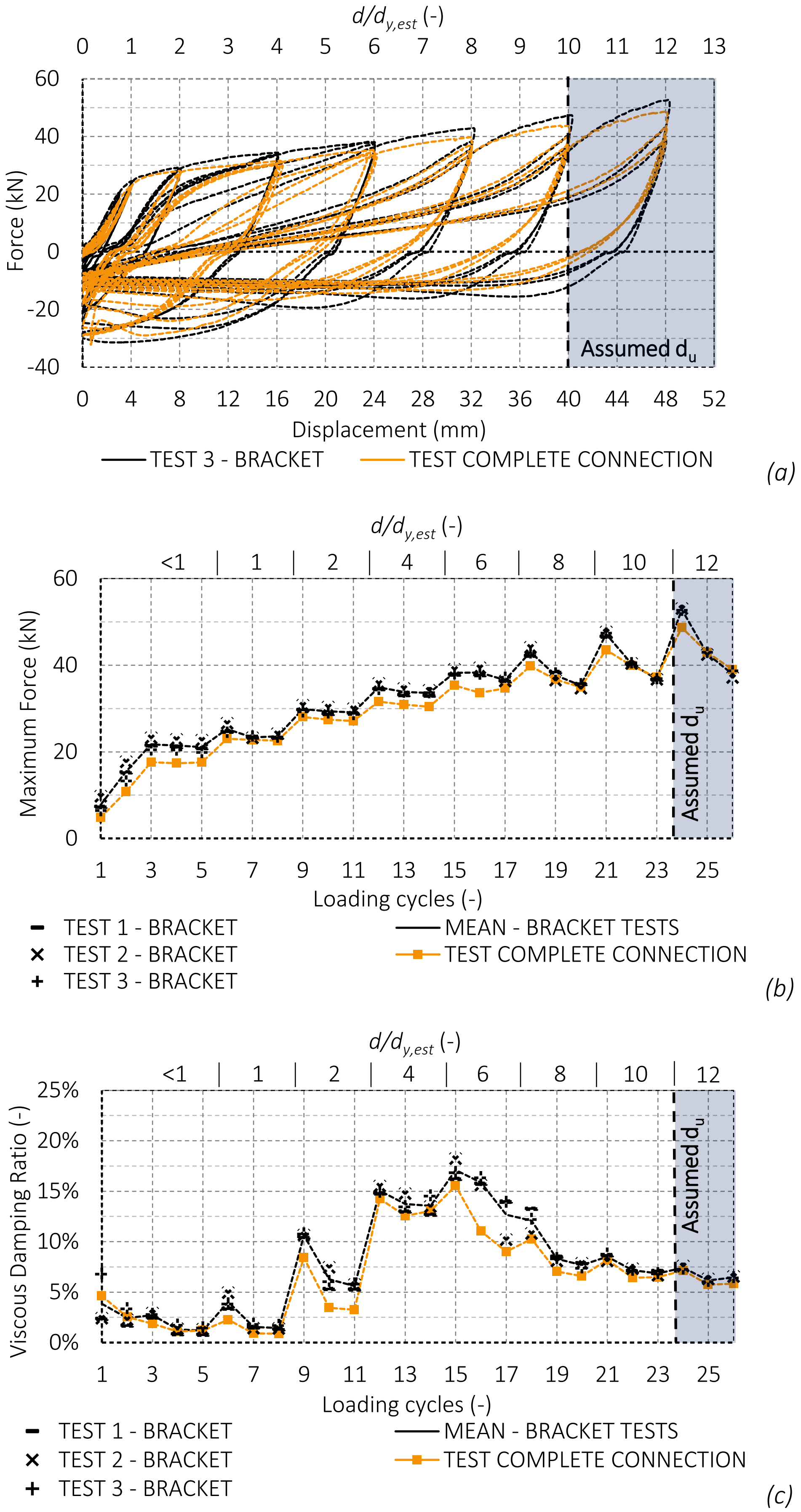

Figure 5. Comparison among tests of brackets and of the complete connection in tension: (a) hysteresis cycles; (b) maximum force per loading cycle; (c) equivalent viscous damping ($d_{y,est}$ = 4.00 mm)

The overstrength factor can be split into the product of two sub-factors, γ_{sc} and γ_{an}. The first accounts for the scattering of the peak strength of the ductile part of the connection. Therefore, a high γ_{sc} means that the ductile component is intrinsically characterized by uncertainty in its mechanical response. The second overstrength sub-factor is dependent on the accuracy of an analytical procedure and relative parameters in evaluating the actual strength of a connection. Therefore, a high γ_{an} means that the strength of the ductile component is strongly underestimated by the Code. This underestimation is normally conservative in the static design of a connection, but it may become non-conservative in the seismic design according to capacity rules, when a non-sufficient overstrength factor is used.

The conceptual model has been characterized for both *traditional* and *innovative connections* and referring to results from the latest experimental tests. The model has been finally applied to design the brittle component of the innovative bracket (i.e., steel plate screwed to CLT panel). A test of the complete connection system proved the correct application of the capacity design.

The main conclusion of this work is that it is fundamental to provide reliable overstrength factors to design the brittle components of a connection, in order to assure that the deformability and failure are localized always in the ductile part. The use of *innovative connections*, which exploit the hysteretic behaviour of steel to confer to the structure a high ductility and dissipative behaviour, can simplify and make more reliable the application of the capacity design than the use of *traditional connections*, thanks to a well-defined behaviour of the ductile component and reliable response of the structural steel.

This work highlights that overstrength factors are affected not only by the statistical variability of the strength of the ductile element but also by the analytical method adopted to estimate its characteristic strength, according to specific Code or ETA provisions. Moreover, the γ_{Rd} factor, to be used in the capacity design, should be associated to each ductile connection employed in the structure (e.g., nails, screws, dowels, etc...) and not to the constructive system (e.g., CLT, light timber frame…) as proposed in (*Follesa et al.* 2015; *Follesa et al.* 2016). However, it is evident that a γ_{Rd} for any possible connection cannot be provided by a Code or a Standard. Therefore, proper values suitable for families of connections with similar mechanical responses and applications should be given, coherently with the analytical procedure and parameters adopted to compute their load-bearing capacity.

Concepts and results provided in this work may be useful for a future implementation into Codes of capacity design rules for CLT and timber buildings and to give a procedure to characterize *innovative connections* also in terms of overstrength factor.

5 References

Baird, A, Smith, T, Palermo, A, Pampanin, S (2014): Experimental and numerical study of U-shape flexural plate (UFP) dissipators. In New Zealand Society for Earthquake Engineering Conference, Auckland, New Zealand.

Blass, HJ, Schmid, M, Litze, H, Wagner, B (2000): Nail plate reinforced joints with dowel-type fasteners. Proceedings of the World Conference on Timber Engineering (WCTE), Whistler, Canada.

Ceccotti, A (2008): New technologies for construction of medium-rise buildings in seismic regions: the XLAM case. Structural Engineering International 18(2):156-165.

ETA-11/0027 (2016) Screws for use in timber constructions, ETA-Danmark A/S, Denmark.

European Committee for Standardization (2006): EN 12512 - Timber Structures. Test Methods. Cyclic Testing of Joints Made with Mechanical Fasteners. CEN, Brussels.

European Committee for Standardization (2009): EN 1995-1-1 Eurocode 5 - Design of timber structures, Part 1-1, General: Common rules and rules for buildings. CEN, Brussels.

European Committee for Standardization (2010): EN 1990 - Eurocode - Basis of structural design. CEN, Brussels.

European Committee for Standardization (2013): EN 1998-1-1 Eurocode 8 - Design of structures for earthquake resistance, part 1: general rules, seismic actions and rules for buildings. CEN, Brussels.

European Committee for Standardization (2014): EN 1993-1-1 Eurocode 3 - Design of steel structures - Part 1-1: General rules and rules for buildings. CEN, Brussels.

Flatscher, G, Schickhofer, G (2015): Shaking-table test of a cross-laminated timber structure. Proceedings of the ICE - Structures and Buildings, 168(11):878-888. DOI 10.1680/stbu.13.00086.

Foliente, GC (1996): Issues in seismic performance testing and evaluation of timber structural systems. Proceedings of the International Wood Engineering Conference, New Orleans, LA, USA.

Follesa, M, Fragiacomo, M, Vassallo, D, Piazza, M, Tomasi, R, Rossi, S, Casagrande, D (2015): A proposal for a new Background Document of Chapter 8 of Eurocode 8. Proceedings of the 2nd International Network on Timber Engineering Research (INTER), Šibenik, Croatia.

Follesa, M, Fragiacomo, M, Casagrande, D, Tomasi, R, Piazza, M, Vassallo, D, Rossi, S (2016): The new version of Chapter 8 of Eurocode 8. Proceedings of the World Conference on Timber Engineering (WCTE), Vienna, Austria.

Fragiacomo, M, Dujic, B, Sustersic, I (2011): Elastic and ductile design of multi-storey crosslam massive wooden buildings under seismic actions. Engineering Structures 33(11):3043-3053.

Gavric, I, Fragiacomo, M, Ceccotti, A (2013): Capacity seismic design of X-LAM wall systems based on connection mechanical properties. Proceedings of Meeting 46 of the Working Commission W18-Timber Structures, CIB, Vancouver, Canada.

Gavric, I, Fragiacomo, M, Ceccotti, A (2015): Cyclic behaviour of typical metal connectors for cross-laminated (CLT) structures. Materials and structures, 48:1841-1857.

Izzi, M, Flatscher, G, Fragiacomo, M, Schickhofer, G (2016): Experimental investigations and design provisions of steel-to-timber joints with annular-ringed shank nails for Cross-Laminated Timber structures. Construction and Building Materials, 122:446-457.

Johansen, KW (1949): Theory of timber connections. Int Assoc Bridge and Struct Eng 9:249-262.

Jorissen, A, Fragiacomo, M (2011): General notes on ductility in timber structures. Engineering Structures, 33(11):2987-2997.

Latour, M, Rizzano, G (2015): Cyclic Behavior and Modeling of a Dissipative Connector for Cross-Laminated Timber Panel Buildings. Journal of Earthquake Engineering, 19(1):137-171. DOI: 10.1080/13632469.2014.948645.

Loo, WY, Kun, C, Quenneville, P, Chouw, N (2014): Experimental testing of a rocking timber shear wall with slip-friction connectors. Earthquake Engineering and Structural Dynamics 43(11):1621-1639.

Marchi L, Trutalli D, Scotta R, Pozza L, Ceccotti A (2016): A new dissipative connection for CLT buildings. Structures and Architecture. CRC Press, pp 169–177.

Paulay, T, Priestley, MJN (1992): Seismic design of reinforced concrete and masonry buildings. Wiley.

Pozza, L, Scotta, R, Trutalli, D, Polastri, A, Smith, I (2016): Experimentally based q-factor estimation of cross-laminated timber walls. Proceedings of the ICE - Structures and Buildings, 169(7):492-507. DOI: 10.1680/jstbu.15.00009.

Pozza, L, Trutalli, D (2016): An analytical formulation of q-factor for mid-rise CLT buildings based on parametric numerical analyses. Bulletin of Earthquake Engineering 15(5):2015-2033. DOI 10.1007/s10518-016-0047-9.

Ramberg, W, Osgood, WR (1943): Description of stress-strain curves by three parameters. NACA, TN-902.

Sarti, F, Palermo, A, Pampanin, S (2016): Quasi-Static Cyclic Testing of Two-Thirds Scale Unbonded Posttensioned Rocking Dissipative Timber Walls. Journal of Structural Engineering, 142(4). DOI: 10.1061/(ASCE)ST.1943-541X.0001291.

Scotta, R, Marchi, L, Trutalli, D, Pozza, L (2016): A dissipative connector for CLT buildings: concept, design and testing. Materials, 9(3):139. DOI:10.3390/ma9030139.

Sustersic, I, Fragiacomo M, Dujic, B (2011): Influence of connection properties on the ductility and seismic resistance of multi-storey cross-lam buildings. Proceeding of Meeting 44 of the Working Commission W18-Timber Structures, CIB, Alghero, Italy.

Discussion

The paper was presented by R Scotta

H Blass commented about nail connection tests with one nail in that the scatter would be reduced had connections with more nails were considered. R Scotta agreed.

M Li asked about the sample size for the connection tests. R Scotta said that 3 replicates in some cases and the statistical method used had an adjustment procedure to account for sample size.

R Jockwer and A Palermo both commented about rope effects influence on values in ETA. A Palermo suggested to check more credible equations and see how this could influence the procedure. R Scotti responded that similar procedures would be used and would consider the capacity based on the required loading.

Post-Tensioned CLT Wall Systems with Multiple Rocking Segments

Dominic Sanscartier Pilon, Laval University, Quebec, Canada

Alexander Salenikovich, Laval University, Quebec, Canada

Alessandro Palermo, University of Canterbury, Christchurch, New Zealand

Francesco Sarti, PTL Structural Timber Consultants, formerly University of Canterbury, Christchurch, New Zealand

Keywords: Pres-Lam, massive timber panels, seismic design, single rocking segment, multiple rocking segments, CLT

1 Introduction

Due to major earthquakes that inflicted significant damage to cities around the world, thus rendering many buildings unusable and unrepairable, the seismic design codes are moving towards a low-damage philosophy (Priestley, et al., 1999; Naeim & Kelly, 1999; Palermo, et al., 2004). The interest in tall timber buildings has been growing in the last decade as a more environmentally friendly choice than concrete and steel. For timber to be a viable alternative, further research needs to be done, especially on low-damage lateral-force-resisting systems. Previous research on the Pre-Stressed Laminated (Pres-Lam) system (Palermo, et al., 2005) proposed for mass timber walls as an adaptation of the PREcast Seismic Structural System (PRESSS) (Priestley, 1991) has shown promising results when used with Laminated Veneer Lumber (LVL) in low-rise buildings. Since multi-storey timber buildings and Cross-Laminated Timber (CLT) are gaining popularity all over the world, further research is needed on the application of CLT Pres-Lam systems to mid-rise timber buildings.

As timber is a more flexible material than concrete, multi-storey timber buildings are more susceptible to a dynamic amplification of the seismic forces. In the original configuration, Pres-Lam walls had a single rocking interface at the wall base allowing the formation of a plastic hinge at the base. Recent research on multiple rocking segment systems in concrete buildings (Wiebe & Christopoulos, 2009) showed that by introducing connections at construction joints that allow a gap opening, the dynamic amplification effects, i.e., additional bending moments due to higher modes, can be reduced. At the same time, the need for expensive over-strength connections at construction joints is eliminated resulting in simple cost effective connections.

The first objective of this project is to demonstrate the reduction of the dynamic amplification of forces and moments in CLT multiple rocking segment systems in comparison with single rocking segment systems evaluated in previous research (Sanscartier Pilon, et al., 2017). The second objective is to develop the design procedure for the Pres-Lam system with multiple rocking segments using an 11-storey case study CLT building in Canada. Additional attention is put on the design of the connections that allow a gap opening at construction joints. To achieve these goals, non-linear numerical models of the wall segments with multi-spring elements were developed and calibrated using pushover analyses to match the analytical models. Then, a selection of strong-motion earthquakes was used to perform non-linear time history analyses (NLTHA) on the calibrated models to analyze the behavior of single and multiple rocking segment systems.

2 Single and Multiple Rocking Segments Comparison

2.1 Concepts

Like the PRESSS technology, the Pres-Lam uses a combination of pre-stressed steel bars designed to remain elastic inside the mass timber wall and replaceable yielding steel dissipaters positioned at the bottom corners of the walls, thus providing re-centering and energy dissipation to the system. So far, single rocking segment systems have been developed and analyzed assuming rigid connections between the panels, resulting in a dynamic amplification of the forces in the upper storeys and higher costs (*Figure 1(a)*). Previous research demonstrated through numerical modeling that this amplification can be reduced by introducing simple connections allowing a gap opening at the construction joints, which will lead to a more flexible structure and cost savings. (*Figure 1(b)*).

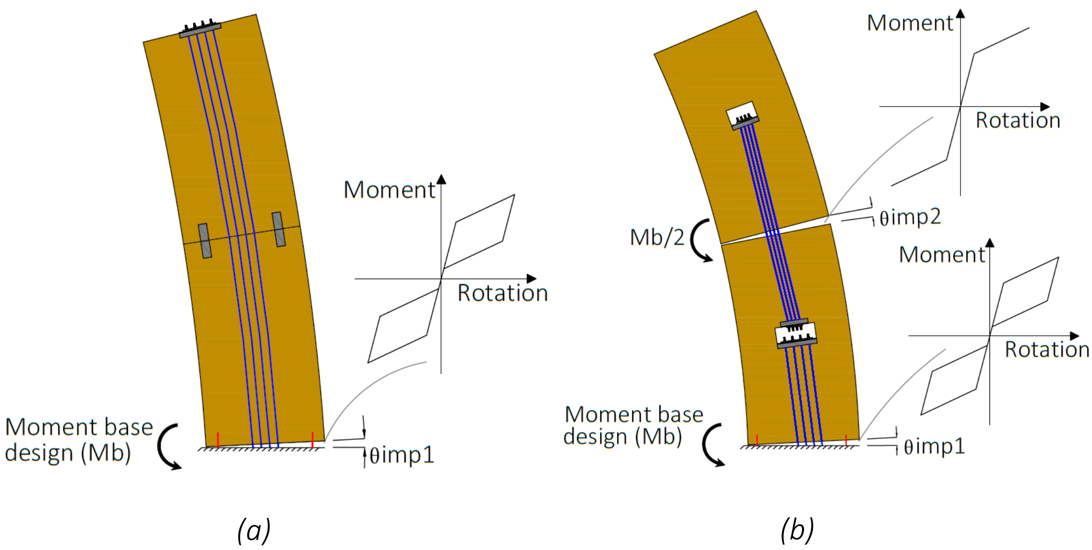

Figure 1 - Schematic systems representations: (a) Single rocking segment, and (b) Multiple rocking segments

2.2 Case Study Buildings and Seismic Analysis

To perform the analysis with the objective to demonstrate the reduction of the dynamic amplification of forces and moments by comparing CLT single and multiple rocking segment systems, several case study buildings were used (Sarti, 2015). Eight configurations of the office buildings with variable number of storeys and inter-storey heights, while having the same plan geometry, were considered (*Figure 3*). The lateral force-resisting systems consisted of post-tensioned mass timber walls with single and multiple rocking segments. A Displacement-Based Design (DBD) procedure (Priestley, et al., 2007) was performed for each case study building to obtain the design base shear (V_b) and the design base moment (M_b). The study parameters and results are presented in *Table 1*.

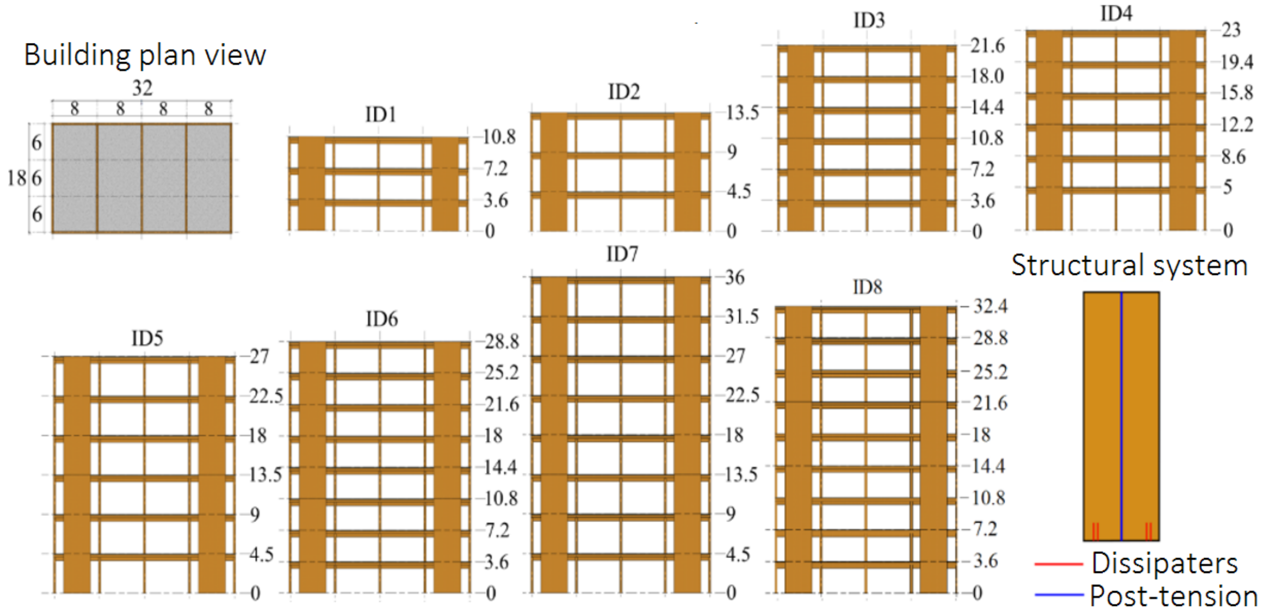

Figure 2 - Case study buildings

Table 1 - Design seismic loads

ID	No. of Storeys	h_1 (m)	h_i (m)	H (m)	Storey Mass (Ton)	V_b (kN)	M_b (kNm)
1	3	3.6	3.6	10.8	320	3946	33146
2	3	4.5	4.5	13.5	320	3475	36488
3	6	3.6	3.6	21.6	320	5128	79997
4	6	5.0	3.6	23.0	320	4979	83149
5	6	4.5	4.5	27.0	320	4108	80106
6	8	3.6	3.6	28.8	320	5148	105019
7	8	4.5	4.5	36.0	320	4118	105009
8	9	3.6	3.6	32.4	320	5682	130400

2.3 Analysis comparisons

2.3.1 Analytical Study

An analytical study has been performed on CLT single and multiple rocking segment systems to compare sizes of panels, post-tensioning bars and dissipaters needed to resist the design base shear and design base moment of the case study buildings. The Modified Monolithic Beam Analogy (MMBA) (Pampanin, et al., 2001) (Newcombe, et al., 2008) was used to perform the analytical study and to obtain the preliminary design presented in *Table 2* (only case study building 8 is shown).

The multiple rocking segment system was designed to reduce the load demand on the structure due to the dynamic amplification observed in the single rocking segment system design. As presented in *Table 2*, the cross-section areas of post-tensioning bars are reduced at the upper segments due to less pre-stress forces and the dissipaters are only used at the base. These reductions of materials in the multiple rocking segment system allow reduction of constructions costs.

Table 2 - Case study building 8 - Single and multiple rocking segments design

Single rocking segment					
Wall segment storey	Wall length (m)	Wall thickness (m)	P_t size (mm)	P_t force (kN)	Dissipater size (mm)
1 to 9	7.2	0.314	2 Ø60	3465	4 Ø50
Multiple rocking segments					
1 to 3	7.2	0.314	2 Ø70	2694	4 Ø50
4 to 6	7.2	0.314	2 Ø55	1710	-
7 to 9	7.2	0.314	2 Ø40	634	-

2.3.2 Modelling and calibration

To compare the seismic forces induced in the single and multiple rocking segment systems and to demonstrate the effects of the dynamic amplification in the upper levels, non-linear time history analyses (NLTHA) were performed on numerical models. The multi-spring numerical models have been developed in OpenSEES (MecKenna, 2011). The model shown on *Figure 3*, presents an overview of the parallel zero-length multi-spring model used to simulate the contact between the base of the wall and the foundation as well as the rocking motion. The post-tensioning bars and external tension-compression yielding dissipaters were modelled as truss elements. Multi-spring elements were added in the upper levels to model the multiple rocking segment systems. The numerical models were calibrated by comparing the resulting curve from the pushover analysis of the numerical and the analytical studies.

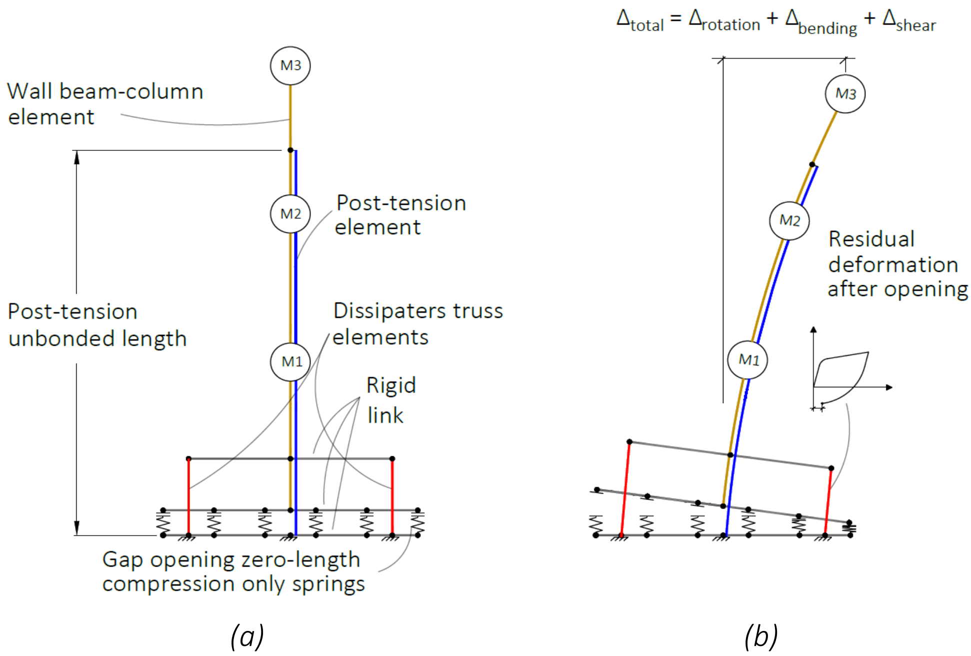

Figure 3 - Single wall multi-spring model overview: (a) initial state, and (b) deformed state

2.3.3 *NLTHA results (building 8)*

To compare the shear envelope, the bending moment envelope and the storey drift of single and multiple rocking segment systems, the numerical models were subjected to NLTHA, which consisted of ten ground motion records calibrated and selected from the Pacific Earthquake Engineering Research Center (PEER) Next-Generation Attenuation (NGA) database (Chiou, et al., 2008). The spectral acceleration of each ground motion record was scaled to match the design spectrum around the fundamental period of the building. *Figure 4* shows a list of the chosen earthquakes and the mean scaled records spectra compared to the design spectrum for Building 5 as an example.

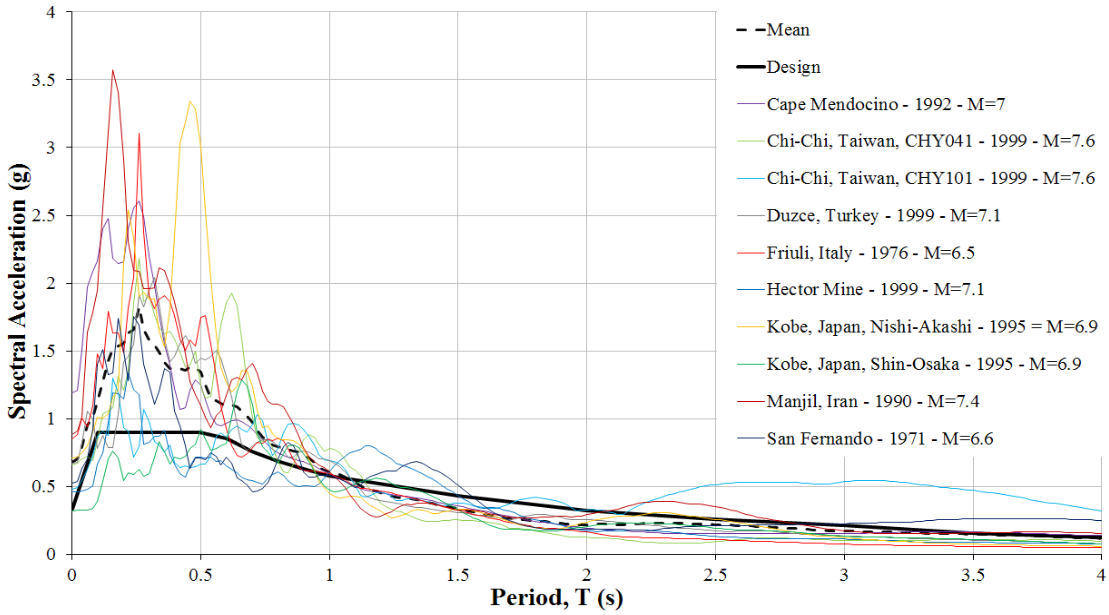

Figure 4 - Mean scaled records spectra compared to the design spectrum of case study building 5 (scaled at T=1.18s)

The resulting curves in *Figure 5*, show that the single rocking segment systems are strongly marked by an effect of dynamic amplification in the upper levels, whereas the multiple rocking segment system envelopes show a significant reduction of that effect. In Figure 5c, the storey drift is presented as a ratio of the average peak storey drift to the building height.

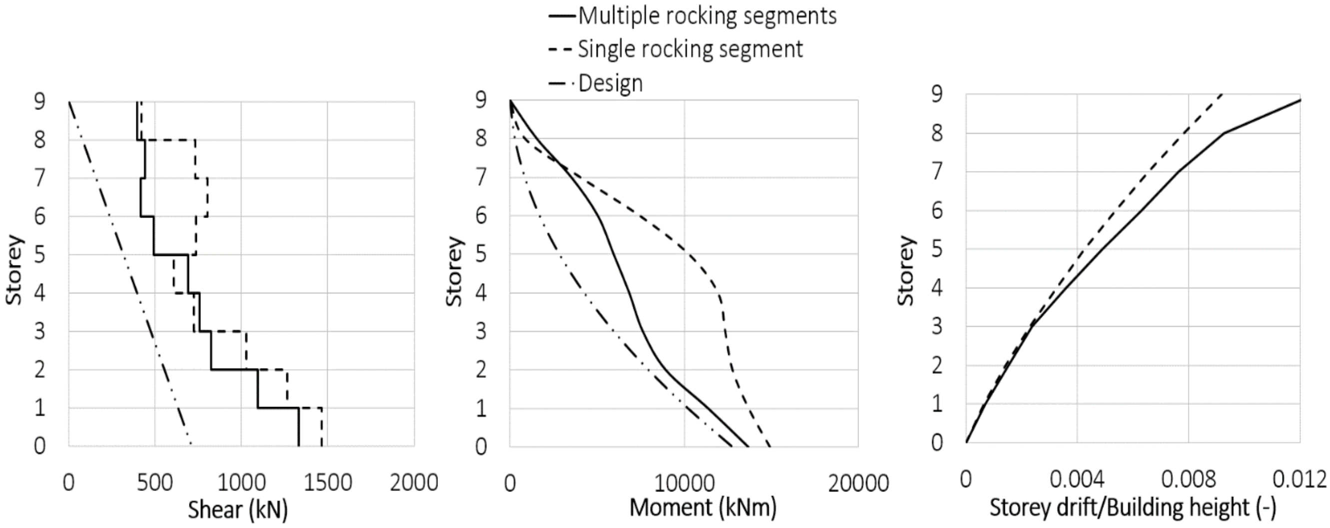

(a) *(b)* *(c)*

Figure 5 - Case study building 8 - NLTHA and design results for single and multiple rocking segments: (a) Shear envelope, (b) Bending moment envelope, and (c) Average peak drift

3 CLT Multiple Rocking Segments Case Study Building in Canada

3.1 Case Study Building

A complete seismic analysis and design of an 11-storey timber building located in Vancouver was performed using CLT single and multiple rocking segments. Each storey of the residential building has the same plan of 47.8 m long by 18.8 m wide at its maximum (*Figure 6*) with an inter-storey height of 3 m and a total height of 34.6 m. The gravity loads are resisted by a system of glulam timber posts and beams with CLT floors. It was designed for load combinations with snow loads and wind loads in accordance with the National Building Code of Canada (NRCC, 2015) and the CSA O86 (CSA Group, 2014). Results of the calculations showed that the wind loads would not govern the lateral-force-resisting system design. Seismic loads of 485 tons at each floor were considered for the DBD performed to determine the design base shear (V_b) and moment (M_b). The lateral-force-resisting system consists of 6 walls in X-direction and 7 walls in Y-direction. The length of walls in X-direction is 6.3 m, walls M1Y, M2Y, M6Y, M7Y are 7.3 m and walls M3Y to M5Y are 2.44 m. This paper presents, the DBD procedure, the analytical study, the modelling considerations, the NLTHA and an example of a connection detailing.

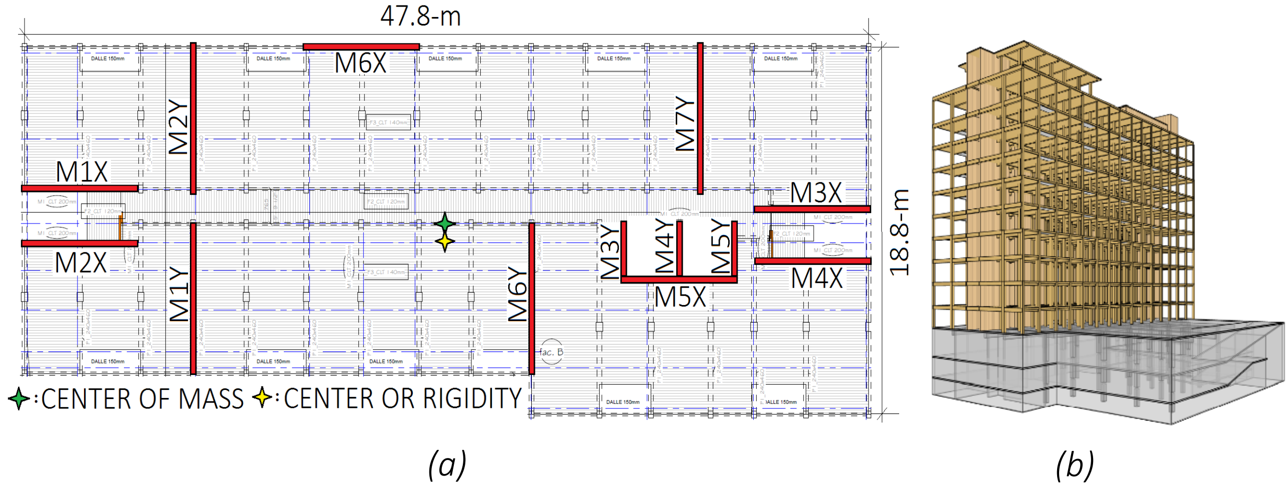

Figure 6 - Case study building: (a) Plan view, and (b) 3D view (Courtesy of Douglas Consultants)

3.2 Displacement-Based Design Analysis

The DBD procedure is based on Priestley (2007). *Figure 7(a)* presents the design acceleration spectrum for Vancouver (NRCC, 2015) and *Figure 7 (b)* the design displacement spectrum calculated based on Priestley (2007) and used to obtain the effective period of the structure (T_e). The results of the DBD analysis are presented in

Table 3. To evaluate T_e, the design displacement (Δ_d) was selected based on code drift limits and calculated following Sarti (2015) recommendations. In the preliminary design phase, the design base shear (V_b) and design base moment (M_b), considering P-delta effects, are distributed equally among each wall of the same length. The torsion effects are being treated in the model and in the final design phases.

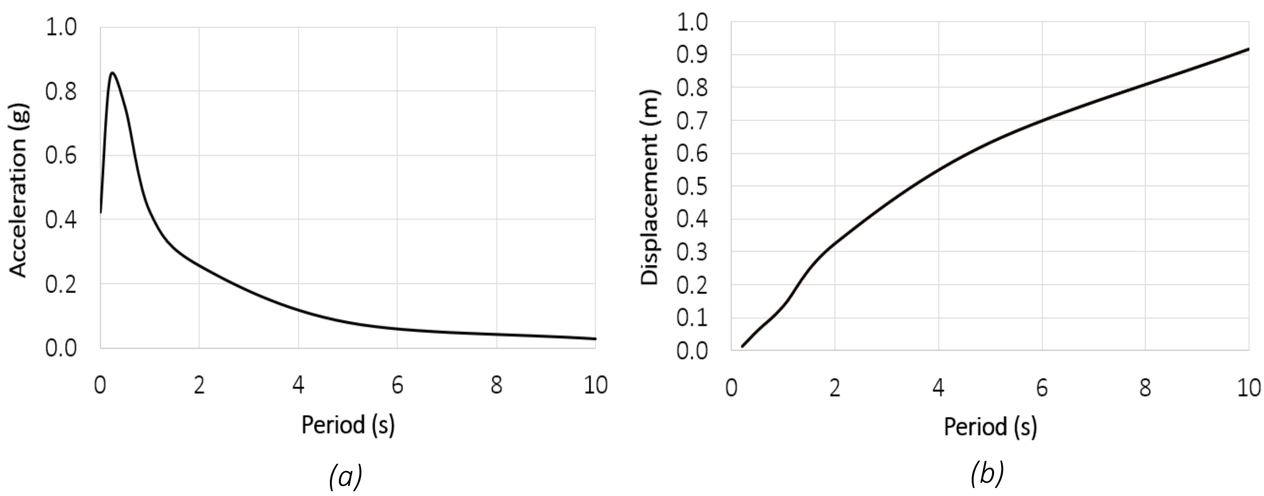

Figure 7 - (a) Design acceleration spectra, and (b) Design displacement spectra

Table 3 - Displacement-based design results

Parameters	Symbols	Units	Values
Design displacement	Δ_d	m	0.523
Effective height	H_e	m	21.9
Effective mass	m_e	Ton	3930
Equivalent viscous damping	ξ	%	9.33
Reduction factor for ξ	R_ξ	-	0.79
Effective period	T_e	s	3.76
Secant stiffness	K_e	kN/m	10964
Design base shear	V_b	kN	5735
Design base moment	M_b	kNm	145976

3.3 Analytical Study

The analytical study, or preliminary design of the walls, was performed in accordance to the Modified Monolithic Beam Analogy (MMBA). *Table 4* presents only the design results for wall M1X in X-Direction and for walls M1Y, M3Y in Y-Direction. The preliminary design of walls M2X to M6X is the same as for wall M1X; walls M2Y, M6Y, M7Y are the same as M1Y, and walls M4Y, M5Y are the same as wall M3Y. The results show the reduction of the wall cross sections, post-tension rod diameter and post-tension forces in the upper segments, thus lowering the costs of the lateral-force-resisting system in comparison to a single rocking segment system.

Table 4 - Multiple rocking segments design

Wall segment storey	Wall length (m)	Wall thickness (m)	P_t size (mm)	P_t force (kN)	Dissipater size (mm)
X-Direction - M1X					
1 to 3	6.3	0.314	4 Ø55	3905	4 Ø30
4 to 6	5.0	0.314	4 Ø55	5912	-
7 to 9	4.5	0.314	4 Ø50	4452	-
10 to 11	3.8	0.314	4 Ø40	2660	-
Y-Direction - M1Y					
1 to 3	7.3	0.314	4 Ø60	3616	4 Ø35
4 to 6	6.5	0.314	4 Ø55	5266	-
7 to 10	5.5	0.314	4 Ø50	4086	-
Y-Direction - M3Y					
1 to 3	2.44	0.314	2 Ø65	4837	4 Ø25
4 to 6	2.44	0.314	2 Ø60	3442	-
7 to 10	2.44	0.314	2 Ø50	2585	-

3.4 Modelling

To perform the NLTHA analyses and to complete the final design by considering the torsion effects of the entire building, non-linear 3D multi-spring numerical models were built and calibrated in OpenSEES (MecKenna, 2011). Multi-spring elements were added in upper levels to model the multiple rocking segment systems and all levels were attached to the mass located at the centre of mass. The analysis revealed that the shift between the centre of rigidity and the centre of mass was small enough; therefore, the hypothesis that walls of the same length and rigidity are subjected to the same forces and moment is valid. To compare the behaviour of single and multiple rocking segment systems, numerical models of the building using a separately designed single rocking segment system were built and subjected to the same NLTHA.

3.5 NLTHA Results

To observe the shear envelope, the bending moment envelope and the average peak drift of single and multiple rocking segment systems, the numerical models were subjected to NLTHA, which consisted of the same ground motion selected in section 2.3.3. *Figure 8* presents the resulting envelopes of the wall M1X in X-Direction for single and multiple rocking segment systems. The shapes of the envelopes show a significant reduction in the shear forces and bending moments in the multiple rocking segment system. In storeys 2 to 6, the bending moments in the walls are reduced by nearly 50%. It also can be noted that whilst reducing an important part of the dynamic amplifications, there is still some residual effect in the upper storeys due to the increased flexibility of a timber building structure made of multiple rocking segments. The story drift curves show that, naturally, the multiple rocking segment system is more flexible. Nevertheless, it stayed within the drift limits prescribed by the code.

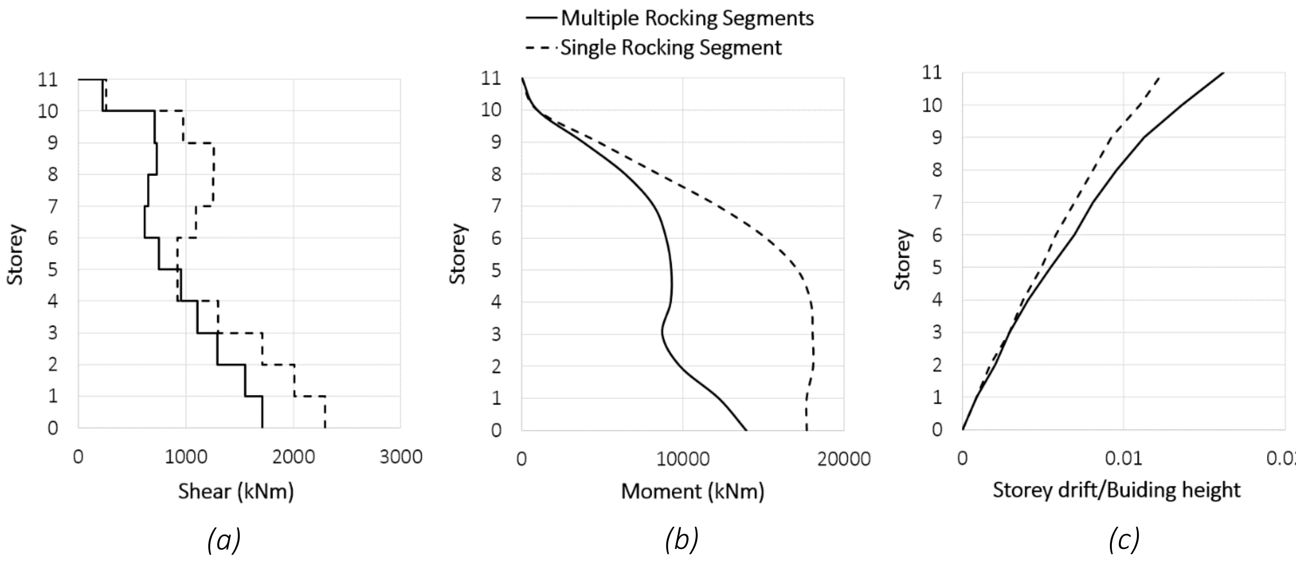

Figure 8 - NLTHA results for wall M1X: (a) Shear envelope, (b) Bending moment envelope, and (c) Average peak drift

Figure 9 presents the resulting envelopes for the wall M1Y in Y-Direction for single and multiple rocking segment systems. The shapes of the envelopes also show a significant reduction in the shear forces and bending moments for the multiple rocking segment system. Story drifts in Y-Direction are also within the code drift limits.

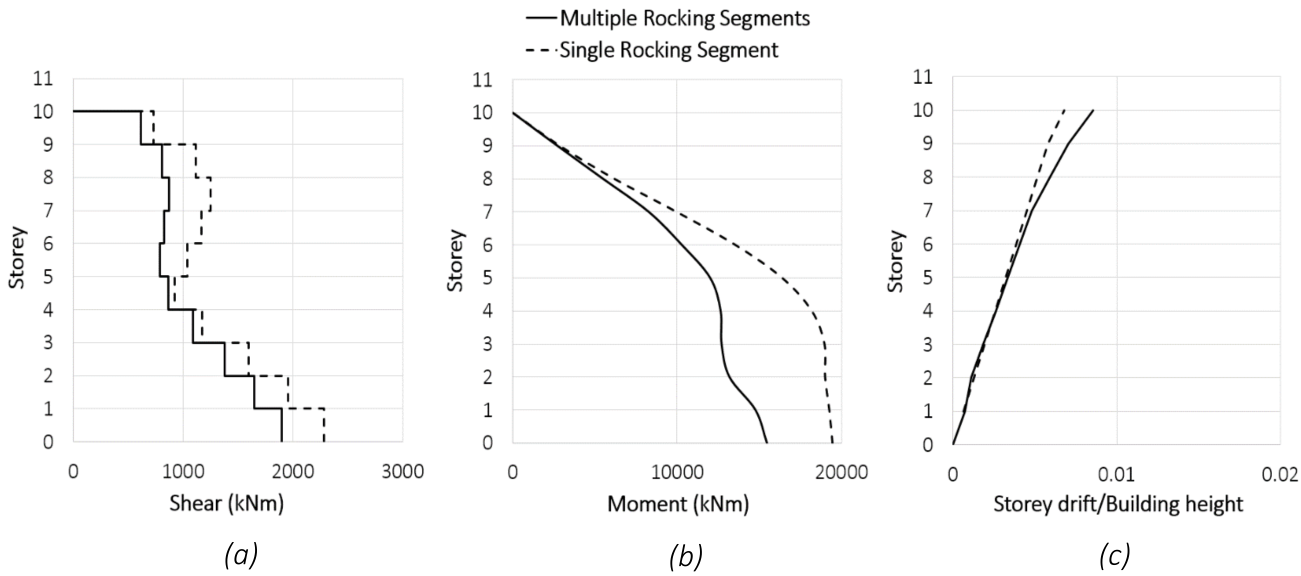

Figure 9 - NLTHA results for wall M1Y: (a) Shear envelope, (b) Bending moment envelope, and (c) Average peak drift

3.6 Connection design example

It is important to design the connections between the panels of the multiple rocking segment systems properly to avoid localized damage during seismic events. *Figure 10* presents details of the connection design for wall M1X between segments 3 and 4. The post-tensioning bars are attached to a C-channel with nuts, and steel washer plates are installed in an opening cut in the wall panel. The C-channel is designed to resist the maximum bending moment developed under a uniformly distributed load resulting from the contact with the timber-bearing surface and the force in the post-tensioning bars. The area of the C-channel is determined to satisfy the following condition $0.4\sigma_r \geq \sigma_f$, where σ_r is the design strength on the timber-bearing surface considering the creep phenomena and σ_f is the applied stress due to the maximum force developed in the post-tensioning bars. The shear and moment strength of the panel reduced section must be checked to resist the envelopes of the NLTHA results. Also, to allow the maximum resistance to the shear through thickness induced by the post-tensioning bars, the opening in the panel is positioned in the middle of the height of the panel to maximize the length of the shear planes.

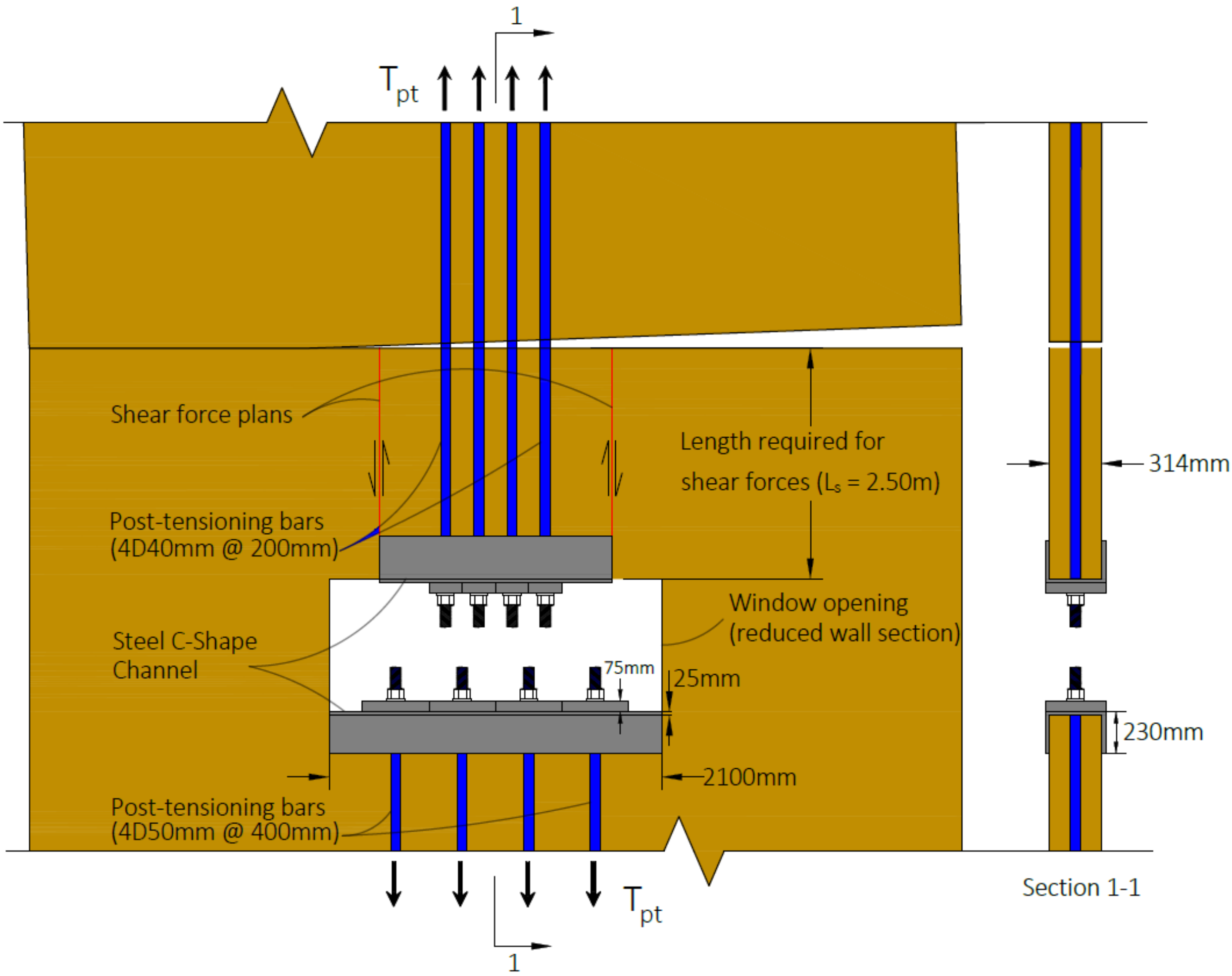

Figure 10 - Connection design for multiple rocking segment system of wall M1X

4 Conclusion

The current study is focused on the analysis of a CLT multiple rocking segment system to resist the seismic forces. First, a comparison of the NLTHA results for the single and multiple rocking segment systems developed in a previous research is shown. Second, an 11-storey case study building in Vancouver, Canada, is designed using the DBD procedure. The NLTHA of the lateral-force-resisting system is performed to determine the inelastic seismic demands and displacements of the building. The results of this research demonstrate relevant ideas for further development and implementation of the low-damage seismic design methodology and consideration of higher mode effects in the building codes. Base on the analyses, the following conclusions have been made:

- NLTHA results comparing CLT single and multiple rocking segment systems showed that the shear and bending moment envelopes can be significantly reduced by allowing a gap opening between the wall segments along the height of the building. Due to the lower forces, it is possible to design a system with reduced walls cross sections, post-tensioning bar areas and lower initial pre-stressing, resulting in material and labour costs savings.

- The design considerations and NLTHA results on the numerical models of an 11-storey building showed that the CLT multiple rocking segment system is viable for this type of structure and location. The connection detailing between the panel segments requires only a C-channel beam and a few plates and nuts, thus resulting in a more economical solution than the rigid connection of the single rocking segment system which requires thousands of fasteners.

5 Acknowledgments

This research was sponsored in part by the Research Center on Renewable Materials and the Canadian Natural Sciences and Engineering Research Council (NSERC) (Grant no. RDCPJ 445200-12 and RGPIN 06483-2017). It was also made possible due to an internship of Dominic Sanscartier Pilon at the University of Canterbury in Christchurch (New Zealand) funded with the Queen Elizabeth Diamond Jubilee Scholarship. The Pres-Lam system was developed at the University of Canterbury, New Zealand, in collaboration with the timber industry. The global patent is owned by Prestressed Timber Ltd, New Zealand.

6 References

Chiou, B., Darragh, R., Gregor, N. & Silva, W., 2008. NGA Project Strong-motion Database. *Earthquake Spectra,* 24(1), pp. 23-44.

CSA Group, 2014. *Engineering Design in Wood*: CSA Group, Mississauga, ON, Canada.

MecKenna, F., 2011. Opensees: A Framework for Earthquake Engineering Simulation. *Computing in Science and Engg,* 13(4), pp. 58-66.

Naeim, F. & Kelly, J. M., 1999. *Design of Seismic Isolated Structures: From Theory to Practice.* Har/Cdr edition ed. s.l.:Wiley.

Newcombe, M., Pampanin, S., Buchanan, A. & Palermo, A., 2008. Section Analysis and Cyclic Behavior of Post-tensioned Jointed Ductile Connections for Multi-Story Timber Buildings. *Journal of Earthquake Engineering,* 12 ((S1)), pp. 83-110.

NRCC, 2015. *National building code of Canada,* Ottawa: National Research Council Canada.

Palermo, A., Pampanin, S., Buchanan, A. & Newcombe, M., 2005. *Seismic Design of Multi-Storey Buildings Using Laminated Veneer Lumber (LVL).* Department of Civil Engineering, University of Canterbury, Christchurch, New Zeland, New Zealand Society of Earthquake Engineering Annual Cofnerence.

Palermo, A., Pampanin, S. & Calvi, G. M., 2004. *The Use of Controlled Rocking in the Seismic Design of Bridges,* Milan: PhD Thesis.

Pampanin, S., Priestley, M. & Sritharan, S., 2001. Analytical Modelling of the Seismic Behaviour of Precast Concrete Frames Designed with Ductile Connections. *Journal of Earthquake Engineering,* 5((3)), pp. 329-367.

Priestley, M., 1991. Overview of PRESSS Research Program.. *PCI Journal,* 36((4)), pp. 50-57.

Priestley, M., Galvi, G. & Kowalsky, M., 2007. *Displacement-Based Seismic Design of Structures,* Pavia, Italy: IUSS Press.

Priestley, M., Sritharan, S., Conley, J. R. & Pampanin, S., 1999. Preliminary Results and Conclusions from the PRESSS Five-Story Precast Concrete Test Building. *PCI journal,* 44(6), pp. 42-67.

Sanscartier Pilon, D., Palermo, A., Sarti, F. & Salenikovich, A., 2017. Submited on 3rd of July 2017- Benefits of Multiple Rocking Segments for CLT and LVL Pres-Lam Wall Systems. *Journal of Earthquake Engineering.*

Sarti, F., 2015. *Seismic Design of Low-Damage Post-Tensioned Timber Wall Systems,* Christchurch, New Zealand: PhD Thesis.

Wiebe, L. & Christopoulos, C., 2009. Mitigation of Higher Mode Effects in Base-Rocking Systems by Using Multiple Rocking Sections. *Journal of Earthquake Engineering,* 13(S1), pp. 83-108.

Discussion

The paper was presented by A Salenikovich

A Buchanan commented that looking at deflection seemed to indicate not much gap opening. Shear stress and crushing under the steel plate must be high. He received confirmation about the size of the window being 1.2 m in width. He commented that the details were important. A Palermo responded that cutting out the high mode would be the intent of post tension system. With large opening would imply large bending moments and more expensive connection designs.

M Li commented about the shear connection design. Local bearing would imply needing large plates. He asked what their thickness was. A Salenikovich responded 35 mm thick washer + C Channel.

R Scotta asked would buckling and compression effects at the end of the wall require additional bracing elements. A Salenikovich said that this could be done.

P Quenneville and A Salenikovich discussed the dampers and the connections between the CLT and dampers.

H Blass commented that rocking could lead to crushing at the compression end. This could lead to permanent deformation.   A Salenikovich said that there was experimental work in US looking into improvement with reinforcement. A Buchanan stated that experience in NZ indicated that it was not a problem. F Lam commented that the NZ work would be based on LVL which would have higher compression strength compared to CLT. H Blass commented that after strong motion localized damage could occur which might need repair and therefore not damage-free. A Palermo agreed that compression of CLT could be a problem but would try to avoid this issue via design calculations. H Blass further commented that the compression strength would decrease by 10 to 15 % considering end grain to end grain compression.

Design parameters for timber members protected by clay plaster at elevated temperatures

Johanna Liblik, Tallinn University of Technology

Alar Just, Tallinn University of Technology, RISE Fire Research

Keywords: clay plaster, fire resistance, timber structures, fire protection material

1 Introduction

The primary protection for timber structures in fire is provided by the cladding. Design standard EN 1995-1-2 (2004) gives expressions for a limited number of protective claddings. Traditional building materials such as natural plasters are not included in the standard, and thus their fire protection ability cannot be taken into account.

Clay plaster has been used for centuries to cover interior walls and ceilings in timber buildings. Today, clay plaster has been recognised as a high-quality material in terms of indoor climate, low embodied energy and aesthetics. It has great potential to substitute conventional wall finish materials as they are met with a renewed interest in their beneficial use in energy efficient buildings (Klinge 2016, Melià 2014).

Furthermore, clay plaster is an authentic material used in conservation and renovation of historical timber buildings. Today, the lack of information about the fire protective effect of clay plaster prevents its wider use with timber.

This paper presents a design model for clay plaster as a fire protection material for timber. Clay plaster requires a support system to be applied on timber. Therefore, commonly used traditional substrates such as reed mat and reed board are examined. The investigation of different clay plaster systems on timber are carried out in small and model scale. Design parameters for clay plaster with common support systems are proposed in order to give an input to the revision of EN 1995-1-2 to improve the effective cross-section method.

2 Fire design of initially protected timber structures

The fire design of timber structures is specified in EN 1995-1-2 (2004). Charring of timber is the dominating effect that influences the mechanical resistance of timber structures. The fire protection for timber against charring is primarily ensured by claddings. In EN 1995-1-2 (2004) important design parameters are stated for different protection materials: the start time of charring, the charring rate behind the cladding and the fall-off time of cladding.

The charring depth $d_{\mathrm{char},0}$ is the distance between the outer surface of the original timber member and the position of the char-line. It is calculated using the time of fire exposure t and the relevant notional charring rate β_{n}.

$$d_{\mathrm{char},0} = \beta_{\mathrm{n}}\, t \tag{1}$$

The notional charring rate of initially protected timber is influenced by two different protection phases. The charring of protected timber is considered as the protection phase. Post-protection phase is considered when the fall-off of the cladding has occurred.

$$\beta_{\mathrm{n}} = k_{\mathrm{pr}}\, \beta_0 \tag{2}$$

k_{pr} is the protection factor that is taken as k_2 for the protection phase and k_3 for the post-protection phase.

β_0 is the basic design charring rate of timber, β_0 = 0,65 mm/min for coniferous species.

The basic design charring rate is taken as the basis of this research since clay plaster is applied on large timber surfaces that are usually exposed to fire on one side.

The failure of fire protective claddings mainly occurs due to the mechanical degradation of the cladding material or insufficient fixation into non-charred timber. This may be caused by insufficient penetration depth or large distances between fastenings. The fall-off time of cladding with respect to pull-out failure of fasteners may be calculated according to the given expression (C.11) given in Annex C in the current EN 1995-1-2 (2004).

3 Clay plaster

Plaster is a surface finish, which includes a mixture of different materials. Terms such as earth, clay, loam and mud are often used while describing the respective plaster. It is proposed to use the term clay as it refers to the binder in plaster.

Currently there is no product standard for clay plaster at European level. In 2013, the first product standard DIN 18947 was published for clay plaster. It is strongly based on the standards of conventional plasters and is used for plastering walls and ceilings in interior and weather proof external applications. DIN 18947 does not apply to stabilised plasters and applies only to clay plasters with a thickness over 3 mm. For thin-layered plasters a technical data sheet TM 06 has been published.

Clay plaster has recently been incorporated into the superior standards of application - DIN 18550-2 where it is implemented alongside other conventional plasters. Since 2016, clay plaster is also described in the European standard for interior plasters - EN 13914-2.

3.1 Composition of clay plaster

In general, clay plasters are composed of sand, silt, clay and natural fibres. Aggregates such as sand and silt are relevant components for modifying the mechanical and physical properties of clay plaster. Sand and silt give the structure, bulk and strength to the plaster. Generally there is 5 – 12 % of clay in the plaster.

Clay acts as a binding agent developing the adhesive and binding forces. Water activates the binding forces of clay. In contrast to other binding agents where hardening is a product of chemical curing, the cohesive effect of clay minerals derives primary from the physical attraction of the particles while the excess water added during the application process is lost (Röhlen 2011).

Plant fibres are added to strengthen the inner cohesion of the mixture and to reduce the effect of drying shrinkage. There are various fibres used in clay plaster: straw, cattail, flax, hemp, wood aggregates, etc. (Laborel-Préneron 2016). The addition of fibres in plaster improves the workability and pliability of plaster. Fibres act as a reinforcement and help to resists stresses in the plaster caused by the movement in the substrate or tensile forces originating from thermal expansion or contraction (Röhlen 2011).

Clay plaster can benefit from additional stabilisation through the embedding of reinforcement mesh across the entire surface such as flax, jute or glass-fibre fabric. The reinforcement is bedded in the upper third of the entire plaster coat (Röhlen 2011).

Types of clay plaster are distinguished according to their function and granularity. Undercoat plasters consist of coarse constituents with a particle size range of 0 – 4 mm and provide a stable base for subsequent layers. As a rule, the undercoat plaster is covered with topcoat or fine-finish plasters with size ranges of 0 – 2 mm and 0 – 1 mm, respectively (Röhlen 2011).

3.2 Properties of clay plaster

DIN 18947 determines the terms, requirements and test methods for clay plaster. Important mechanical requirements for clay plaster mortars are the compressive strength 1.5 – 5 N/mm² and the linear shrinkage of drying that should be not more than 2 %. The colour of clay is not an indication of its properties (Röhlen 2011). Studies by Ashour (2010) indicate that the equilibrium moisture content in clay plasters is not more than 7%.

The effect of elevated temperatures upon the properties of clay plaster has hardly been examined. During the heating process, there is a series of changes in particle size distribution, mass loss, mineralogy and permeability (Zihms 2013).

Research about clay at elevated temperatures by Han (2016) indicate that when temperature reaches more than 100 °C, free and absorbed water dissipates and pores are filled with air. The porosity increases while the temperature continues to rise to 400 °C. In the temperature range of 400 – 600°C the original minerals of clay transform and the chemically bound water is lost.

Above 400 °C the properties of clay are close to rock. The inner structure recombines due to the dehydration of kaolinite in clay and phase transformation of quartz. Changes in kaolinite are considered the primary cause of the variation of physical and mechanical properties of clay under elevated temperatures (Sun 2016). The dehydration of kaolinite improves the bond between particles. Around 900 °C the clay particles start to fuse and form ceramic structures.

3.3 Plaster substrates

Clay plaster does not chemically react with the background and therefore the surface has to be sufficiently rough in order to develop a good physical bond. For that reason, various plaster support systems are used on timber before plastering. Mainly traditional substrates such as a reed mat and a reed board are fixed on timber to improve the adhesion of plaster.

Reed mat is a plaster base consisting of ca. 6-10 mm thick reed stems with approx. 70 stems per linear metre. Reed stems are bound together by a galvanized carrier wire and a thinner binding wire. The carrier wire is fixed with staples to timber. The carrier wire presses the reed stems against timber. The distance between staples is usually 5 – 10 cm.

Reed board is a rigid building board which is made from natural reeds that are laid in parallel and tightly bound using a thin gauge galvanised wire. Reed board is fixed with screws using fastening clips on the wires. The distance between screws on the wire support should not be more than 150 mm.

4 Methodology

The aim of the experimental study was to determine the fire protective effect of clay plaster systems on timber. There is limited data available about the fire protection properties of clay plaster. One of the few accessible studies on natural plasters as a fire protection material has been made by Watchling (2013), Küppers (2015). Tests with various plasters were conducted with cone heater and model-scale furnace. It was demonstrated that clay plaster can be classified as $K_2 60$ according to EN 13501-2 (2010).

Studies by Liblik and Just (2016, 2017) were carried out in small-scale to determine the basic properties of clay plaster that influence the fire resistance of protected timber members. Small-scale tests enabled a rough indication for predicting larger scale fire behaviour of clay plaster systems in combination with timber. Tests were carried out using the cone heater apparatus according to ISO 5660.

The cone tests were followed by model-scale fire tests which were carried out in a cubic furnace that corresponded to the ISO 834 standard fire curve. After tests, the timber specimens were cut along the line of thermocouples to measure the charring depth. The charring rate and protection factors were calculated from the measured residual cross-section.

In this study, commonly used clay plasters with an average dry density in the range of 1500 to 1900 kg/m³ were tested. This value corresponds to gross density classes of 1.6, 1.8 and 2.0 according to DIN 18947. Preparation of the specimens was done in Estonia. Plastering was conducted by a professional craftsman according to the application requirements. All tests were performed at RISE Fire Research in Stockholm.

4.1 Small-scale tests

The cone heater provides controlled levels of continuous radiant heating to the exposed specimens. The construction, preparation and conditioning of the test specimens were made in accordance with ISO 5660. The tests approx. followed the ISO 834 curve using heat flux levels of 50 and 75 kW/m². Test specimens were placed directly under the cone heater as defined in ISO 5660. The duration of the tests was 40 and 60 minutes. After testing, specimens were selectively cooled down with water or left to cool down naturally.

The dimensions of each timber member were 100x100x100 mm. Timber specimens were instrumented with thermocouples on the exposed surface under plaster. Reed mats and reed boards were used as a plaster support on timber. In case of reed boards, extra thermocouples were located on the interface of plaster and the reed board. Clay plaster was applied mechanically by trowel.

The first study by Liblik (2016) was conducted with ready-mix plasters and three different mixtures of clay plasters with various clay/sand ratios with constant 5% straw fibre content. Plaster thickness in the range of 10 – 40 mm was used.

An extended research followed after the first study. Tests consisted of a wide selection of various combinations of clay plasters. Different plant fibres such as straw, cattail and hemp were selected to examine plaster mixtures where 5% and 30 % of fibre content were tested. Additionally a plaster mixture without any fibres was used. Various reinforcement meshes were embedded within plasters to examine if any detachment of plaster layers or other damage could occur. A reed mat and a reed board were examined.

In total, the following test series of specimens were prepared and tested in small-scale:

- Plaster thicknesses in range of 10 – 40 mm
- Plant fibre additives: straw, hemp, cattail
- Reinforcement meshes: jute, flax, glass-fibre
- Undercoat and topcoat plasters: DIN 19847, not standardised
- Plaster substrate: reed mat, 50 mm reed board

4.2 Model-scale tests

Different thicknesses and combinations of clay plasters and plaster support systems on a solid timber panel were tested in vertical and horizontal position in a cubic metre furnace. A total of 9 tests were conducted following the standard fire curve according to ISO 834 which corresponds to EN 1363-1.

Each test specimen consisted of 40-mm thick timber planks (200 x 1200mm) to form a solid background for plaster. The average density of the timber was 428 kg/m³. Timber planks were secured by a particle board and supporting construction on the unexposed side to guarantee the integrity and stiffness of the specimen throughout testing.

The fire exposed side of the timber specimen was covered with the plaster system using two different substrates for plastering: a reed mat and a 50 mm reed board, see sections of test specimens in Figure 1a. The set-up of the specimens in horizontal position is presented in Figure 1b.

Selected clay plasters were Estonian- and German-based according to DIN 18947. Commonly used plaster systems were prepared with undercoat, topcoat and fine finish plasters with respect to its use in practice. Test specimens were prepared with and without a reinforcement mesh.

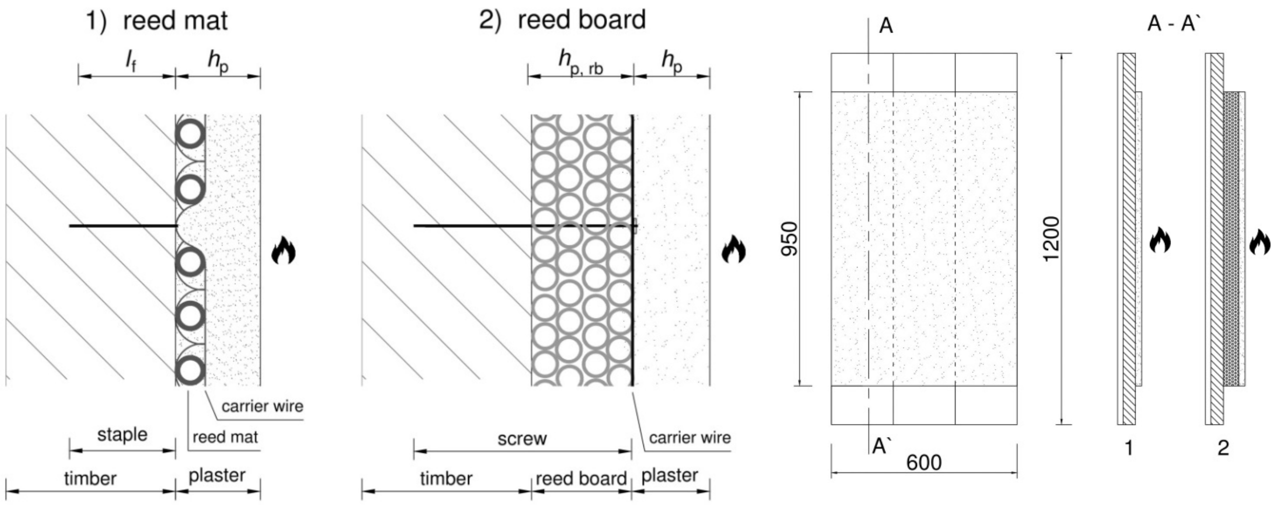

a) Plaster support systems 1 and 2 b) Test specimen in horizontal position

Figure 1.Schematic of model-scale test specimens

The set-up of vertical test specimens is illustrated in Figure 2. In two tests, the exposed surface of the specimen was divided into 4 separate areas in order to investigate clay plasters with different substrate, grain size distribution, type of clay and fibre.

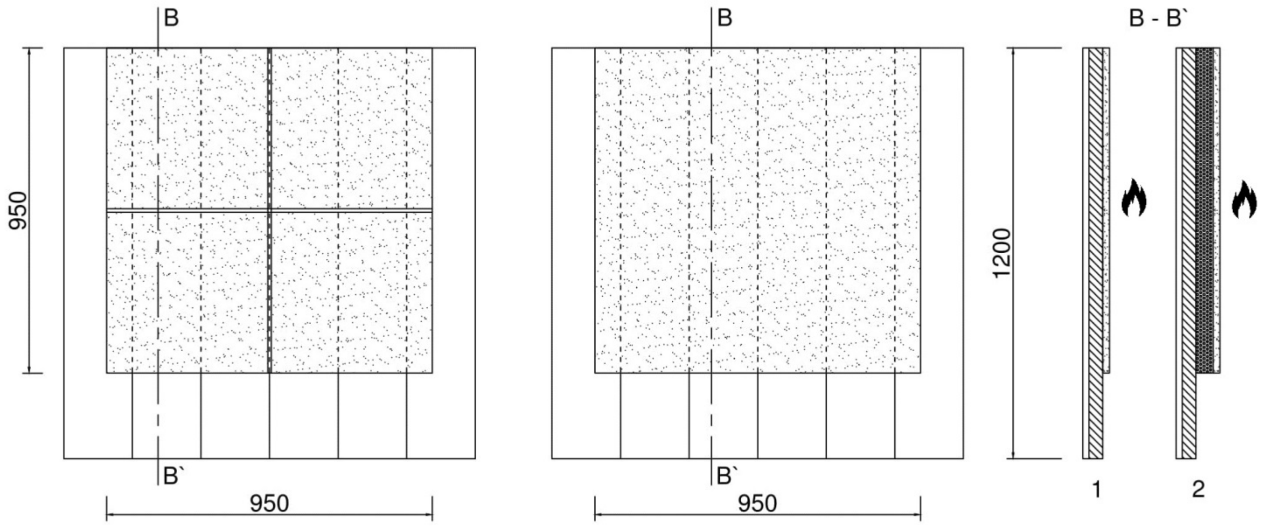

a) Surface divided into 4 areas   b) Full surface   c) Sections

Figure 2.Model-scale test specimens in vertical position

The carrier wire of the reed mat was used to fix the mat on timber with 25 mm staples. The distance between the staples was approx. 5 – 10 cm. The reed board was fixed with 80 mm screws using the fastening clips for the wire. Thermocouples were placed on the timber surface directly under plaster. In the tests with reed boards, additional thermocouples were embedded on the interface of the reed board and plaster. Specimens were conditioned in an ambient atmosphere of 50 % relative humidity at 23 °C before testing.

4.3 Results and analysis

Main parameters such as the start time of charring, the charring rate and the fall-off time of cladding were determined in this study. Test results indicate that the fire protection ability of clay plaster is mostly influenced by its thickness. The start time of charring of timber is increasingly delayed by thicker coats of plaster. Different combinations of clay/sand proportions in plaster show minimal effect (Liblik 2016).

Test results indicated that neither the variation of grain size distribution, fibre type nor clay have any significant influence on the charring of timber. Slight variations in results can be caused by the density of plaster, fibre content, mineralogical transformations, variation in positioning of the reed stems and application process of the plaster. Various reinforcement meshes tested under cone heater did not show any detachment of plaster layers (Liblik 2016).

The relationship between the plaster thickness and the start time of charring is presented in Figure 3a. The charring is considered to start when the temperature under the plaster reaches 300°C. Average time based on thermocouple recordings is considered for each test. Plaster thickness is defined in Figure 1a. Small and model scale test results show good agreement.

Plaster becomes harder and remains solid while being exposed to elevated temperatures. No significant shrinkage was detected. However, a few cracks developed on the plaster surface after approx. 20 minutes after the start of fire in furnace. The density of plasters before and after the tests remained approx. the same. No self-ignition of plaster, smokes, fumes or other perceptible combustible gases of plaster were detected.

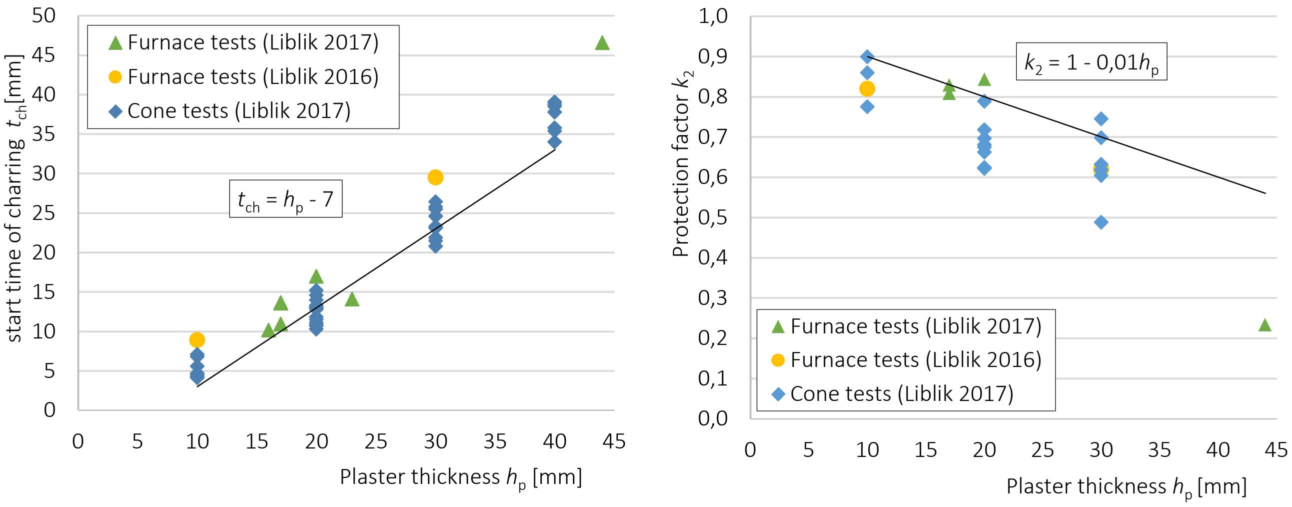

a) Start time of charring behind clay plaster

b) Protection factor for charring behind clay plaster

Figure 3. Determination of design parameters for clay plaster according to test results

Tests show that the thickness of plaster and the charring rate of timber are in negative correlation. A trend between plaster thickness and the calculated protection factor is presented in Figure 3b. The presented expression for protection factor k_2 is given with respect to the model-scale tests. Results from the cone tests are illustrated, however not considered due to the peculiarities in the test method. All conducted model-scale tests (2016, 2017) are listed in Table 1.

Tests showed that the fall-off time of clay plaster depends principally on the substrate and its fastening system. The reinforcement mesh within plaster has no significant influence on the performance of clay plaster at elevated temperatures. Throughout the fire exposure a few longitudinal cracks developed within the plaster. The fall-off time of plaster with thickness up to 30 mm appeared not to be related to its thermal decomposition nor cracking. However, during Test 7 where the plaster thickness was 44 mm, a local decomposition in thickness was observed. This is not considered as fall-off of plaster but it requires further research with plasters thicker than 30 mm.

Clay plaster shows a strong bond with the steel galvanized wires of the reed mat. The wires act as a fastening system in plaster and prevent the fall-off of plaster. As a result, the fall-off time of plaster is dependent on the penetration length of fasteners in timber if a reed mat is used as a substrate.

Table 1.Test specimens in 1m³ furnace

Test No	Position	Dimensions [mm]	Substrate	Plaster thickness [mm]	Reinforcement mesh in plaster	Start time of charring of timber [min]	Recession speed of reed board [mm/min]	Fall-off time of plaster [min]
1	hor	600 x 950	reed mat	17	jute	13,7		75
2	hor	600 x 950	reed mat	17	no	13,6		62
3	hor	600 x 950	reed board	17	no	36,7	2,5	17
4	hor	600 x 950	reed board	16	jute	32,5	3,6	18,5
5	ver	4x (475x475)	reed mat	20	jute	17,0		>90
6	ver	4x (475x475)	reed board	23	jute	68,6	1,3	29**/ >120
7	ver	950 x 950	reed mat	44	jute	46,6		64***/ >79
8*	ver	1000 x 1000	no	10	no	8,9		n.f.
9*	ver	1000 x 1000	reed mat	30	no	29,5		n.f.

*(Liblik 2016)

** Earliest fall-off time

*** Partial decomposition in thickness

n.f. – No fall-off of cladding detected

Fall-off times observed in model-scale tests are stated in Table 1. In the case of reed board substrate, the fall-off time of plaster occurs relatively early compared to the reed mat. After the reed board is carbonized behind plaster, the bond between plaster and reed board is highly reduced. Reed board embodies only few carrier wires compared to the reed mat. Therefore, it does not provide sufficient fastening for plaster. Tests showed that plaster remained intact longer in the vertical position than in the horizontal position.

After the fall-off of plaster the carbonizing reed board still protected timber from charring thus delaying the start time of charring of timber. Therefore, the recession speed of reed board should be introduced in order to take this phenomenon into account. Recession speed expresses the propagation of the 300° C isotherm through the reed board.

The results gained from small and model-scale tests are considered reliable; however full-scale tests should be carried-out to confirm the results.

5 Design model for clay claddings

Proposed design model is limited to clay plasters that are tested according to DIN 18947 and belong to plaster density class 1.8. The selection, design and application of clay plaster shall be in accordance to the EN 13914-2. It is recommended to use a reinforcement mesh. It is mandatory to adhere to the manufacturer's recommendations while applying clay plaster and substrates on the walls and ceilings.

Design parameters are given with respect to the traditional substrates for plastering:

- reed mat
- reed board

The substrates should be fastened on timber in accordance with the manufacturer's guidance following these minimal requirements:

Reed mat is fixed on timber using staples on the carrier wire to press the reed stems firmly against timber surface. Distance between the staples should not be more than 100 mm.

Reed board is fixed with screws using fastening clips on thin gauge galvanised wires. Distance between the screws should not be more than 150 mm along the wire support.

It is shown by this study that the proposed design model is valid for clay plasters with the maximal thickness of 30 mm for walls and 17 mm for ceilings. Proposed design models for clay plaster are illustrated in Figure 4.

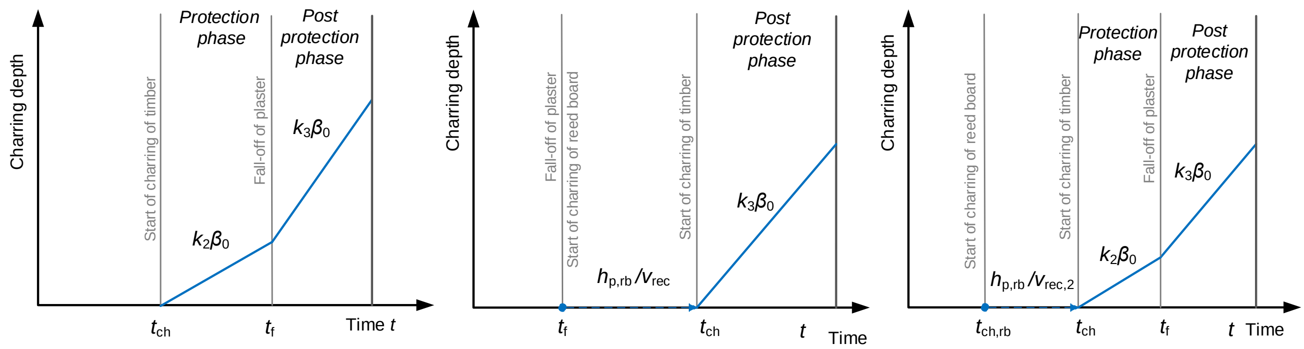

a) Reed mat as a substrate b) Reed board as a substrate, $t_{ch} > t_f$ c) Reed board as a substrate, $t_f > t_{ch}$

Figure 4.Design models for clay plaster with different substrates on timber.

5.1 The start time of charring

The start time of charring of timber depends on the plaster thickness and substrate.

For clay plaster applied directly on wood-based surfaces using a reed mat the start time of charring of timber t_{ch} should be taken as

$$t_{ch} = h_p - 7 \tag{3}$$

where h_p is the thickness of clay plaster on timber (see Figure 1a).

For clay plaster applied on a reed board, the start time of charring of timber t_{ch} should be taken as a combination from the following:

- the start time of charring of the reed board $t_{ch, rb}$
- the fall-off time of plaster t_f
- the recession speed of the reed board v_{rec} (see Figure 4b and Figure 4c)

The recession speed of the reed board should be determined by furnace tests. For 50 mm thick reed board $v_{rec} = 4$ mm/min could be used.

When the fall-off time of plaster occurs before the start time of charring of timber (see Figure 4b), the start time of charring of timber should be taken as

$$t_{ch} = t_f + \frac{h_{p,rb}}{v_{rec}} \tag{4}$$

where

t_f is the fall-off time of plaster,

$h_{p,rb}$ is the thickness of the reed board (see Figure 1a),

v_{rec} is the recession speed of the reed board.

When the fall-off time of plaster occurs after the start time of charring of timber (see Figure 4c), the start time of charring of timber should be taken as

$$t_{ch} = t_{ch,rb} + \frac{h_{p,rb}}{v_{rec,2}} \tag{5}$$

where

$t_{ch,rb}$ is calculated according to Equation (3), $t_{ch,rb} = t_{ch}$

$h_{p,rb}$ is the thickness of the reed board (see Figure 1a),

$v_{rec,2} = k_2 v_{rec}$

$v_{rec,2}$ is the recession speed of the reed board and is multiplied by the protection factor k_2 according to Equation (8).

When $t_{ch,rb} < t_f < t_{ch}$ then the interpolation between Equations (4) and (5) could be performed.

5.2 The charring rate

For protection phase when $t_{ch} \leq t \leq t_f$ the basic design charring rates of the timber member given in EN 1995-1-2 should be multiplied by a factor k_2. After the fall-off of plaster the charring rates should be multiplied by a factor k_3.

The notional charring rates should be taken as

$$\beta_n = k_2 \beta_0 \tag{6}$$

$$\beta_n = k_3 \beta_0 \tag{7}$$

where β_0 is the basic design charring rate of timber.

The protection factor k_2 should be taken as

$$k_2 = 1 - 0{,}01\, h_p \tag{8}$$

where h_p is the thickness of plaster (see Figure 1a).

The post-protection factor $k_3 = 2$ according to EN 1995-1-2.

5.3 Fall-off time of plaster

For clay plaster with reed mat as a substrate the fall-off time of plaster can be calculated as

$$t_f = t_{ch} + \frac{l_f - 10}{k_2 \beta_0} \tag{9}$$

where l_f is the length of the fastener (see Figure 1a).

The Equation (9) applies to clay plaster with a thickness up to 17 mm for horizontal positioning and up to 30 mm for vertical positioning. The extension of these limits has to be verified by furnace tests.

For clay plaster with a reed board as a substrate the fall-off time of plaster is recommended to be taken as

$$t_f = t_{ch,\, rb} \tag{10}$$

where $t_{ch,\, rb}$ is the start time of charring of reed board.

If the fall-off time of plaster is not determined then the Equation (10) should be used. Else, the design scenario in Figure 4c should be followed.

Proposed design equation for the fall-off time of clay plaster is illustrated in Figure 5. Figure 5a presents the fall-off time of plaster with respect to the penetration length of fasteners (see Equation 9). In the case of reed board, the recommended design model (see Equation 10 and 3) is presented in Figure 5b. Fall-off time of plaster with reed mat and reed board could be determined by EN 13381-7.

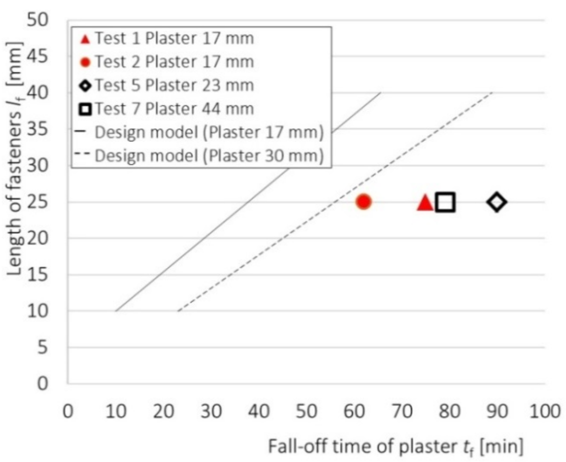

a) Reed mat as a substrate

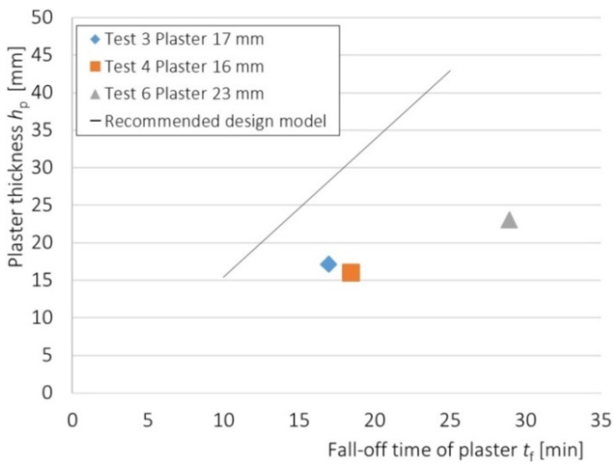

b) Reed board as a substrate

Figure 5.Fall-off time of plaster depending on the substrate

6 Conclusion and further work

This paper presents a comprehensive analysis of clay plaster as a fire protection material for timber structures based on the experimental studies in small and model-scale tests. A design model for clay plaster, which corresponds to DIN 18947, is proposed to give an input to the revision of EN 1995-1-2 to improve the effective cross-section method. Clay plaster requires a support system on timber that influences the charring behaviour of initially protected timber. Traditional substrates such as a reed mat and a reed board are considered in the presented design model.

Plaster thickness is the most significant factor influencing the charring of timber behind plaster. The proposed design parameters for horizontal and vertical positions are based on the plaster thicknesses that were experimentally tested. Further research is required for plasters thicker than 30 mm, due to some local decomposition of thicker plaster coat appears to occur. Fall-off time of clay plaster for reed mat is determined by the fastening system. In regards to the implementation of traditional fire protection materials to the building codes, earth based panels and lime plaster should also be investigated.

Acknowledgements

The authors wish to express their deep gratitude to Marko Kikas, Martin Hütt, Kerti Vissel, Andres Uus, Prof. Christof Ziegert and Manfred Lemke for their cooperation, knowledge and support. The authors acknowledge the network of COST Action FP1404 WG2 for the contribution. This research was supported by the European Union through the European Regional Development Fund and the Estonian Research Council grant PUT 794, TAR 16012.

7 References

EN 1995:1-2 (2004): Design of timber structures - Part 1-2: General – Structural Fire Design; CEN.

EN 1363–1:2012 (2012) Fire Resistance Tests–Part 1: General Requirements; CEN.

EN 13381-7 (2002) Test methods for determining the contribution to the fire resistance of structural members - Part 7: Applied protection to timber members.

EN 13501-2 (2010) Fire classification of construction products and building elements. Classification using data from fire resistance tests, excluding ventilation services.

EN 13914-2 (2016) Design, preparation and application of external rendering and internal plastering - Part 2: Internal plastering; CEN.

DIN 18947 (2013): Earth plasters –Terms and definitions, requirements, test methods. Deutsches Institut für Normung (Hrsg.) (in German)

TM 06:2015-06 (2015). Technische Merkblätter Lehmbau: TM 06 Lehmdünnlagenbeschichtungen. Begriffe, Anforderungen, Prüfverfahren, Deklaration.

Dachverband Lehm e.V. Weimar, Germany.

ISO 5660:2015. Reaction-to-fire tests -- Heat release, smoke production and mass loss rate -- Part 1: Heat release rate (cone calorimeter method) and smoke production rate (dynamic measurement); CEN.

ISO 834-1 (1999) Fire-resistance tests – Elements of building construction – Part 1: General requirements; CEN.

Ashour, T., Georg, H., Wu, H. (2010) An experimental investigation on equilibrium moisture content of earth plaster with natural reinforcement fibres for straw bale buildings. Applied Thermal Engineering 31, 293 – 303.

Han, J., Sun, Q., Xing, H., Zhang, Y., Sun, H. (2016) Experimental study on thermophysical properties of clay after high temperature. Applied Thermal Engineering 111, 847 – 854.

Klinge, A., Roswag-Klinge, E., Fontana, P., Hoppe, J., Richter, M., Sjöström, C. (2016) Reducing the need for mechanical ventilation through the use of climate-responsible natural building materials. Lehm 7th International Conference on Building with Earth. Weimar, Germany.

Küppers, J., Hosser, D., Zehfuβ, J. (2015) Neue Forschungergebnisse zum Brandchutz für mehrgeschossige Strohballenbauten. Vfdb Zeitschrift 1/2015.

Laborel-Préneron, E. et al. (2016) Plant aggregates and fibres in earth construction materials: A review. Construction and Building Materials 111, 719 – 734.

Liblik, J. (2016) Performance of constructions with timber and clay plaster at elevated temperatures. Comparison of different methods in small and model-scale. SP Report 2016:69. Stockholm, Sweden.

Liblik, J., Just, A. (2016) Performance of constructions with clay plaster and timber at elevated temperatures. SBE16 Tallinn and Helsinki Conference Build Green and Renovate Deep. Energy Procedia 96:717-728.

Liblik, J. (2017) Model-scale tests with clay plaster. Test Report 4P06479-05. RISE Fire Research. Stockholm, Sweden.

Melià (2014) Environmental impacts of natural and conventional building materials: a case study on earth plasters. Journal of Cleaner Production 80, 179 – 186.

Röhlen, U., Ziegert, C. (2011) Earth Building Practice. Planning-Design-Building. Beauwerk. Beuth Verlag GmbH, Berlin.

Sun, Q. et al (2016) Variations of Strength, Resistivity and Thermal Parameters of Clay after High Temperature Treatment. Acta Geophysica 64 (6).

Zihms, S.G. et al. (2013) Effects of high temperature processes on physical properties of silica sand. Engineering Geology 164, 139 – 145.

Wachtling, J., Hosser, D., Zehfuβ, J. (2013) Fire protection of multi-storey straw bale buildings. Research and Applications in Structural Engineering, Mechanics and Computation – Zingoni (Ed.). Taylor and Francis Group.

Discussion

The paper was presented by J Liblik

A Buchanan asked about the non standard product considered. For example can one buy the reed mat? J Liblik said this could be bought in Estonia and Germany. There is strong interest to use natural material in buildings.

H Blass asked how to guarantee that plaster would conform to the product. J Liblik said that the clay plaster was tested as standardized product.

J W Van de Kuilen discussed fitting of the data shown in Slide 18. J Liblik said that the fitting results were considered safe and conservative.

A Buchanan commented about the ISO fire in small scale versus full scale tests as there was no standardization.

H Blass commented that test standard to determine charring rate was missing. D Brandon responded that it was difficult to standardize this test procedure as the procedure aimed to simulate the charring rate and there would be difficulties with respect to control and measurement of heat flux etc.

Parametric fire design – zero-strength-layers and charring rates

Daniel Brandon, RISE Research Institutes of Sweden

Alar Just, RISE Research Institutes of Sweden

David Lange, RISE Research Institutes of Sweden

Mattia Tiso, Tallinn University of Technology

Keywords: Parametric fire, zero-strength-layer, charring rate

1 Introduction

In the field of fire safety engineering, performance based design methods are increasingly used to demonstrate that building designs are safe. However, performance based design is not commonly used for the design of timber structures, as there are not many relevant assessment methods available (Östman et al. 2010). For assessment whether the design of a building meets certain criteria, a design fire scenario is needed. Design fires often describe the temperature throughout a fire and are often based on dimensions, ventilation conditions and the fuel load of the compartment. Parametric fires are such design fires, used for structural calculations corresponding to ventilation controlled post-flashover fires in compartments, based on the compartment's dimensions, ventilation openings, lining materials, and the fuel load. Eurocode 1 (EN1991-1-2, 2004) includes parametric fires.

Annex A of Eurocode 5 (EN1995-1-2, 2004) offers a calculation method (the effective cross-section method) to determine charring rates of timber under parametric fire exposure of unprotected softwood only. However, Annex A is not accepted for use in all European countries, as the provided charring rates are questioned. Additionally, thicknesses for *zero-strength-layers* are missing, which take into account the strength reduction of uncharred but heated wood in the structural member. There is, furthermore, no distinction made between (1) a notional charring rate which accounts for increased charring around the corners of timber elements and (2) a one-dimensional charring rate.

As timber is combustible it contributes to the fuel load of a fire. If large surfaces of wood are exposed, its contribution should be included in the fuel load used to determine the parametric fire. It was previously shown that a relatively small amount of exposed timber, for example one wall of non-delaminating exposed timber in a compartment (Medina Hevia, 2014), does not significantly influence the temperature and fire duration of a compartment fire. This study focuses on parametric fires for compartments with a relatively small amount of exposed timber. The inclusion of the contribution of large exposed timber surfaces to the fuel load is out of the scope of this paper and is studied in ongoing work. This paper presents an experimental and numerical study performed to determine one-dimensional charring rates, notional charring rates and zero-strength-layers corresponding to a range of parametric fire curves. The experimental and numerical studies are used as a benchmark for a proposed improvement of the effective cross-section method, which in 1995-1-2 (2004) is referred to as a reduced cross-section method.

2 Eurocode 1, Parametric fire exposure

Temperature curves for parametric fires were proposed by Wickström (1986) and were based on the standard fire and so called Swedish fire curves by Magnusson and Thelanderson (1970). The relationship between the fire temperature, *Θ*, and the time, *t*, is given by (EN 1991-1-2, 2002):

$$\Theta = 20 + 1325(1 - 0.324e^{-0.2t\cdot\Gamma} - 0.204e^{-1.7t\cdot\Gamma} - 0.472e^{-19t\cdot\Gamma} \qquad (1)$$

where Γ is a factor that changes the heating rate corresponding to the thermal inertia of the compartment boundaries and the opening factor, *O*, of a compartment:

$$\Gamma = (O/\sqrt{pc\lambda})^2/(0.04/1160)^2 \qquad (2)$$

Where, p is the density in kg/m3, c is the specific heat J/kgK and λ is the thermal conductivity in W/mK of the compartment's boundary.

The duration of the heating phase t_{max} (h) is related to the fuel load within the compartment:

$$t_{\max} = \max\left[(0.2\cdot 10^{-3} q_{t,d}/O); t_{\lim}\right] \qquad (3)$$

Where: $q_{t,d}$ is the fuel load divided by the total surface area of the compartment boundaries (including walls and ceiling) in MJ/m^2; t_{lim} is the lower limit of the duration of the heating phase, which is 0:15h, 0:20h or 0:25h for slow, medium and fast fire growth, respectively. After the start of the cooling phase at t_{max}, the temperature decreases linearly until it reaches 20°C.

3 Eurocode 5, effective cross-section method

Eurocode 5 (EN 1995-1-2, 2004) provides an effective cross-section method for the assessment of structures exposed to fire. Following this method, a char layer and a so called zero-strength-layer on exposed sides of structural timber elements are subtracted from the original cross-section before the structural calculation is performed. The sum of the char layer thickness d_{char} and the zero strength layer thickness d_0 is termed the ineffective layer thickness d_{inef} (see Figure 1). As the strength of char is negligible in comparison with that of timber, charred material should be disregarded for the structural calculation. The zero-strength-layer compensates for heated but uncharred timber and its thickness is dependent on the exposure. Eurocode 5, however, does not provide any information about the calculation of zero-strength-layer thickness corresponding to parametric fires.

Charring rates for parametric fires are provided in Annex A of EN 1995-1-2 (2004). The charring rates during the heating phase originate from Hadvig (1981):

$$\beta_{par} = 1.5\beta_n \frac{0.2\sqrt{\Gamma} - 0.04}{0.16\sqrt{\Gamma} + 0.08} \tag{4}$$

where, β_n is the notional charring rate (mm/min)

For a duration of t_0, which is shorter than the duration of the heating phase, the charring rate for parametric fires, β_{par}, is taken into account. The charring rate for the cooling phase, linearly decreases to zero for a duration equal to two times t_0 (see Figure 1, right). The charring depth at any time can then be calculated from the integral of the charring rate function shown in the figure.

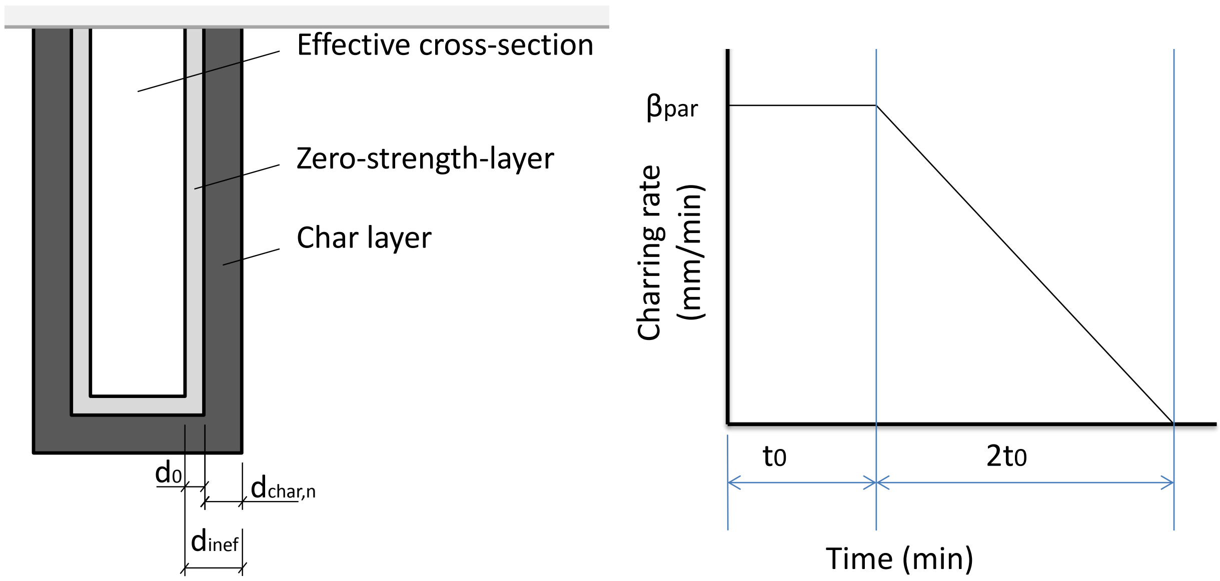

Figure 1: Char layer and zero-strength-layer of a beam cross-section exposed on three sides (left) and charring rate during the heating and cooling phases (right)

4 Experimental study

The number of parametric fire test results available is very limited. Therefore, two test series have, recently, been performed of which the second series (Series B) is also discussed by Lange et al. (2015). The tests of the two series were exposed to, in total, five different parametric fires in agreement with Eurocode 1, EN1991-1-2 (2002). The implemented fires were within a range that is relevant for under ventilated compartment fires.

Test series A comprised of model scale furnace tests and consisted of less specimens than test series B. However, due to the smaller scale it was possible to perform temperature measurements at a large number of positions in each beam. Test series A is, therefore, used to set up a numerical method to predict material temperatures.

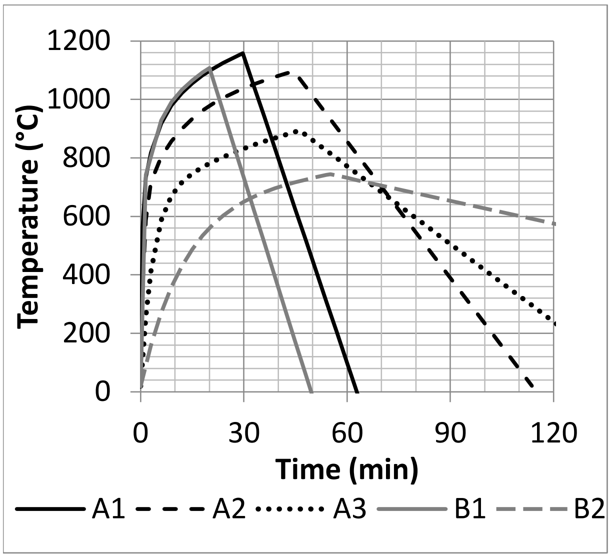

Table 1. Parameters of tested fire curves

Name	Fuel load density $q_f(q_{td})$ (MJ/m^2)	Thermal inertia (J/m^{2}s$^{1/2}$K)	Opening factor (m$^{1/2}$)	Heating rate factor
A1	675(149)	600	0.06	8.41
A2	675(149)	600	0.04	3.74
A3	675(149)	350	0.02	0.93
B1	250(92)	1160	0.12	9.00*
B2	250(92)	0.02	0.02	0.25*

Figure 2: Parametric temperature curves **medium fire growth rate*

4.1 Setup of test series A (model scale tests)

Ten glued laminated timber beams were exposed to parametric fires (A1 to A3) in a fire testing furnace. The series comprised of six 4-point bending tests of strength graded glued laminated beams (see Figure 3) and four unloaded tests of glued laminated beams with cross-sections of 180x260mm. The loads were chosen so that the two specimens tested under the same parametric fire exposure failed at different times during the cooling phase. The time to failure and the deflection of the beam was recorded. For all tests, the charring rates were determined in horizontal and vertical directions using three thermocouple series of 10 thermocouples for each specimen positioned in the timber. Figure 3 shows the positions of one of those sets.

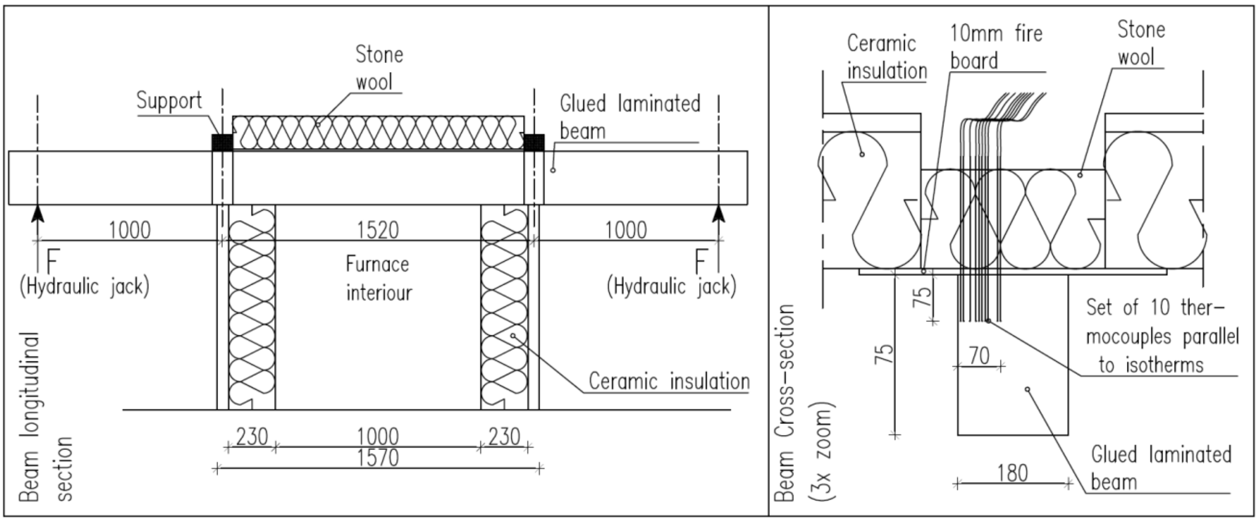

Figure 3: Longitudinal section (left) and cross-section (right) of a glued laminated beam in a four-point bending test on top of a model-scale furnace

In order to assess the validity of structural calculations of fire exposed timber, its strength at ambient conditions should be known. Therefore, glued laminated beam specimens were made of lamellas that were strength graded in accordance with Olsson and Oscarsson (2016). Out of 105 strength graded lamellas, eight beams were glued using six lamellas that had similar estimated strengths, with less than $1N/mm^2$ difference between the strongest and weakest lamella in one beam. The average moisture content of all lamellas was 12.0% with a standard deviation of 0.4%.

4.2 Setup of test series B (full scale tests)

This series of 4 tests was based on EN 1363-1 and EN 1365-3, with 2 significant deviations. Firstly, 2 of the tests used the standard fire temperature-time curve, whereas the other two tests used temperature-time curves based on the parametric fire model of EN 1991-1-2 (2002), with two different opening factors. Secondly, for the entire series the beams spanned the short axis of a 3 m x 5 m horizontal furnace, with a distance between the supports of 3300 mm (see Figure 4). This meant that 8 glulam beams with cross-section 139 mm x 269 mm could be tested in each test. The beams in 3 of the 4 tests were subjected to 4 point bending, with different loads applied to the beams in pairs. The loads were chosen to encourage failure at different times during the fire tests. As the beams failed, the hydraulic loading cylinders were retracted and any openings in the top of the furnace were sealed with mineral wool. At the end of the tests, all of the beams were removed from the furnace as quickly as possible, burning was extinguished and the char layer was mechanically removed.

45 beams were divided into 5 groups (4 groups of 8, and 1 of 10- leaving 3 spare) using a dynamic estimate of their stiffness. Each group had a very similar mean and standard deviation in stiffness. The group of 10 was then subject to static testing until failure, with the assumption that the distribution of strength and stiffness of this group was the same as the four to be used in the fire tests. During the fire test, various measurements were taken, including deflection and temperatures in the cross-section. A detailed sectional analysis was also carried out after the tests.

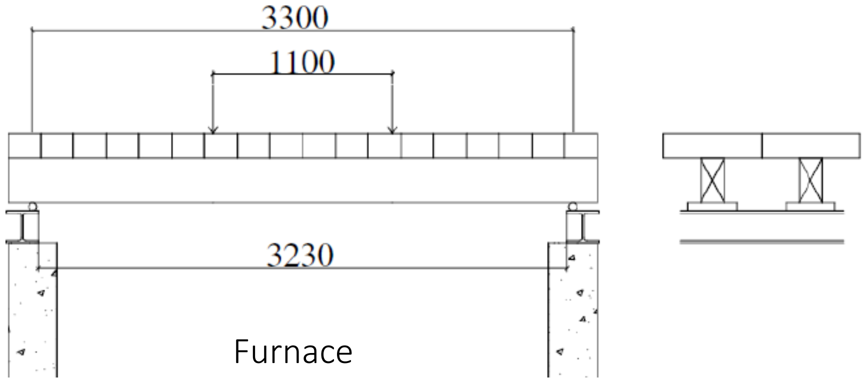

Figure 4: Setup of a four-point bending test on top of a full-scale furnace

5 Numerical analysis

A combination of a numerical heat transfer analysis for calculation of material temperatures in a large number of locations (step 1) and a numerical structural analysis to determine the structural capacity based on temperatures calculated in step 1 (step 2) is performed. For the structural calculation in step 2, a reduction of tensile and compressive strength (f_t and f_c) and tensile and compressive Young's modulus (E_t and E_c) is based on temperatures as shown in Figure 5 (König and Walleij, 2000).

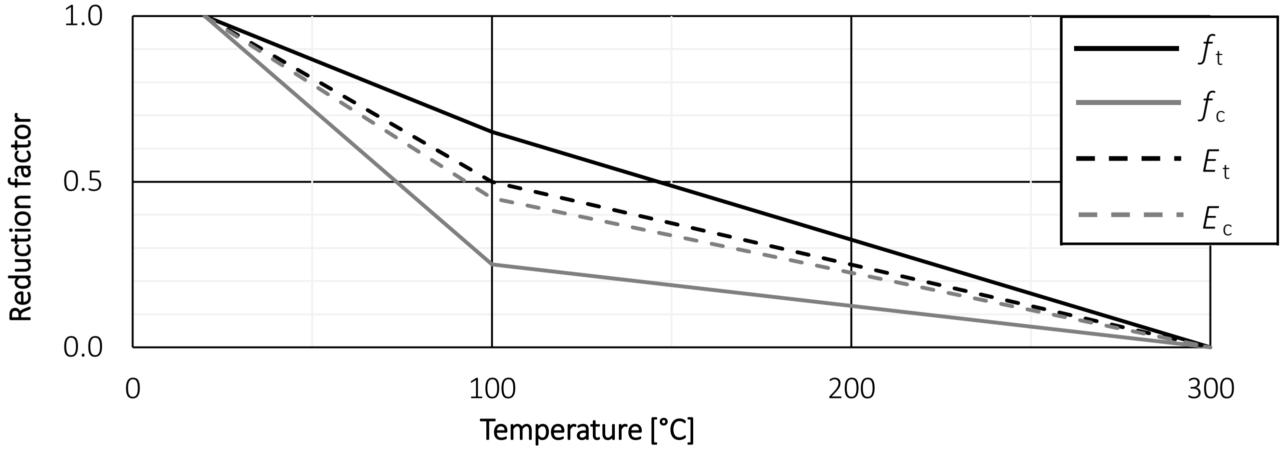

Figure 5. Temperature dependent reduction factors for strength and Young's modulus

The heat transfer analysis of step 1 is performed using a set of thermal properties that is effective to calculate temperatures within timber elements for the full duration of a parametric fire assuming solely conductive, radiative and convective heat transfer. Additionally, it is assumed that the heat source is in the compartment and not within the surface of the timber, as done in multiple previous studies (e.g. König and Walleij, 2000). In reality, mass transfer (moisture and gasses), fissures in the char layer and oxidation have an influence on the temperature development in timber exposed to fires. Due to the simplifications it is not possible to have a single set of thermal properties that is effective to predict temperatures in timber exposed to all possible parametric fires (Hopkin et al. 2011).

5.1.1 Thermal simulations of experiments

In this section sets of thermal properties are presented that result in accurate temperature predictions in the heating phase as well as the cooling phase. Although, it is recognized that changes of thermal properties are mostly irreversible in a fire (for example, char does not turn back to timber), it is assumed that these properties are reversible. This assumption allows the search for effective thermal properties that are effective in, both, the heating and the cooling phase of a fire.

Using computer algorithm by Mäger et al. (2016) and numerical temperature calculations performed with SAFIR 2007, the set of thermal properties shown in Table 2 was obtained. The used convection coefficient and emissivity are 25 W/m^{2}K and 0.8, respectively, which are in accordance with EN 1991-1-2 (2002) and EN 1994-1-2 (2004).

In order to have one framework that fits a range of parametric fires, the thermal conductivity corresponding to temperatures of 250°C and higher are multiplied by a factor, α. α was determined for three tests corresponding to different heating rates, Γ, and results are shown in Table 2. The thermal properties can be obtained by linear interpolation with respect to temperature. In order to demonstrate the validity of the framework the predicted and the experimentally determined temperature distributions corresponding to fire curves A1 to A3 are given in Figure 6 and Figure 7. Good agreement was seen between the calculated and measured internal temperatures.

Table 2. Temperature and effective thermal properties

Temperature (°C)	Thermal conductivity (W/mK)	Specific heat (J/kgK)	Density (kg/m^3)
20	0.12	1530	495
98	0.133	1770	495
99	0.265	13600	495
120	0.272	13500	495
121	0.137	2120	495
200	0.150	2000	495
250	0.136 x α*	3337	460
300	0.106 x α*	1463	257
350	0.077 x α*	1751	188
400	0.084 x α*	2060	163
500	0.099 x α*	2472	155
600	0.194 x α*	2884	139
800	0.385 x α*	3399	129
1200	1.65 x α*	3399	0

*α that results in the best fit with experimental data is determined for three tests of series A.

**ω is the initial moisture content

Table 3. α for different heating rates

Parametric fire	Heating rate factor Γ	α
A1	8.41	1
A2	3.74	1.1
A3	0.93	1.35

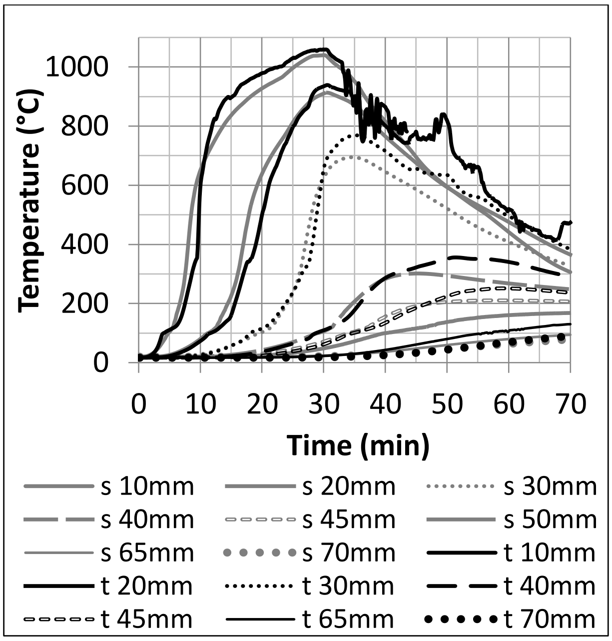

Figure 6. Numerical and experimentally determined temperatures at different depths. Parametric curve A1

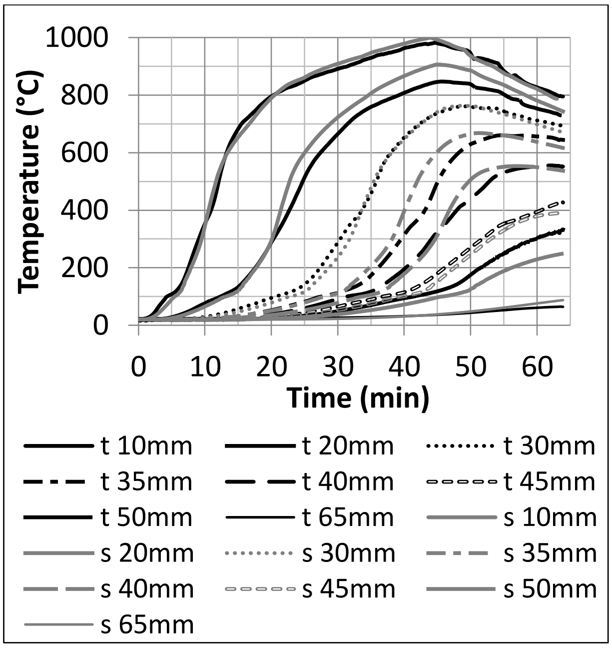

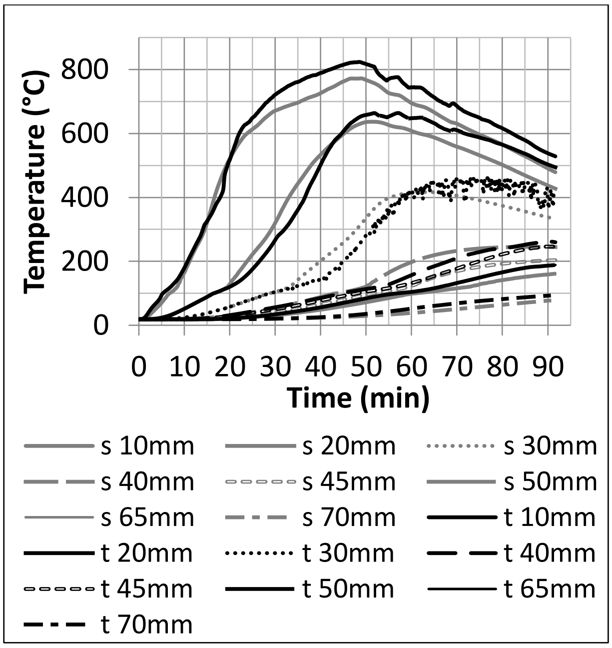

Figure 7. Numerical and experimentally determined temperatures at different depths. Parametric curve A2 (left) A3 (right)

For the heat transfer model (step 1 of the analysis) a symmetrical half of the beams cross-section (180/2 x 260mm) was discretised using square elements of 1x1mm. The two exposed sides of the symmetrical half were subjected to the parametric temperature curves, assuming the same convection and emissivity as mentioned before. There was no heat transfer on the other sides, to simulate a symmetry plane and the unexposed side of the beam. The average temperature (of four nodes) of every element was calculated and a numerical calculation according to Schmid and König (2010) with the same element mesh using the reduction coefficients of Figure 5 was performed, to determined the moment capacity of the heated beam.

6 Generation of a new effective cross-section method for parametric fires

For application of the effective cross-section method to calculate the structural capacity of timber members exposed to fire, charring rates and the zero-strength-layer are necessary input parameters. In the standard ISO 834 fire, the zero-strength-layer can be taken as constant after 20 minutes according to Eurocode 5. In the cooling phase of a parametric fire, the correlation between the charring rate and the reduction of load bearing capacity is not as straightforward. The charring rate will decrease and charring can completely stop during the cooling phase. However, after the charring has stopped the capacity of the beam continues to decrease. In the numerical model, the end of charring is taken as the time at which the 300°C isotherm stops to advance. After that, internal material with temperatures lower than 300°C continues to heat up as a result of diffusion from the hotter char layer, meaning that the load bearing capacity of the cross-section still reduces as the thickness of the temperature affected timber increases. The zero-strength-layer is, therefore, not constant in the cooling phase. Consequently, predictions of the real charring rate in the cooling phase are not practical, as its use for calculations only complexifies the calculation of the thickness of the zero-strength layer. Instead, an effective charring rate is introduced so that a constant zero-strength-layer can be assumed. The zero-strength-layer is dependent on the heating rate, *Γ*.

The numerical model was used to predict the width of the ineffective layer, d_{inef}, that should be subtracted from the initial cross-section to calculate the load bearing capacity for the full duration of the fire. The thickness of this layer can be obtained by solving the following equation to d_{inef}.

$$W_{ef} = \frac{(b-2d_{inef})(h-d_{inef})^2}{6} = \frac{M_{ult}}{f_b} \tag{5}$$

where: W_{ef} is the effective section modulus; M_{ult} is the failure load; b is the initial beam width; h is the initial beam depth; f_b is the estimated bending strength of the beam.

The thickness of the zero-strength-layer can be estimated by solving the following equation to d_0:

$$W_{300} = \frac{(b-2(d_{inef}-d_0))(h-d_{inef}+d_0)^2}{6} \tag{6}$$

where: W_{300} is the section modulus of the part of the cross-section with temperatures lower than 300°C, which can be based on heat transfer analyses. The zero-strength-layer corresponding to the start time of the cooling phase is determined numerically for parametric fires A1, A2 and A3. It should be noted that the zero-strength-layer is approximately, but not exactly constant. The following empirical equation is proposed for the heating rate dependence of the zero-strength layer:

$$d_0 = 8.0 + 0.02\Gamma - 0.05\Gamma^2 \tag{7}$$

In Section 7 the extrapolation of the above equation is tested for heating rate factors of 0.25 and 9.0. Care should be taken to extrapolate the function any further as it is an empirical relationship.

The charring rate during the heating phase is based on the series of experimental results. The charring rates where determined from the location and time at which the last thermocouple of one thermocouple series reached 300°C. To avoid unreliably results, only thermocouples that were positioned parallel to the isotherms, in agreement with Annex C of EN 1363-1 (2012), were used for determining the charring rate. Additionally, experimental results of test series B1 were not included as none of the thermocouple readings exceeded 300°C during the heating phase. The following equation is proposed for the one dimensional charring rates corresponding to different fire heating rates: $\beta_{par,0} = \beta_0 \Gamma^{0.28}$ (8)

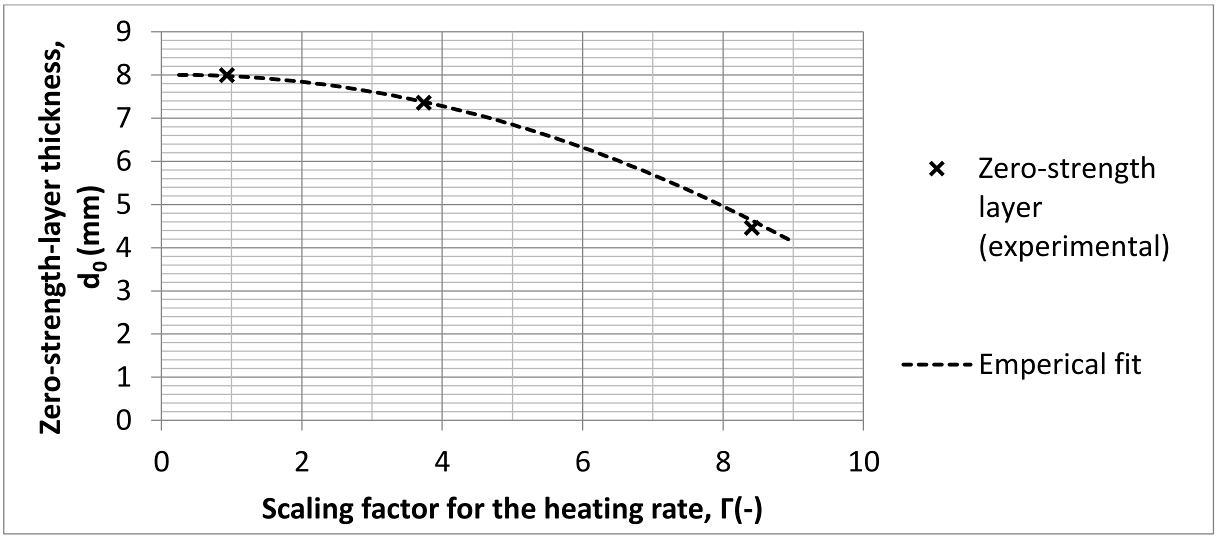

Figure 8. Relationship between Γ and zero-strength-layer (numerical)

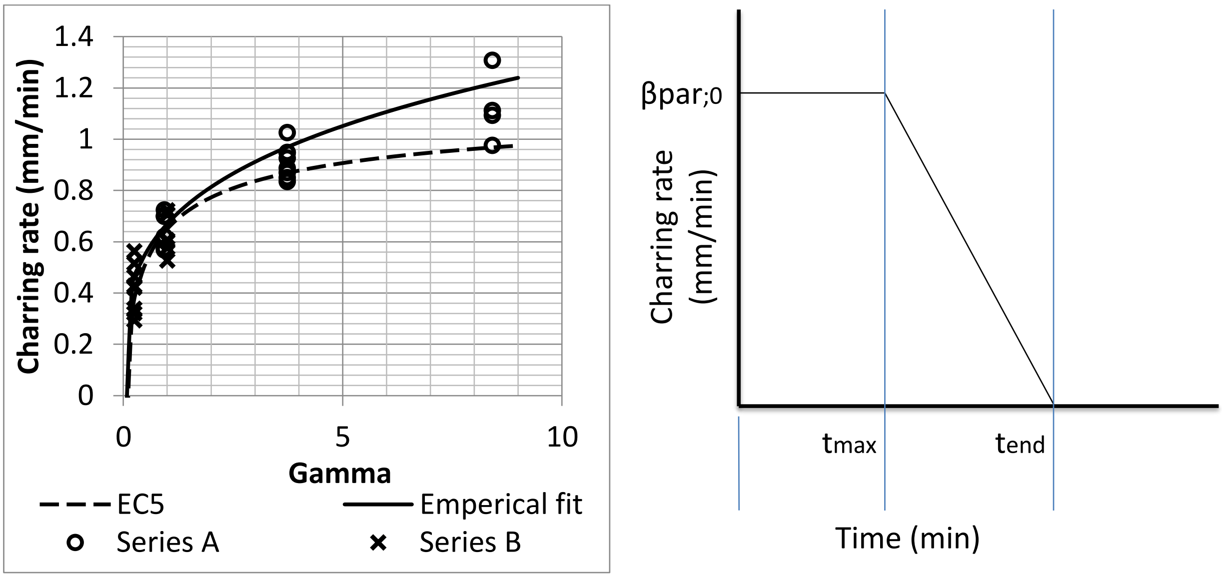

Figure 9. Relationship between Γ and the one-dimensional charring rate(left) proposed effective charring model (right)

An effective charring model is proposed with significant differences from the current charring model in EN1995-1-2 (2004). In the proposed model the charring rate is constant for the entire heating phase. It should be noted that t_0 of the Eurocode 5 model is not equal to the duration of the heating phase, t_{max}. t_{end} is the time at which the temperature of the parametric fire curve returns back to 20°C:

$$t_{end} = \frac{625 t_{\max} x \cdot \Gamma + \Theta_{\max} - 20}{625 \cdot \Gamma} \quad \text{if} \quad t_{\max} \cdot \Gamma \leq 0.5 \tag{9}$$

$$t_{end} = \frac{-250 t_{\max}^2 x \cdot \Gamma^2 + 750 t_{\max} x \cdot \Gamma + \Theta_{\max} - 20}{250 \cdot \Gamma (t_{\max} \cdot \Gamma - 3)} \quad \text{if} \quad 0.5 < t_{\max} \cdot \Gamma < 2 \tag{10}$$

$$t_{end} = \frac{250 t_{\max} x \cdot \Gamma + \Theta_{\max} - 20}{250 \cdot \Gamma} \quad \text{if} \quad t_{\max} \cdot \Gamma \geq 2 \tag{11}$$

The maximum fire temperature Θ_{max} can be obtained by substituting t_{max} for t in Eq.(1). The effective charring depth, $d_{char;ef,}$ at any time can be calculated using:

$$\beta_{par;eff} = k_{char}\beta_{par;0} \tag{12}$$

$$d_{char;eff} = \beta_{par;ef}\, t \qquad \text{for } t \le t_{\max} \tag{13}$$

$$d_{char;ef} = \beta_{par;ef}\, t_{\max} + 0.5 * \left(\frac{-\beta_{par;ef}}{t_{end} - t_{\max}}\right) \cdot (t - t_{\max})^2 + \beta_{par;ef}\,(t_{end} - t_{\max}) \quad \text{for } t > t_{\max} \tag{14}$$

Where k_{char} is a factor that accounts for corner roundings and is the ratio between the one-dimensional charring depth and the notional charring depth.

The notional charring rate at the end of the heating phase was estimated from the numerical study:

$$\beta_{par;n} = \frac{d_{inef} - d_0}{t} \tag{15}$$

The one-dimensional charring rate was determined from a one dimensional heat transfer model using the same thermal properties and fire exposure. The ratios between the average notional and one-dimensional charring rates at the end of the heating phase were 1.10, 1.03 and 1.12 for parametric fires A1, A2 and A3, respectively. A ratio of k_{char}=1.1 corresponds well with the numerical results and is approximately similar to the ratio between the one-dimensional and notional charring rates according to EN1995-1-2 (2004). This ratio is used for predictions discussed further in this paper.

In the next section, the validity of the proposed effective cross-section method applied to parametric fires is assessed using comparisons with experimental and numerical results.

7 Assessment of the new effective cross-section method

The effective cross-section method proposed in Section 6 is assessed using results of the experimental and numerical studies discussed in Section 4 and 5. Numerically and experimentally determined thicknesses of the ineffective layer, $d_{inef,}$ together with predictions using the proposed effective cross-section method for parametric fire curves A1, A2, A3, B1 and B2 (see Table 1) are given in Figure 10 and Figure 11. Additionally, predictions of the charring depth according to the Eurocode are given.

It can be seen that the numerically predicted charring depth and the effective depth deviate significantly in the cooling phase of the fire. The charring rate prediction of EN 1995-1-2 (2004) is based on experimental results (Hadvig, 1981) and shows good agreement with the numerical predictions. The effective char depth according to the proposed model deviates significantly from predicted charring rates. However, it seems effective to predict the ineffective depth using only a constant zero-strength-layer, because the predicted ineffective depth corresponds well with the numerical and experimental results. The ineffective depth corresponding to experiments is calculated and is defined as the ineffective depth that leads to failure of the beam, using the predicted strength properties of the beam.

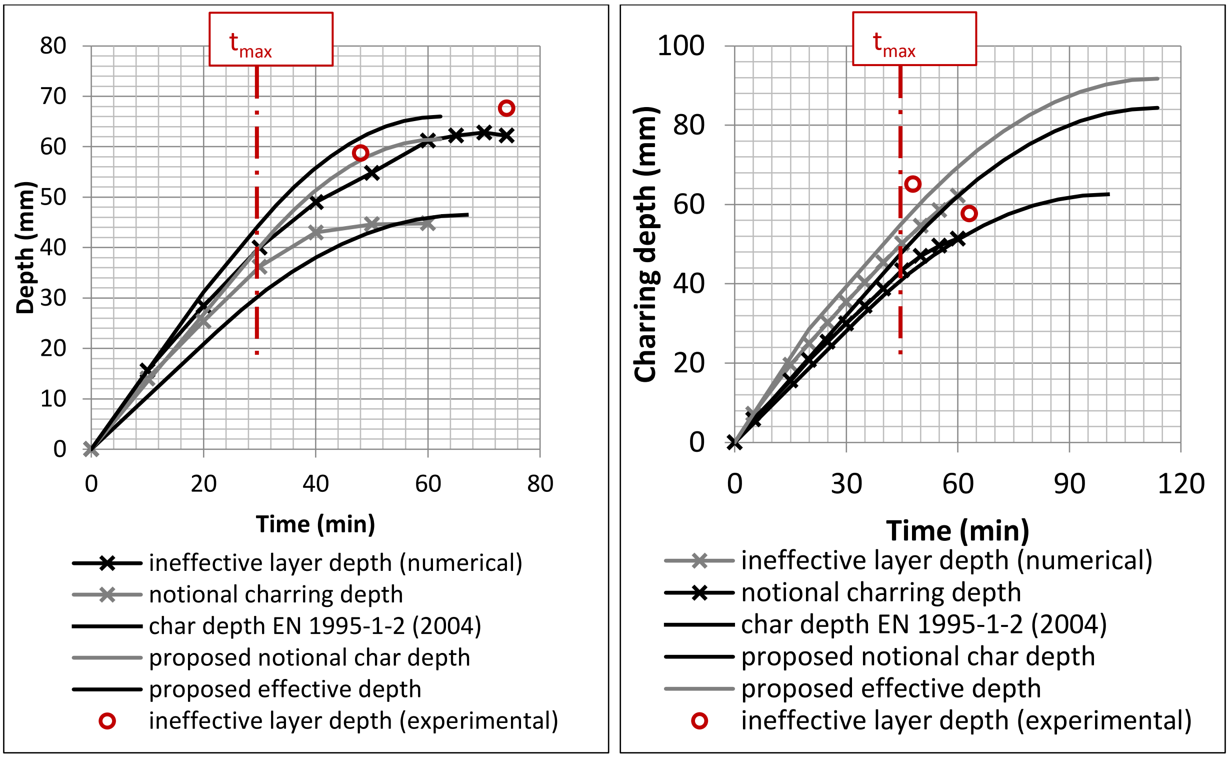

Figure 10. Numerical, analytical predictions of the charring depth, d_{char}, and ineffective depth, d_{inef}, and experimental results. Parametric fire A1 (left) and A2 (right)

Figure 12 shows comparisons between the experimental and predicted load bearing of glued laminated beams exposed to parametric fires, at the time of failure. Predictions were made using the proposed model and the current model of EN1995-1-2 (2004). For the latter, a zero-strength-layer of 7mm was taken for all fire exposures irrespective of the heating rate, as there is no zero-strength-layer specified for parametric fires. It can be seen that the calculated load bearing capacity using the proposed approach is generally more similar to the tested load bearing capacity. The current calculation method of EN1995-1-2 (2004) generally leads to unsafe predictions, indicating that the model should be updated in the next version of Eurocode 5.

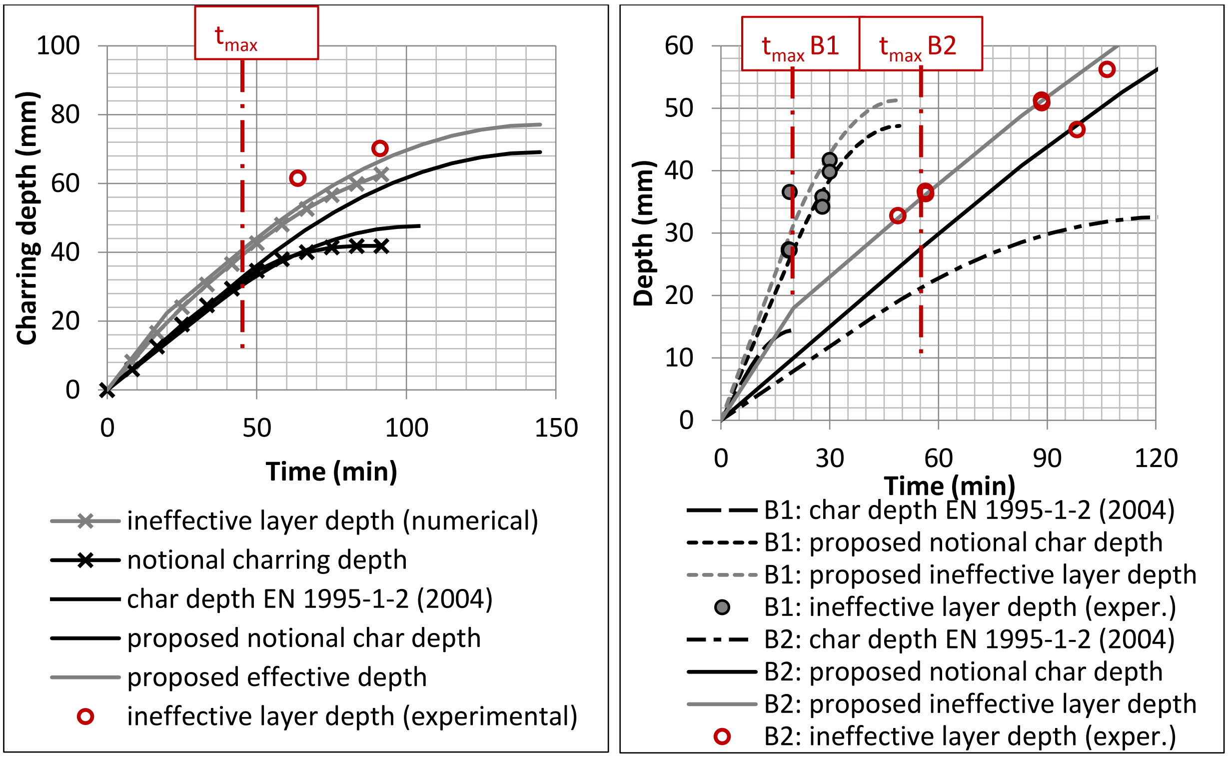

Figure 11. Numerical, analytical predictions of the charring depth, d_{char}, ineffective depth, d_{inef}, and experimental results. Parametric fire A3 (left) B1 and B2 (right)

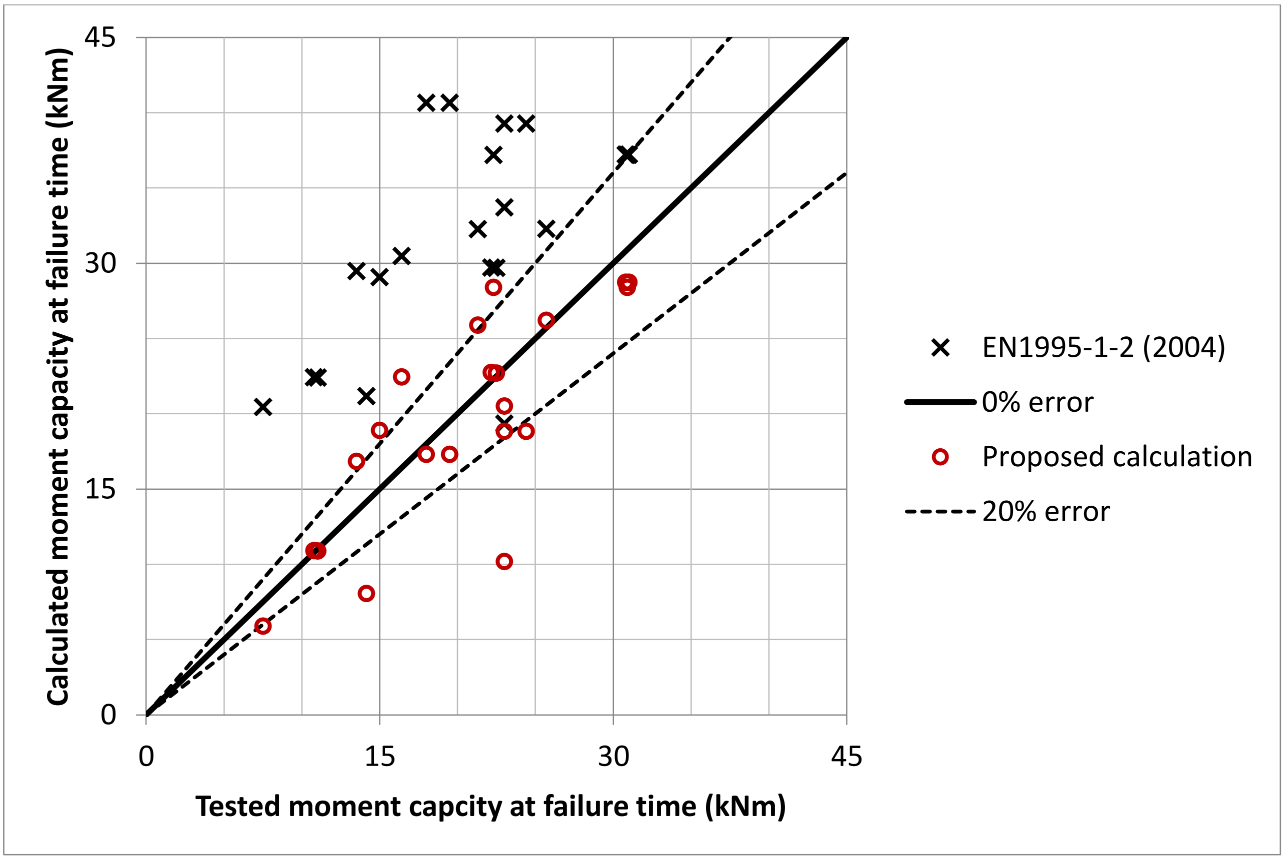

Figure 12. Calculated versus tested moment capacity at failure time

8 Conclusions

A new effective cross-section method for predictions of structural failure of timber exposed to parametric fires is proposed. Comparisons with experimental and numerical results showed that the current method given in EN1995-1-2 (2004) is unconservative and that the proposed model predicts structural failure more accurately.

References

EN1363-1 (2012). Fire resistance tests. General requirements. CEN, Brussels.

EN1995-1-2 (2004). Eurocode 5: Design of timber structures - Part 1-2: General - Structural fire design. CEN, Brussels.

EN1991-1-2 (2002) Eurocode 1: Actions on structures - Part 1-2: General actions - Actions on structures exposed to fire. CEN, Brussels.

Hadvig S. (1981). Charring of wood in building fires. Technical University of Denmark, ISBN 87-87 245-83-3.

Hopkin, D., El-Rimawi, J., Silberschmidt, V., and Lennon, T. (2011) An effective thermal property framework for softwood in parametric design fires. Journal of Construction & Building Materials 25(5), pp 2584-2595.

König J., Walleij L. (2000) Timber frame assemblies exposed to standard and parametric fires, Part 2. Institutet för träteknisk forskning, Stockholm, Sweden.

Lange D., Boström L., Schmid J., Albrektsson J. (2015) The reduced cross section method applied to glulam timber exposed to non-standard fire curves. Fire Technology DOI: 10.1007/s10694-015-0485-y

Mäger K.N., Brandon D., Just A. (2016) Determination of the effective thermal properties for thermal simulations. in: Proceedings of INTER, Graz, Austria.

Magnusson S.E., Thelanderson S. (1970) Temperature-time curves of complete process of fire development. *Acta Polytechnica Scandinavica,* 65.

Medina Hevia A.R. (2014). *Fire resistance of partially protected cross-laminated timber rooms*. Master thesis. Department of Civil and Environmental Engineering Carleton University, Ottawa, Ontario, Canada.

Olsson A. and Oscarsson J. (2016) Strength grading on the basis of high resolution laser scanning and dynamic excitation. *Eur. J. Wood Prod*.

Östman et al. (2010). Fire safety in timber buildings. Technical guideline for Europe. SP Technical Research Institute of Sweden, SP-Report 2010:19. Stockholm, Sweden.

Schmid J., König J., Köhler J. (2010) Fire exposed cross-laminated timber–modelling and tests. In: World conference on timber Engineering 2010. Riva del Garda, Italy.

Wickström U. (1986). *Application of the standard fire curve for expressing natural fires for design purposes*. Fire Safety: Science and Engineering, ASTM STP 882

Discussion

The paper was presented by D Brandon

A Buchanan commented that as the fire went out the temperature would decrease; however, the temperature within the panel would keep increasing. He wondered if the simulation work extended beyond the fire going out. He stated that this was a huge problem and there was a lot of work going on worldwide. He suggested to the authors to coordinate with others.

J W Van de Kuilen asked whether the modified charring rate included delamination of layers. D Brandon responded that falling off did not seem to occur when char reached the bond line in this study. Depending on the type of adhesive delaminating could occur at around 220°C. This would be a complicated problem

Zero-Strength Layers for Timber Frame Assemblies in a Standard Fire

Mattia Tiso, Alar Just, Tallinn University of Technology

Michael Klippel, Joachim Schmid, ETH Zürich

Daniel Brandon, RISE Research Institutes of Sweden

Keywords: timber frame assemblies; zero-strength layer; insulation materials; fire resistance; mechanical simulations

1 Introduction

Structural behaviour of timber members under fire conditions is influenced by material properties, geometrical characteristics, protection and boundary conditions. Fire resistance of timber members exposed to standard fire can be evaluated by an analytical design model known as the Effective Cross-Section Method (ECSM). Following this method, the effective cross-section in fire conditions is determined decreasing the original cross-section by a notional charring depth and a zero-strength layer. The ECSM for timber frame assemblies (TFA) exposed to a standard fire has been earlier presented. This design model considers the fire protection provided by claddings and insulation materials, for which design values for zero-strength layers are still missing. The zero-strength layer has been determined by means of a series of heat-transfer analyses combined with mechanical simulations. A model scale furnace test was performed in order to validate the results of the numerical simulations.

1.1 Charring models for timber frame assemblies exposed to standard fire

The charring of timber members of wall and floor assemblies exposed to fire is influenced by the protective properties of cladding and cavity insulation materials. A primary protection for a timber member is achieved by the cladding on the fire exposed side. The charring phase prior to fall-off (failure) of protective cladding is defined as the protection phase. After the fall-off of cladding, a secondary protection of the timber member might be provided by cavity insulation materials. The charring phase after the fall-off of protective cladding is defined as the post-protection phase.

Annex C of the current Eurocode 5 part 1-2 (2004) presents a design model that considers fire protection provided by claddings and stone wool as cavity insulation during the protection and post-protection phases (Fig. 1b). In this design model the charring of the timber element is taken into account as one-dimensional (König & Walleij, 2000). The model is applied for timber frame assemblies with glass wool as cavity insulation at the protection phase only. In the European technical guideline Fire Safety in Timber Buildings (FSITB) (Östman et al., 2010) a design model that takes into account the contribution of glass wool to the fire resistance during the post-protection phase is included. The design model for glass wool considers also charring from the lateral sides of the timber element, giving a trapezoidal shape to the residual cross section (Fig. 1c).

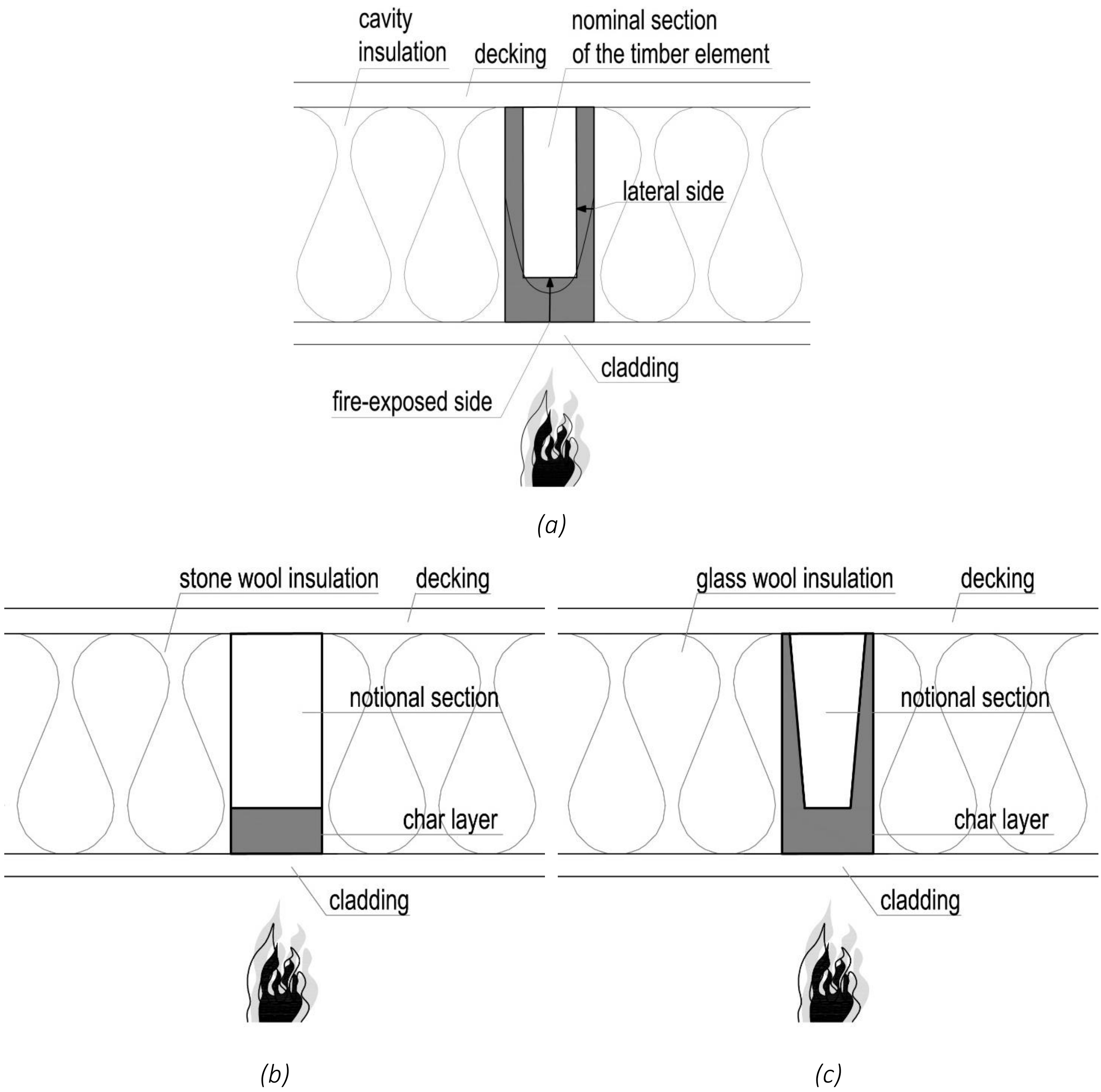

Figure 1. (a) Cross-section of a timber frame assembly used as a floor. Charring models for TFA insulated with (b) stone wool and (c) glass wool.

This model was proposed due to a significantly faster recession of the glass wool compared to stone wool under fire conditions. The recession speed of glass wool was introduced to describe the development of charring on the lateral sides (Just, 2010).

An improved design approach independent of the material of the cavity insulation has been published by the authors of this paper (Tiso & Just, 2017). This approach introduces the concept of protection levels (PL) of insulation materials. The protection level of an insulation material indicates its capability to protect timber against charring. The protection level is evaluated by means a standard test set-up. Three different protection levels can be assigned to an insulation material, where PL3 indicated the weaker protection level and PL1 indicates the stronger protection level. This improved design approach includes also a design model where the charring of the timber element can be considered from the fire side or from three (Fig. 1a) sides according to the fire protection provided by the insulation (i.e. protection level).

1.2 Reduction of the load-bearing capacity

Behind the char layer of a timber member exposed to fire there is a heated zone where the strength and stiffness properties of the timber are reduced compared to the respective initial properties at normal temperature.

Current Eurocode 5 Part 1-2 (2004) includes two methods to determine the mechanical resistance of timber members exposed to fire:

- The effective cross-section method (which is also known as the reduced cross-section method) in which the decrease of strength and stiffness properties of timber member are compensated by using zero-strength layers while initial strength and stiffness properties are used in calculations;
- The reduced properties method in which the strength and stiffness of the residual cross-section is reduced by modification factors.

Values for zero-strength layers for the effective cross-section method (ECSM) for timber frame assemblies with cavities completely filled with stone wool and glass wool were published in FSITB (2010). The values are based on backwards calculations from results of fire tests corresponding to a limited range of cross-sections with reduced strength and stiffness properties. In this study, improved values for zero-strength layers for TFA with cavity insulations of PL1 in different load conditions are proposed. For PL1 stone wool and high temperature extruded (HTE) mineral wool are chosen as representative examples. The improvement is based on thermo-mechanical simulations and fire tests. The resulting model is based on a significantly wider range of cross-sections than previous studies.

2 Improved design model for timber frame assemblies

The design model proposed by Tiso and Just (2017) considers three different charring scenarios for timber frame assemblies with cavities completely filled with insulation. If the cavities are completely filled with insulation materials qualified as PL1 (Tiso &

Just, 2017) the charring occurs mainly on the fire-exposed side of the member, while the lateral sides are protected by the insulation (Fig. 2a). Fire exposed side and lateral sides of cross-section are defined in Figure 1a. In that case, the lateral charring can be neglected. If the cavities are completely filled with insulation materials qualified as PL2 (Tiso & Just, 2017), the charring is regarded from one side during the protection phase and from three sides of the cross-section during the post-protection phase due to the degradation (recession) of the insulation material. When the cavities are completely filled with insulation materials qualified as PL3 (Tiso & Just, 2017), the charring is regarded from three sides of the cross-section already during the protection phases.

The charring depth along the fire exposed side ($d_{char,1,n}$) is calculated as:

$$d_{char,1,n} = \beta_0 \, k_{s,n} \, k_2 \, (t_f - t_{ch}) + \beta_0 \, k_{s,n} \, k_{3,1} \, (t - t_f) \quad (1)$$

After the start of lateral charring, the charring depth on the lateral sides can be evaluated as:

$$d_{char,2,n} = \beta_0 \, k_{s,n} \, k_{3,2} \, (t - t_{ch,2}) \quad (2)$$

The coefficient $k_{s,n}$ is a cross-section factor, used to consider the influence of cross-section width and depth on the charring rate. Different charring rates in different protection phases are described using the protection coefficients k_2 and $k_{3,1}$ like in the current version of Eurocode 5 (2004). The start time of charring from lateral sides ($t_{ch,2}$) is assumed to occur after the cladding has fallen off. The factor $k_{3,2}$ considers the influence of the recession of the insulation material on fire protection on the lateral sides.

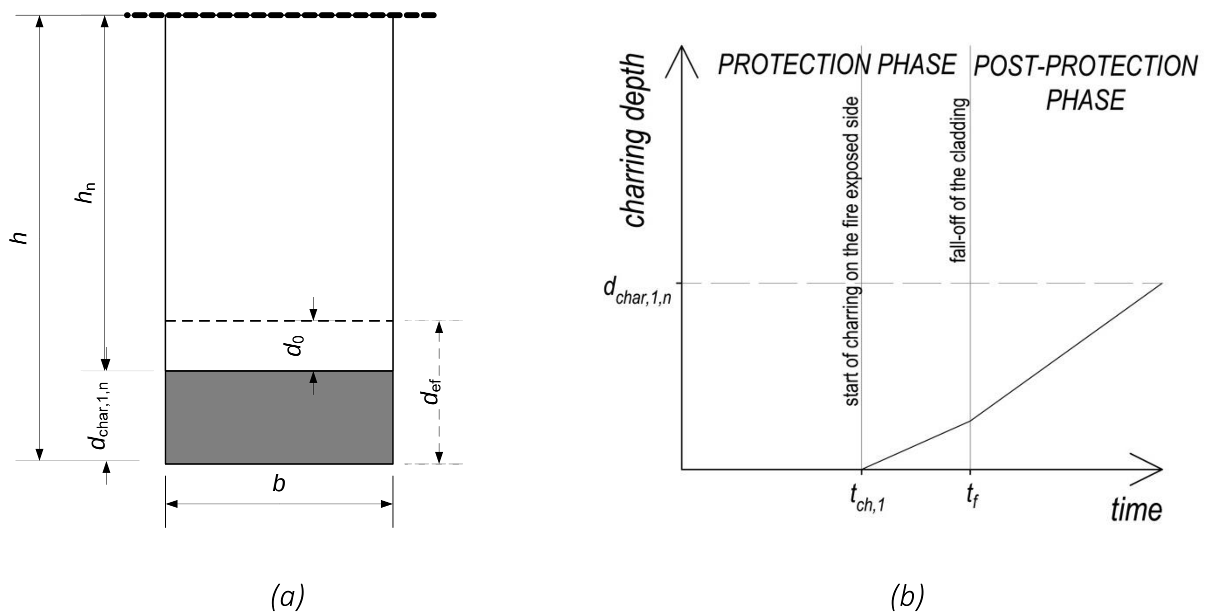

Figure 2. Improved design model for timber frame assemblies with PL1 insulation ; (a) determination of the residual cross-section; (b) different charring phases of the design model.

An effective charring depth can be calculated by increasing the notional charring depth by a zero-strength layer (d_0):

$$d_{ef} = d_{char,n} + d_0 \quad (3)$$

An effective cross section is obtained by subtracting the effective charring depth from the original cross-section. The effective cross-section enables to predict the load bearing capacity of the element under fire conditions by using the initial strength and stiffness properties.

3 Calculation of the load-bearing capacity of timber frame assemblies in fire

The load-bearing capacities were predicted using thermo-mechanical simulations. For this, a two-step process was adopted:

1. Temperature distributions through the cross-section were obtained by means of two-dimensional heat-transfer analysis,
2. Load-bearing capacity with temperature dependent reduction of strength and stiffness was calculated.

The output of the thermo-mechanical simulations were used to calculate corresponding zero-strength layers.

3.1 Heat transfer analysis

In order to investigate the temperature distribution within the cross-section, two-dimensional (2D) models were implemented in SAFIR software package (Franssen, 2005).

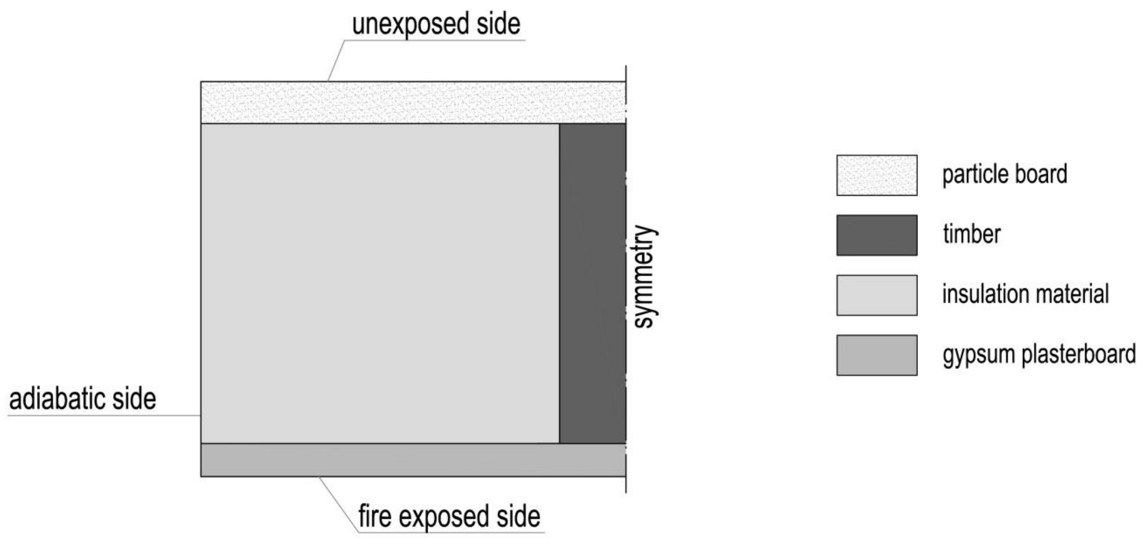

Figure 3. Schematization of the heat-transfer simulations.

The thermal exposure was described by means of the standard fire time-temperature curve. The heat transfer by convection and radiation to the exposed side of the model was considered (Fig. 3) using a convection coefficient of 25 W/ m^2 K and emissivity of 0.8, as prescribed in Eurocode 1 part 1-2.

Heat transfer through the timber member was modelled by using the effective thermal properties given in Eurocode 5 part 1-2. Gypsum plasterboards and particle board were described by using the effective thermal properties given in FSITB. Two different materials were considered as insulation: a stone wool (SW) and a high temperature extruded (HTE) mineral wool as cavity insulations. Effective thermal properties of stone wool insulations and HTE mineral wool were calibrated for this study (Fig.4). The heat transfer calculations considered 90 minutes of fire exposure.

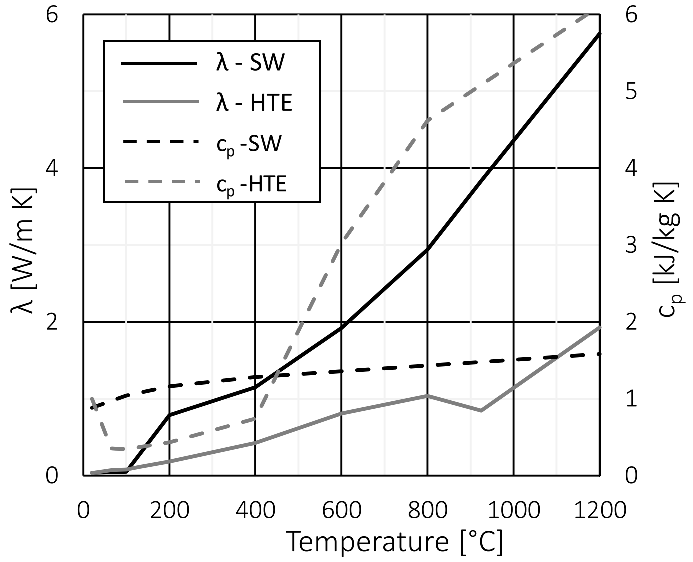

Figure 4. Effective thermal properties vs. temperature of HTE mineral wool and SW.

3.2 Mechanical analysis

For the structural analysis of the timber member, CST Fire was used (Schmid & König, 2010). This program is capable of calculating the bending moment capacities of timber members exposed to fire. The calculations are performed by means of an iterative process.

The program (i) takes the temperature distribution of the timber cross-sections from the heat transfer analysis, (ii) assigns strength and stiffness reduction depending on the temperature, (iii) calculates the geometrical properties of the residual cross-section, (iv) determines the bending moment capacities (M_{fi}) and related curvatures (κ_{fi}) during the time.

Reduction of strength and stiffness in tension and compression were as assumed according to Eurocode 5 part 1-2 (Fig 5). Furthermore, a brittle behaviour of timber in tension and full-plastic behaviour in compression were considered.

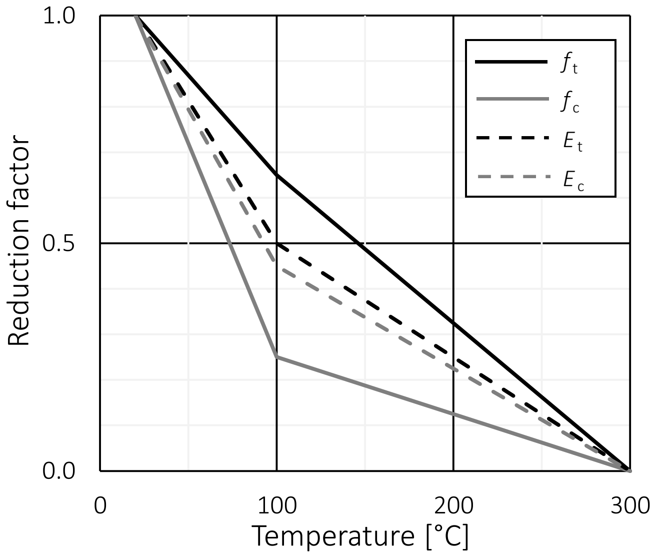

KEY: f_t-tensile strength, f_c-compressive strength, E_t- modulus of elasticity in tension, E_c-modulus of elasticity in compression

Figure 5. Reduction factors for strength and stiffness properties in compression and tension according to Eurocode 5 part 1-2.

3.3 Simulation programme

Different cross-section dimensions and claddings were investigated. Set-ups are summarized in Table 1. The type of claddings considered corresponding to the different cross-sections dimensions are also given.

Table 1. Claddings on the fire side of investigated set-ups.

		Initial height of cross-section			
		h = 95 mm	*h* = 145 mm	*h* = 195 mm	*h* = 295 mm
Initial width of cross-section	*b* = 45 mm	-	GtF 15 mm	GtF 15 mm	GtF 15 mm
	b = 60 mm	GtF 15 mm	GtF 15 mm	GtF 20 mm	GtF 20 mm
	b = 75 mm	-	GtF 15 mm	GtF 20 mm	GtF 20 mm
	b = 90 mm	GtF 15 mm	GtF 15 mm	GtF 20 mm	GtF 20 mm
	b = 120 mm	GtF 15 mm	GtF 15 mm	GtF 20 mm	GtF 20 mm

*GtF – Gypsum Plasterboard type F

For each set-up, at least two different fall-off times (t_f) of the claddings were considered. Furthermore, for each configuration, both, tension and compression side of the cross-section exposed to fire were considered. For each insulation material, at least 72 different simulations were performed. Results of the thermo-mechanical simulations are shown in Figure 6.

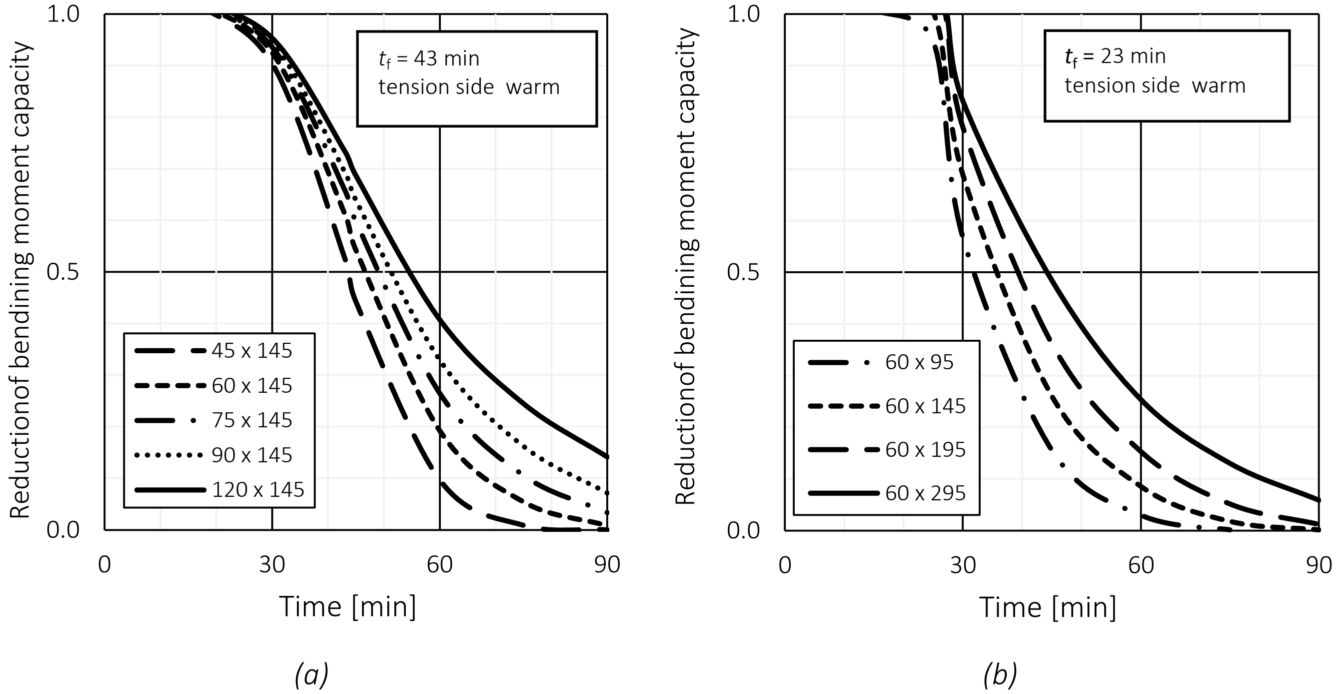

Figure 6. Reduction of bending moment capacity against the time for assembly insulated with stone wool. Comparison of different (a) widths and different (b) heights.

4 Determination of zero-strength layers

Zero-strength layers for members in bending and compression have been determined by using the output of the thermo-mechanical simulations.

4.1 Bending members

The bending moment capacities and related curvatures are calculated using CST Fire, see Figure 6. In order to determine the depth of the zero-strength layer d_0 for a member in bending, the bending capacity of the heated cross-section was taken as equal to the bending capacity of the effective cross-section at ambient temperature. For timber frame assemblies insulated with a material qualified as PL1 the bending capacity in fire is:

$$M_{fi}=W_{ef}\, f_{m,20°C}=\frac{(h_n\text{-}d_0)^2 b}{6}\, f_{m,20°C} \tag{4}$$

where: W_{ef} is the section modulus of the effective cross-section; $f_{m,20°C}$ is the bending strength value at ambient temperature; h_n is the notional height of the cross-section and b is the initial width of the cross-section.

Then depth of zero-strength layer for a member in bending is derived as:

$$d_0=h_n\text{-}\sqrt{\frac{6\, M_{fi}}{b\cdot f_{m,20°C}}} \tag{5}$$

4.2 Compression members

Buckling is most the relevant failure mode for axially loaded compression members. For timber frame wall assemblies, out-of-plane buckling or in-plane buckling of load-bearing studs might occur. In general, the buckling resistance of a member (N_{crit}) in fire is:

$$N_{crit} = \frac{\pi^2 (EI)_{fi}}{l_0^2} \tag{6}$$

where: $(EI)_{fi}$is the stiffness of a member in fire conditions, l_0 is the effective buckling length of a member.

The stiffness in fire, can be evaluated from CST Fire as:

$$(EI)_{fi} = \frac{M_{fi}}{\kappa_{fi}} \tag{7}$$

where: κ_{fi} is the curvature of a member in fire conditions.

Zero-strength layers for bucking were evaluated by comparing the buckling resistance with an effective cross-section at ambient temperature:

$$N_{crit} = \frac{\pi^2 E_{20°C} I_{ef}}{l_0^2} \tag{8}$$

where: $E_{20°C}$ is the modulus of elasticity (MOE) value at ambient temperature; I_{ef} is the moment of inertia of the effective cross-section.

The moment of inertia of the cross-section for out-of-plane buckling can be calculated as:

$$I_{ef} = \frac{(h_n - d_0)^3\, b}{12} \tag{9}$$

And for in-plane buckling can be calculated as:

$$I_{ef} = \frac{(h_n - d_0)\, b^3}{12} \tag{10}$$

By combining the Equations (6), (8) and (9) is possible to derive the expression to calculate the zero-strength layer for out-of-plane buckling elements:

$$d_0 = h_n \left(1 - \sqrt[3]{\frac{E_{fi}}{E_{20°C}}}\right) \tag{11}$$

where: E_{fi} is the MOE of a member in fire.

On the same way, combining the Equations (6), (8) and (10) the expression to calculate the zero-strength layer for in-plane buckling is derived:

$$d_0 = h_n \left(1 - \frac{E_{fi}}{E_{20°C}}\right) \quad (12)$$

4.3 Results

Depths of zero-strength layers for compression and bending have been calculated for timber frame assemblies insulated with high temperature extruded mineral wool and stone wool (see an example in Fig. 7a). Results are compared for different fall-off times of cladding (Fig. 7b). The comparison shows that there is no significant difference in the maximum value of d_0 for different fall-off times (t_f), as the different curves peak at similar value of d_0. Furthermore, it can be seen that the only difference between assemblies that were unprotected (t_f = 0 in Fig. 7b) and protected for 90 min (t_f = 90 in Fig. 7b) is the time when the maximum d_0 occurred.

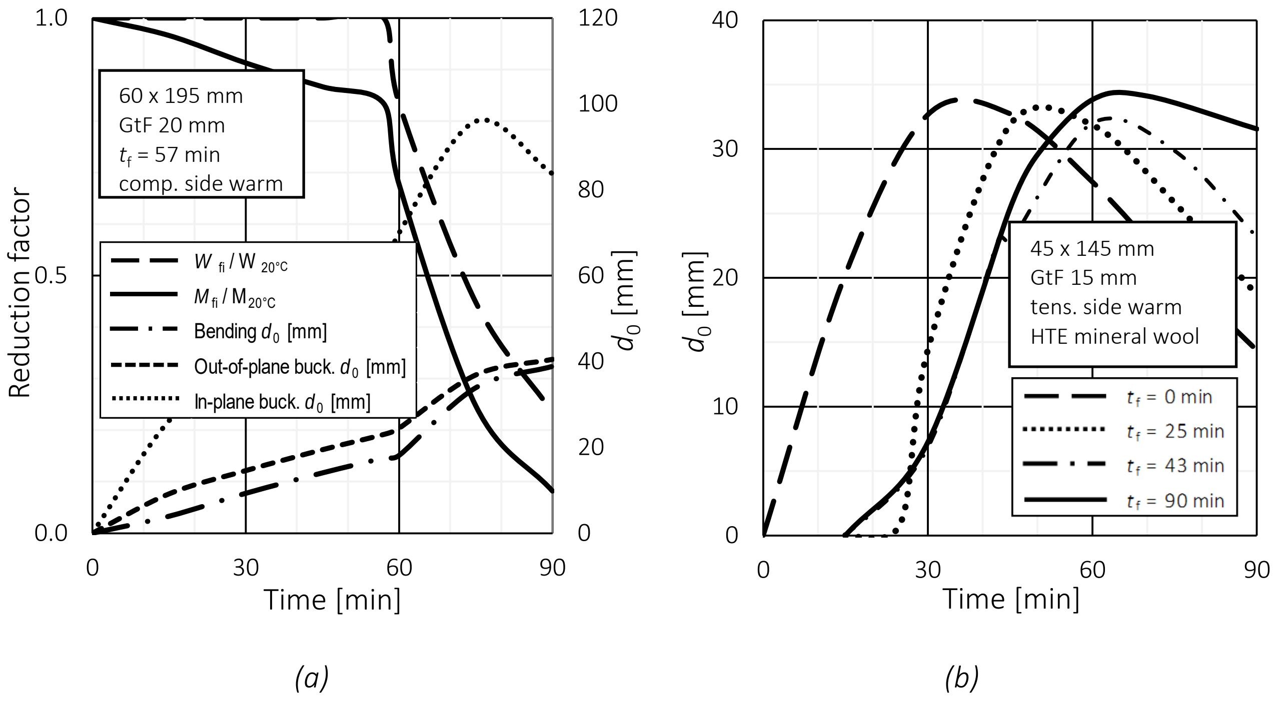

Figure 7. (a) Bending moment capacity, section modulus and depth of zero-strength layers for an assembly insulated with stone wool; (b) depth of zero-strength layer for elements in bending for different fall-off times of the cladding for assemblies with HTE wool.

In order to provide a simple approach for the designer, it is reasonable to assume the depth of zero-strength layer is independent of time. By means of multi-regression analyses, factors influencing the zero-strength layers were determined.

For timber frame assemblies insulated with stone wool, the following expressions are proposed:

- bending member with the fire exposed side in tension:

$$d_0 = 9 + 0.25\,h - 0.18\,b \quad (13)$$

- bending member with the fire exposed side in compression:

$$d_0 = 27.9 + 0.14\,h - 0.26\,b \quad (14)$$

- out-of-plane buckling of compression member:

$$d_0 = 29.1 + 0.16\, h - 0.26\, b \tag{15}$$

- in-plane buckling of compression member:

$$d_0 = 43.6 + 0.43\, h - 0.37\, b \tag{16}$$

For timber frame assemblies insulated with HTE mineral wool, the following expressions are proposed:

- bending member with the fire exposed side in tension:

$$d_0 = 18.6 + 0.17\, h - 0.18\, b \tag{17}$$

- bending member with the fire exposed side in compression:

$$d_0 = 27.9 + 0.14\, h - 0.28\, b \tag{18}$$

- out-of-plane buckling of compression member:

$$d_0 = 25.5 + 0.17\, h - 0.26\, b \tag{19}$$

- in-plane buckling of compression member:

$$d_0 = 36.4 + 0.45\, h - 0.37\, b \tag{20}$$

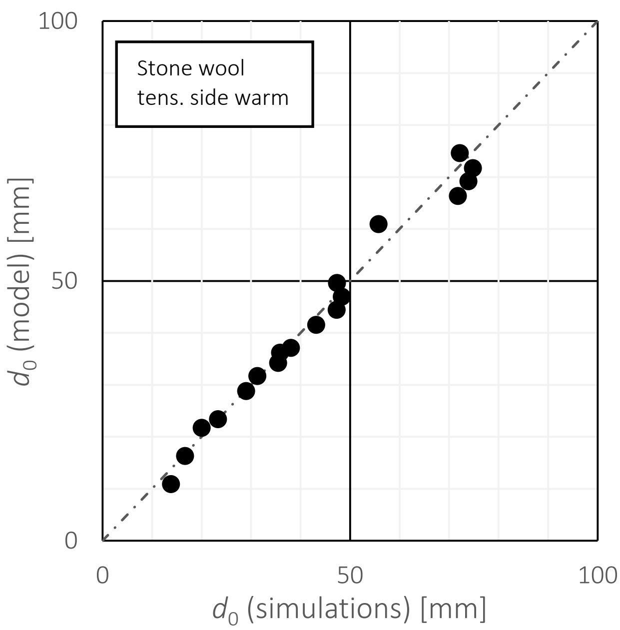

(a)

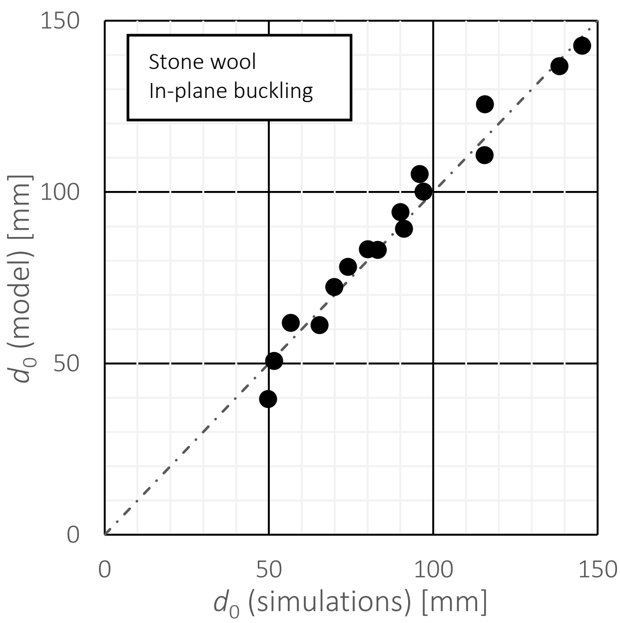

(b)

Figure 8. Zero-strength layers calculated by means of numerical simulations compared with the models proposed for assemblies insulated with stone wool. Comparison for (a) bending members with tension side exposed to fire and (b) compression members with in-plane buckling.

5 Reference fire test

A loaded model-scale furnace test has been carried out as benchmarks for the simulations. A cubic meter furnace was used for fire testing. A portion of a floor (dimensions 800 x 1000 mm) was subjected to the standard fire exposure according to ISO 834 (1999). The floor specimen was composed of a load bearing timber element, gypsum plasterboard cladding and HTE mineral wool. The load bearing timber element (cross-section dimension 50 x200 mm) was loaded in four-point bending, with the tension side exposed to the fire. The exposed side of the assemblies was protected by a 15 mm thick gypsum plasterboard (Type F) held in place by screws. Prior to the test, the Modulus of Elasticity (MOE) and the bending strength of the beams were assessed by means of high resolution laser scanning and dynamic excitation in accordance with Olsson & Oscarsson (2016). Results of the tested beam are shown in Table 2.

Table 2. Overview of the loaded test performed

Cross-section dimensions [mm]	Fire protection	Fall-off of fire protecticion [min]	Bending moment applied [kNm]	Predicted MOE [GPa]	Predicted bending strength [MPa]
50 × 200	GtF 15 mm	34	5.27	13.2	52.7

The timber element was loaded with a constant bending moment of 5.27 kNm along the fire-exposed part (which corresponds to 30% of the ultimate moment capacities at ambient temperature).

The gypsum plasterboard has fallen in one piece at 34 minutes from the beginning of the test. The end of the test was determined when rupture of the beams occurred, at 53.3 min. The zero-strength layer has been calculated according to Eq. (5) and resulted to be equal to 36.1 mm. The same set-up was simulated according to the methodology described in Chapter 3. From the simulation a zero-strength layer equal to 37.3 mm was obtained. The good agreement between the experimental and numerical results indicates that the numerical simulations are suitable to predict the fire resistance of bending beams. The zero-strength layer calculated according to Eq. (17) for this set-up resulted to be equal to 43.6 mm. The predictions according to the proposed expression of Eq. (17) give only the peak values of d_0 during fire exposure. The empirical approach is simple but conservative with respect to fire tests and numerical simulations.

6 Conclusions

The purpose of this study was to investigate the depths of zero-strength layers of timber members in wall and floor assemblies. Thermo-mechanical analyses of different set-ups of cross-sections and cavity insulations were performed. Comparisons of numerous simulations have shown that the depth of zero-strength layer depends on cross-section dimensions, and fire exposure time. In order to validate the results of the mechanical simulations, one loaded fire test has been performed.

Design values for depths of zero-strength layers for bending and compression has been proposed for assemblies with two different cavity insulation materials qualified as PL1. This approach is proposed for a maximum of 90 minutes standard fire exposure.

This research will serve as a basis for future studies on zero-strength layer of timber frame assemblies with different insulation materials applied.

7 Acknowledgements

The authors acknowledge the network of COST Action FP1404 WG2 for the contribution.

8 References

Eurocode 5 Part 1-2 (2004): Design of timber structures – Part 1-2: General – Structural fire design, (EN 1995-1-2:2004).

Eurocode 1 Part 1-2 (2002): General Actions – Actions on structures exposed to fire, (EN 1991-1-2:2002).

ISO 834–1:1999: Fire Resistance Tests – Elements of Building Construction – Part 1: General Requirements., 1999.

Östman, B. et al. (2010): Fire safety in timber buildings, SP Technical Research Institute of Sweden.

König, J., Walleij, L. (2000): Timber frame assemblies exposed to standard and parametric fires: part 2: a design model for standard fire exposure. Rapport-Institutet för Träteknisk Forskning, (0001001).

Just, A. (2010):Post protection behaviour of wooden wall and floor structures completely filled with glass wool, in: Struct. Fire Proceeding 6th Int. Conf., East Lansing (USA), pp. 584–592.

Tiso, M., Just, A. (2017): Fire protection provided by insulation materials - a new design approach for timber frame assemblies, Struct. Eng. Int., Vol. 27, N. 2, pp. 231-237

Franssen, J. M. (2005). SAFIR: A thermal/structural program for modeling structures under fire. Engineering Journal-American Institute of Steel Construction Inc, 42(3), 143-158.

Schmid, J., König, J. (2010): Cross-laminated timber in fire. SP Report 2010:11.

Olsson, A., Oscarsson, J. (2016): Strength grading based on high resolution laser scanning – performance of a procedure newly approved for the European market, Eur. J. Wood Wood Prod., pp. 232–240. doi:10.1007/s00107-016-1102-6.

Discussion

The paper was presented by M Tiso

H Blass commented that comparison of test results with calculated results would need assumption or prediction of bending strength. It would not make sense to present the results with this level of accuracy. H Blass further asked about the in- or out- of plane buckling load. Which model was used to determine the compression capacity? M Tiso said a model developed by T Konig on constitutive properties was used.

A Buchanan discussed the approach used and one equation should be good enough considering the accuracy. M Tiso said that in the buckling situation there would be panel on side of wall. He further discussed about the type of product used and they planned to investigate other products.

Improved fire resistance of connected nail plate trusses

Geir Glasø, Norwegian Institute of Wood Technology

Kristine Nore, Norwegian Institute of Wood Technology

Arnold Sagen, Norwegian Truss Producers Association

Keywords: Timber truss, nail plate, fire sealant, fire testing, fire resistance.

1 Introduction

Nail plate timber trusses utilize the timber properties by connecting slender timber members in torque stiff joints. Nail plate trusses are produced efficiently and erected quickly. For smaller buildings, this construction system is widely used, it is cost-efficient and robust.

During a fire nail plates will fail very early if the nail plate is not protected. Trusses with nail-plates are normally used with sheathing (ceiling, floor or wall) and therefore normally not directly exposed to fire.

For larger constructions, additional requirements apply. Nail-plate timber trusses are shown to be cost efficient also as larger and open trusses. To ensure fire safety, several trusses are connected to form a larger combined structure which allows an open truss construction.

When connecting several timber trusses, only the outer two surfaces with nail-plates will be exposed directly to fire while the rest will be inside the structure and protected. Small gaps between each truss in top and bottom created by the thickness of the nail-plates can be closed with protection material or by having enough distance from open surface to nail-plates.

Examples are *Almenningstråkket* commercial centre built in 2015 in Gran, Norway. In this project, the truss system spans up to 23 meters. See Figure 1a. Another example is a commercial store in Vestby, built in 2016, see Figure 1b.

a) b)

Figure 1a) Connected timber truss beams at Almenningstråkket in Gran, Norway. B) Nail-plate truss system in roof (R60). Commercial food store outside Oslo in Norway.

Due to national fire regulations in Norway (TEK17, 2017), this construction has to withstand 60 minutes fire resistance (R60) for use in commercial buildings as shown in Figure 1a and 1b.

Preliminary calculations show that for combined truss construction with nail-plates to withstand fire resistance of 60 minutes, the cross section must be increased (increased height) to make sure edge distance between nail-plates and wood surface is satisfied. To make this truss system cost-effective and to compete with other solutions and materials, fire tests was conducted to see how different configurations acts during fire.

The most important factor for fire resistance for nail-plates is temperature. Increase in temperature will decrease the strength in the nail-plate. At 300˚C the yield value of steel has decreased with about 20%, and at 600 ˚C with to about 80%.

In this fire test, we wanted to see how the different configurations behaved during fire and to measure the temperature increase for nails-plates with different gap depth distances and different local protections of the nail plate.

2 Construction principle

The principles of this construction system are based on several single trusses with nail-plates that are linked together to form a larger combined structure for increased span, specially in roof constructions. Figure 2 shows a small part of the structures with nail-plate connection for a five-layer truss system. Fire sealant is applied around the outer edges of the nail-plates before next truss is connected to the first. The fire sealant fill the gap between the trusses. This is done for all nail-plates in every interface.

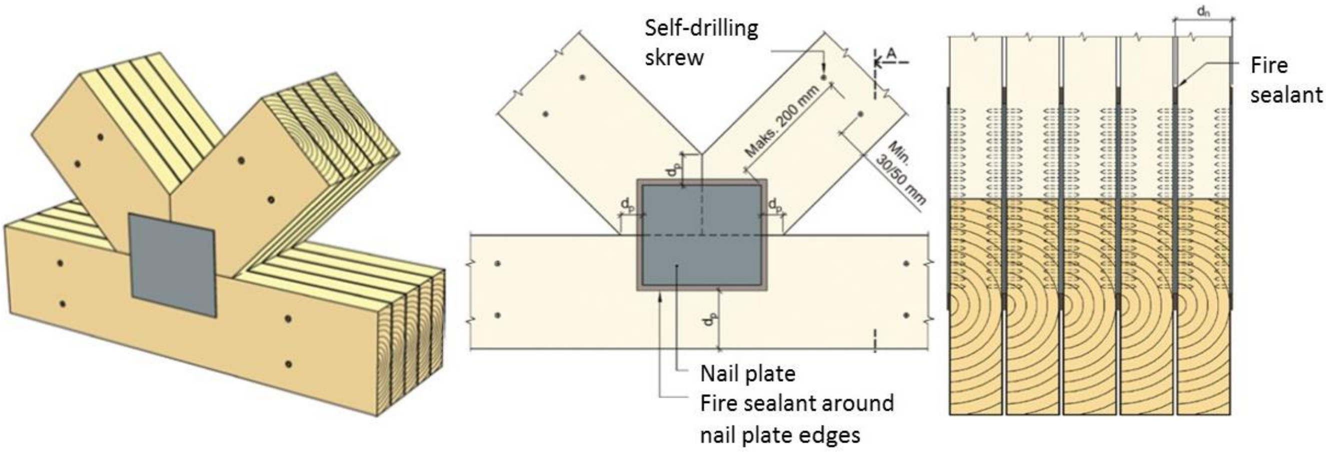

Figure 2. Principle of linked wood trusses with nail plates. Assembled joint (left), section with end distances and fire sealant (middle), cross section with penetration depth and fire sealant (right).

The manufactures of nail plate trusses with in Norway, has a nationally technical approval for this construction system.

To fulfil fire requirements in long-span constructions, connected timber trusses were tested in full scale in fire laboratory. The research is based on tests done by Roald and Aasheim (1991).

Fire sealant is not mentioned in Eurokode 5 (2014) Part 2 (fire design). However, narrow steel plate protection is given in the simplified rules, in chapter 6.2.1.3 Additional rules for connections with internal steel plates. It states that fire resistance of 60 minutes can be achieved with more than 60 mm gap depth. When the steel plate is protected by glued in strips, d_g, 60 minutes can be achieved with a glued in strip greater than 30 mm.

3 Materials and method

3.1 Samples for testing

For the fire tests, a total of 5 different test elements was tested. Table 1 shows the different test set up. Only one element per set up was tested. The main differences in test setups are type of fire protection of nail-plates and gap depth. Some test elements have nail plates have fire sealant around the edges and/or coated with fire-retardant, or are covered with plywood or fire insulation.

The configuration of the five test elements show the calculate fire resistance.

Table 2 present the type and placing of the nail plates used.

Table 1. Test element for fire test and type of protection for nail plates

Test element	Dimension [mm]	Number of trusses	Fire resistance*	Interface no.	Fire protection nail plates
1	198x198	4 pcs	R30	All	Non
2		5 pcs	R60	1	Fire retardant paint and fire sealant
				2	Fire sealant
				4	Fire-retardant paint and fire sealant
3.1	73x148	1 pcs	R30		Plywood
3.2		1 pcs	R30		Plywood
4	73x148	1 pcs	R15		Fire retardant paint** and plywood
5	73x198	1 pcs	R15		Fire retardant insulation

**Calculated fire resistance based on reduced cross section method in EN 1995-1-2.*

***One interface of fire retardant paint on one side and two interfaces on the other side.*

Table 2. Specification of the internal nail plates for each test element

Test element	Thickness nail plate [mm]	Width b_{st} [mm]	Interface no.	Gap depth d_g [mm]	Panel thickness h_p [mm]
1	1.5	<<timber member	1	37.5	-
			2	37.5	-
			3	12.0	-
2	1.5	145	1	55.0	-
		145	2	55.0	-
		145	3	55.0	-
		226	4	20.0	-
3.1	1.5	<<timber member		15.0	14.0
3.2	1.5	245		15.0	14.0
4	1.5	245		15.0	14.0
5	1.5	245		48.5	

3.1.1 Test element 1

Figure 3 shows the test set up for test element 1. Two different nail plate sizes were used. For interface 1 and interface 2 nail-plate 123 × 245 GN-T150S was used. while 174 × 226 GN-T150S was used in interface 3. Nail-plate for test element 1 had no fire sealant. The thickness of each truss was 48 mm.

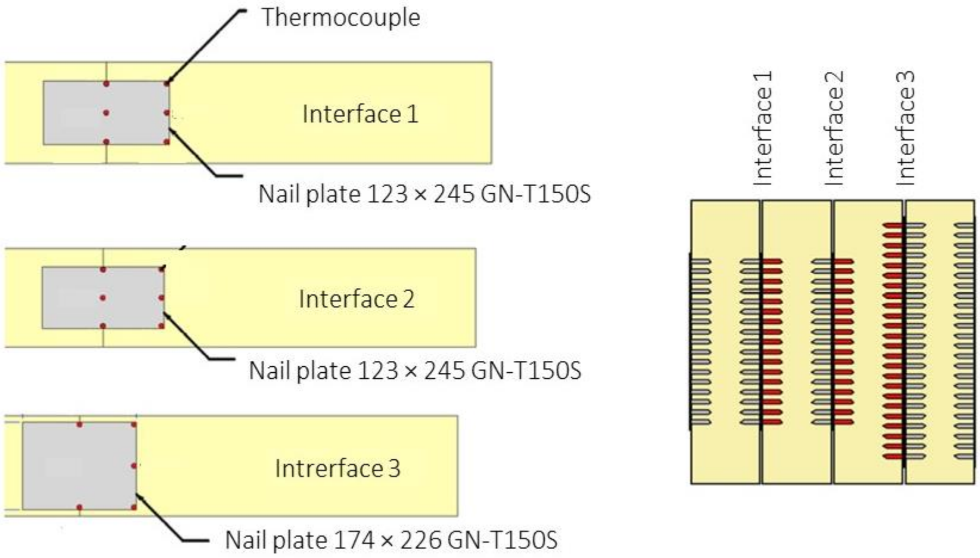

Figure 3. Test element 1. Four connected trusses. The red dots show the position of thermocouples installed in interface 1, 2 and 3 on the red nail plates (right Figure).

3.1.2 Test element 2

Figure 4 shows the teste set up of test element 2. Two different nail-plate sizes were used. For interface 1 and interface 2 nail-plate 145 ×205 GN-T150S was used. while 174 × 226 GN-T150S was used in interface 4.

The nail plates in interface 1 and 4 had fire-retardant paint and fire sealant around the edges of nail-plate.

The thickness of each truss was 48 mm.

3.1.3 Test element 3

Figure 5 shows the teste set up of test element 3 with a plywood plate for fire protection. The thickness of truss was 73 mm. Expected fire resistance of 15 minutes.

3.1.4 Test element 4

Figure 6 shows the teste set up of test element 4. The thickness of truss was 73 mm. Fire resistance with a plywood plate and fire retardant paint combined was tested.

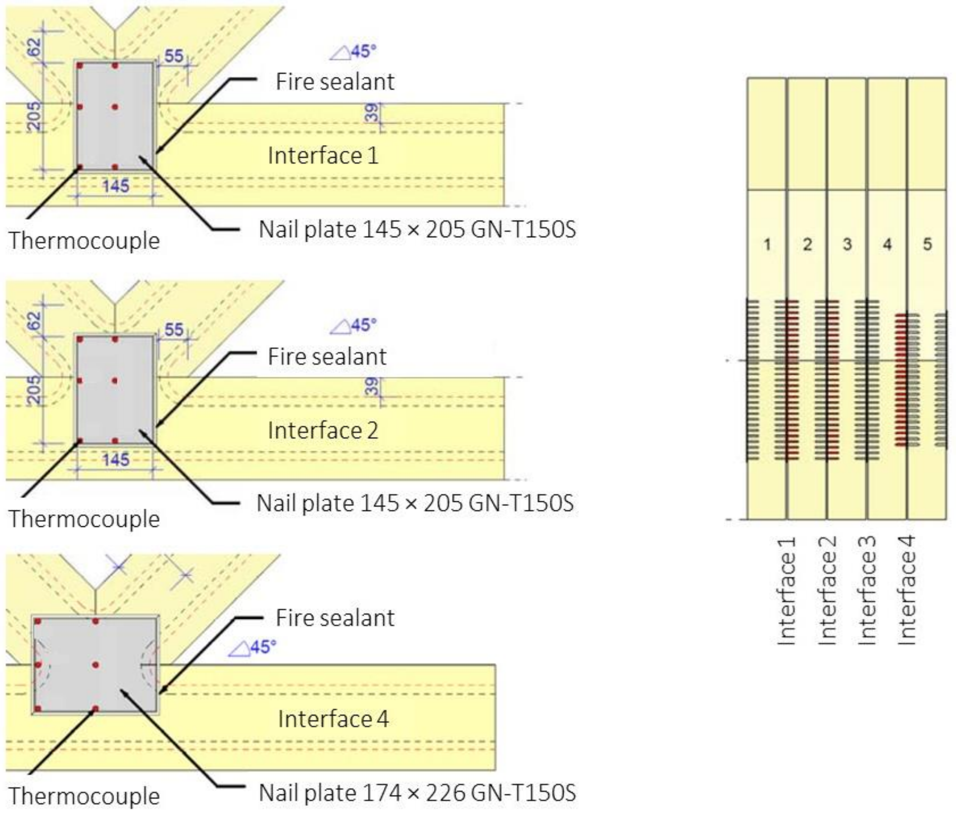

Figure 4. Test element 2. Five connected trusses. Thermocouples were installed in interface 1, 2 and 4 on the red nail plates.

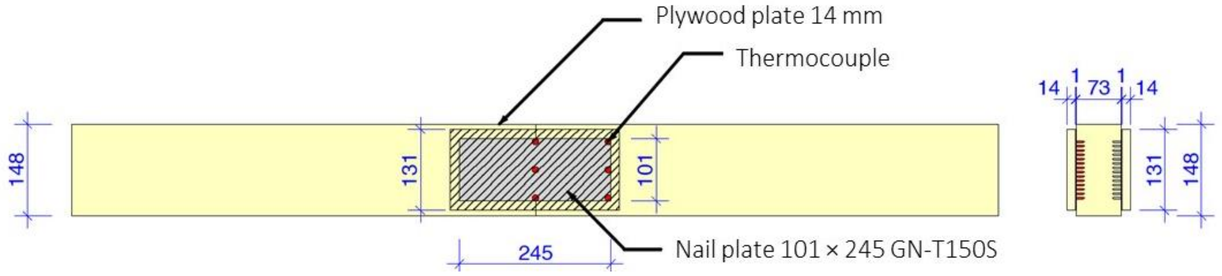

Figure 5. Test element 3 with one truss protected with 14 mm plywood. Thermocouples were installed between plywood and nail plate on one side on the red nail plate.

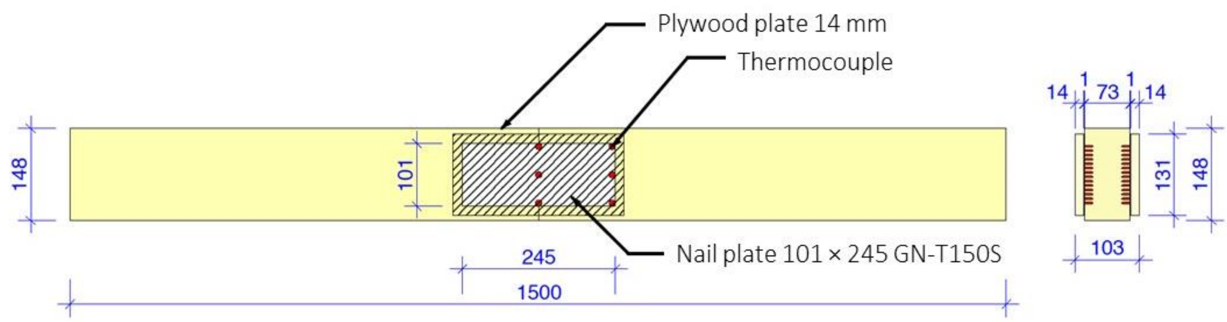

Figure 6. Test element 4 with one truss. Thermocouples installed between plywood and nail plate.

3.1.5 Test element 5

Figure 7 shows the teste set up of test element 5. The thickness of truss was 73 mm. In this test fire resistance with a fire retarding insulation is tested.

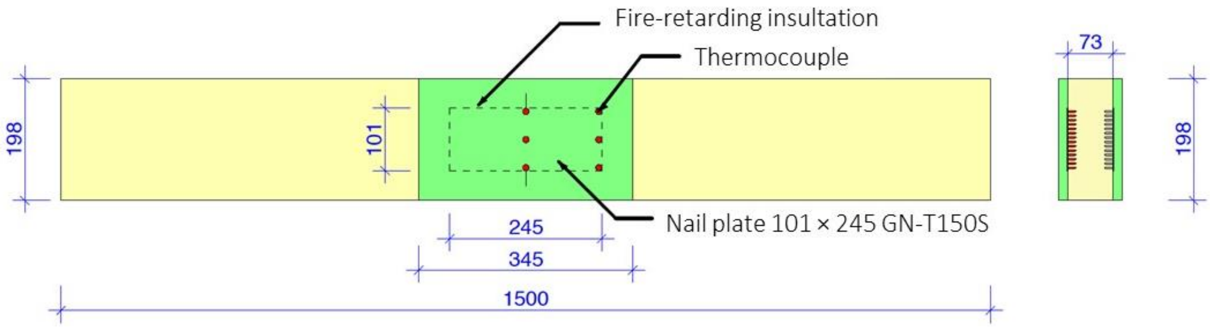

Figure 7. Test element 5 with one truss and fire insulation.

3.2 Moisture content

The moisture content was measured in the wood trusses before fire testing. Mean moisture content in all trusses was 11.7 %. Lowest moisture content was 9.0 % and highest was 15.5 %. Wood trusses had been stored indoors and moisture was as expected.

3.3 Fire-retardant paint and fire sealant

For nail plates treated with fire retardant the paint, the thickness was measured. The average paint thickness was measured to 0.23 mm. Minimum thickness was 0.19 mm and largest thickness was 0.31 mm. Primer (Epoxy Yacht HB) was added the nail-plates before fire retardant paint (Firetex FX2000. Leighs Paints). Fire sealant (Firesafe Acryl). was used around the nail plate edges. Figure 8 shows the fire-retardant paint and fire sealant.

3.4 Fire protection with plywood

Plywood with thickness of 14 mm was added as protection on external nail plates for test element 3 and 4.

3.5 Fire protection with insulation

Insulation plate (Isover FireProtect. Saint-Gobain Isover AB) with density 153 kg/m3 was used for test element 5.

3.6 Loads

The fire test was conducted without any loading of the test elements.

Figure 8. Nail plate painted with fire-retardant painting and fire sealant added around the nail plate edges.

3.7 Thermocouples

Thermocouples was installed between nail plates and wood, see Figure 9. In cross section of each test samples. interface marked with red colour has installed thermocouples. Six thermocouples are installed for each nail-plate and red dotes in figures for the test samples shown the exact position of thermocouples.

Temperature development for each thermocouple and average for each instrumented nail-plate were recorded.

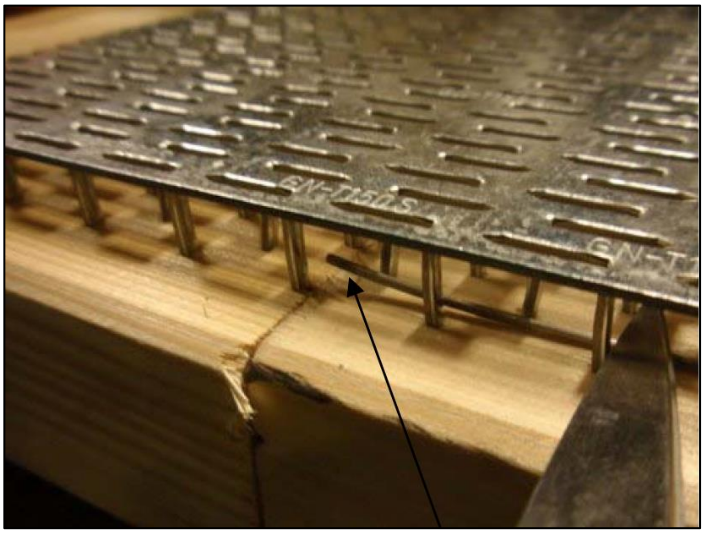

Figure 9. Picture shows installation of thermocouple before pressing the nail plate into wood.

4 Results and discussion

The fire test was conducted according to time and temperature curves given in NS-EN 1363-1. The size of the oven was B × D × H = 4060 × 3080 × 1500 [mm^3]. All tests were run simultaneous. The fire test lasted 110 minutes. Figure 10 shows the time – temperature curve of the oven.

Temperature increase is recorded for all thermocouples during testing. A 300°C threshold is set as a limitation for failure point of nail plates. For simplification, the average temperature values for each test element is given.

4.1 Test element 1

For the non-protected nail plates of element 1, the results given in Figure 11 show, as expected, the great impact the gap depth has a on the nail plate temperature increase. For interface 1 and 2 the gap depths were 37.5 mm compared to only 12.0 mm for interface 3. Interface 3 with gap depth 12.0 mm had a temperature above 300°C after 35 minutes. Interface 1 rise to above 300°C after 45 minutes due to a rapid increase in temperature caused by the slender truss (48 mm). Interface 2 (in the middle of cross section) rises above the 300°C threshold after about 65 minutes.

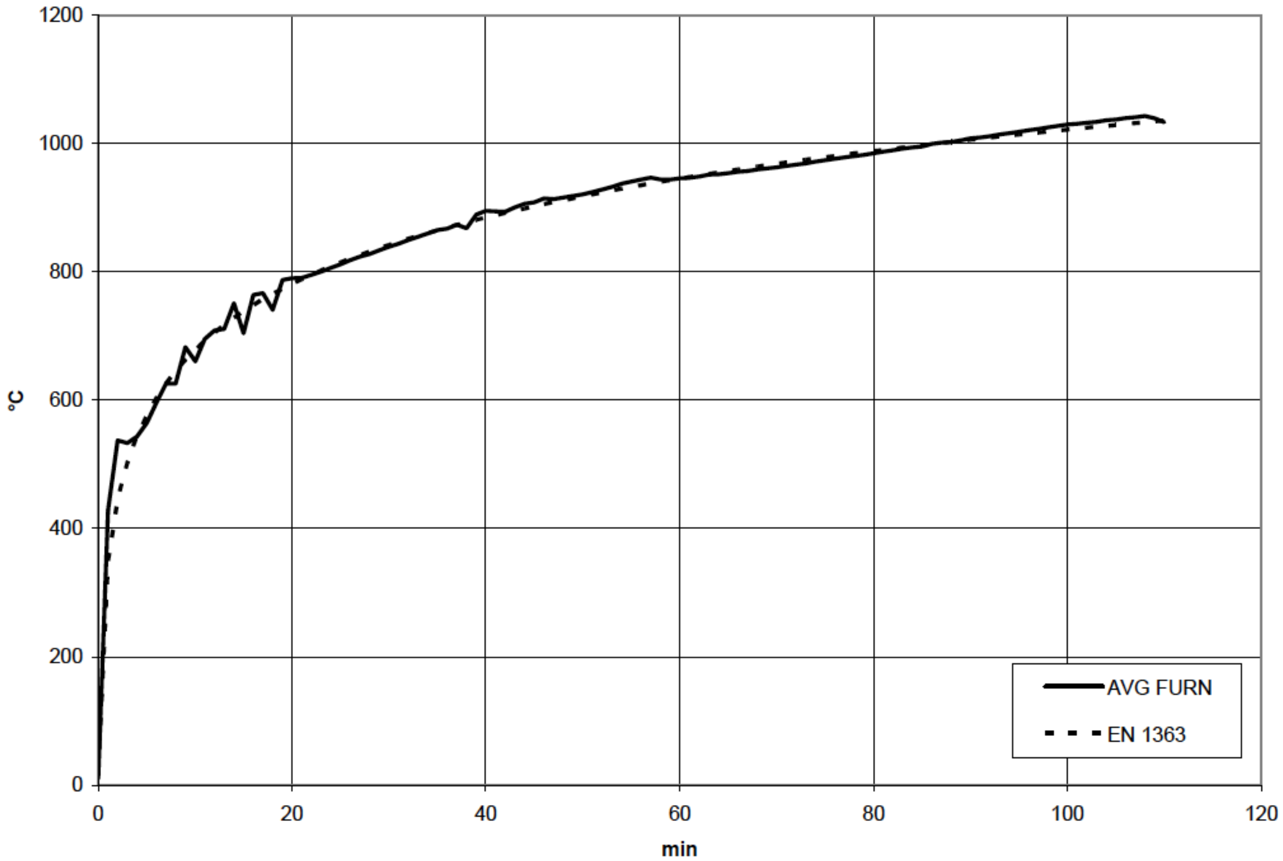

Figure 10. Average temperature in oven for test. The standard time/temperature curve given in EN 1363-1:2012 is also given.

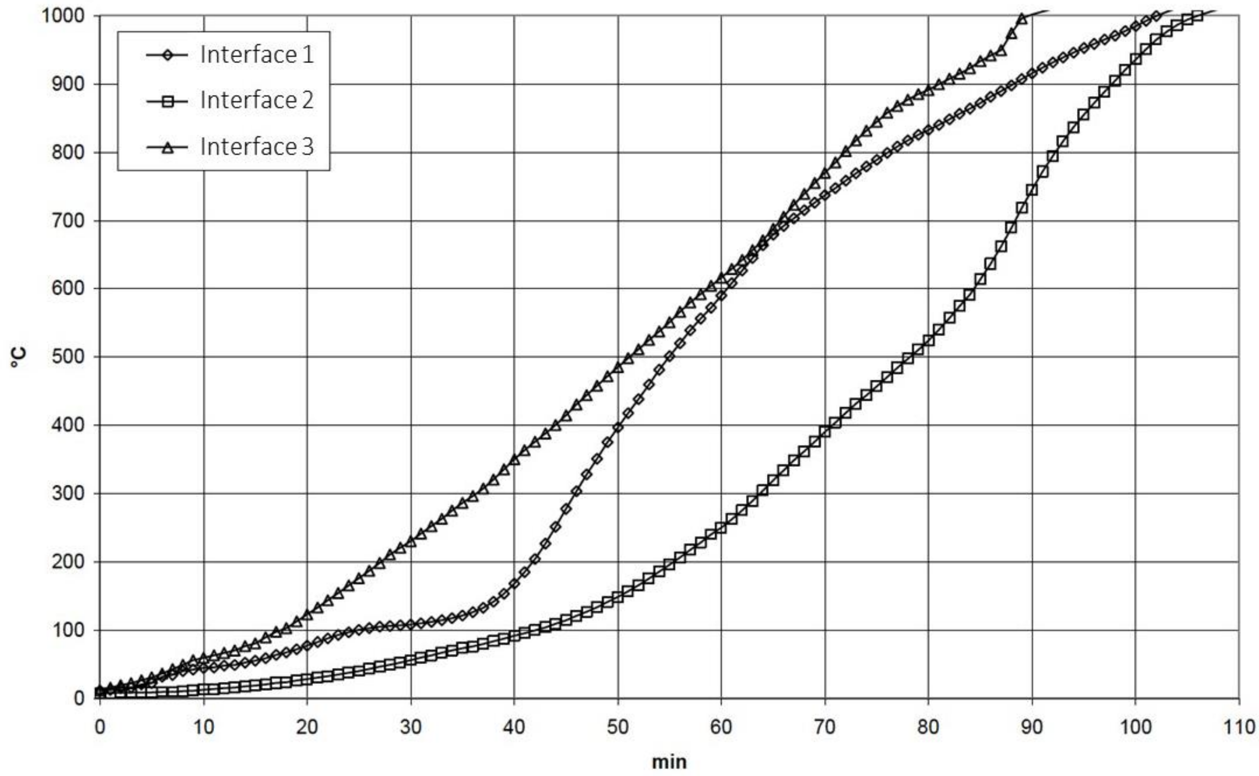

Figure 11. Average temperature increases in nail plates during testing for interface 1, 2 and 3 in element 1. Interface 2 is clearly better protected in the middle of test element 1.

4.2 Test element 2

Test element 2 has both fire-retardant paint and fire sealant, see the results in Figure 12. Interface 1 and interface 4 has both fire-retardant painting and fire sealant around the edges of the nail plates, and showed the same temperature increase during the fire test. The gap depth was different for these two interfaces. But this seemed to have small influence. From 35 to 60 minutes there was almost no temperature increase. The nail plate was totally covered by wood and fire sealant. At this time period, it is excepted that heat energy mainly goes to evaporating water before a temperature increase in nail plates can occur.

Both interface 1 and 4 met the 300°C thresholds after around 75 minutes.

Interface 2 was protected by more wood (increased thickness) and had no fire-retardant painting. It showed an increase in temperature after 95-100 minutes when water had evaporated in the wood. The threshold of 300°C was met just before the test finished at 110 minutes.

By comparing interface 2 without any protection of nail-plate and nail-plates with fire sealant around the edges, it was shown that fire sealant slows down the temperature increase in nail plate considerably.

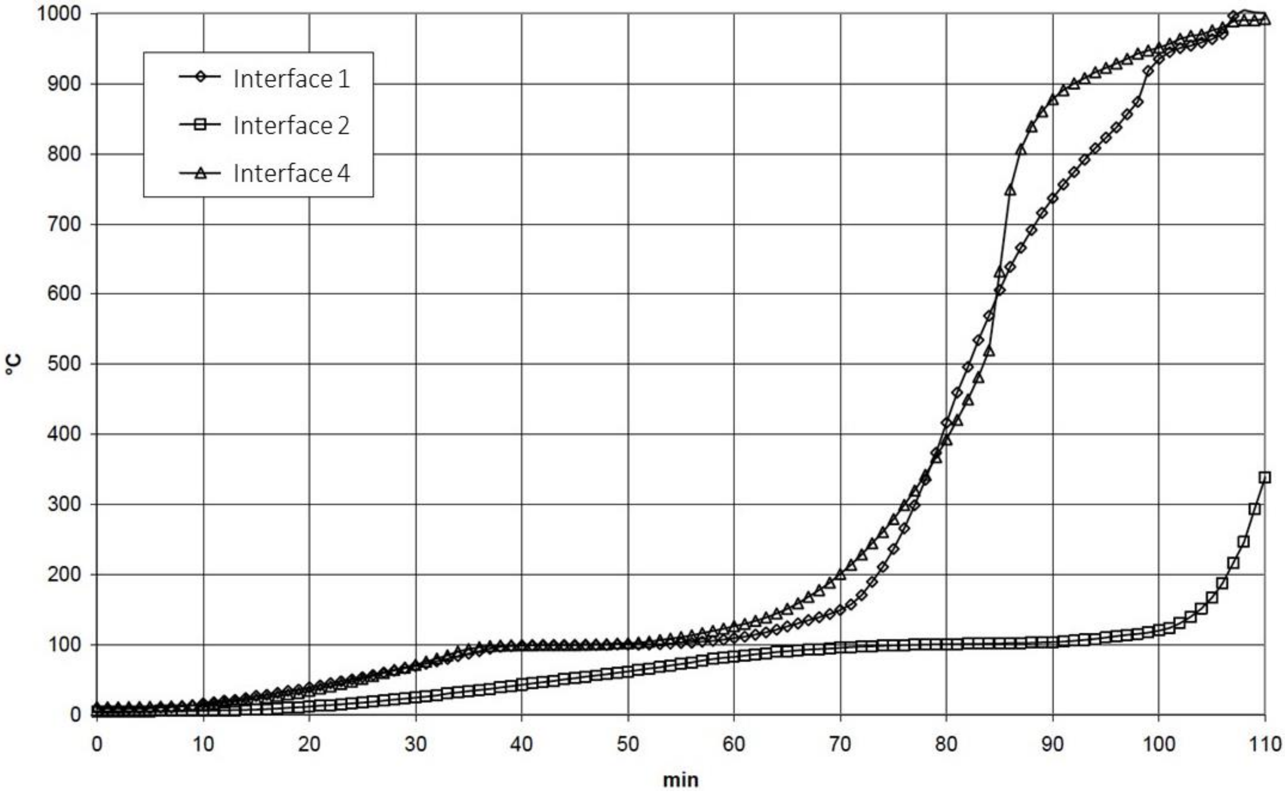

Figure 12. Average temperature increases in nail plates during testing for interface 1, 2 and 4 in test element 2.

4.3 Test element 3.1 and 3.2

Both test elements were protected by 14 mm plywood, see Figure 13. They showed quite the same behaviour, except an earlier increase in temperature for test element 3.1 after 15 minutes. Test element 3.1 rises above the 300°C thresholds after 18 minutes, while element 3.2 rises above threshold after 22 minutes.

4.4 Test element 4

Both nail plates were covered with 14 mm plywood and fire-retardant, see Figure 14. The nail plate with two layers of fire-retardant painting showed less increase in temperature after 20 minutes compared to the nail plate with only one layer of fire retardant painting. Both nail plates reach the 300°C threshold around 25 minutes.

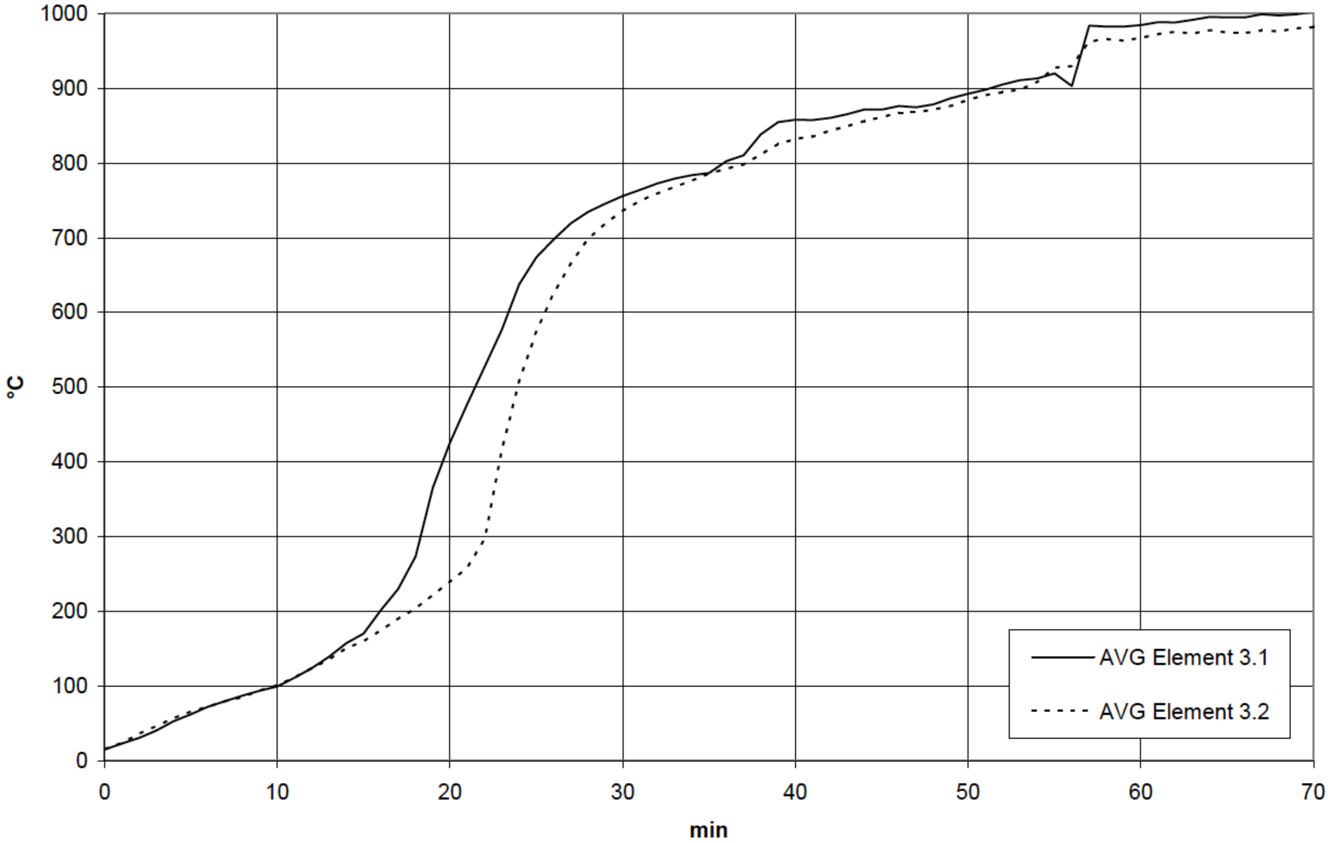

Figure 13. Average temperature increases in nail plates during testing for test element 3.1 and 3.2.

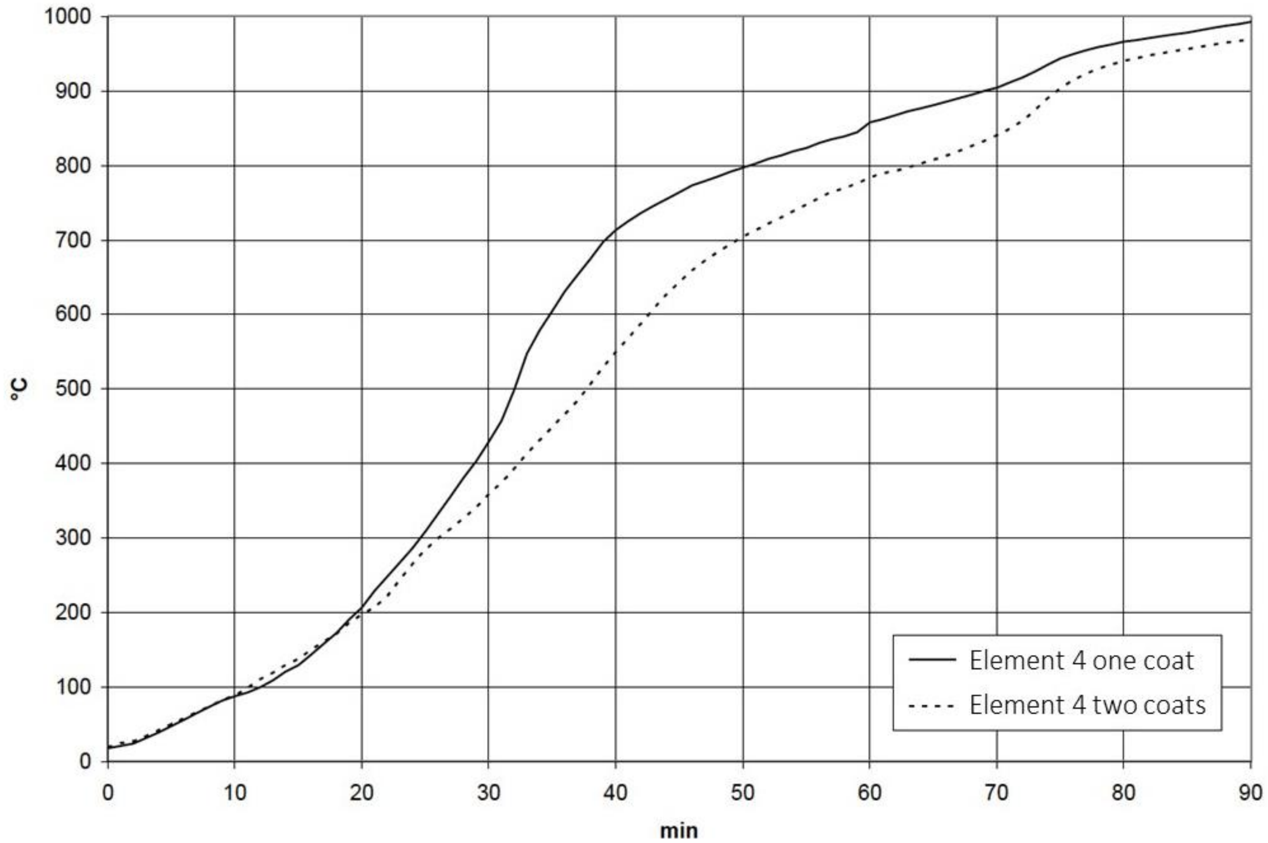

Figure 14. Average temperature increases in nail-plates during testing for test element 4 with one layer of fire-retardant painting on one side and two layer on the other side.

4.5 Test element 5

Test element with nail plates covered by fire retardant insulation met the 300°C threshold after 40 minutes, see Figure 15. The increase in temperature was almost constant to around 200°C. before an increase up to 300°C and further.

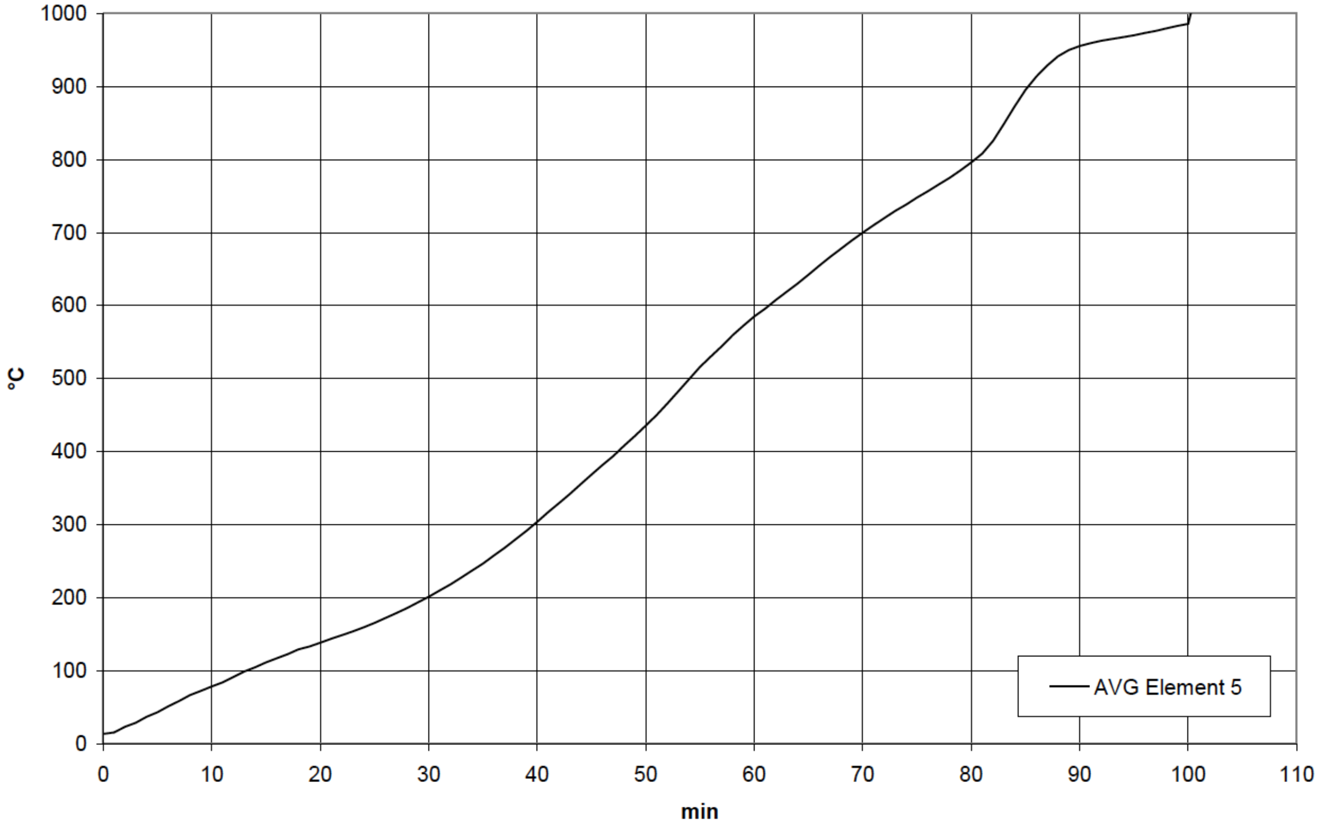

Figure 15. Average temperature increases in nail plates during testing for test element 5.

5 Conclusion

For larger and exposed truss construction with nail plate connections it is possible to achieve improved fire resistance by connecting two or more trusses compared to a single truss.

Testing shows fire behaviour with several nail plate timber trusses connected. The thickness of each truss and level of local protection of nail plates has a huge impact on fire resistance for the structure. Nail plates protected with fire sealant around the edges of the nail plate shows a huge impact in temperature increase compared to plates without protection. Fire sealant protects the joint on all sides and influence the needed gap depth in the joint to obtain a certain fire resistance. Use of fire sealant will make this system more cost efficient and slimmer cross sections can be archived. This alternative should be included in Eurokode 5 Part 2 in the future.

6 References

Eurocode 5 (2014): Design of timber structures - Part 1-2: General - Structural fire design. CEN. (EN 1995-1-2).

ETA (2015): European Technical Assessment ETA-15/0687. 11.11.2015 Fire sealant.

NS-EN 1363-1: 2012 Fire resistance tests. Part 1: General Requirements

Roald. B and Aasheim. E (1991): Fire testing of nail plate connected wood trusses. Timber engineering conference. London

TG 20079 (2017): Nail plate connections with fire resistance (in Norwegian). Technical approval. Sintef certification. Oslo. https://www.sintefcertification.no/no/product/index/2234/tg_20079.

TEK17 (2017): Regulations on technical requirements for building works (Technical Regulations, in Norwegian). Norwegian Building Authority. Oslo. https://dibk.no/byggereglene/byggteknisk-forskrift-tek17/

Sintef NBL (2010): Fire properties nail plate connections [In Norwegian]. Report 10301123-1. Trondheim. Norway

Discussion

The paper was presented by K Nore

H Blass asked if protection of the timber was needed. K Nore said it was not needed as the timber were screwed together and did not char in between.

A Buchanan received confirmation that fully threaded screws were used.

D Brandon commented about embedment failure versus steel failures at high temperature. He commented that it would be interesting to do some tests.

Protection by fire rated claddings in the Component Additive Method

Katrin Nele Mäger, Tallinn University of Technology

Alar Just, Tallinn University of Technology, RISE Fire Research

Andrea Frangi, ETH Zürich

Daniel Brandon, RISE Fire Research

Keywords: Fire rated cladding, component additive method

1 Introduction

The Component Additive Method has been developed to calculate the fire resistance of structures exposed to standard fire (ISO834), in order to assess the temperature rise on the unexposed side of timber frame assemblies against insulation criteria.

The Component Additive Method considers the insulation ability of the material layers present in the timber frame assemblies. The method is based on the contributions of each layer to the protection ability of the assembly considering different heat transfer paths. The average temperature rise behind the layer on the fire unexposed side of the assembly is limited to 140K and to 250K behind all the preceding layers. At the time these temperature criteria are reached, the layer is not considered anymore in the calculations.

Fire rated claddings can provide longer protection time compared to these limits. In the original version of the Component Additive Method (Schleifer, 2009) increased temperature limits are used behind the fire rated gypsum boards. For walls, the cladding is assumed to stay in place until 600°C behind the layer is reached. For ceilings the temperature limit is 400°C.

An increased fire protection compared to non-fire-rated claddings is taken into account by adding a correction time Δt to the protection time of the subsequent layer. The protection provided by the fire rated cladding depends on the duration the protective cladding is able to stay in place. As shown by Just (2010) there is no good correlation between the fall-off temperature and the actual fall-off time. The boards can stay in place for longer time after the temperature criteria assumed by Schleifer are reached. Therefore, the real behaviour of the claddings and assemblies is underestimated in most cases. In this study a new approach to determine the correction time Δt is proposed based on fall-off times of the gypsum boards.

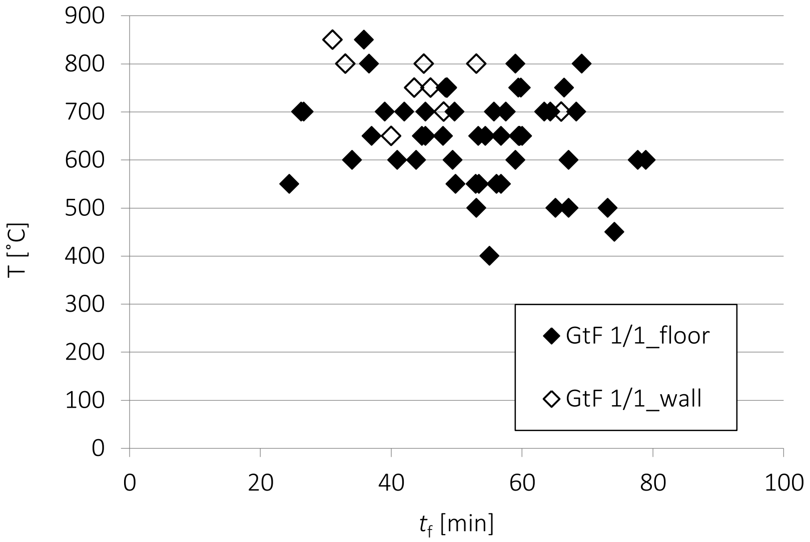

Figure 1. Fall-off temperatures behind gypsum plasterboards (Just, 2010)

Correction times are therefore important parameters for taking into account the effect of improved fire protection in the fire resistance calculations for insulation criterion. Fall-off times of the claddings can be determined by tests according to EN 13381-7 or by calculations. The fall-off time is depending on the fasteners (i.e. type, anchoring length, distances, etc.) or thermal degradation of the board.

2 Component additive method

The Component Additive Method is based on the contributions of each layer to the fire resistance of the whole assembly considering different heat transfer paths. This method is applicable to timber frame assemblies consisting of unlimited number of layers of inorganic claddings, wood-based materials, insulations and their combinations.

The fire resistance of the assembly to fulfil the insulation criterion is the time between the start of the fire exposure and the time when the temperature on the unexposed side of the structure reaches a temperature rise of 140 K on average over the whole surface or 180 K in a single point (EN 13501-2). Generally, the starting (ambient) temperature is 20°C, therefore the temperature criteria become 160°C and 200°C, respectively.

As the assembly usually consists of multiple layers that fulfil different functions, different names and symbols are used according to Figure 2. The layer on the fire unexposed side is a layer with insulating function. For this layer the insulation time is determined. All the other layers have a protecting function and the protection time is determined.

In analogy to the classification of fire protective claddings according to EN 13501-2, the protection time is the time until the temperature rise behind the considered layer is 250 K on average or 270 K at any point. Ambient conditions are usually 20°C, hence the temperature criteria become 270°C and 290°C, respectively. These criteria are approximations to account for the failure (or fall-off) of thermally degraded material layers. They are also close to the charring temperature of timber (300°C). Therefore, the sum of protection times of the layers preceding the timber elements may be used as a slightly conservative starting time of charring.

The insulation time of the last material layer is the time during which the temperature rise on the unexposed side is equal to 140 K on average over the whole area and 180 K at any point. The same temperature criteria are used for the fire resistance (insulation time) of the whole assembly.

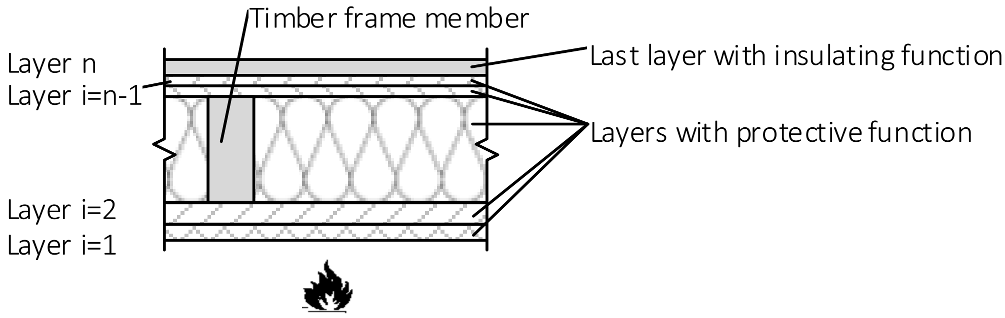

Figure 2 – Numbering and function of the layers in a timber frame structure

The time of fire resistance for insulation criterion of the whole assembly is calculated as shown in (1).

$$t_{ins}=\sum_{i=1}^{i=n-1} t_{prot,i} + t_{ins,n} \qquad (1)$$

where

t_{ins} is the total insulation time of the assembly [min];

$t_{prot,i}$ is the protection time of each layer in the direction of the heat flux [min];

$t_{ins,n}$ is the insulation time of the last layer of the assembly on the unexposed side [min].

The protection times of layers before the last layer can be calculated taking into account the basic values of the layers, the position coefficients and joint coefficients by equation (2).

$$t_{prot,i}=\left(t_{prot,0,i}\cdot k_{pos,exp,i}\cdot k_{pos,unexp,i}+\Delta t_i\right)\cdot k_{i,j} \qquad (2)$$

where

$t_{prot,i}$ is the protection time of the considered layer *i* [min];

$t_{prot,0,i}$ is the basic protection value of the considered layer *i* [min];

$k_{pos,exp,i}$ is the position coefficient that takes into account the influence of layers preceding the layer considered;

$k_{pos,unexp,i}$ is the position coefficient that takes into account the influence of layers backing the layer considered;

Δt_i is the correction time for considered layer *i* protected by fire rated cladding [min];

$k_{i,j}$ is the joint coefficient for layer *i*.

Insulation time of the last layer is calculated similarly to protection time, taking into account the basic values of the layers, the position coefficients and joint coefficients.

The coefficients and basic values are dependent on the material of the considered layer and the preceding and backing layers. Generic values of the basic protection times, basic insulation times and coefficients for gypsum boards, timber and mineral wool insulations are presented in the European technical guideline Fire Safety in Timber Buildings (2010) based on the work of Schleifer (2009).

3 Determination of improved correction times

In this study correction times for the Component Additive Method are determined for wooden and gypsum claddings, stone wool and glass wool insulations protected by fire rated gypsum boards.

The results presented in the following are based on extensive thermal simulations of different configurations of assemblies with wooden layers, gypsum plasterboards and gypsum fibreboards, stone wool and glass wool insulations. Generic effective thermal properties of the materials used in the simulations are taken from Fire Safety in Timber Buildings (2010). The equations are developed to fit the aforementioned simulation results. Finally, the equations have been verified with full-scale fire test results.

Thermal simulations of the assemblies are performed with constructions according to Figure 3.The FE software used in this study is SAFIR v2014a1 (Franssen, 2012). It is a software capable of solving the Fourier' heat transfer equation numerically.

In all the simulations, the maximum mesh size was 2 mm and maximum time steps used were 1 second. This is to ensure a proper accuracy of calculations and to achieve converging calculations while calculation times are kept reasonable. The model consisted of one connected row two-dimensional square elements. Convection and radiation boundary conditions were implemented at the element sides at the two ends of the row. For these boundary condition an emissivity of 0.8, a convection coefficient of 25 KW/m^2 at the exposed side and a convection coefficient of 9 kW/m^2 at the unexposed side, which are in accordance with EN 1991-1-2 (2002) and EN 1995-1-2 (2004). There was no heat flux going through the longitudinal sides of the row of elements. Each element had temperature dependent thermal properties which corresponded to the material of the layer it represents. After the times t_1

or t_f, of layer 1 were reached, the elements of layer 1 were removed from the model and the convective and radiative boundary condition was moved to the end of the second layer.

For the purpose of developing unified equations for correction times, an extensive system of configurations was simulated. The simulated configurations are shown in Tables 1 and 2 and illustrated in Figure 3.

Table 1. Backing materials used as layer 2 (see Figure 3)

Material and density	**Thickness [mm]**								
	10	20	30	40	50	95	145	200	295
Stone wool (26 kg/m^3)	v	v	v	v	v	v	v	v	v
Stone wool (100 kg/m^3)	v				v				
Glass wool (15 kg/m^3)	v	v	v	v	v	v	v	v	v
Massive timber panel (450 kg/m^3)	v	v	v	v	v				
Gypsum boards (850 kg/m^3)	v	v							

Table 2. Combinations of materials of layers 1 and 2 (see Figure 3)

Cladding material, thickness	**Backing layer**				
	Stone wool 26 kg/m^3	Stone wool 100 kg/m^3	Glass wool	Massive timber panel	Gypsum board
Gypsum plasterboard, Type F, 12,5 mm	v	v	v	v	v
Gypsum plasterboard, Type F, 15 mm	v		v	v	
Gypsum plasterboard, Type F, 25 mm	v	v	v	v	v

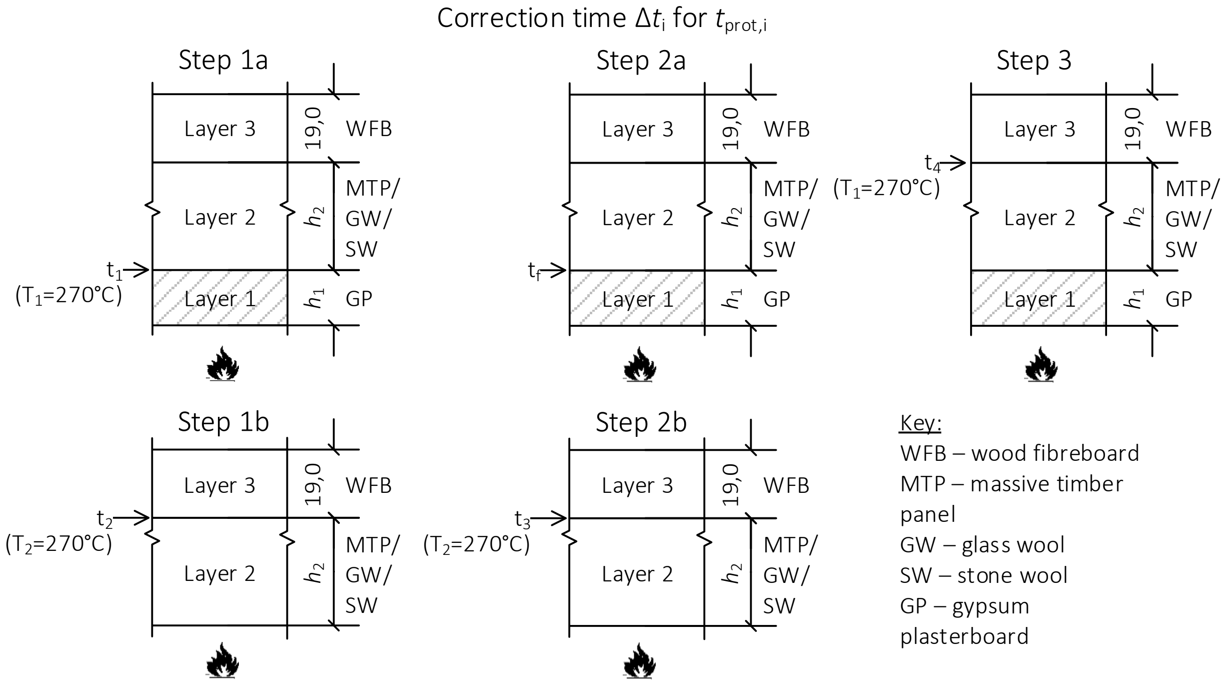

Figure 3 – Simulation set-ups

The thermal simulations are performed according to the following procedure:

Firstly, the simulation is conducted until the temperature behind the protective board reaches 270°C (step 1a). This time is recorded as t_1. The board is removed and the simulation continued until the temperature behind the next layer reaches 270°C (step 1b). This time is recorded as t_2.

Secondly, the initial configuration is simulated until the specified fall-off time is reached (step 2a). This time is recorded as t_f and can be chosen arbitrarily or based on existing knowledge. In this study, the fall-off times of gypsum plasterboards were calculated based on the equations presented in Fire Safety in Timber Buildings (2010). The simulation is continued without the protective board until the temperature behind the next layer reaches 270°C (step 2b). This time is recorded as t_3.

The correction time can be defined as the difference between t_2 and t_3. Therefore, according to the simulations the correction time is calculated as

$$\Delta t_{sim} = t_3 - t_2 \qquad (3)$$

Thirdly, the simulation configuration shown as step 3 was simulated with the protective board until the temperature reached 270°C behind the next layer. This time is recorded as t_4. The difference between the times when 270°C was reached behind the protective board and the next layer represents the maximum protection time for the considered layer

$$t_{prot,max,sim} = t_4 - t_1 \qquad (4)$$

The upper limit for the correction time is therefore

$$\Delta t_{max,sim} = t_4 - t_2 \qquad (5)$$

Thus, based on the evaluation of the thermal simulations, the limits for the correction times are defined as it follows (see Figure 4):

- When the fall-off time of the cladding $t_{f,p}$ is smaller than or equal to the protection time of the cladding $t_{prot,p}$, then no correction time is applied.

  $t_{f,p} \leq t_{prot,p}$, $\Delta t_i = 0$

- When the fall-off time of the cladding $t_{f,p}$ is larger than the sum of protection time of the cladding and maximum possible protection time of the layer *i*, then the maximum correction time for layer *i* is applied.

  $t_{f,p} \geq t_{prot,p} + t_{prot,max,i}$, $\Delta t_i = \Delta t_{max,i}$

where layer *i* is the layer protected by cladding layer *p*.

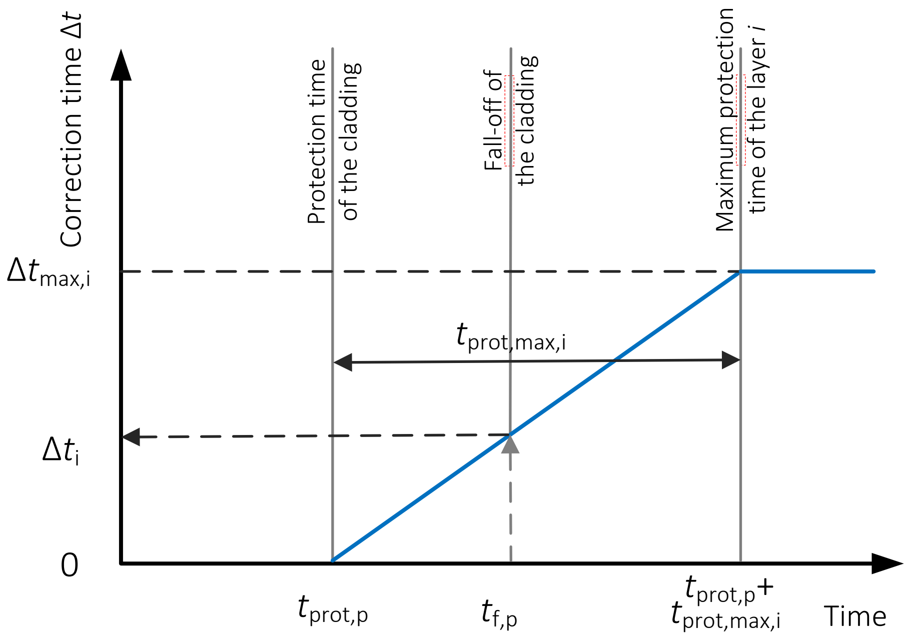

Figure 4 – Limits of the correction time

Based on the results of the thermal simulations, the following relationships between correction times and fall-off times considering the maximum protection times are determined.

If $t_{prot,p} \leq t_{f,p} \leq t_{prot,max,i} + t_{prot,p}$

$$\Delta t_i = \frac{\left(t_{f,p} - t_{prot,p}\right) \cdot \Delta t_{max,i}}{t_{prot,max,i}} \qquad (6)$$

If $t_{f,p} \geq t_{prot,max,i} + t_{prot,p}$

$$\Delta t_i = \Delta t_{max,i} \qquad (7)$$

where

$t_{f,p}$ is the fall-off time of the cladding (system).

The protection time of the considered layer without correction time is expressed as

$$t_{p,i} = t_{prot,0,i} \cdot k_{pos,exp,i} \cdot k_{pos,unexp,i} \quad (8)$$

In agreement with equation (5) the maximum correction time that can be considered is expressed as

$$\Delta t_{max,i} = t_{prot,max,i} - t_{p,i} \quad (9)$$

where the maximum possible protection time of the considered layer is taken as

$$t_{prot,max,i} = \frac{t_{prot,0,i}}{k_2} \quad (10)$$

where k_2 is protection coefficient.

For gypsum plasterboards the coefficient is taken according to Eq (C.3) from EN 1995-1-2 (2004):

$$k_2 = 1,05 - 0,0073 \cdot h_p \quad (11)$$

where h_p is thickness of gypsum plasterboard(s) in millimetres.

For other fire rated claddings the coefficient k_2 could be determined with fire test according to EN 13381-7.

Correction time Δt can be applied for the next layer after the fire rated cladding system which can consist of single or multiple layers.

The comparison between the results of calculations with the proposed equations and thermal simulations of assemblies with stone wool, glass wool, gypsum and wooden layers covered by gypsum claddings are shown in Figures 5, 6 and 7. To illustrate the pure effect of correction time, the protection times t_{prot} of the claddings, time t_1 from simulations has been used in the calculations with the proposed design equations shown in Figures 5, 6 and 7. Other coefficients and basic values were taken from *Fire Safety in Timber Buildings*.

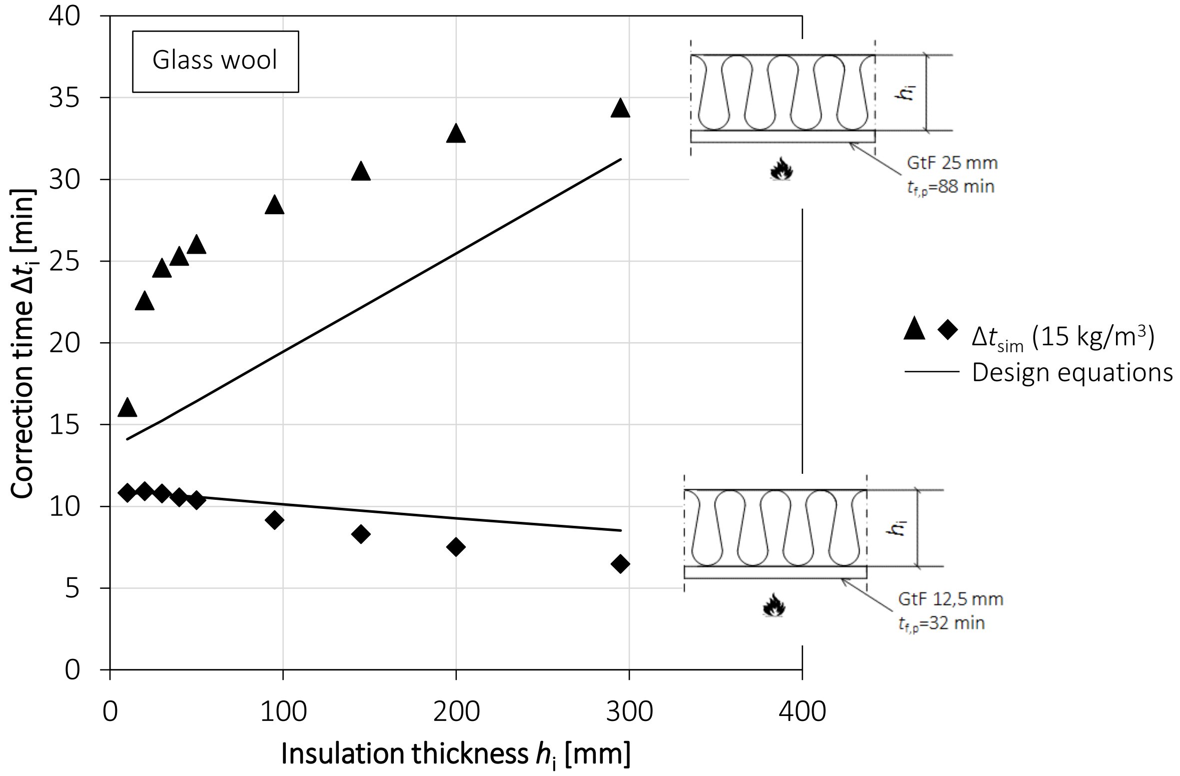

Figure 5 – Correction time for glass wool insulation related to insulation thickness. Comparison between thermal simulations and derived equations.

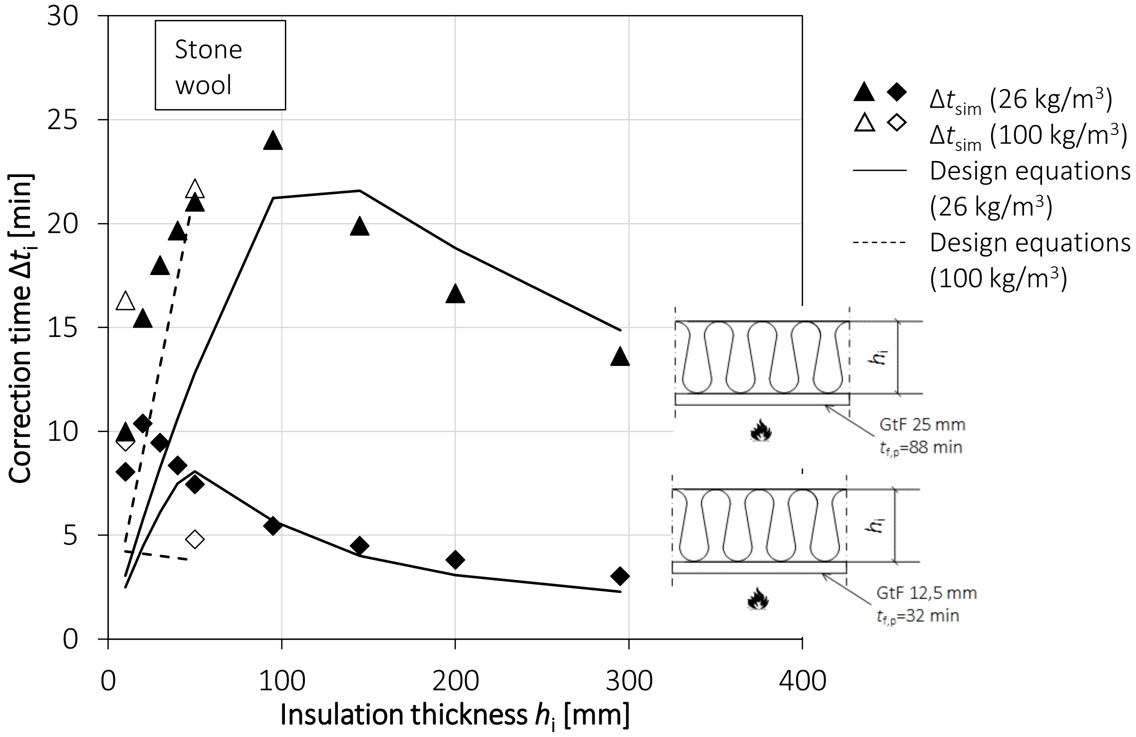

Figure 6 – Correction time for stone wool insulation related to insulation thickness. Comparison between thermal simulations and derived equations.

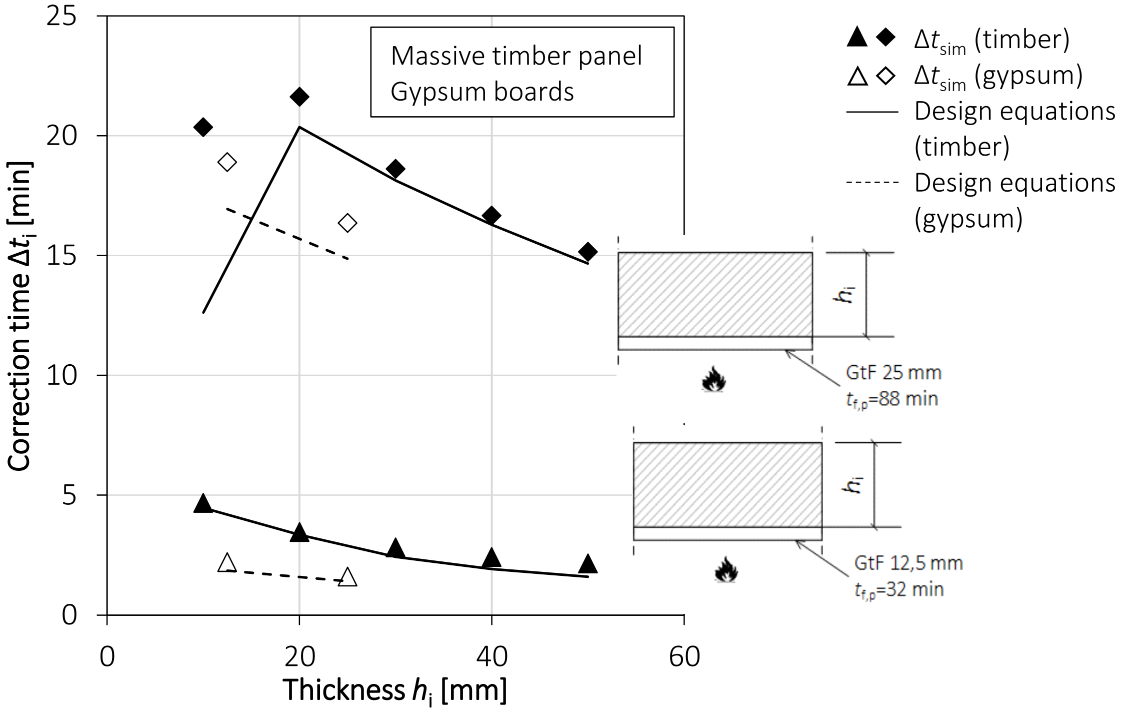

Figure 7 – Correction time for gypsum and wood based claddings related to substrate thickness. Comparison between thermal simulations and derived equations.

The equations proposed in this paper show good correlation with the simulation results.

The same procedure as shown in this study may be followed to derive the necessary equations for other fire rated claddings and substrates.

4 Comparison to fire tests

Selected full scale test results from the database (SP Report 2010:28) have been compared with calculations according to the Component Additive Method using the improved correction times. Comparison of calculated results with test results are shown in Figure 8.

The calculated fire resistance of tested structures using the improved correction times are on the safe side with one exception.

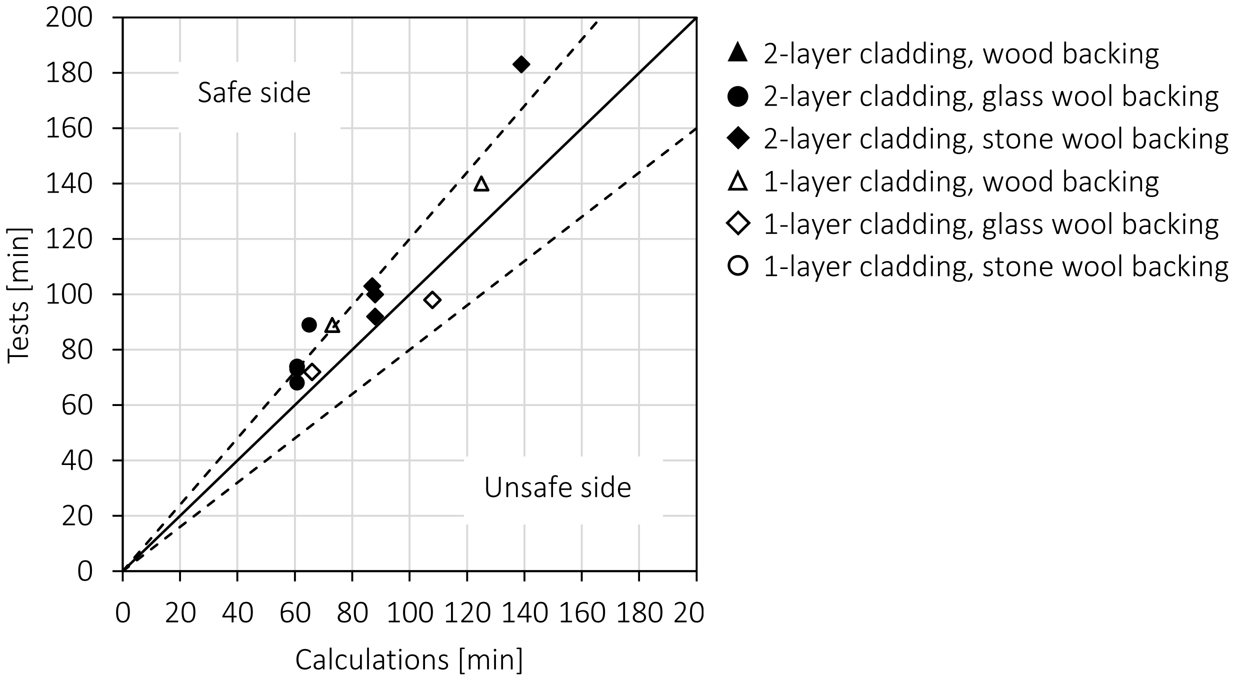

Figure 8 – Comparison of insulation criteria of the assemblies determined by full scale tests and by the component additive method with the improved correction times.

5 Impact

The improved Component Additive Method will be included into the revised EN 1995-1-2. This study allows a more accurate consideration of fire rated claddings in the Component Additive Method. By considering the fall-off times in the calculation of the separating function, there is less calculations for the designer and strong links with existing calculation methods for the design of load-bearing capacity in the fire scenario.

6 Acknowledgements

The authors wish to express their deep gratitude to Karl Õiger Foundation for supporting this study. This research was also supported by the Estonian Research Council grant PUT 794. The authors acknowledge the network of COST Action FP1404 WG2 for the contribution.

7 References

Schleifer, V (2009) Zum Verhalten von raumabschliessenden mehrschichtigen Holzbauteilen im Brandfall. Zürich, Switzerland.

EN 1995-1-2:2004. Eurocode 5: Design of timber structures - Part 1-2: General - Structural fire design. CEN, Brussels.

Mäger, K. N. (2016). Implementation of new materials to the component additive method for fire design of timber structures. Master's thesis at Tallinn University of Technology, Tallinn, Estonia.

B. Östman et al. (2010). Fire safety in timber buildings. Technical guideline for Europe, Stockholm, Sweden: SP Technical Research Institute of Sweden, 2010.

EN 13501-2:2016. Fire classification of construction products and building elements. Classification using data from fire resistance tests, excluding ventilation services. CEN, Brussels.

Just, A (2010). Structural Fire Design of Timber Frame Assemblies Insulated by Glass Wool and Covered by Gypsum Plasterboards. PhD thesis. Tallinn University of Technology. Tallinn, Estonia.

Just, A, Schmid, J, König, J, Gypsum plasterboards used as fire protection – Analysis of a database. In preparation. SP Report 2010:28, Stockholm, 2010.

ISO 834–1:1999: Fire Resistance Tests – Elements of Building Construction – Part 1: General Requirements., 1999.

Franssen, J. M. (2012). User's manual for SAFIR 2013b2. Liège, Belgium

EN 1991-1-2:2004. Eurocode 1: Actions on structures - Part 1-2: General actions - Actions on structures exposed to fire. CEN, Brussels.

Discussion

The paper was presented by K N Mäger

A Buchanan commented that this study tried to make something complicated simpler for designers. He asked if it would be possible to use this type of method for structural components. In NZ different manufacturers would have their own data and would not rely on same method. K N Mäger responded that different factors and parameters would be needed. He also responded that in Europe manufacturers might not be happy with the current conservative method; hence, this study was needed.

M Gershfeld also commented on approaches in US.

Reliability of large glulam members Part 2: Data for the assessment of partial safety factors for the tensile strength

Matthias Frese, Sebastian Egner, Hans Joachim Blaß
Karlsruher Institut für Technologie, Holzbau und Baukonstruktionen

Keywords: size effect, *k*-factor, strength modification

1 Introduction and concept

Eurocode 5 allows considering the influence of the member volume on the glulam tensile strength. It is explicitly possible to raise the tensile strength for tension members with a depth (*d*) smaller than 0.6 m. The depth *d* results from the sum of the single lamination thicknesses of a tension member. This raise for the tensile strength is limited to 10 % of the reference value, which ideally results from tension tests on glulam members with reference size 0.6 m in depth and 5.4 m in free length (ℓ) according to the provisions in EN 14080 and EN 408, respectively.

Until now, no Eurocode 5 provisions exist how to modify the tensile strength of members longer than 5.4 m. Among others, the reason is that at least experimental strength data of very long tension members are not available. It was therefore not possible to derive purposeful strength modifications. Consequently, the partial safety factor γ_M has to compensate effects arising from those member lengths which are longer than 5.4 m. As a practical example, the roof structure of the Aquatic Centre Surrey (Fast and Ratzlaff 2017) shows the relevance to look into the subject of a strength modification for very long glulam members. The catenary roof structure consists of suspended glulam tension members, acting as “timber cables”, with a free length of up to 55 m and a member depth of 0.27 m.

In agreement with the Eurocode 5 concept using various *k*-factors, the authors have already proposed an exponent for the modification of the tensile strength applicable to members up to 60 m in length. The corresponding k_ℓ-factor is given by Eq. (1), Frese and Blaß 2010.

$$k_\ell = (5.4/\ell)^{1/10.8} \qquad \ell \text{ in m and } 0.15\text{ m} \le \ell \le 60\text{ m} \tag{1}$$

However, this modification proposal initially results from an adaption to the length-depending 5th percentiles of tensile strength distributions. The corresponding strength values were obtained by simulated tension tests on glulam members. In doing so, only a single strength level was examined. Due to the adaption to the 5th percentiles and the examination of a single strength level, restrictions arise and k_ℓ from Eq. (1) does, therefore, not necessarily yield balanced reliability between short and long glulam members. Consequently, there remained a lack of knowledge.

Compared to the data basis for Eq. (1), this paper enables an insight into new tensile strength data for glulam members. Using efficient scientific computing, these new data were also obtained from simulations. The basis are 375 thousand realisations of simulated tension tests in order to create data as accurately as possible. With that, it was intended to reduce statistical uncertainties arising generally from the amount of data (Thoft-Christensen and Baker 1982, P. 7). The tension tests reproduce the test procedure in EN 408. The data contain strength values in a range between short members (ℓ = 0.15 m) and long members (ℓ = 108 m). With the new simulations, two different strength levels and classes, respectively, were examined to consider also the influence arising from a variation of the material quality.

The work aims at showing that a newly determined k_ℓ-factor given with Eq. (2) actually enhances the tensile strength modification regarding the member reliability which should be independent of its length. This will be confirmed by simplified reliability analyses with subsequent determination of the reliability index β.

$$k_\ell = (5.4/\ell)^{1/13} \qquad \ell \text{ in m and } 1.5\text{ m} \le \ell \le 108\text{ m} \tag{2}$$

A benefit of the work is that the strength data will be made available. Reliability experts are asked to use the new data for the reassessment or determination of the level of partial safety factors or modification factors in particular for long glulam members. With that, they may establish a more consistent reliability between short and long members. The authors will provide the original data sets on demand[1] so that interested experts can themselves make interpretations or fit theoretical probability distributions. Data sets are available as single txt files for all possible combinations between five member depths and fifteen lengths. Each depth-length combination contains 2500 modelled tensile strength values, evaluated for both strength levels.

This paper is the second part of a two-part contribution. The first part published last year (Frese and Blaß 2016) reported on new bending strength data of small and large glulam members.

---

[1] Experts are asked to express their interest by sending an email to matthias.frese@kit.edu

2 Methods

2.1 Computational model

The computational strength examinations were conducted with the Karlsruhe Rechenmodell in its latest amended version. The main features of this computer model are described in the following. For further model features, see Frese and Blaß 2016 and Frese 2016. The Karlsruhe Rechenmodell is a validated finite element based computer model using the structural analysis system ANSYS and its corresponding processors. The integrated design language was employed to control the general programme flow and to build the model with realistic mechanical properties of glulam. A visual or mechanical grading process is computationally reproduced prior to the Monte Carlo analyses to obtain the two examined strength levels and material qualities, respectively (see section 2.2). Fig. 1 shows the basic model to simulate a tension test. The member size of the modelled specimen depends on the numbers of elements *n* (150 mm in length, 30 mm in depth and arbitrary lamination width inside of limits with practical relevance) along the total length and depth. After being empirically represented by regression equations, stochastically distributed and auto-correlated mechanical properties are assigned discretely and systematically to the elements of the model. Physical uncertainties, as defined in Thoft-Christensen and Baker 1982, P. 6, are covered by considering the residual scatter in the regression equations used. In doing so, the natural occurrence of knots and glulam specific characteristics as finger joints are taken into account with regard to the local mechanical properties. This enables the computation of local tensile stresses ($\sigma_{t,i}$), which are quantitatively different, and finally of realistic statistical distributions describing load-carrying capacities for the computationally tested members.

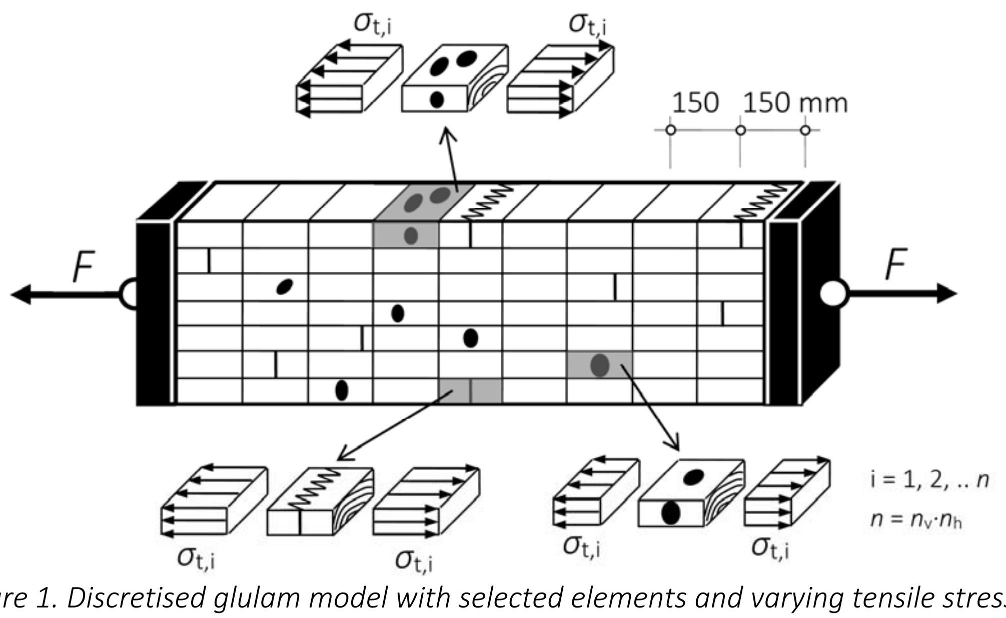

Figure 1. Discretised glulam model with selected elements and varying tensile stresses.

2.2 Computationally examined strength levels and member sizes

The computational test programme covers two strength levels reflecting the target strength classes GL23h and GL33h. Table 1 shows the 5th percentiles for corresponding bending and tension tests. These percentiles were determined from sample sizes with 2500 modelled values. The differences between the nominal strength values (e. g. 23) and modelled values (e. g. 23.1) are due to the stochastic nature of the simulation process. The 5th percentiles for tension enclose a range of 10 N/mm². The ratio between the 5th percentiles belonging to tension and bending amounts to 20.2/23.1 = 0.87 and 29.9/33.2 = 0.90, respectively. The grading method indicates whether a visual or mechanical grading procedure is computationally reproduced.

Table 1. Target strength class, grading method, bending and tensile strength.

Target strength class	Computationally modelled grading method	reference strength in N/mm² bending	tension	COV %
GL23h	visual	23.1	-	15.5
		-	20.2	11.1
GL33h	mechanical	33.2	-	14.1
		-	29.9	9.57

The computational test programme encompasses a large range of examined member sizes. Fig. 2 exemplifies the key sizes: the shortest of 150 mm (left), the longest of 108,000 mm (right), the narrowest of 120 mm (above) and the deepest of 600 mm (below). The depth was varied by changing the number of laminations (n_v) in equal steps of four laminations resulting in five member depths; the length was varied by changing the number of elements in longitudinal direction (n_h) in unequal steps resulting in fifteen different member lengths.

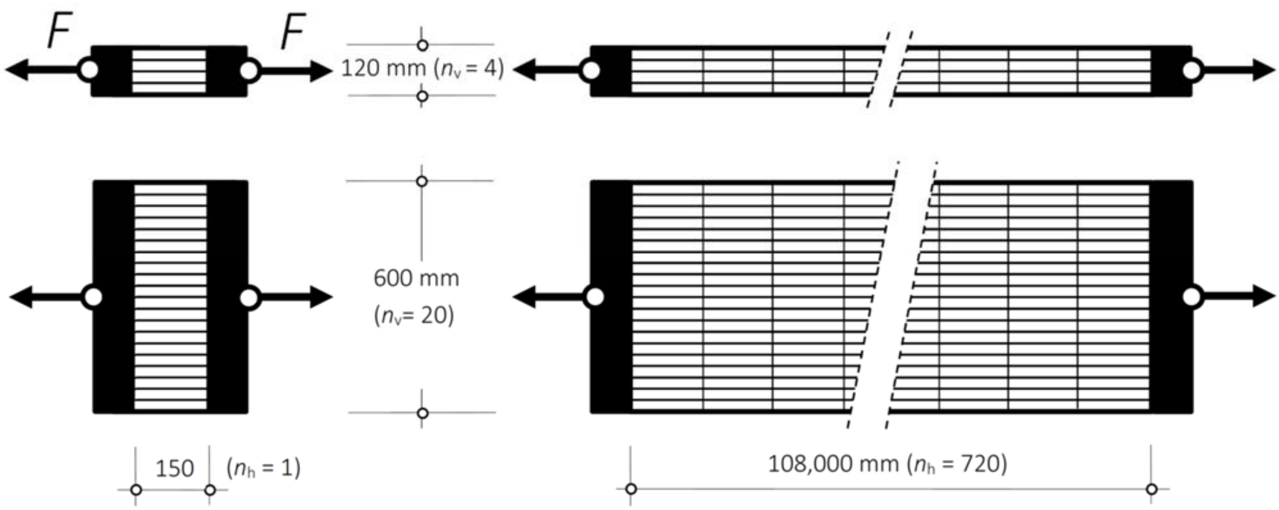

Figure 2. Modelled tension members: key sizes

3 Results

3.1 Representation of the strength data

The results of the computationally examined target strength classes are presented in annexes A and B. In order to impart the strength data as clearly and simply as possible, the two data annexes are uniformly arranged.

An annexe begins with histograms and appertaining probability plots in the same line (Fig. 4 and 6, respectively). The boxes in the histograms contain the minimum value (MIN), the 5th percentile (5th P.), the mean value (Mean) and the standard deviation (SD) of the computationally obtained tensile strength values. The first five lines in each Figure refer to the depth of 0.24 m and the next five to 0.60 m. The diagram pairs represent data for the key lengths 2.7, 5.4, 27, 54 and 108 m. With that, the data selection has practical relevance. Each histogram contains a fitted three-parameter Weibull density also represented as a cumulative frequency distribution in the appertaining probability plot. The shape parameter C is quoted below the probability plots. In these plots, the Weibull distributions are compared with the 2500 computationally obtained tensile strength values (f_t).

The following Tables 2 and 3, respectively, provide the full set of the parameters for the fitted Weibull distributions, also for the in-between lengths 1.35 and 16.2 m and the five examined depths. In the two last columns in the Tables, the mean values and standard deviations belonging to the Weibull fit are specified.

The two diagrams on top of each other in Fig. 5 and 7, respectively, impart an overview of percentiles and their dependence on the member length. For each class, the member depths of 0.24 and 0.60 m are presented. The courses were evaluated from 0.15 to 108 m. The horizontal axis is logarithmically scaled. The vertical broken lines point out the same member lengths of 1.35, 2.7, 5.4, 16.2, 27, 54 and 108 m as in the Tables 2 and 3. The purple lines mark the reference strength ($f_{t,k}$), calculated as mean value based on the 5th percentiles for the depths 0.24, 0.36, 0.48 and 0.60 m. The red ones represent the calculated design strength using the partial safety factor γ_M = 1.3 and a modification factor k_{mod} = 1. The blue and green curves are explained in the following.

3.2 Data analysis and discussion

With a length of 2.7 m, the frequency distributions and the Weibull densities in the histograms, respectively, are more or less symmetrical; with a length of 27 m, they finally show a negative skewness. The parameter estimation for the Weibull distributions follows an automatic procedure available in SAS 9.4. In all cases, this procedure provides a purposeful set containing threshold, scale and shape parameter C, respectively. The comparisons between the cumulative frequency distributions of the computationally obtained tensile strength data and the linearised Weibull fit prove – even representative for depth-length combinations of which comparisons are not shown here – that the fitted Weibull distributions suitably capture the empirically represented strength values. The tabulated mean values and standard deviations belonging to the theoretical

Weibull distributions (Table 2 and 3) show only marginal differences with the means and standard deviations given in the boxes of the corresponding histograms (Fig. 4 and 6). Therefore, the fitted Weibull distributions at least represent the mean and standard deviation of the original computational data. For a given length, there is no pronounced influence of the examined depth on the strength.

The diagrams with the percentile courses (Fig. 5 and 7) show independently of the strength classes and the two examined depths that minimum values and percentiles decrease with increasing member length. This general trend becomes evident by comparing the decreasing percentile courses with the characteristic tensile strength (purple line) and the design value (red line). As an example, minimum values and first percentiles fall below the design strength at a certain length if the design strength is supposed to be constant. Hence, the four diagrams visualise that an unbalanced reliability may exist, if no modification is applied in the calculation of the design strength. The blue curves reflect a length-depending strength value, which results from the modification of the corresponding characteristic tensile strength with the proposed k_ℓ-factor in Eq. (2). These curves seem to ensure balanced reliability along the member length because of its affinity with the percentile courses. The green curves finally represent a length-depending design strength using $\gamma_M = 1.3$.

3.3 Reliability analyses

Reliability analyses, performed for this contribution, aim at showing that modifying the resistance (R) with the proposed length-depending k_ℓ-factor (Eq. 2) actually results in a more or less balanced reliability along the examined member length. In total, four different configurations for the reliability analyses are examined. In doing so, the limit state function g (Eq. 3) is evaluated based on billions of Monte Carlo simulations (cf. Spaethe 1992, P. 131-136) resulting in corresponding failure probabilities (P_f) and reliability indices (β) as defined in Eurocode "0". Model uncertainties, as defined in Thoft-Christensen and Baker 1982, P. 7, were not taken into account in the analyses.

$$g = \frac{1}{k_\ell} \cdot R - E \rightarrow P_f = \text{Probability } (g < 0) \tag{3}$$

The numerical procedure was validated using analytically examined case studies published in Loebjinski et al. 2017, P. 67-69 and Thoft-Christensen and Baker 1982, P. 192-193.

The four different configurations for the reliability analyses and the Monte Carlo simulations, respectively, are composed in the terms (4). In the configurations, in which the k_ℓ-factor is considered, the strength data was first used directly as obtained from the simulated tests and secondly processed indirectly by reproducing the strength data with the fitted Weibull distributions (see Table 2 and 3). The first configuration is termed as "with k_ℓ - direct" and the second one "with k_ℓ - indirect". In the third and fourth configuration the k_ℓ-factor is set to 1 independently of the actual length and the strength data is used directly and indirectly as described above. The corresponding terms are "without k_ℓ - direct" and "without k_ℓ - indirect".

$k_\ell = (5.4/\ell)^{1/13}$ $\quad 0.15 \text{ m} \leq \ell \leq 108 \text{ m}$ (with k_ℓ)

R as modelled random variable (- direct)

R as random variable from fitted Weibull distribution (- indirect) (4)

$k_\ell = 1$ (without k_ℓ)

R as modelled random variable (- direct)

R as random variable from fitted Weibull distribution (- indirect)

Each of the four configurations was applied to the two target strength classes. The randomly distributed stress values representing *E* are reproduced with a Normal distribution (cf. Eurocode "0", C6). The corresponding parameters are given in the terms (5). The mean values (μ_x) result from a calibration process so that the reliability index approximately amounts to 3.8 in case of the reference length of 5.4 m. The coefficient of variation is set to 10 %. With that, the stress *E* features a purposefully chosen scatter to consider its stochastic character in the reliability analyses. In doing so, the influence, which the k_ℓ-factor exerts in Eq. (3), becomes evident.

E: normally distributed stress

μ_x=11.50 N/mm², COV = 10 % (if *R* from GL23h) (5)

μ_x=18.63 N/mm², COV = 10 % (if *R* from GL33h)

The four configurations for the reliability analyses were performed for each examined length and each examined depth resulting in five more or less different β-values for a given length. However, if a single reliability analysis yields a failure probability of zero, no β-value exists. This is particularly the case in configurations with short members and $k_\ell = 1$.

Fig. 3 represents the result: above for GL23h and below for GL33h. The β-values obtained from the differently configured reliability analyses are grouped and represented by different symbols. The mean β-values, calculated from the single values for the five depths, are connected each by straight lines. Independently of the examined strength class, the representation shows:

- There is an evident drop of the reliability index for an increasing member length, if the k_ℓ-factor is set to 1 and hence is not considered.
- Modifying the tensile strength with the proposed length-depending k_ℓ-factor results in a more or less balanced reliability index along the examined member length.
- The analyses based on indirectly processed data produce similar β-values. The shape of the corresponding β-courses obtained from reliability analyses with direct and indirect configurations even feature a certain affinity.

4 Conclusions

Based on a computationally determined tensile strength for glulam members with varying depth and length, it is shown that an inconsistent reliability between short and long members may exist. This assumption refers to computationally examined strength classes complying with GL23h and GL33h. Using a k_ℓ-factor with an exponent of 1/13 according to

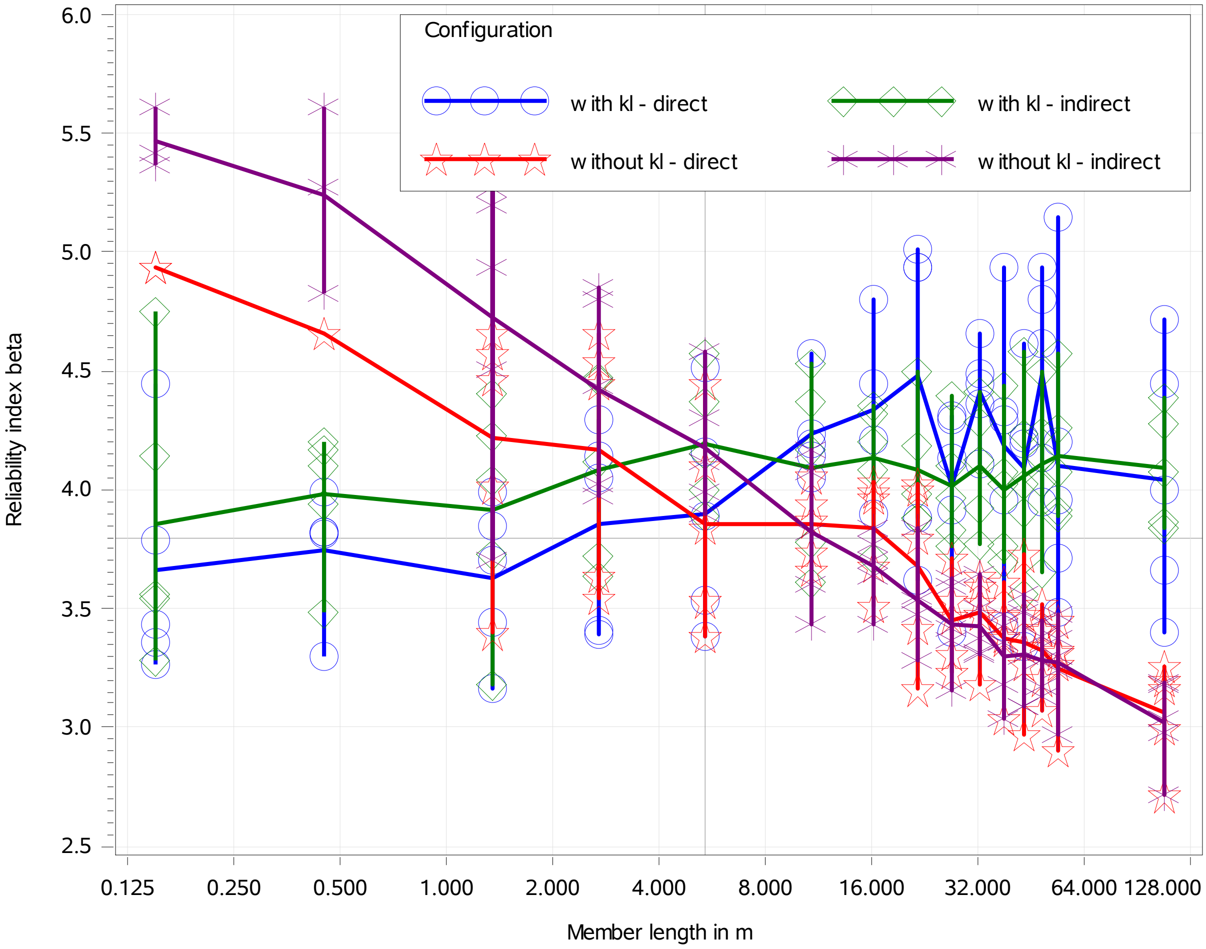

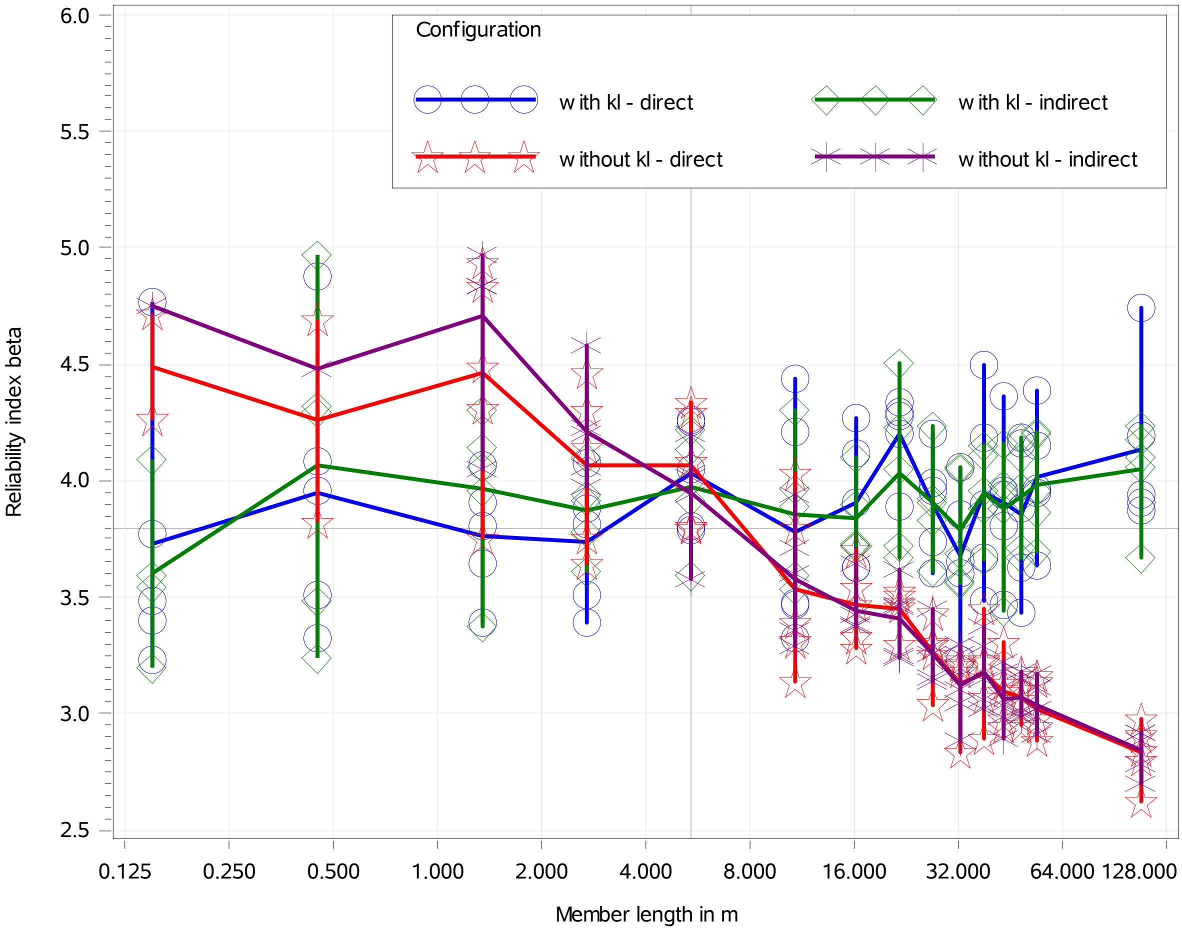

Figure 3. Reliability index and member length; GL23h (top) and GL33h (bottom)

Eurocode 5 format, one could obviously compensate length effects for tension members with a length up to 108 m. In comparison with current provisions, this compensation would be conservative. This is confirmed with reliability analyses performed as Monte Carlo simulations. The computationally determined strength data trigger the reflection whether the extent of consequences in case of tension failure of long members are adequately considered in the current provisions of Eurocodes “0” and 5.
The paper provides purposeful theoretical tensile strength distributions so that reliability experts may define precise strength modifications in order to create a more consistent reliability level throughout a length range from 1.35 up to 108 m. All the computationally determined strength data, described in the paper, will be made available on demand in its current txt format. The complete data encompass 375 thousand single tensile strength values, which are organised in two strength levels, five depths and fifteen lengths.

5 References

EN 1995-1-1:2004 Eurocode 5: Design of timber structures – Part 1-1: General – Common rules and rules for buildings

EN 14080:2013-09 Timber structures – Glued laminated timber and glued solid timber – Requirements

EN 408:2010+A1:2012 Timber structures – Structural timber and glued laminated timber – Determination of some physical and mechanical properties

Fast, P; Ratzlaff, D (2017): Design of the roof for the Grandview Heights Aquatic Centre, Surrey, Canada. The Structural Engineer 95(7), 16-23

Frese, M; Blaß, HJ (2010): System effects in glued laminated timber in tension and bending. CIB-W18/43-12-3, Nelson, New Zealand

Thoft-Christensen, P; Baker, MJ (1982): Structural Reliability Theory and Its Applications. Springer-Verlag, Berlin

Frese, M; Blaß, HJ (2016): Reliability of large glulam members – Part 1: Data for the assessment of partial safety factors for the bending strength. INTER/49-17-1, Graz, Austria

Frese, M (2016): Computergestützte Verfahren zur pragmatischen Beurteilung der Tragwiderstände von Brettschichtholz. Bd. 31 Karlsruher Berichte zum Ingenieurholzbau, KIT Scientific Publishing

Spaethe, G (1992): Die Sicherheit tragender Baukonstruktionen. 2. Aufl., Springer-Verlag, Wien

EN 1990:2002 Eurocode “0”: Basis of structural design

Loebjinski, M; Rug, W; Pasternak, H (2017): Zuverlässigkeitsbewertungen von Holzbauteilen im Bestand. Bauingenieur 92, 65-73

Annexe A Data sheets for GL23h

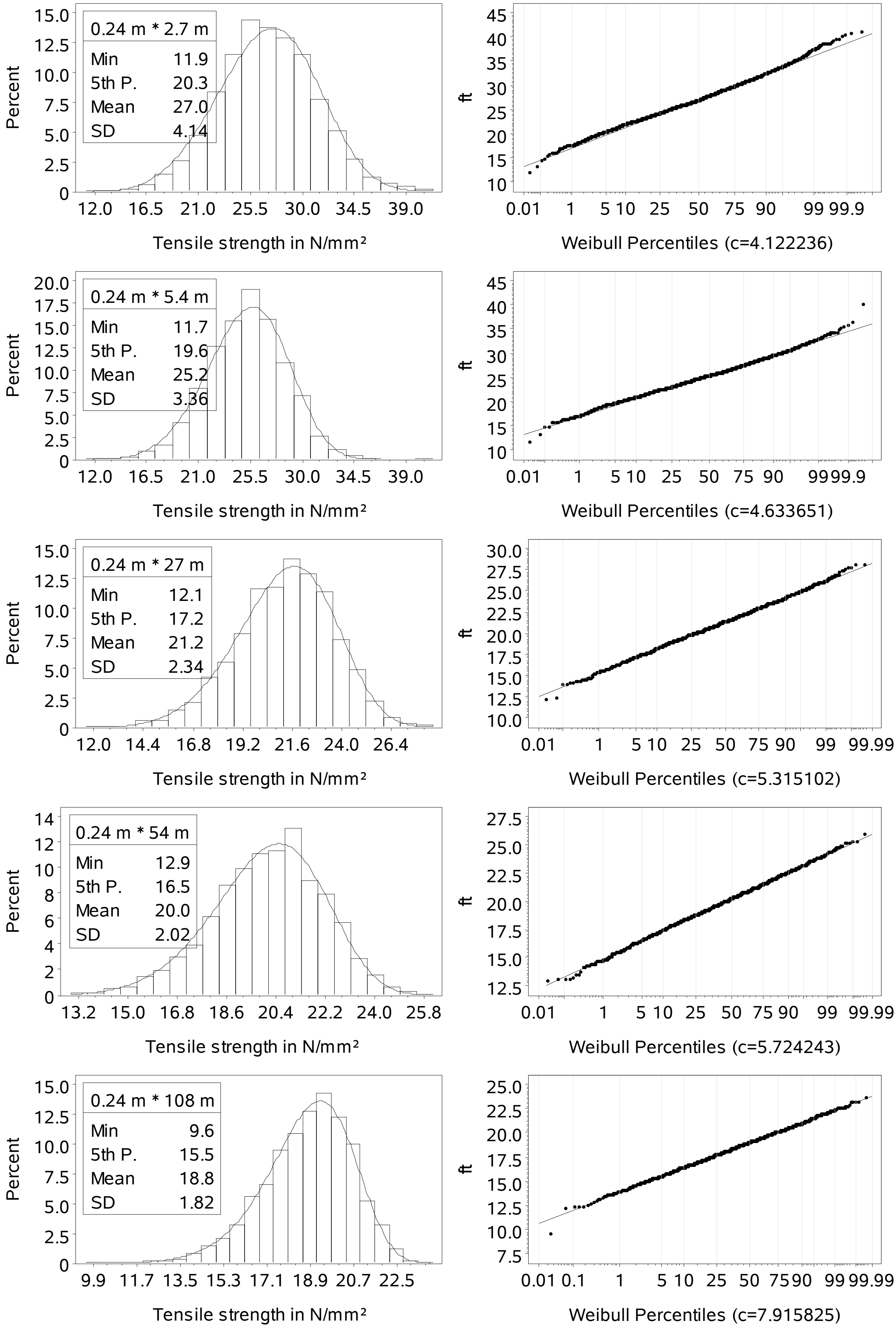

Figure 4. Modelled frequency and fitted probability distributions, 2500 realisations each.

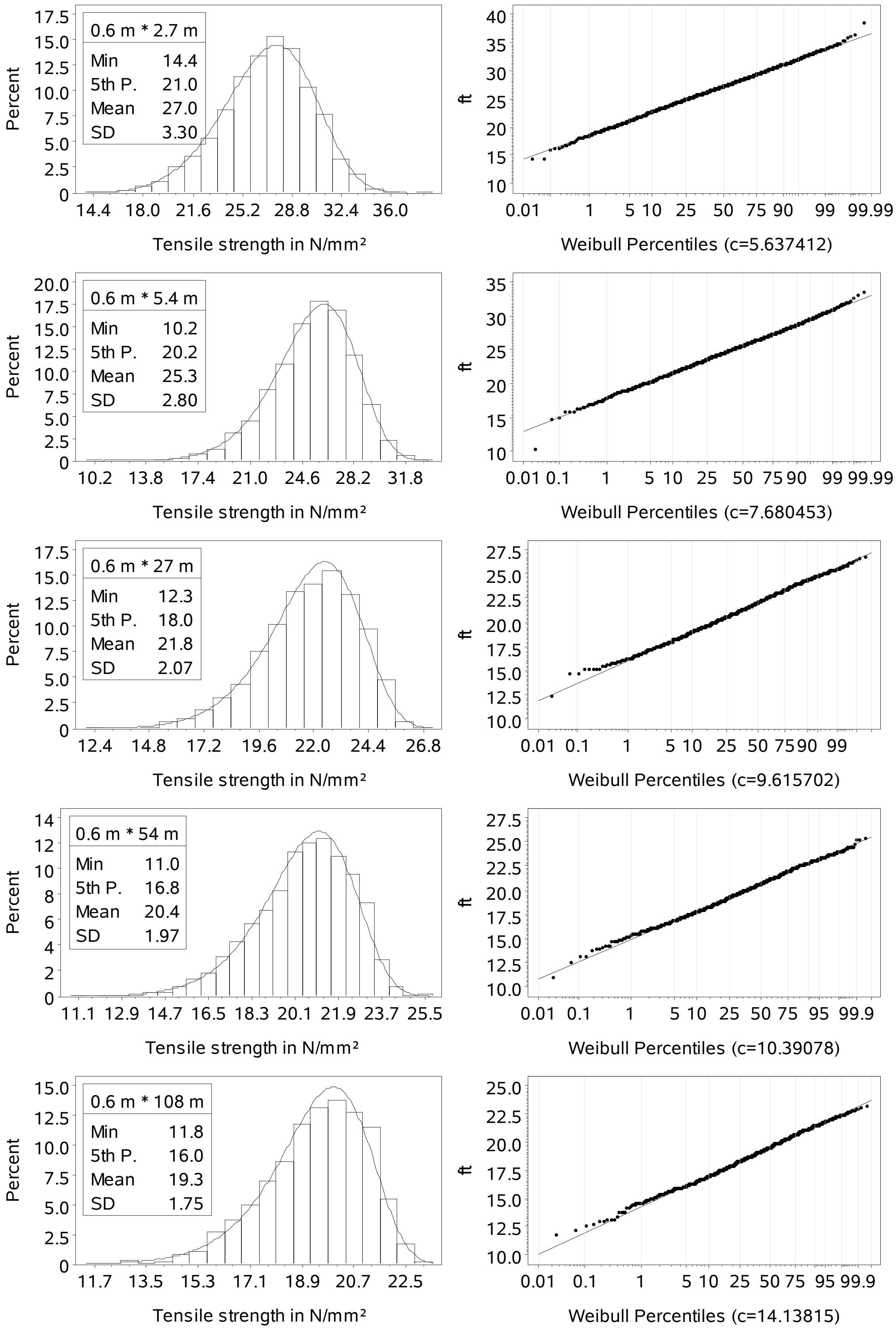

Figure 4 (cont'd). Modelled frequency and fitted probability distributions, 2500 realisations each.

Table 2. Parameters of fitted Weibull distributions.

Depth m	Length m	Threshold N/mm²	Scale N/mm²	C	Mean N/mm²	SD N/mm²
	1.35	11.3	21.2	3.210	30.3	6.48
	2.70	12.3	16.7	3.266	27.2	5.04
	5.40	12.4	14.0	3.729	25.0	3.77
0.12	16.2	11.4	11.7	4.189	21.9	2.85
	27.0	8.50	13.2	5.686	20.7	2.49
	54.0	8.35	11.8	5.880	19.3	2.17
	108	7.28	11.7	6.650	18.2	1.92
	1.35	13.1	18.0	3.347	29.2	5.31
	2.70	11.4	17.1	4.122	27.0	4.25
	5.40	11.1	15.4	4.634	25.2	3.45
0.24	16.2	10.3	13.1	5.367	22.4	2.59
	27.0	10.4	11.8	5.315	21.2	2.35
	54.0	10.0	10.8	5.724	20.0	2.03
	108	6.60	12.9	7.916	18.8	1.83
	1.35	13.7	16.8	3.528	28.8	4.76
	2.70	13.5	15.0	4.079	27.1	3.75
	5.40	11.7	14.9	4.959	25.3	3.15
0.36	16.2	9.89	13.8	5.939	22.7	2.50
	27.0	6.65	15.9	7.727	21.6	2.29
	54.0	8.00	13.2	7.160	20.3	2.03
	108	7.89	12.0	7.340	19.2	1.82
	1.35	13.6	16.8	3.985	28.8	4.28
	2.70	12.9	15.5	4.701	27.0	3.43
	5.40	11.8	14.7	5.418	25.3	2.88
0.48	16.2	8.15	15.5	7.063	22.6	2.42
	27.0	4.09	18.5	9.510	21.7	2.22
	54.0	6.07	15.1	8.535	20.4	2.00
	108	5.99	14.0	9.047	19.3	1.76
	1.35	13.7	16.4	4.297	28.7	3.93
	2.70	10.8	17.5	5.637	27.0	3.32
	5.40	6.93	19.5	7.680	25.3	2.83
0.60	16.2	1.16	22.6	11.20	22.8	2.34
	27.0	5.24	17.4	9.616	21.8	2.07
	54.0	3.46	17.8	10.39	20.4	1.97
	108	-0.911	21.0	14.14	19.3	1.75

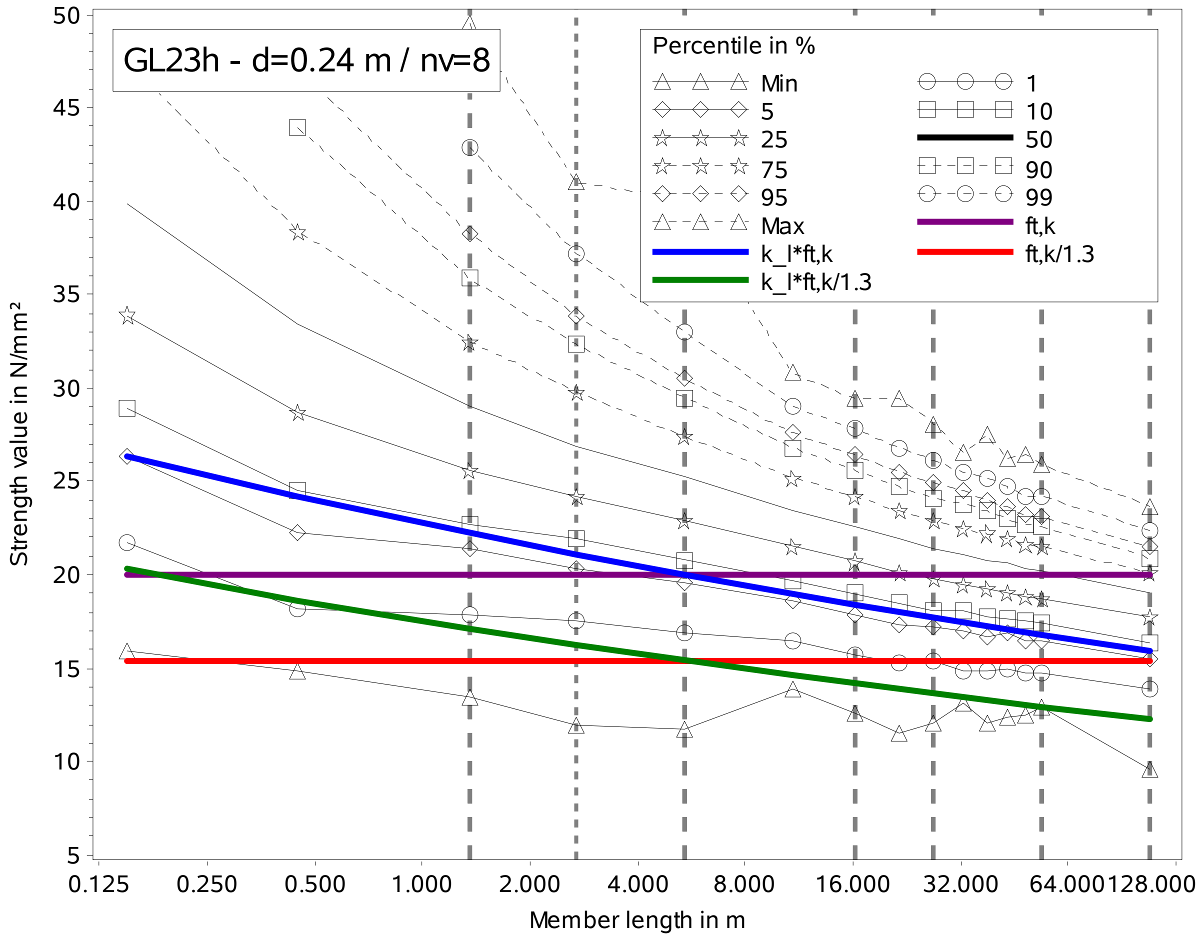

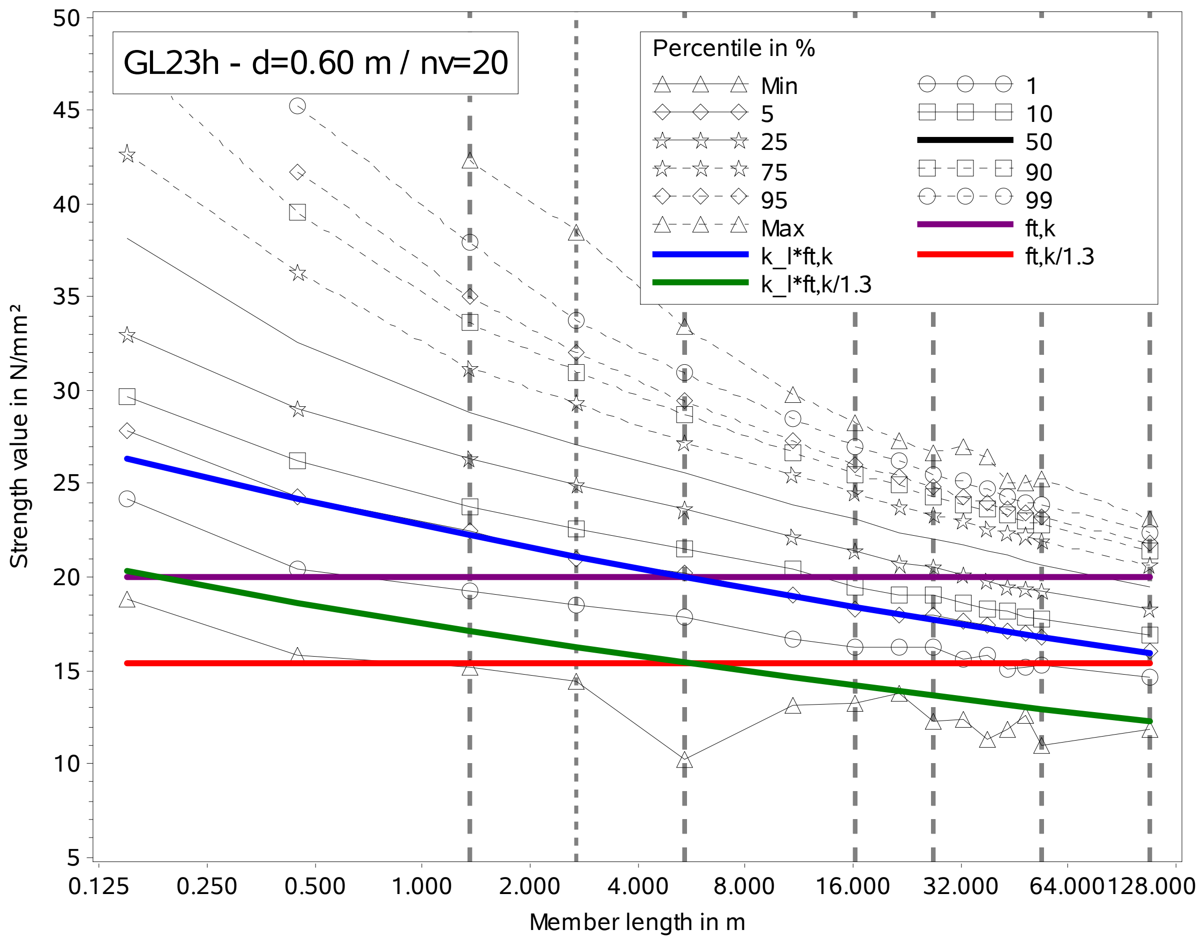

Figure 5. Selected percentiles of the tensile strength over member length.

Annexe B Data sheets for GL33h

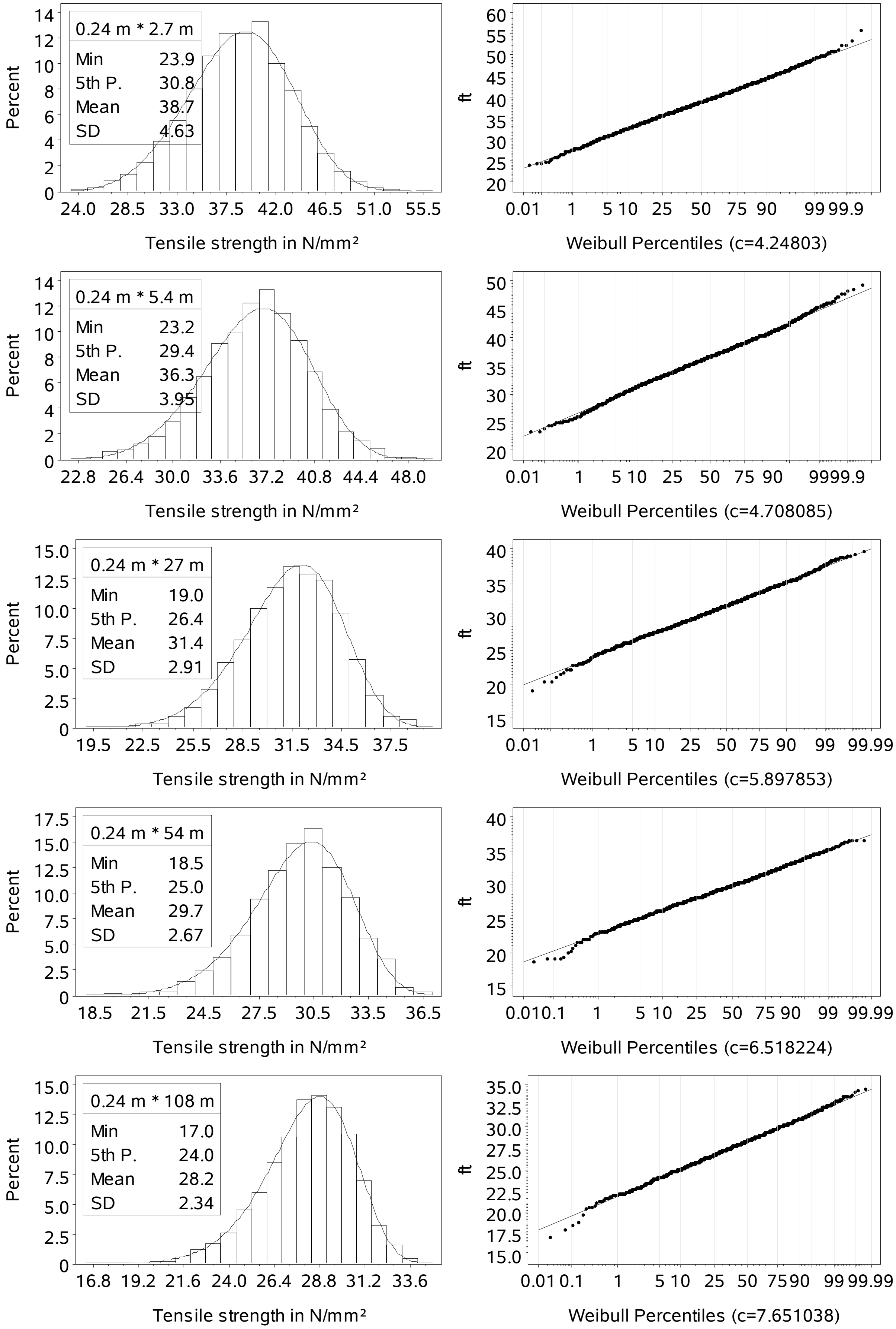

Figure 6. Modelled frequency and fitted probability distributions, 2500 realisations each.

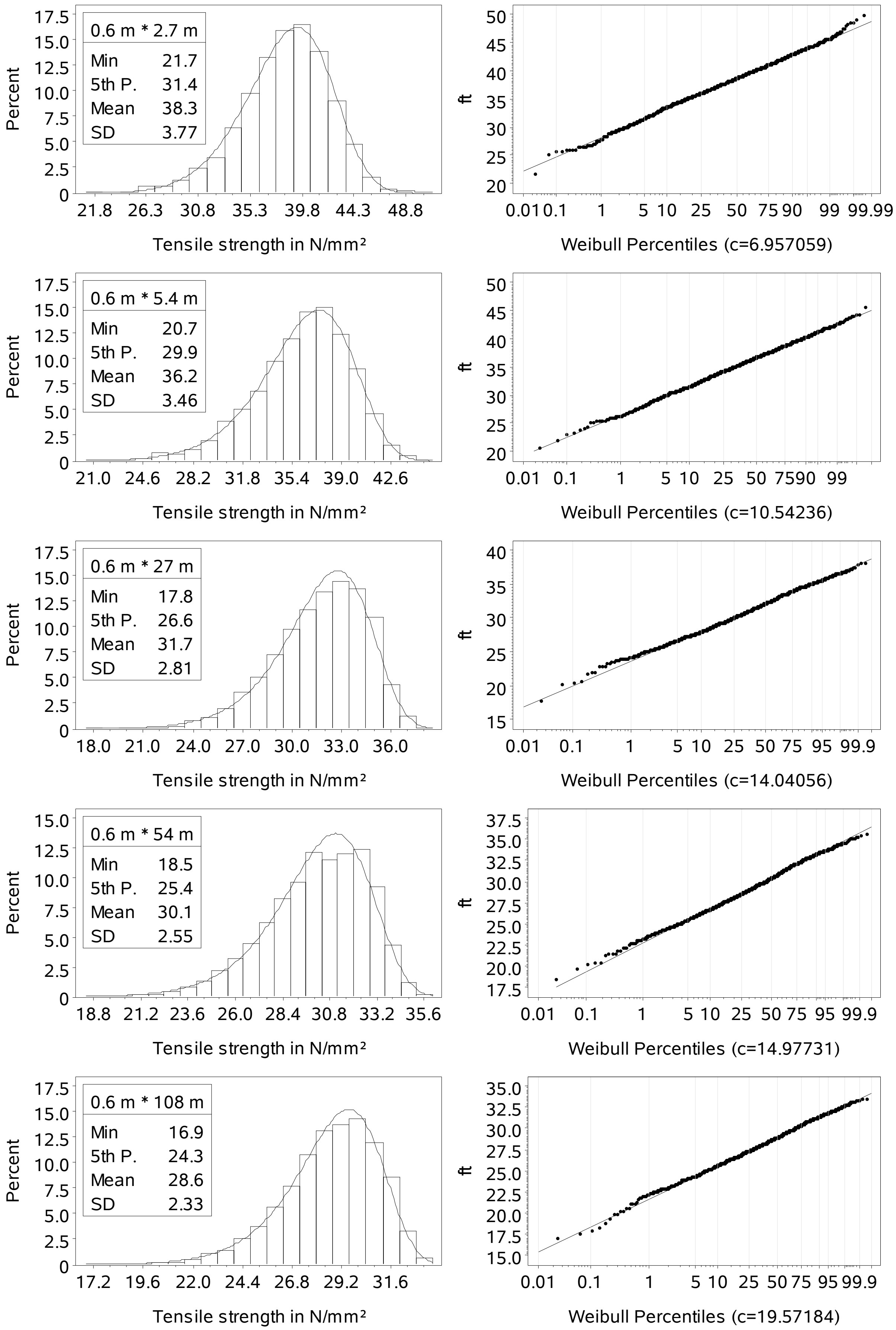

Figure 6 (cont'd). Modelled frequency and fitted probability distributions, 2500 realisations each.

Table 3. Parameters of fitted Weibull distributions.

Depth m	Length m	Threshold N/mm²	Scale N/mm²	C	Mean N/mm²	SD N/mm²
	1.35	19.8	26.1	3.499	43.2	7.42
	2.70	20.0	21.2	3.553	39.1	5.96
	5.40	19.8	18.0	3.960	36.2	4.63
0.12	16.2	17.1	16.5	4.953	32.2	3.50
	27.0	15.4	16.7	5.685	30.8	3.14
	54.0	14.0	16.2	6.380	29.1	2.77
	108	13.1	15.6	7.044	27.6	2.43
	1.35	23.6	19.9	3.388	41.4	5.82
	2.70	21.1	19.3	4.248	38.7	4.66
	5.40	19.8	18.0	4.708	36.3	3.98
0.24	16.2	14.7	19.4	6.400	32.8	3.29
	27.0	16.5	16.1	5.898	31.4	2.94
	54.0	14.7	16.1	6.518	29.7	2.70
	108	12.9	16.2	7.651	28.2	2.35
	1.35	21.0	21.9	4.552	41.0	5.00
	2.70	18.0	22.0	5.253	38.3	4.44
	5.40	16.9	20.8	6.086	36.3	3.70
0.36	16.2	15.0	19.2	6.911	32.9	3.05
	27.0	11.9	20.8	8.054	31.5	2.89
	54.0	13.7	17.3	7.307	30.0	2.62
	108	10.8	18.7	8.981	28.5	2.36
	1.35	22.0	20.2	4.457	40.5	4.69
	2.70	17.3	22.6	6.125	38.3	3.99
	5.40	16.4	21.2	6.657	36.2	3.49
0.48	16.2	8.04	26.3	9.872	33.1	3.05
	27.0	8.72	24.1	9.796	31.7	2.81
	54.0	7.65	23.5	10.27	30.0	2.62
	108	10.0	19.6	9.438	28.6	2.36
	1.35	22.2	20.0	5.017	40.5	4.19
	2.70	15.9	23.9	6.957	38.3	3.78
	5.40	6.00	31.6	10.54	36.2	3.45
0.60	16.2	6.01	28.3	11.07	33.0	2.95
	27.0	-0.456	33.4	14.04	31.7	2.80
	54.0	-0.983	32.2	14.98	30.1	2.55
	108	-8.23	37.9	19.57	28.6	2.33

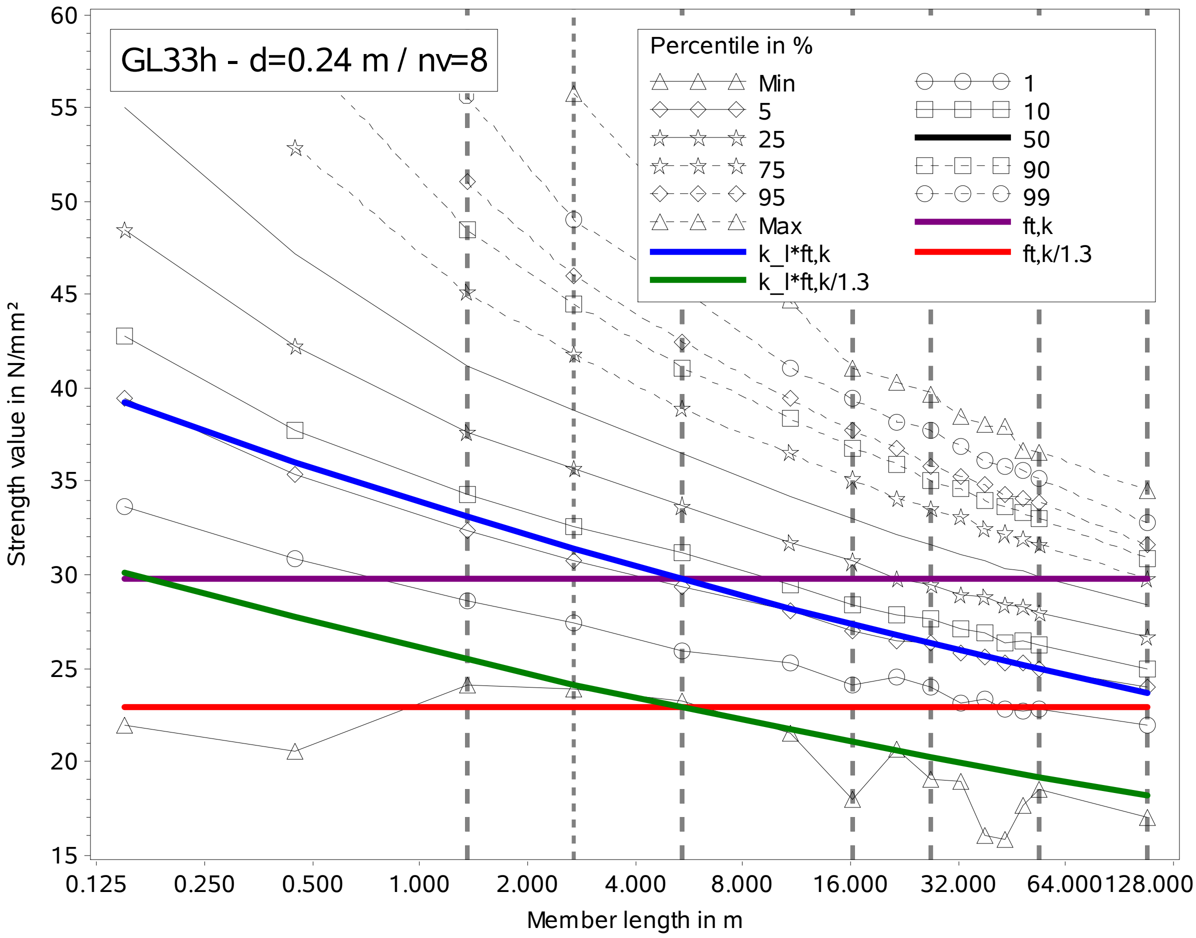

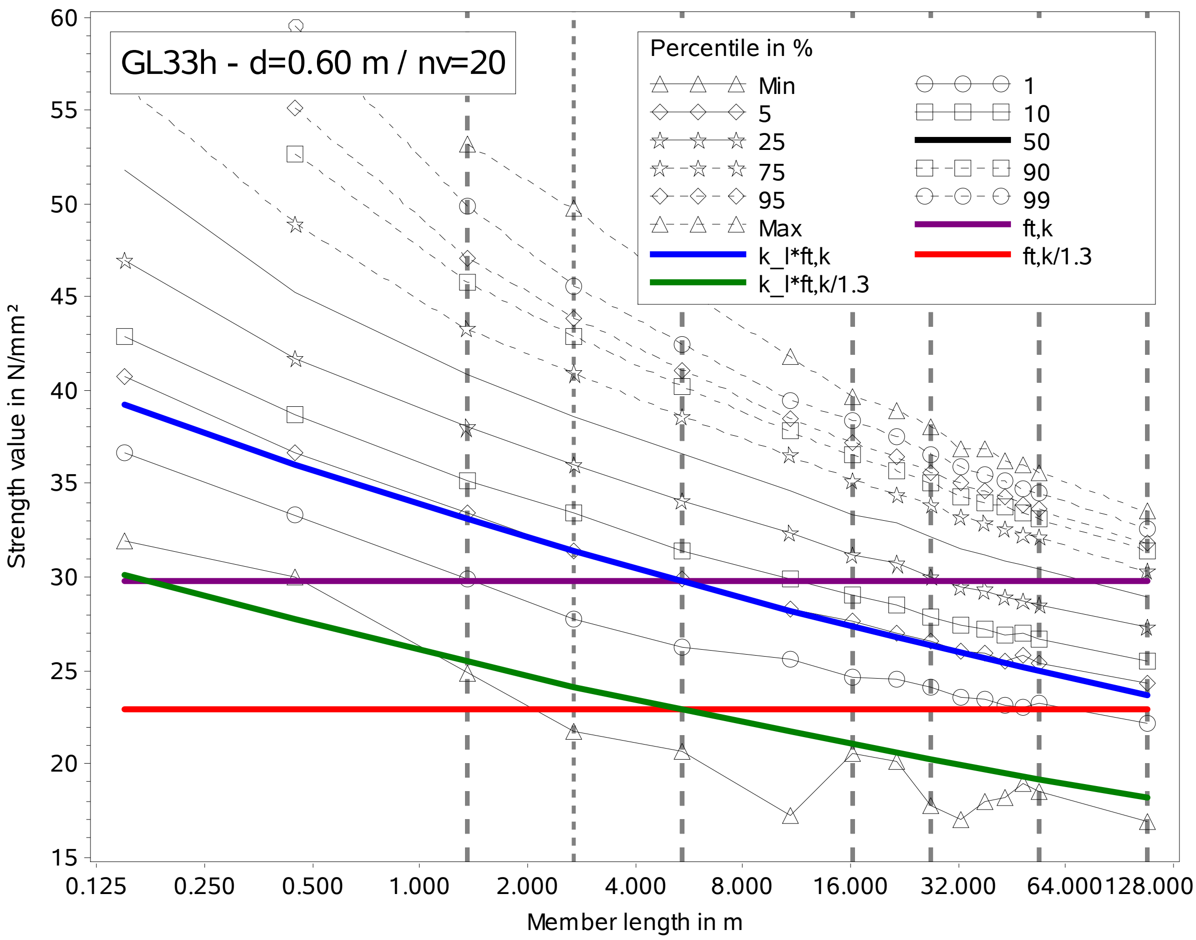

Figure 7. Selected percentiles of the tensile strength over member length.

Discussion

The paper was presented by M Frese

F Lam commented that the scope of the paper is wider than the title suggested. The author should consider changing the title to reflect the paper content. M Frese responded that this paper was the second part of a paper from last year with similar title and would be appropriate to keep the title for consistency.

F Lam asked about the use of Normal distribution rather than extreme value distribution to represent the load in reliability study. M Frese responded that Normal distribution can be used to represent some loads in Eurocode approach.

P Dietsch asked about the assumption of 30 mm laminate thickness. There are many producers in Europe producing glulam with 40 mm thick laminates. Why 40 mm thick laminates were not considered. M Frese said that the database is based on 30 mm thick material and changing the laminate thickness might yield different results. H Blass responded that if 40 mm thick material was used fewer laminates would be used for a given beam depth. Results would have already considered laminate number and hence thickness effects.

There were discussions about the normal forces in truss lower chord might not be constant and what would be a length to be used for consideration. F Lam said that UBC had done work in this area and results were presented in CIB W18 paper which could be considered here.

S Aicher commented that the results indicated no significant depth effect whereas volume effect existed in bending of timber.

R Jockwer commented that consideration of minimum value rather than 5th percentile value would be confusing.

S Aicher received clarification of the mean and standard deviation of the laminate length.

4 INTER Notes, Kyoto, Japan 2017

An improved design model for fire exposed Cross Laminated Timber

Joachim Schmid, Michael Klippel, Andrea Frangi, ETH Zurich

Alar Just, Mattia Tiso, Tallinn Technical University

Keywords: fire, cross laminated timber, design model, effective cross section method

1 Introduction

The effective cross section method (ECSM) is a popular design method for the fire design of timber members. Based on simulations, which were verified by testing in model and large scale, a design model for CLT (cross laminated timber) was presented (Schmid et al., 2010) and implemented in the European handbook Fire Safety In Timber Buildings (Östman et al., 2010). As for other timber members, the design model specifies a so called zero-strength layer d_0 to compensate strength losses of the heated member due to elevated temperatures by reducing the residual cross section by means of a fictive layer with no strength to obtain an effective cross section with material properties as at normal temperature. Contrary to Eurocode (EN 1995-1-2) where a constant d_0-value is implemented, linear equations were presented for CLT. Obtained results exceed d_0 values for beams and columns mainly due to the structure of CLT with cross layers (negligible strength and stiffness in the load bearing direction) and the actual definition of d_0. This note summarizes approaches to improve the actual proposal (Schmid et al., 2010).

2 Model development

The model presented in 2010 was the result from simulations of available structures and testing. Thermal simulations were performed to determine temperature profiles for initially unprotected and protected CLT. Temperature gradients for about 40 protection scenarios were determined. Then the maximum bending capacity was calculated with CSTFire, an Excel based macro program; the simulation procedure is shown in Fig. 1. Results are $d_{0,fm}$values for the compensation of strength losses (based on the section modulus W_{fi} of the heated section) and $d_{0,E}$values for the compensation of stiffness losses (based on the curvature κ_{fi} of the heated section). The $d_{0,E}$ results can be used for the development of a buckling model, for which the stiffness reduction is crucial. Simulations were verified with ca. 30 fire tests and ca. 20 reference tests at normal temperature. Further, large scale tests were performed at IVALSA (Fiori, 2009) and used for verification.

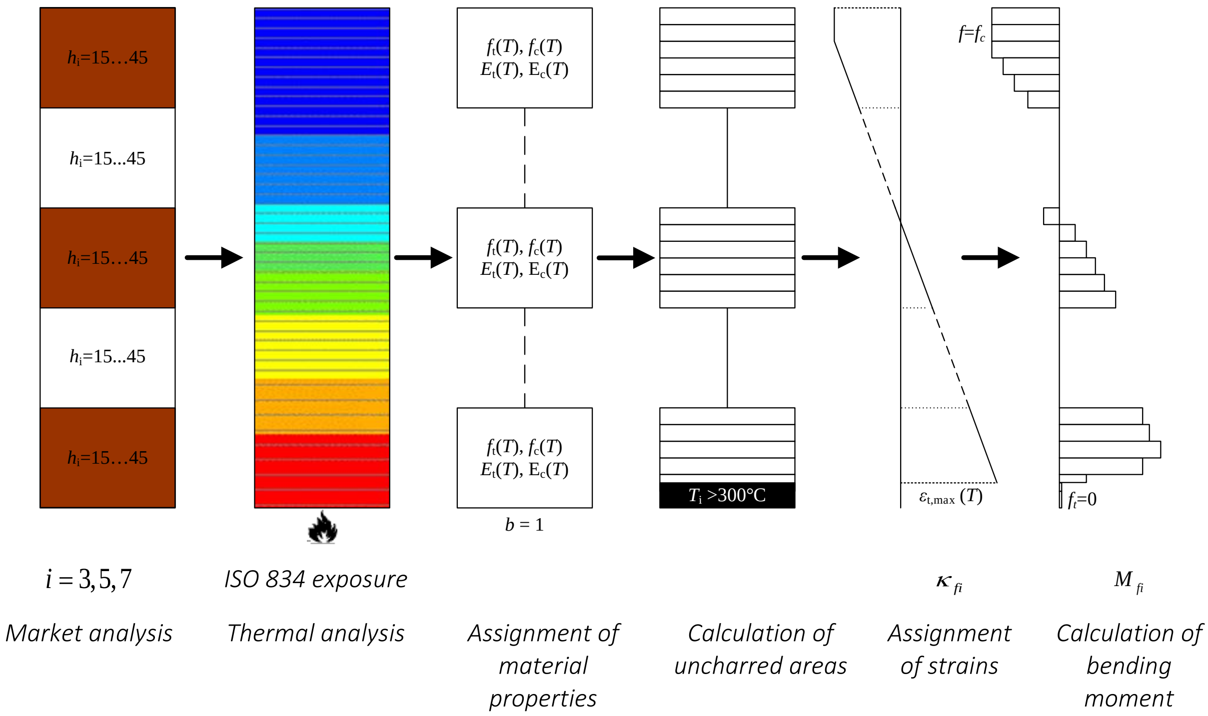

Fig. 1. Calculation process of CSTFire adopted for CLT to determine the curvature and bending capacity of the heated cross-section (example for CLT with exposed side in tension).

3 Improved model

As defined by the Horizontal Group Fire (HGF), Eurocode design may follow (a) tabulated data (b), simplified or (c) advanced models. Tabulated data (a) is not the inclusion of single fire test results but can be based on multiply, systematic testing and/or advanced calculations. To address (a) and (b) as well as weaknesses of the model presented in 2010, which are (1) the large product portfolio of CLT and (2) the unfavourable definition of d_0, currently a re-analysis and complementary calculations are performed at ETH Zurich and TU Munich. Recently, a task group "CLT" within the COST Action FP1404 has collected 12 preferred CLT structures (solely three and five layer CLT) based on industry input. Next, it is aimed to describe the load bearing performance in fire in terms of tabulated data for these structures, i.e. appropriate d_0 values for 30, 60 and 90 min fire exposure. Further, a systematic analysis will be performed to optimize the linear equations from the actual 2010 proposal in terms of a simplified model. Initially unprotected and protected CLT will be analysed with respect to different definitions of d_0, see Section 3.1, and the temperature performance of the glue line, see Section 3.2. Results will be presented at the task group "CLT" meeting in October 2017 and subsequently published.

3.1 Definition of the zero-strength layer d_0

In the model presented in 2010, $d_0$was defined in line with the Eurocode model for solid members, where d_0 describes the difference between the effective and residual cross section at a certain time of fire exposure, i.e. the zero-strength layer with respect to the residual cross section, $d_{0,res}$. The use of $d_{0,res}$ is very simple, but it may lead to very conservative (and uneconomic) fire design for CLT. Fig. 2 (b) shows the determination of $d_{0,res}$ and $d_{0,ef}$ for the same cross section. It should be noted that $d_{0,ef}$ comprises only "effective" layers, i.e. longitudinal layers while $d_{0,res}$ is simply the difference between the residual cross section and the effective cross section, $d_{0,res} = h_{res} - h_{ef}$.

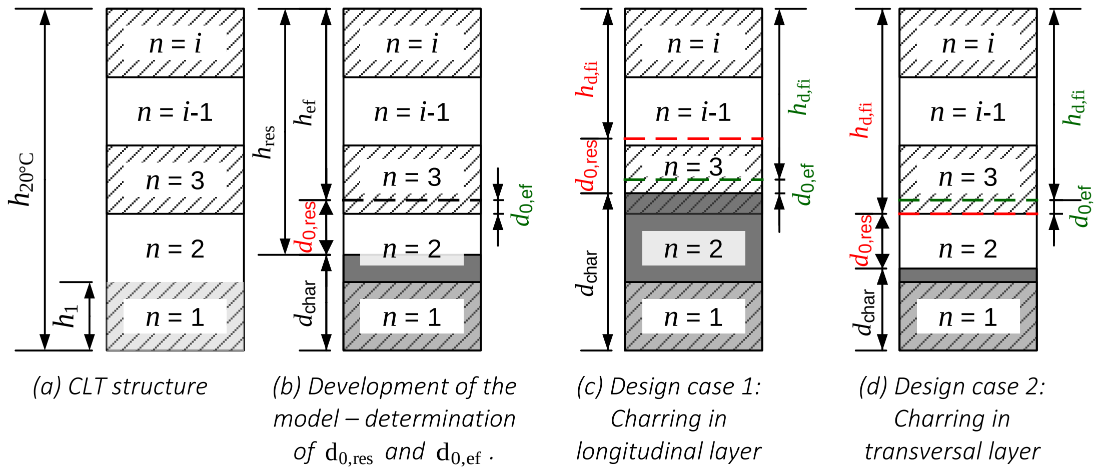

Fig. 2. Determination of $d_{0,res}$ and $d_{0,ef}$ for a cross section and two different design cases.

Fig. 2 shows advantages of the use of $d_{0,ef}$: in the design case 1 (c), layer 3 would be reduced completely by $d_{0,res}$. However, design case 2 (d) shows that the designer has to consider that layer 2 is a transversal layer, which might be seen as an additional step and disadvantage in the design process. In case 2, the reduction of layer 3 is justified by the heated depth of 40 to 80 mm beyond the char line depending on the protection case for which the $d_0$values where developed (b).

3.2 Failure of the glue line – fall-off of the charred layers

In many experimental studies (local) fall-off of the charred layers is documented, which is a property of the adhesive used for surface gluing. This fall-off has a negative effect on the charring rate which would be increased to some extent. However, there is no negative effect of this fall-off on the d_0-value since the temperature profile will be steeper and, thus the heat affected depth reduced. However, as fall-off of charred layers cannot be guaranteed it will not be considered further in the model.

4 References

EN 1995-1-2 (2004): Design of timber structures - Part 1-2: General and rules for buildings. CEN.

Fiori, S. (2009). Analisi Numerico-Serimentale di Panelli di Solaio in Legno Lamellare incrociato esposti al Fuoco. Master Thesis, Trieste.

Schmid, J., König, J., & Köhler, J. (2010). Fire-exposed cross-laminated timber-Modelling and tests. In World Conference on Timber Engineering.

Östman B. (editor). Fire safety in timber buildings – Technical guideline for Europe, SP Report 2010:19, 2010. ISBN 978-91-86319-60-1

Impact and detection of grain direction in European beech wood

Thomas Ehrhart, ETH Zürich - Institute of Structural Engineering, Zürich, Switzerland

René Steiger, Empa - Structural Engineering Research Lab, Dübendorf, Switzerland

Andrea Frangi, ETH Zürich - Institute of Structural Engineering, Zürich, Switzerland

Keywords: European beech wood, grain direction, strength grading, medullary ray spindles, non-contact method, machine grading

1 Introduction

Within a project on the mechanical properties of glued laminated timber (GLT) made from European beech wood (*Fagus sylvatica* L.), 6499 timber boards from five different sawmills located in Switzerland were investigated and strength graded. Thereof, 423 timber boards were subjected to tensile tests and 100 were used for assessing the tensile and bending strength of finger joints as well as the quality of face bonding in delamination tests. The remaining majority of the timber boards was used to produce GLT beams, columns and lamination bundles later on to be subjected to bending, shear, compression and tensile tests parallel to the grain, respectively. In the tensile tests on single boards the dominating failure mechanism was shear failure in the *LR*-plane along the medullary rays (Figure 1.1 and Figure 1.2). It could be concluded that the grain pattern plays an important role with regard to the tensile strength of the board and, hence, should be accounted for in the strength grading process.

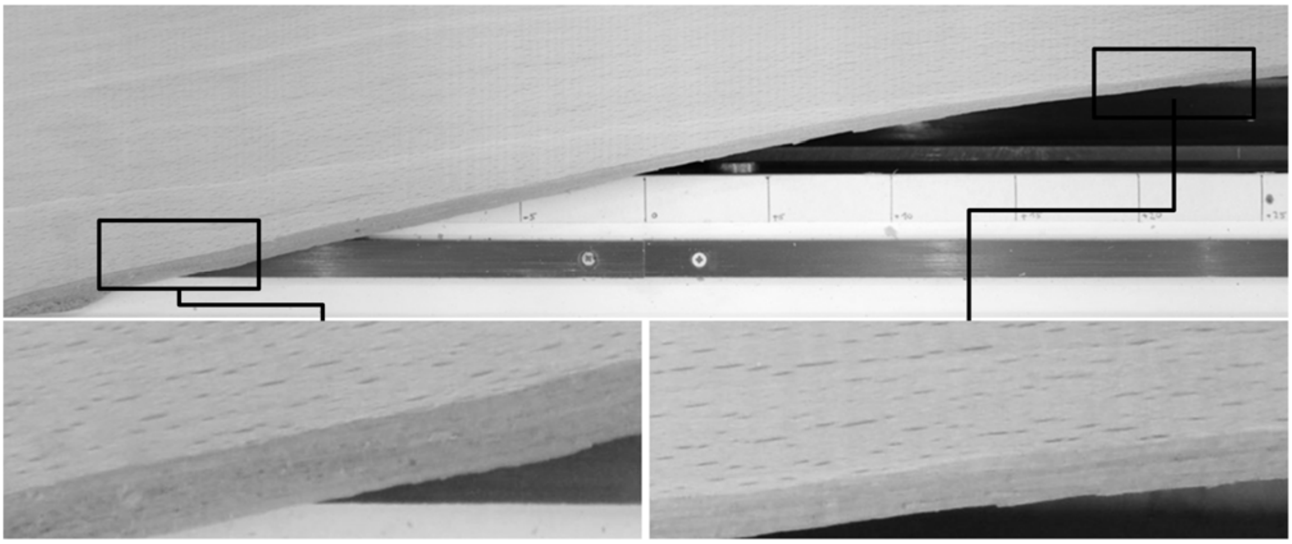

Figure 1.1. Shear failure along the medullary rays observed in tensile testing “parallel to the grain”.

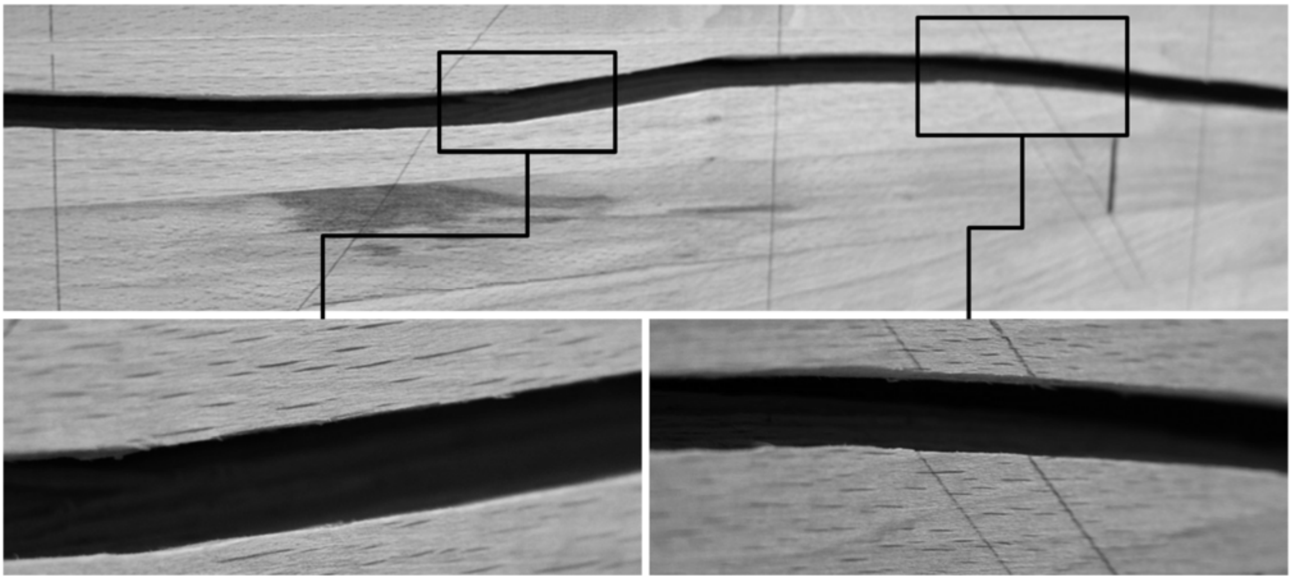

Figure 1.2. Shear failure in a GLT beam made from European beech wood (top) and detailed view of the fracture path along the medullary ray spindles (bottom).

Standardised methods to determine the grain direction, such as the scribing method (EN 1310) and the alignment of drying checks on the flat sawn face (DIN 4074-5), were reported not to be expedient when applied to beech wood (Frühwald & Schickhofer 2005). Methods based on electric field strength measurement, microwave scanning, and tracheid effect, as often used for softwoods, were reported to be hardly applicable to beech wood too (Schlotzhauer et al. 2016). Due to the lack of appropriate methods for its measurement, the grain direction has been explicitly excluded as an indicator for the strength grading of beech according to DIN 4074-5. However, grain direction plays a key role in predicting the mechanical behaviour of beech wood (Aicher et al. 2001; Frühwald & Schickhofer 2005; Ehrhart et al. 2016).

2 Materials and methods

To allow for the identification, quantification, and documentation of grain direction, a non-contact method, based on an automated visual analysis of the medullary ray spindle pattern, was developed. Initially, all faces of a board are photographed using a device that assures standardised perspective, object position and distance, resolution and illumination level. The information of the resulting images is reduced to the objects of interest (spindles) by means of image feature analysis and the objects identified are documented regarding their location, size and orientation (Figure 2.1).

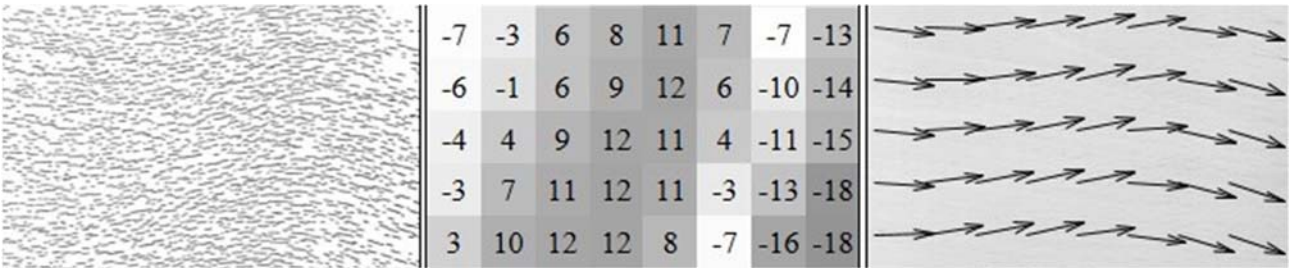

Figure 2.1. Identified medullary ray spindles and estimated field of grain direction in numerical (inclination in degree) and vectorised form (left to right).

3 First results and outlook

The first results are highly promising. The fracture path of the (dominating) mechanism *shear failure along the medullary rays* could be predicted accurately using the described method. For all kinds of shear failure, i.e. local slope of grain (with or without knots, Figure 3.1, left), global slope of grain (Figure 3.1, right), or splinter failure, the estimated field of grain orientation and the actual fracture path are congruent.

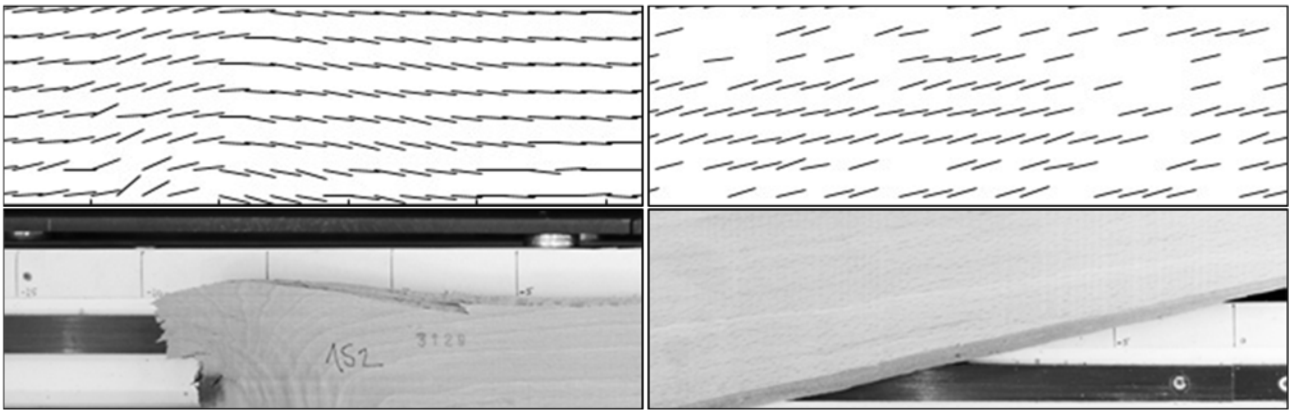

Figure 3.1. Estimated field of grain orientation (top) and failure pattern observed in tensile tests.

The presented method will be further improved and advanced models to estimate the tensile strength, taking into account the field of grain direction, are being developed. Based on (i) the developed models for the tensile strength and (ii) well documented GLT beams, investigations on the laminating effect will be conducted and experimentally verified.

4 References

Aicher, S., Höfflin, L. & Behrens, W., 2001. A study on tension strength of finger joints in beech wood laminations. *Otto-Graf-Journal*, 12, pp.169–186.

CEN European Committee for Standardization, 1997. EN 1310: Round and sawn timber - Method of measurement of features.

DIN German Institute for Standardization, 2008. DIN 4074-5: Strength grading of wood – Part 5: Sawn hard wood.

Ehrhart, T. Fink, G., Steiger, R. & Frangi, A., 2016. Experimental investigation of tensile strength and stiffness indicators regarding European beech timber. *WCTE*. Vienna, Austria.

Frühwald, K. & Schickhofer, G., 2005. Strength grading of hardwoods. In: *Proceedings of the 14th International Symposium on Nondestructive Testing of Wood*. Hannover, Germany.

Schlotzhauer, P., Wilhelms, F., Lux, C. & Bollmus, S., 2016. Machine grain angle determination on spruce, beech, and oak lumber for construction use. *WCTE*. Vienna, Austria.

The Displacement Paradox for Seismic Design of Timber Buildings

A.H. Buchanan, T. Smith, PTL Structural Consultants, New Zealand

1 Introduction

Seismic design to control displacements is essential, to reduce the potential costs of structural and non-structural damage. The damage potential of displacement is far beyond the damage potential of acceleration, however displacements are too often overlooked.

The displacement paradox occurs because, on the one hand, designers need to control lateral displacements to reduce damage and the possibility of structural collapse, but on the other hand, they must provide enough displacement to activate non-linear response and thereby reduce seismic forces. These two objectives sometimes clash, creating a paradox. There is a danger that an “improved” design process to reduce accelerations and seismic forces can lead to “poorer” behaviour because of increasing displacements which will cause unintended damage. For some building systems, this displacement paradox may make it very difficult to provide sufficient ductility in the seismic design of the building while still meeting lateral displacement limits.

Most design codes have very different displacement limits for Ultimate Limit State (ULS) compared with the Serviceability Limit State (SLS) loading conditions. The ULS limits are imposed to protect structural stability of the building, whereas the SLS limits are intended to control non-structural damage with regard to appearance, repair, and weather-tightness. Non-structural damage can also be caused by very high accelerations, but accelerations are not limited in the design codes.

Precise calculation of displacements is not always easy, and they are usually only checked late in the design procedure, unless displacement based design procedures are followed. Ductile design is only possible if there is a sufficiently large displacement window between onset of yield and the ultimate displacement limits. The increased flexibility of timber structures can limit this window.

2 The “DISPLACEMENT WINDOW”

The “displacement window” is the difference in lateral displacement between the onset of yielding and the upper bound prescribed by codes to maintain structural stability, shown in Figure 1. The larger the displacement window, the easier it is to ensure that the design level of in-elastic response will be provided by a structure under earthquake loading.

The bounds of the displacement window:

The upper bound of the displacement window is the maximum code-specified displacement for ULS loading, or the maximum likely displacement of the structure under the design earthquake. In New Zealand ULS loading (Section 7 of NZS 1170.5) is limited to 2.5% lateral drift (75mm inter-storey displacement for a 3.0m storey height).

The lower bound of the displacement window is the displacement at which yielding occurs. This depends heavily on the structural system, the structural materials, and the geometry of the structural members and connections.

For SLS loading in New Zealand, deflection limits usually range from H/600 (0.17% drift, or ~5mm) for unreinforced masonry to H/200 (0.5% drift, or ~15mm) for paper-finished gypsum board walls, for both wind or seismic loading. The Canadian code specifies a SLS limit of H/500 (0.2% drift, or ~6mm) for both wind and earthquake loading.

3 The need for in-elastic response

A very stiff building designed for only elastic response will be subjected to high accelerations and high seismic forces. High seismic forces result in expensive buildings, and high accelerations lead to high levels of possible damage to contents. Engineers have two weapons against these high accelerations: ductility and damping.

Force based design requires an assumption regarding the initial period of the structure and the amount of ductility that the structure will possess at its performance point. It is normally assumed that a structure with ductility will also have hysteretic damping. It is important to recognise that ductility influences seismic response separately from the influence of hysteretic response (damping).

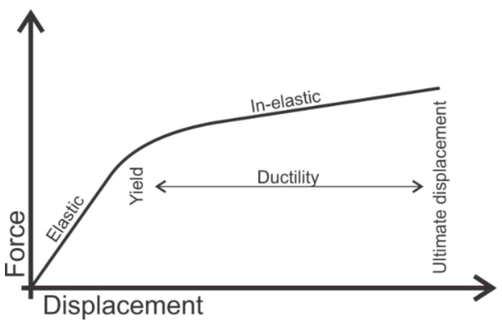

Figure 1. a) The displacement window

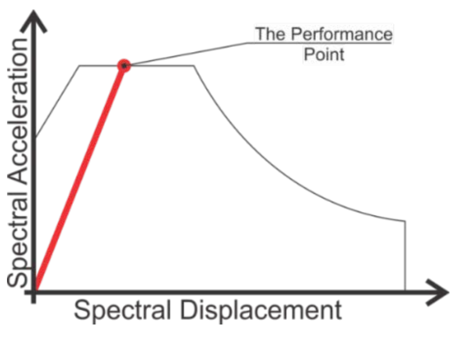

Figure 2. Structural capacity ADRS curve of an elastic SDOF system.

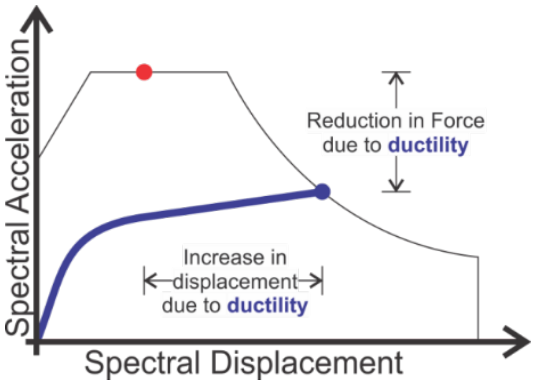

Figure 3. The structural capacity curve of a ductile SDOF system without hysteretic damping.

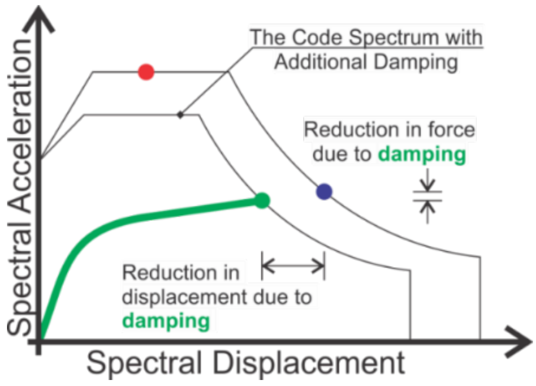

Figure 4. The structural capacity curve of a ductile SDOF with hysteretic damping.

Consider the dimensionless Acceleration Displacement Response Spectrum (ADRS) of a single degree of freedom system shown in Figure 2. This spectrum allows visualisation of the non-linear response of the non-linear SDOF system by presenting both the structural capacity (pushover) curve and the demand spectrum, plotted in spectral-acceleration versus spectral displacement coordinates. Period is represented on an ADRS spectrum as radial lines originating from the origin.

The code response spectrum is presented with a damping ratio of 5%. This represents the inherent elastic damping of the structure, not captured by the hysteretic model used to further reduce seismic forces. Inherent damping can also result from impact damping, foundations and the interaction between structural and non-structural elements.

If a building remains elastic it will respond to earthquake loading as shown in red in Figure 2, being loaded and unloaded with the same stiffness, and thus the same period. For most low and medium rise structures the performance point of the elastic structure will be on the constant acceleration section of the demand spectrum.

Introducing ductility creates a reduction in the stiffness of the building as shown by the curved blue line in Figure 3. This change in stiffness elongates the period. This period shift moves the performance point of the structure, reducing the force and increasing the lateral displacement, as expected. The spectrum shown in Figure 3 has not been altered from the elastic spectrum and maintains the damping ratio of 5%. This movement of the performance point is thus only attributable to the period shift created by the change in stiffness through ductility.

The addition of hysteretic damping is represented on the ADRS as the reduction of the demand with increasing hysteretic damping shown by the inner curve in Figure 4. This creates a new performance point for the damped system, as shown, with a minor decrease in force due to damping beyond that already created by the period shift, but a significant decrease in displacement. Iteration is normally required to find the performance point of a hysteretic system because a reduction in final displacement will lower the hysteretic energy release from the system.

4 Relevance to timber buildings:

The low Modulus of Elasticity (E) of wood compared with concrete or steel can result in larger elastic displacements of timber buildings in most loading conditions, hence a smaller "displacement window". A small displacement window may be a particular problem for timber buildings with moment-frames or slender walls, where the elastic displacements will be larger than for similar concrete or steel buildings. For example, in a reinforced concrete building, if yielding occurs at 0.5% drift with a design limit of 2.5% drift, there is a displacement window of 2% drift for ductility and energy dissipation. In comparison for a very flexible timber building, if yielding does not occur until 2% drift, the displacement window has been drastically cut to only 0.5% drift.

5 Solutions

Possible solutions to the problem caused by the small displacement window in multi-storey timber buildings are stiffer materials, stiffer geometry, concentrated inelastic behaviour, stiffer connections and reduction of deformations in compression perpendicular to the grain.

5.1 Stiffer materials

The stiffness of a structure is mainly related to EI, through material properties and structural geometry. Hence the two ways to design a stiffer structure are to increase one or both of E or I.

The E value of sawn timber can vary widely, depending on species and grading. An advantage of engineered wood products such as laminated veneer lumber (LVL) is that mechanical properties are accurately defined. All New Zealand manufacturers can produce LVL with E=11GPa, some able to produce E=13GPa and even E=16GPa in smaller quantities. Stiffness can be been increased by using higher E timber materials in some locations, or by using hybrid structures with some reinforced concrete components.

5.2 Stiffer geometry

The way to increase the structural stiffness I is to change the geometry, by increasing the size of structural elements, adding walls in line with structural frames to create dual systems, stitching walls together in order to change their structural form (i.e. I-section and C-section structural walls around lift shafts). The use of cross bracing can also give a significant increase in stiffness.

5.3 Concentrated inelastic behaviour at specific points

It is also possible to increase the displacement window by concentrating inelastic behaviour at a small number of discrete points within a structure, or by using base isolation. Combining the dissipative devices with an elastically responding system reduces the amount of period shift in the structure, so careful positioning of the devices can result in earlier activation and increased damping.

5.4 Stiffer connections

In timber structures, damping energy tends to be designed into discrete steel yielding devices. With a small displacement window, the yielding devices will never be activated if they are too flexible or have sloppy connections. This is especially critical for dissipative cross bracing where the connections and the members themselves must be treated as a series of springs designed for stiffness in addition to strength.

5.5 Local reinforcement to increase stiffness

It is possible to limit elastic deflections through local reinforcement of timber members. This can be done through the addition of stiffer materials into the beam, column or wall members, for example by adding steel plates or using long screw reinforcing at beam-column joints to reduce deformations in compression perpendicular to the grain.

6 Conclusions

- The displacement paradox comes because designers try to increase displacements to increase ductility, and try to reduce displacements to reduce seismic damage.
- Ductile design is only possible if there is a sufficiently large displacement window between onset of yield and the ultimate displacement.
- This displacement window is often small in timber structures, but can be increased by using stiffer materials, stiffer geometry, or stiffer connections.
- Providing ductility reduces seismic forces and increases displacements. Providing additional damping reduces the displacements but has little effect on forces.

Estimation of Bending Stiffness and Moment Carrying Capacity of Japanese CLT panels by Monte Carlo Method

Minoru Okabe, Centre for Better Living, Japan
Atsushi Miyatake, The Forestry and Forest Products Research Institute, Japan
Motoi Yasumura, Shizuoka University, JAPAN
Kenji Kobayashi, Shizuoka University, JAPAN

1 Introduction

For satisfaction of required performance of CLT Japanese Agricultural Standard, it is important to estimate the bending stiffness and moment carrying capacity before manufactured CLT panels. Purpose of the verification of bending performance, CLT panels were manufactured under different species, number of layers, and different width. Three types of Species, Japanese sugi (Cryptomeria japonica), hinoki (Japanese cypress) and karamatsu (Japanese Larch) were selected. Before manufactured CLT panels, MOE of lumber was measured by grading machine. JAS standard shows four types the lumber modulus of elasticity (MOE) (M120, M90, M60 and M30) and arranged lumber at the outer and inner layer. On the other hand, based on the MOE of lumber, bending stiffness of CLT would be calculated and relationship between the MOE and MOR of lumber, moment carrying capacity would be calculated. Bending stiffness and moment carrying capacity would be calculated based on the distribution of lumber MOE by Monte Carlo method.

2 Prediction of structural performance of CLT panel

Bending stiffness EI_{eff} and moment carrying capacity M_{max} of CLT panel are calculated in equation (1) and (2). Equation (2) is based on the composite stress of bending and tensile and failure criteria calculated second power equation.

$$EI_{eff} = E_{ref} \sum_{i=1}^{n} (I_i + A_i N_i^{\,2}) \qquad (1) \qquad M_{\max} = \frac{EI_{CLT}}{E_i} \times \frac{2 f_{bi} \cdot f_{ti}}{\sqrt{t_i^{\,2} \cdot f_{ti}^{\,2} + 4N_i^{\,2} \cdot f_{bi}^{\,2}}} \qquad (2)$$

Where

E_{ref}: MOE of reference layer. Generally outer layer of tensile side
I_i: Moment of inertia of i-th layer A_i: Equivalent section area of i-th layer
N_i: Distance from neutral axes to the centroid of each i-th layer.
E_i: Lumber MOE of i-th layer t_i: Lumber thickness of i-th layer
fb_i, ft_i : Bending and tensile strength of i-th layer's lamina

3 Monte Carlo method

MOE of lamina determined by Monte Carlo Method assumed normal distribution and f_b determined based on the relations of MOE and F_b. Assumption of 18% COV based on normal distribution, F_b on each MOE shows variation value using random number function. F_t shows 60 % value of F_b and F_t on each MOE shows variation value using random number function.

4 Bending properties of lamina

Bending test of lamina was carried out for relations of MOE and modulus of rapture (MOR) of machine graded lumber. MOR was determined by the bending test according to the bending method C of structural Glulam by Japanese Agricultural Standards (JAS). Finger joint was arranged at the center of lumber.
Prediction of maximum moment carrying capacity of CLT panels was used bending property of lumber with finger joint and tensile strength of lumber assumed 60% of bending strength.

5 Bending test of CLT panels

4-point bending test was carried out that the span shows 21 times of CLT thickness and load applied one-third of span. Number of test specimen is 210 and 36 types of CLT panels were tested. Number of test specimen of same type is almost 6. Test procedure was followed by JAS standard. **Figure 1** shows the cross section of CLT bending test specimen. Four kind of species were used, Sugi CLT, outer hinoki and inner sugi lamina arranged CLT, Japanese larch CLT and hinoki CLT.

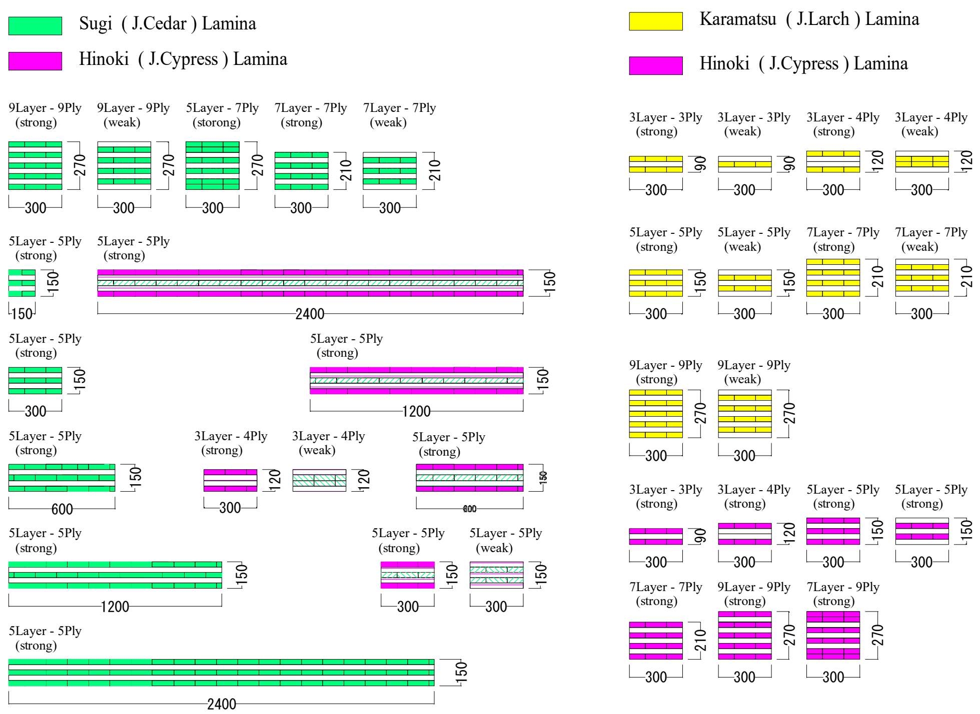

Figure 1 Cross section of CLT bending test

6 Comparison of structural performance

Figure 2 shows the relationship between the calculated bending stiffness EI and experimental bending stiffness EI. Calculated value shows average of 1000 times simulated by Monte Carlo method. And experimental value shows average of almost 6 test results. Bending stiffness EI of CLT panels could be estimated by adopting composite theory and equivalent section area

Figure 3 shows the relationship between the calculated and experimental average moment carrying capacity M_{cal} and M_{exp}. Experimental moment carrying capacity showed 28% higher value than the calculated moment carrying capacity by average lumber failure method due to the reinforcement of the outer layer by the neighbouring cross layer.

Figure 4 shows the relationship between the calculated and experimental 5th percentile moment carrying capacity M_{cal} and M_{exp}. Experimental moment carrying capacity showed 17% higher value than the calculated moment carrying capacity

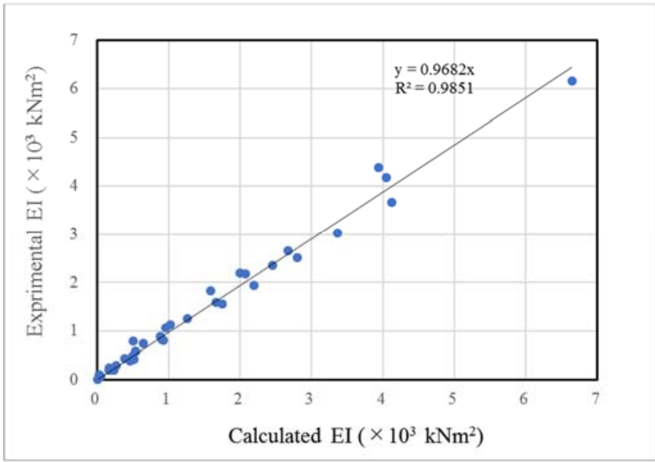

Figure 3 Relationship between calculated and experimental average bending stiffness of CLT panel

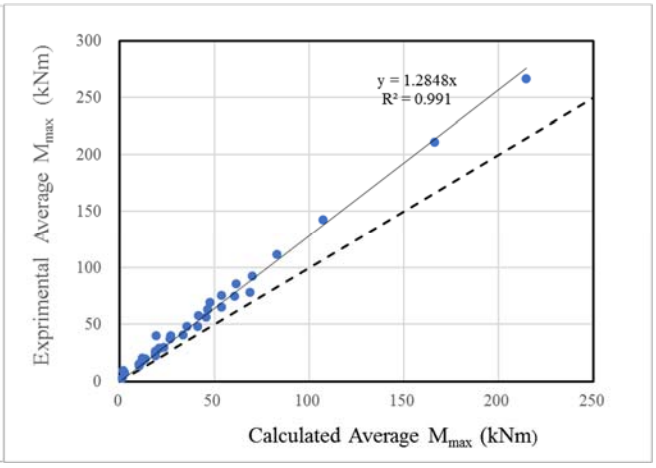

Figure 2 Relationship between calculated and experimental average moment carrying capacity of CLT panels

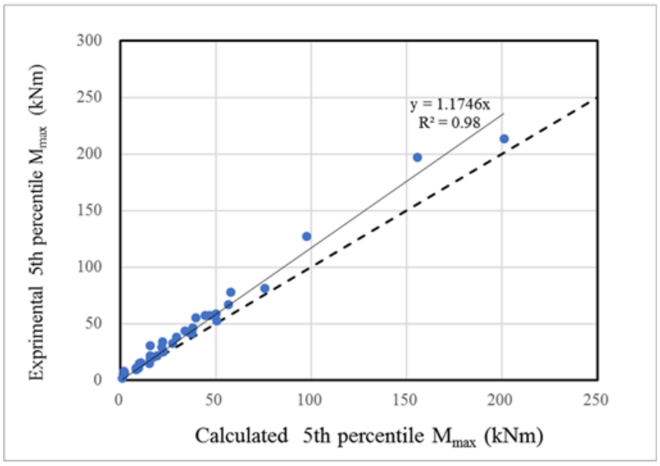

Figure 4 Relationship between calculated and experimental 5th percentile moment carrying capacity of CLT panels

5 Peer review of papers for the INTER Proceedings

Experts involved:

Members of the INTER group are a community of experts in the field of timber engineering.

Procedure of peer review

- Submission of manuscripts: all members of the INTER group attending the meeting receive the manuscripts of the papers at least four weeks before the meeting. Everyone is invited to read and review the manuscripts especially in their respective fields of competence and interest.
- Presentation of the paper during the meeting by the author
- Comments and recommendations of the experts, discussion of the paper
- Comments, discussion and recommendations of the experts are documented in the minutes of the meeting and are printed on the front page of each paper.
- Final acceptance of the paper for the proceedings with
    - no changes
    - minor changes
    - major changes
    - or reject
- Revised papers are to be sent to the editor of the proceedings and the chairman of the INTER group
- Editor and chairman check, whether the requested changes have been carried out.

6 Meetings and list of all CIB W18 and INTER Papers

CIB Meetings:

1 Princes Risborough, England; March 1973
2 Copenhagen, Denmark; October 1973
3 Delft, Netherlands; June 1974
4 Paris, France; February 1975
5 Karlsruhe, Federal Republic of Germany; October 1975
6 Aalborg, Denmark; June 1976
7 Stockholm, Sweden; February/March 1977
8 Brussels, Belgium; October 1977
9 Perth, Scotland; June 1978
10 Vancouver, Canada; August 1978
11 Vienna, Austria; March 1979
12 Bordeaux, France; October 1979
13 Otaniemi, Finland; June 1980
14 Warsaw, Poland; May 1981
15 Karlsruhe, Federal Republic of Germany; June 1982
16 Lillehammer, Norway; May/June 1983
17 Rapperswil, Switzerland; May 1984
18 Beit Oren, Israel; June 1985
19 Florence, Italy; September 1986
20 Dublin, Ireland; September 1987
21 Parksville, Canada; September 1988
22 Berlin, German Democratic Republic; September 1989
23 Lisbon, Portugal; September 1990
24 Oxford, United Kingdom; September 1991
25 Åhus, Sweden; August 1992
26 Athens, USA; August 1993
27 Sydney, Australia; July 1994
28 Copenhagen, Denmark; April 1995
29 Bordeaux, France; August 1996
30 Vancouver, Canada; August 1997
31 Savonlinna, Finland; August 1998
32 Graz, Austria; August 1999

33 Delft, The Netherlands; August 2000
34 Venice, Italy; August 2001
35 Kyoto, Japan; September 2002
36 Colorado, USA; August 2003
37 Edinburgh, Scotland; August 2004
38 Karlsruhe, Germany; August 2005
39 Florence, Italy; August 2006
40 Bled, Slovenia; August 2007
41 St. Andrews, Canada; August 2008
42 Dübendorf, Switzerland; August 2009
43 Nelson, New Zealand; August 2010
44 Alghero, Italy; August 2011
45 Växjö, Sweden; August 2012
46 Vancouver, Canada; August 2013

INTER Meetings:

47 Bath, United Kingdom; August 2014
48 Šibenik, Croatia; August 2015
49 Graz, Austria; August 2016
50 Kyoto, Japan; August 2017

The titles of the CIB W 18 and INTER papers (starting from 2014) are included in the complete list of CIB/INTER papers: http://holz.vaka.kit.edu/392.php